



COOPERATIVE POWER EXCHANGE BETWEEN TWO ROOFTOP SOLAR PLANTS INTERFACED WITH ARDUINO IOT CLOUD

Pragada Dheeraj Abhinav¹

Gorantla Anil Kumar

Sunkara Veerababu

P. S. Brahmanandam

Keywords:

A B S T R A C T



The main aim of this paper is to develop a system which enables the sharing of excess power generated by the solar panels to maximize the use of renewable energy sources and reduce the reliance on traditional power grids. The monitoring system collects data from the two rooftop solar plants and transmits it to the cloud for visualization, retrieval, and data storage. The Arduino IOT Cloud provides a platform for the monitoring of power generation and consumption, and the Node MCU ESP8266 enables communication between the two solar plants. The system implements a cooperative power exchange algorithm that allows the two rooftop solar plants to exchange power based on their energy production levels. The system operates on a peer-to-peer instantaneous energy monitoring, where the two rooftop solar plants can share excess power to each other.

© 202x Published by Faculty of Engineering

1. INTRODUCTION

In order to minimize the negative environmental effects of conventional energy producing techniques, there has been an increasing focus on renewable energy sources in recent years. Rooftop solar power production has become one of the most popular renewable energy sources because of its accessibility, scalability, and potential for decentralization. The idea of cooperative power exchange (Yamaguchi et al., 2023) between two rooftop solar plants has emerged as a workable solution to this problem. A network of linked solar power plants may be built, allowing excess energy from one plant to be shared with a plant that is facing a deficit, resulting in stable and balanced energy ecology. This collaborative strategy improves the overall efficiency and dependability of the renewable energy infrastructure while

optimizing power use and reducing waste (Strielkowski et al., 2019). In this project, a sophisticated platform for monitoring, managing, and coordinating cooperative power exchange between two rooftop solar plants is provided by the combination of the Arduino IOT Cloud and NodeMCU ESP8266 microcontroller board. Real-time data from solar power plants can be collected and visualized using Arduino IOT Cloud, and NodeMCU ESP8266 allows communication and coordination between the plants to ensure effective power exchange (Li, et al., 2020).

¹ Corresponding author: Pragada Dheeraj Abhinav
Email: dheerajabhinav32@gmail.com

2. LITERATURE SURVEY

A literature review of two rooftop solar plants cooperating to trade electricity using an Arduino IoT Cloud-enabled NodeMCU 8266 interface shows that interest in decentralized energy management systems is rising. It presents a concept for the implementation of Peer-to-Peer energy network based on the circuit-switching framework (Salvi et al., 2020). The proposed system also provides users with the ability to track and sell energy remotely using IoT architecture and cloud computing. They propose an integrated auctioning-scheduling mechanism that auctions the surplus energy and done by making use of Arduino IOT cloud as mainly the following features one is thing interaction and the other is Arduino IOT cloud web editor as features allow user to program and communicate. Schedules its consumption on a cloud datacenter. The auction part incentivizes the inter-datacenter cloud workload migrations, while the scheduling part ensures that migrated workloads do not exceed the destination datacenter capacity (Abada et al., 2022).

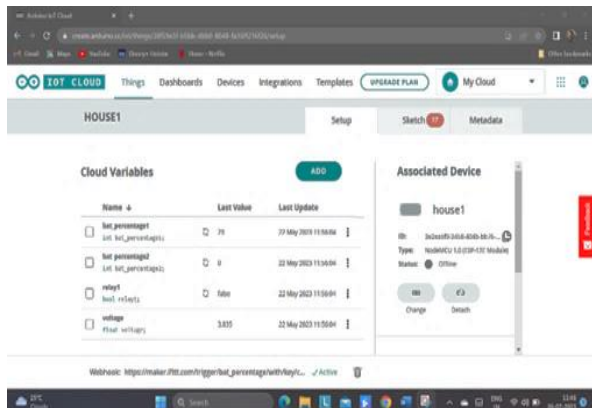


Figure 1. Cloud variables of house 1

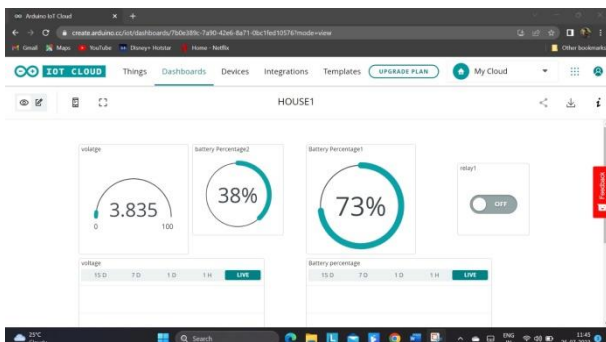


Figure 2. Dashboard of house1

3.0 ARDUINO IOT CLOUD

The cloud-based (Atlam et al., 2017) Arduino IoT Cloud platform enables users to safely connect to, manage, and control their IoT projects and devices. For creating IoT apps and connecting them with the

Arduino ecosystem, it offers a combination of tools and services. The platform makes it easier to remotely manage and update devices, gather and analyze data, and connect to and operate IoT devices (Oton et al., 2021).

3.1 Thing Interactions

The Arduino IoT Cloud offers a simple interface for defining interactions between objects. Devices may react to events or changes in other devices thanks to these interactions (De Oliveira Cavalcanti et al., 2023). For instance, you may set up a device such that it performs a given action when it gets a certain message or when a property value reaches a predetermined level.

3.2 Arduino IoT Cloud Web Editor

The Arduino IoT Cloud Web Editor provides community support, accessibility, integrated IoT capability, cloud integration, collaboration tools, and device management capabilities. For creating, deploying, and administering IoT applications utilizing Arduino boards, it offers a comprehensive and user-friendly environment (Panagiotakis et al., 2022).

4.0 EXPERIMENTAL SETUP

A cutting-edge combination of hardware elements including NodeMCU ESP8266, TP4056 charging module, lithium-ion battery, voltage divider circuit, and relay module, all smoothly interfaced with the Arduino IoT Cloud platform can be shown in the experimental setup for the solar power exchange project as shown in fig 3 (Salvi et al., 2020). This technological convergence represents a fundamental change in the way we organize and distribute renewable energy sources.

The NodeMCU acts as a link between the actual hardware parts and the digital world thanks to its integrated Wi-Fi capabilities, enabling bidirectional communication and control. The proper operation of the Lithium-Ion battery (Abu et al., 2023) is maintained by the TP4056 charging module. This module makes sure the energy storage component is secure and lasts a long time by controlling and managing the battery charging process. Along with the visual indications, the TP4056 charging IC ensures effective charging and protects against overcharging or undercharging of the lithium-ion battery. Speaking about batteries, the Lithium-Ion kind, often the 18650 types, is in charge of both storing and supplying energy. This arrangement is perfect for its high energy density and rechargeable design. Using a voltage divider circuit, the Analog-to-Digital Converter (ADC) of the NodeMCU is cleverly used to monitor the battery voltage level and translate it into a readable range.

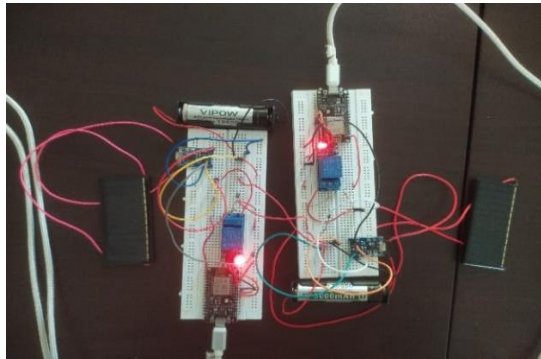


Figure 4. Prototype model of P2P connection between two solar power plant

4.1 SOFTWARE SETUP

The ArduinoCloud.update () method is used in the loop () function to update the cloud variables and attributes. The analogRead() method is used to read the sensorValue from the analog input pin A0. By translating the sensor data to voltage and adding a calibration factor, the voltage is computed. By converting the voltage value to a % between 0 and 100 while considering the battery cut-off voltage and maximum voltage, the bat_percentage1 variable is created. For monitoring reasons, the computed values are then output to the serial monitor. Using the digitalWrite() method, the relay pin is set to HIGH or LOW depending on the bat_percentage2 and bat_percentage1 values.

The relaypin is set to HIGH if the bat_percentage2 is less than 40 and the bat_percentage1 is more than 60. The default setting is LOW. The mapfload() method is designed to translate values across ranges. It is used to determine the bat_percentage1 variable's value. Finally, anytime the relay1 variable from the IoT Cloud changes, the onRelay1Change() method is invoked. Using the digitalWrite() method, the relaypin is set to either LOW or HIGH depending on the value of the relay1 variable and vice versa.

5.0 RESULTS

A revolutionary approach to increase energy efficiency and promote sustainable energy sharing is the cooperative power exchange system. It uses the ESP8266 and automated relay operation on the Arduino IoT Cloud platform. This system enables power transfer from one rooftop solar plant to another when one of the batteries reaches the critical 40% voltage barrier, ensuring a continuous energy supply and efficient energy management. This comprehensive summary of the implementation's results will include the key findings involving power transfer, automatic relay operation, monitoring on the Arduino IoT Cloud platform, and real-time Gmail alerts through web hooks.

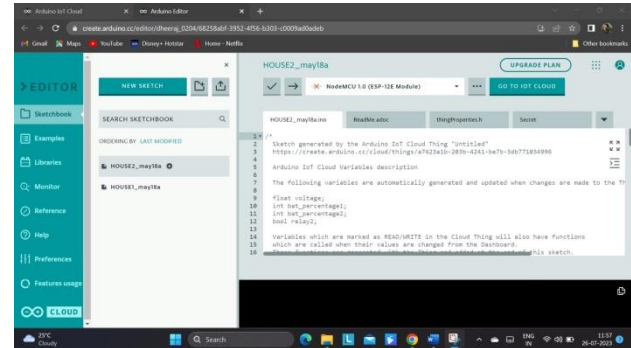


Figure 5. Arduino Web Editor

5.1 Transfer of Power at Low Battery Voltage

One of the remarkable results of the cooperative power exchange system is the seamless power transfer between the two rooftop solar plants when one of the batteries reaches a low voltage level. The power exchange procedure begins at the preset critical voltage level of 40%. Once the power from input is low, then for an instance the battery voltages show 1% as shown in figure 6, which may indicate an energy deficiency, which indicates one

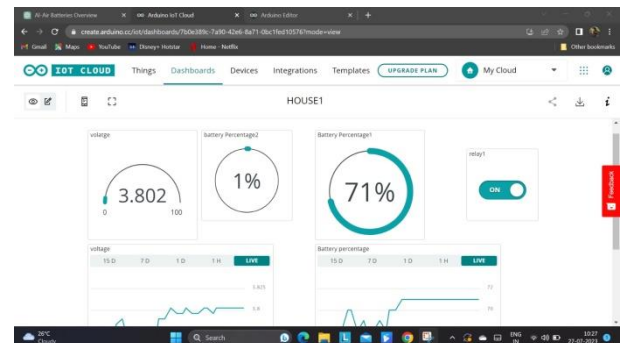


Figure 6. Power transfer from house 2 to house 1

plant requires outside energy support. The system activates the automatic relay function to make the power transfer from the second solar plant, which has surplus energy. This real-time decision-making ensures that energy is continuously exchanged, and it also promotes energy balance and reduces energy waste.

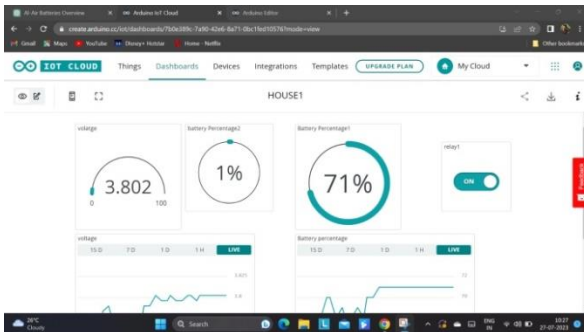


Figure 7. Power transfer from house1 to house 2

5. 2 Operation of Automatic Relays

The cooperative power exchange system, which regulates the power flow between the two rooftop solar systems, is very dependent on the automated relay functioning. The ESP8266 microcontroller (Lal et al., 2022), which serves as the control point, continuously monitors the battery voltage levels and energy needs. When the battery percentage in one plant drops below the predetermined level, the Arduino IoT Cloud platform activates the relay, allowing power transfer.

The automatic relay operation, which ensures a smooth transmission of power, allows the two solar plants to operate together independently. The quick activation and deactivation of the relays maximizes energy efficiency and minimizes energy waste throughout the exchange operation (Lee, 2019). By requiring less human involvement, this automated procedure improves system efficiency and simplifies energy management.

5. 3 Monitoring in the IoT Cloud Platform

The integration of the Arduino IoT Cloud platform has given the cooperative power exchange system considerable monitoring features. The user-friendly interface allows users to get real-time data on voltage levels, battery percentages, and relay statuses for both rooftop solar plants (Chen, 2018). This real-time monitoring helps users to make educated choices by allowing them to view the system's performance and the ongoing power exchange process.



Figure 8. Live data of battery voltage and percentage

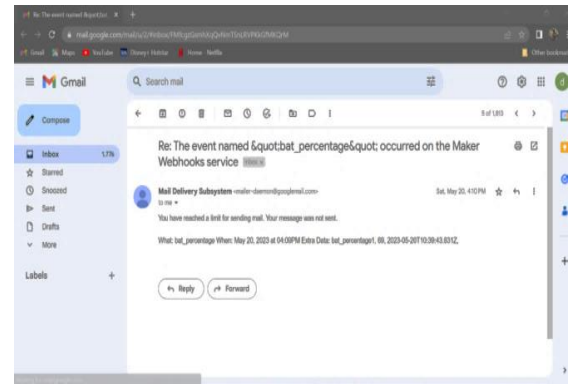


Figure 9. Webhook notification through Gmail

5. 4 Webhook notifications for Gmail

A unique feature of the cooperative power exchange system is the incorporation of Gmail notifications through web hooks, as shown in Figure 9. The Arduino IoT Cloud platform sends real-time time alerts to a selected Gmail account (Cheng et al., 2019) when certain events occur, such as the turning on or off of the relay or critical battery levels. The ESP8266 and Arduino IoT Cloud-based cooperative power exchange system promises promising results in terms of optimizing energy utilization, stimulating the sharing of renewable energy, and creating a sustainable energy ecosystem. When the power transfer mechanism is activated and when one of the batteries hits a vital 40% voltage level, it ensures steady energy delivery and minimizes potential energy shortages. Automated relay operation controls power flow, maximizes energy efficiency, and minimizes energy loss.

6. CONCLUSION

The cooperative power exchange system between two solar rooftop plants, enabled by ESP8266 and Arduino IoT Cloud, with a focus on Thing Interaction and Gmail notifications through web hooks, represents a remarkable advancement in renewable energy utilizations (Hannan et al., 2020) and sustainable energy sharing. This method has shown to be effective in developing a greener and more robust energy infrastructure, improving energy distribution, and encouraging energy self-sufficiency. We have examined the technique, application, and outcomes of this ground-breaking system throughout this project, and it is clear that it has enormous potential for influencing the direction of energy management in the future. The system's performance in fostering energy self-sufficiency, improving energy distribution, and lowering carbon emissions highlights its potential to fundamentally alter the energy landscape.

References

- Abada, A., M. St-Hilaire and W. Shi (2022). Auction-Based Scheduling of Excess Energy Consumption to Enhance Grid Upward Flexibility. *IEEE Access*, 10, 5944-5956, 2022, doi: 10.1109/ACCESS.2021.3139985.
- Abu M., Sayem M., et al., (2023). State of the art of lithium-ion battery material potentials: an analytical evaluations, issues and future research directions. *J. Clean. Prod.*, 394 doi: 10.1016/j.jclepro.2023.136246.
- Atlam, H. F., Alenezi, A., Alharthi, A., Walters, R. J., & Wills, G. B. (2017). Integration of cloud computing with Internet of things: challenges and open issues. In 2017 IEEE International Conference on Internet of Things (iThings) and IEEE Green Computing and Communications (GreenCom) and IEEE Cyber, Physical and Social Computing (CPSCom) and IEEE Smart Data (SmartData) (pp. 670- 675). doi: 10.1109/ItThings-GreenCom-CPSCom-SmartData.2017.105.
- Cheng, L., Yu, T., Jiang, H., Shi, S., Tan, Z., Z. Zhang, (2019). Energy internet access equipment integrating cyber-physical systems: concepts, key technologies, system development, and application prospects. *IEEE Access* 7, 23127–23148. doi: 10.1109/ACCESS.2019.2897712.
- Chen, X., Li, C., Tang, Y., Xiao, Q., (2018). An Internet of Things based energy efficiency monitoring and management system for machining workshop. *J. Clean. Prod.* 199, 957–968. doi:10.1016/j.jclepro.2018.07.211.
- De Oliveira Cavalcanti, G., and H. C. D. Pimenta (2023). Electric energy management in buildings based on the internet of things: a systematic review. *Energies*. 16 (15), 5753. doi: 10.3390/en16155753.
- Hannan, M.A., Tan, S.Y., Al-Shetwi, A.Q., Jern, K.P., Begum, R.A., (2020a). Optimized controller for renewable energy sources integration into microgrid: functions, constraints and suggestions. *J. Clean. Prod.*, 256. doi: 10.1016/j.jclepro.2020.120419.
- Lal, R., B. Singh and M. A. Wassay (2022). IoT in Smart Irrigation and Node MCU ESP 8266 Wi-Fi Module. 2022 International Conference on Computational Modelling, Simulation and Optimization (ICCMOSO), Pathum Thani, Thailand, pp. 296-300, doi: 10.1109/ICCMOSO58359.2022.00065.
- Lee, S., D. H. Choi (2019). Reinforcement learning-based energy management of smart home with rooftop solar photovoltaic system, energy storage system, and home appliances. *Sens. (Switz.)*, 19 (18), 3937. doi:10.3390/s19183937.
- Li, Y., Zhao, X., H. Liang (2020). Throughput maximization by deep reinforcement learning with energy cooperation for renewable ultradense IoT networks. *IEEE Internet Things J.*, 7 (9), 9091–9102. doi: 10.1109/JIOT.2020.3002936.
- Oton C. N. and M. T. Iqbal (2021). Low-Cost Open Source IoT-Based SCADA System for a BTS Site Using ESP32 and Arduino IoT Cloud. 2021 IEEE 12th Annual Ubiquitous Computing, Electronics & Mobile Communication Conference (UEMCON), New York, NY, USA, 2021, pp. 0681-0685, doi: 10.1109/UEMCON53757.2021.9666691.
- Panagiotakis et al. (2022). Remote Arduino Labs for Teaching Microcontrollers and Internet of Things Programming. 2022 31st Annual Conference of the European Association for Education in Electrical and Information Engineering, Coimbra, Portugal, 2022, pp. 1-6, doi: 10.1109/EAEEIE54893.2022.9820605.
- Salvi, S. K., N. D. Jacob, S. Sikka (2020). An IoT based Prototype of Basic Solar Power Trading Platform for Independent Distributed Nano-Grids. 2020 Fourth International Conference on I-SMAC (IoT in Social, Mobile, Analytics and Cloud) (I-SMAC), Palladam, India, 144-149, doi: 10.1109/I-SMAC49090.2020.9243560.
- Strielkowski, W., Streimikiene, D., Fomina, A., Semenova, E., (2019). Internet of energy (IoE) and high-renewables electricity system market design. *Energies*, 12 (24), 4790. doi:10.3390/en12244790.
- Yamaguchi, T., Takayuki Matsumoto (2023). Autonomous Control for Cooperative Operation between Energy Storage Systems, *IEEE Journal of Emerging and Selected Topics in Power Applications*. doi:10.1109/JESTPA.2023.36507605

Pragada Dheeraj Abhinav

Jawaharlal Nehru Technological University,
Kakinada
India
e-mail: dheerajabhinav32@gmail.com
ORCID 0009-0004-6351-8189

Gorantla Anil Kumar

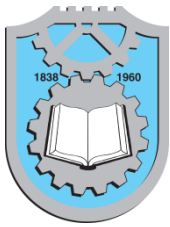
Jawaharlal Nehru Technological
University,
Kakinada
India
e-mail: gorantlaanilkumar@gmail.com
ORCID 0000-0001-8679-9260

Sunkara Veerababu

Shri Vishnu Engineering College For
Women (A), Bhimavaram
India
e-mail: sveerababu5@gmail.com
ORCID 0000-0002-9126-0312

Potula Sree Brahmanandam

Shri Vishnu Engineering College For
Women (A), Bhimavaram
India
e-mail: dranandpotula@svecw.edu.in
ORCID 0000-0001-8679-9260



EFFECT OF COVID-19 ON PSYCHOSOCIAL BEHAVIOUR OF AUTOMOBILE WORKERS PERFORMANCE - AN ERGONOMIC STUDY

Syam Babu Bokka

Anil Kumar Birru*

Netai Chandra Dey

Amandeep kaur

Sibaji Ch Dey

Hari Krishna Ch

Keywords:

Automobile Employees; Cardiovascular Endurance; Health Care Services; Musculoskeletal Disorders; Psychosocial Behavior; Worker Motivation

A B S T R A C T

The COVID-19 lockdown has had a significant negative impact on the automotive industry, particularly on the small and medium-sized businesses and daily wage workers who rely on autonagar industrial area as their main source of income. Employees experienced increased physiological and psychological stress during the lockdown period. Many people lost their jobs, finding work and surviving for food and shelter became worse for daily wagers. To suggest the behavioural changes needed to improve the quality of worker performance there is need of worker motivation during the work that suits the type of work and design of work including adequate rest period needed during a working shift. Consequently, it is felt necessary to study the behaviour including estimation the heart rates of various groups of workers after determining their maximum heart rate including maximum limit of continued work. This comparison can help workers achieve better performance at their workplaces having prescribed training to enhance their work efficiency and health conditions. Out of 307 samples, 110 participants had a limit of continuous work that was less than their maximum working heart rate while performing a task, demonstrating the need for better posture, work rest breaks, and customised work study models to improve performance, persistence and to lower stress levels. Continuous employee monitoring is a challenging task. However, improved worker productivity and employee health benefits support socio-cultural advancement of the firm's products and services.



© 202x Published by Faculty of Engineering

1. INTRODUCTION

According to 2021 data, India is fourth largest automobile producer in the world with a target of 4.4 million and has the fifth-highest GDP in the world. Due to the industry's extensive applications in the fields of manufacturing, product development, marketing,

mining, road and transportation, petroleum and gasoline, many new employment avenues have generated in these sectors. The quick economic growth of India has resulted in an enormous rise in the demand for exports. In addition, the government's most well-known programs, such as Digital India, Made in India, Start-up India, the Smart City Mission, and the Atal

* Corresponding author: Dr. Anil Kumar Birru
Email: anilbirru@gmail.com

Mission for Urban Transformation and Rejuvenation, have given momentum. According to the automotive mission plan, the Indian automotive industry currently accounts for roughly 7% of the nation's GDP and is soon predicted to reach 12%. The National Health Mission (NHM), which is divided into the National Rural Health Mission (NRHM) and the National Urban Health Mission (NUHM), is a government-funded healthcare initiative, assists States and UTs in improving their health care systems to ensure that everyone has access to economical, cost-effective, and high-quality healthcare services. These programmes involve infant care, nutrition assistance, and communicable and non-communicable diseases. A total of 2 996 635 hospitals fights these illnesses, and the total number of households that benefited was 8.03 crores across India under various standard deprivation parameters and total families covered and Ayushman Bharat - Pradhan Mantri Arogya Yojana (AB-PMJAY) provided benefits to 10.74 crore rural and urban families.

The anticipated loss per day during the lockdown was 2300 crores, and the 3.45 lakh job losses indicate a sharp decline in the number of workers in this industry. All major original component manufacturers reduced their production to 18–20% as recommended by the committee of the auto industry association (Shanahan et al. 2022).

According to surveys, 65% of families had an improvement in their quality of life during lockdown, but many people also experienced loneliness, worry, and discomfort, and 40% of respondents stated they missed their regular social and working lives (Shanahan et al. 2022).

In September 2021, the Union Cabinet approved the INR 26,058 Crore production linked incentive (PLI) Programme to increase domestic production of drones and fuel cell and electric vehicles shows the importance of automobile and manufacturing sector growth in India. Hence, as World Health Organization (WHO) Statistics 2018 in detail it was cited, however, not much research was made an attempt on covid-19 on psychosocial behavior of Automobile workers performance in ergonomic perspective.

2. THE TYPE OF EMPLOYMENT AND CONTRIBUTING FACTORS FOR MUSCULOSKELETAL DISORDERS

The automobile supply chain is dependent on manufacturers, manufacturing, dealers, and customers. It is complicated and susceptible owing to general transportation concerns based on demand and supply (Ali et al. 2018).

The production of two-wheelers has significantly expanded as young, middle-class Indians have

transitioned into rural market segments and in fiscal year 2022(FY-2022),India produced 22.93 million vehicles (Gupta 2013). Due to multiple initiatives, government funding, and predicted future growth, India has risen to the leading two-wheeler and four-wheeler manufacturer and developing supplier. Occupational stress grew as a result impact of COVID-19 on staff accessibility and increasing demand. This led to spike in workload to compensate for the increased demand and enhance the production of automobiles (Dennerlein 2008; Yassierli 2017). As a result, physiological, psychological, and psychosocial pressures developed due to increased commitment in the industrial sector and concurrently increased work pressure on the available workforce. Long working hours contributed to the development of musculoskeletal disorders (Bailey et al. 2019; Bertera 1990; Bhushan Mandal et al. 2018; Shanahan et al. 2012)

3. MORBIDITY AND MORTALITY AS A RESULT OF MUSCULOSKELETAL DISORDERS

The majority of those who work in the automotive industry, including drivers, mechanics, assemblers, repairers, load pullers, and other personnel who operate on machinery and vehicles, suffer from musculoskeletal disorders and psychological issues (Das et al., 2022; Dennerlein 2008; Mačužić and Lukić 2017; Philip et al. 2014; Valirad et al. 2015). Due to different working culture and requirements in the industry the administrative, executive, and operational levels of the automobile hierarchy encounter work-related musculoskeletal disorders, physical, psychosocial, and psychological stress (Dianat et al. 2017; Engineering 2016; James et al. 2019; Luger et al. 2019). The automobile manufacturing companies are showing exponential growth. At the operational and maintenance level employees are more prone to cardiac stress during their task in the shift. Assessment of their cardiac stress gives estimation of levels of works that can be assigned and the requirement of work breaks (Cortes-Ramirez et al. 2018; James et al. 2019).

4. INCREASE IN THE POVERTY LEVEL IN THE INDIA DURING LOCKDOWN AND ITS EFFECT ON WORK RELATED STRESSES

The World Health Organization estimates that more than half a billion individuals fell below the poverty line as a result of having to pay for health care services with the increase in population of India at a rate of 2.2% per year, decrease in agriculture productivity, and rising unemployment number of below the poverty line(BPL) has increased (Dennerlein 2008). Lack of proper medical facilities at the operational level as a result of the pandemic have made the situation worse. Significant changes in the auto industry brought on by the increased

use of automation, constantly changing safety and environmental regulations, new developments in manufacturing, and applications of robotics, the industry has an unprecedented need for training as a requirement. Despite the fact that adequate training can avoid physical injuries, industries are under enormous pressure to cut corners on safety, making employees in these industries more susceptible to occupational risks (Luger et al. 2019). Sustained stress has a negative impact on health. Training can give motivation to handle the job and stresses. Unlike distress, eustress has positive effects on health that increases the efficiency of employees (Lavie et al. 2019; Scott et al., 2012). It is important to apply the concept of Astrand to evaluate job heaviness for all such work categories. This will help increase profile of workers more accurately to prescribe befitting conditions to achieve workers comfort and safety in the automotive supply chain (ÅStrand et al. 1960; WSH Council 2014).

5. EFFECT OF WORKING ENVIRONMENT ON FATIGUE LEVELS OF EMPLOYEE

The environmental conditions play a crucial role in the work performance of the worker. Around 12 million individuals die each year as a result of the unsanitary conditions in the workplace and domiciles (Brusseau et al. 2019; Das et al. 2022; Dey and Sharma 2013; Engineering, 2016). Due to the difficult working circumstances, more workers are suffering from accidents and cuts as well as musculoskeletal diseases in the automotive manufacturing and operating industries, which are under intense pressure (Lin 2016; Valirad et al. 2015; Yassierli 2017).

The human body adjusts its temperature in response to the environment and working conditions in order to maintain homeostasis while achieving a new dynamic equilibrium. People survive if homeostasis is successful but are prone to serious health problems if it is not maintained (Cortes-Ramirez et al. 2018; James et al. 2019).

6. DATA COLLECTION

Data collecting for the study began in the Autonagar region of Vijayawada, which is situated on the bank of the River Krishna in Andhra Pradesh. Daily high temperatures are around 40°C. Various parameters were used to assess the cardiac stress including demographic details, height, weight, body mass index, body surface area, resting heart rate, working heart rate. From these parameters, the net cardiac cost (NCC), relative cardiac costs are calculated using the formulas as follows.

$$\text{Body mass Index (BMI)} = \frac{\text{Weight (kg)}}{(\text{height (m)})^2} \quad \dots(1)$$

Body Surface area (BSA)

$$= \sqrt{\text{Height (Cm)} * \text{weight (kg)}} / 3600 \quad \dots(2)$$

$$\text{The maximum heart rate (MHR)} = 220 - \text{age} \quad \dots(3)$$

$$\text{The heart rate reserve (HRR)} = \text{Maximum heart rate (MHR)} - \text{Resting heart rate (RHR)} \quad \dots(4)$$

$$\text{Net cardiac cost(NCC)} = \text{Average Working heart rate (WHR)} - \text{Resting Heart Rate (RHR)} \quad \dots(5)$$

$$\text{Relative Cardiac Cost (RCC)} = (\text{NCC}/\text{HRR}) * 100 \quad \dots(6)$$

$$\text{Limit of continuous work (LCW)} = \text{Resting hear rate (RHR)} + 35 \quad \dots(7)$$

For a healthy adult, the BMI ranges from 18.5 to 24.9 kg/m², with a BMI of 18.5 kg/m² or less indicating underweight, 25.0 to 29.9 kg/m² indicating overweight, and 30 kg/m² or more being considered obese. Due to decreased activity levels, a lack of motivation to lose weight, and the use of steroids as a component of medications, the prevalence of obesity has grown during the pandemic (Bhaskaran et al. 2022; Lavie et al. 2019; Scott et al. 2012).

The environmental parameters such as temperature, humidity, are taken from Continuous Air Quality Measuring System (CAQMS) to calculate e heat index temperature. An average individual has 1.9m² of surface area; the larger the surface, the greater the heat loss or gain by conduction, convection, and radiation. Thermal radiation can damage human cells, diminishing the worker performance and propensity to unsafe work behaviour (Dey and Sharma 2013; Sharma et al. 2016; Valirad et al. 2015).

Employees working at the operational level in the automobile industry are more prone to tobacco and alcohol habits due to high stress from the working environment and the influence of the surrounding people (Bhaskaran et al. 2022; Dey et al. 2007). A healthy person's heart rate typically ranges from sixty beats to one hundred per minute. Lower heart rate is an indication of a strong heart and good health. However, factors such as age, degree of exercise and fitness, smoking, cardiovascular disease, high cholesterol, diabetes, air temperature, posture, emotions, body size, and medication affects heart rate (Chung 2018; Scott et al. 2012; Shanahan et al. 2022).

The relative cardiac cost values indicate the strain on the workers' hearts. 0–19 is described as light, 20–39 as moderate, and 40–69 as severe(Pancardo et al. 2015). People exhibiting high RCC values, which fall under the vigorous category, they needing work breaks in between to bring the level down to the light work group.

According to a National Geographic research of major towns in India, Vijayawada will experience an increase in temperature over the next 50 years, with average

maximum temperatures rising to 35°C and minimum average temperatures rising to 18°C or higher.

7. RESULTS AND DISCUSSION

The recorded and derived data were analyzed to predict the overall performance of the employees and to increase their productivity.

According to the present study conducted on Autonagar employees, the average resting heart rate (RHR) is 84.6 beats per minute (BPM), which is higher than the average heart rate of 80 BPM. This indicates that the majority of people do not have healthy heart rates. Employees with $LCW < HR W_{max}$, have average heart rate of 81.21 BPM, which is also higher than the average and indicates high levels of stress. RHR and HRR vary in parallel, the values were 96.07 BPM for 307 samples and 101.67 BPM for 110 samples of the people having $LCW < HR W_{max}$ in the present study.

From the bar graphs shown in figures 1, 2, and 3 and tables 2 and 3, it is observed that there is no proper linear relationship between height and weight to age, but BMI has a direct relationship with both height and weight. However, Ding et al. (2020) observed a conflicting correlation between BMI and cardiovascular endurance, with an increase in BMI leading to a decrease in cardiovascular endurance(Ding and Jiang n.d.). From the results shown in table 2, average BMI is 25.94 kg/m² which is an indication of increased sedentary behavior, decreased activity levels and cardiovascular endurance. Employees having $LCW < HR W_{max}$ (table 3), the average BMI was 26.05 kg/m². This is indicative of drop in exercise levels and an increase in sedentary behavior. These in turn are indicators of increased risk for heart-related disorders due to reduced cardiovascular strength.

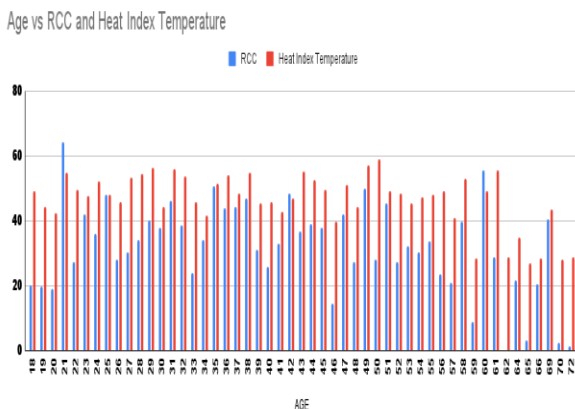


Fig.1. Age vs Relative Cardiac Cost (RCC) and Heat Index temperature (°C).

Age vs LCW and HR W Max

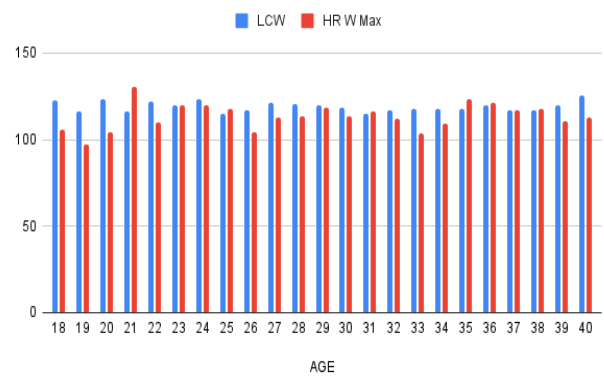


Fig. 2. People (Age<40 Years) with limit of continuous work less than working maximum heart rate

Age Vs LCW and HR W Max

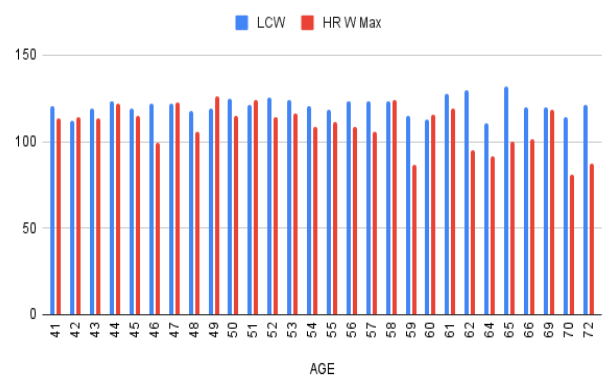


Fig. 3. People (Age>40 Years) with limit of continuous work less than working maximum heart rate

The general perception is that the summer temperatures of up to 45°C are the only element contributing to heat stress. People experience higher temperatures than expected because temperature and relative humidity are inversely related. In the present study, it was found that in addition to work-related stress and psychological strain, participants experienced temperatures of up to 62°C, a symptom of significant heat stress and an increased risk of heart-related disorders. The minimum, maximum and average values of different parameters are shown in the Table 1. The bar graphs (figures 1 and 3) depict that RCC is directly related to employee attitude and performance during the working hours. Also, it was observed that the exposure to sunlight can cause high heat stress irrespective of the age and employee attitude. During working hours, dehydration is also a severe problem in order to maintain the homeostasis of the body.

To cope with physiological and work-related stress, majority of employees addict to unhealthy habits. Therefore, to minimize work pressure and other job-related musculoskeletal problems, the working intensity should be kept within the range that allows for

continuous work, with short breaks in the work process (Bhaskaran et al. 2022; Dey et al. 2007; James et al. 2019).

Table 2 gives the details of the different categories of people with the parameters- considered and the effect of work-related stress in terms of net cardiac cost (NCC), relative cardiac cost (RCC), Thermal stress in terms of Heat index (HI) are shown during the working shift.

Light pollution is also a significant factor for human health and wildlife

Parameter	Avg. value	Min. Value	Max. Value
Age (years)	39.32	18	72
RHR(BPM)	84.6	60	104
HR W _{max} (BPM)	112.89	69	145
Max. HR(BPM)	180.68	148	202
NCC(BPM)	28.26	0	68
RCC	34.48	0	93.33
LCW (BPM)	119.62	95	139
DBT(°C)	36	25	41
RH(%)	51.99	45.6	54.7
WBT(°C)	28.2	17.3	32.9
WBGT (°C)	30.61	19.61	35.33
HI(°C)	48.06	25	62

Table 1: The Average, minimum and maximum values of different parameters

8. CONCLUSIONS

Excessive work stress can cause cumulative trauma disorder (CTD) having lasting damage to various body parts including development of psychological stresses, excessive cardiac strain and musculoskeletal disorders. The working and resting heart rates play a significant part in determining the employee limit of continuous work. The application of ergonomics is of utmost importance in these sectors. Also increased number of short breaks in between work spells would create improvement. Consequently, job adherence would increase bringing forth job interest and team spirit. To maintain the homeostasis of the body drinking sufficient amount of water is also must during working.

BMI= Body Mass Index	BSA=Body Surface Area (m ²)	HRR=heart rate reserve
NCC = Net Cardiac cost	RCC =Relative cardiac cost	LCW = Limit of continuous work
RHR= Resting heart rate	HR =maximum working hear rate	W _{max}
DBT =Dry bulb temperature	WBGT= Wet bulb globe temperature	

References:

- Åstrand, Irma, Per-Olof Åstrand, Erik Hohwü Christensen, and Rune Hedman. 1960. Intermittent Muscular Work. *Acta Physiologica Scandinavica* 48(3–4):448–53. doi: 10.1111/j.1748-1716.1960.tb01879.x.
- Bailey, Daniel P., Anselm Ting Su, Jean-Frédéric Brun, Frédéric Dutheil, Gil Boudet, Pierre Chausse, David Thivel, Sylvie Rousset, Martial Mermilliod, Julien S. Baker, Lenise M. Parreira, Yolande Esquirol, Martine Duclos, and Frédéric Dutheil. 2019. How to Measure Sedentary Behavior at Work?. *Frontiers in Public Health* 7(JUL):1–11. doi: 10.3389/fpubh.2019.00167.
- Bertera, R. L. (1990). The Effects of Workplace Health Promotion on Absenteeism and Employment Costs in a Large Industrial Population. *American Journal of Public Health* 80(9):1101–5. doi: 10.2105/AJPH.80.9.1101.
- Bhaskaran, Krishnan, Ian Douglas, Harriet Forbes, Isabel dos-Santos-Silva, David A. Leon, and Liam Smeeth (2022). Body-Mass Index and Risk of 22 Specific Cancers: A Population-Based Cohort Study of 5·24 Million UK Adults. *The Lancet* 384(9945):755–65. doi: 10.1016/S0140-6736(14)60892-8.
- Bhushan mandal, Bibhuti, Shivkumar shrinarayan prajapati, Syed aftab hussain, and Rahul anup mishra (2018). Monitoring and Evaluation of Whole-Body Vibration Exposure of Equipment Operators and Assessment of Associated Health Risk in an Indian Underground Pb-Zn Mine. *Current World Environment* 13(3):403–15. doi: 10.12944/cwe.13.3.13.
- Brusseau, M. L., M. Ramirez-Andreotta, I. L. Pepper, and J. Maximillian (2019). *Environmental Impacts on Human Health and Well-Being*. 3rd ed. Elsevier Inc.
- Chung, Dingyu (2018). The Eight Stages of Psychosocial Protective Development: Developmental Psychology. *Journal of Behavioral and Brain Science* 08(06):369–98. doi: 10.4236/JBBS.2018.86024.
- Cortes-Ramirez, Javier, Suchithra Naish, Peter D. Sly, and Paul Jagals (2018). Mortality and Morbidity in Populations in the Vicinity of Coal Mining: A Systematic Review. *BMC Public Health* 18(1):1–17. doi: 10.1186/s12889-018-5505-7.
- Das, Kunal, Devi Prasad Mishra, and Ram Madhab Bhattacharjee (2022). Heat and Humidity Problems in Indian Coal Mines Mass Production Panels and Their Remedies. *Journal of The Institution of Engineers (India): Series D*. doi: 10.1007/s40033-022-00364-8.
- Dennerlein, J. T. (2008). Ergonomics/Musculoskeletal Issues. *International Encyclopedia of Public Health* 443–52. doi: 10.1016/B978-012373960-5.00288-4.
- Department of the Army and Air Force Headquarters (2003). Heat Stress Control and Heat Casualty Management. *Technical Bulletin Medical* 507 152(I):1–65.
- Dey, Netai Chandra, Samanta Amalendu, and Ratnadeep Saha. 2007. ssessment of Cardiac Strain amongst Underground Coal Carriers-A Case Study in India. *International Journal of Industrial Ergonomics* 37(6):489–95. doi: 10.1016/j.ergon.2007.01.005.
- Dey, Netai Chandra, and Gourab Dhara Sharma (2013). A Critical Study on the Underground Environment of Coal Mines in India-an Ergonomic Approach. *Journal of The Institution of Engineers (India): Series D* 94(1):1–6. doi: 10.1007/s40033-013-0023-3.
- Dianat, Iman, Soleyman Rahimi, Moein Nedaei, Mohammad Asghari Jafarabadi, and Ali E. Oskouei (2017). Effects of Tool Handle Dimension and Workpiece Orientation and Size on Wrist Ulnar/Radial Torque Strength, Usability and Discomfort in a Wrench Task. *Applied Ergonomics* 59:422–30. doi: 10.1016/j.apergo.2016.10.004.
- Ding, Chen, and Yumei Jiang (2020). The Relationship between Body Mass Index and Physical Fitness among Chinese University Students: Results of a Longitudinal Study. doi: 10.3390/healthcare8040570.
- Engineering, Civil (2016). Safety and Ergonomics Study for High Rise Construction Project.

Gupta, Sadanand (2013). Automobile Industry in India : A Cluster Approach. 228.

Irzmańska, Emilia, and Tomasz Tokarski (2017). A New Method of Ergonomic Testing of Gloves Protecting against Cuts and Stabs during Knife Use. *Applied Ergonomics* 61:102–14. doi: 10.1016/j.apergo.2017.01.002.

Lavie, Carl J., Cemal Ozemek, Salvatore Carbone, Peter T. Katzmarzyk, and Steven N. Blair (2019). Sedentary Behavior, Exercise, and Cardiovascular Health. *Circulation Research* 124(5):799–815. doi: 10.1161/CIRCRESAHA.118.312669.

Lin, Jia-hua (2016). Office Ergonomics Evaluation in a Naturalistic Work Environment. (August).

Luger, Tessy, Christopher G. Maher, Monika A. Rieger, and Benjamin Steinhilber. 2019. “Work-Break Schedules for Preventing Musculoskeletal Symptoms and Disorders in Healthy Workers.” *Cochrane Database of Systematic Reviews* 2019(7). doi: 10.1002/14651858.CD012886.pub2.

Mačužić, Slavica, and Jovanka Lukić. 2017. “Ergonomics Analysis of Automobile Seat Comfort.” 16(March):412.

Pancardo, Pablo, Francisco D. Acosta, José Adán Hernández-Nolasco, Miguel A. Wister, and Diego López-de-Ipiña. 2015. “Real-Time Personalized Monitoring to Estimate Occupational Heat Stress in Ambient Assisted Working.” *Sensors (Switzerland)* 15(7):16956–80. doi: 10.3390/s150716956.

Scott, Karen A., Susan J. Melhorn, and Randall R. Sakai (2012). Effects of Chronic Social Stress on Obesity. *Current Obesity Reports* 1(1):16–25. doi: 10.1007/S13679-011-0006-3.

Shanahan, Lilly, Annekatrin Steinhoff, Laura Bechtiger, Aja L. Murray, Amy Nivette, Urs Hepp, Denis Ribeaud, and Manuel Eisner (2022). Emotional Distress in Young Adults during the COVID-19 Pandemic: Evidence of Risk and Resilience from a Longitudinal Cohort Study. *Psychological Medicine* 52(5):824–33. doi: 10.1017/S003329172000241X.

Sharma, Gourab Dhara, Shibaji Dey, and N. C. Dey (2016). Rationalising Postural Demand of Side Discharge Loading Machine Operators with Respect to Musculoskeletal Pain and Discomfort in Underground Coal Mines in India.” *International Journal of Human Factors and Ergonomics* 4(1):60–72. doi: 10.1504/IJHFE.2016.076573.

Valirad, Fateme, Mostafa Ghaffari, Alireza Abdi, Mirsaeed Attarchi, Seyed F. arzi. Mircheraghi, and Saber Mohammadi (2015). Interaction of Physical Exposures and Occupational Factors on Sickness Absence in Automotive Industry Workers. *Global Journal of Health Science* 7(6):276–84. doi: 10.5539/gjhs.v7n6p276.

WSH Council (2014). Workplace Safety and Health Guidelines, Improving Ergonomics in the Workplace. *Workplace Safety and Health Council* (January):1–29. doi: 10.1016/0022-1694(88)90090-X.

Yassierli (2017). Implementation of Ergonomic Programs to Reduce Sick Leave Due to Low Back Pain among Nickel Mining Operators. *International Journal of Industrial Ergonomics* 61:81–87. doi: 10.1016/j.ergon.2017.05.013.

Syam Babu Bokka
National institute of technology
Manipur,
Imphal,
India-795004
syam4ever@yahoo.co.in

Anil Kumar Birru
National Institute of Technology
Manipur,
Imphal,
India-795004
anilbirru@gmail.com

Amandeep Kaur
Post Graduate Institute of Medical
Education and Research,
Sangrur,
Punjab,
India,
amandoc24@gmail.com

Netai Chandr Dey
Indian Institute of Engineering Science
and Technology,
Shibpur,
Kolkata,
India,

Sibaji Ch Dey
Indian Institute of Engineering Science
and Technology,
Shibpur,
Kolkata,
India,

Harikrishna Ch
Shri Vishnu Engineering College for
Women (A), Bhimavaram,
Andhra Pradesh,
India

ncdey63@gmail.com

sibsde@gmail.com

harinityw@gmail.com

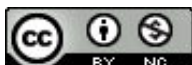


VARIABILITY OF IONOSPHERIC F2 REGION DUE TO SUDDEN STRATOSPHERIC WARMING EVENT OF 2017

Qadeer Ahmed
Anshul Singh
Ankit Gupta
Arti Bhardwaj
P. S. Brahmanandam
A. K. Upadhyaya¹

Keywords:

Sudden stratospheric warming (SSW); ionosphere; electron density; stratospheric temperature; quasi-stationary planetary waves.



A B S T R A C T

We analyzed the impact of minor Arctic sudden stratospheric warming (SSW) event of 2017 on the ionospheric F2 region, using Digisonde data from a low-mid latitude Indian station, Delhi (28.6°N , 77.2°E , 19.2°N geomagnetic latitude, 42.4°N dip). Our study revealed significant ionospheric changes, with electron densities exhibiting variations of more than 200% during this warming event. To further investigate, we examined the deviation in critical frequency $\Delta f_{\text{of}F2}$ from median values in the first six months of 2017 and found that the F2 layer critical frequency experiences maximum and minimum variations during the SSW period. Additionally, we observed periodicities of 7, 11, 14 and 30 days in characteristic F2 layer frequency during this event.

© 202x Published by Faculty of Engineering

1. INTRODUCTION

Ionosphere is the part of Earth's upper atmosphere extending from $\sim 60\text{km}$ to above 500km , mainly created by incoming high frequency solar radiations (EUV and X-ray) and the particle precipitation from the Sun. Significant numbers of electrons and ions that are present in the ionosphere influence the radio signals, satellite signals and Global Navigation Satellite Systems (GNSS) passing through it. One of the primary causes of error in GPS precise positioning and navigation is the ionospheric delay in the propagation of GPS signals. However, ionosphere shows variability in density, composition, and distribution of the ionized gases over time that causes delay in GPS signal and results in positioning error in single frequency GPS. Yu & Liu,

2021 reported ~ 7.1 to ~ 7.9 times positioning error relative to ionospheric quite day in GPS signal during 2013 tropical cyclone Usagi event in the Hong Kong region. Besides the diurnal and seasonal variations, ionosphere undergoes changes during severe space weather events such as solar flares and geomagnetic storms (Uma et al., 2012). In addition to the upper atmospheric phenomena such as solar flares and geomagnetic storms known for primarily perturbing the ionosphere, ionospheric variability is also driven by planetary waves, gravity waves under stable solar and geomagnetic conditions (Hocke & Schlegel, 1996). Studies such as (Gupta & Upadhyaya, 2017; Tulasi Ram et al., 2017) reported ionospheric variability associated with seismological events.

¹ Corresponding author: A K. Upadhyaya
Email: upadhyayaak@nplindia.org

Among the other lower atmospheric phenomenon Sudden Stratospheric Warming is one such phenomenon known to perturb the ionosphere. Sudden stratospheric warming that was first observed by Scherhag in 1952, is a meteorological phenomenon when polar stratospheric temperature during the winters increases by up to $\sim 50^{\circ}\text{C}$ within a few days accompanied by alteration of wind circulation pattern. This phenomenon is more prominent in northern hemisphere, brought on by planetary-scale waves that travel upward from the troposphere. SSWs have a significant impact on the chemistry, temperatures, winds, neutral (non-ionized) particles and electron densities in the stratosphere that extend beyond mesosphere (Baldwin et al., 2021).

Through dynamical processes, the stratospheric state influences the light-ion dominated protonosphere. The ionosphere's O⁺ may be transported by upward disturbance drifts to the protonosphere, where it is primarily converted to H⁺ by chemical coupling and the ionosphere contracts (Zhang et al., 2023). It is known that the tropical upper atmosphere experiences significant changes related to SSW, including an increase in amplitudes of semi-diurnal tides on the order of 10-15 m/s in comparison to the usual period (Susanth, 2021). (Gupta & Upadhyaya, 2017a) investigated ionospheric response to seven SSW events from 2010 to 2016 for wide latitude from 26.6°N to 45.1°N of Asian region and observed the latitudinal dependence of semidiurnal variations and perturbations in ionospheric F2 region in form of enhancements and depressions in electron density.

Recently, Goncharenko et al., 2021 studied the impact of SSW 2019 of southern hemisphere on mid latitude ionosphere (northern hemisphere) and reported anomalies in Total electron content (TEC). Pedatella, 2022 used a combination of Constellation Observing System for Meteorology, Ionosphere, and Climate-2 (COSMIC-2) observations and the Whole Atmosphere Community Climate Model with thermosphere-ionosphere extension (WACCM-X) simulations to investigate the variability in the ionosphere during the 2020–2021 sudden stratospheric warming (SSW) and observed a reduction in the diurnal and zonal mean ionosphere total electron content (ITEC) and decreased amplitude of the diurnal variation in the ionosphere during the SSW.

Most of the studies are carried out at different latitudes except a few studies at Indian latitude. We attempted to quantify the extent of ionospheric perturbation in F2 region associated with sudden stratospheric warming at Indian station Delhi. We found the perturbations in ionosphere in form of enhancements in electron density around the stratospheric warming peak. Further we also examined 6 months data and noticed maximum deviation in critical frequency values during the SSW months.

An important part of our study is that it investigates the pharmacophores model to learn more about how the functional group interacts with the amino acids of the receptor at the molecular level. The utilization of a singular pharmaceutical agent that may effectively target several molecular targets has the potential to be a promising therapeutic approach for the treatment of many types of cancer (Hu et al. 2022). Further, to conduct a molecular docking analysis on the epidermal growth factor receptor (EGFR) using potential lead molecules to forecast their pharmacokinetic characteristics.

2. DATA AND METHODOLOGY

The variation in Ionospheric F2 region following the sudden stratospheric warming is illustrated by critical frequency (foF2) and virtual height (h`F) values obtained after 5 minutes by using Digisonde installed at low-mid latitude Indian station (CSIR-National Physical Laboratory), Delhi (28.6°N, 77.2°E, 19.2°N geomagnetic latitude, 42.4°N dip). Auto scaled Ionograms recorded after every 5 minutes are then manually scaled by using the SAO explorer software. SAO Explorer is the flagship software tool for working with Global Ionosphere Radio Observatory (GIRO) ionograms (<https://ulcar.uml.edu/SAO-X/SAO-X.html>). To eliminate the diurnal variability, we have then calculated the deviation in critical frequency values (ΔfoF2) by taking the difference of foF2 values from average foF2 values of 5 quiet days. The data of international quiet days can be downloaded from http://www.ga.gov.au/oracle/geomag/iqd_form.jsp.

The Polar stratospheric parameters like temperature at 90° N and 10hpa level, temperature at 60-90°N, amplitudes of planetary wave1 and planetary wave 2 and mean zonal wind at 60°N are taken from NASA's Global Space Flight Center, available on website http://acdb-ext.gsfc.nasa.gov/Data_services/met/ann_data.html.

To calculate peak warmings in stratospheric temperature we have taken the daily average stratospheric temperature from 1979 to 2020 and stratospheric temperature during the SSW period available on above website. For determining the influence of solar and geomagnetic activity on ionosphere during the SSW period, F_{10.7} flux and K_p index have been obtained from <https://omniweb.gsfc.nasa.gov/form/dx1.html>.

To isolate ionospheric variability linked to SSW, seismic data available on India Meteorological Department's website <https://riseq.seismo.gov.in/riseq/earthquake> is used to check any influence of earthquake events occurring during the SSW period. Following formula have been used to calculate percentage change in electron density for determining enhancement and depression.

$$\Delta N_e = (f_o F_2)^2_{obs} - (f_o F_2)^2_{avg}$$

ionosphere total electron content (ITEC) and decreased amplitude of the diurnal variation in the ionosphere during the SSW.

Most of the studies are carried out at different latitudes except a few studies at Indian latitude. We attempted to quantify the extent of ionospheric perturbation in F2

region associated with sudden stratospheric warming at Indian station Delhi. We found the perturbations in ionosphere in form of enhancements in electron density around the stratospheric warming peak. Further we also examined 6 months data and noticed maximum deviation in critical frequency values during the SSW months.

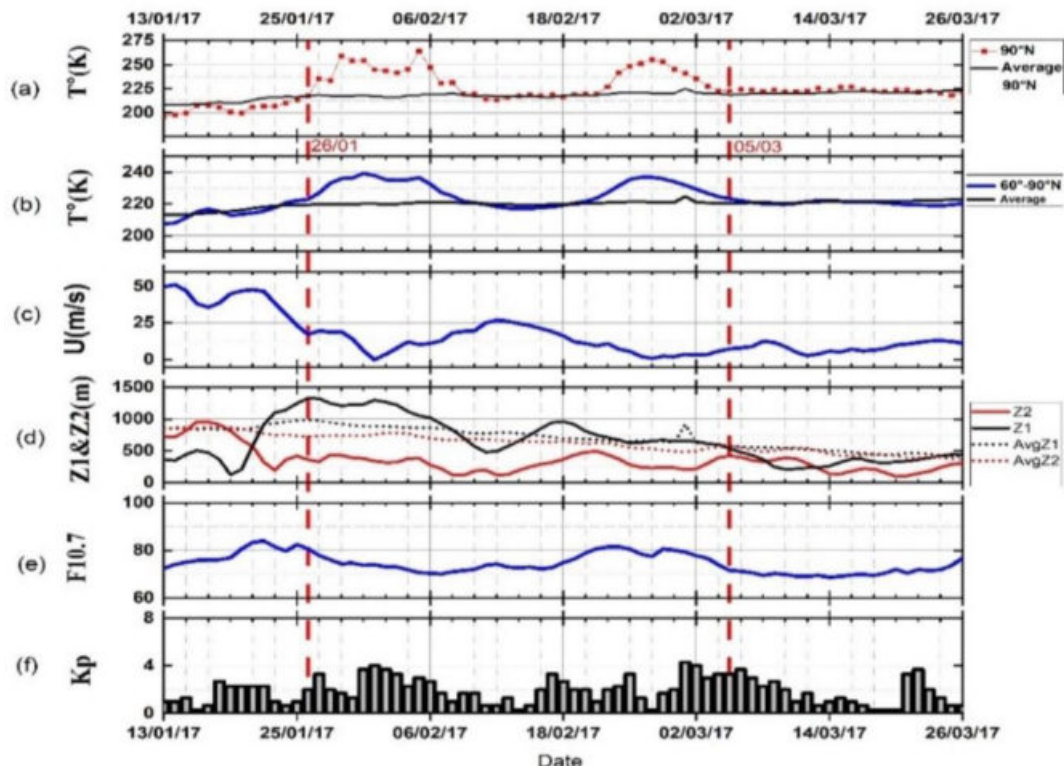


Figure 1. Stratospheric summary during the SSW event of 2017:(a) Stratospheric temperature at 90°N, 10 hPa level (b) zonal mean stratospheric temperature at 60°N–90°N, 10 hPa level (c) Mean zonal wind at 60°N, 10 hPa level, (d) Planetary wave 1 & wave 2 activity at 60°N, 10 hPa level, (e) F10.7 daily average solar radio flux in SFU and (f) daily average Kp index.

An important part of our study is that it investigates the pharmacophores model to learn more about how the functional group interacts with the amino acids of the receptor at the molecular level. The utilization of a singular pharmaceutical agent that may effectively target several molecular targets has the potential to be a promising therapeutic approach for the treatment of many types of cancer (Hu et al. 2022). Further, to conduct a molecular docking analysis on the epidermal growth factor receptor (EGFR) using potential lead molecules to forecast their pharmacokinetic characteristics.

2. DATA AND METHODOLOGY

The variation in Ionospheric F2 region following the sudden stratospheric warming is illustrated by critical frequency (f_{oF2}) and virtual height ($h'F$) values obtained after 5 minutes by using Digisonde installed at low-mid latitude Indian station (CSIR-National Physical

Laboratory), Delhi (28.6°N, 77.2°E, 19.2°N geomagnetic latitude, 42.4°N dip). Auto scaled Ionograms recorded after every 5 minutes are then manually scaled by using the SAO explorer software. SAO Explorer is the flagship software tool for working with Global Ionosphere Radio Observatory (GIRO) ionograms (<https://ulcar.uml.edu/SAO-X/SAO-X.html>). To eliminate the diurnal variability, we have then calculated the deviation in critical frequency values (Δf_{oF2}) by taking the difference of f_{oF2} values from average f_{oF2} values of 5 quiet days. The data of international quiet days can be downloaded from http://www.ga.gov.au/oracle/geomag/iqd_form.jsp. The Polar stratospheric parameters like temperature at 90°N and 10hpa level, temperature at 60–90°N, amplitudes of planetary wave 1 and planetary wave 2 and mean zonal wind at 60°N are taken from NASA's Global Space Flight Center, available on website <http://acdb->

ext.gsfc.nasa.gov/Data_services/met/ann_data.html. To calculate peak warmings in stratospheric temperature we have taken the daily average stratospheric temperature from 1979 to 2020 and stratospheric temperature during the SSW period available on above website. For determining the influence of solar and geomagnetic activity on ionosphere during the SSW period, $F_{10.7}$ flux and K_p index have been obtained from <https://omniweb.gsfc.nasa.gov/form/dx1.html>.

To isolate ionospheric variability linked to SSW, seismic data available on India Meteorological Department's website <https://riseq.seismo.gov.in/riseq/earthquake> is used to check any influence of earthquake events occurring during the SSW period. Following formula have been used to calculate percentage change in electron density for determining enhancement and depression.

Figure 1 represents the SSW summary i.e., stratospheric temperature, mean zonal wind, solar and geomagnetic conditions prevailing during the SSW event of 2017. The vertical red dashed line in Fig.1 marks the start and end of the warming period. This stratospheric warming at 10hpa level (~32km) remained for 38 days extending from 26 January to 05 March 2017. The black line in Fig 1(a) shows the daily average stratospheric temperature calculated from 1979 to 2017 and the red dotted line shows the stratospheric temperature for the SSW period. During this event maximum increase in stratospheric temperature by ~47K is observed, wherein temperature enhanced from 217K to 264K (as shown in fig.1(a)). Three instances of Peak warming are seen on 29 January, 05 February, and 26 February with temperature anomaly (ΔT) of 42K, 47K and 35K, respectively, in contrast to the average temperature.

$$\text{Change in electron density} = \frac{\Delta N_e}{N_e} \times 100\%$$

Where, $(f_o F_2)_{obs}$ is the $f_o F_2$ values obtained after every 5 minutes and $(f_o F_2)_{avg}$ is the average of 5 quiet days during the month.

The first largest value in stratospheric temperature at 90°N was attained three days following the onset of the warming period. After a slight decrease in temperature by 19K, it showed a second peak after an interval of 6 days. After the recovery phase of the second peak, it remained near the average temperature for 12 days from 09 February to 21 February and again reached a maximum temperature of 255K, where the temperature was enhanced by 35K. Similar variations in stratospheric temperature at $60^\circ\text{-}90^\circ\text{N}$ were seen as shown in Fig1(b).

Table1.Cases of enhancement in critical frequency values during SSW event of 2017.

Date	Time	foF2	Average foF2	Δ foF2	% Change in electron density
20-01-2017	09:15:00	9.9	5.2	-4.7	259
03-03-2017	04:55:00	10.2	5.6	-4.5	223
01-03-2017	04:45:00	10	5.8	-4.2	199
18-01-2017	09:40:00	8.8	5.1	-3.6	196
07-03-2017	06:35:00	11.9	7.3	-4.6	167
18-03-2017	10:15:00	11.7	7.5	-4.1	140
26-02-2017	03:55:00	10.3	6.8	-3.5	130

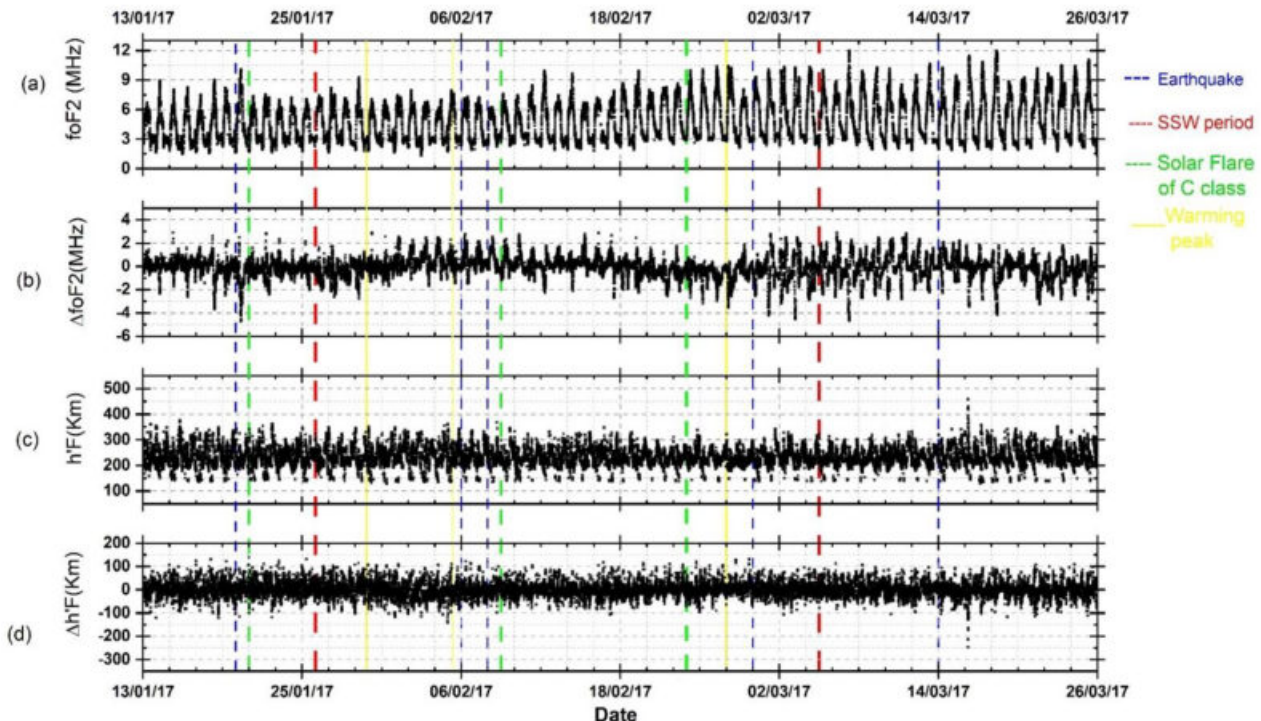


Figure 2. Plot of (a) F2 layer critical frequency (foF2) in MHz (b) Deviation in F2 layer critical frequency (Δ foF2) from quiet time average (c) Virtual height h'F in Km and (d) Deviation in virtual height from (Δ h'F) quiet time average.

This event of 2017 was a minor SSW event, as in this case, zonal mean wind at 60°N became weak, as illustrated in Fig 1(c), and the polar vortex shifted off the pole but did not change the direction. Figure 1(d) shows amplification in planetary wave Z1 (black line) at 60°N and 10 hPa level beginning from 19 January which continued throughout the warming period. Z1 activity dominates the circulation over Z2 during this SSW period, as illustrated in Fig 1(d). This increased wave activity causes significant changes in the neutral

composition of the atmosphere and thus contributes to perturbations in the ionosphere due to the lower atmosphere. The first Maximum peak of planetary wave activity Z1 coincided with the onset of the warming period, and the second peak occurred three days before the beginning of the third peak of stratospheric warming at 90°N . Similarly, the third peak of stratospheric temperature at 90°N coincided with the amplification peak of planetary wave Z. The solar (F10.7 flux) and geomagnetic activity (Kp index) during this period are

presented in Figure 1(e) & 1(f), respectively, because the state of the ionosphere is well known to be strongly controlled by solar and geomagnetic activity. To associate ionospheric variability with SSW, other conditions like solar and geomagnetic activity needs to be constant. During this event, the F10.7 flux (~70 to 80 SFU) remained low and stable. Geomagnetic conditions (K_p index) are also considered to investigate the SSW influence on the ionosphere. It can be seen from Figure 1(f) that geomagnetic activity remained quiet ($K_p < 4$, except in one case when $K_p = 4.3$) during this entire period of warming.

To examine ionospheric response during the SSW event of 2017, the critical frequency of the F2 layer (f_{oF2}) and deviation in critical frequency (Δf_{oF2}) from quiet time average from 13 January 2017 to 26 March 2017(2 weeks before and 3 weeks after warming period) is presented in Fig.2, where the vertically drawn red dashed line marks the beginning and ending of SSW event. Peak warming dates (29 January, 05 February and 26Feb) are shown by a solid yellow line in Fig.2. In this case, we assumed variation in Δf_{oF2} to be anomalous if $|\Delta f_{oF2}| \geq 3.5\text{MHz}$, where $\Delta f_{oF2} \leq -3.5\text{ MHz}$ and $\Delta f_{oF2} \geq 3.5\text{MHz}$ refers to enhancement and depression respectively, calculated by taking the difference from quiet time average values.

During this entire duration, we observed 7 cases of enhancement in critical frequency values of the F2 layer, i.e. When $\Delta f_{oF2} \leq -3.5\text{MHz}$ (shown in table 1). However, no case of depression in f_{oF2} values was found. A maximum enhancement of 4.7MHz from the quiet time average is observed in f_{oF2} ($f_{oF2}=9.9\text{MHz}$ as shown in table) with the enhancement in electron density by ~260% on 20 January, five days before the start of the warming period, which coincided with an earthquake event shown by blue dotted lines in Fig.2. Another enhancement of 4.5MHz ($f_{oF2}=10.22\text{MHz}$) corresponding to enhancement in electron density by 223 % is seen during this warming period on 03 March 2017, which occurred 05 days after the 2nd warming peak. Two days after the peak warming (26 February), an enhancement of 4.2MHz occurred on 01 March, increasing electron density by ~200%. In addition to these changes, enhancement in f_{oF2} values on other occasions with changes in electron density varying from ~130 % to ~260% (as shown in the table) is seen. Apart from enhancements in critical frequency values, Virtual height $h^{\prime}F$ also shows enhancements and depressions during and after the warming period as shown in Figure .2(d). Maximum enhancement of height by 247km compared to the average quite time value was seen on 16 March, 11 days after the warming period. Maximum depression in $h^{\prime}F$ by 132km is observed on 27 February, a day after third warming peak.

3. RESULTS AND DISCUSSION

This work focuses on ionospheric response of F2 region to the minor SSW event of 2017 at low mid latitude Indian station Delhi. In this analysis we have shown variations in F2 layer critical frequency (f_{oF2}) and virtual height $h^{\prime}F$ following this event. Anomalous behavior in terms of enhancement was found in both f_{oF2} and $h^{\prime}F$. The SSW event of 2017 showed 05 cases of enhancement in f_{oF2} values with change in electron density varying from ~130% to ~223%. A total of 07 cases are observed during the 73 days, out of which 02 cases of enhancement occurred before the SSW event and 05 cases of enhancements are seen during and after the warming period. Virtual height ($h^{\prime}F$) also shows enhancement and depression during and after the warming period. Solar and geomagnetic conditions which are primarily known for perturbing the ionosphere remained quiet and stable ($F10.7$ index<80 and K_p index<4) before and during the warming period which indicates the possibility of SSW perturbing the otherwise neutral composition of atmosphere. (Gupta & Upadhyaya, 2017b) reported seismo-ionospheric coupling perturbing the ionosphere in form of enhancement (3-4 days prior to an earthquake) and depression in F2 layer critical frequency. On the similar pattern we analysed ionospheric variations associated with earthquake events shown by blue dashed line in Fig.2. Out of five cases enhancement in F2 layer critical frequency on one occasion is seen two days prior to the earthquakes (coinciding with warming peak). We also examined deviation in critical frequency Δf_{oF2} from median values during the first six months of 2017 presented in Fig.3, where blue dot shows the maximum value of Δf_{oF2} during the SSW period red dot shows hourly median of Δf_{oF2} values. We found that maximum deviation in critical frequency from median values, particularly from 06:00 to 10:00hrs (LT) occurred during the SSW period of 2017, which points toward the contribution of SSW causing deviation in critical frequency from median values. To check the influence of quasi stationary planetary waves we have performed Lomb-Scargle (illustrated in figure 4) spectral analysis. We utilized the detrended values of F2 layer critical frequency (Δf_{oF2}) for two weeks before and three weeks after the Sudden Stratospheric Warming (SSW) period, encompassing a total of thirty-eight days during the SSW. The normalized power spectral densities, generated through the Lomb-Scargle periodogram, depict periods where dominant and secondary components of the wave are observed.

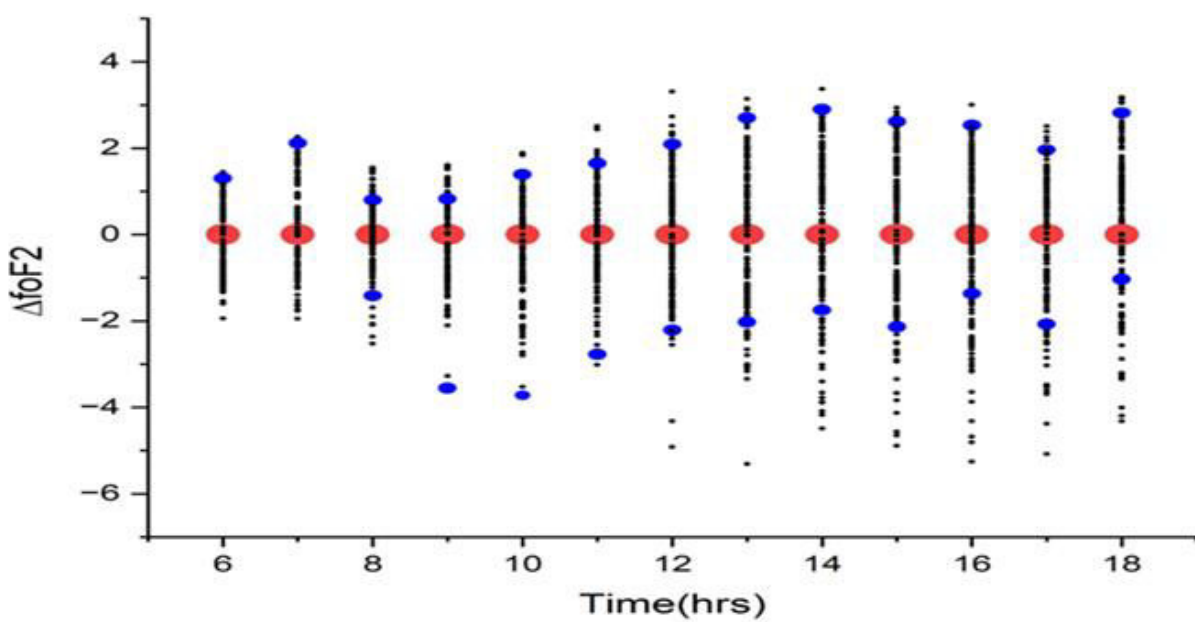


Figure 3. Six months plot of hour wise (0600 to 1800 LT) deviation of critical frequency Δf_{oF2} from median values for SSW events of 2017.

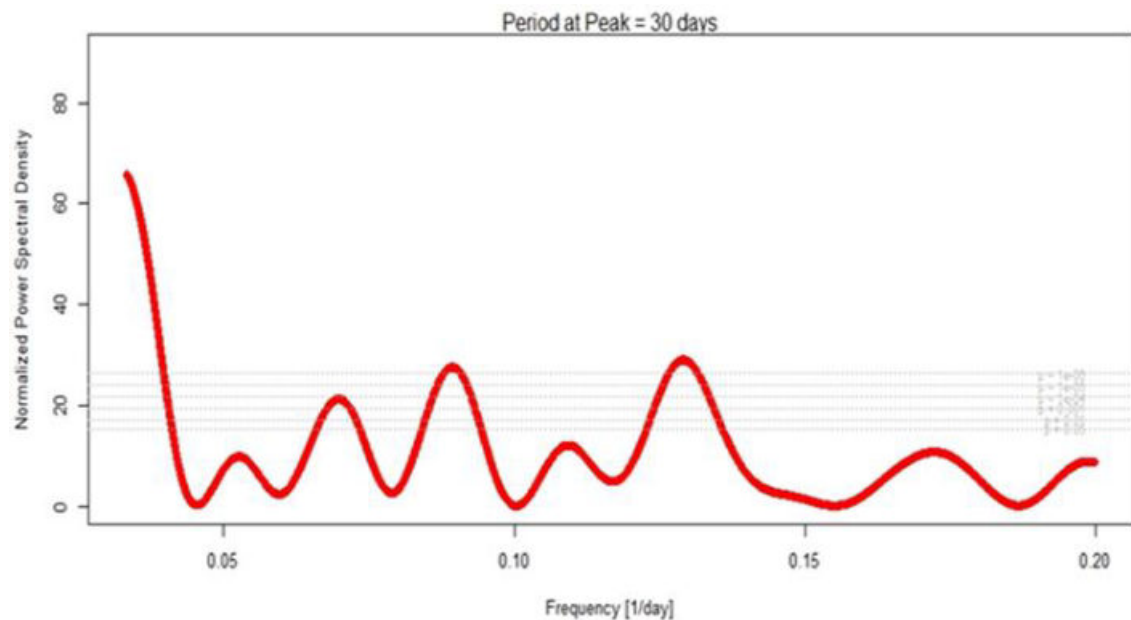


Figure 4. Lomb-Scargle periodogram showing periodicities and period of peak for the SSW events of 2017.

It is essential to highlight that, post-normalization, the spectral power density exhibits an exponential probability distribution with a mean of unity in these plots. We have found peak periodicity of 30 days in addition to the periodicities of 7, 11 and 14 days during the 2017 SSW event. Recently, (Liu et al., 2023) demonstrated that 14 days periodicity is mainly driven by low-level geomagnetic activity represented by K_p index. Several other studies such as (Gupta & Upadhyaya, 2017a; Sripathi & Bhattacharyya, 2012; Upadhyaya & Mahajan, 2013) also reported periodicities ranging from 2 to 30 days. The SSW events are characterized by a rapid increase in temperatures in the stratosphere, particularly over the Polar Regions. This warming can disrupt the usual temperature and pressure patterns in the upper atmosphere, leading to vertical coupling that influences the layers below, including the mesosphere and ionosphere. The reports have shown that the SSW events are often associated with the propagation of planetary waves from the troposphere into the stratosphere. These waves can subsequently modulate the atmospheric circulation and temperatures, impacting the ionosphere.

4. CONCLUSION

Despite solar and geomagnetic conditions being quiet and stable we find perceptible ionospheric variations in electron densities during the minor SSW event of 2017 with enhancement in electron density varying from 130% to 223% and enhancements in electron density were pronounced around and during the warming peak. Six-month plot of deviation in critical frequency values from median values also indicates maximum perturbation during the SSW period. It has been observed that SSW brings significant perturbations in F2 region of ionosphere. Thus, we suggest, inclusion of the SSW phenomena in the models for prediction of ionospheric behaviour. However, in order to assess the extent of variability in the ionosphere associated with SSW, it is crucial to investigate additional events.

Acknowledgement: The authors are thankful to CSIR-NPL for providing the research facilities and NASA Goddard space flight Centre for making the data available on its website. The authors are also thankful to CSIR and UGC for granting Fellowship.

References:

- Baldwin, M. P., Ayarzagüena, B., Birner, T., Butchart, N., Butler, A. H., Charlton-Perez, A. J., Domeisen, D. I. V., Garfinkel, C. I., Garny, H., Gerber, E. P., Hegglin, M. I., Langematz, U., & Pedatella, N. M. (2021). Sudden Stratospheric Warmings. In *Reviews of Geophysics* (Vol. 59, Issue 1). Blackwell Publishing Ltd. doi:10.1029/2020RG000708
- Goncharenko, L. P., Harvey, V. L., Greer, K. R., Zhang, S. R., Coster, A. J., & Paxton, L. J. (2021). Impact of September 2019 Antarctic Sudden Stratospheric Warming on Mid-Latitude Ionosphere and Thermosphere Over North America and Europe. *Geophysical Research Letters*, 48(15). doi:10.1029/2021GL094517
- Gupta, S., & Upadhyaya, A. K. (2017a). Morphology of ionospheric F2 region variability associated with sudden stratospheric warmings. *Journal of Geophysical Research: Space Physics*, 122(7), 7798–7826. doi:10.1002/2017JA024059
- Gupta, S., & Upadhyaya, A. K. (2017b). Preearthquake anomalous ionospheric signatures observed at low-mid latitude Indian station, Delhi, during the year 2015 to early 2016: Preliminary results. *Journal of Geophysical Research: Space Physics*, 122(8), 8694–8719. doi:10.1002/2017JA024192
- Hocke, K., & Schlegel, K. (1996). A review of atmospheric gravity waves and travelling ionospheric disturbances: 1982–1995. *Annales Geophysicae*, 14(9), 917–940. doi:10.1007/s00585-996-0917-6
- Liu, H., Otsuka, Y., Hozumi, K., & Yu, T. (2023). Day-to-day variability of the equatorial ionosphere in Asian sector during August–October 2019. *Frontiers in Astronomy and Space Sciences*, 10. doi:10.3389/fspas.2023.1198739
- Pedatella, N. (2022). Ionospheric Variability during the 2020–2021 SSW: COSMIC-2 Observations and WACCM-X Simulations. *Atmosphere*, 13(3). doi:10.3390/atmos13030368
- Sripathi, S., & Bhattacharyya, A. (2012). Quiet time variability of the GPS TEC and EEJ strength over Indian region associated with major sudden stratospheric warming events during 2005/2006. *Journal of Geophysical Research: Space Physics*, 117(5). doi:10.1029/2011JA017103
- Susanth, S. G. (2021). A brief review on the Atmosphere-Ionosphere coupling during Stratospheric sudden warming over the tropical region. *Indian Journal of Science and Technology*, 14(11), 956–963. doi:10.17485/IJST/v14i11.251
- Tulasi Ram, S., Sunil, P. S., Ravi Kumar, M., Su, S. Y., Tsai, L. C., & Liu, C. H. (2017). Coseismic Traveling Ionospheric Disturbances during the Mw 7.8 Gorkha, Nepal, Earthquake on 25 April 2015 From Ground and Spaceborne Observations. *Journal of Geophysical Research: Space Physics*, 122(10), 10,669–10,685. doi:10.1002/2017JA023860

- Uma, G., Brahmanandam, P. S., Kakinami, Y., Dmitriev, A., Latha Devi, N. S. M. P., Uday Kiran, K., Y. H. Chu (2012). Ionospheric responses to two large geomagnetic storms over Japanese and Indian longitude sectors. *Journal of Atmospheric and Solar-Terrestrial Physics*, 74, 94–110. doi:10.1016/j.jastp.2011.10.001
- Upadhayaya, A. K., & Mahajan, K. K. (2013). Ionospheric F2 region: Variability and sudden stratospheric warmings. *Journal of Geophysical Research: Space Physics*, 118(10), 6736–6750. doi:10.1002/jgra.50570
- Yu, S., & Liu, Z. (2021). The ionospheric condition and GPS positioning performance during the 2013 tropical cyclone Usagi event in the Hong Kong region. *Earth, Planets and Space*, 73(1). doi:10.1186/s40623-021-01388-2
- Zhang, R., Liu, L., Chen, Y., Le, H., & Li, W. (2023). The Stratosphere-Ionosphere-Protonosphere Coupling: Evidence From the Ion Composition Observations During the 2009 Sudden Stratospheric Warming. *Geophysical Research Letters*, 50(2). doi:10.1029/2022GL101707

Qadeer Ahmed

1-Accademy of Scientific and Innovative ResearchGhaziabad,Uttar Pradesh,India
2-CSIR-National Physical Laboratory, New Delhi, India
gahmed785@gmail.com

ORCID 0000-0001-8133-0252

Arti Bhardwaj

1-Accademy of Scientific and Innovative ResearchGhaziabad,Uttar Pradesh, India
2- CSIR-National Physical Laboratory, New Delhi, India
arti.bhardwaj0@gmail.com

Anshul Singh

1-Accademy of Scientific and Innovative ResearchGhaziabad,Uttar Pradesh, India
2- CSIR-National Physical Laboratory, New Delhi, India
phy.anshul@gmail.com
ORCID 0009-0008-3484-7740

Arun Kumar Upadhyaya

CSIR-National Physical Laboratory, New Delhi, India
upadhyayaak@nplindia.org
ORCID 0000-0002-2314-5259

Ankit Gupta

1-Accademy of Scientific and Innovative ResearchGhaziabad,Uttar Pradesh, India
2- CSIR-National Physical Laboratory, New Delhi, India
akki.ankitgupta1995@gmail.com

Potula Sree Brahmanandam

R & D Cell, Shri Vishnu Engineering College for Women (A), Bhimavaram 534202, India dranandpotula@svecw.edu.in
ORCID: 0000-0001-9777-3496



Investigation of Anomalous Ionospheric Signature as Possible Precursor to Earthquakes

Nitesh Kumar Devrani¹

Puja Goel

Qadeer Ahmed

Anshul Singh

Ankit Gupta

Arti Bhardwaj

P. S. Brahmanandam

A. K Upadhyaya*

Keywords:

A B S T R A C T

Earthquake, Ionospheric response, Seismo-ionosphere precursor, Critical Parameter ($f_{\text{OF2}}.h'm_{\text{F2}}$)Digisonde, Delhi

We have examined the ionospheric response to a magnitude 6.6 earthquake that occurred in the Hindu Kush region of Afghanistan on March 21, 2023. This seismic event impacted the ionosphere in the Indian region. Our analysis utilized critical parameters of the F2 layer (f_{OF2} , $h'F$), obtained through Digisonde measurements from a low-mid latitude Indian station located in New Delhi (28.6°N, 77.2°E, 19.2°N geomagnetic latitude, 42.4°N dip). The routine day-to-day fluctuations in the ionosphere are removed by computing variations in the critical frequency and peak height of the F layer (Δf_{OF2} , $\Delta h'F$) in comparison to its standard normal behaviour during quiet periods. We observe noteworthy disturbances in the ionospheric F2 region over Delhi about 8 days before the earthquake event, leading to a substantial variation in peak electron density of approximately 90%. These observed perturbations suggest the potential existence of seismo-ionospheric coupling, given the solar and geomagnetic indices remained relatively quiet and stable during the period. Notably, the precursory impact of the earthquake was observed beyond the earthquake preparation zone, as given by Dobrovolsky et al. (1979).



© 2023 Published by Faculty of Engineering

1. INTRODUCTION

The most devastating natural event, earthquakes, arise from the abrupt release of energy in the Earth's crust, producing seismic waves. Predicting an impending earthquake is a significant scientific challenge, and

reliably forecasting them with high accuracy remains an ongoing pursuit. The notion of ionospheric anomalies as earthquake precursors was initially introduced by Antselevich in 1971. Subsequent to this, several lithosphere-atmosphere-ionosphere coupling mechanisms have been postulated, involving factors

* Corresponding author: AK Upadhyaya
Email: upadhyayaak@nplindia.org

such as radon radioactivity, the release of CH₄, CO₂, He, and H₂ carrier gases (Pulinets et al., 2000, 2002; Pulinets, 2004; Pulinets and Ouzounov, 2011). These mechanisms ionize the near-ground atmosphere (Sorokin and Hayakawa, 2013), generating an anomalous vertical electric field (Singh et al., 2012; Pundhir et al., 2015), which, in turn, perturbs the ionosphere (Pulinets and Davidenko, 2014).

Other proposed mechanisms include the generation of acoustic pressure waves (Astafyeva et al., 2013) and the underground emission of aerosols (Pulinets et al., 2000), emitting electromagnetic radiation that can alter the ionospheric electron density distribution. Importantly, not only the ionosphere above the earthquake epicenter but also its magnetically conjugated region (Pulinets et al., 2003, 2007) and the surrounding area known as the earthquake preparation zone (Dobrovolsky et al., 1979) are affected. The extent and intensity of these pre-earthquake ionospheric anomalies (PEIAs) depend on factors such as the earthquake's magnitude, depth, location, and the distance between its epicenter and the ionosphere monitoring station (Pulinets, 2004; Liu et al., 2006; Le et al., 2011, Bhardwaj et al., 2023).

PEIAs, in the form of changes in total electron content (TEC) and anomalies in F2, E, and Es layer ionospheric parameters, have been reported for various earthquake events. For instance, Ouzounov et al. (2015) found a close correlation between ionospheric anomalies and the M7.8 and M7.3 earthquakes in Nepal in April 2015. Similar studies by Pundhir et al. (2015) on the April 2013 M7.8 earthquake in Pakistan showed GPS TEC data anomalies 5–7 days before the event. Shah and Jin (2015) demonstrated ionospheric anomalies for events with $M \geq 6$ and focal depth less than 60 km based on global $M \geq 5$ earthquake events during 1998–2014. Liu et al. (2015) analyzed Electromagnetic Emissions Transmitted from Earthquake Regions data to reveal nighttime electron and ion density depression and daytime ion temperature enhancement 1–6 days prior to the epicenter of the May 2008 M8 Wenchuan earthquake. Other examples include anomalies detected around the epicenter of the 11 March 2011 M9 Tohoku-Oki earthquake in Japan (Heki, 2011), the 6 April 2009 M6.3 L'Aquila earthquake in Italy (Tsolis and Xenos, 2010), and the 20 September 1999 M7.7 Chi-Chi earthquake in Taiwan (Liu et al., 2001). In these cases, anomalies in ionospheric parameters were observed days to weeks before the seismic events, highlighting the potential of ionospheric monitoring for earthquake prediction. In light of above we examine whether (a) the earthquake event of March 21, 2023 affected the ionospheric F2 region over the low-mid latitude Indian station, Delhi, (2) the effect of earthquake can be seen outside the radius of earthquake preparation zone, as given by Dobrovolsky et al. (1979), and if so,

(c) the magnitude in electron density variation because of this earthquake event.

2. METHODOLOGY

The ionosphere's temporal variability, spanning hourly to seasonal scales and responding to solar activity, necessitates round the clock monitoring. The Digisonde instrument, situated at the "low mid-latitude ionospheric monitoring Indian station" in Delhi (28.6°N, 77.2°E, 19.2°N geomagnetic latitude, 42.4°N dip), is employed for our study. Operating at 5-minute intervals, it generates ionograms, showcasing sounding frequency on the x-axis and virtual reflection height on the y-axis (Gupta and Upadhyaya, 2017).

Ionogram data manually scaled with SAO-X software to derive critical ionospheric parameters (foF2, h'F2). The critical parameters exhibit variation which allow us to quantify ionospheric variability by measuring the deviation of these parameters from their normal statistical behavior. Ionospheric parameters (foF2, ΔfoF2, h'F and Δh'F) are analyzed 15 days prior and 20 days after ((i.e. from March 6, 2023, to April 10, 2023).) the seismic event of 21 March 2023. Ionospheric variabilities stem from day-to-day, hourly, and seasonal fluctuations, observed as deviations from average values based on ten geomagnetically quiet days (IQD). The deviation of foF2 is then estimated based on these comparisons (Gupta and Upadhyaya, 2017).

$$\Delta foF2 (\text{MHz}) = foF2 - \text{quiet} \quad (1)$$

"Quiet" denotes the median foF2 from ten IQDs. Positive ΔfoF2 signifies increased critical frequencies and electron density, while negative ΔfoF2 indicates decreased electron density. Electron density variations were calculated as percentage change using the following equation.

$$\text{ElectronDensity (\%)} = \left(\frac{foF2 - \text{quiet}}{\text{quiet}} \right) \times 100 \quad (2)$$



Figure 1. Schematic of earthquake epicentre to Ionospheric monitoring station(NPL, New Delhi)

Table 1. Details of Earthquake Event

Earthquake date	Detail of Earthquake					Distance from Delhi (Km)	Radius of Influence Zone "R" (Km)
	Lat.(deg.)	Long.(deg.)	Depth(Km)	Mag.	Time(UT)		
21 Mar 2023	36.09° N	71.35° E	156	6.6	16.47	988	668.65

3. OBSERVATIONS AND ANALYSIS

We examine the earthquake event of 21 March 2023 with a magnitude greater than 6.0 in the Hindu Kush region with epicentre in Tajikistan (36.09° N, 71.35° E) with a focal depth of 156 km. This area is marked by intense seismic activity, resulted from collisional tectonics between the Indian Plate and Eurasian Plate. Ionospheric observations were conducted in Delhi, India. It can be noticed from Table 1 that the distance of the observing station, Delhi (~1105 km), was outside the radius of earthquake preparation zone (~1023 km) as given by (Dobrovolsky et al. (1979)).

Figures 1a–1e depict the F_2 layer critical frequency, the deviation in F_2 layer frequency ($\Delta foF2$), and the background space weather conditions during 6th March to 11th April 2023. The global geomagnetic storm index (K_p), the Disturbance Storm Time Index (Dst), an index of magnetic activity, and the solar index F10.7 in sfu (solar flux unit, 1 SFU = 10^{-22} W/m²/Hz) are shown in Figure to ascertain the space weather conditions during the period of investigation. On March 15th, the Dst indices exhibited a minimum of -38 nT at 23 UT, accompanied by a K_p index of 5.6. While the Dst index remains tranquil and steady, the K_p index suggests an elevated level of geomagnetic activity. It's important to note that although there exists a general correlation between Dst and K_p , these metrics gauge distinct facets of geomagnetic activity and are influenced by different factors. Typically, during geomagnetic storm episodes, both Dst and K_p are prone to register elevated values. Nevertheless, in certain instances, such as on March 15th, K_p may be heightened while Dst does not exhibit a corresponding significant negative deviation. This inconsistency might arise when the effects of the storm are unevenly distributed across the Earth. Additionally, when evaluating the influence of geomagnetic storms at equatorial and low to low-mid latitude stations, the Dst (Disturbance Storm Time) index, offering a measure of the global, low-latitude disturbance in the Earth's magnetic field, is generally more appropriate than the K_p index. The geomagnetic and solar conditions depicted in Figures 1c, 1d, and 1e before the earthquake event, barring the disturbance observed in K_p on the 15th, are quiet and stable. This presents an ideal scenario to examine potential anomalous ionospheric variations triggered by other sources, such as earthquakes, sudden stratospheric warming, etc.

Prior to the earthquake event, enhancement more than 15 MHz in $foF2$ are seen on 7th, 9th, 13th, 16th and 19th March 2023. However, after de-trending ($\Delta foF2$) two notable peaks (shown in green) are observed on March

16 and March 13 leading to an electron density variation of 120% and 90% respectively. On average, variations range 15-25%, corresponding to day-to-day ionospheric changes. This abrupt increase in $\Delta foF2$ on March 16 and on March 13 signifies a distinctive anomaly in the ionosphere prior to the earthquake event. The increase in $\Delta foF2$ on March 16 could be because of the increase in geomagnetic activity however, the enhancement seen in $\Delta foF2$ on 13th March warrant a detailed investigation.

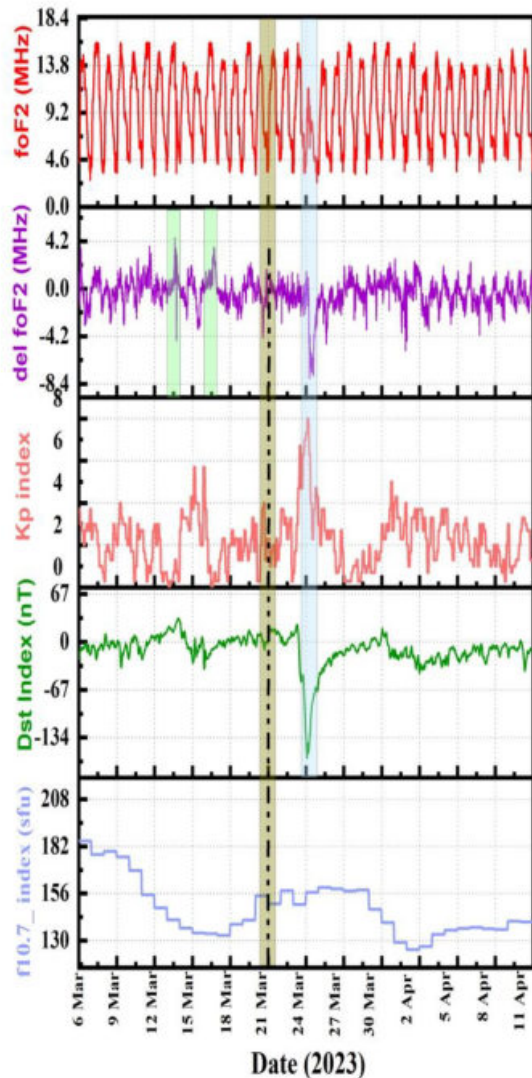


Figure 2. Plots depicting ionospheric parameters, geomagnetic, and solar indices from March 6th to April 11th, 2023.

In Figure 2, the plot shows the variation in F2 layer critical frequency (foF_2) from March 6th to April 10th, 2023. It includes the median value on quiet days and highlights its fluctuations on March 13th and 24th, where anomalous variations were observed. It can be seen from this figure that prominent large variation varying from 3 to 16 MHz is seen on 13th March. Furthermore, there is a distinct decrease mostly in foF_2 throughout the day in comparison to other days, aligning with the geomagnetic storm on March 24th (-163nT).

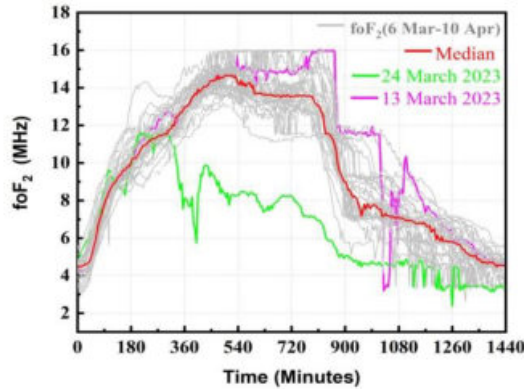


Figure 3. foF_2 variations from 06 March 2023 to 10 April 2023.

A clear anomalous variation in F2 layer frequency on 13th March can be seen in Figure 3 where, we have plotted the variation in the deviation of F2 layer frequency (ΔfoF_2) from the median values observed during quiet days in the month of March. A positive deviation of 4.5 MHz at 14.30 UT followed by a negative deviation of -4.6 MHz is seen at 17.25 UT. This anomalous variation of about 9 MHz on 13th March happened in just four hours of interval is strange and unexpected.

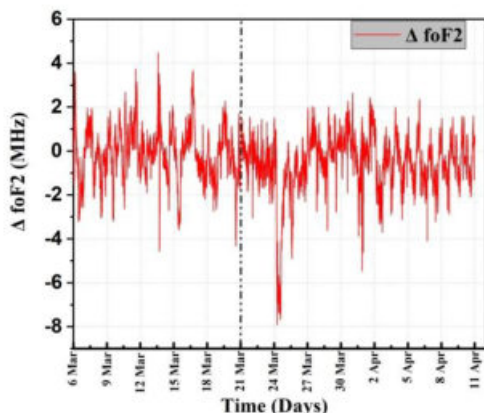


Figure 4. H'F variation from 06 March 2023 – 10 April 2023

We further examine the F layer base height behaviour during 6th March 2023 to 11th April 2023 for this earthquake event. In figure 4, the variation in F layer

base height ($h'F$) is plotted, for the period from 6th March to 10th April 2023, the median value of quiet days along with its variation on 13th and 24th March respectively. On the Geomagnetic storm day of March 24, 2023, a considerable fluctuation of approximately 425 km in $h'F$ is evident. However, despite the notable variation in foF_2 , no significant disturbances were noted in $h'F$ on March 13th.

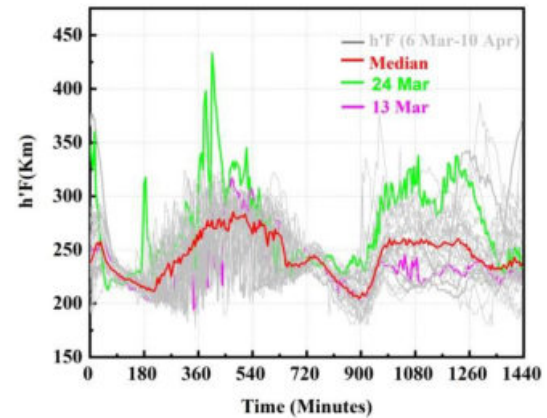


Figure 5. Plot of variation in $h'F$ from March 6, 2023, to April 10, 2023.

Similar behaviour, i.e., no prominent variation in $\Delta h'F$ was seen on 13th March 2023 as can be seen in Figure 5, where the deviation in F layer base height ($\Delta h'F$) from the quiet median is plotted, for the period from 6th March to 10th April 2023. However, a large variation of 175 km and 125 km was observed on 24th March and 16th March respectively.

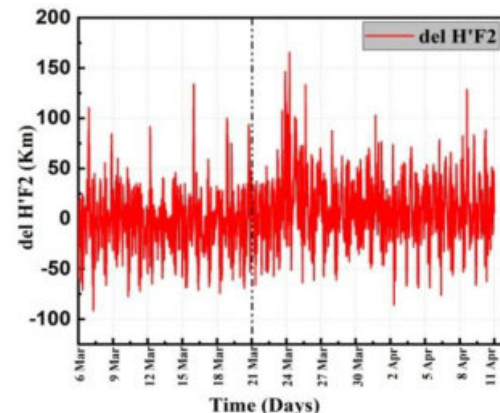


Figure 6. Plot of variation in $\Delta h'F$ from March 6, 2023, to April 10, 2023.

4. DISCUSSION:

The investigation of the ionospheric response in the F2 region to the earthquake event on March 21, 2023, with a magnitude of 6.6 on the Richter scale, at the low-mid latitude Indian station, Delhi, has revealed two significant anomalous disturbances on March 16 and March 13, resulting in electron density variations of 120% and 90%, respectively. The anomaly detected in the F layer of the ionosphere on March 16 appears to be

associated with geomagnetic factors, as evidenced by a registered K_p value of 5.6 on March 15. Conversely, the disruptions noted in the ionosphere on March 13 seem to be attributable to the seismo-ionospheric coupling effect, arising from the earthquake event, as the geomagnetic and solar indices remained tranquil and stable during this timeframe. Many researchers have documented comparable ionospheric disturbances occurring within the two weeks preceding the onset of the earthquake event for e.g. (Liu *et al.*, 2008; Liu *et al.*, 2010; Tojiev *et al.*, 2013; Gupta and Upadhyaya, 2017; Tariq *et al.*, 2021; (Eshkuvatov *et al.*, 2023). Therefore, the anomalous variation observed on March 13, eight days before the earthquake event, can be regarded as a precursor to the earthquake event of March 23, 2023. However, the complexity and thus the elusiveness of the F2 region are well known. Often unexpected variability in the ionospheric F2 region is seen even at times when the solar and geomagnetic indices are low and quite stable also such abrupt variations in ionosphere is also linked to sudden stratospheric warming events however; it affects the ionosphere in winter time. In our previous study (Gupta & Upadhyaya, 2017); from the same monitoring station as well as in other reports, we have noted unusual perturbations in foF2 occurring one to two weeks before an earthquake. These observations have been recognized as potential precursors to seismic events. In the absence of any alternative source to which we can attribute the observed large variations in ΔfoF2, and based on our prior observations, we believe that these variations resulted from the earthquake event.

On the precursor day, March 13th, there were minimal variation in the F layer height; nevertheless, these changes were not as noticeable as those observed in the frequencies. (Maruyama *et al.*, 2011) in their study noted F2-layer height increase at Kokubunji station, 440 km from the Tohoku-Oki earthquake epicentre, supporting the notion of layer height changes. The main ionospheric variations what is being insisted occur prior to earthquakes, and the behavior of ionospheric base height ($h'F$) in relation to seismic events is a complex phenomenon that is not fully understood. It is established that some earthquakes can trigger disturbances in the ionosphere, causing changes in $h'F$. However, not every earthquake will necessarily have such effects. Several factors play a role, including the magnitude and depth of the earthquake (smaller or deeper earthquakes may have minimal or undetectable impact on the ionosphere), the distance between the epicenter and the observation point (effects may be unnoticed if the earthquake is far from the measurement area), and the specific ionospheric conditions at the time (pre-existing disturbances or irregularities may overshadow earthquake-induced effects).

However, a depth of 156 km is unusual for a magnitude of (6.6) earthquake, researchers (Kon *et al.*, 2011)

analyzed seismic events with focal depths exceeding 40 km, even for low-magnitude earthquakes and showed Ionospheric anomalies associated with the event.

The seismic event under investigation occurred at a considerable distance from the Delhi station, beyond its zone of influence. Our findings are reinforced by the reported work of Dabas *et al.* (2007), who examined foF2 variations at Varanasi and Delhi in response to moderate to low-magnitude earthquakes exceeding 1000 km away. These earthquakes, with magnitudes ranging from 5 to 7.5, were primarily located in China, Myanmar, Indonesia, and Japan.

Furthermore, Gupta and Upadhyaya (2017) also investigated ionospheric anomalies associated with seismic events, analyzing five earthquakes. Interestingly, the effects of the earthquakes were observed even when the observation station was located outside the earthquake preparation zone.

It's important to emphasize that while there is evidence of ionospheric anomalies preceding earthquakes, the exact mechanisms and causal relationships are still not fully understood. One possible explanation could be the generation of a powerful electric field in the vicinity of the Earth's surface. Pulinets(2004) proposed a coupling model providing a block diagram of seismo-ionospheric coupling mechanism that suggested that radon is emitted from the region where the earthquake epicentre is located, both during and preceding the occurrence of the earthquake. Other similar schematic depiction of the causative mechanism is reported by (Xiong *et al.*, 2021, Revathi *et al.*, 2011). The increased concentration of ions in the seismic zone initiates a process known as nucleation, leading to the formation of ion clusters (Pulinets and Ouzounov, 2011). The diffusion of radon is facilitated by carbon dioxide and methane (Khilyuk *et al.*, 2000), which, in turn, incite the generation of acoustic gravity waves. The movement of air disrupts the ion clusters, causing a rapid enrichment of ions in the near-Earth atmosphere. Consequently, an anomalously strong vertical electric field of approximately kV/m magnitude is produced through a process of charge separation. This intense electric field can penetrate into the ionosphere, altering its dynamics and electron density (Pulinets *et al.*, 2000).

4. CONCLUSION

Following our examination of the ionospheric response to the seismic event that occurred on March 21, 2023, in the Hindu Kush region of Afghanistan, registering 6.6 on the Richter scale, the following conclusions are drawn from the analysis.

- a) Distinct ionospheric perturbations are observed at the low-mid latitude Indian station, Delhi, indicating the impact of the seismo-ionospheric coupling mechanism. These perturbations

manifested eight days prior to the earthquake event, exhibiting both enhancements and depressions in foF2, corresponding to a maximum peak electron density variation of approximately 90%

- b) The anomalous perturbation in foF2 can be taken as precursor to earthquakes. However, no notable variations are observed in h'F that could be identified as distinctive signatures of earthquake events
- c) The ionospheric perturbations caused by the earthquake event are seen even when the observing station is located outside the earthquake preparation zone (Dobrovolsky et al., 1979).

5. Acknowledgement:

The authors express deep gratitude to CSIR-NPL, New Delhi, for their invaluable academic and instrumental support in conducting this research. Authors are also thankful to GBPUAT , Pantnagar for their support. The authors AB, AU, and QA are thankful to UGC, and AS is thankful to CSIR for granting the Senior Research Fellowship. They are also thankful to Academy of Scientific and Innovative Research (AcSIR), Ghaziabad, India

References:

- Astafyeva, E., Shalimov, S., Olshanskaya, E., & Lognonné, P. (2013). Ionospheric response to earthquakes of different magnitudes: Larger quakes perturb the ionosphere stronger and longer. *Geophysical Research Letters*, 40(9), 1675-1681.<https://doi.org/10.1002/grl.50398>.
- Bhardwaj A, Gupta A, Ahmed Q, Singh A, Gupta S, Sarkhel S, Sunil Krishna MV, Pallamraju D, Pant T and Upadhyay A K (2023), Signature of Y-forking in ionogram traces observed at low-mid latitude Indian station, New Delhi, during the earthquake events of 2020: ionosonde observations. *Front. Astron. Space Sci.*, doi: 10.3389/fspas.2023.1170288.
- Dabas, R. S., Das, R. M., Sharma, K. & Pillai, K. G. M. (2007). Ionospheric pre-cursors observed over low latitudes during some of the recent major earthquakes. *Journal of Atmospheric and solar-terrestrial physics*, 69(15), 1813-1824.doi: 10.1016/j.jastp.2007.09.005
- Dobrovolsky, I. P., Zubkov, S. I. & Miachkin, V. I. (1979). Estimation of the size of earthquake preparation zones. *Pure and applied geophysics*, 117(5), 1025-1044. doi:10.1007/BF00876083
- Eshkuvatov, H. E., Ahmedov, B. J., Tillayev, Y. A., Tariq, M. A., Shah, M. A. & Liu, L. (2023). Ionospheric precursors of strong earthquakes observed using six GNSS stations data during continuous five years (2011–2015). *Geodesy and Geodynamics*, 14(1), 65-79.doi: 10.1016/j.geog.2022.04.002.
- Gupta, S., & Upadhyay, A. K. (2017). Preearthquake anomalous ionospheric signatures observed at low-mid latitude Indian station, Delhi, during the year 2015 to early 2016: Preliminary results. *Journal of Geophysical Research: Space Physics*, 122(8), 8694-8719.<https://doi.org/10.1002/2017JA024192>
- Heki, K. (2011). Ionospheric electron enhancement preceding the 2011 Tohoku-Oki earthquake. *Geophysical Research Letters*, 38(17).<https://doi.org/10.1029/2011GL047908>.
- Khilyuk, L. F., Chilingar, G. V., Robertson, J. O., and Endres, B. (2000). “Chapter 15 - gas migration,” in Gas migration. Editors L. F. Khilyuk, G. V. Chilingar, J. O. Robertson, and B. Endres (Houston: Gulf Professional Publishing), 223–237. doi:10.1016/B978- 088415430-3/50016-1.
- Kon, S., Nishihashi, M. & Hattori, K. (2011). Ionospheric anomalies possibly associated with $M \geq 6.0$ earthquakes in the Japan area during 1998-2010: Case studies and statistical study. *Journal of Asian Earth Sciences*, 41(4), 410-420.doi: 10.1016/j.jseaes.2010.10.005
- Le, H., Liu, J. Y., & Liu, L. (2011). A statistical analysis of ionospheric anomalies before 736 M6. 0+ earthquakes during 2002–2010. *Journal of Geophysical Research: Space Physics*, 116(A2).<https://doi.org/10.1029/2010JA015781>
- Liu, J. Y., Chen, Y. I., Chuo, Y. J., & Tsai, H. F. (2001). Variations of ionospheric total electron content during the Chi-Chi earthquake. *Geophysical Research Letters*, 28(7), 1383-1386.<https://doi.org/10.1029/2000GL012511>
- Liu, J. Y., Chuo, Y. J., Shan, S. J., Tsai, Y. B., Chen, Y. I., Pulinet, S. A. & Yu, S. B. (2004). Pre-earthquake ionospheric anomalies registered by continuous GPS TEC measurements. In *Annales Geophysicae*, 22(5), 1585-1593.doi: 10.5194/angeo-22-1585-2004
- Liu, J. Y., Tsai, H. F., Lin, C. H., Kamogawa, M., Chen, Y. I., Lin, C. H., ... & Yeh, Y. H. (2010). Coseismic ionospheric disturbances triggered by the Chi-Chi earthquake. *Journal of Geophysical Research: Space Physics*, 115(A8). <https://doi.org/10.1029/2010JA015313>

- Liu, J. Y., Tsai, Y. B., Chen, S. W., Lee, C. P., Chen, Y. C., Yen, H. Y., ... & Liu, C. (2006). Giant ionospheric disturbances excited by the M9. 3 Sumatra earthquake of 26 December 2004. *Geophysical Research Letters*, 33(2). <https://doi.org/10.1029/2005GL023963>
- Liu, J. Y., Y. I. Chen, C. C. Huang, M. Parrot, X. H. Shen, S. A. Pulinets, Q. S. Yang, and Y. Y. Ho (2015), A spatial analysis on seismo-ionospheric anomalies observed by DEMETER during the 2008 *M*8.0 Wenchuan earthquake, *J. Asian Earth Sci.*, **114**, 414–419, doi:10.1016/j.jseaes.2015.06.012.
- Maruyama, T., T. Tsugawa, H. Kato, A. Saito, Y. Otsuka, & M. Nishioka (2011). Ionospheric multiple stratifications and irregularities induced by the 2011 off the Pacific coast of Tohoku earthquake, *Earth, planets and space*, **63**(7), 869–873. doi: 10.5047/eps.2011.06.008.
- Ouzounov, D., Pulinets, S., & Davidenko, D. (2015). Revealing pre-earthquake signatures in atmosphere and ionosphere associated with 2015 *M*7. 8 and *M*7. 3 events in Nepal. Preliminary results. *arXiv preprint arXiv:1508.01805*. <https://doi.org/10.48550/arXiv.1508.01805>.
- Pulinets, S. (2004). Ionospheric precursors of earthquakes: *Recent advances in theory and practical applications*. *Terr. Atmos. Ocean. Sci.* **15**, 413–435. doi:10.3319/TAO.2004.15.3.413(EP).
- Pulinets, S. A., Boyarchuk, K. A., Hegai, V. V., & Karelina, A. V. (2002). Conception and model of seismo-ionosphere-magnetosphere coupling. *Seismo-Electromagnetics: Lithosphere-Atmosphere-Ionosphere Coupling*, 353-361.
- Pulinets, S. A., Boyarchuk, K. A., Hegai, V. V., Kim, V. P., and Lomonosov, A. M. (2000). Quasielectrostatic model of atmosphere-thermosphere-ionosphere coupling. *Adv. Space Res.* **26**, 1209–1218. doi:10.1016/S0273-1177(99)01223-5
- Pulinets, S. A., Kotsarenko, A. N., Ciraolo, L., & Pulinets, I. A. (2007). Special case of ionospheric day-to-day variability associated with earthquake preparation. *Advances in Space Research*, **39**(5), 970-977. <https://doi.org/10.1016/j.asr.2006.04.032>
- Pulinets, S. A., Legen'Ka, A. D., Gaivoronskaya, T. V., & Depuev, V. K. (2003). Main phenomenological features of ionospheric precursors of strong earthquakes. *Journal of atmospheric and solar-terrestrial physics*, **65**(16-18), 1337-1347. <https://doi.org/10.1016/j.jastp.2003.07.011>
- Pulinets, S., & Davidenko, D. (2014). Ionospheric precursors of earthquakes and global electric circuit. *Advances in Space Research*, **53**(5), 709-723. <https://doi.org/10.1016/j.asr.2013.12.035>
- Pulinets, S., and Ouzounov, D. (2011). Lithosphere–Atmosphere–Ionosphere Coupling (LAIC) model – an unified concept for earthquake precursors validation. *J. Asian Earth Sci.* **41**, 371–382. doi:10.1016/j.jseaes.2010.03.005.
- Pundhir, D., Singh, B., Lakshmi, D. R., & Reddy, B. M. (2015). A study of ionospheric precursors associated with the major earthquakes occurred in Pakistan region. *J Ind Geophys Union*, **19**(1), 71-76.
- Revathi, R., Brahmanandam, P. S., Vishnu, T., & Uma, G. (2011). Possible prediction of earthquakes by utilizing multi precursor parameters in association with ground and satellite-based remote sensing techniques. *International Journal of Earth Sciences and Engineering*, **4**(6), 978-981.
- Shah, M., & Jin, S. (2015). Statistical characteristics of seismo-ionospheric GPS TEC disturbances prior to global $Mw \geq 5.0$ earthquakes (1998–2014). *Journal of Geodynamics*, **92**, 42-49. <https://doi.org/10.1016/j.jog.2015.10.002>
- Sharma, K., Dabas, R. S., Sarkar, S. K., Das, R. M., Ravindran, S. & Gwal, A. K. (2010). Anomalous enhancement of ionospheric F2 layer critical frequency and total electron content over low latitudes before three recent major earthquakes in China. *Journal of Geophysical Research: Space Physics*, **115**(11), 1-14. doi: 10.1029/2009JA014842
- Sorokin, V., & Hayakawa, M. (2013). Generation of seismic-related DC electric fields and lithosphere-atmosphere-ionosphere coupling. *Modern Applied Science*, **7**(6), 1. doi:10.5539/mas.v7n6p1
- Singh, A. K., S. Kumar, R. Singh, and A. K. Singh (2012), Pre-earthquake Ionospheric anomalies observed using ground based multiinstruments, *Int. J. Adv. Earth Sci.*, **1**(1), 13–1
- Tariq, M. A., Shah, M., Li, Z., Wang, N., Shah, M. A., Iqbal, T. & Liu, L. (2021). Lithosphere ionosphere coupling associated with three earthquakes in Pakistan from GPS and GIM TEC. *Journal of Geodynamics*, **147**(1), 1-11. doi: 10.1016/j.jog.2021.101860
- Tojiev, S. R., Ahmedov, B. J., Tillayev, Y. A. & Eshkuvatov, H. E. (2013). Ionospheric anomalies of local earthquakes detected by GPS TEC measurements using data from Tashkent and Kitab stations. *Advance in. Space Research*, **52**(6), 1146-1154. doi: 10.1016/j.asr.2013.06.011
- Tsolis, G. S., & Xenos, T. D. (2010). A qualitative study of the seismo-ionospheric precursors prior to the 6 April 2009 earthquake in L'Aquila, Italy. *Natural Hazards and Earth System Sciences*, **10**(1), 133-137. <https://doi.org/10.5194/nhess-10-133-2010>
- Xiong, P., Long, C., Zhou, H., Battiston, R., De Santis, A., Ouzounov, D., et al. (2021). Pre-earthquake ionospheric perturbation identification using CSES data via transfer learning. *Front. Environ. Sci.* **9**. doi:10.3389/fenvs.2021.779255.

Nitesh Kumar Devrani
Govind Ballabh Pant University
of Agriculture and Technology
Pantnagar,
India
Niteshdevrani10@gmail.com

Qadeer Ahmed
1-Accademy of Scientific and Innovative Research (AcSIR) Ghaziabad, Uttar Pradesh, India
2-CSIR-National Physical Laboratory, New Delhi, India
qahmed785@gmail.com

Dr. Puja Goel
Govind Ballabh Pant University of Agriculture and Technology, Pantnagar, India
pujagoel@gmail.com

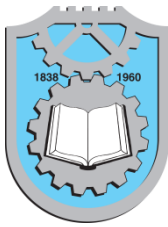
Anshul Singh
1-Accademy of Scientific and Innovative Research (AcSIR) Ghaziabad, Uttar Pradesh, India
2- CSIR-National Physical Laboratory, New Delhi, India
phy.anshul@gmail.com

Dr. Arun Kumar Upadhyaya
CSIR-NPL
New Delhi,
India
upadhyayaak@nplindia.org

Ankit Gupta
1-Accademy of Scientific and Innovative Research (AcSIR) Ghaziabad, Uttar Pradesh, India
2- CSIR-National Physical Laboratory, New Delhi, India
akki.ankitgupta1995@gmail.com

Arti Bhardwaj
1-Accademy of Scientific and Innovative Research (AcSIR) Ghaziabad, Uttar Pradesh, India
2- CSIR-National Physical Laboratory, New Delhi, India
arti.bhardwaj0@gmail.com

Potula Sree Brahmanandam
R & D Cell, Shri Vishnu Engineering College for Women (A), Bhimavaram 534202, India
dranandpotula@svecw.edu.in
ORCID: 0000-0001-9777-3496
&
RnD Cell, Shri Vishnu Engineering College for Women(A), Bhimavaram 534 202, India



FPGA IMPLEMENTATION OF HYBRID ADDER

K. Bala Sindhuri

G. Challa Ram¹

M. Venkata Subbarao

M. Aravind kumar

B. Kalivaraprasad

Keywords:

Hancarlson Adder; Weinberger Adder; Energy Efficient Design; Binary to Excess-1 Converter (BEC); Hybrid Adder



A B S T R A C T

In applications of Digital Electronics, the primary aim is precision, emphasizing accurate outcomes while concurrently minimizing power dissipation and latency. This precision is especially crucial in arithmetic operations, notably addition and multiplication, where the critical path plays a substantial role in influencing the delay of electronic devices. To enhance the speed of these operations, various adder architectures such as Linear Carry Select Adder (CSELA), Square Root CSELA (SQRT CSELA), Ling, Hancarlson, and Weinberger adders are surveyed. This survey serves as motivation for the development of a hybrid adder, which combines different addition techniques to optimize the speed of addition. The proposed hybrid adder architecture is synthesized and simulated using the Xilinx Vivado 2017.2 ISIM tool, with subsequent hardware implementation on the Zedboard. Experimental findings indicate that the introduced hybrid adder exhibits improved speed compared to other conventional adders.

© 2023 Published by Faculty of Engineering

1. INTRODUCTION

The fundamental building block extensively employed in computer arithmetic, originating from Digital Signal Processing (DSP) Filters to Ultra Low Power Biomedical Frequency Low Pass Filters, is the binary adder (Anil Kumar et al., 2023). The Ripple Carry Adder (RCA) (Koyada et al., 2017) is recognized as the most fundamental and straightforward binary adder. Nevertheless, a significant drawback of ripple carry adders lies in their speed dependence on the time needed to propagate a carry throughout the entire adder. Consequently, the Carry Select Adder (CSLA) finds extensive use due to its enhanced computational speed, particularly in integrated systems (Sreevani et al., 2021). CSLA incorporates both adders and multiplexers in its

structure. Describing CSLA as an alternative to regular adders, it emphasizes the simultaneous computation of multiple intermediate values, leading to a more rapid addition process. The Carry Select Adder (CSLA), while effective in its function, is noted for its inefficiency in terms of area utilization. This inefficiency arises from the use of multiple Ripple Carry Adder (RCA) pairs, which generate partial sum and carry data by considering carry information. The final sum and carry are then selected using multiplexers (mux) (Balasubramanian and Mastorakis, 2018). To address this issue and enhance area efficiency while minimizing power consumption, the conventional RCA is replaced with a Binary to Excess-1 Converter (BEC) in the regular CSLA. This substitution achieved a more streamlined and resource-efficient design, optimizing the overall performance of the adder. The integration of

¹ Corresponding author: G. Challa Ram
Email: challaram.grandhi@svecw.edu.in

a BEC reduced the area usage and power consumption compared to the traditional approach employing multiple RCAs (Gudala et al., 2021; Patil et al., 2015).

Another most precisely used adder is parallel-prefix adder designed for efficient binary number addition. Unlike traditional ripple-carry adders that process carries sequentially, parallel-prefix adders compute carries signals in parallel, thereby decreasing overall delay and enhancing performance. These adders play a crucial role in high-performance computing applications like microprocessors and digital signal processors, where rapid arithmetic operations are indispensable. They bring advantages in terms of speed, efficiency, and reduced carry propagation delay when compared to conventional adders such as ripple-carry adders. The selection of a specific parallel-prefix adder depends on the application's needs and the desired trade-offs between speed, area, and power efficiency.

The Ling adder (Guo et al., 2023), Han-Carlson adder (Rao et al., 2018), Brent-Kung adder, and Kogge-Stone adder (Penchalaiah and Siva Kumar 2018) belong to the category of parallel-prefix adders, designed to enhance binary addition in digital circuits. The Ling adder utilizes a network of binary full adders and carry-select adders, prioritizing efficiency in terms of speed and minimized carry propagation delay. The Han-Carlson adder excels in high-speed carry propagation through a tree-based structure. The Brent-Kung adder adopts a hierarchical tree structure, emphasizing low fan-out and a balance between speed and area efficiency. In contrast, the Kogge-Stone adder features a balanced binary tree structure, known for its simplicity, regularity, and a well-balanced combination of speed and area efficiency. The Weinberger adder integrates the concept of parallel carry computation (Varshney and Arya 2019), (Gaur et al., 2019) to boost circuit speed. Each adder provides distinct advantages, catering to various preferences in digital circuit design based on specific application requirements (Priya and Kumar 2013). Until now, several adders (Suganya and Meganathan 2015; Thamizharasan and Kasthuri 2021) have been designed to enhance the performance of the adder. This paper introduces a hybrid adder that is meticulously designed by integrating diverse addition techniques, with the goal of improving the speed of the addition process.

In this paper, Section 2 focuses on detailing the design of the proposed VLSI architecture for the adder. Sections 3 and 4 delve into the presentation of results, discussions, and conclusions.

2. PROPOSED HYBRID ADDER

Designing an energy-efficient hybrid adder involves integrating basic components like Half Adder and Full

Adder, Ripple Carry Adder and the latest adders exploring low-power adder designs, and optimizing with techniques such as clock gating, power gating, and pipeline staging. The choice of semiconductor technology and dynamic voltage scaling are critical, and parallelism, bit-level optimizations, and data-dependent power management contribute to efficiency. Considering error tolerance and employing simulation tools for power analysis are essential, followed by rigorous testing and continuous optimization based on real-world performance feedback. The proposed hybrid adder is designed based on Power efficient adders such as different adders such as Hancarlson Adder (Lakshmanan et al., 2006), Ling and Weinberger adder (Sudhakar et al., 2012) at different stages (Ram et al., 2023), (Raju et al., 2023). Considering the major constraints, architecture of the 16-bit hybrid adder is proposed which is depicted in Figure1, is built upon the SQRT CSELA architecture and is organized into five distinct groups, each with a designated function in the addition process:

First and Second Groups:

The inputs for these groups encompass bits 0-1, a carry input (cin), and bits 2-3. Utilizing 2-bit Ripple Carry Adders (RCA), these groups perform the addition operation on their respective inputs.

Third Group:

Comprising a 3-bit Weinberger adder, a Binary to Excess-1 Converter (BEC) for input carry 'one' to reduce the area and a Multiplexer (MUX) unit to select the final output. Responsible for handling inputs from bits 4-6, the MUX unit selects the output from either the Weinberger adder or the BEC based on the specific requirements of the addition process.

Fourth Group:

Similar to the third group in structure, with a 4-bit Hancarlson adder replacing the Weinberger adder. This group is designed to add inputs from bits 7-10.

Fifth Group:

Resembling the structure of the third and fourth groups, the fifth group integrates a 5-bit Ling adder, a Binary to Excess-1 Converter (BEC) for input carry 'one' to reduce the area and a Multiplexer (MUX) unit to select the final output. It is specifically configured to add inputs from bits 11-15.

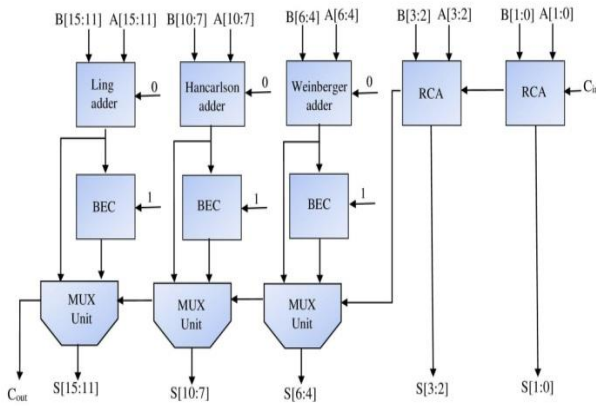


Figure 1. Architecture of Proposed 16-bit Hybrid Adder.

In summary, the hybrid adder employs a combination of various adder types, including 2-bit RCA, 3-bit Weinberger, 4-bit Hancarlson, and 5-bit Ling adders. Each group is strategically designed to handle a specific range of input bits, optimizing the addition process for different segments of the 16-bit input (Parvathi 2020). This approach is intended to enhance efficiency and speed in binary addition within the context of a 16-bit computational system.

3. ANALYSIS OF ADDER ARCHITECTURE USING THEORITICAL APPROACH

The analysis of the various adder architectures using a theoretical approach is tabulated in Table 1 which involves assessing the estimated delay and area metrics provided for each design. Here's a summary of the analysis based on the theoretical approach:

i. Ripple Carry Adder (RCA):

High delay may become impractical for large bit-widths due to carry propagation.

ii. Linear CSELA:

Speed is improved compared to RCA due to parallelism. The area is higher than RCA due to additional components.

iii. Modified Linear CSELA:

Slight reduction in area compared to Linear CSELA due to incorporation of BEC.

iv. SQRT CSELA:

Improved performance in terms of area and delay compared to Linear CSELA.

v. Modified SQRT CSELA with BEC:

Similar to SQRT CSELA, potentially modified for optimizations which balances delay and area considerations.

vi. Ling Based Linear CSELA:

Incorporates Ling adder for potentially faster linear addition with moderate increase compared to Linear CSELA.

vii. Ling Based SQRT CSELA:

Utilizes Ling adder in square root carry select architecture with balanced approach between delay and area.

viii. Hancarlson Based Linear CSELA:

Utilizes Hancarlson adder for potential improvement in linear addition. With slight increase in area due to additional components.

ix. Hancarlson Based SQRT CSELA:

Utilizes Hancarlson adder in square root carry select architecture aims for a balance between delay reduction and moderate area increase.

x. Weinberger Based Linear CSELA:

Incorporates Weinberger adder for linear addition with relatively higher area due to additional components.

xi. Weinberger Based SQRT CSELA:

Uses Weinberger adder in square root carry select architecture for Potential trade-off between delay, area, and additional features.

The Proposed Hybrid Adder aims for a balance between delay reduction and moderate area increase.

Table 1. Theoretical Delay and Area of Adders

Adder	Theoretical Delay	Theoretical Area
Ripple Carry Adder (RCA)	$T_{XOR} + 30T_{OR} + 15T_{AND}$	$32A_{XOR} + 48A_{AND} + 32A_{OR}$
Linear CSELA	$3T_{MUX} + 4T_{AND} + 8T_{OR}$	$15A_{MUX} + 47A_{XOR} + 3A_{XNOR} + 69A_{AND} + 47A_{OR}$
Modified Linear CSELA	$3T_{MUX} + 2T_{XOR} + 4T_{AND} + 5T_{OR}$	$15A_{MUX} + 38A_{XOR} + 51A_{AND} + 29A_{OR} + 3A_{NOT}$
SQRT CSELA	$T_{MUX} + 2T_{XOR} + 4T_{AND} + 6T_{OR}$	$18A_{MUX} + 48A_{XOR} + 4A_{XNOR} + 70A_{AND} + 48A_{OR}$
Modified SQRT CSELA	$T_{MUX} + 3T_{XOR} + 4T_{AND} + 6T_{OR}$	$18A_{MUX} + 38A_{XOR} + 50A_{AND} + 28A_{OR} + 4A_{NOT}$
Ling Based Linear CSELA	$4T_{MUX} + 2T_{XOR} + 4T_{AND} + T_{OR}$	$25A_{MUX} + 38A_{XOR} + 50A_{AND} + 45A_{OR} + 3A_{NOT}$
Ling Based SQRT CSELA	$3T_{MUX} + 2T_{XOR} + T_{AND} + T_{OR}$	$26A_{MUX} + 38A_{XOR} + 48A_{AND} + 43A_{OR} + 4A_{NOT}$
Hancarlson Based Linear CSELA	$3T_{MUX} + 2T_{XOR} + 3T_{AND} + 3T_{OR}$	$15A_{MUX} + 38A_{XOR} + 58A_{AND} + 20A_{OR} + 3A_{NOT}$
Hancarlson Based SQRT CSELA	$4T_{MUX} + 2T_{XOR} + T_{AND} + T_{OR}$	$18A_{MUX} + 38A_{XOR} + 53A_{AND} + 18A_{OR} + 4A_{NOT}$
Weinberger Based Linear CSELA	$4T_{MUX} + 2T_{XOR} + 2T_{AND} + T_{OR}$	$33A_{MUX} + 33A_{XOR} + 14A_{AND} + 8A_{OR} + 20A_{AND} + 24A_{NOR} + 3A_{NOT}$
Weinberger Based SQRT	$5T_{MUX} + T_{XOR} + T_{AND} + T_{OR} + T_{NOT}$	$33A_{MUX} + 32A_{XOR} + 16A_{AND} +$

CSELA		$10A_{OR} + 17A_{NAND} + 18A_{NOR} + 41A_{NOT}$
Proposed Hybrid adder	$3T_{MUX} + 4T_{AND} + 5T_{OR}$	$20A_{MUX} + 37A_{XOR} + 50A_{AND} + 31A_{OR} + 3A_{NAND} + 3A_{NOR} + 8A_{NOT}$

4. PERFORMANCE ANALYSIS OF SENSOR

The Table 2 provides a comparison of different adder designs based on LUT count and power consumption. The proposed hybrid adder seems to have relatively lower power consumption (11.532W) compared to some other designs.

Table. 2. Practical Comparative analysis of Power, LUT'S for various adders.

Adder	LUTs	Power(W)
Ripple Carry Adder (RCA)	16	11.014
Linear CSELA	30	11.615
Modified Linear CSELA	28	11.644
SQRT CSELA	33	12.017
Modified SQRT CSELA	36	11.680
Ling Based Linear CSELA	29	11.629
Ling Based SQRT CSELA	30	11.400
Hancarlson Based Linear CSELA	29	11.659
Hancarlson Based SQRT CSELA	32	11.683
Weinberger Based Linear CSELA	28	11.553
Weinberger Based SQRT CSELA	33	11.634
Proposed Hybrid adder	29	11.532

From Table 3, the proposed hybrid adder outperforms the other designs in terms of setup delay, hold delay, and PDP, indicating superior performance and energy efficiency. Lower setup and hold delays suggest faster and more stable operation. The lower PDP for the proposed hybrid adder implies a more efficient use of power resources compared to the other adders in the list. In practical terms, the proposed hybrid adder seems to be a promising design if the goal is to achieve a balance between speed and power efficiency in adder circuits.

Table. 3. Practical Comparative analysis of Delay and PDP for various adders.

Adder	Setup Delay(ns)	Hold Delay(ns)	PDP
Ripple Carry Adder (RCA)	11.359	2.448	125.108
Linear CSELA	9.662	2.511	112.224
Modified Linear CSELA	10.144	2.498	118.117
SQRT CSELA	9.339	2.511	112.227

Modified SQRT CSELA	9.227	2.417	107.771
Ling Based Linear CSELA	9.997	2.474	116.255
Ling Based SQRT CSELA	9.987	2.477	113.852
Hancarlson Based Linear CSELA	10.140	2.514	118.222
Hancarlson Based SQRT CSELA	9.222	2.484	107.741
Weinberger Based Linear CSELA	10.166	2.496	117.448
Weinberger Based SQRT CSELA	9.230	2.512	107.382
Proposed Hybrid adder	9.096	2.467	104.895

5. HARDWARE IMPLEMENTATION

The process of implementing and validating a hybrid adder design is outlined with meticulous detail, involving the use of Verilog Hardware Description Language (HDL) and the Vivado 2017.2 toolset. Simulation is conducted using Vivado ISIM, and synthesis takes place on a system equipped with an INTEL Core i5 processor boasting a 64-bit operating system, 16GB of RAM, and a clock frequency of 2.50GHz.

For the validation of the proposed design on the ZedBoard Zynq Evaluation and Development Kit (xc7z020clg484-1), crucial components from the IP Catalog, namely the Virtual Input Output (VIO) and Integrated Logic Analyzer (ILA) packages, are employed. The VIO package plays a pivotal role in configuring inputs and outputs, establishing a virtual environment conducive to configuration. On the other hand, the ILA package designates all probes as inputs, facilitating the capture and subsequent analysis of internal signals within the adder during the verification process.

The ZedBoard is selected as a robust platform for the implementation and validation of the hybrid adder design. Leveraging the VIO and ILA packages enhances the verification process by providing the capability to analyze input-output relationships and internal signals that are critical for the proper functioning of the adder. In the implementation phase, a Verilog file undergoes meticulous creation and modification for the purpose of port mapping. This involves the selection of the clock pin as a Y9 package pin, with I/O standards set to LVCMOS33 as shown in Figure 2.

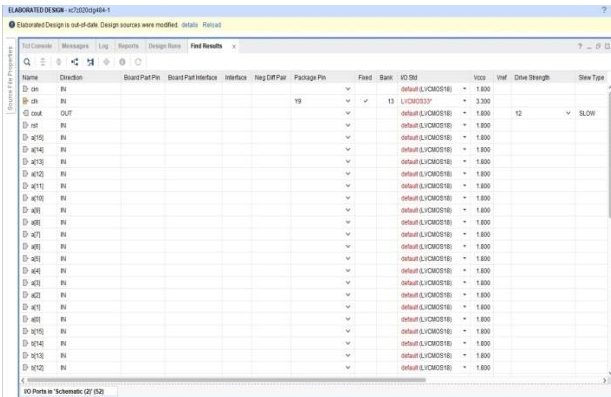


Figure 2. Clock pin selection.

Successful Bitstream generation follows this stage. The ZedBoard is then powered on, and the connection is established through hardware management. The implemented hybrid adder architecture is visually represented in Fig. 3.

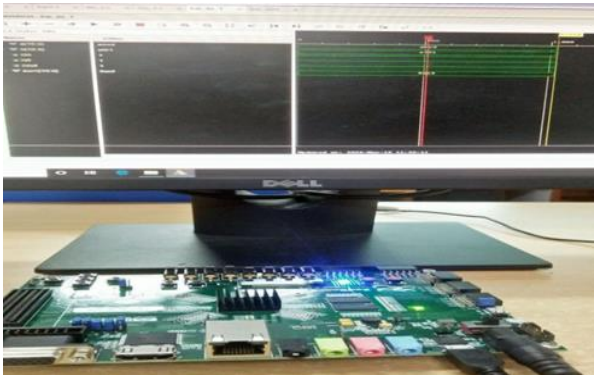


Figure 3. Implementation of hybrid adder on Zedboard.

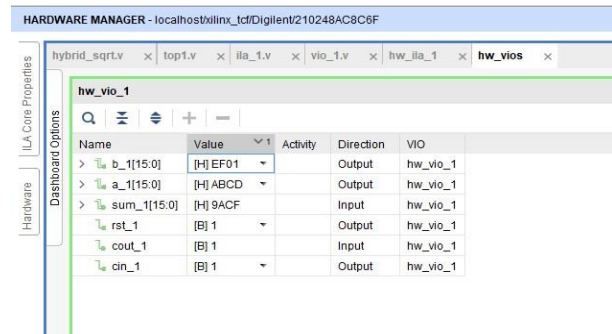


Figure 4. Hardware manager to provide inputs.

Subsequently, in Fig. 4, all pins are selected, inputs are modified, and the run trigger is activated, leading to the presentation of simulation results in Fig. 3. This comprehensive process ensures a thorough evaluation and validation of the proposed hybrid adder design.

6. CONCLUSION

In this research, an energy-efficient hybrid adder is proposed, designed utilizing Ling, Hancarlson, Weinberger Adders, and BEC Circuit. The resultant hybrid adder demonstrates reduced delay and power delay product. The architecture of the hybrid adder is synthesized and simulated using Xilinx Vivado 2017.2 isim tool, with subsequent hardware implementation on zedboard. Experimental results reveal a speed enhancement of 19.92%, 5.86%, 10.33%, 2.60%, 1.42%, 9.01%, 8.92%, 10.29%, 1.37%, 10.52%, and 1.45% when compared To Ripple Carry Adder, Linear Csela, Modified Linear CSELA, SQRT CSELA, Modified SQRT CSELA, Ling-Based Linear CSELA, Ling-Based SQRT CSELA, Hancarlson-Based Linear CSELA, Hancarlson-Based SQRT CSELA, Weinberger-Based Linear CSELA, And Weinberger-Based SQRT CSELA respectively.

References:

- Anil Kumar, U., Bharadwaj, S. V., Pattaje, A. B., Nambi, S., & Ahmed, S. E. (2023). CAAM: Compressor-Based Adaptive Approximate Multiplier for Neural Network Applications. *IEEE Embedded Systems Letters*, 15(3), 117-120. doi: 10.1109/LES.2022.3199273
- Balasubramanian, P., & Mastorakis, N. (2018). Performance comparison of carry-lookahead and carry-select adders based on accurate and approximate additions. *Electronics*, 7, 369. doi: 10.3390/electronics7120369
- Gaur, N., Mehra, A., Kumar, P., & Kallakuri, S. (2019). 16-bit power efficient carry select adder. *Sixth International Conference on Signal Processing and Integrated Networks*, 558-561. doi: 10.1109/SPIN.2019.8711565
- Gudala, N. A., Ytterdal, T., Lee, J. J., & Rizkalla, M. (2021). Implementation of high-speed and low-power carry select adder with BEC. *International Midwest Symposium on Circuits and Systems*, Lansing, MI, USA, 377-381. doi: 10.1109/MWSCAS47672.2021.9531750
- Guo, P., Xie, G., Chen, X., Han, J., & Zhang, Y. (2023). A variable latency Ling adder based on Brent-Kung parallel-prefix topology. *23rd International Conference on Nanotechnology*, Jeju City, Korea, 1-5. doi: 10.1109/NANO58406.2023.10231157
- Koyada, B., Meghana, N., Jaleel, M. O., & Jeripotula, P. R. (2017). A comparative study on adders. *International Conference on Wireless Communications, Signal Processing and Networking*, Chennai, India, 2226-2230. doi: 10.1109/WiSPNET.2017.8300155

- Lakshmanan, A., Meamar, & Othman, M. (2006). High-speed hybrid parallel-prefix carry-select adder using Ling's algorithm. *International Conference on Semiconductor Electronics*, 598-602. doi: 10.1109/SMELEC.2006.380702
- Parvathi, M. (2020). High-Accurate, Area-Efficient Approximate Multiplier for Error-Tolerant Applications. *Soft Computing: Theories and Applications, Advances in Intelligent Systems and Computing*, 1154, 91–102. doi: 10.1007/978-981-15-4032-5_10
- Patil, N., Joshi, A., Eskandari, N., & Nikoubin, T. (2015). RCA with conditional BEC in CSLA structure for area-power efficiency. *Sixth International Conference on Computing, Communication and Networking Technologies*, Dallas-Fortworth, TX, USA, 1-4. doi: 10.1109/ICCCNT.2015.7395199
- Penchalaiah, U., & Siva Kumar VG. (2018). Design of high-speed and energy-efficient parallel prefix Kogge Stone adder. *International Conference on System, Computation, Automation and Networking*, Pondicherry, India, 1-7. doi: 10.1109/ICSCAN.2018.8541143
- Priya, R., & Kumar, J. S. (2013). Implementation and comparison of effective area efficient architectures for CSLA. *International Conference on Emerging Trends in Computing, Communication and Nanotechnology*, Tirunelveli, India, 287-292. doi: 10.1109/ICE-CNN.2013.6528510
- Raju, G. R. L. V. N. S., Nikitha, T. N., Ram, G. C., Chary, U. G., Vardhan, J. N. V., & Kumar, J. D. (2023). Area optimized efficient multiplication using modified round square approximation. *International Conference on Integrated Circuits and Communication Systems*, Raichur, India, 1-5. doi: 10.1109/ICICACS57338.2023.10099920
- Ram, G. C., Subbarao, M. V., Varma, D. R., & Kumar, M. P. (2023). Delay enhancement of Wallace tree multiplier with binary to excess-1 converter. *Fifth International Conference on Smart Systems and Inventive Technology*, Tirunelveli, India, 113-117. doi: 10.1109/ICSSIT55814.2023.10061043
- Rao, E. J., Ramanjaneyulu, T., & Kumar, K. J. (2018). Advanced multiplier design and implementation using Hancarlson adder. *International Conference on Intelligent and Innovative Computing Applications*, Mon Tresor, Mauritius, 1-5. doi: 10.1109/ICONIC.2018.8601252
- Sreevani, M., Lakshmanachari, S., Manvitha, B., Pravalika, Y. J. N., Praveen, T., Vijay, V., & Ratna Vallabhuni, R. (2021). Design of Carry Select Adder Using Logic Optimization Technique. *International Conference on Advances in Computing, Communication, and Control*, Mumbai, India, 1-6. doi: 10.1109/ICAC353642.2021.9697189.
- Sudhakar, S. M., Chidambaram, K. P., & Swartzlander, E. E. (2012). Hybrid Han-Carlson adder. *55th International Midwest Symposium on Circuits and Systems*, Fukuoka, Japan, 818-821. doi: 10.1109/MWSCAS.2012.6292146
- Suganya, R., & Meganathan, D. (2015). High performance VLSI adders. *Third International Conference on Signal Processing, Communication and Networking*, Chennai, India, 1-7. doi: 10.1109/ICSCN.2015.7219919
- Thamizharasan, V., & Kasthuri, N. (2021). Design of proficient two operand adder using hybrid carry select adder with FPGA implementation. *IETE Journal of Research*. doi: 10.1080/03772063.2022.2071771.
- Varshney, N., & Arya, G. (2019). Design and execution of enhanced carry increment adder using Han-Carlson and Kogge-Stone adder technique: Han-Carlson and Kogge-Stone adder is used to increase speed of adder circuitry. *International conference on Electronics, Communication and Aerospace Technology*, Coimbatore, India, 1163-1170. doi: 10.1109/ICECA.2019.8822194

K. Bala Sindhuri

Department of ECE

S. R. K. R Engineering College,
Bhimavaram, India.
kbsindhuri@srkrec.ac.in
ORCID 0000-0001-7892-2062

G. Challa Ram

Department of ECE

Shri Vishnu Engineering College for
Women, Bhimavaram, India.
challaram.grandhi@svecw.edu.in
ORCID 0000-0002-3790-1318

M. Venkata Subbarao

Department of ECE,

Shri Vishnu Engineering College for
Women, Bhimavaram, India.
mvssubbarao@svecw.edu.in
ORCID 0000-0001-5840-2190

M. Aravind kumar

Department of ECE,

West Godavari Institute of Science and
Engineering, Tadepalligudem, India.
drmaravindkumar@gmail.com
ORCID 0000-0003-4718-5738

B. Kalivaraprasad

Department of ECE,

Koneru Lakshmaiah Education
Foundation (KLEF), Vaddeswaram, India
baditakali@gmail.com
ORCID 0000-0001-7817-2062



ASSESSMENT OF DRIVING BEHAVIOUR AT TOLL PLAZA UNDER HETEROGENEOUS TRAFFIC CONDITIONS USING VISSIM

V L N Murthy G¹
Ramprasad Naik D
Anjankumar M
Gireesh Kumar Pala

Keywords:

Traffic Simulation; Heterogeneous Traffic; Calibration; Driving behavior; VISSIM.

A B S T R A C T

Traffic Simulating and Evaluating Traffic Patterns at heterogeneous traffic Situations in the Indian Context is extremely increasing. Many researchers from all over the world are trying to explore driving behavior and simulate traffic flow conditions under heterogeneous traffic environments. Simulating Traffic at a Microscopic Level with VISSIM is used in this study identifying every element that contributes to traffic at various traffic stages. Further, the VISSIM model was calibrated based on the desired safety distance and car-following theory. Traffic metrics including flow volume, speed, acceleration, and deceleration were all input parameters in the VISSIM model for simulation purposes. Furthermore, the analysis part of different cases of driving behavior models, such as the default case, and calibration values based on measurement were compared to find out if there was a significant improvement. Moreover, the linear regression model was proposed to understand the calibrated model versus the default case parameters, and it was identified that it is significant when plotting the data. The proposed study results highlighted driving behavior under heterogeneous traffic conditions using VISSIM at Toll Plaza.

© 2021 Published by Faculty of Engineering



¹ Corresponding Author: G V L N Murthy
e-mail: gvlnmurthy98@gmail.com

1. INTRODUCTION

In India, there is significant improvement in the highway network, and it is essential to have national highways as long-distance roads for any nation. The improvement of infrastructure will be generally considered based on the toll plazas, which significantly raises the financial requirements for such an improvement of the road network. The driver's behavior abruptly changes at toll plazas, either to minimize their queue length or due to multiple services at toll plaza vehicular movement patterns. Generally, the new highway has advantages like minimizing average travel time on its route; however, the toll plaza's blockages at tolls. The adverse effects of heavy vehicles include environmental damage and fuel loss (Wang, 2017; Mittal and Sharma, 2020; Mittal and Sharma, 2022). Moreover, waiting times and queue length have been widely studied by researchers (Sharma et al., 2010), including queue length at tolls. The driving behavior at tolls is less explored under improved toll operations such as payments by Radio Frequency Identification (RFID) system, which tries to minimize the delay at tolls. Recently, in India, the National Highway Authorities of India (NHAI) have implemented FASTag, an RFID-enabled toll collection system, to streamline traffic flow and reduce waiting times at toll plazas.

Typically, toll plazas are organized into three key zones: merging areas, queuing areas, and toll booths, facilitating a systematic approach to traffic management. Further, in order to minimize the queue length, a growth in the number of toll booths has been observed, and such scenario merging areas are critical, which creates queues in the queuing area (Kim, 2009; Abdel Wahab, 2017). There are several contributing factors to effectively manage queue formation during peak hours, a microscopic simulation of toll plaza dynamics is required to explore the contributing factors that influence queue formation. Furthermore, attention to microscopic simulation for traffic analysis has intensified, as simulation models prove adept at scrutinizing traffic patterns, vehicle types, and queuing patterns through a refined calibration process. Moreover, it requires a high-accuracy calibration process that can forecast traffic for various complex conditions with varied driving behavior. Within this framework, the study specifically concentrates on the driving behavior observed at the toll plaza based on Verkehr in Städten – simulation model (VISSIM) simulation software.

2. LITERATURE REVIEW

The study on driving behavior has been considered an essential approach for identifying solutions to improve roadway levels of services by reducing congestion, delays, and accidents. Driving behavior modeling has been developed to measure the effects of individual differences in traffic flow characteristics, driving behavior, and their interaction. Driving behavior parameters are calibrated by micro-simulation and subsequently used to develop driving behavior models. In the recent past, to account for additional traffic situations and driver behaviors, researchers have sought to calibrate several microscopic tools (Al-Deeket al., 1996; Al-Deeket al., 2000; Wang et al., 2018; Mehar et al. 2014).

Researchers have explored the waiting and traffic queues at toll plazas using PTV VISSIM and generating different scenarios for improving the existing congestion of toll plazas (Al-Deek et al., 2000; Dubedi et al., 2012). They have used Electronic Toll Collection (ETC) in toll plazas to increase the efficiency of revenue collection of toll plazas as manual collection is time consuming process before using ETC. Lane configuration in mixed traffic approach-based approach has been used. The author found that having lanes more or less than required also leads to traffic congestion in the toll plaza. The result shows that using E-tag in lanes gives an improvement of 75.9 %, 93.6% and 57.7% in throughputs, waiting time and queue length respectively (Dubedi et al., 2012). Researchers have used PTV VISSIM for simulate the existing condition of toll plazas and generate some scenarios for decreasing waiting time and also checking calibration results with existing results (Aycin et al., 2009; Ozbay 2005). From the result, it was found that calibrated parameters like queue length, average service time, etc. are the same as existing parameters with plus or minus 2% error and it was also found that for exempted and fast-tag vehicles average service time that is waiting time is less compared to card or cash payment. Studies have explored the effect of toll booth shape on waiting time and queue length. For this, the PTV VISSIM microsimulation tool was used to represent the Kurnakoy toll booth. It was discovered that this operation was the best since delays caused by barriers and delays caused by bottlenecks were avoided (Neuhold et al., 2019).

The suggested approach by researchers involves the integration of queuing theory and VISSIM for traffic simulation, aiming to estimate traffic flow conditions at

toll plazas (Ceballos and Curtis, 2004). Studies have analyzed traffic at toll plazas based on the AIMSUN simulation model to figure out the complete financial yield from toll collections (Poon and Dia, 2005). The time taken for tax collection at toll booths has been a focal point in research studies, serving as a crucial metric for evaluating traffic flow (Poon and Dia, 2005). Researchers have estimated driver behavior based on toll plaza traffic and driver behavior analyzed based on the number of lanes and vehicle types (Klodzinski et al., 2002, 2007). Studies have focused on understanding the dynamics of vehicle lane selection patterns at toll booths through the implementation of microsimulation-based traffic simulation models (Dubedi et al., 2012). Researchers have explored the effect of vehicle speeds on capacity on multilane highways (Velmurugan et al., 2010).

Researchers have engineered a simulation framework for toll plazas for varied lane configurations and vehicle characteristics (Al-Deek et al. 1996; 2000). The study incorporated multiple factors, namely vehicle speed, acceleration, and deceleration, with a focus on analyzing traffic flow and delays as the output variables. The exploration of driving behavior in this study centered on lane choice, with a specific emphasis on minimizing the queue length at the toll booth. Further, researchers have used the VISSIM to analyze the delays at tolls and queuing analysis was carried out (Ceballos and Curtis, 2004). Researchers have developed a traffic simulation model corresponding to a lane-changing

model (Mahdi et al., 2019). These existing studies have proven that micro-simulation is an effective tool for analyzing driver behaviour in heterogeneous traffic conditions. Researchers have studied vehicle speed-flow relationships on the multilane highway to analyze the effect of speed on the capacity of various roadways using micro-simulation tools (Velmurugan et al., 2010). Researchers have estimated the passenger equivalency factor based on the traffic flow models based on various categories of vehicles using micro-simulation tools (Coelho et al., 2005). In contrast to earlier studies conducted in developing countries, this research focused on analyzing driving behavior in lane selection utilizing PTV VISSIM. Additionally, driver behavior parameters were calibrated within the VISSIM model at the toll plaza.

3. METHODOLOGY

The proposed procedure for the measurement of driving behavior parameters and calibration of different driving behavior values is based on microscopic traffic flow simulation. The proposed study methodology is shown in Figure 1. The study methodology involves selecting the study area, conducting field data collection, and extracting relevant data. Further development of model calibration, including network building, introducing input parameters to the model, appropriate driving behavior model selection, calibration, and validation process using VISSIM PTV.

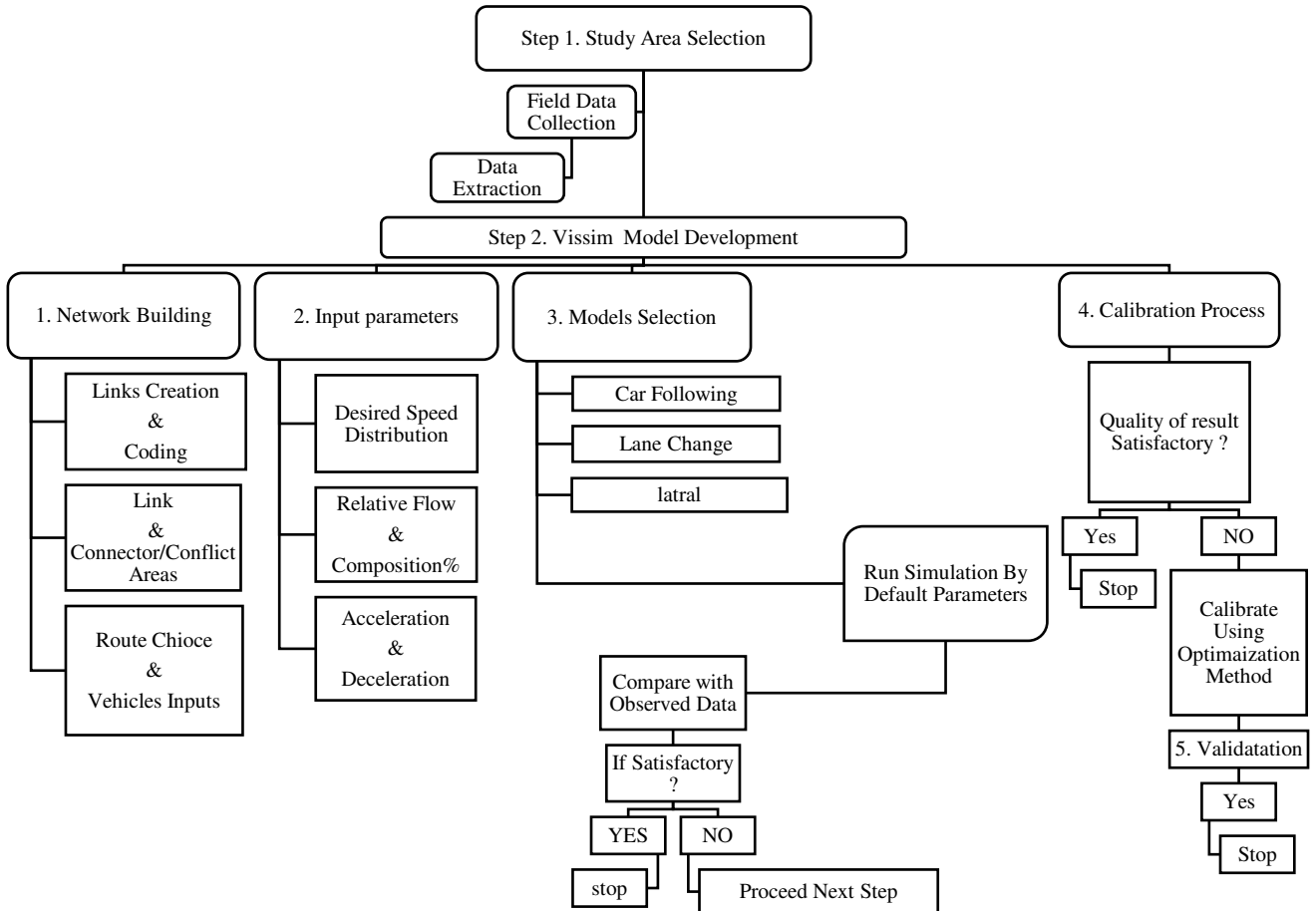


Figure 1. The envisioned research methodology

4. STUDY AREA AND DATA COLLECTION

Traffic data collection took place at the Panthangi toll plaza located on NH-65, 70 kilometres from Hyderabad, India, and a satellite image (bird view) is shown in Figure 2. Data was gathered from morning to evening, encompassing peak hours (7:00 AM to 8:00 PM). The

overall count of four cameras was used; two were at the entrance and two were at the exit points of Toll Plaza to capture a video graphic image of all lanes of Toll Plaza. The traffic extractor software was used to extract the following data: vehicular traffic, speed, acceleration, and deceleration at entry, as well as exit points of the toll plaza.



Figure 2. Satellite Image of Study Area

LAYOUT OF PANTHANGI TOLL PLAZA

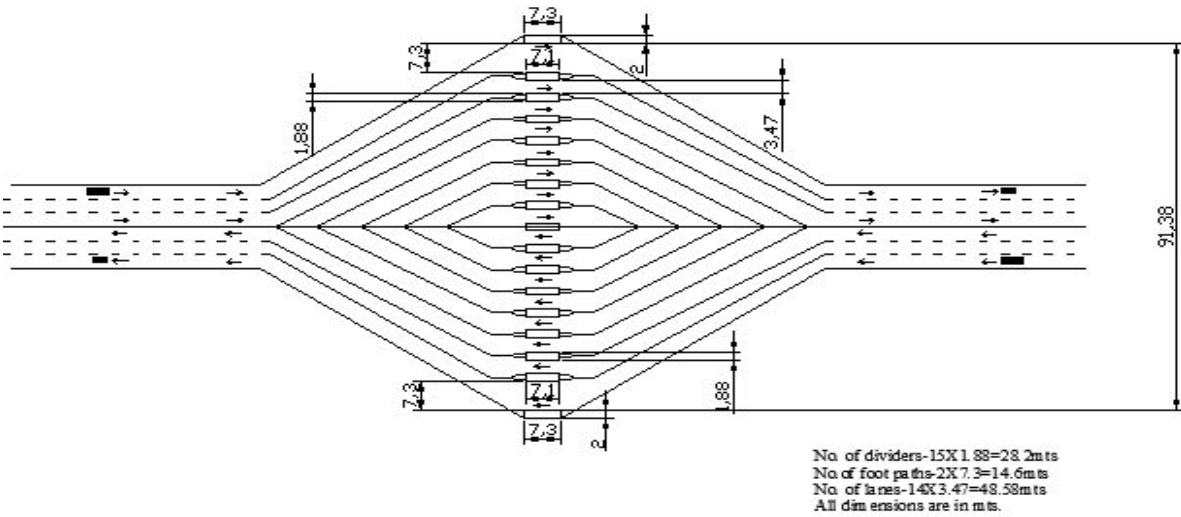


Figure 3. Layout Image of Study Area

From the video survey data, the gathered data includes details such as the quantity of traffic flow, types of traffic composition, parameters related to velocity, dynamics of acceleration, patterns of deceleration, specifications of vehicles, characteristics of road structure, attributes of roadway geometry, and configuration of the transportation network were extracted. The extracted traffic volume data as well as average vehicle speed are presented in Table 1, and the

traffic composition is presented in Figure 4. From the survey results, it is observed that 40% of the traffic composition is small cars that pass through the toll plaza, followed by big cars with 22%. The residual vehicular movement is constituted by heavy-duty vehicle categories, incorporating light commercial vehicles, buses, heavy commercial vehicles, mixed-axle vehicles and trailer-type vehicles.

Table 1. Traffic Flow and Speed Data observed at Panthangi Toll Plaza

S.NO	Traffic Flow				Speed	
	Traffic Flow	NO	PCU	Traffic Composition %	Average (m/s)	KMPH
1	Small Car	525	525	40	13.2	48
2	Big Car	294	294	22.4	11.25	41
3	LCV	168	168	12.8	13.5	49
4	HCV	189	567	14.4	9.8	35
5	Bus	60	210	4.6	10	36
6	MAV	63	189	4.8	8	29
7	Trailer	12	36	1	7.5	27
	Total	1311	1989	100		

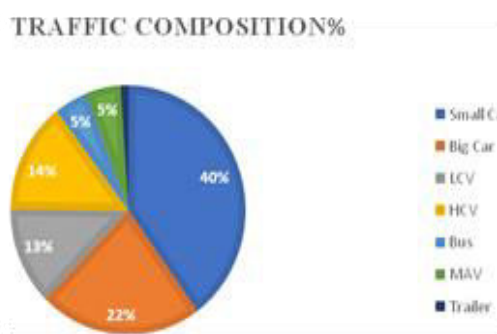


Figure 4. Traffic Composition at Panthangi Toll Plaza

From the video survey results, it is observed that the maximum acceleration 4.73 m/sec^2 on extreme toll booth and the minimum acceleration is observed in inner lanes as shown in Table 2. From the deceleration

data, it is observed that the highest deceleration is observed in inner lanes as compared to the extreme lanes maybe when the driver decelerates their vehicles and changes lanes to reduce the queuing.

Table 2. Traffic Acceleration and Deceleration Data Observed at Panthangi Toll Plaza

Acceleration			Deceleration		
Mean Acceleration (m/sec^2)	Minimum	Maximum	Mean Deceleration (m/sec^2)	Minimum	Maximum
0.056	0	4.73	-0.6	-4.36	0
0.056	0	4.73	-0.605	-4.37	0
0.0019	0	3.9	-0.63	-4.34	0
0.0069	0	3.5	-0.63	-4.208	0
0.0059	0	3.5	-0.47	-4.659	0
0.0088	0	3	-0.437	-4.65	0
0.0088	0	3	-0.42	-4.012	0

5. MICRO SIMULATION MODEL DEVELOPMENT

The VISSIM micro-simulation model was developed and calibrated based on the selected parameters of vehicular movement and speed. The network of the simulated model of the toll plaza is shown in Figure 5. In the initial step, the model is simulated with default parameters, and from the simulated model, the traffic comparison as well as speed are observed and contrasted with the field data. Executing the calibration

process for the simulation model, route choice, car following model of Wideman74, and safety additive distances were considered, and the vehicle composition and relative flow were observed as well as compared with field observed data.

According to field observations, the state of conflict areas is determined. As shown in Figure 6, there are

four different types of conflict areas in the VISSIM model: one waits for 2, two holds for 1, undecided, and passive. The first two states imply that vehicles on major and minor routes are given preference when entering a conflict zone. When the major street crosses the minor street, these should be utilized. Use either indeterminate or passive when two major highways intersect. Undetermined means that traffic on both crossing roads behaves as though it were a single link. The modeling of traffic movement at merging and diverging portions considered this situation of

conflicting regions. A passive state assumes that no priority is allocated at all, which will lead to vehicle collisions during the simulation run. As soon as the simulation model notices the conflict zones where traffic from intersecting roadways collides, it automatically assigns itself this classification. This status must also be determined based on the observations made in the field and may differ from one road facility to another.

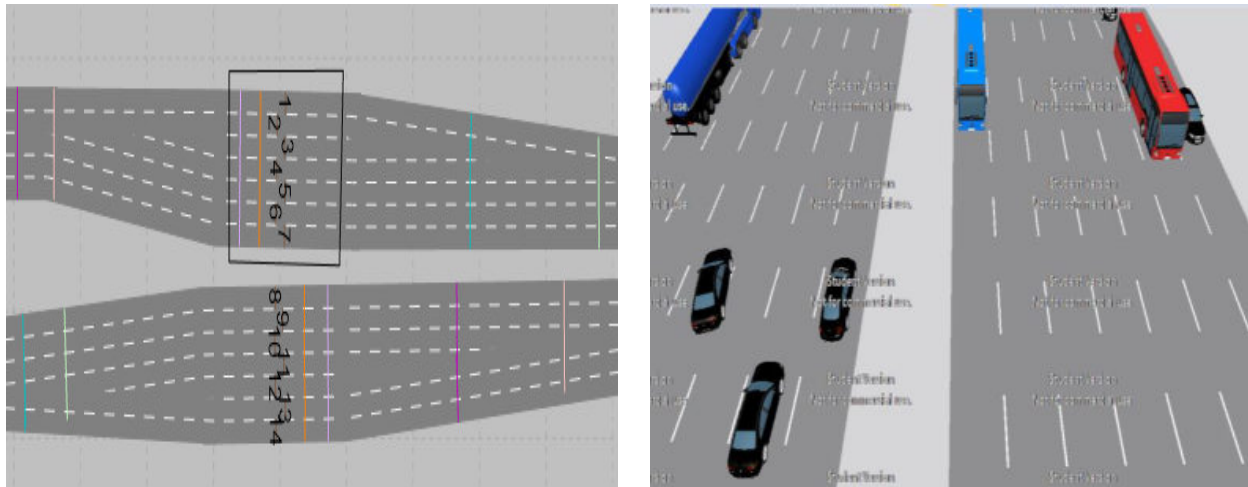


Figure 5. The VISSIM Network of the Simulated Toll Plaza

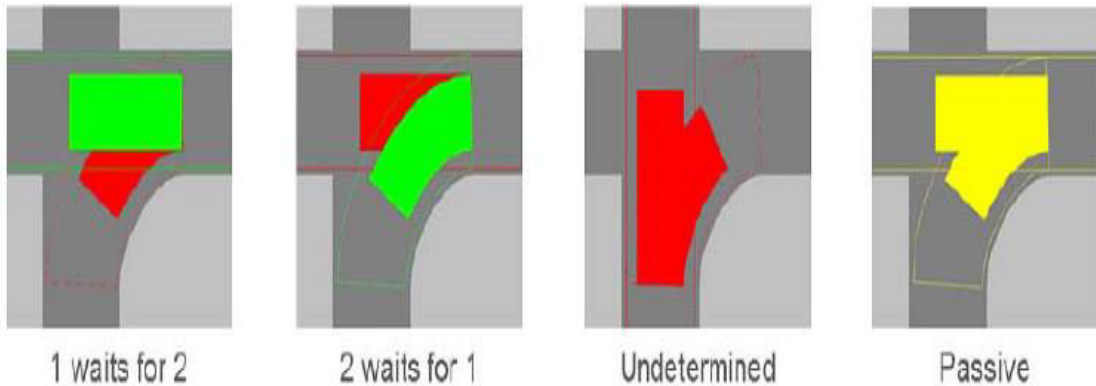


Figure 6. States of Conflict Areas in Simulated Model

For the study according to Indian traffic conditions, the traffic composition based on the Indian scenario was introduced and applied to the model. Vehicle composition in the model, relative flow, and speed measures were calibrated according to the field-observed data. The driving behavior and link behavior models were calibrated using default values. Also, data

collection points at the link sections and link evaluation parameters were introduced for the model. The result obtained from the micro-simulation was configured and evaluated using default parameters. Urban motorized vehicle driving behaviors were introduced for each link (see Table 3).

Table 3. Default Parameter for Driving Behaviour (Wiedemann 74)

Wiedemann 74 Parameters		Description	Value	
Following	Look head distance	Minimum	0.00 m	
		Maximum	250.00 m	
		No interaction objects	4	
		No interaction vehicles	99	
	Look back distance	Minimum	0.00 m	
		Maximum	150.00 m	
	Behavior during recovery from speed breakdown (Slow recovery)	Speed	60.0%	
		Acceleration	40.0%	
		Safety distance	110.0%	
		Distance	2000.00 m	
	Standstill distance for static obstacles	0.50 m		
	Model Parameter	Range		
Car Following Model	(AX)Average Standstill Distance	2.00 m		
	Additive Part of a Safety distance	2.00 m		
	Multiplicative Part of safety Distance	3.00 m		
Lane Change	Necessary lane changes (route)	Parameter	Following Vehicle	Trailing Vehicle
		Maximum Deceleration	-4.00m/s ²	-3.00 m/s ²
		-1 m/s ² per distance	100.00m	100.00m
		Accepted Deceleration	-1.00 m/s ²	-1.00 m/s ²
	Waiting Time before diffusion	60.00 sec		
	Min clearance (front/rear)	0.50 m		
	To the slower lane, if the collision time is above	11.00 sec		
	Safety Distance reduction factor	0.60		
	Maximum Deceleration for cooperative breaking	-3.00 m/s ²		
	Cooperative lane change	Maximum speed difference	10.80 Km/h	
		Maximum Collision time	10.00 sec	
		Max speed	3.00 Km/h	
	Rear Correction of lateral positions	Active during a time period from	1.00 sec	10.00 sec

6. CALIBRATIONS AND VALIDATIONS

This study incorporates the Weidman-74 driving behavior model in the context of varied traffic conditions. The car-following model's safety distance is established by referencing prior research, which considers parameters such as the average standstill distance, the additive element of the safety distance, and the multiplicative component of the safety distance

(Matthew and Radhakrishnan, 2010). These values were chosen by the results of the trial-and-error procedure and the traffic patterns in the chosen research region. The calibrated results of additive safety distance are presented in Table 4. The AX additive and BX multiplicative distances were computed based on equations 1 to 8.

Table 4. Calibrated Safety Distance Parameters for Different Vehicular Categories

Vehicles Type	AX	BX Additive	BX Multiplicative
Small Car	0.90	0.70	0.50
Big Car	0.90	0.50	0.40
MAV	1	0.5	1
Bus	1.00	0.50	1.00

HCV	1.00	0.50	1.00
LCV	1.00	0.50	1.00
Trailer	1	0.5	1

The calculated safety margin, identified as d, is computed as:

$$d = ax + bx \quad (1)$$

$$\text{Where } bx = (bx_{add} + bx_{mult} * z) * \sqrt{v} \quad (2)$$

In this context, v represents the speed of the vehicle in meters per second, while z is a value within the range of 0 to 1. This value follows a normal distribution centered around 0.5, with a standard deviation of 0.15..

$$Ax(\text{mixed}) = Ax.\text{Car} * \% \text{car} + Ax.\text{Big car} * \% \text{Big Car} + AxLCV * \% \text{LCV} + AxHCV * \% \text{HCV} + AxBus * \% \text{Bus} + AxMAV * \% \text{MAV} + Ax \text{ Trailer} * \% \text{Trailer} \quad (3)$$

$$bxadd(\text{mixed}) = Bx.\text{Car} * \% \text{car} + Bx.\text{Big car} * \% \text{Big Car} + BxLCV * \% \text{LCV} + BxHCV * \% \text{HCV} + BxBus * \% \text{Bus} + BxMAV * \% \text{MAV} + Bx \text{ Trailer} * \% \text{Trailer} \quad (4)$$

$$\begin{aligned} Bxmulti(\text{mixed}) &= Bx.\text{Car} * \% \text{car} + Bx.\text{Big Car} * \% \text{Big Car} + BxLCV * \% \text{LCV} + BxHCV * \% \text{HCV} \\ &\quad + BxBus * \% \text{Bus} + BxMAV * \% \text{MAV} + Bx \text{ Trailer} * \% \text{Trailer} \end{aligned} \quad (5)$$

By substituting the values, we get,

$$Ax(\text{mixed}) = 0.9(0.4) + 0.9(0.22) + 1(0.012) + 1(0.015) + 1(0.046) + 1(0.048) + 1(0.01) = 0.691 \quad (6)$$

$$\begin{aligned} Bxadd(\text{mixed}) &= 0.7(0.4) + 0.7(0.22) + 0.5(0.012) + 0.6(0.015) + 0.5(0.046) + 0.5(0.048) + 0.5(0.01) \\ &= 0.494 \end{aligned} \quad (7)$$

$$BxMult(\text{mixed}) = 0.5(0.4) + 0.4(0.22) + 1(0.012) + 1(0.015) + 1(0.046) + 1(0.048) + 1(0.01) = 0.42 \quad (8)$$

From the calibrated VISSIM model, the look head distance, look back distance, behavior during recovery, and standstill distance were computed for the following model (see Table 5). The calibrated values pertaining to the average distance during standstill, the additive portion of safety distance, and the multiplicative

segment of safety distance are 0.7, 0.5, and 0.42, respectively. From the lane changing case, it is observed that the minimum clearance (front and rear) and safety distance reduction factor were observed at 0.45m and 0.4 m, respectively.

Table 5. Calibrated Wiedemann – 74 Parameters for Different Vehicular Categories

Wiedemann 74 Parameters		Parameter	Default Value	Calibrated Value
Following	Look head distance	Minimum	0.00 m	30 m
		Maximum	250.00 m	150 m
		No. of interaction objects	4	4
		No. of interaction vehicles	99	25
	Look back distance	Minimum	0.00 m	30
		Maximum	150.00 m	150 m
	Behavior during recovery from speed breakdown (Slow recovery)	Speed	60.0%	
		Acceleration	40.0%	
		Safety distance	110.0%	
		Distance	2000.00 m	
	Standstill distance for static obstacles	0.50 m		
Car Following Model	Model Parameter	Default Value	Calibrated Value	
	(AX)Average Standstill Distance	2.00 m	0.7	
	Additive Part of Safety distance	2.00 m	0.5	
	Multiplicative Part of safety Distance	3.00 m	0.42	

Lane Change	Necessary lane changes (route)	Own	Trailing Vehicle
		Maximum deceleration	-4.65 m/s ²
		-1 m/s ² per distance	100.00m
		Accepted deceleration	-1.00 m/s ²
	Waiting Time before diffusion	60.00 sec	Calibrated value
	Min clearance (front/rear)	0.50 m	0.45 m
	To slower lane, if collision time is above	11.00sec	
	Safety Distance reduction factor	0.60	0.40
	Maximum Deceleration for cooperative breaking	-3.00 m/s ²	-4.65
	Cooperative lane change	Maximum speed difference	10.80 Km/h
		Maximum Collision time	10.00 sec
	Rear Correction of lateral positions	Maximum speed	3.00 Km/h
		Active during time period from	1.00 sec. 10.00 sec.

Table 6. Simulation Result of Predicted and Observed Traffic Volume at Panthangi Toll Plaza based on Default Case and Calibrated Values of Driving Behaviour Parameters using VISSIM

Simulation 600 second	No	Vehicles	Traffic Volume (Veh/hr)		No	Vehicles	Traffic Volume (Veh/hr)	
			Observed	Simulated			Observed	Simulated
	1	Small Car	525	434	1	Small Car	525	490
	2	Big Car	294	100	2	Big Car	294	148
	3	MAV	63	37	3	MAV	63	42
	4	Bus	60	79	4	Bus	60	50
	5	LCV	168	90	5	LCV	168	140
	6	HCV	189	52	6	HCV	189	156
	7	Trailer	12	4	7	Trailer	12	4
	Total		1311	796		Total	1311	1030
	Default Parameters				Calibrated Parameters			

From the calibrated VISSIM model, the traffic volumes were compared between the observed and simulated cases of default as well as calibrated parameters (see Table 6). The results show that a clear difference is observed between the default parameter and calibrated parameters, and the total volume is observed as 1030 veh/hr, corresponding to the calibrated parameters. From the results, it is also identified that small as well as big cars can be accurately predicted with modified parameters. After the simulation of the model using the default parameters for the car-tracking mechanism and the lane-changing algorithm using Weidman-74 driving behavior options under heterogeneous traffic conditions, a linear regression analysis line was fitted between the

observed and simulated values of the calibrated parameters.

Figure 7 indicates the correct predicted accuracy of the calibrated model of the VISSIM simulation. Whereas, the default case of the observed versus simulated result indicates R^2 as 0.82, which is not adequate and further needs the parameters to be calibrated. Further, the calibrated value for the driving behavior model was entered into VISSIM, and after running simulation with calibrated values, it was observed that the model line fit with the data analysis using the regression trend line, and it was observed that the R^2 value was 0.93, which is an acceptable value and indicates significant improvement in the model.

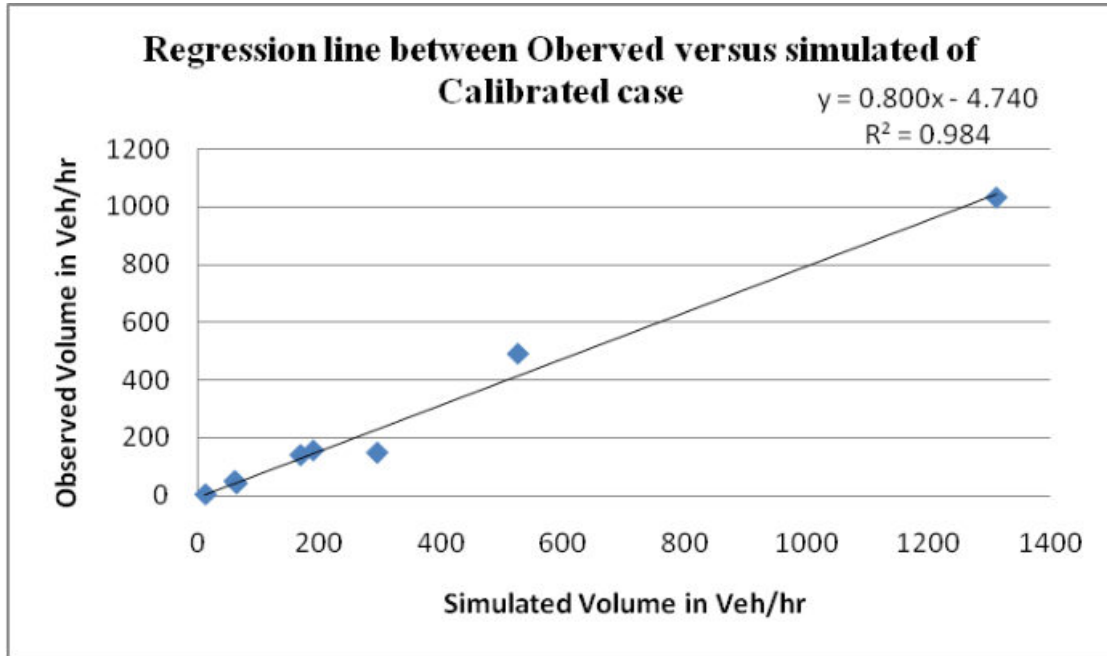


Figure 7. Simulated Fit Plot for Traffic Data using Calibrated Values for Driving Behaviour Parameters

Validation Target

The simulation results were validated using mean absolute percentage error (MAPE), root mean square error (RMSE), and correlation coefficient to ensure that the process of fine-tuning of the driving behavior parameter that was determined in the model achieved

the target simulation. This was done to ensure the validity of the calibrating values introduced in the VISSIM model. From the validation results, it was observed that MAPE, RMSE, and correlation coefficient values are 0.25, 0.09, and 0.994, respectively.

Mean absolute percentage error measures the size of the percentage error and is expressed as:

$$MAPE = \frac{1}{n} \sum_{i=1}^n \left| \frac{y_{sim} - y_{obs}}{y_{obs}} \right| * 100 = 0.25 < 5\% \quad (9)$$

In this scenario, n denotes the total quantity of observations taken for traffic measurements, y_{sim} and y_{obs} are simulated and observed data points exist within a time-space domain, while, and y_{sim} denotes the average calculated from the entire set of simulated outputs.

$$RMSE = \sqrt{\frac{1}{N} \sum N(X_i - Yy_i)^2} = 0.09 \quad (10)$$

The strength of the linear link between the simulated and observed data was expressed as a correlation coefficient (CC). A perfect and direct association is shown by a correlation coefficient of 1, whereas a perfect and inverse relationship is indicated by a CC of -1. A correlation coefficient of 0.85 is regarded as satisfactory for model calibrations.

$$Correlation Coefficient = \frac{1}{N} \sum_{i=1}^n \frac{(Yi_{sim} - Yi_{sim})(Yi_{obs} - Yi_{obs})}{\sigma_{sim} * \sigma_{obs}} = 0.994 \quad (11)$$

Where n is the overall number of traffic measurement observations, and Yi_{sim} and Yi_{obs} represent the means of the simulated and observed data, respectively. The standard deviations of the simulated and observed measurements are σ_{sim} and σ_{obs} , respectively.

7. CONCLUSION

The current research delved into microscopic traffic simulation at a toll plaza to comprehend driving behavior at the toll booth through the utilization of VISSIM. The driving behavior was explored based on the acceleration, and deceleration parameters and

modified the driving behavior parameters in VISSIM. In this research paper, a three-phase step methodology is outlined for creating, fine-tuning, and verifying the simulation framework. Parameters that influence the driving behavior at merging and diverging locations.

The required phase-wise procedure indicates the collecting and processing of field data and the creation of a detailed simulative structure at the microscopic level using PTV VISSIM. The field data were assigned to the model and different driving behavior parameters were defined to calibrate and validate using field data. Using the default case parameters, the result of the model output indicates the model fit of ($R^2 = 0.82$) which was in competent to reproduce the observed conditions, although, after multiple simulations running with changing the most influencing attributes such as safety impact factor and headway distance between vehicles, the results showed the higher value of model fit represented as ($R^2 = 0.93$) which is significantly an acceptable value. From the validation test results, it can be seen that the RMSE for all types of vehicles observed and simulated vehicular movement ($0.09 < 0.2$) was found acceptable. The MAPE value shows that the value is in the range of 0.25 which is less than 5% and it is satisfactory. Overall validation results were satisfactory, with minimal error. Therefore, it can be concluded that the model was successfully calibrated and validated.

The study concluded that based on the calibrated model, the driving behavior parameters were observed with as much accuracy with respect to the car following behavior and lane change behavior. Compared to the results of the default model, the statistics of the calibrated model show a significant improvement. It is clear that the MAPE error measurement is less than 5%, which suggests that the observed and simulated traffic statistics are reasonably matched. The RMSE for all simulated and real-world vehicle categories is less than 10%, which is regarded as acceptable for mixed-traffic model validations. In conclusion, all combinations of design characteristics and traffic demand patterns showed good agreement between measured and projected values. In general, the following parameters in Wiedemann 74 are the primary variables that influence the simulation precision. Factors such as AXE, BX additive, and BX multiplicative, and the lane change model parameters, including minimum headway and safety distance reduction factor, were considered, and it was concluded that these factors significantly influence driving behavior.

REFERENCES

- Abdelwahab, M.P (2017). Traffic micro-simulation model for design and operational analysis of barrier toll stations. *Ain Shams Engineering Journal*, Vol. 8, no. 4, pp. 507-513, 2017. doi: 10.1016/j.asej.2016.05.010.
- Aycin, M., Kiskel, K. Papayannoulis, V. and Davies G (2009). Development of Methodology for Toll Plaza Delay Estimation for Use in Travel Demand Model Postprocessor. *Transportation Research Record: Journal of the Transportation Research Board*. Vol. 2133, no. 1, pp. 1-10, 2009, doi: 10.3141/2133-01.
- Al-Deek, H. M., Mohamed, A. A., and , E. A. Radwan (2000). New model for evaluation of traffic operations at electronic toll collection plazas. *Transportation Research Record*, 1710 (1), pp. 1-10.
- Al-Deek H., Radwan A., Mohamed A., and J. Klodzinski (2000). Evaluating the Improvements in Traffic Operations at a Real-Life Toll Plaza with Electronic Toll Collection. *Transportation Research Record Journal of the Transportation Research Board*. 1710 (1), pp. 1-10. doi: 10.3141/2133-01.
- Ceballos, G., and Curtis, O. (2004). Queue analysis at toll and parking exit plazas: a comparison between multi-server queuing models and traffic simulation. *ITE Annual Meeting, Institute of Transportation Engineers*.
- Coelho, M. C., Farias, T. L., and Rouphail, N. M. (2000). Measuring and Modeling Emission Effects for Toll Facilities. *Transportation Research Record: Journal of the Transportation Research Board*, 141 (1), pp. 136-144. doi: 10.3141/1941-17
- Dubedi, A., Chakraborty, P., Kundu, D., and, K. H. Reddy (2012). Modeling automobile drivers' toll-lane choice behavior at a toll plaza. *Journal of Transportation Engineering*, 138(11), pp. 1350-1357.
- Kim, S., (2009). The toll plaza optimization problem: Design, operations, and strategies", *Transportation Research Part E: Logistics and Transportation Review*, Vol.45, no.1, pp 125-137.
- Klodzinski, J., Gordin, E., and Al-Deek, H. M. (2007). Evaluation of impacts of open road tolling on main-line toll plaza. *Transportation research record*, Vol. 2012 (1), pp.72-83.
- Klodzinski J, Al-Deek H, Asce M., (2002). New Methodology for Defining Level of Service at Toll Plazas. *Journal of Transportation Engineering-ASCE*, 128 (2), pp.173-181.
- Mahdi, M. B., Leong, L. V., and Sadullah, A. F. M. (2019). Use of Microscopic Traffic Simulation Software to Determine Heavy-Vehicle Influence on Queue Lengths at Toll Plazas. *Arabian Journal for Science and Engineering*, 44 (8), pp. 1–15. doi: 10.1007/s13369-019-03809-7.
- Mehar, A., Chandra, S., and Velmurugan, S., (2013). Speed and Acceleration Characteristics of Different Types of Vehicleson Multi-Lane Highways. *European Transport*, 55 (1), pp. 1–12.
- Mittal, H., and Sharma, N. (2020). Assessment of Delhi NCR Traffic Using Queuing Model. *International Journal of Advanced Science and Technology*, 29 (7), pp. 5418-5424.
- Mittal, H., and Sharma, N., (2012). Modeling of Communication Network with Queuing Theory under Fuzzy Environment. *Mathematical Statistician and Engineering Applications*, Vol. 71 (2), pp. 122-137, 2022.
- Neuhold, R., Garolla, F., Sidla, O., Fellendorf, M. (2019). Predicting and Optimizing Traffic Flow at Toll Plazas. *Transportation Research Procedia*, 37, pp. 330-337. doi:10.1016/j.trpro.2018.12.200.
- Poon, N., and Dia, H., (2005). Evaluation of toll collection performance using traffic simulation. *27th Conference of Australian Institutes of Transport Research (CAITR 2005)*, AITR, Brisbane, pp. 7-9.
- Ozbay K, Mudigonda S, Bartin B., (2005). Development and calibration of an integrated freeway and toll plaza model for New Jersey Turnpike using Paramics microscopic simulation tool. *IEEE Conference on Intelligent Transportation Systems, Proceedings, ITSC 2005*, pp. 1165- 1170.
- Sharma, N., Mishra, G.D., and Kumar, A. (2010). Simulation of Service Station of Vehicles With One Server. *International Journal of Computer, Mathematical Sciences and Application*, 4(1-2), pp. 85-97.
- Velmurugan S., Errampalli M., Ravinder K., Sitaramanjaneyulu K., and Gangopadhyay S. (2010). Critical evaluation of roadway capacity of multi-lane high speed corridors under heterogeneous traffic conditions through traditional and microscopic simulation models. *Journal of Indian Roads Congress*, 71 (3), pp. 235-264, 2010.
- Wang, C., (2017). Study on Toll Plaza Design Based on M/M/1 Queue Theory. 7th International Conference on Education, Management, Computer and Society (EMCS 2017). Atlantis Press.
- Wang, C., Xu, C., Xia, J., Qian, Z., and Lu, L. (2018). A combined use of microscopic traffic simulation and extreme value methods for traffic safety evaluation. *Transportation Research Part C: Emerging Technologies*, Vol. 90, pp. 281-291.

G V L N Murthy

Researcher Scholar,
GIET University,
Gunupur, Odisha,
India.
gvlnmurthy98@gmail.com
ORCID 0009000860559830

Ramprasad Naik D

Professor,
GIET University,
Gunupur, Odisha,
India.
dnaik@giet.edu
ORCID 0000000346336987

Anjankumar M

Professor and Principal,
DNR College of Engineering and
Technology,
Bhimavaram, Andhra Pradesh,
India
principal@dnrcet.org
ORCID 0009000860559830

Gireeesh Kumar Pala

Professor & Head
Shri Vishnu Engineering College for Women (A)
Bhimavaram, Andhra Pradesh,
India
gireeshcivil@svecw.edu.in
ORCID 0000-0003-3945-7553



DIELECTRIC STUDIES ON TSP: NaNO_3 BIOPOLYMER-BASED POLYMER ELECTROLYTES

M. Gnana Kiran¹

Sharmila. D

Rao. M. C

Naveen Kumar. V

Krishna Jyothi. N

P. S. Brahmanandam

Keywords:

TSP, NaNO_3 , conductivity, impedance analysis, dielectric constant.



ABSTRACT

The solution cast method made free-standing tamarind seed polysaccharide (TSP): Sodium Nitrate (NaNO_3) based solid polymer electrolyte films with various weight percentages. The conductance and dielectric properties of the polymer films were evaluated using AC impedance spectroscopy. This polymer electrolyte's conductance varied with temperature. By raising the temperature for different concentrations, the conductivity was increased. The maximum conductivity was obtained for 70:30 films at 373 K. According to dielectric studies, dielectric constants and dielectric loss were higher at low frequencies and lower at higher frequencies. At 303 K, the dielectric constant (ϵ') was 899.1, and the dielectric loss (ϵ'') was 1393.8 for 70:30 (TSP: NaNO_3) composition. The minimal tangent loss was 1.54×10^{-4} for 30% film.

© 202x Published by Faculty of Engineering

1. INTRODUCTION

Solid biopolymer electrolytes (SBPE) are a thrust area compared to other research domains. There are several benefits to using these electrolytes. These material samples can be easily prepared in a lab. Solid polymer electrolytes are mechanically strong, offer more conductivity, and have less leakage (Singh et al., 2016). Over the past few decades, substantial research has been carried out on electrolytes using synthetic polymers (Raju et al. 2019). These polymers, therefore, take a very long time to decompose.

Consequently, biopolymers overcome the issue above (Park et al., 2003). Proteins, polyesters, and

polysaccharides are the three subcategories of biopolymers. Pectin, starch, agar-agar, cellulose, chitosan, and agarose are some such polysaccharides (Kulkarni et al., 2021) Polysaccharide-based biopolymers are extremely useful in electrochemical devices since they are eco-friendly, quickly degrading materials. Tamarind Seed Polysaccharide (TSP) is a special biopolymer with outstanding properties and uses. For example, effective gelling agents, simple film-forming abilities, etc. A lot of polar groups are present in this highly branched polysaccharide. 3:1:2 molar ratios of glucose, galactose, and xylose sugar monomers can be found in TSP (Saha et al., 2023). Numerous applications of TSP have been the subject of substantial research. Recent studies on TSP for various medicine formulations

¹ Gnana Kiran. M,
Email: gnanakiran33@gmail.com

have shown other distinctive properties, such as its potent antidiabetic activity (Bharathi et al., 2023), which decreases blood sugar levels. It is also an excellent excipient for ocular preparations because of its capacity to create flexible films with high tensile strength.

The characteristics of this film include transparency, non-hygroscopicity, non-stickiness, shape preservation even after harsh handling, and ferning patterns like those of natural tear film (Basha et al., 2017). TSP works as a binder, thickener, stabilizer, and good gelling agent. It increases viscosity in various industries, including cosmetics, food packaging, medicine, and numerous drug products (Rambabu et al., 2023). At 60 to 80 °C, it can only be completely resolved in inorganic liquids like water. Only a few research have been reported on TSP biopolymers until now. Fig. 1 represents the molecular structure of TSP (Selvakumar et al. 2008). This research prepares a biopolymer electrolyte by adding biopolymer TSP with dopant salt NaNO₃ for various concentrations of dopant salt NaNO₃ by solution cast procedure in laboratory methods. AC impedance spectroscopy allows it to observe electrical conductivity studies and dielectric properties (Vijay et al., 2017, Pandi et al., 2016).

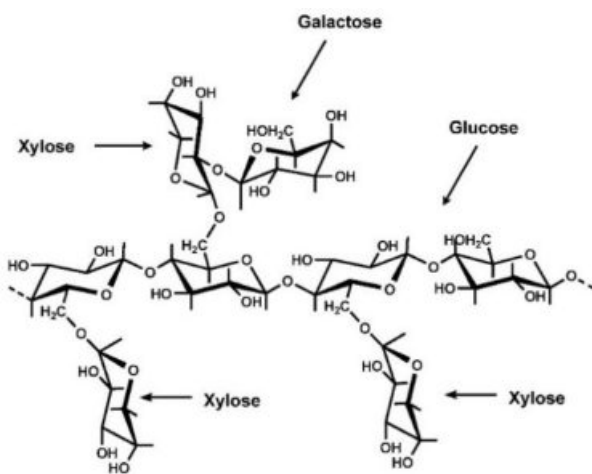


Figure 1. Molecular Structure of Tamarind Seed Polysaccharides

2. MATERIAL AND METHODS

TSP is purchased from Tokyo Chemical Industries (TCI) in Japan. The solid biopolymer electrolyte films were made using the solution cast technique in this study. TSP is dissolved in double-distilled water (H₂O) with NaNO₃ added in the compositional ratios of (90:10), (80:20), (70:30), and (60:40), and the mixture is stirred for 12 hours at a temperature of 60 °C using magnetic stirrers. After forming a very homogeneous and viscous solution, transparent or partially transparent thin films ranging from 0.08 to 0.11 mm are generated after 24 h when the mixture is poured into Petri dishes and deposited in a

vacuum chamber with the temperature kept at 60 °C. A computer equipped HIOKI 3532 LCR testing meter measures solid biopolymer electrolyte's electrical and ionic conductivity properties at 42 to 1 MHz temperatures.

3. RESULTS AND DISCUSSIONS

3.1 Conductivity Studies

The electrical relaxations in AC frequency are split into three states. In the first state, high-frequency electrical relaxations are correlated with short-range ion movement (Majid et al. 2005). In second-state middle frequencies, the relaxations are associated with the long-range direction of ions. Dopants, point defects, and grain boundaries influence the relaxations. At a lower frequency, the relaxation is assigned to charge transfer. Third low region, asymmetric plots that gradually increase from a lower end to a higher end are due to ions moment and charge carrier concentrations (Premalatha et al., 2017). The conductance of ions is defined by the density and flow rate (Kiran et al., 2019).

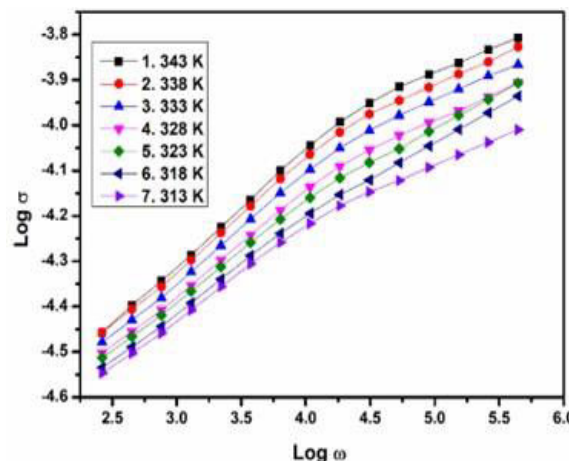


Figure 2. Conductance plot between Log ω vs. Log σ at various temperatures for 30% film

Fig. 2 is drawn between ‘Log ω ’ and ‘Log σ ’. Here by raising the temperature, conductance increases gradually with respect to frequency. This plot shows two different regions; one is a low-frequency region and another one is a high-frequency region. At the first low region, all plots look merged and overlapped. At high-frequency regions, conductance increases by increasing the temperature and frequency (Premalatha et al., 2016). Here, the conductance is increased due to the migration of ions.

3.2 Conductivity vs. Composition

Fig. 3 shows the plot between the composition concentration and conductivity of the materials at different temperatures. Pure TSP and TSP with a salt of

various concentrations are taken in this composition. By increasing the temperature of each composition, the conductivity is also increased gradually. Initially, the conductivity is very low for pure TSP at room temperature. By raising the temperature for different concentrations, the conductivity is increased. Finally, the maximum conductivity is obtained for 70:30 film at 373 K. Yet the conductivity decreases by raising the salt concentration to the polymer. The conductivity change can be observed as shown in the given plots with respect to temperature. The conductivity is raised due to the migration and movement of ions through the material (Hamsan et al., 2020).

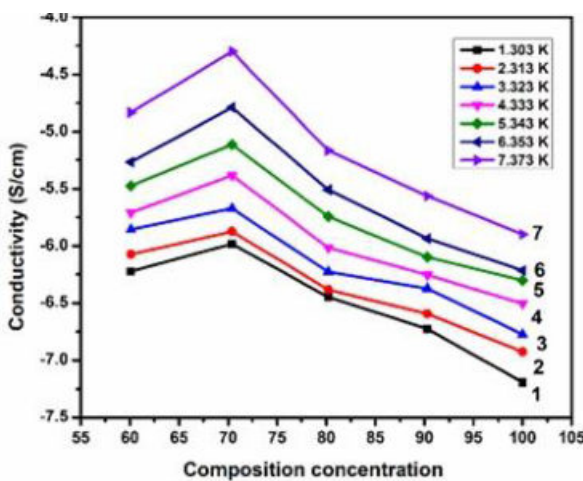


Figure 3. Composition Concentration vs. Conductivity plot for various wt.% ratios of TSP: NaNO₃

Due to the movement of ions in the polymer material, the polymer chain segments are increased, which finally causes the conductivity of the ions (Jyothi et al. 2022). At various temperatures, plots were drawn between the Conductivity and Composition of the films (Fig. 3). For a particular film composition, the conductivity progressively increases as the temperature is enhanced (Ma et al., 2007). At a specific temperature, the conductivity increases as the percentage of NaNO₃ increases to 30%. Then onwards, again, the conductivity decreased.

3.3 Dielectric Properties

The dielectric parameters are measured from the electrical properties of pure and doped films. Fig. 4 and 5 show the frequency dependence of ϵ^1 and ϵ^{11} . At low frequencies, ϵ^1 and ϵ^{11} are higher. As the frequency increases, the values decrease gradually and remain constant at high frequencies (Sikkantha et al., 2015). The decrease in dielectric constant and dielectric energy loss for ions at high frequencies may be due to the space charge effect and polarization (Kiran et al., 2021). Moreover, it can be deduced from the graphs that the 30% film has demonstrated the largest dielectric constant (ϵ^1) and dielectric loss (ϵ^{11}).

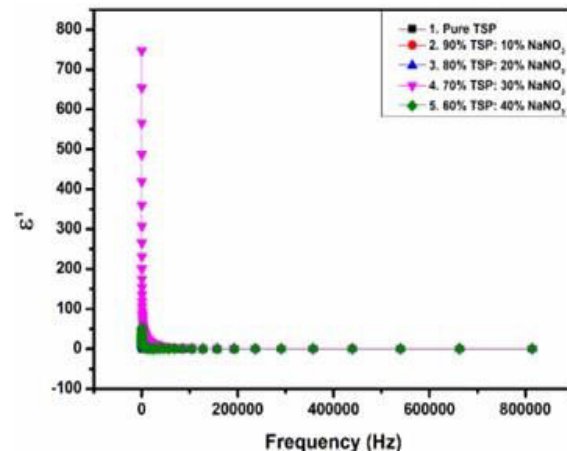


Figure 4. Dielectric plot between frequency vs. ϵ^1 for TSP: NaNO₃ at various wt.% ratios

The information is displayed in Table 1. The parameters are decreased with a decrease in salinity or an increase in salinity (Gnana Kiran et al. 2023). For pure TSP, the computed permittivity (dielectric constant) is 14.4. However, the dielectric permittivity of TSP films with 10%, 20%, and 30% NaNO₃ doping is 30.0, 42.7, and 899.1, respectively. However, the dielectric constant is once more reduced to 62.2 with a 40% doped layer. Similar to this, pure TSP has a dielectric loss of 34.2. However, the dielectric losses for 10%, 20%, and 30% NaNO₃ doped TSP films are 64.6, 67.1, and 1393.8, respectively. Again, the dielectric loss is reduced to 134.8 in a 40% doped layer. The 30% film has a higher dielectric constant and dielectric loss than the other films because it is more conductive and amorphous (Mishra et al. 2011).

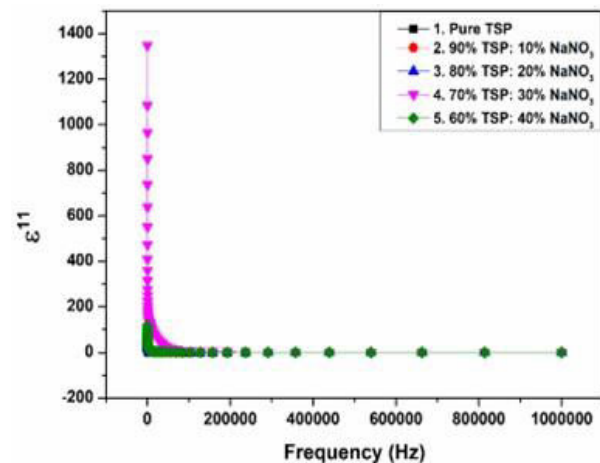


Figure 5. Dielectric plot between frequency vs. ϵ^{11} for TSP: NaNO₃ at various wt.% ratios

The relation time may be responsible for these differences in the parameters. At low frequencies, the electric dipoles have enough time to align themselves in the field's direction (Armstrong et al., 1972).

However, at high-frequency ranges, the dipoles cannot spend enough time aligning themselves with the field direction, which results in a low dielectric constant and dielectric loss (Marzantowicz et al., 2007).

Table 1. Dielectric constant and dielectric loss of TSP: NaNO₃ at various wt.% ratios

S. No	Composition wt. % (TSP: NaNO ₃)	ϵ^1	ϵ^{11}
1	Pure TSP	14.4	34.2
2	90: 10	30.0	64.6
3	80: 20	42.7	67.1
4	70: 30	899.1	1393.8
5	60: 40	62.2	134.8

3.4 Tangent loss

Fig. 6 is drawn between 'Log ω ' and tangent loss ($\tan \delta$) of pure TSP and TSP with various wt.% ratios of the salt. The tangent loss represents the total energy loss in the system. And it is the ratio between dielectric energy loss and dielectric constant (ϵ^{11}/ϵ^1). The peak maximum indicates energy loss (Adachi et al. 2002). It may be inferred from the plot that with pure TSP, energy loss is more than in other composite films. The data is presented in Table 2. The calculated tangent loss for pure TSP is 2.34×10^{-4} . But with 10%, 20%, and 30% NaNO₃ doped TSP films, the tangent energy losses are 2.26×10^{-4} , 2.12×10^{-4} , and 1.54×10^{-4} , respectively. But with 40% doped film, the tangent energy loss again increases to 1.72×10^{-4} . The tangent loss is obtained by the following formula,

$$\tan \delta = \frac{\epsilon^{11}}{\epsilon^1} \quad (1)$$

Table 2. Tangent loss of TSP: NaNO₃ at various wt.% ratios

S. No	Composition wt. % (TSP: NaNO ₃)	$\tan \delta$
1	Pure TSP	2.34×10^{-4}
2	90: 10	2.26×10^{-4}
3	80: 20	2.12×10^{-4}
4	70: 30	1.54×10^{-4}
5	60: 40	1.72×10^{-4}

As the salt concentration is increased in the host material from 10% to 30%, tangent energy losses are decreased gradually. The lowest energy loss is observed with 30% film. Further increasing the dopant concentration up to 40% increases the tangent energy loss. The tangent loss is evaluated as per equation (Jyothi et al., 2022).

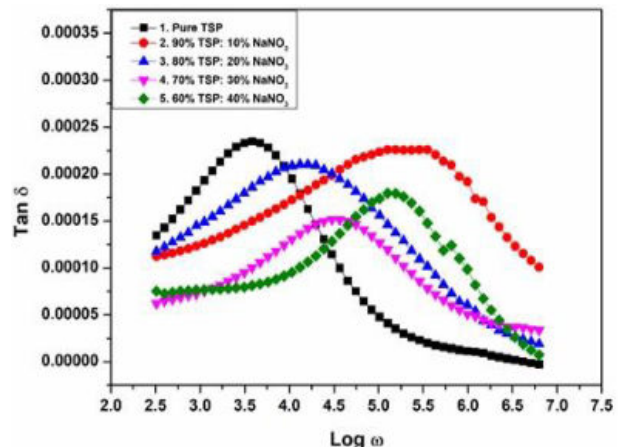


Figure 6. Tangent loss plot of TSP: NaNO₃ at various wt.% ratios

4. CONCLUSION

This study uses the solution cast method to examine synthesized TSP-based polymer electrolyte membranes with different NaNO₃ concentrations (10, 20, 30, and 40%). Electrical features, including conductance analysis, dielectric properties, tangent loss, and electrical modulus, are assessed for the films at various compositions to characterize them. By raising the temperature for different concentrations, the conductivity is increased. The maximum conductivity is obtained for 70:30 films at 373 K. Furthermore, the dielectric measurements show that the "dielectric constant" and "dielectric losses" are maxima for 30% film: 899.1 and 1393.8, respectively. The tangent energy loss is minimum for 30% film and is 1.54×10^{-4} .

Acknowledgement: Thanks to the Department of Science and Technology (DST, Delhi), Government of India, for providing the Department of Physics with the DST-FIRST Level-1 (SR/FST/PS-1/2018/35) initiative. We thank the KLEF for providing the facilities, infrastructure, basic instruments, and assistance for the current project.

References:

- Adachi, K., & Urakawa, O. (2002). Dielectric study of concentration fluctuations in concentrated polymer solutions. *Journal of Non-Crystalline Solids*, 307, 667-670. doi:10.1016/S0022-3093(02)01527-2
- Armstrong, R. D., Dickinson, T., & Whitfield, R. (1972). The impedance of the silver-solid electrolyte interphase. *Journal of Electroanalytical Chemistry and Interfacial Electrochemistry*, 39(2), 257-262. doi:10.1016/S0022-0728(72)80150-5
- Basha, S. S., Gnanakiran, M., Ranjit Kumar, B., Veera Bhadra, K., Reddy, M., & Rao, M. (2017). Synthesis and spectral characterization on PVA/PVP: GO based blend polymer electrolytes. *Rasayan Journal of Chemistry*, 10, 1159-1166. <http://dx.doi.org/10.7324/RJC.2017.1041756>
- Bharathi, R. V., Raju, M. K., Shanmukhi, P. S. V., Kiran, M. G., Murali, N., Parajuli, D., & Samatha, K. (2023). Enhanced DC electrical resistivity and magnetic properties of transition metal cobalt substituted spinel MgFe₂O₄ ferrite system. *Inorganic Chemistry Communications*, 111713. doi:10.1016/j.inoche.2023.111713
- Gnana Kiran, M., N. K. Jyothi, M. C. Rao, S. K. Babu, P. Pardhasaradhi, G. R. K. Prasad, M. P. Rao, & K. Samatha. (2023). Structural, electrical, and dielectric studies of PVA-based NaNO₃ Polymer electrolytes for battery applications. *International Journal of Ambient Energy*, 44(1), 246-255. DOI: 10.1080/01430750.2022.2126521
- Hamsan, M. H., Shujahadeen B. Aziz, Muaffaq M. Nofal, M. A. Brza, Rebar T. Abdulwahid, Jihad M. Hadi, Wrya O. Karim, & M. F. Z. Kadir. (2020). Characteristics of EDLC device fabricated from plasticized chitosan: MgCl₂ based polymer electrolyte. *Journal of Materials Research and Technology*, 9(5), 10635-10646. doi:10.1016/j.jmrt.2020.07.096
- Jyothi, N., Krishna, K., Tarakeswara Rao, K., Naveen Kumar, V., Gnana Kiran, M., Deepthi, K., Rao, M. C., Vijaya Kumar, K., & Inthiyaz, S. (2022). Synthesis and dielectric properties of PAN-based Na⁺ ion polymer electrolytes. *Materials Today: Proceedings*, 51, 1168-1171. doi:10.1016/j.matpr.2021.07.123
- Jyothi, N., Krishna, M. Gnana Kiran, Naveen Kumar, V., Nageswara Rao, B., Vijaya Kumar, K., & Rao, M. C. (2022). Structural and impedance analysis of PAN-based Na⁺ ion conducting gel polymer electrolytes for energy storage device application. *Materials Today: Proceedings*, 51, 1164-1167. doi:10.1016/j.matpr.2021.07.122
- Kiran, M. Gnana, N. Krishna Jyothi, K. Samatha, M. P. Rao, & V. B. V. N. Prasad. (2021). Studies on optical properties of PVA-based complex polymer electrolyte. *RASAYAN Journal of Chem*, 14, 760-767. <http://dx.doi.org/10.31788/RJC.2021.1425964>
- Kiran, M. Gnana, N. Krishna Jyothi, M. Narasimha Rao, & K. Vijaya Kumar. (2019). AC conductivity and dielectric studies of PVA-based solid polymer electrolyte. *Journal of the Indian Chemical Society*, 96(1), 76-77.
- Kulkarni, G. T., Paritala, S., & Siddaiah, M. K. (2011). Effect of tamarind seed polysaccharide on dissolution behaviour of ibuprofen tablets. *Journal of Chronotherapy & Drug Delivery*, 2, 49-56.
- Ma, X., Yu, J., He, K., & Wang, N. (2007). The effects of different plasticizers on the properties of thermoplastic starch as solid polymer electrolytes. *Macromolecular Materials and Engineering*, 292(4), 503-510. doi:10.1002/mame.200600445
- Majid, S. R., & Arof, A. K. (2005). Proton-conducting polymer electrolyte films based on chitosan acetate complexed with NH₄NO₃ salt. *Physica B: Condensed Matter*, 355(1-4), 78-82. doi:10.1016/j.physb.2004.10.025
- Marzantowicz, M., Dygas, J. R., Krok, F., Florjańczyk, Z., & Zygałdo-Monikowska, E. (2007). Influence of crystalline complexes on electrical properties of PEO: LiTFSI electrolyte. *Electrochimica Acta*, 53(4), 1518-1526. doi:10.1016/j.electacta.2007.03.032
- Mishra, M. U., & Khandare, J. N. (2011). Evaluation of tamarind seed polysaccharide as a biodegradable carrier for colon-specific drug delivery. *International Journal of Pharmacy and Pharmaceutical Sciences*, 3(1), 139-142.
- Pandi, D. Vinod, S. Selvasekarapandian, R. Bhuvaneswari, M. Premalatha, S. Monisha, D. Arunkumar, & Junichi, K. (2016). Development and characterization of proton conducting polymer electrolyte based on PVA, amino acid glycine, and NH₄SCN. *Solid State Ionics*, 298, 15-22. doi:10.1016/j.ssi.2016.10.016
- Park, C. H., Kim, D. W., Prakash, J., & Sun, Y.K. (2003). Electrochemical stability and conductivity enhancement of composite polymer electrolytes. *Solid State Ionics*, 159(1-2), 111-119. doi: 10.1016/S0167-2738(03)00025-0
- Premalatha, M., Mathavan, T., Selvasekarapandian, S., Monisha, S., Vinod Pandi, D., & Selvalakshmi, S. (2016). Investigations on proton conducting biopolymer membranes based on tamarind seed polysaccharide incorporated with ammonium thiocyanate. *Journal of Non-Crystalline Solids*, 453, 131-140. doi:10.1016/j.jnoncrysol.2016.10.008
- Premalatha, M., Mathavan, T., Selvasekarapandian, S., Monisha, S., Selvalakshmi, S., & Vinod Pandi, D. (2017). Tamarind seed polysaccharide (TSP)-based Li-ion conducting membranes. *Ionics*, 23, 2677-2684. doi:10.1007/s11581-017-1989-x
- Raju, G., Murali, N., Prasad, M. S. N. A., Suresh, B., Babu, D. Apparao, Kiran, M. Gnana, Ramakrishna, A., Wegayehu, M. Tulu, & Babu, B. Kishore. (2019). Effect of chromium substitution on the structural and magnetic properties of cobalt ferrite. *Materials Science for Energy Technologies*, 2(1), 78-82. doi:10.1016/j.mset.2018.11.001
- Rambabu, C., Aruna, B., Shanmukhi, P. S. V., Kiran, M. G., Murali, N., Mammo, T. W., & Narayana, P. L. (2023). Effect of La³⁺/Cu²⁺ and La³⁺/Ni²⁺ substitution on the synthesis, magnetic and dielectric properties of M⁻ type Sr₁₋

- xLaxFe12-xMxO19 (M= Cu and Ni) hexaferrite. Inorganic Chemistry Communications, 111753. doi:10.1016/j.inoche.2023.111753
- Saha, A., Kumar, K. V., Jyothi, N. K., Kiran, M. G., & Rao, M. C. (2023). Structural and electrical properties of TSP: CH₃COONa amorphous Biopolymer electrolytes for electrochemical cell applications. Journal of Non-Crystalline Solids, 616, 122465. doi:10.1016/j.jnoncrysol.2023.122465
- Selvakumar, M., & Krishna Bhat, D. (2008). LiClO₄ doped cellulose acetate as a biodegradable polymer electrolyte for supercapacitors. *Journal of Applied Polymer Science*, 110(1), 594-602. doi:10.1016/j.mset.2018.11.001
- Sikkanthar, S., Karthikeyan, S., Selvasekarapandian, S., Vinoth Pandi, D., Nithya, S., & Sanjeeviraja, C. (2015). Electrical conductivity characterization of polyacrylonitrile-ammonium bromide polymer electrolyte system. *Journal of Solid-State Electrochemistry*, 19(5), 987-999. doi:10.1007/s10008-014-2697-3
- Singh, R., Polu, A. R., Bhattacharya, B., Rhee, H. W., Varlikli, C., & Singh, P. K. (2016). Perspectives for solid biopolymer electrolytes in dye-sensitized solar cell and battery application. *Renewable and Sustainable Energy Reviews*, 65, 1098-1117. doi:10.1016/j.rser.2016.06.026
- Vijaya, N., Selvasekarapandian, S., Sornalatha, M., Sujithra, K. S., & Monisha, S. (2017). Proton-conducting biopolymer electrolytes based on pectin doped with NH₄X (X= Cl, Br). *Ionics*, 23(10), 2799-2808. doi:10.1007/s11581-016-1852-5

M. Gnana Kiran

Department of Engineering Physics,
KLEF, Vaddeswaram,
Andhra Pradesh,
India
gnanakiran33@gmail.com
ORCID: 0000-0002-1465-5265

Sharmila. D

Dept. of E&IT,
Aacharya Nagarjuna University,
Nambur, Guntur, Andhra Pradesh
INDIA
sharmilad@gmail.com
ORCID: 0000 0002 9121 0702

Rao M. C.

Department of Physics,
Andhra Loyola College,
Vijayawada,
Andhra Pradesh,
India
raomc72@gmail.com
ORCID: 0000-0001-9136-9679

Naveen Kumar. V

Department of Basic Sciences and
Humanities, Seshadri Rao Gudlavalleru
Engineering College, Gudlavalleru,
Andhra Pradesh, India
vnkbjs@gmail.com
ORCID: 0000-0002-3838-6733

Krishna Jyothi. N

Department of Physics, Sri Sathya Sai
University for Human Excellence,
Kalaburagi, Karnataka,
India
jyothinadella82@gmail.com
ORCID: 0000-0003-0721-0695

P. S. Brahmanandam

Department of Physics
Shri Vishnu Engineering College for
Women (A), Vishnupur, Bhimavaram,
India
dranandpotula@svecw.edu.in
ORCID: 0000-0001-9777-3496



TEXT DESCRIPTION TO IMAGE GENERATION USING GENERATIVE ADVERSARIAL NETWORK

Kayal Padmanandam^{1*}

Yeshasvi Mogula

Nikitha Pitla

P.S Brahmanandam

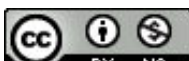
Keywords:

A B S T R A C T

Generative Adversarial Network (GAN), Attention Generative Adversarial Network, Generator, Discriminator, Style based Generator, Text to image

*The progression of translating text into images has been an imperative topic of research. The significant challenges arise from translating visual to textual information and vice versa. High-quality images can be generated from text using a Generative Adversarial Network (GAN), however, there are challenges associated with accurately portraying the content of the sentence provided to the model. Text-to-image conversion strategies can produce examples that closely reflect the descriptions' intended meaning. The user descriptions may however lack crucial details. To create the conditioned text descriptions, this study employs an Attention-Generative Adversarial Network to generate 256*256-pixel images that are image-sensitive. In the initial phase of GAN sketches, the input text descriptions serve solely to inform the basic form and color scheme of the devices. The information gleaned from the first stage, along with the textual descriptions, is fed into a GAN which generates images with high resolution and realistic detail. The conditional GAN training may be stabilized using conditioning augmentation, and the generated samples can have higher quality. Using Style based Generator, samples for each style of the image can be drawn. The proposed system can generate photorealistic visuals of an object when the user inputs the textual descriptions in the application's GUI.*

© 202x Published by Faculty of Engineering



1. INTRODUCTION

Image Caption generator is one of the most prevalent topics in Natural Language processing and computer Vision. Similarly, generating images from natural language as text is the vice versa process. These are research problems in a broad sense, identical to those that arise during linguistic translation. Like different languages can convey the same meaning in different ways, images and text can encode similar information. Because of the multimodal characteristics issues, text-image and image-text conversions are not the same. The

text description stating, "This is a magnificent red flower", has few possible translations into English. A broad variety of mental images could correspond to this description if one tried to create one. This multimodal behaviour is not exclusive to image captioning challenges, nonetheless, the sequential nature of language simplifies the difficulty there. The text-to-image structure is more tedious than image captioning. Potential uses for image synthesis based on natural language are vast, once the technology is ready for widespread use. By using the existing textual descriptions(words) as a basis for generating new ones, the proposed system can be put to good use. Instead of

spending a lot of time looking for relevant images, users could tell a computer what they want and the proposed system will generate it. Creators and machines could work more closely together to make content using natural language (Saleem Raja et al.,2022).

Creating high-quality images from a word-based description prevails to be a complex research obstacle. The resulting synthetic image must be accurate to the given description with high quality. If the process is automated, it can be used in the fashion industry to prototype new designs which is invaluable to designers. In addition, the ability to generate various designs of apparel items based on human-written descriptions would facilitate the discovery and intuitive selection of one's favourite designs. Since the generated images are crisper than those of the previous deep generative representation, GAN has gained a lot of attention recently. It has been shown that GANs can be trained with additional knowledge to guide the data generation process like Class labels, attributes, images, texts and other condition variables. Researching text-to-image structured algorithms, predominantly GAN-based approach implementing cutting-edge methods, allows researchers to compare the effectiveness of various methods and gain insights into this field. Also, Photo editing, CAD, and other fields could benefit greatly from this system. Creating synthetic versions of real-world images using GANs has shown encouraging results. Figure 1 shows the sample generation text to an image.



Figure 1. Sample image of text description to image generation

There's a discussion of related works in Section II, a description of the proposed Text Description to Image Generation system in Section III, and an explanation on methodology and experimental results are discussed in Sections IV & V respectively.

2. RELATED WORKS

High-resolution image generation from text descriptors is essential for several real-world applications, including

art creation and computer-aided architecture. Significantly, the advent of deep generative models has led to progress in this area (Ian Goodfellow, 2014), (Diederik P Kingma et al,2014) and (Aaron van den oord et al, 2016) (Elman Mansimov et al, 2016) extending AlignDRAW led to the discovery of a model Deep Recurrent Attention Writer (DRAW) (Karol Gregor et al ,2015) to sketch texture features iteratively while paying close attention to the pertinent words in the caption. The Paper (Anh Nguyen et.al., 2017) proposed an estimated Lagrangian approach for generating images from annotations. (Scott Reed et al, 2017) have been using conditional Pixel CNN (Aaron van den oord et al, 2016) to summarise the images from text using a multi-scale model structure. In comparison to various deep generative models, generative adversarial networks (GANs) (Ian Goodfellow, 2014), have demonstrated outstanding performance to generate cleaner samples. (Emily L et al, 2015) (Phillip Isola et al, 2017) (Christian Ledig, et al. 2017),(Christian Szegedy, 2016), (Alec Radford, 2016), (Edeh Michael Onyema,2023) and (Tim Salimans et al 2016). Their subsequent work illustrated that GAN can be capable of producing better sample data by integrating multiple conditions (e.g., objects and locations). (Han Zhang et al, 2017) and (Han Zhang et al, 2017) used distinctive GANs to generate pictures of varying dimensions after stacking numerous GANs for textual content-to-photo structure. Nevertheless, all of their GANs are constrained to the global sentence vector, so image generation is missing best-grained phrase-degree statistics. The attention mechanism has also been incorporated into models of sequence transmission. It has been used effectively in responding to questions (Kelvin Xu et al., 2015) about image subtitling (Zichao Yang et al, 2016) and machine translation to model multilevel dependencies. (Vaswani et al., 2017) have also shown that, with the aid of an attention model, machine translation models produce state-of-the-art results. Despite these advances, the attention mechanism in GANs for textual content-to-picture structure has until now to be investigated. It should be noted that AlignDRAW (Elman Mansimov et al, 2016) and (Olga Russakovsky et al, 2015) pre-owned LAPGAN (Emily L et al, 2015) to expand the copy of the photograph to a superior resolution. As a result, GANs were not given much consideration in their framework (Rinon Gal et al,2022). In our opinion, the proposed AttnGAN is the GAN to employ multi-level (e.g., word and sentence level) conditioning to generate fine-grained greater images.

3. PROPOSED SYSTEM

A high-resolution, detailed image is obtained with the proposed method. There is also a Deep Attentional Multimodal Similarity Model (DAMSM) included with the AttnGAN. Based on global sentence-level data and fine-grained word-level information, the DAMSM calculates the similarity between the generated source

image and the statement. To generate a training dataset for the generator, DAMSM applies a fine-grained loss for image capture matching. The technique includes three obligations, i) An Attentional Generative Adversarial Network projected for structure and quality image for the text descriptions. There are two attentional generative networks: the DAMSM and the Attentional Generating Network which are two dissimilar elements introduced in the Attention GAN field. (ii) a complete and accurate study is conducted to analytically assess the projected ATTNGAN. The experiments demonstrate that AttnGAN outperforms original condition GAN's models significantly. (iii) A comprehensive scrutiny is carried out by depicting the AttnGAN's attention layers. It is demonstrated for the first time that the patterned conditional GAN can instantaneously attend to the appropriate terms from image generation.

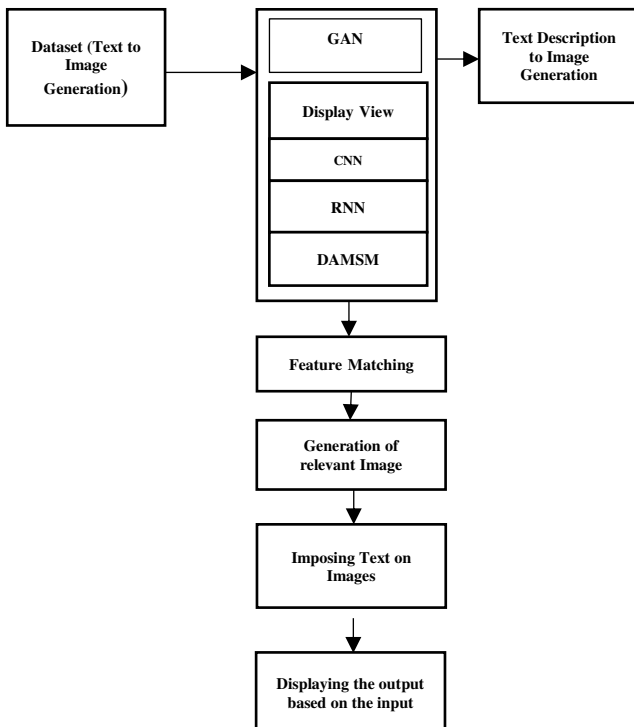


Figure 2. Progressive Diagram of GAN

Figure 2 shows the working of GAN with the given dataset. The algorithms used in the Text Description to Image Generation are AttnGAN (Attentional Generative Adversarial Network), and DAMSM (Deep attentional multimodal similarity model). The system first detects the Attn GAN from the context and considers the mapping between keywords and images. Then the trained output of DAMSM is sent to the discriminator to find the real and fake images. Style-based generator is used to reshape and resize the image for the clear visibility of the images.

3.1 System Architecture

Using Global Attention, we can design and build text to image generation system that automatically extracts key phrases and words from a written description. A low-resolution picture is generated from phrase attributes and the random noise vector is used as the backdrop environment in a generative neural network. Figure 3 is to resolve the issue of false positive caused by erroneously authenticating fake photos, a discriminative network is employed. The generators and discriminators for a high-resolution picture are arranged like a tree.

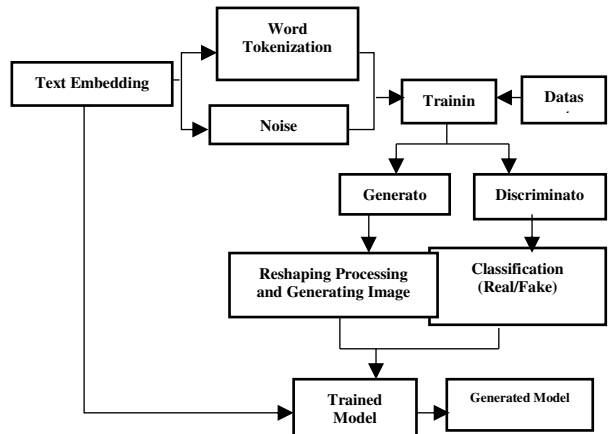


Figure 3. System architecture

3.2 Working model of Attention Generative Adversarial Network

Existing GAN-based text-to-image generation models (Han Zhang et al, 2017) and (Han Zhang et al, 2017) encode the entire sentence text description into a single word vector. This approach, however, creates an innovative model of attention that generates different graphics from the subregions according to words. The used attentional generative network has m Generators which will take hidden states of the generator and generate the smaller extent of images to the larger scale of images. As shown in Equation 1, the sampled standard normal distribution is represented by the noise vector Z. The vector \hat{e} is considered to be the sentence vector, while e is considered as the matrix of the sentence vector. At the i^{th} stage of the attention GAN as a neural network, f^{ca} represents the acclimatizing (Conditional) Augmentation for the sentence vector, from which f^{attn} forms the attention model

$$\begin{aligned} \mathbf{h}_0 &= f_0(\mathbf{z}, f^{ca}(\hat{\mathbf{e}})) \\ \mathbf{h}_i &= f_i(\mathbf{h}_{i-1}, f_i^{attn}(e, \mathbf{h}_{i-1})) \end{aligned} \quad (1)$$

$$\hat{\mathbf{x}}_i = \mathbf{G}_i(\mathbf{h}_i)$$

The two features word and image features from the preceding hidden layer are taken as inputs for the

following single-layer perceptron. The word features are initially transformed into the image features shared semantic space by creating a new feed-forward neural layer, $e' = Ue$, where $U \in R$. To find the right word for each j^{th} sub-region of the picture, a word-context vector is created using hidden features. Each column of h indicates a feature representation of an image sub-region. The word context vector for the j^{th} sub-region is a dynamic description of word vectors pertinent to h_j derived by $s' j, i = hTj e'i$, where j, i is the weight given to the i^{th} word by the model while creating the j^{th} sub-region of the picture. Finally, the image feature and the equivalent word-context features are combined to generate images at the later level of the discriminator. To generate realistic images, one can use the generative attentional network, which has as its objective function the generation of images at various levels (Tao Xu et al,2017).

$$L = L_G + L_{DAMSM}, \text{ where } L_G = \sum_{i=0}^{z^{-1}} L_{G_i} \quad (2)$$

In this λ defined as the hyperparameter used to equilibrium the two GAN losses that estimated the conditional and unconditional distributions jointly. The generator G_i has an identical discriminator I_i , the i^{th} phase of AttnGAN. Figure 4 explains the flow diagram of GAN. The adversarial forfeiture of G_i decides whether the photos are real or fake, whereas the Conditional loss distinguishes between images and phrases that match and those that do not. In addition to being trained on the generative model, each discriminator is taught to classify inputs as real or false. ATTN: GAN discriminators are fundamentally discontinuous, allowing them to be trained to focus on one picture only.

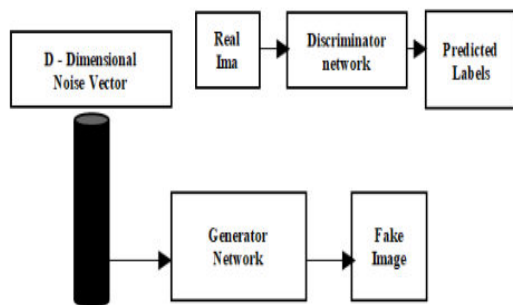


Figure 4. Flow Diagram of ATTN GAN

3.3 Working process of Deep Attentional Multimodal Similarity Model (DAMSM) for visualizing and comparing the similarity of multiple object categories

The DAMSM get trained to deuce computational models that maps imageries segments & sentence phrases to a common latent space, assessing the

researchers sought to estimate a fine-grained loss for image generation by comparing the similarity of images with their text counterparts, only at the word level. Image-Text similarity is a matching algorithm used to measure the correspondence between the image descriptions and the corresponding text segments. The results can be used to calculate a comparison matrix for all possible pairings of arguments in the sentences and images. Finally, the cosine comparison between the corresponding words c_i and e_i is used to determine whether or not the i^{th} word is related to the image. The attention-consumed per-character, per-word correlation between the full image (Q) and the entire text description (D) is defined as the function of the lowest error classification.

3.4 Working of Style based Generator for the images

In a feedforward network, the latent code is typically sent from the input layer to the generator. It deviates from this format by substituting a learned constant for the input stage in constructing the model's initial conditions. A non-linear mapping network ($f: Z \rightarrow W$) will return "W" as a starting point if a latent code z is given as input from the input latent space Z . For consistency and ease of use, to the proposed system standardize the measures. Instead of just passing the latent code through the input layer as is done in a traditional generator, it instead transfer to a latent space W that acts as a controller for the generator through adaptive instance normalization (AdaIN) at each convolution layer. After each convolution, the outcomes of the nonlinear analysis and the addition of Gaussian noise are shown. A learned affine transform and scaling parameters specific to the B channel are then applied to the noise input. There is a total of eight layers in the mapping network f (two for each resolution) and eighteen in the synthesis network g . A separate 1×1 convolution technique is employed to transform the final layer's output to RGB. Compared to the standard in the industry of 23.1M trainable parameters, the proposed generator has 26.2M. Based on the findings of the research conducted, it was determined that a Multi-Layer Perceptron (MLP) with 8 layers would be the optimal architecture for realizing the 512-dimensional mapping f . Affine transformations learned at the end of each convolution layer in the synthesis network regulate the AdaIN procedure, which specializes w to styles $y = (y_s, y_b)$.

4. METHODOLOGY

Initially, the model was presented as a system of trained modules, each of which had a brief description of its purpose and function. as the proposed system has a standardized web application to let users' query rationalization go as smoothly as possible. An appealing user interface has been developed so that users may

quickly grasp the information presented and quickly apply it to their personalized imagination. The web application design has a user-friendly GUI allowing for simple navigation and users' text-based image generation.

4.1. Text Feature Extraction

Semantic vectors, which represent the meaning of words, are extracted from the text description using the bidirectional LSTM, allowing for the extraction of text features. Here we have two hidden states for each word, one for each conceivable orientation generated using a two-way LSTM. Therefore, we represent the importance of a word by combining its two hidden states. The feature vector for each word is stored in a separate column of the feature matrix, and the final hidden states of the bidirectional LSTM are then put together to generate the sentence vector. Figure 5 shows how the features of the given input are extracted.

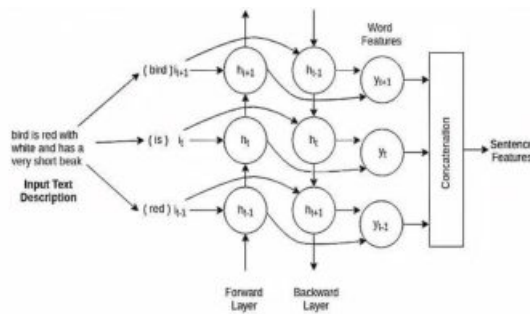


Figure 5. Architecture of text feature extraction

4.2. Priming- (Conditional Augmentation)

When it comes to text embedding, the latent space is typically quite high dimensional even above a hundred. When learning the generator with a small amount of data, it is not ideal to have gaps in the latent data manifold. Figure 6 is about the condition augmentation. The latent variables are drawn at random from a separate Gaussian distribution.

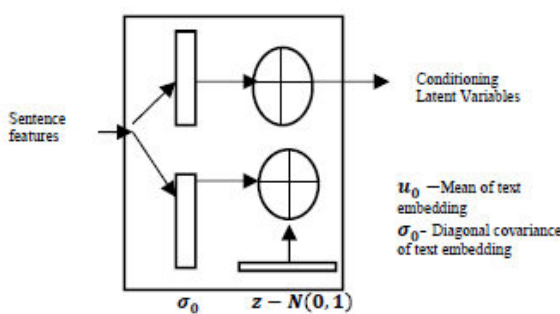


Figure 6. Architecture of Conditional Augmentation

4.3. Making Pictures - (Generative Network)

The picture creation module has a tree-like structure with numerous generators to produce images at varying scales, and it receives a conditional variable and noise vector generated by the pre-processing phase as input. Figure 7 shows the visuals produced at the first branch level are very simple in terms of colour and structure. When this is done, the generators at the subsequent branches can concentrate on filling in the remaining details in order to produce images with a better resolution.

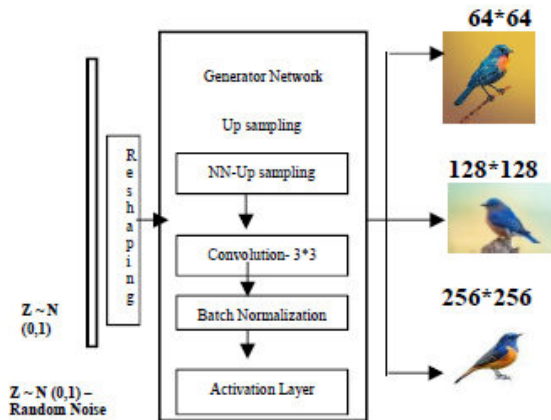


Figure 7. Architecture of image generation

4.4. A genuine method of identifying images- (Discriminative Network)

Figure 8 the image produced by the generative network is reduced in dimension by the discriminator, which comprises down-sampling, convolution, residual blocks, and the sentence characteristics are appended. A comparison is then made between the original image in the dataset and the created image. The discriminator determines the generator and discriminator losses based on the output.

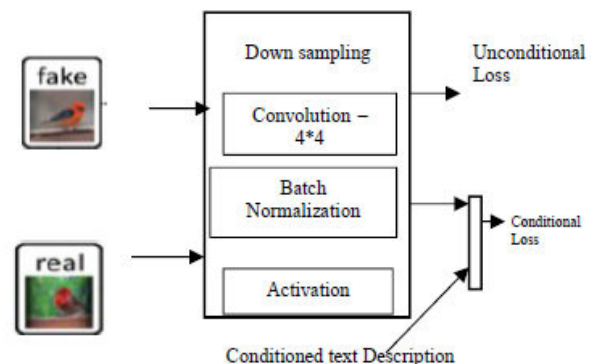


Figure 8. Architecture of image identification

This causes the generator's weights to change. There is a concurrent training process for both the generator and the discriminator.

5. EXPERIMENTAL RESULTS

To assess the generative model's performance, two well-known measures, the Inception Score (IS) and the Frechet Inception Distance (FID), were employed. The IS uses a pre-trained Inception Network model to recognize patterns in sensory data to determine class probabilities for simulated data. Higher IS scores suggest more objective and diverse material. Our IS calculations are carried out using the same Inception Networks as were used in our prior in-depth comparisons. There are networks available on StackGAN that are tailored to the CUB and Oxford-102 datasets. The IS is flawed since it does not take statistical information. An excellent IS score would be achieved by a generative model with minimal diversity that generates just a few high-quality examples for each class. To circumvent this issue, the Frechet Inception Distance was devised (FID). Using FID, one may determine if a generative model produced a distribution with statistical properties that are comparable to those of the training data. To be more specific, an Inception Network is used by FID to calculate activation characteristics of both training set photos and final images. Table 1 (Yeshasvi Mogula et al., 2023) shows the measures of the images and scores of the input text. The Frechet Distance is then determined by comparing the genuine and fake image characteristics. When the FID score is low, the produced pictures statistically reflect the training set as nearly as possible.

Table 1. Metrics for the image measurement

Met ric	The Ima ge Qua lity	The Ima ge Driv ers	Obj ect Fide lity	The Menti oned Objec ts	The Num erical Alig ment	The Posit onal Alig ment	Parap hrase Robus tness	Text Relev ance	Auto matic
IS	✓		✓						✓
FID	✓	✓							✓
Scor e FID			✓						✓
R- Prec					✓			✓	✓
SO A				✓				✓	✓
Capt ion Img								✓	✓

A. Evaluation Measures

i. Inception Score (IS):

The entropy of the distribution of classes over the sampled data is a measure of diversity; a high value indicates a lack of dominant classes and a more evenly distributed training set. Here is the scoring equation: where the probability distribution is a KL-divergence.

Given the label and the generated image, the conditional probability is denoted by $p(y/x)$, with $p(y)$ standing for the marginal probability. Information loss due to the approximation of an empirical distribution is quantified by the KL-distance.

ii. Fractional Frechet-Inception Distance (FID):

It has been reported that scores for FID generated by the TensorFlow and Pytorch implementations are different, even though there are quantitative measures of quality. While style-attn GAN results may appear to be on the lower end compared to SOTA, a closer look at the generated images reveals otherwise. After looking at a few hundred examples, it is observed that the style-AttnGAN-generated photos are more consistent and appear more photorealistic. Table 2 shows the dataset performances comparison with different scores.

Table 2. Performance Comparison

Data set	Frechet Inception distance	Inception score	Human Rank
CUB-200	16.89	4.08 ±.04	1.29±.03
OXFORD-102	48.88	3.27±.05	1.30±.03

iii. R-Precision:

To calculate the R-precision, R-precision ranks potential text explanations for each image based on their process of similarity and relies on selecting the most relevant descriptions. The Rth place, accuracy equals recall. Table 3, the Best inception score is an indicator of how well a particular GAN model performs on the CUB dataset. R-precision rate is a measure of accuracy that reflects how closely each generated image matches the original photo. (Tao Xu et al, 2017).

Table 3. Calculated Scores of Inception Score and R-precision

Method	Inception Score	R- Precision Score
AttnGAN2, no StyleAttnGAN	3.99±.05	10.38 ±5.8
AttnGAN2, StyleAttnGAN=0.1s	4.20±.07	16.58 ±4.85
AttnGAN2, StyleAttnGAN=1	4.38±.08	34.98± 4.03
AttnGAN2,StyleAttnGAN=5	4.39±.05	58.69 ±5.42
AttnGAN2, StyleAttnGAN=10	4.30±.08	63.88± 4.86

6. CONCLUSION

In this paper, we present an updated version of the neural network with information flow, called "Captioner," which is an integral part of the GAN architecture. The proposed network architecture may be thought of as a chain: text > picture > text, with the central idea being to use the restored original text as input to the network. We base our comparison of the existing StackGAN framework to four different variant implementations. Based on this study, it is observed that the Captioner module can generate images with more authentic expressions and preservations of primitive

elements. To further enhance the image data quality, the embeddings are used in error calculation. Moreover, both synthesized image data and real picture data are useful for bolstering quality. We anticipate that integrating these diverse implementations will certainly elevate to cutting-edge GAN designs. It is a novel approach to create generations that approximate real-world situations with GANs that provide trustworthy outcomes.

References:

- Aaron van den Oord, Nal Kalchbrenner, Lasse Espeholt, koray kavukcuoglu, Oriol Vinyals, Alex Graves. (2016). Conditional image generation with pixel CNN decoders. doi.org/10.48550/arXiv.1606.05328
- Ashish Vaswani, Noam Shazeer, Niki Parmar, Jakob Uszkoreit, Llion Jones, Aidan N. Gomez, Łukasz Kaiser, Illia Polosukhin. (2017). Attention is all you need. arXiv:1706.03762, doi.org/10.48550/arXiv.1706.03762
- Anh Nguyen, Jeff Clune, Yoshua Bengio, Alexey Dosovitskiy, Jason Yosinski. (2017). Plug & play generative networks: Conditional iterative generation of images in latent space. In *Computer Vision and Pattern Recognition Conference (CVPR)*, doi.org/10.48550/arXiv.1612.00005
- Alec Radford, Luke Metz, Soumith Chintala (2016). Unsupervised representation learning with deep convolutional generative adversarial networks. In *the International Conference on Learning Representations*, doi.org/10.48550/arXiv.1511.06434
- Christian Ledig, Lucas Theis, Ferenc Huszar, Jose Caballero, Andrew Cunningham, Alejandro Acosta, Andrew Aitken, Alykhan Tejani, Johannes Totz, Zehan Wang, Wenzhe Shi. (2017). Photo-realistic single image superresolution using a generative adversarial network. In *Computer Vision and Pattern Recognition Conference (CVPR)*, [doi: 10.1109/CVPR.2017.19](https://doi:10.1109/CVPR.2017.19)
- Christian Szegedy, Vincent Vanhoucke; Sergey Ioffe; Jon Shlens; Zbigniew Wojna (2016). Rethinking the inception Architecture. [doi: 10.1109/CVPR.2016.308](https://doi:10.1109/CVPR.2016.308)
- Diederik P Kingma, Max Welling. (2014). Auto-encoding variational bayes. In *the International Conference on Learning Representations*. doi.org/10.48550/arXiv.1312.6114
- Edeh Michael Onyema, Sundaravadivazhagn Balasubaramanian, Kanimozhi Suguna S, Celestine Iwendi, B.V.V. Siva Prasad, Chinecherem Deborah Edeh.(2023). Remote monitoring system using slow-fast deep convolution neural network model for identifying anti-social activities in surveillance applications,Measurement: Sensors,Vol 27, [sciencedirect, doi.org/10.1016/j.measen.2023.100718](https://sciencedirect.com/science/article/pii/S1364546X2300718).
- Elman Mansimov, Emilio Parisotto, Jimmy Lei Ba, Ruslan Salakhutdinov (2016). Generating images from captions with attention. In *the International Conference on Learning Representations*. doi.org/10.48550/arXiv.1511.02793
- Emily L. Denton, Soumith Chintala, arthur szlam, Rob Fergus. (2015). Deep Generative Image Models using a Laplacian Pyramid of Adversarial Networks. doi.org/10.48550/arXiv.1506.05751
- Han Zhang, Tao Xu, Hongsheng Li, Shaoting Zhang, Xiaogang Wang, Xiaolei Huang, Dimitris Metaxas. (2017). Text to photo-realistic image synthesis with stacked generative adversarial networks. *International Conference on Computer Vision*. [doi: 10.1109/ICCV.2017.629](https://doi:10.1109/ICCV.2017.629)
- Han Zhang, Tao Xu, Hongsheng Li, Shaoting Zhang, Xiaogang Wang, Xiaolei Huang, Dimitris Metaxas.(2017). Realistic image synthesis with stacked generative adversarial networks. [arXiv: 1710.10916](https://arXiv:1710.10916), doi.org/10.48550/arXiv.1710.10916
- Ian Goodfellow, Jean Pouget-Abadie, Mehdi Mirza, Bing Xu, David Warde-Farley, Sherjil Ozair, Aaron Courville, Yoshua Bengio. (2014), Generative adversarial nets. <https://arxiv.org/abs/1406.2661>, doi.org/10.48550/arXiv.1406.2661
- Kelvin Xu, Jimmy Ba, Ryan Kiros, Kyunghyun Cho, Aaron Courville, Ruslan Salakhutdinov, Richard Zemel, Yoshua Bengio. (2015). Show, attend and tell: Neural image caption generation with visual attention. arXiv:1502.03044, doi.org/10.48550/arXiv.1502.03044
- Karol Gregor, Ivo Danihelka, Alex Graves, Danilo Jimenez Rezende, Daan Wierstra. (2015). A recurrent neural network for image generation. In *the International Conference on Machine Learning*. <https://arxiv.org/abs/1502.04623>, doi.org/10.48550/arXiv.1502.04623
- Olga Russakovsky, Jia Deng, Hao Su, Jonathan Krause, Sanjeev Satheesh, Sean Ma, Zhiheng Huang, Andrej Karpathy, Aditya Khosla, Michael Bernstein, Alexander C. Berg, Li Fei-Fei. (2015). ImageNet Large Scale Visual Recognition Challenge. *IJCV*, 115(3):211–252. doi.org/10.48550/arXiv.1409.0575

- Phillip Isola; Jun-Yan Zhu; Tinghui Zhou; Alexei A. Efros. (2017). Image-to-image translation with conditional adversarial networks. In Computer Vision and Pattern Recognition Conference (CVPR). doi.org/10.1109/CVPR.2017.632
- Rinon Gal, Yuval Alaluf, Yuval Atzmon, Or Patashnik, Amit H. Bermano, Gal Chechik, Daniel Cohen-Or (2022). An Image is Worth One Word: Personalizing Text-to-Image Generation using Textual Inversion. doi.org/10.48550/arXiv.2208.01618
- Saleem Raja .A, Sundarvadivazhagan. B , Vijayarangan.R and S. Veeramani (2022). Malicious Webpage Classification Based on Web Content Features using Machine Learning and Deep Learning. International Conference on Green Energy, Computing and Sustainable Technology (GECOST), Miri Sarawak, Malaysia, 2022, pp. 314-319, doi: 10.1109/GECOST55694.2022.10010386.
- Scott Reed, Aäron Oord, Nal Kalchbrenner, Sergio Gómez Colmenarejo, Ziyu Wang, Yutian Chen, Dan Belov, Nando Freitas (2017). parallel multiscale autoregressive density estimation, Proceedings of the 34th International Conference on Machine Learning, PMLR 70:2912-2921. <https://proceedings.mlr.press/v70/reed17a.html>
- Tim Salimans, Ian Goodfellow, Wojciech Zaremba, Vicki Cheung, Alec Radford, Xi Chen, Xi Chen (2016). Improved techniques for training gans. In NIPS.for computervision. In Computer Vision and Pattern Recognition Conference (CVPR). doi.org/10.48550/arXiv.1606.03498
- Tao Xu, Pengchuan Zhang, Qiuyuan Huang, Han Zhang, Zhe Gan, Xiaolei Huang, Xiaodong He. (2017). AttnGAN: Fine-Grained Text to Image Generation with Attentional Generative Adversarial Networks. ArXiv. doi.org/10.48550/arXiv.1711.10485.
- Yeshasvi Mogula., Kayal, P., Subetha, T. (2023). A Survey on Text Description to Image Generation Using GAN. In: Ranganathan, G., Fernando, X., Piramuthu, S. (eds) Soft Computing for Security Applications. Advances in Intelligent Systems and Computing, vol 1428. Springer, Singapore, doi.org/10.1007/978-981-19-3590-9_52
- Zichao Yang, Xiaodong He, Jianfeng Gao, Li Deng, Alex Smola. (2016). Stacked attention networks for image question answering. In Computer Vision and Pattern Recognition Conference (CVPR). doi.org/10.48550/arXiv.1511.02274

Kayal Padmanandam

BVRIT HYDERABAD College of
Engineering for Women,
Hyderabad,
India
kayalpaddu@gmail.com
0000-0002-3872-8422

Yeshasvi Mogula

BVRIT HYDERABAD College of
Engineering for Women,
Hyderabad,
India
yeshasvireddy26@gmail.com
0009-0007-2233-2320

Nikitha Pitla

BVRIT HYDERABAD College of
Engineering for Women,
Hyderabad,
India
nikitap121@gmail.com
0009-0000-7997-2547

P. S. Brahmanandam

Dept. of Physics
&
R&D Cell
Shri Vishnu Engineering College for
Women(A),
Bhimavaram
dranandpotula@svecw.edu.in
0000-0001-9777-3496



MOLECULAR DOCKING SIMULATIONS ON EPIDERMAL GROWTH FACTOR RECEPTOR (EGFR) WITH POTENTIAL LEAD MOLECULES

K Ganesh Kadiyala¹

K. Jagadeesh

B. N. Suresh Varma Dendukuri¹

Rama Swamy Guttula

TDL Suneetha

Kiranmai Devi

B. Kanaka Durga

Sumalatha Sagi

Keywords:

A B S T R A C T

The Epidermal Growth Factor Receptor (EGFR) has received significant interest in the field of lung cancer due to its pivotal involvement in the development and progression of certain types of the illness, particularly non-small cell lung cancer (NSCLC). The study used molecular docking simulations to examine the molecular interactions between ten lead compounds and the EGFR protein. In the study of EGFR inhibitors, Tepotinib had the most advantageous docking energy of -7.92 Kcal/mol ($IC_{-1.57\mu M}$), whereas Dacomitinib and Lazertinib demonstrated docking energies of -6.96 Kcal/mol ($IC_{-7.91\mu M}$) and -6.63 Kcal/mol ($IC_{-13.77\mu M}$), respectively, which were in close proximity. The binding affinities of these medicines towards the EGFR, as observed, suggest their potential efficacy as inhibitors. The results obtained from this research suggest that several lead medications, specifically Tepotinib, Dacomitinib, Lazertinib, and Sotorasib, demonstrate promise as inhibitors of the EGFR in the context of therapy for prostate cancer.

© 202x Published by Faculty of Engineering



1. INTRODUCTION

Lung adenocarcinoma is a frequently diagnosed disease and a leading contributor to cancer-related mortality on a global scale (Thai et al. 2021). In the global context, it is projected that there will be around 2.2 million newly diagnosed cases of lung cancer in the year 2020, constituting approximately 11.4% of the total number of cancer cases (Liu et al. 2023). Although smoking is well recognized as the primary contributor to the development of lung cancer, it is important to acknowledge that this disease is frequently diagnosed among those who engage in smoking behavior (Thandra et al. 2021). It is widely recognized that tobacco smoking is the primary preventable factor contributing

to mortality on a global scale. Research has found that tobacco smoking is responsible for up to 90% of lung cancer cases. If current trends persist, tobacco consumption is expected to contribute to a rise in cancer rates worldwide, particularly impacting developing countries like China, Russia, and India.

Tobacco smoking is widely recognized as the leading cause of preventable death worldwide. It is responsible for a significant proportion, up to 90%, of lung cancer cases. Tobacco consumption is expected to cause a global increase in cancer rates, particularly in developing countries like China, Russia, and India. The EGFR mutation is widely prevalent in cases of non-small-cell lung cancer. The acronym EGFR represents

¹ K Ganesh Kadiyala, E-mail: kganeshkadiyala@gmail.com

¹ B. N. Suresh Varma Dendukuri, Email: sureshvarma60@gmail.com

the epidermal growth factor receptor. The cell surface receptor protein in question is significant in the regulation of cell growth, division, and survival. Upon binding to the epidermal growth factor receptor (EGFR) located on the cellular membrane, a ligand, such as epidermal growth factor (EGF), initiates a cascade of intracellular signaling events (Pache 2006). The presence of irregularities in the signaling pathway of the epidermal growth factor receptor (EGFR) can have a role in the pathogenesis and advancement of specific medical conditions, such as cancer (Sigismund 2018). Cancer often starts because of problems with the EGFR gene, like mutations or overexpression, which causes cells to divide and multiply in ways that are not controlled (Wee and Wang 2017). This phenomenon is considered a distinctive feature of the disease. EGFR-targeted therapeutics encompass both small-molecule inhibitors and monoclonal antibodies that selectively target the epidermal growth factor receptor (EGFR) or its related signaling pathways (Seshacharyulu et al. 2012 & Bethune et al. 2010). These pharmaceutical agents effectively manage several malignancies, including non-small cell lung carcinoma, colorectal carcinoma, and head and neck carcinoma, among other types.

In the case of EGFR-positive lung cancer, individuals can enhance their prognosis by undergoing a therapeutic intervention that specifically targets the mutation, such as the administration of an EGFR inhibitor (Thandra et al. 2021). Numerous laboratory investigations have been conducted in pursuit of inhibitors capable of efficiently impeding the mutation of EGFR, yielding successful outcomes in the identification of these pharmaceutical agents (Nan et al. 2017).

Therefore, searching small molecular inhibitors that can target both EGFR may help lung cancer treatment (Yang et al. 2023). The molecular docking and molecular dynamics (MD) methods were used to find the binding sites on target molecules, study how biomolecules' shapes change, check for stability, and look at how proteins fold (Jayakanthan et al. 2015) (Rajendra Prasad et al. 2013). Molecular modeling techniques were used to investigate the drug-receptor interaction to figure out whether the ligands might bind to EGFR (Nasab et al. 2018). The evaluation of ligand appropriateness for receptor binding necessitates careful consideration of their physicochemical features (Reddy et al. 2014). These properties play a crucial role in guiding subsequent modifications of the ligands, ultimately preparing them for clinical trials (Ali et al. 2016). Nevertheless, the reports fail to provide explicit details regarding the exact target receptors or cellular pathways through which the medication exerts its effects. Consequently, the researchers conducted a molecular docking analysis to evaluate the efficacy of inhibitors in preventing EGFR mutations (Sangande et al. 2021).

An important part of our study is that it investigates the pharmacophores model to learn more about how the functional group interacts with the amino acids of the receptor at the molecular level. The utilization of a singular pharmaceutical agent that may effectively target several molecular targets has the potential to be a promising therapeutic approach for the treatment of many types of cancer (Hu et al. 2022). Further, to conduct a molecular docking analysis on the epidermal growth factor receptor (EGFR) using potential lead molecules to forecast their pharmacokinetic characteristics.

2. MATERIALS AND METHODS

2.1 Determine target receptors and the lead ligands

The significance of the EGFR in lung cancer is of utmost importance (Bethune et al. 2015). The presence of DNA changes in the intracellular epidermal growth factor receptor (EGFR), which can be found using polymerase chain reaction (PCR), has been observed in most cases. The EGFR receptor has been selected as the receptor of interest for the subsequent docking investigations. The use of epidermal growth factor receptor inhibitors Gefitinib, Erlotinib, Afatinib, Dacomitinib (Ellis 2015), Mobocertinib (Wang et al. 2022), Lazertinib (Myung-Ju et al. 2019), Osimertinib, Tepotinib (Smit et al. 2022), Sotorasib (Skoulidis et al. 2021), Poziotinib (Le et al. 2022) are considered as key ligands for ligands.

2.2 Target protein preparation for docking studies using autodock

Epidermal Growth Factor Receptor (EGFR)

The protein obtained from the Protein Data Bank (PDB) possesses a fully assigned charge. Therefore, polar hydrogens and Kollman charges were included in the macromolecule prior to the docking process, utilizing the AutoDock software (ADS). The outcome of the macromolecule docking process may exhibit variability when water molecules are present. Water molecules were eliminated from the macromolecule to mitigate any undesired protein behavior during the execution of docking tests. The protein EGFR mutant (exon-19 deletion) (Huang et al. 2022) was obtained from the Protein Data Bank (PDB) due to its well-documented association with the development of lung cancer.

The utilized structure consists of a crystal structure complexed with ligands. Consequently, to perform docking of the required ligand with the protein at the specific location, it is necessary to eliminate the bound ligand by deleting the heteroatoms from the PDB file using the auto dock software. The precise location of the active site inside the protein remains undetermined. Blind docking was employed in this study, wherein the full protein surface was selected for the purpose of protein-ligand interaction. After establishing the grid

box for blind docking, the protein is subsequently stored in the PDBQT format.

2.3 Collecting Ligands from sources and Preparation for docking studies using autodock

Ligand preparation

The employed structure entails a crystal structure that is bound to the ligand(s). Consequently, to successfully dock the intended ligand at the specific location inside the protein, it is necessary to eliminate the associated ligand by eliminating the heteroatoms from the PDB file through the utilization of autodock software. The precise location of the active site inside the protein remains undetermined. The method of blind docking was employed, wherein the entirety of the protein surface was chosen to facilitate the interaction between the protein and ligand. After establishing the grid box for blind docking, the protein is subsequently stored in the PDBQT format.

Analysis of the docking results

The analysis of the .DLG file, generated through the execution of autogrid and autodock procedures, is conducted to derive essential parameters such as docking energy, RMSD (Root Mean Square Deviation), representing the disparity between the initial and final positions of native ligands, total internal energy, and inhibition constant (IC). These values hold significant significance in characterizing both the ligand and protein involved in the docking process. The tabulation of the values corresponding to the 10 distinct ligands is conducted in order to identify the optimal protein-ligand pairings. The findings were analyzed using Discovery Studio software, which allowed for both 3-D and 2-D visualization formats. The photos depict the spatial arrangement of the ligand in relation to the protein's surface, presented in both three-dimensional (3-D) and two-dimensional (2-D) formats. Additionally, it provides insights into the many types of contacts, such as van der Waals forces, pi-lone pair interactions, alkyl interactions, pi-alkyl interactions, and traditional hydrogen bonding, that occur between the atoms of the protein and the ligand.

3. RESULTS AND DISCUSSION

Molecular docking is an important method used in drug development because it helps scientists guess how ligands will fit into their specific binding sites and how they will interact with other molecules. At present, Autodock is widely recognized as the molecular docking program that enjoys the highest level of popularity. The great level of accuracy and versatility exhibited by this technology has significantly broadened its range of applications. The AutoDock software was utilized to dock all the processed ligands onto the surface of the EGFR. The obtained results are presented below. The binding affinity between a ligand and the

active site of a protein is positively correlated with the number of interactions. Consequently, an increase in the number of interactions leads to an improvement in binding affinity, ultimately resulting in the development of a favorable docking score. The inhibition constant (IC) is a measure of the concentration of the ligand needed to effectively inhibit the activity of the corresponding protein. If the IC value is lower for a specific ligand, it indicates that the ligand is superior and exhibits a strong affinity at the active site for the specific protein. Table 1 and Figures 1.1 to 1.10 depict the interaction of the lead ligands on the surface of the EGFR.

As can be seen in Figure 1.1, the ligand Tepotinib has a docking score of -7.92 Kcal/mol and an inhibitory constant (IC) of 1.57 μ M when it comes to interacting with the EGFR mutant. The ligand Tepotinib has exhibited a diverse array of bonding interactions within the active site of the EGFR, encompassing more than 12 interactions. The interactions between the amino acids of the EGFR protein and the tepotinib ligand can be characterized as follows: Van der Waals interaction occurs with TYR 915; a conventional hydrogen bond is formed with GLY 917, ASP 916, and SER 912; and alkyl and pi-alkyl interactions are observed with PRO 934 and ARG 932.

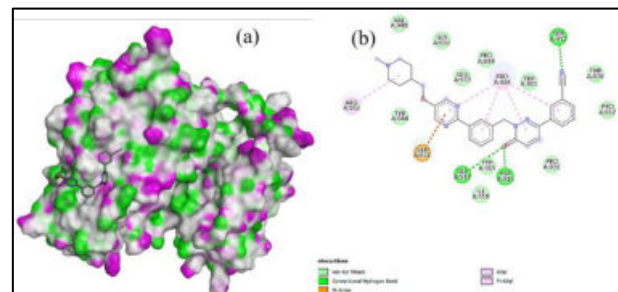


Figure 1.1. (a): 3-D representation of EGFR protein and Tepotinib ligand interaction, (b): 2-D representation of EGFR protein and Tepotinib ligand interaction.

In Figure 1.2, the ligand Dacomitinib shows that it has a docking score of -6.96 Kcal/mol and an inhibitory constant (IC) of 7.9 μ M when it comes to interacting with the EGFR mutant. The EGFR protein's amino acids engage in many types of interactions with the Dacomitinib ligand, including Van der Waals contacts with ARG 889 and SER 885, as well as pi-cation interactions with ARG 836. The presence of a covalent bond is shown by the interaction between the amino acid residues isoleucine (ILE) at position 890 and threonine (THR) at position 892. A high docking score is obtained due to the strong covalent contact between the ligand and the EGFR.

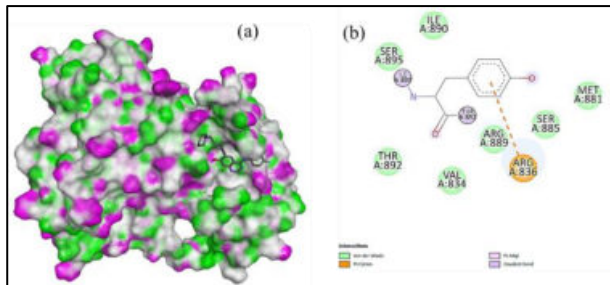


Figure 1.2. (a): 3-D representation of EGFR protein and Dacomitinib ligand interaction, (b): 2-D representation of EGFR protein and Dacomitinib ligand interaction.

The ligand Lazertinib, which can be seen in Figure 1.3, has a docking score of -6.63 Kcal/mol and an inhibitory constant (IC) of 13.77 μ M when it comes to interacting with the EGFR mutant. The ligand Lazertinib has exhibited a diverse array of bonding interactions within the active site of the EGFR, encompassing more than 12 interactions. The EGFR protein's amino acids engage in many types of interactions with the Lazertinib ligand. In particular, PRO 699 and VAL 769 make Van der Waals contacts, ARG 831, ASN 700, and TYR 827 make conventional hydrogen bonds, and LEU 703 makes pi- lone pair contacts. It was looked into how alkyl and pi-alkyl groups interact with amino acid residues ARG 831, ALA 702, ALA 767, LEU 777, and LEU 703.

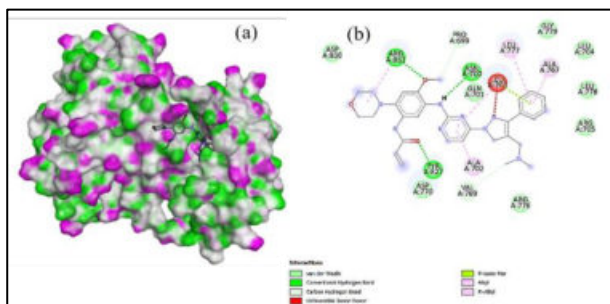


Figure 1.3. (a): 3-D representation of EGFR protein and Lazertinib ligand interaction, (b): 2-D representation of EGFR protein and Lazertinib ligand interaction

The ligand Sotorasib can be seen in Figure 1.4, has a docking score of -6.49 Kcal/mol and an inhibitory constant (IC) of 17.44 μ M when it comes to interacting with the EGFR mutant. The ligand Sotorasib has exhibited a diverse array of bonding interactions within the active site of the EGFR, encompassing more than 12 interactions. The amino acids of the EGFR protein exhibit a diverse array of interactions with the sotorasib ligand. The interactions between the amino acids of EGFR proteins and the Sotorasib ligand can be described as follows: a conventional hydrogen bond with THR 993, LYS 728, and PRO 794; a pi-cation interaction with LYS 716; a pi-sigma interaction with PHE 795; and an amide pi-stacked interaction with PHE 795. The present study investigates the interactions of alkyl and pi-alkyl groups with PRO 990, PHE 795, and LEU 718 residues.

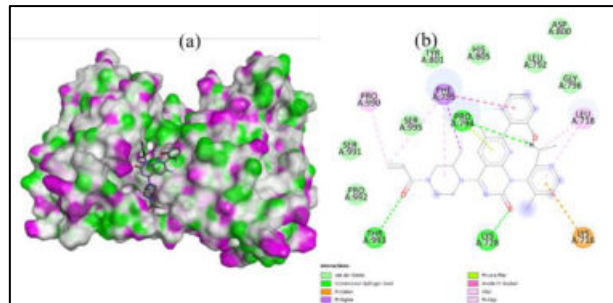


Figure 1.4. (a): 3-D representation of EGFR protein and Sotorasib ligand interaction, (b): 2-D representation of EGFR protein and Sotorasib ligand interaction

In Figure 1.5, the ligand Afatinib shows that it has a docking score of -6.47 Kcal/mol and an inhibitory constant (IC) of 18.02 μ M when it comes to interacting with the EGFR mutant. There exists a total of nine interactions between the Afatinib ligand and the EGFR protein. The interactions between the amino acids of EGFR proteins and the Afatinib ligand involve conventional hydrogen bonding with LEU 704 and GLN 701. The halogen interacts with the amino acid TYR 764, while the ALA 702 amino acid engages in a pi-sigma contact. Additionally, there is a pi-pi stacked interaction involving TYR 764. Furthermore, ALA 702, ALA 767, LEU 704, and LEU 703 exhibit alkyl and pi-alkyl interactions.

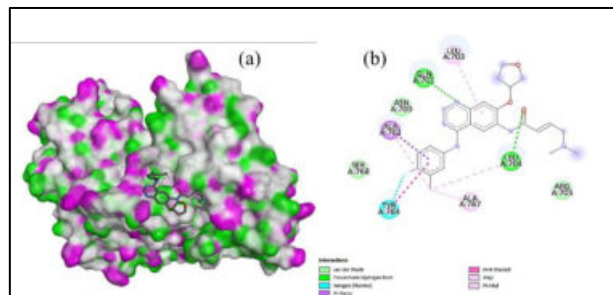


Figure 1.5. (a): 3-D representation of EGFR protein and Afatinib ligand interaction, (b): 2-D representation of EGFR protein and Afatinib ligand interaction

In Figure 1.6, the ligand Poziotinib shows that it has a docking score of -6.28 Kcal/mol and an inhibitory constant (IC) of 24.89 μ M when it comes to interacting with the EGFR mutant. A total of ten interactions have been observed between the Poziotinib ligand and the EGFR receptor. The EGFR protein's amino acids engage in many types of interactions with the Poziotinib ligand. Specifically, ARG 705 exhibits Van der Waals contacts, LEU 777 forms a conventional hydrogen bond, LEU 703 also participates in a conventional hydrogen bond, ALA 767 engages in a halogen interaction, and ALA 702, ARG 705, LEU 777, ALA 767, and LEU 703 are involved in alkyl and pi-alkyl interactions.

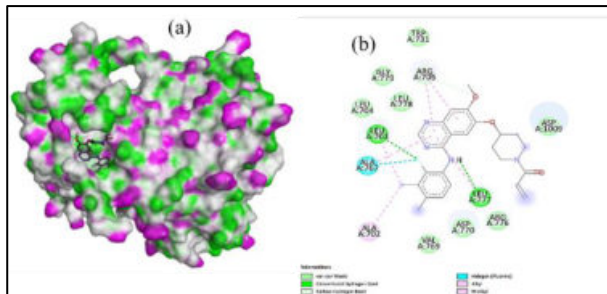


Figure 1.6. (a): 3-D representation of EGFR protein and Pozotinib ligand interaction, (b): 2-D representation of EGFR protein and Pozotinib ligand interaction

In Figure 1.7, the ligand Osimertinib shows that it has a docking score of -6.10 Kcal/mol and an inhibitory constant (IC) of 33.93 μ M when it comes to interacting with the EGFR mutant. A total of thirteen interactions were observed between the Osimertinib ligand and the EGFR receptor. The EGFR protein's amino acids engage in many types of interactions with the Osimertinib ligand. Specifically, Van der Waals contacts occur with ASP 800 and ASP 855, a conventional hydrogen bond is formed with MET 793, a carbon hydrogen interaction takes place with GLN 791, a pi-sigma interaction occurs with LEU 718 and LEU 814, and a pi-sulfur connection is established with MET 766. The present study investigates the interactions of alkyl and pi-alkyl groups with the amino acid residues CYS 775, ALA 743, and VAL 726.

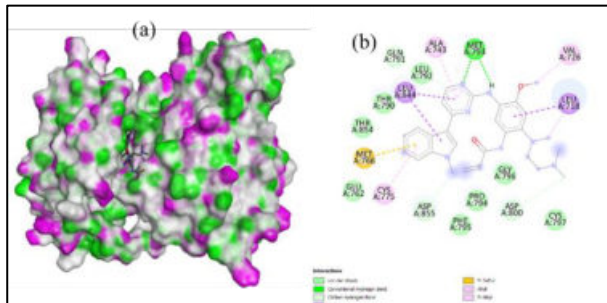


Figure 1.7. (a): 3-D representation of EGFR protein and Osimertinib ligand interaction, (b): 2-D representation of EGFR protein and Osimertinib ligand interaction

The observed elevation in the concentration of inhibitory constant (IC) values for ligands in the presence of the protein suggests that a substantial concentration of a certain ligand or lead molecule is required to effectively impede the functioning of a particular protein. Ligands that exhibit a favorable docking score and lower IC values are deemed suitable candidates for targeting the active site of the selected targets.

Therefore, the ligands Gefitinib, Mobocertinib, and Erlotinib exhibits a high IC value (greater than 40 μ M) and minimal docking score (less than -6.0 Kcal/mol) with EGFR. The docking energy of Gefitinib,

Mobocertinib, and Erlotinib ligands has been seen to be less than -6.0 Kcal/mol, and their IC values with EGFR are greater than 40 μ M. This observation indicates that the three ligands depicted in Figures 1.8 to 1.10 have minimal interaction with the EGFR. The potential explanation for the lower docking scores and higher concentrations of IC values seen for Gefitinib, Mobocertinib, and Erlotinib may be attributed to a reduced number of interactions between these ligands and the active site of the EGFR protein.

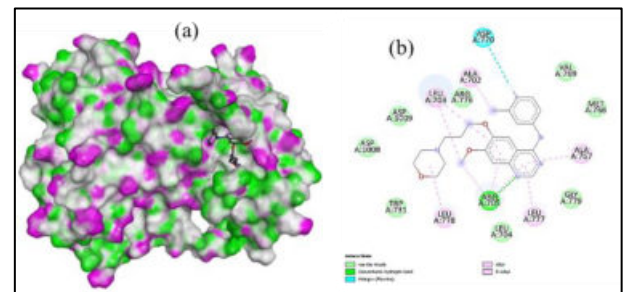


Figure 1.8. (a): 3-D representation of EGFR protein and Gefitinib ligand interaction, (b): 2-D representation of EGFR protein and Gefitinib ligand interaction

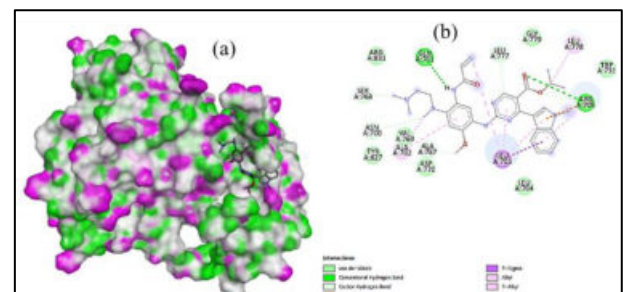


Figure 1.9. (a): 3-D representation of EGFR protein and Mobocertinib ligand interaction, (b): 2-D representation of EGFR protein and Mobocertinib ligand interaction

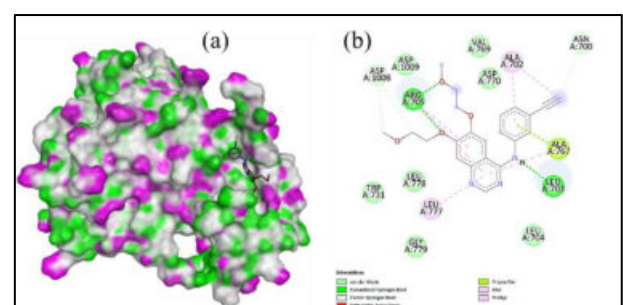


Figure 1.10. (a): 3-D representation of EGFR protein and Erlotinib ligand interaction, (b): 2-D representation of EGFR protein and Erlotinib ligand interaction.

Table 1. Docking results and IC values of multiple ligands (Lead Ligands) with Epidermal Growth Factor Receptor (EGFR) mutant

S. No	Lead Molecule (Ligand)	Target Protein	Docking Energy	Inhibition Constant (IC)
1.	Tepotinib	Epidermal Growth Factor Receptor (EGFR) mutant	-7.92 Kcal/mol	1.57 μM
2.	Dacomitinib	Epidermal Growth Factor Receptor (EGFR) mutant	-6.96 Kcal/mol	7.91 μM
3.	Lazertinib	Epidermal Growth Factor Receptor (EGFR) mutant	-6.63 Kcal/mol	13.77 μM
4.	Sotorasib	Epidermal Growth Factor Receptor (EGFR) mutant	-6.49 Kcal/mol	17.44 μM
5.	Afatinib	Epidermal Growth Factor Receptor (EGFR) mutant	-6.47 Kcal/mol	18.02 μM
6.	Pozotinib	Epidermal Growth Factor Receptor (EGFR) mutant	-6.28 Kcal/mol	24.89 μM
7.	Osimertinib	Epidermal Growth Factor Receptor (EGFR) mutant	-6.10 Kcal/mol	33.93 μM
8.	Gefitinib	Epidermal Growth Factor Receptor (EGFR) mutant	-5.95 Kcal/mol	43.38 μM
9.	Mobocertinib	Epidermal Growth Factor Receptor (EGFR) mutant	-5.72 Kcal/mol	64.01μM
10.	Erlotinib	Epidermal Growth Factor Receptor (EGFR) mutant	-5.02 Kcal/mol	208.39 μM

4. CONCLUSION

The EGFR protein is the primary target in lung cancer cases. In this study, we have selected 10 lead ligands to conduct docking studies on EGFR to find the affinity of the ligands with the help of the docking energy and inhibition constant (IC) values. The objective is to predict the binding affinity of these ligands towards Epidermal Growth Factor Receptor (EGFR) mutant receptors known to be associated with lung cancer.

The lead ligand Tepotinib has a docking score of -7.92 Kcal/mol and an inhibitory constant (IC) of 1.57 μM when it comes to interacting with the EGFR mutant, which has demonstrated a favorable binding affinity with EGFR when compared to the remaining lead ligands (Table 1). The analysis of the docking poses revealed that the ligand Tepotinib exhibited a Van der Waals interaction at TYR 915; a conventional hydrogen bond is formed with GLY 917, ASP 916, and SER 912; and alkyl and pi-alkyl interactions are observed with PRO 934 and ARG 932. Nevertheless, the docking score of the Lazertinib ligand exhibits a little drop due to the unfavorable interaction between the donor and acceptor at LEU 703. The docking score exhibits a

modest drop when comparing the interaction between the Sotorasib ligand and EGFR to that of Tepotinib, which can be attributed to the lack of Van der Waals interaction. The binding affinity between the osimertinib ligand and EGFR is lower in comparison to the tepotinib ligand. The reduced level of interactions observed may be attributed to a decrease in the number of Van der Waals connections as well as a significant decrease in conventional hydrogen bond interactions between Osimertinib and EGFR. No covalent interaction between osimertinib and EGFR is detected. Based on the findings, it may be inferred that tepotinib exhibits favorable binding affinity as a ligand towards the EGFR compared to other selected lead ligands. Hence, out of the 10 lead ligands that were chosen, four to five ligands have demonstrated favorable binding interactions with the specified protein, namely the EGFR mutant with good docking energy and a lower inhibition constant value.

Acknowledgement: The authors would like to express their gratitude towards the management of Shri Vishnu Engineering College for Women (A), Bhimavaram, India for their logistic support, without which it would not have been possible to carry out this work.

References:

- Ali, A. A., Lee, Y. R., Chen, T. C., Chen, C. L., Lee, C. C., Shiau, C. Y., Huang, H. S. (2016). Novel Anthra[1,2-c][1,2,5]Thiadiazole-6,11-Diones as Promising Anticancer Lead Compounds: Biological Evaluation, Characterization & Molecular Targets Determination. *PLOS ONE*, 11(4), e0154278. doi:10.1371/journal.pone.0154278

- Bethune, G., Bethune, D., Ridgway, N., & Xu, Z. (2010). Journal of Thoracic Disease, Epidermal growth factor receptor (EGFR) in lung cancer: an overview and update. *Journal of thoracic disease*, 2(1), 48–51.
- Ellis, P. M., Coakley, N., Mlis, R., Feld, M. D., Kuruvilla, S., & Ung, Y. C. (2015). Use of the epidermal growth factor receptor inhibitors gefitinib, erlotinib, afatinib, dacomitinib, and icotinib in the treatment of non-small-cell lung cancer: a systematic review. *Curr Onco*, 22(3), e183–e215. doi: 10.3747/co.22.2566.
- Hu, L., Fan, M., Shi, S., Song, X., Wang, F., He, H., & Qi, B. (2022). Dual target inhibitors based on EGFR: Promising anticancer agents for the treatment of cancers. *European Journal of Medicinal Chemistry*, 227, 113963. doi:10.1016/j.ejmech.2021.113963
- Huang, L. T., Zhang, S. L., Han, C. B., & Ma, J. T. (2022). Impact of EGFR exon 19 deletion subtypes on clinical outcomes in EGFR-TKI-Treated advanced non-small-cell lung cancer. *Lung Cancer*, 166, 9–16. doi:10.1016/j.lungcan.2022.01.014
- Jayakanthan, M., Jubendradass, R., D'Cruz, S. C., & Mathur, P. P. (2015). A use of homology modeling and molecular docking methods: To explore binding mechanisms of nonylphenol and bisphenol A with antioxidant enzymes. *Methods in Molecular Biology*, 1268, 273–289. doi:10.1007/978-1-4939-2285-7_12
- Le, X., Cornelissen, R., Garassino, M., Clarke, J. M., Tchekmedyian, N., Goldman, J. W., Socinski, M. A. (2022). Poziotinib in Non-Small-Cell Lung Cancer Harboring HER2 Exon 20 Insertion Mutations After Prior Therapies: ZENITH20-2 Trial. *Journal of Clinical Oncology*, 40(7), 710–718. doi:10.1200/JCO.21.01323
- Liu, H. I., Chiang, C. J., Su, S. Y., Jhuang, J. R., Tsai, D. R., Yang, Y. W., Lee, W. C. (2023). *Scientific Reports*, 13, article no.: 1655.
- Myung-Ju, A., Ji-Youn, H., Ki Hyeong Lee., Sang-We, K., & Yun-Gyoo, L. (2019). Lazertinib in patients with EGFR mutation-positive advanced non-small-cell lung cancer: Results from the dose escalation and dose expansion parts of a first-in-human, open-label, multicentre, phase 1–2 study, 20(12), 1681–1690.
- Nan, X., Xie, C., Yu, X., & Liu, J. (2017). EGFR TKI as first-line treatment for patients with advanced EGFR mutation-positive non-small-cell lung cancer. *Oncotarget*, 8(43), 75712–75726. doi:10.18632/oncotarget.20095
- Nasab, R. R., Mansourian, M., Hassanzadeh, F., & Shahlaei, M. (2018). Exploring the interaction between epidermal growth factor receptor tyrosine kinase and some of the synthesized inhibitors using combination of in-silico and in-vitro cytotoxicity methods. *Research in Pharmaceutical Sciences*, 13(6), 509–522. doi:10.4103/1735-5362.245963
- Pache, J. C. (2006) Epidermal Growth Factors, encyclopedia of respiratory medicine Cambridge, MA: Academic Press, 129–133. doi:10.1016/B0-12-370879-6/00138-1
- Rajendra Prasad, V. V. S., Deepak Reddy, G., Appaji, D., Peters, G. J., & Mayur, Y. C. (2013). Chemosensitizing acridones: In vitro calmodulin dependent cAMP phosphodiesterase inhibition, docking, pharmacophore modeling and 3D QSAR studies. *Journal of Molecular Graphics and Modelling*, 40, 116–124. DOI:10.1016/j.jmgm.2012.12.009
- Reddy, G. D., Kumar, K. P., Divya, R., Kumar Reddy, K. P., & Prasad, V. V. S. R. (2015). Structural insights of JAK2 inhibitors: pharmacophore modeling and ligand-based 3D-QSAR studies of pyrido-indole derivatives. *Journal of receptor and signal transduction research*, 35(2), 189–201. doi:10.3109/10799893.2014.948556
- Sangande, F., Juliani, E., & Tjahjono, D. H. (2021). *International Journal of Molecular Sciences*, 21/20, 7779. doi:10.3390/ijms21207779
- Seshacharyulu, P., Ponnusamy, M. P., Haridas, D., Jain, M., Ganti, A. K., & Batra, S. K. (2012). Targeting the EGFR signaling pathway in cancer therapy. *Expert Opinion on Therapeutic Targets*, 16(1), 15–31. doi:10.1517/14728222.2011.648617.
- Sigismund, S., Avanzato, D., & Lanzetti, L. (2018). Emerging functions of the EGFR in cancer. *Molecular Oncology*, 12(1), 3–20. doi:10.1002/1878-0261.12155.
- Skoulidis, F., Li, B. T., Dy, G. K., Price, T. J., Falchook, G. S., Wolf, J., Govindan, R. (2021). Sotorasib for Lung Cancers with KRAS p.G12C Mutation. *New England Journal of Medicine*, 384(25), 2371–2381. doi:10.1056/NEJMoa2103695
- Smit, E., Dooms, C., Raskin, J., Nadal, E., Tho, L. M., Wu, Y. (2022). INSIGHT 2: A phase II study of tepotinib plus osimertinib in MET -amplified NSCLC and first-line osimertinib resistance. *Future Oncology*, 18(9), 1039–1054. doi:10.2217/fon-2021-1406
- Thai, A., Solomon, B. J., Sequist, L. V., Gainor, J. F., & Heist, R. S. (2021). Lung cancer. *Lancet*, 398(10299), 535–554. doi:10.1016/S0140-6736(21)00312-3
- Thandra, K. C., Barsouk, A., Saginala, K., Aluru, J. S., & Barsouk, A. (2021) Epidemiology of lung cancer. *Contemporary Oncology*, 25(1), 45–52. doi:10.5114/wo.2021.103829.
- Wang, J., Lam, D., Yang, J., & Hu, L. (2022). Discovery of mobocertinib, a new irreversible tyrosine kinase inhibitor indicated for the treatment of non-small-cell lung cancer harboring EGFR exon 20 insertion mutations. *Medicinal Chemistry Research*, 31(10), 1647–1662. doi:10.1007/s00044-022-02952-5
- Wee, P., Wang, Z. (2017). Epidermal Growth Factor Receptor Cell Proliferation Signaling Pathways. *Cancers*, 9(5), 52. doi:10.3390/cancers9050052
- Yang, H., Zhang, Z., Liu, Q., Yu, J., Liu, C., & Lu, W. (2023). Identification of dual-target inhibitors for epidermal

growth factor receptor and AKT: Virtual screening based on structure and Molecular Dynamics study. *Molecules*, 28(22), 7607. doi:10.3390/molecules28227607.

K Ganesh Kadiyala

Shri Vishnu Engineering College for Women,
Bhimavaram-534202, Andhra Pradesh, India.
kganeshkadiyala@gmail.com
ORCID 0000-0001-7357-0504

Rama Swamy Guttula

Department of BS, Vishnu Institute of
Technology, Bhimavaram-534202, Andhra
Pradesh, India.
ramaswamy.g@vishnu.edu.in
ORCID 0000-0001-7321-6660

B. Kanaka Durga

Shri Vishnu Engineering College for Women,
Bhimavaram-534202, Andhra Pradesh, India.
kanakadurga1711@gmail.com
ORCID 0009-0009-4571-430X

K. Jagadeesh

Shri Vishnu Engineering College for
Women, Bhimavaram-534202,
Andhra Pradesh, India.
kadali.jc@gmail.com
ORCID 0000-0002-3805-4931

TDL Suneetha

Shri Vishnu Engineering College for
Women, Bhimavaram-534202,
Andhra Pradesh, India.
tdlsunithache@svecw.edu.in
ORCID 0009-0007-9621-0748

Sumalatha Sagi

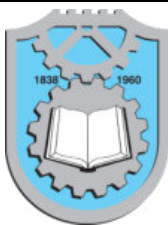
Department of BS&H,
Sri Vasavi Engineering College,
Tadepalligudem, Andhra Pradesh,
India. sagisumalatha@gmail.com
ORCID: 0009-0007-7331-4501

B. N. Suresh Varma Dendukuri

Department of Chemistry, Shri Vishnu
Engineering College for Women,
Bhimavaram-534202, Andhra Pradesh,
India. sureshvarma60@gmail.com
ORCID 0000-0002-9921-9461

Kiranmaai Devi

Shri Vishnu Engineering College for
Women, Bhimavaram-534202, Andhra
Pradesh, India.
kkiranmaiche@svecw.edu.in
ORCID: 0009-0004-2661-4139



SYNTHESIS AND PHOTOLUMINESCENCE STUDIES OF YTTRIUM ZIRCONATE (YZO) PHOSPHORS POWDERS DOPED WITH Bi³⁺ IONS

K. Suresh¹

A. Ganesh

B. V. Naveen Kumar

C. V. Krishna Reddy

A B S T R A C T

In this research work, Yttrium Zirconate ($Y_2Zr_2O_7$ =YZO) phosphors doped with varying percentages of Bi^{3+} ions ($x = 1.0, 1.5, 2.0$, and 2.5) were successfully synthesized using simple co-precipitation method and subsequently annealed at $1300^{\circ}C$. Through X-ray diffraction, it was determined that the pure YZO sample had an average crystallite size of 0.63 nm, whereas the Bi^{3+} doped YZO samples averaged at 18.36 nm. Scanning electron microscopy (SEM) revealed the prepared samples as spherical agglomerates with particle sizes ranging between 110 nm and 120 nm. Exciting the samples at a UV wavelength of 305 nm, the photoluminescence emission spectra displayed a peak at 437 nm (blue), attributed to the $3P1 \rightarrow 1S0$ transition of Bi^{3+} ions. Emission intensity increased beyond a doping concentration of 1.5 at. % Bi^{3+} , indicating a concentration quenching effect, establishing the optimal doping concentration at 1.5 at. %. Additionally, CIE color chromatic parameters were computed for the Bi^{3+} doped samples, pinpointing the optimized Bi^{3+} content (1.5 at. %) within the "Cyan" region, showcasing its potential for use in near-ultraviolet (NUV) blue emitting chips for display applications.

© 202x Published by Faculty of Engineering



1. INTRODUCTION

Yttrium zirconate ($Y_2Zr_2O_7$ = YZO) is a promising fluorescent material with a wide bandgap (5.3 eV) and excellent chemical stability (Zhang, Lü, Qiu, Zhou, & Ma, 2008). It has been extensively studied as a host for several rare earth dopants such as Eu^{3+} , Dy^{3+} and Tb^{3+} that emit visible light when excited with UV radiation (Q. Du, Zhou, Zhou, Jia, & Zhou, 2013; Gao et al., 2011; Papan, Vuković, Ahrenkiel, Jovanović, & Dramićanin, 2017). This type of mixed oxide is usually from the pyrochlore system (space group Fd-3m) or the fluorite system (space group Fm-3m). As the bond radius ratio decreases, the structure of $A_2B_2O_7$ gradually changes from fully ordered pyrochlore structure to disordered defective pyrochlore structures (Q. Du, Zhou, Zhou, & Yang, 2012; Xiao et al., 2021). The material exhibits remarkable optical transparency across an extensive wavelength range. Its substantial unit cell allows for extensive doping with trivalent

lanthanide elements. Moreover, it can be co-doped with Bi^{3+} or Ce^{3+} to enhance fluorescence sensitivity (Ting, Chiu, Chang, & Chuang, 2011; Tong, Chen, Wang, & Huo, 2015).

Bi^{3+} ions are also known as photoactive activators and have been used to activate various host networks including YZO. When doped in YZO, Bi^{3+} ions can emit blue light through the $^3P_1 \rightarrow ^1S_0$ (Whittle, Cranswick, Redfern, Swainson, & Lumpkin, 2009) transition. According to the results of many researchers, the emission spectra of Bi^{3+} ions are broad and the peaks range from blue to green for different host lattices, because the outer $6S^2$ electronic structures of Bi^{3+} ions depend on their environmental conditions, namely covalent and coordination No. etc. and place are equal. Therefore, from the results, Bi^{3+} ions can be used as a sensitizer to transfer their energy to the surrounding dopant ions and increase the doping emission intensity. Therefore, Bi^{3+} ion proved to be a

¹ Corresponding author: Kurudi Suresh
Email: kurudisuresh@gmail.com

very good sensitizer for common rare earth ions such as Eu³⁺, Tb³⁺ and Dy³⁺ etc., with greatly enhanced fluorescence efficiency through energy transfer and broadening of excitation spectrum (Awater & Dorenbos, 2017; Q. Du et al., 2012; Talari, Chirauri, Rambabu, & Ramachandra Rao, 2023; Talari, Chirauri, Reddy, & Rao, 2022). In this study, the synthesis and photoluminescence properties of YZO phosphors with different doping concentrations of Bi³⁺ ions ($X = 1.0$, 1.5 , 2.0 and 2.5) are reported.

These phosphors were synthesized through a straightforward co-precipitation process, which is of low cost, very effective in comparison with other chemical synthesis methods such as “polyol” or “sol-gel”. The precipitate formation in this method is often quick and the chemicals get well mixed in the solution forming a homogenous final product which is then subsequently annealed at 1300°C .

The crystal structure, morphology, and photoluminescence characteristics were examined using X-ray diffraction (XRD), scanning electron microscopy (SEM), and photoluminescence spectroscopy.

2. SYNTHESIS PROCEDURE

A straightforward wet-chemical technique called the “Co-Precipitation method” was used to prepare the samples of undoped and Bi³⁺ doped YZO phosphors. The $\text{Y}(\text{NO}_3)_3 \cdot 6\text{H}_2\text{O}$, $\text{Zr}(\text{NO}_3)_3 \cdot 6\text{H}_2\text{O}$, and $\text{Bi}(\text{NO}_3)_3 \cdot 5\text{H}_2\text{O}$ precursors used in the production of YZO were bought from Sigma-Aldrich in 99.99% purity. The above-mentioned powders were weighed in the appropriate amounts and properly combined with 20 milliliters of distilled water in a round-bottom flask to create YZO in pure form. This concoction was placed on a heated magnetic stirrer to act as a reduction agent. The mixture was agitated for two hours until a white precipitate formed, and NH_4OH was gradually added to the mixture from a burette. The precipitate-containing solution was washed three times with methanol, collected, centrifuged, and allowed to dry overnight in a dust-free environment. Following that, the dried samples were calcined in a furnace at 1300°C before being collected by grinding them in an agate mortar. This same procedure was repeated to create $x\%$ Bi³⁺ (where $x = 1.0$, 1.5 , 2.0 , and 2.5) YZO samples by dissolving the required amount of $\text{Bi}(\text{NO}_3)_3 \cdot 5\text{H}_2\text{O}$ in distilled water along with additional reagents.

3. RESULTS AND DISCUSSION

3.1 XRD Results

The XRD patterns of single-phase YZO: Pure and Bi³⁺ doped samples calcinated at temperature 1300°C are shown in Figure 1. The reason for high calcinations temperature may be ascribed due to the fact that, higher

calcinations temperature can easily produce nanoparticles bonding, formation of high-sized aggregates which affect the luminescence performance of the samples (Geng, Shang, Zhang, Lian, & Lin, 2013; Samuel & Kamal, 2022). The pyrochlore structure, denoted as $\text{A}_2\text{B}_2\text{O}_7$ (where $\text{A}=\text{Y}^{3+}$ and $\text{B}=\text{Zr}^{4+}$), aligns with the $\text{Fd}\bar{3}\text{m}$ space group, numbered as #227 (with $Z = 8$). The ions A, B, O, and O' reside in the 16c, 16d, 48f, and 8b crystallographic sites, respectively, inside this structure. The oxygen vacancy is represented by an empty '8a' site. The exact location of this vacancy is at the tetrahedral interstitial site between nearby B-site cations (Zr^{4+}). As a result, the coordination number of the A cation (La^{3+}) is still 8, while the coordination number of the B cation decreases to 6 from 8. ZrO_6 octahedra at the vertex corners and La^{3+} in the hexagonal holes constitute the framework of YZO's Ordered Pyrochlore (OP) structure, which creates a network of vertex corners and hexagonal holes (Tang et al., 2016).

Consequently, the introduction of Bi³⁺ ions through doping is anticipated to substitute Y³⁺ ions in the YZO structure, resulting in a singular-phase structure inclusive of the dopant ions. **Figure 1** showcases diffraction peaks that closely align with the reported cubical phase of YZO (JCPDS-01-077-2117). Notably, there's no detection of a secondary phase, signifying the comprehensive dissolution of the Bi³⁺ ions within the YZO host lattice (Chen et al., 2018; Sashmeetha, Chitrarasu, & Thangadurai, 2019).

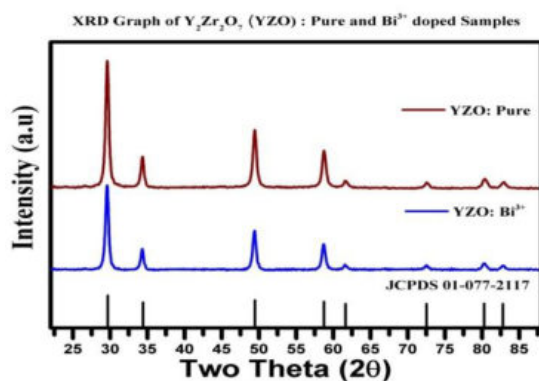


Figure 1. XRD graph of YZO: Pure and Bi³⁺ doped sample calcinated at 1300°C .

Table 1 shows the average crystallite size which was estimated from the peak width (i.e, FWHM) of the few most intense peaks from the XRD pattern using Scherrer's equation (1).

$$\text{Average Crystallite Size, } D = \frac{0.9\lambda}{\beta \cos \theta} \text{ nm} \quad \text{-- (1)}$$

Where λ is the wavelength of X-rays = 1.5406 \AA^0 and β is the corrected full width at half maximum (FWHM) of an observed peak and θ is the Bragg's Diffraction angle.

The average crystallite sizes are calculated using equation (1) and are found to be 20.63 nm for the pure YZO sample and 18.36 nm for the Bi³⁺ doped YZO sample. The distortion observed in the size is attributed to lattice strain, necessitating the introduction of charge-compensating defects and leading to the creation of oxygen vacancies. This arises from the mismatch in size between Y³⁺ ions of ionic radius 1.019 Å⁰ and Bi³⁺ ions of ionic radius 1.17 Å⁰. This phenomenon confirms the substitution of Bi³⁺ ions within the Y₂Zr₂O₇ (YZO) host lattice, replacing the Y³⁺ ions at tetrahedral sites without significantly altering the structure. (Kumar et al., 2018; Prasad, Walke, & Bhame, 2019; Shaik, Kumar, Chirauri, & Rao, 2022).

Table 1. Crystal Parameters of YZO: Pure and Bi³⁺ doped samples

Compound	a=b=c Å ⁰	V (Å ⁰) ³	Crystallite Size (nm)
YZO: Pure	5.21000	141.420	20.63
YZO: Bi ³⁺	5.21022	141.439	18.36

3.2 Morphology Results

The morphological studies of the YZO: Pure and Bi³⁺ doped phosphor powders were investigated by utilizing FEI Thermo Fisher Quanta 200F (SEM) instrument and are depicted in Figure 2. A collection of crystalline granules and particles are observed in the SEM images of the phosphorus.

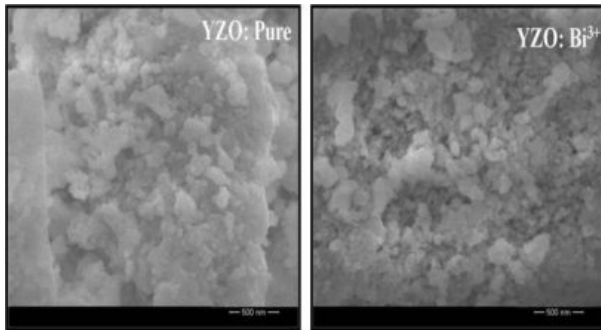


Figure 2. SEM images of (a) YZO: Pure, (b) YZO doped with Bi³⁺ sample

Owing to the phosphor particle aggregation that occurs during the calcinations, all the particles are discovered to be spherical in shape and the values of Avg. Particle size distribution of YZO pure and Bi³⁺ doped samples are 120 nm and 110.12 nm respectively. Figure 3 displays the particle size distribution between the Bi³⁺ doped and pure samples as determined by graphing histograms. The results revealed that the particle size decreases upon doping the sample with Bi³⁺ ions; this can be attributed to Coalescence effect. The difference in ionic radius between Y³⁺& Bi³⁺ ions lead to this

pseudo-distortion, resulting in a reduction in particle size (Edgar, 2007; Ju et al., 2011).

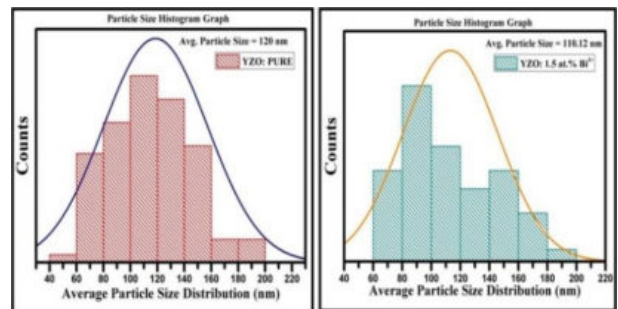


Figure 3. Avg. Particle Size distribution graphs of YZO: Pure and Bi³⁺ doped sample

3.3 Photoluminescence Results

The photoluminescence excitation and emission spectra of YZO: x at%. Bi³⁺ (x= 1.0, 1.5, 2.0 & 2.5) ions is depicted in Figure 4. Rare Earth ions such as bismuth are multipurpose since they can be used as activators and sensitizers. This indicates that it can both directly contribute to luminescence (activator role) and increase the luminescence of other ions (sensitizer role). The Bi³⁺ ions exhibit a variety of energy levels, including the ground state (¹S₀) and excited states (³P₀, ³P₁, ³P₂, and ¹P₁). The luminous behaviour of Bi³⁺ is significantly influenced by the transitions between these states. Transitions between states are guided by spin-selection rules. For instance, the $\Delta S = 0$ rule governs the transition from ¹S₀ to ¹P₁, while the ¹S₀ to ³P₀ transition is prohibited because of the constant total angular momentum ($\Delta J = 0$) (Jafer et al., 2015; Ju et al., 2011). The ¹S₀ to ³P₁ transition, which is frequently forbidden by spin-selection criteria, becomes permissible when singlet and triplet states are coupled. The experimental results are shown in Figure 4, which depicts the Photoluminescence spectra of YZO: x at% Bi³⁺ for different concentrations such as x= 1.0, 1.5, 2.0 & 2.5.

The ¹S₀ to ³P₁ transition of Bi³⁺ ions is responsible for a broad excitation band that peaks at about 305 nm and extends from 250 nm to 400 nm. The excitation wavelength at which the emission spectra were recorded ($\lambda_{ex} = 305$ nm) revealed a unique emission band at around 430 nm (blue), which is associated with the ³P₁→¹S₀ transition of Bi³⁺ ions in the host structure. The intensity of emission at 430 nm increases as the concentration of Bi³⁺ ions rises to 1.5 at%. Nevertheless, a concentration quenching effect causes the emission intensity to drop beyond this concentration. (Basina et al., 2023). Thus, the optimal composition is determined to be YZO: 1.5 at. % Bi³⁺ ions. Further, the relative emission intensities as a function of the dopant concentration is represented in Figure 4(c).

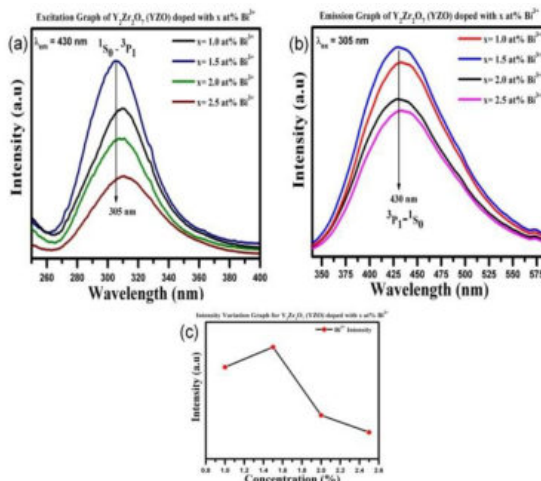


Figure 4. Photoluminescence Spectra (a) Excitation, (b) Emission and (c) Concentration Vs Emission Intensity graph of Bi³⁺ doped LZO samples

However, the emission spectrum was used to determine the chromaticity colour coordinates in accordance with the CIE (Commission Internationale de l'Eclairage) 1932 in order to understand the luminous properties of the manufactured phosphor granules. **Figure 5** shows the CIE diagram specifically for YZO doped with 1.5 at.% Bi³⁺. Using the (x, y) colour coordinates and specialized software, the CIE parameters were used to measure colour saturation. The color-correlated temperature (CCT) values (Figure 5) were calculated from the emission profiles of the prepared samples using a ratio that was derived from the chromaticity epicentre and the inverse slope line. (F. Du, Tang, Zhao, Du, & Xia, 2023; Suresh et al., 2018). The colour variables for optimized Bi³⁺ content (i.e., 1.5 at%) fall on the "Cyan" region with CIE coordinate values at X = 0.2068, Y = 0.3268, CCT value 14754 K, colour purity value 43.2%, and CRI value 37%, respectively (Li et al., 2022). Because of this, the YZO host sample doped with Bi³⁺ ions are thought to be appropriate for use in NUV blue emitting chips for display applications. Since the sample emits blue emission, it might be applicable for latent fingerprint detection, LED lighting and fluorescent lamps.

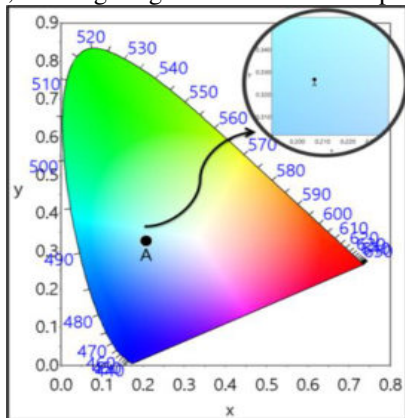


Figure 5. CIE Chromaticity diagram of optimized Bi³⁺ doped YZO sample

4. CONCLUSIONS

Yttrium Zirconate (YZO) phosphors powders doped with various concentrations of Bi³⁺ ions (x=1.0, 1.5, 2.0 & 2.5) were effectively synthesized through a straightforward "co-precipitation" method and subsequently annealed at 1300°C. XRD analyses demonstrated distinct crystallite size variations, with average sizes measuring 20.63 nm for pure YZO and 18.36 nm for the Bi³⁺ doped samples. SEM examinations highlighted spherical agglomeration morphology, ranging in size from 110 nm to 120 nm. The Photoluminescence studies unveiled the emission peak associated with the $^3P_1 \rightarrow ^1S_0$ transition of Bi³⁺ ions, occurring at approximately 430 nm when excited at around 305 nm. Notably, there's a decline in emission intensity beyond a 1.5 at. % Bi³⁺ doping concentration due to a concentration quenching effect, leading to the identification of the optimal concentration as YZO: 1.5 at. % Bi³⁺. Evaluation of CIE color parameters indicated that the optimized Bi³⁺ content (1.5 at. %) exhibited characteristics within the "Cyan" region, with CIE coordinates at X = 0.2068, Y = 0.3268, along with color purity and CRI values of 43.2% and 37% respectively. Conclusively, the photoluminescence studies revealed that the prepared YZO sample doped with Bi³⁺ ions could be a promising material for the use in NUV blue emitting chips for display, LED and fluorescent lamp applications.

References

- Awater, R. H. P., & Dorenbos, P. (2017). The Bi³⁺ 6s and 6p electron binding energies in relation to the chemical environment of inorganic compounds. *Journal of Luminescence*, 184, 221-231. doi:10.1016/j.jlumin.2016.12.021
- Basina, V. N. K., Yerramalla, N. R., Shaik, E. B., K, V., K, R. R., & Cole, S. (2023). Enhanced Luminescence and Energy Transfer of Bi³⁺/Dy³⁺ Co-doped La₂Zr₂O₇ Nanophosphors for pc-LED Applications. *Physical Chemistry Research*, 11(1), 23-31. doi:10.22036/pcr.2022.333784.2050
- Chen, Y., Xu, J., Xie, S., Tan, Z., Nie, R., Guan, Z., . . . Zhu, J. (2018). Ion Doping Effects on the Lattice Distortion and Interlayer Mismatch of Aurivillius-Type Bismuth Titanate Compounds. *Materials*, 11(5). doi:10.3390/ma11050821
- Du, F., Tang, Z., Zhao, Q., Du, L., & Xia, W. (2023). Ba₅GeO₄Br₆:Bi³⁺, a promising cyan phosphor for high-quality full-spectrum white light illumination. *Journal of Luminescence*, 255, 119592. doi:<https://doi.org/10.1016/j.jlumin.2022.119592>
- Du, Q., Zhou, G., Zhou, H., & Yang, Z. (2012). Novel multiband luminescence of Y₂Zr₂O₇:Eu³⁺, R³⁺ (R=Ce, Bi) orange-red phosphors via a sol-gel combustion approach. *Optical Materials*, 35(2), 257-262. doi:<https://doi.org/10.1016/j.optmat.2012.08.014>
- Du, Q., Zhou, G., Zhou, J., Jia, X., & Zhou, H. (2013). Enhanced luminescence of novel Y₂Zr₂O₇:Dy³⁺ phosphors by Li⁺ co-doping. *Journal of Alloys and Compounds*, 552, 152-156. doi:<https://doi.org/10.1016/j.jallcom.2012.10.074>
- Edgar, A. (2007). Luminescent Materials. In S. Kasap & P. Capper (Eds.), *Springer Handbook of Electronic and Photonic Materials* (pp. 983-996). Boston, MA: Springer US.
- Gao, L., An, Y., Zhu, H., Wang, L., Chen, J., Wang, N., & Ou, G. (2011). Hydrothermal synthesis and photoluminescence properties of Y₂Zr₂O₇:Tb³⁺ phosphors. *Journal of Materials Science*, 46(5), 1337-1340. doi:10.1007/s10853-010-4924-3
- Geng, D., Shang, M., Zhang, Y., Lian, H., & Lin, J. (2013). Color-Tunable and White Luminescence Properties via Energy Transfer in Single-Phase KNaCa₂(PO₄)₂:A (A = Ce³⁺, Eu²⁺, Tb³⁺, Mn²⁺, Sm³⁺) Phosphors. *Inorganic Chemistry*, 52(23), 13708-13718. doi:10.1021/ic402305x
- Jafer, R. M., Coetsee, E., Yousif, A., Kroon, R. E., Ntwaeborwa, O. M., & Swart, H. C. (2015). X-ray photoelectron spectroscopy and luminescent properties of Y₂O₃:Bi³⁺ phosphor. *Applied Surface Science*, 332, 198-204. doi:<https://doi.org/10.1016/j.apsusc.2015.01.009>
- Ju, G., Hu, Y., Chen, L., Wang, X., Mu, Z., Wu, H., & Kang, F. (2011). White-Light Generation and Energy Transfer in Y₂O₃:Bi,Eu Phosphor for Ultraviolet Light-Emitting Diodes. *Journal of The Electrochemical Society*, 158(10), J294. doi:10.1149/1.3615934
- Kumar, B. V. N., Balla, P. K., Chirauri, S. K., Rao, T. K. V., Ramakrishna, Y., & Rao, K. R. (2018). Synthesis and characterization of copper particles decorated reduced graphene oxide nano composites for the application of supercapacitors. *AIP Conference Proceedings*, 1992(1). doi:10.1063/1.5047973
- Li, Z.-J., Liu, B., Zhang, Y.-Y., Zhang, N.-N., Shi, Q., Wei, L., . . . Wang, X.-P. (2022). Cyan, deep red and white light emission generated by SrLaGa₃O₇:Bi³⁺, SrLaGa₃O₇:Mn⁴⁺ and SrLaGa₃O₇:Bi³⁺/Mn⁴⁺ phosphors. *Journal of Alloys and Compounds*, 894, 162455. doi:<https://doi.org/10.1016/j.jallcom.2021.162455>
- Papan, J., Vuković, K., Ahrenkiel, S. P., Jovanović, D. J., & Dramićanin, M. D. (2017). Detailed study of structural and luminescent properties of Y_{2-x}Eu_xZr₂O₇ (0 ≤ x ≤ 1) nanophosphors. *Journal of Alloys and Compounds*, 712, 437-444. doi:10.1016/j.jallcom.2017.04.139
- Prasad, R., Walke, P. S., & Bhame, S. D. (2019). Structural and optical studies on flowerlike strontium doped zinc oxide synthesized by hydrothermal method. *Materials Research Express*, 6(11), 1150b1158. doi:10.1088/2053-1591/ab4deb
- Samuel, T., & Kamal, C. h. S. (2022). Investigation of Luminescence properties of Bi³⁺, Dy³⁺ doped LaAlO₃ nanophosphors for radiation dosimetry applications. *International journal of health sciences*, 6(S1), 11638-11642. doi:10.53730/ijhs.v6nS1.7851
- Sashmeetha, M., Chitrarasu, K., & Thangadurai, P. (2019). Tuning electrical properties of nanocrystalline Y₂Zr₂O₇ pyrochlores by engineering the size of their particles. *Ionics*, 25(12), 5949-5961. doi:10.1007/s11581-019-03138-7
- Shaik, E. B., Kumar, B. V. N., Chirauri, S. K., & Rao, K. R. (2022). Realization of effective energy transfer and color tunability between Tb³⁺ and Eu³⁺ ions in LaAlO₃ host for LED display applications. *Journal of Materials Science: Materials in Electronics*, 33(1), 105-114. doi:10.1007/s10854-021-07257-8
- Suresh, C., Nagabhushana, H., Darshan, G. P., Basavaraj, R. B., Kavyashree, D., Sharma, S. C., . . . Amith Yadav, H. J. (2018). Facile LaOF: Sm³⁺ based labeling agent and their applications in residue chemistry of latent fingerprint and cheiloscopy under UV-visible light. *Arabian Journal of Chemistry*, 11(4), 460-482. doi: 10.1016/j.arabjc.2017.09.014
- Talari, S., Chirauri, S. K., Rambabu, A., & Ramachandra Rao, K. (2023). Development of single phase pink light-emitting Bi³⁺/ Eu³⁺ co-doped LaAlO₃ phosphors for LED applications. *Materials Research Innovations*, 27(2), 61-68. doi:10.1080/14328917.2022.2079898
- Talari, S., Chirauri, S. K., Reddy, P. V. S. S. S. N., & Rao, K. R. (2022). Photoluminescence studies of Bi³⁺/Dy³⁺ co-doped LaGaO₃ nanophosphors for display device applications. *Materials Today: Proceedings*, 52, 2224-2227. doi:10.1016/j.matpr.2021.08.042

- Tang, Z., Wang, D., Khan, W. U., Du, S., Wang, X., & Wang, Y. (2016). Novel zirconium silicate phosphor $K_2ZrSi_2O_7:Eu^{2+}$ for white light-emitting diodes and field emission displays. *Journal of Materials Chemistry C*, 4(23), 5307-5313. doi:10.1039/C6TC01449F
- Ting, C.-C., Chiu, Y.-S., Chang, C.-W., & Chuang, L.-C. (2011). Visible and infrared luminescence properties of Er^{3+} -doped $Y_2Ti_2O_7$ nanocrystals. *Journal of Solid State Chemistry*, 184(3), 563-571. doi:10.1016/j.jssc.2011.01.001
- Tong, Y., Chen, X., Wang, Q., & Huo, H. (2015). Crystal growth dynamics and structural characterization of re-doped $Y_2Zr_2O_7$ nanocrystals. *Materials Letters*, 157, 106-108. doi:10.1016/j.matlet.2015.05.089
- Whittle, K. R., Cranswick, L. M. D., Redfern, S. A. T., Swainson, I. P., & Lumpkin, G. R. (2009). Lanthanum pyrochlores and the effect of yttrium addition in the systems $La_{2-x}Y_xZr_2O_7$ and $La_{2-x}Y_xHf_2O_7$. *Journal of Solid State Chemistry*, 182(3), 442-450. doi:10.1016/j.jssc.2008.11.008
- Xiao, Z., Zhang, Z., Li, J., Zhang, B., Wu, B., Wang, F., . . . You, W. (2021). Preparation and luminescent properties of $Y_2Zr_2O_7:Eu^{3+}$ phosphor for W-LED application. *Applied Physics A*, 127(11), 866. doi:10.1007/s00339-021-05024-4
- Zhang, A., Lü, M., Qiu, Z., Zhou, Y., & Ma, Q. (2008). Multiband luminescence of Eu^{3+} based on $Y_2Zr_2O_7$ nanocrystals. *Materials Chemistry and Physics*, 109(1), 105-108. doi: 10.1016/j.matchemphys.2007.10.042

K. Suresh

Department of Humanities & Basic Sciences, G. Pulla Reddy Engineering College (Autonomous), Kurnool-518 007, A.P India
e-mail: kurudisuresh@gmail.com
ORCID: 0000-0002-9779-0955

A. Ganesh

Department of Humanities & Basic Sciences, G. Pulla Reddy Engineering College (Autonomous), Kurnool-518 007, A.P India
e-mail: ambaliganesh85@gmail.com
ORCID: 0000-0002-2936-9245

B. V. Naveen Kumar

Shri Vishnu Engineering College for Women (Autonomous), Bhimavaram – 534 202, A.P India
e-mail: bvnkbs@svecw.edu.in
ORCID: 0000-0003-4700-5442

C. V. Krishna Reddy

Department of Physics,
Rayalaseema University,
Kurnool – 518 002, A.P, India
e-mail: reddycvk02@yahoo.co.in
ORCID: 0000-0001-7091-5482



ESTIMATING COMMON PARAMETERS OF DIFFERENT CONTINUOUS DISTRIBUTIONS

Abbarapu Ashok¹
Nadiminti Nagamani

Keywords:

Maximum likelihood estimation; Confidence interval; Gamma distribution; Weibull distribution; Rayleigh distribution; Lomax distribution.



A B S T R A C T

Estimating a common parameter is the most essential and quite fascinating task across various probability distributions. This article addresses the challenge of estimating this parameter through the application of Maximum Likelihood Estimation (MLE). Numeric determination of common parameters is conducted for several distributions, including the Lomax distribution, Gamma distribution, Rayleigh distribution, and Weibull distribution. In cases where distributions lack a closed-form solution, estimation of MLEs is achieved using the Newton-Raphson technique. Furthermore, asymptotic confidence intervals are computed utilizing the Fisher information matrix tailored to each distribution. The performance evaluation of these estimators centers on the assessment of bias and mean squared error. To enable a numerical comparison of these estimators, the Monte Carlo simulation method is employed. Finally, these techniques are applied to real-time rainfall data to assess parameter estimates for each distribution.

© 202x Published by Faculty of Engineering

1. INTRODUCTION

Measuring the entire population would be too difficult, parameters serve as descriptive measures of the population as a whole. Consequently, we resort to estimating parameters by selecting a sample from the population since we lack knowledge of their exact values. Various popular methods for parameter estimation include Bayes estimation, least square estimation, method of moments, uniformly minimal variance unbiased estimation (UMVUE) method, and others. However, owing to its distinctive characteristics, the most effective and renowned method for parameter estimation is the Maximum Likelihood (ML) approach.

The British statistician, geneticist, and eugenicist R.A. Fisher, often referred to as the father of statistics, demonstrated (Aldrich, 1977) that the method of

moments may not be effective when calculating the parameters of Pearson Type III distributions. He recommended applying the MLE approach instead. MLE is a straightforward technique for obtaining an estimate of an unknown parameter. A new distribution named as Generalized Exponential (GE) distribution introduced by (Gupta, 2001) estimated the unknown parameters of $GE(\alpha, \lambda)$ using MLE and compared with other estimation methods. While the estimation of parameters for various continuous distributions has been tackled individually by different authors in distinct ways, the comparative estimation of parameters for different distributions has received little attention. The primary objective of this study is to estimate the common parameter of different populations in order to determine which distribution provides the best estimates for the collected rainfall data, considering their bias and mean squared error.

¹ Corresponding author: Nagamani Nadiminti
Email: maniinadiminti999@gmail.com

In this study, common parameters are estimated for a variety of distributions, including the Lomax, Rayleigh, Weibull, and Gamma distributions. For each distribution, maximum likelihood estimators are determined numerically, and for those that lack a closed form, the MLEs are estimated using the Newton-Raphson technique. Asymptotic confidence intervals have also been calculated using the Fisher information matrix of each distribution. Let's consider these distributions one by one.

Lomax distribution:

The Lomax distribution, first proposed by K.S. Lomax in 1954 for lifetime data analysis and modelling business failure data, is a special type of Pareto distribution, also known as the Pareto Type II distribution. Widely applied in various contexts, the Lomax distribution is known for its heavy-tailed characteristics. According to Hassan and Al Ghamdi, the Lomax distribution proves useful in reliability modelling and life testing problems. This distribution has unquestionably served as a model for various datasets in numerous studies. Harris, for instance, used the Lomax distribution for income and wealth data in 1978. When dealing with heavily tailed data, the Lomax distribution is preferred over the exponential distribution. Moreover, it finds numerous applications across a range of disciplines, including biology, business, economics, actuarial modelling, queuing theory, and reliability modelling.

Let us consider two independent Lomax populations with a common scale parameter ' δ ' and different shape parameters σ_1 and σ_2 respectively. Let $X = (X_1, X_2 \dots, X_m)$ and $Y = (Y_1, Y_2 \dots, Y_n)$ be m and n random samples taken from two Lomax Populations $L(\delta, \sigma_1)$ and $L(\delta, \sigma_2)$ respectively. Here $L(\delta, \sigma_1)$ denotes the Lomax population having the probability density function.

$$f(x; \delta, \sigma_1) = \frac{\sigma_1}{\delta} \left[1 + \frac{x}{\delta}\right]^{-(\sigma_1+1)} ; x \geq 0, \sigma_1, \delta > 0 \quad (1.1)$$

likewise, $L(\delta, \sigma_2)$ denotes the Lomax population which has the probability density function,

$$f(y; \delta, \sigma_2) = \frac{\sigma_2}{\delta} \left[1 + \frac{y}{\delta}\right]^{-(\sigma_2+1)} ; y \geq 0, \sigma_2, \delta > 0 \quad (1.2)$$

Giles (2013) discussed MLE for the parameters of the Lomax distribution and alternative techniques for reducing this bias when the sample size is small. Hasanain (2022) delved into the parameter estimation of the Lomax distribution using three different loss functions, employing both MLE and Bayesian estimation methods. The Lindley approximation was utilized to obtain the best estimates. To draw conclusions about the parameters of a Lomax distribution, (He, 2023) established objective Bayesian

techniques. Al-Zahrani and Sobhi (2013) estimated the parameters of the Lomax distribution under general progressive censoring by considering the probability density function of the two-parameter Lomax distribution.

Rayleigh distribution:

Among all probability distributions, the Rayleigh distribution is one of the most frequently used. Introduced by Lord Rayleigh in 1880, it generally appears as a special case of the Weibull distribution. The Rayleigh distribution finds significant applications in statistical communication theory and target theory. It is widely used in reliability analysis, applied statistics, and clinical investigations, all of which are extremely important fields. This distribution is in fact, a specific example of the Weibull distribution with two parameters scale and location.

Let us consider two independent Rayleigh populations with a common scale parameter λ and different location parameters μ_1 and μ_2 respectively. $X = (X_1, X_2 \dots, X_m)$ and $Y = (Y_1, Y_2 \dots, Y_n)$ be m and n random samples taken from two Rayleigh Populations $Ray(\lambda, \mu_1)$ and $Ray(\lambda, \mu_2)$ respectively. Here $Ray(\lambda, \mu_1)$ denotes the Rayleigh population having the probability density function,

$$f(x; \lambda, \mu_1) = 2\lambda(x - \mu_1)e^{-\lambda(x-\mu_1)^2}; x > 0, \mu_1, \lambda > 0 \quad (1.3)$$

likewise, $Ray(\lambda, \mu_2)$ denotes the population which has the probability density function,

$$f(y; \lambda, \mu_2) = 2\lambda(y - \mu_2)e^{-\lambda(y-\mu_2)^2}; y > 0, \mu_2, \lambda > 0 \quad (1.4)$$

Dey et al. (2014) estimated the parameters of the Rayleigh distribution using various methods, including MLE, method of moments, L-moment estimators, least squares estimators, weighted least squares estimators, percentile-based estimators, and Bayes estimators, all for a single sample (Dey and Dey, 2012) estimated Bayesian estimators and calculated Prediction Intervals for a Rayleigh Distribution using conjugate prior. N. Balakrishnan, in 1989, derived the Approximate MLE of the Scale Parameter of the Rayleigh Distribution with Censoring (Kundu, 2005). They also derived the parameters of the Generalized Rayleigh distribution using different estimation methods. Johnson, Kotz, and Balakrishnan in 1994 briefly discussed the Rayleigh distribution with two parameters. In addition, (Bhat, 2023) formulated a new lifetime probability model named the Power Rayleigh distribution, and the unknown parameters are estimated using MLE.

Weibull distribution:

The Weibull distribution was introduced by Mr. Waloddi Weibull in 1937. It is an adaptable distribution that can take on the characteristics of other types of distributions based on the shape parameter value. This distribution is particularly useful for analyzing life statistics and determining the reliability of items. The Weibull distribution finds extensive applications in life data analysis and reliability analysis due to its versatility, which is of paramount importance. It is primarily employed to model the range of behaviors for a given function, depending on the parameter values. The distribution function is typically well described by the probability density function. The Weibull distribution method represents one of the distinctive ways to analyze real-world data significantly. Several approaches are typically employed to assess the reliability of the data in a specific manner.

Let us consider two independent Weibull populations with a common scale parameter ‘ α ’ and different shape parameters β_1 and β_2 respectively. $X = (X_1, X_2 \dots, X_m)$ and $Y = (Y_1, Y_2 \dots, Y_n)$ be m and n random samples taken from two Weibull Populations Weibull(α, β_1) and Weibull(α, β_2) respectively. Here Weibull(α, β_1) denotes the Weibull population having the probability density function,

$$f(x; \alpha, \beta_1) = \beta_1 \alpha^{-\beta_1} x^{-\beta_1-1} e^{-(\frac{x}{\alpha})^{\beta_1}}; x \geq 0, \alpha, \beta_1 > 0 \quad (1.5)$$

likewise, Weibull(α, β_2) denotes the population which has the probability density function

$$f(y; \alpha, \beta_2) = \beta_2 \alpha^{-\beta_2} y^{-\beta_2-1} e^{-(\frac{y}{\alpha})^{\beta_2}}; y \geq 0, \alpha, \beta_2 > 0 \quad (1.6)$$

(Tan, 2009) in the year came to the conclusion that there is no analytical solution for the restricted MLE of the scale parameter for a given shape parameter, and he finally developed a new approach that is thought to be more effective and efficient at handling interval data than regular MLE methods, directly developed EM algorithms, as well as genetic algorithms. Stone (1977) used the maximum likelihood method to find the Weibull distribution’s parameters, and they also gave a method for calculating confidence intervals. As can be seen from an example, the confidence intervals for sample sizes often used in dielectric life tests can be wide. Lai (2011) provided comprehensive explanations of a variety of extensions, parameter estimation techniques, and fundamental Weibull distribution characteristics that are useful for modelling complex data sets. N. Balakrishnan and Kateri proposed an alternative approach based on a simple and easy-to-apply graphical method (Balakrishnan and Kateri (2008) also readily shows the existence and uniqueness of the maximum likelihood estimators. Yang et al (Yang, 2007) proposed a new approach called Modified MLE (MMLE) In the case of complete and Type II censored

data, the bias of the MLE can be substantial. This is noticeable even when the sample size is large.

Gamma distribution:

The Gamma distribution is a widely used and versatile statistical distribution in fields such as Business, Science, Reliability, Modelling, and Climate Analysis Centre (CAC), among others. It was first discovered by James Clerk Maxwell and later developed by Ludwig Boltzmann. In 2021, Eric U., Oti Michael, Olusola, and Francis studied the properties and applications of the Gamma distribution in real-life situations.

Let us take two independent irregular samples from two Gamma populations with a common scale parameter ‘ η ’ and different shape parameters ρ_1 and ρ_2 respectively. $X = (X_1, X_2 \dots, X_m)$ and $Y = (Y_1, Y_2 \dots, Y_n)$ be m and n random samples taken from two gamma populations Gamma(η, ρ_1) and Gamma(η, ρ_2) respectively. Here Gamma(η, ρ_1) denote the gamma population having the probability density function,

$$f(x; \eta, \rho_1) = \frac{1}{\Gamma(\rho_1 \eta)} x^{\rho_1-1} e^{-\frac{x}{\eta}}; x > 0, \eta > 0, \rho_1 > 0 \quad (1.7)$$

likewise, Gamma(η, ρ_2) denotes the population which has the probability density function

$$f(y; \eta, \rho_2) = \frac{1}{\Gamma(\rho_2 \eta)} y^{\rho_2-1} e^{-\frac{y}{\eta}}; y > 0, \eta > 0, \rho_2 > 0. \quad (1.8)$$

Several studies have attempted to address the problem of estimating parameters of the Gamma distribution. Chapman (Hirose, 1995), S. C. Choi and R. Wette (Choi, 1969), Cohen and Whitten (Wilks, 1990), Daniel S. Wilks and Hideo Hirose (Nagamani, 2017) in 2017 have applied the Maximum Likelihood Estimation (MLE) method to estimate parameters of the Gamma distribution. In addition to calculating the common shape parameter (Tripathy, 2017), they also estimated the parameters for the Gamma distribution using MLE (Husak, 2007). Husak (Shenton, 1969) estimated the MLEs of the Gamma distribution for monthly rainfall data in Africa. David E. Giles and Hui Feng (Shenton, 1969) demonstrated how the methodology suggested by Cox and Snell in 1968 can be easily used to construct a closed-form adjustment to these MLEs.

2. MAXIMUM LIKELIHOOD ESTIMATION AND THE ASYMPTOTIC CONFIDENCE INTERVALS OF VARIOUS CONTINUOUS DISTRIBUTIONS

In this part, we examine our model and provide a numerical approach for calculating the maximum likelihood estimate of the parameters, as well as asymptotic 95% confidence intervals for the parameters of Lomax, Weibull, Rayleigh, and Gamma distributions individually.

2.1 MLE and Asymptotic confidence intervals of “Lomax distribution”:

In this sub section 2.1 we are going to estimate the maximum likelihood estimates of Lomax distribution as well as the confidence intervals for its parameters.

Let us consider the joint probability density function of X and Y is,

$$f(x, y; \delta, \sigma_1, \sigma_2) = \frac{\sigma_1^m \sigma_2^n}{\delta^{m+n}} \times \prod_{i=1}^m \left[1 + \frac{x_i}{\delta}\right]^{-(\sigma_1+1)} \times \prod_{j=1}^n \left[1 + \frac{y_j}{\delta}\right]^{-(\sigma_2+1)}$$

here $\sigma_1, \sigma_2 > 0, \delta > 0$ and $x, y > 0$.

The log-likelihood function of $f(x, y)$ is given by,

$$L(x, y; \delta, \sigma_1, \sigma_2) = m \log \sigma_1 + n \log \sigma_2 - (\sigma_1 + 1) \sum_{i=1}^m \log \left[1 + \frac{x_i}{\delta}\right] - (\sigma_2 + 1) \sum_{j=1}^n \log \left[1 + \frac{y_j}{\delta}\right] - (m + n) \log \delta$$

the maximum value of $L(x, y; \delta, \sigma_1, \sigma_2)$ can be obtained by differentiating with respect to δ, σ_1 and σ_2 and equating to zero. Then solving for δ, σ_1 and σ_2 we get the MLEs. After certain calculations the system of three nonlinear equations are obtained as follows.

$$\begin{aligned} -(m + n) + \sum_{i=1}^m \left[\frac{x_i(\sigma_1+1)}{\delta+x_i} \right] + \sum_{j=1}^n \left[\frac{y_j(\sigma_2+1)}{\delta+y_j} \right] &= 0 \\ \frac{m}{\sigma_1} - \sum_{i=1}^m \log \left[1 + \frac{x_i}{\delta} \right] &= 0 \\ \frac{n}{\sigma_2} - \sum_{j=1}^n \log \left[1 + \frac{y_j}{\delta} \right] &= 0 \end{aligned}$$

next, we derive the information matrix and hence the expression for asymptotic variance of the MLEs of the parameters associated to our model.

We have the log-likelihood function for our model as,

$$L(x, y; \delta, \sigma_1, \sigma_2) = m \log \sigma_1 + n \log \sigma_2 - (\sigma_1 + 1) \sum_{i=1}^m \log \left[1 + \frac{x_i}{\delta} \right] - (\sigma_2 + 1) \sum_{j=1}^n \log \left[1 + \frac{y_j}{\delta} \right] - (m + n) \log \delta$$

we denote $\theta_1 = \sigma_1$, $\theta_2 = \sigma_2$ and $\theta_3 = \delta$. The Fisher information matrix for our model is after certain calculations, we obtain the Fisher information matrix as follows.

$$I(\sigma_1, \sigma_2, \delta) = (I_{ij}), \quad i, j = 1, 2, 3$$

$$\text{where } I_{ij} = E(P_{ij}), P_{ij} = -\frac{\partial^2 L}{\partial \theta_i \partial \theta_j}$$

$$I(\sigma_1, \sigma_2, \delta) = \begin{bmatrix} \frac{-m}{\sigma_1^2} & 0 & \frac{m-\delta \sum_{i=1}^m t_1}{\delta} \\ 0 & \frac{-n}{\sigma_2^2} & \frac{n-\delta \sum_{j=1}^n t_1}{\delta} \\ \frac{m-\delta \sum_{i=1}^m t_1}{\delta} & \frac{n-\delta \sum_{j=1}^n t_1}{\delta} & \frac{L_1}{\delta^2} \end{bmatrix}$$

here, $L_1 = m + n - (\sigma_1 + 1)(m - \delta^2 \sum t_1^2)$
 $-(\sigma_2 + 1)(n - \delta^2 \sum t_2^2)$, $t_1 = \frac{1}{\delta+x_i}$ and $t_2 = \frac{1}{\delta+y_j}$
then, the inverse of this matrix is obtained as,

Let $X = (X_1, X_2, \dots, X_m)$ and $Y = (Y_1, Y_2, \dots, Y_n)$ be two independent random samples taken from $\text{Lomax}(\delta, \sigma_1)$

$$I(\sigma_1, \sigma_2, \delta)^{-1} = \begin{bmatrix} a_{11} & \frac{\sigma_1^2 \sigma_2^2 (m-a\delta)(n-b\delta)}{D_1} & \frac{\sigma_1^2 n \delta (m-a\delta)}{D_1} \\ \frac{\sigma_1^2 \sigma_2^2 (m-a\delta)(n-b\delta)}{D_1} & a_{22} & \frac{\sigma_2^2 m \delta (n-b\delta)}{D_1} \\ \frac{\sigma_1^2 n \delta (m-a\delta)}{D_1} & \frac{\sigma_2^2 m \delta (n-b\delta)}{D_1} & \frac{\delta^2 mn}{D_1} \end{bmatrix}$$

$$\text{here, } a_{11} = \frac{-\sigma_1^2 [d\sigma_2^2 \delta^2 - 2n\sigma_2^2 b\delta + \sigma_2^2 n^2 + Bn]}{D_1},$$

$$a_{22} = \frac{-\sigma_2^2 [c\sigma_1^2 \delta^2 - 2ma\delta \sigma_1^2 + \sigma_1^2 m^2 + Bm]}{D_1},$$

$$D_1 = (\sigma_1^2 a^2 \delta^2 n - 2mn\sigma_1^2 a\delta + \sigma_1^2 m^2 n + \sigma_2^2 b^2 \delta^2 m - 2mn\sigma_2^2 b\delta + \sigma_2^2 mn^2 + Bmn),$$

$$a = \sum t_1, b = \sum t_2, c \sum t_1^2, d = \sum t_2^2 \text{ and}$$

$$B = m + n - (\sigma_1 + 1) \left(m - \delta^2 \sum t_1^2 \right) - (\sigma_2 + 1) \left(n - \delta^2 \sum t_2^2 \right)$$

by using the above information, we can easily calculate the asymptotic 95% confidence intervals for the parameters δ, σ_1 and σ_2 . The 95% confidence interval for θ_j is obtained as,

$$\theta_j \pm 1.96 \sqrt{(I(\theta))_{jj}^{-1}}$$

the 95% confidence interval for the common scale parameter δ , shape parameters σ_1 and σ_2 are estimated as follows,

$$\hat{\delta}_{ML} \pm 1.96 \sqrt{\frac{\hat{\delta}_{ML}^2 mn}{D_1}},$$

$$\hat{\sigma}_{1ML} \pm 1.96 \sqrt{a_{11}} \quad \text{and} \quad \hat{\sigma}_{2ML} \pm 1.96 \sqrt{a_{22}}$$

2.2 MLE and Asymptotic confidence intervals of “Rayleigh distribution”:

Let $X = (X_1, X_2, \dots, X_m)$ and $Y = (Y_1, Y_2, \dots, Y_n)$ be independent random samples taken from $\text{Ray}(\lambda, \mu_1)$ and $\text{Ray}(\lambda, \mu_2)$ (as given in 1.3 and 1.4) respectively, with common scale parameter λ and different Shape parameters μ_1 and μ_2 . In this sub section 2.2 we are going to estimate the maximum likelihood estimates of Rayleigh distribution as well as the confidence intervals for its parameters.

The joint probability density function of X and Y is obtained as,

$$f(x, y; \lambda, \mu_{\{1\}}, \mu_{\{2\}}) = (2\lambda)^{m+n} \prod_{i=1}^m (x_i - \mu_1) \prod_{j=1}^n (y_j - \mu_2) e^{-\lambda(\sum_{i=1}^m (x_i - \mu_1)^2 + \sum_{j=1}^n (y_j - \mu_2)^2)}$$

the log-likelihood function of $f(x, y)$ is given by,

$$L(x, y; \lambda, \mu_1, \mu_2) = (m+n)\log(2\lambda) + \sum_{i=1}^m \log(x_i - \mu_1) \\ \Sigma_{j=1}^n \log(y_j - \mu_2) - \lambda \left(\sum_{i=1}^m (x_i - \mu_1)^2 + \sum_{j=1}^n (y_j - \mu_2)^2 \right)$$

the maximum value of $L(x, y; \lambda, \mu_1, \mu_2)$ can be obtained by differentiating with respect to μ_1 , μ_2 and λ and equating to zero. Then solving for λ , μ_1 and μ_2 we get the MLEs. After certain calculations the system of three nonlinear equations are obtained as follows,

$$\hat{\lambda} = \frac{m+n}{\sum_{i=1}^m (x_i - \mu_1)^2 + \sum_{j=1}^n (y_j - \mu_2)^2} \\ \frac{-1}{\sum_{i=1}^m (x_i - \mu_1)} + 2\lambda \sum_{i=1}^m (x_i - \mu_1) = 0 \\ \frac{-1}{\sum_{j=1}^n (y_j - \mu_2)} + 2\lambda \sum_{j=1}^n (y_j - \mu_2) = 0$$

next, we derive the information matrix and hence the expression for asymptotic variance of the MLEs of the parameters associated to our model. We have the log-likelihood function for our model as,

$$L(x, y; \lambda, \mu_1, \mu_2) = (m+n)\log(2\lambda) + \sum_{i=1}^m \log(x_i - \mu_1) \\ \Sigma_{j=1}^n \log(y_j - \mu_2) - \lambda \left(\sum_{i=1}^m (x_i - \mu_1)^2 + \sum_{j=1}^n (y_j - \mu_2)^2 \right)$$

we denote $\theta_1 = \mu_1$, $\theta_2 = \mu_2$ and $\theta_3 = \lambda$.

The Fisher information matrix for our model is obtained as,

$$I(\mu_1, \mu_2, \lambda) = (I_{ij}), \quad i, j = 1, 2, 3, \quad I_{ij} = E(P_{ij}) \\ P_{ij} = -\frac{\partial^2 L}{\partial \theta_i \partial \theta_j}$$

after certain calculations, we obtain the Fisher information matrix as follows,

$$I(\mu_1, \mu_2, \lambda) = \\ \begin{bmatrix} (-2ma\lambda - 1)/a & 0 & -2b \\ 0 & (-2nc\lambda - 1)/c & -2d \\ -2b & -2d & \frac{-(m+n)}{\lambda^2} \end{bmatrix}$$

here, $a = \sum_{i=1}^m (x_i - \mu_1)^2$, $b = \sum_{i=1}^m (x_i - \mu_1)$,

$$c = \sum_{j=1}^n (y_j - \mu_2)^2 \text{ and } d = \sum_{j=1}^n (y_j - \mu_2)$$

the inverse of the matrix $I(\mu_1, \mu_2, \lambda)$ is obtained as,

$$I(\mu_1, \mu_2, \lambda)^{-1} = \\ \begin{bmatrix} b_{11} & -\frac{4\lambda^2 abcd}{D_1} & -\frac{2ab\lambda^2 [2cn\lambda + 1]}{D_1} \\ -\frac{4\lambda^2 abcd}{D_1} & b_{22} & -\frac{2cd\lambda^2 [2am\lambda + 1]}{D_1} \\ -\frac{2ab\lambda^2 [2cn\lambda + 1]}{D_1} & -\frac{2cd\lambda^2 [2am\lambda + 1]}{D_1} & b_{33} \end{bmatrix}$$

$$\text{here, } b_{11} = -\frac{a[2cn^2\lambda - 4c\lambda^2 d^2 + 2cmn\lambda + m + n]}{D_1},$$

$$b_{22} = -\frac{c[2am^2\lambda - 4a\lambda^2 b^2 + 2amn\lambda + m + n]}{D_1}, \\ b_{33} = -\frac{\lambda^2 [2am\lambda + 1][2cn\lambda + 1]}{D_1},$$

$$D_1 = 4\lambda^2 ab^2 + 4\lambda^2 cd^2 - 2m^2 a\lambda - 2n^2 c\lambda - \\ 2amn\lambda - 2cmn\lambda - 4\lambda^2 acmn^2 - 4\lambda^2 acm^2 n + \\ 8\lambda^3 ab^2 cn + 8\lambda^3 acd^2 m - m - n.$$

Using above information, we can easily calculate the asymptotic 95% confidence intervals for the parameters λ , μ_1 and μ_2 . The 95% confidence interval for θ_j is obtained as,

$$\theta_j \pm 1.96 \sqrt{(I(\theta)_{jj})^{-1}}$$

the 95% confidence intervals for the common rate parameter λ and shape parameters μ_1 and μ_2 are estimated respectively as follows.

$$\hat{\lambda}_{ML} \pm 1.96 \sqrt{b_{33}}, \\ \hat{\mu}_{1ML} \pm 1.96 \sqrt{b_{11}} \quad \text{and} \quad \hat{\mu}_{2ML} \pm 1.96 \sqrt{b_{22}}.$$

2.3 MLE and Asymptotic Confidence Intervals of “Weibull Distribution”:

Let $X = (X_1, X_2, \dots, X_m)$ and $Y = (Y_1, Y_2, \dots, Y_n)$ be independent random samples taken from Weibull(α, β_1) and Weibull(α, β_2) (as given in 1.5 and 1.6) respectively, with common scale parameter α and different shape parameters β_1 and β_2 . In this sub section 2.3 we are going to estimate the maximum likelihood estimates of Weibull distribution as well as the confidence intervals for its parameters.

Let us consider the joint probability density function of X and Y is,

$$f(x, y; \alpha, \beta_1, \beta_2) = \beta_1^m \beta_2^n \alpha^{-(m\beta_1 + n\beta_2)} \times \\ (\prod_{i=1}^m x_i^{\beta_1 - 1})(\prod_{j=1}^n y_j^{\beta_2 - 1}) e^{-\left\{ \frac{\sum_{i=1}^m x_i^{\beta_1} - \sum_{j=1}^n y_j^{\beta_2}}{\alpha^{\beta_1}} \right\}}$$

the log-likelihood function of $f(x, y)$ is given by,

$$L(x, y; \alpha, \beta_1, \beta_2) = m \log \beta_1 + n \log \beta_2 \\ -(m\beta_1 + n\beta_2) \log \alpha + (\beta_1 - 1) \sum_{i=1}^m \log x_i \\ + (\beta_2 - 1) \sum_{j=1}^n \log y_j - \left\{ \frac{\sum_{i=1}^m x_i^{\beta_1}}{\alpha^{\beta_1}} + \frac{\sum_{j=1}^n y_j^{\beta_2}}{\alpha^{\beta_2}} \right\}$$

the maximum value of $L(x, y; \alpha, \beta_1, \beta_2)$ can be obtained by differentiating with respect to α , β_1 and β_2 and equating to zero. Then solving for α , β_1 and β_2 we get the MLEs. After certain calculations the system of three nonlinear equations are obtained as follows.

$$\begin{aligned} \beta_1 \sum_{i=1}^m x_i^{\beta_1} \alpha^{-\beta_1} + \beta_2 \sum_{j=1}^n y_j^{\beta_2} \alpha^{-\beta_2} - m\beta_1 - n\beta_2 &= 0 \\ \frac{m}{\beta_1} - m \log \alpha - \sum_{i=1}^m \log x_i - \left(\frac{\sum_{i=1}^m x_i}{\alpha} \right)^{\beta_1} \log \left(\frac{\sum_{i=1}^m x_i}{\alpha} \right) \\ \frac{n}{\beta_2} - n \log \alpha - \sum_{j=1}^n \log y_j - \left(\frac{\sum_{j=1}^n y_j}{\alpha} \right)^{\beta_2} \log \left(\frac{\sum_{j=1}^n y_j}{\alpha} \right) \end{aligned}$$

next, we derive the information matrix and hence the expression for asymptotic variance of the MLEs of the parameters associated to our model. We have the log-likelihood function for our model as,
we have the log-likelihood function for our model as,

$$\begin{aligned} L(x, y; \alpha, \beta_1, \beta_2) &= m \log \beta_1 + n \log \beta_2 \\ &\quad - (m\beta_1 + n\beta_2) \log \alpha + (\beta_1 - 1) \sum_{i=1}^m \log x_i \\ &\quad + (\beta_2 - 1) \sum_{j=1}^n \log y_j - \left\{ \frac{\sum_{i=1}^m x_i^{\beta_1}}{\alpha^{\beta_1}} + \frac{\sum_{j=1}^n y_j^{\beta_2}}{\alpha^{\beta_2}} \right\} \end{aligned}$$

we denote $\theta_1 = \beta_1$, $\theta_2 = \beta_2$ and $\theta_3 = \alpha$. The Fisher information matrix for our model is obtained as,

$$I(\beta_1, \beta_2, \alpha) = (I_{ij}), \quad i, j = 1, 2, 3, \quad I_{ij} = E(P_{ij})$$

$$P_{ij} = -\frac{\partial^2 L}{\partial \theta_i \partial \theta_j}$$

after certain calculations, we obtain the Fisher information matrix as follows,

$$I(\alpha, \beta_1, \beta_2) = \begin{bmatrix} \frac{k_1}{\beta_1^2} & 0 & \frac{k_2}{\alpha} \\ 0 & \frac{k_4}{\beta_2^2} & \frac{k_3}{\alpha} \\ \frac{k_2}{\alpha} & \frac{k_3}{\alpha} & \frac{k_5}{\alpha^2} \end{bmatrix}$$

Here,

$$\begin{aligned} k_1 &= -m - \beta_1^2 \left(\frac{\sum_{i=1}^m x_i}{\alpha} \right)^{\beta_1} \left(\log \frac{\sum_{i=1}^m x_i}{\alpha} \right)^2, \\ k_2 &= -m + \left(\frac{\sum_{i=1}^m x_i}{\alpha} \right)^{\beta_1} \left[\beta_1 \log \left(\frac{\sum_{i=1}^m x_i}{\alpha} \right) + 1 \right], \\ k_3 &= -n + \left(\frac{\sum_{j=1}^n y_j}{\alpha} \right)^{\beta_2} \left[\beta_2 \log \left(\frac{\sum_{j=1}^n y_j}{\alpha} \right) + 1 \right], \\ k_4 &= -n - \beta_2^2 \left(\frac{\sum_{j=1}^n y_j}{\alpha} \right)^{\beta_2} \left(\log \frac{\sum_{j=1}^n y_j}{\alpha} \right)^2, \\ k_5 &= m\beta_1 + n\beta_2 - \beta_1(\beta_1 + 1) \left(\frac{\sum_{i=1}^m x_i}{\alpha} \right)^{\beta_1} \\ &\quad - \beta_2(\beta_2 + 1) \left(\frac{\sum_{j=1}^n y_j}{\alpha} \right)^{\beta_2} \end{aligned}$$

the inverse of this matrix $I(\alpha, \beta_1, \beta_2)$ is obtained as,

$$I(\alpha, \beta_1, \beta_2)^{-1} = \begin{bmatrix} \frac{-\beta_1^2(k_4k_5 - k_3^2\beta_2^2)}{D_1} & \frac{-\beta_1^2k_2k_3\beta_2^2}{D_1} & \frac{-\beta_1^2k_2k_4\alpha}{D_1} \\ \frac{-\beta_2^2k_2k_3\beta_2^2}{D_1} & \frac{-\beta_2^2(k_1k_3 - k_2^2\beta_1^2)}{D_1} & \frac{k_1k_3\beta_2^2\alpha}{D_1} \\ \frac{-\beta_1^2k_2k_4\alpha}{D_1} & \frac{k_1k_3\beta_2^2\alpha}{D_1} & \frac{-k_1k_4\alpha^2}{D_1} \end{bmatrix} \quad (2.38)$$

Here, $D_1 = k_1k_4k_5 - \beta_2^2k_1k_3^2 - \beta_1^2k_2^2k_4$.

By using above information, we can easily calculate the asymptotic 95% confidence intervals for the parameters α, β_1 and β_2 . The 95% confidence interval for θ_j is obtained as,

$$\theta_j \pm 1.96 \sqrt{(I(\theta)_{jj})^{-1}}$$

the 95% confidence intervals for the parameters α, β_1 and β_2 are as follows

$$\begin{aligned} \hat{\alpha}_{ML} &\pm 1.96 \sqrt{\frac{-k_1k_4\hat{\alpha}_{ML}^2}{D_1}} \\ \hat{\beta}_{1ML} &\pm 1.96 \sqrt{\frac{-\hat{\beta}_{1ML}^2(k_4k_5 - k_3^2\hat{\beta}_{2ML}^2)}{D_1}} \\ \hat{\beta}_{2ML} &\pm 1.96 \sqrt{\frac{-\hat{\beta}_{2ML}^2(k_1k_3 - k_2^2\hat{\beta}_{1ML}^2)}{D_1}} \end{aligned}$$

2.4 MLE and Asymptotic Confidence Intervals of “Gamma Distribution”:

Let $X = (X_1, X_2, \dots, X_m)$ and $Y = (Y_1, Y_2, \dots, Y_n)$ be independent random samples taken from $\text{Gamma}(\rho_1, \eta)$ and $\text{Gamma}(\rho_2, \eta)$ (as given in 1.7 and 1.8) respectively, with common scale parameter η and different Shape parameters ρ_1 and ρ_2 . In this sub section 2.4 we are going to estimate the maximum likelihood estimates of Gamma distribution as well as the confidence intervals for its parameters.

The joint probability density function of X and Y is obtained as,

$$f(x, y | \rho_1, \rho_2, \eta) = \frac{(\prod_{i=1}^m x_i)^{\rho_1-1} (\prod_{j=1}^n y_j)^{\rho_2-1}}{(\Gamma \rho_1)^m (\Gamma \rho_2)^n \eta^{m\rho_1+n\rho_2}} \times e^{-\frac{1}{\eta}(\sum_{i=1}^m x_i + \sum_{j=1}^n y_j)}$$

the log-likelihood function of $f(x, y)$ is given by,

$$\begin{aligned} L(x, y; \rho_1, \rho_2, \eta) &= (\rho_1 - 1) \sum_{i=1}^m \log x_i + n \log(\Gamma \rho_2) \\ &\quad - (\rho_2 - 1) \sum_{j=1}^n \log y_j - m \log(\Gamma \rho_1) \\ &\quad - (m\rho_1 + n\rho_2) \log \eta - \frac{1}{\eta} (\{\sum_{i=1}^m x_i + \sum_{j=1}^n y_j\}) \end{aligned}$$

the maximum value of $L(x, y; \rho_1, \rho_2, \eta)$ can be obtained by differentiating with respect to ρ_1 , ρ_2 , and η and equating to zero. Then solving for ρ_1 , ρ_2 , and η we get the MLEs. After certain calculations the system of three nonlinear equations are obtained as follows,

$$\sum_{\{i=1\}}^m \log x_i - m \psi(\rho_1) - m \log \eta = 0$$

$$\sum_{\{j=1\}}^n \log y_j - n \psi(\rho_2) - n \log \eta = 0$$

$$\eta(m\rho_1 + n\rho_2) - \sum_{\{i=1\}}^m x_i + \sum_{\{j=1\}}^n y_j = 0$$

Where,

$$\psi(\rho_1) = \frac{d}{d\rho_1}(\log \Gamma \rho_1) \quad \text{and} \quad \psi(\rho_2) = \frac{d}{d\rho_2}(\log \Gamma \rho_2)$$

are known as the digamma functions.

next, we derive the information matrix and hence the expression for asymptotic variance of the MLEs of the parameters associated to our model. We have the log-likelihood function for our model as,

$$L(x, y; \rho_1, \rho_2, \eta) = (\rho_1 - 1) \sum_{i=1}^m \log x_i + n \log(\Gamma \rho_2) \\ (\rho_2 - 1) \sum_{j=1}^n \log y_j - m \log(\Gamma \rho_1) - \\ -(m\rho_1 + n\rho_2) \log \eta - \frac{1}{\eta} (\{\sum_{i=1}^m x_i + \sum_{j=1}^n y_j\})$$

we denote $\theta_1 = \rho_1$, $\theta_2 = \rho_2$ and $\theta_3 = \eta$. The Fisher information matrix for our model is obtained as,

$$I(\rho_1, \rho_2, \eta) = (I_{ij}), \quad i, j = 1, 2, 3, \quad I_{ij} = E(P_{ij})$$

$$P_{ij} = -\frac{\partial^2 L}{\partial \theta_i \partial \theta_j}$$

after certain calculations, we obtain the Fisher information matrix as follows.

$$I(\rho_1, \rho_2, \eta) = \begin{bmatrix} m\Psi'(\rho_1) & 0 & \frac{m}{\eta} \\ 0 & n\Psi'(\rho_2) & \frac{n}{\eta} \\ \frac{m}{\eta} & \frac{n}{\eta} & \frac{m\rho_1+n\rho_2}{\eta^2} \end{bmatrix}$$

where $\Psi'(\rho_1)$ and $\Psi'(\rho_2)$ are the derivative of digamma function known as tri gamma functions. The inverse of this matrix is obtained as,

$$I(\rho_1, \rho_2, \eta)^{-1} =$$

$$\begin{bmatrix} \frac{\Psi'(\rho_2)(m\rho_1+n\rho_2)-n}{mD} & \frac{1}{D} & -\frac{\eta\Psi'(\rho_2)}{D} \\ \frac{1}{D} & \frac{\Psi'(\rho_1)(m\rho_1+n\rho_2)-m}{nD} & \frac{\eta\Psi'(\rho_1)}{D} \\ -\frac{\eta\Psi'(\rho_2)}{D} & \frac{\eta\Psi'(\rho_1)}{D} & \frac{\eta^2\Psi'(\rho_1)\Psi'(\rho_2)}{D} \end{bmatrix}$$

by using above information, we can easily calculate the asymptotic 95% confidence intervals for the parameters η , ρ_1 and ρ_2 .

The 95% confidence interval for θ_j is obtained as,

$$\theta_j \pm 1.96 \sqrt{(I(\theta)_{jj})^{-1}}$$

the 95% confidence intervals for the common rate parameter η and shape parameters ρ_1 , ρ_2 are obtained respectively as follows.

$$\hat{\eta}_{ML} \pm 1.96 \sqrt{\frac{\hat{\eta}_{ML}^2 \Psi'(\hat{\rho}_{1ML}) \Psi'(\hat{\rho}_{2ML})}{D}}$$

$$\hat{\rho}_{1ML} \pm 1.96 \sqrt{\frac{(m\hat{\rho}_{1ML} + n\hat{\rho}_{2ML}) \Psi'(\hat{\rho}_{2ML}) - n}{mD}}$$

$$\hat{\rho}_{2ML} \pm 1.96 \sqrt{\frac{(m\hat{\rho}_{1ML} + n\hat{\rho}_{2ML}) \Psi'(\hat{\rho}_{1ML}) - m}{nD}}$$

using the Monte-Carlo simulation approach in R programming, all of the above-mentioned estimators are

numerically compared in section-3 in terms of bias and mean squared error.

3. NUMERICAL COMPARISONS

In this research, we address the problem of estimating parameters for two similar continuous probability distributions, specifically the Lomax, Weibull, Rayleigh, and Gamma distributions, using the Maximum Likelihood Estimation (MLE) method. As the closed form of the ML estimates does not exist, we are going to use a numerical technique named as Newton-Raphson method to find approximate ML estimates of the common parameter by solving the system of equations of different distributions. Furthermore, we compute the 95% confidence intervals with the help of Fisher information matrix. To compare these estimators numerically, we evaluate their performance in terms of bias and mean squared error. For this purpose, we generate 10,000 random samples for each distribution and compute the bias and mean squared error of each parameter.

By taking the different values of parameters we computed the Estimates, from the table 3.1 to 3.4 represents equal sample sizes of both the samples of different continuous probability distributions from 10 to 50 the ML-estimates of all parameters with its Bias and mean squared error are reported. From table 3.5 to 3.8 having different combination of sample sizes from 10 to 50 with unequal sample sizes, the ML-estimates of all parameters with its bias and mean squared error are computed. From Table 3.9 to 3.12 are the values of 95% Asymptotic confidence intervals for the distributions of Lomax, Weibull, Rayleigh and Gamma distributions respectively, with various different values of common parameter are computed.

1. MLE provided consistent and efficient parameter values for every distribution considered in the study.
2. From the simulation data, it can be said that increasing the sample size reduced both the bias and mean square error for each estimator.
3. Larger sample sizes generally resulted in more accurate parameter estimates with lower standard error.
4. With small sample sizes, the MLE estimates had higher variability and larger standard errors.
5. It was observed that, for fixed sample sizes and fixed shape parameters, the common scale parameter of these distributions increased and its mean squared error values decreased.
6. All the parameter values lay inside the confidence intervals, and the length of confidence intervals for all parameters decreased as the sample size grew.

7. The width of the confidence intervals depended on the sample size and the desired level of confidence.
 8. As the sample size increased, the width of the confidence intervals decreased, indicating increased precision in parameter estimation.
 9. Based on the specific context and characteristics of the data, it can be analyzed that every distribution has its own individuality and identity.
 10. Our simulation analysis yielded comparable results for other combinations of sample sizes and parameters.

Table 3.1: Comparing Biases and MSE of Several Estimators of Several distributions For The different parameters when (m,n) = (10,10)

$\Theta \downarrow$	Lomax($\theta=\sigma_1, \sigma_2, \delta$)			Weibull($\theta=\beta_1, \beta_2, \alpha$)			Rayleigh($\theta=\mu_1, \mu_2, \lambda$)			Gamma(ρ_1, ρ_2, η)		
	Mle	Bias	Mse	Mle	Bias	Mse	Mle	Bias	Mse	Mle	Bias	Mse
1	1.26	0.26	0.76	1.11	0.11	0.11	1.19	0.19	0.26	1.21	0.21	0.26
2	1.77	-0.22	0.46	2.25	0.25	0.32	2.40	0.40	0.44	2.45	0.45	0.48
1.5	1.41	-0.09	0.44	1.49	-0.00	0.05	1.35	-0.14	0.26	1.35	-0.14	0.27
1	1.43	0.43	0.39	1.10	0.10	0.11	1.22	0.22	0.24	1.21	0.21	0.24
2	1.93	-0.06	0.09	2.37	0.37	0.71	2.39	0.39	1.18	2.47	0.47	1.24
2.5	2.35	-0.14	1.48	2.50	-0.00	0.15	2.22	-0.22	0.53	2.25	-0.20	0.74
1	1.24	0.24	0.78	1.10	0.10	0.12	1.21	0.21	0.25	1.20	0.20	0.24
2	2.18	0.18	0.15	2.30	0.30	0.53	2.28	0.28	0.61	2.46	0.46	1.21
3.5	3.37	-0.12	0.42	3.46	-0.03	0.29	3.34	-0.15	0.63	3.15	-0.34	1.43

Table 3.2: Comparing Biases and MSE of Several Estimators of Several distributions For The different parameters when (m,n) = (20,20)

$\Theta \downarrow$	Lomax($\theta=\sigma_1, \sigma_2, \delta$)			Weibull($\theta=\beta_1, \beta_2, \alpha$)			Rayleigh($\theta=\mu_1, \mu_2, \lambda$)			Gamma(ρ_1, ρ_2, η)		
	Mle	Bias	Mse	Mle	Bias	Mse	Mle	Bias	Mse	Mle	Bias	Mse
1	1.23	0.23	0.60	1.04	0.04	0.03	1.11	0.11	0.25	1.08	0.08	0.08
2	1.79	-0.20	0.45	2.14	0.14	0.20	2.20	0.20	0.33	2.21	0.21	0.34
1.5	1.37	-0.12	0.39	1.49	-0.00	0.02	-0.05	0.11	0.19	1.42	-0.07	0.13
1	1.34	0.34	0.27	1.05	0.05	0.04	1.11	0.11	0.09	1.09	0.09	0.08
2	1.97	-0.02	0.03	2.12	0.12	0.19	2.21	0.21	0.36	2.22	0.22	0.37
2.5	2.38	-0.11	1.33	2.49	-0.00	0.02	-0.18	0.34	0.22	2.35	-0.14	0.34
1	1.18	0.18	0.74	1.04	0.04	0.03	2.31	-0.18	0.34	1.10	0.10	0.09
2	2.16	0.16	0.13	2.16	0.16	0.18	2.24	0.24	0.48	2.22	0.22	0.35
3.5	3.41	-0.08	0.35	3.49	-0.00	0.00	3.28	-0.22	0.42	3.30	-0.19	0.75

Table 3.3: Comparing Biases and MSE of Several Estimators of Several distributions For The different parameters when (m,n) = (30,30)

$\Theta \downarrow$	Lomax($\theta=\sigma_1, \sigma_2, \delta$)			Weibull($\theta=\beta_1, \beta_2, \alpha$)			Rayleigh($\theta=\mu_1, \mu_2, \lambda$)			Gamma(ρ_1, ρ_2, η)		
	Mle	Bias	Mse	Mle	Bias	Mse	Mle	Bias	Mse	Mle	Bias	Mse
1	1.18	0.18	0.43	1.03	0.03	0.02	1.09	0.09	0.20	1.06	0.06	0.04
2	1.81	-0.18	0.36	2.08	0.08	0.10	2.13	0.13	0.21	2.13	0.13	0.21
1.5	1.42	-0.07	0.28	1.49	-0.00	0.01	1.45	-0.04	0.08	1.45	-0.04	0.09
1	1.15	0.15	0.24	1.03	0.03	0.02	1.05	0.05	0.08	1.06	0.06	0.04
2	1.98	-0.01	0.01	2.08	0.08	0.11	2.13	0.13	0.20	2.14	0.14	0.21
2.5	2.41	-0.08	1.27	2.49	-0.00	0.04	2.41	-0.08	0.22	0.241	-0.08	0.25
1	1.14	0.14	0.68	1.03	0.03	0.02	1.07	0.07	0.04	1.08	0.08	0.05
2	2.11	0.11	0.10	2.09	0.09	0.11	2.13	0.13	0.19	2.18	0.18	0.24
3.5	3.48	-0.00	0.33	3.49	-0.00	0.09	3.41	-0.08	0.38	3.31	-0.18	0.51

Table 3.4: Comparing Biases and MSE of Several Estimators of Several distributions For The different parameters when (m,n) = (50,50)

$\Theta \downarrow$	Lomax($\theta=\sigma_1, \sigma_2, \delta$)			Weibull($\theta=\beta_1, \beta_2, \alpha$)			Rayleigh($\theta=\mu_1, \mu_2, \lambda$)			Gamma(ρ_1, ρ_2, η)		
	Mle	Bias	Mse	Mle	Bias	Mse	Mle	Bias	Mse	Mle	Bias	Mse
1	1.04	0.04	0.08	1.02	0.02	0.01	1.05	0.05	0.07	1.03	0.03	0.02
2	1.91	-0.08	0.22	2.04	0.04	0.05	2.06	0.06	0.11	2.08	0.08	0.10
1.5	1.48	-0.01	0.07	1.49	-0.00	0.01	1.47	-0.02	0.05	1.46	-0.03	0.05
1	1.12	0.12	0.13	1.01	0.01	0.01	1.04	0.04	0.05	1.08	0.08	0.07
2	1.98	-0.01	-0.00	2.06	0.06	0.05	2.08	0.08	0.11	2.18	0.18	0.34
2.5	2.47	-0.02	1.18	2.49	-0.00	0.02	2.43	-0.06	0.14	2.36	-0.11	0.37

1	1.09	0.09	0.45	1.01	0.01	0.01	1.03	0.03	0.02	1.04	0.04	0.02
2	2.04	0.04	0.08	2.05	0.05	0.05	2.07	0.07	0.09	2.10	0.10	0.10
3.5	3.49	-0.00	0.25	3.50	-0.00	0.04	3.47	-0.02	0.02	3.39	-0.10	0.29

Table 3.5: Comparing Biases and MSE of Several Estimators of Several distributions For The different parameters when (m,n) = (10,20)

$\Theta \downarrow$	Lomax($\theta=\sigma_1, \sigma_2, \delta$)			Weibull($\theta=\beta_1, \beta_2, \alpha$)			Rayleigh($\theta=\mu_1, \mu_2, \lambda$)			Gamma(ρ_1, ρ_2, η)		
	Mle	Bias	Mse	Mle	Bias	Mse	Mle	Bias	Mse	Mle	Bias	Mse
1	1.21	0.21	0.24	1.05	0.05	0.06	1.31	0.31	0.89	1.61	0.16	0.17
2	1.79	-0.20	0.21	2.19	0.19	0.22	1.98	-0.01	0.02	0.29	0.29	0.44
1.5	1.42	-0.07	0.05	1.50	-0.00	0.02	1.54	0.04	0.16	1.35	-0.14	0.15
1	1.39	0.39	0.29	1.06	0.06	0.08	1.07	0.07	0.04	1.12	0.12	0.14
2	1.82	-0.17	0.14	2.19	0.19	0.18	1.86	-0.13	0.18	2.15	0.15	0.29
2.5	2.41	-0.08	0.11	2.51	0.01	0.06	2.46	-0.13	0.19	2.39	-0.10	0.36
1	1.22	0.22	0.19	1.10	0.10	0.12	1.07	0.07	0.12	1.06	0.06	0.10
2	1.94	-0.05	0.14	2.12	0.12	0.15	2.04	0.04	0.09	2.32	0.32	0.57
3.5	3.34	-0.15	0.27	3.54	-0.04	0.18	3.47	-0.02	0.04	3.30	-0.19	0.94

Table 3.6: Comparing Biases and MSE of Several Estimators of Several distributions For The different parameters when (m,n) = (20,10)

$\Theta \downarrow$	Lomax($\theta=\sigma_1, \sigma_2, \delta$)			Weibull($\theta=\beta_1, \beta_2, \alpha$)			Rayleigh($\theta=\mu_1, \mu_2, \lambda$)			Gamma(ρ_1, ρ_2, η)		
	Mle	Bias	Mse	Mle	Bias	Mse	Mle	Bias	Mse	Mle	Bias	Mse
1	1.18	0.18	0.45	1.05	0.05	0.04	1.14	0.14	0.74	1.12	0.12	0.11
2	1.82	-0.17	3.1	2.28	0.28	0.54	2.07	0.07	0.26	2.29	0.29	0.66
1.5	1.34	-0.15	0.22	1.49	-0.00	0.04	1.57	0.07	0.25	1.39	-0.1	0.19
1	1.34	0.34	0.28	1.04	0.04	0.03	1.15	0.15	0.42	1.12	0.12	0.10
2	1.94	-0.05	0.19	2.26	0.26	0.53	1.96	-0.03	0.14	2.34	0.34	0.71
2.5	2.39	-0.10	0.14	2.48	0.17	0.13	2.48	-0.01	0.02	2.32	-0.17	0.48
1	1.14	0.14	0.22	1.05	0.05	0.04	1.12	0.12	0.49	1.10	0.10	0.10
2	2.11	0.11	0.17	2.3	0.30	0.57	1.98	-0.01	0.01	2.30	0.30	0.63
3.5	3.42	-0.07	0.15	3.47	-0.02	0.23	3.45	-0.04	0.24	3.32	-0.17	0.99

Table 3.7: Comparing Biases and MSE of Several Estimators of Several distributions For The different parameters when (m,n) = (30,50)

$\Theta \downarrow$	Lomax($\theta=\sigma_1, \sigma_2, \delta$)			Weibull($\theta=\beta_1, \beta_2, \alpha$)			Rayleigh($\theta=\mu_1, \mu_2, \lambda$)			Gamma(ρ_1, ρ_2, η)		
	Mle	Bias	Mse	Mle	Bias	Mse	Mle	Bias	Mse	Mle	Bias	Mse
1	1.14	0.14	0.32	1.03	0.03	0.02	1.04	0.04	0.38	1.04	0.04	0.03
2	1.95	-0.04	3.98	2.05	0.05	0.05	1.95	-0.05	0.15	2.09	0.09	0.12
1.5	1.43	-0.06	0.24	1.49	-0.00	0.11	1.47	-0.02	0.06	1.46	-0.03	0.06
1	1.13	0.13	0.29	1.02	0.02	0.02	1.21	0.21	0.78	1.05	0.05	0.03
2	1.97	-0.02	0.08	2.04	0.04	0.05	1.88	-0.11	0.96	2.09	0.09	0.12
2.5	2.41	-0.08	0.19	2.49	-0.00	0.00	2.43	-0.06	0.73	2.44	-0.05	0.18
1	1.11	0.11	0.39	1.02	0.02	0.02	1.27	0.27	0.85	1.04	0.04	0.03
2	2.05	0.05	0.07	2.05	0.05	0.06	1.87	-0.12	0.41	2.08	0.08	0.12
3.5	3.45	-0.04	0.08	3.48	-0.00	0.05	3.38	-0.11	0.24	3.41	-0.08	0.35

Table 3.8: Comparing Biases and MSE of Several Estimators of Several distributions For The different parameters when (m,n) = (50,30)

$\Theta \downarrow$	Lomax($\theta=\sigma_1, \sigma_2, \delta$)			Weibull($\theta=\beta_1, \beta_2, \alpha$)			Rayleigh($\theta=\mu_1, \mu_2, \lambda$)			Gamma(ρ_1, ρ_2, η)		
	Mle	Bias	Mse	Mle	Bias	Mse	Mle	Bias	Mse	Mle	Bias	Mse
1	1.06	0.06	0.08	1.02	0.02	0.01	1.18	0.18	0.43	1.04	0.04	0.03
2	1.88	-0.11	0.12	2.10	0.10	0.10	1.92	-0.07	0.39	2.11	0.11	0.17
1.5	1.44	-0.05	0.08	1.49	-0.00	0.00	1.41	0.08	0.48	1.45	-0.04	0.07
1	1.11	0.11	0.27	1.02	0.02	0.01	1.22	0.22	0.88	1.04	0.04	0.03
2	1.97	-0.02	0.02	2.08	0.08	0.10	1.87	-0.12	0.76	2.11	0.11	0.15

2.5	2.48	-0.01	0.04	2.49	-0.00	0.04	2.31	-0.28	1.03	2.41	-0.08	0.18
1	1.08	0.08	0.14	1.01	0.01	0.01	1.27	0.27	0.97	1.05	0.05	0.03
2	2.10	0.10	0.31	2.09	0.09	0.10	1.92	-0.07	0.97	1.22	0.11	0.16
3.5	3.48	-0.01	0.01	3.49	-0.00	0.08	3.37	-0.12	0.39	3.37	-0.12	0.38

The Asymptotic Confidence intervals for the parameters of lomax, Weibull, Rayleigh and Gamma Distributions with its parameter values and various combinations of sample sizes are computed in the following tables.

Table 3.9: The 95% confidence intervals of Gamma Distribution for the parameters (ρ_1, ρ_2, η)

(m,n)	Conf($\rho_1 = 2$)	Conf($\rho_2 = 3$)	Conf($\eta = 1.5$)	Conf($\rho_1 = 2$)	Conf($\rho_2 = 3$)	Conf($\eta = 2.5$)
(10,10)	(0.55,4.38)	(1.77,5.60)	(-0.57,3.2)	(0.45,4.55)	(1.75,5.85)	(0.19,4.29)
(15,15)	(0.98,3.58)	(2.10,4.76)	(0.11,2.70)	(0.95,3.61)	(2.09,4.74)	(1.01,3.66)
(30,30)	(1.32,2.98)	(2.39,4.05)	(0.60,2.27)	(1.31,2.93)	(2.42,4.03)	(1.58,3.20)
(50,50)	(1.47,2.71)	(2.51,3.75)	(0.84,2.08)	(1.47,2.65)	(2.52,3.70)	(1.85,3.03)
(10,15)	(0.77,3.98)	(1.94,5.15)	(-0.20,2.98)	(0.79,3.92)	(1.96,5.09)	(0.74,3.87)
(15,10)	(0.80,3.89)	(1.97,5.06)	(-0.14,2.94)	(0.91,3.75)	(2.11,4.94)	(0.89,3.73)
(30,50)	(1.36,2.86)	(2.42,3.92)	(0.70,2.20)	(1.38,2.82)	(2.42,3.86)	(1.77,3.15)
(50,30)	(1.39,2.80)	(2.47,3.87)	(0.76,2.16)	(1.41,2.77)	(2.48,3.84)	(1.75,3.11)

Table 3.10: The 95% confidence intervals of Weibull Distribution for the parameters (β_1, β_2, α)

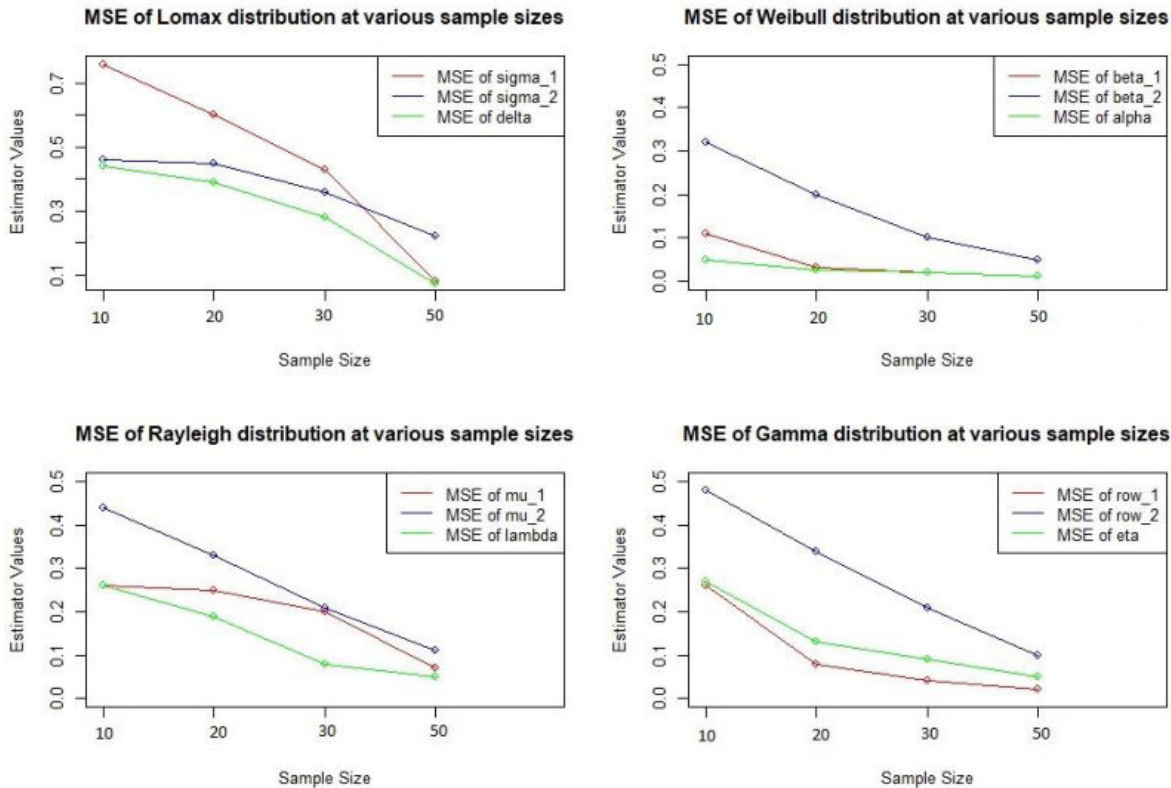
(m,n)	Conf($\beta_1 = 2$)	Conf($\beta_2 = 3$)	Conf($\alpha = 1.5$)	Conf($\beta_1 = 2$)	Conf($\beta_2 = 3$)	Conf($\alpha = 2.5$)
(10,10)	(0.85 , 3.58)	(1.29 , 5.53)	(1.20 , 1.78)	(0.83 , 3.57)	(1.24 , 5.61)	(1.98 , 2.97)
(15,15)	(1.16 , 3.12)	(1.67 , 4.87)	(1.26 , 1.72)	(1.19 , 3.10)	(1.64 , 4.91)	(2.12 , 2.87)
(30,30)	(1.44 , 2.68)	(2.19 , 4.04)	(1.33 , 1.65)	(1.45 , 2.70)	(2.18 , 4.00)	(2.23 , 2.76)
(50,50)	(1.59 , 2.52)	(2.37 , 3.76)	(1.37 , 1.61)	(1.59 , 2.56)	(2.38 , 3.75)	(2.29 , 2.69)
(10,15)	(0.91 , 3.50)	(1.74 , 4.77)	(1.25 , 1.73)	(0.89 , 3.61)	(1.66 , 4.80)	(2.07 , 2.90)
(15,10)	(1.10 , 3.21)	(1.26 , 5.53)	(1.23 , 1.76)	(1.08 , 3.23)	(1.21 , 5.77)	(2.03 , 2.93)
(30,50)	(1.46 , 2.67)	(2.35 , 3.82)	(1.36 , 1.62)	(1.45 , 2.68)	(2.36 , 3.76)	(2.28 , 2.71)
(50,30)	(1.58 , 2.50)	(2.17 , 4.05)	(1.354 , 1.64)	(1.60 , 2.50)	(2.16 , 4.10)	(2.24 , 2.75)

Table 3.11: The 95% confidence intervals of Lomax Distribution for the parameters ($\sigma_1, \sigma_2, \delta$)

(m,n)	Conf($\sigma_1 = 2$)	Conf($\sigma_2 = 3$)	Conf($\delta = 1.5$)	Conf($\sigma_1 = 2$)	Conf($\sigma_2 = 3$)	Conf($\delta = 2.5$)
(10,10)	(-0.30 , 3.63)	(-5.06 , 5.73)	(-1.48 , 10.61)	(-0.11 , 4.38)	(-4.79 , 5.79)	(0.66 , 7.44)
(15,15)	(0.04 , 3.48)	(-5.33 , 5.77)	(-1.47 , 10.59)	(0.23 , 4.17)	(-5.15 , 5.80)	(0.75 , 7.53)
(30,30)	(0.55 , 3.19)	(-5.65 , 5.83)	(-1.46 , 10.58)	(0.78 , 3.94)	(-5.55 , 5.84)	(0.84 , 7.52)
(50,50)	(0.83 , 2.98)	(-5.79 , 5.86)	(-1.47 , 10.61)	(1.21 , 3.75)	(-5.79 , 5.87)	(0.86 , 7.51)
(10,15)	(1.08 , 3.49)	(-5.79 , 5.86)	(-1.21 , 9.83)	(0.62 , 4.13)	(-5.44 , 5.83)	(0.79 , 7.50)
(15,10)	(-1.75 , 3.75)	(-3.77 , 5.48)	(-1.60 , 10.96)	(-0.62 , 4.36)	(-4.43 , 5.73)	(0.54 , 7.77)
(30,50)	(1.39 , 3.72)	(-5.88 , 5.88)	(-1.08 , 9.46)	(1.32 , 3.82)	(-5.84 , 5.87)	(0.89 , 7.42)
(50,30)	(-2.02 , 3.61)	(-3.69 , 5.43)	(-1.72 , 11.36)	(0.16 , 3.84)	(-5.22 , 5.82)	(0.57 , 8.17)

Table 3.12: The 95% confidence intervals of Rayleigh Distribution for the parameters (μ_1, μ_2, λ)

(m,n)	Conf($\mu_1 = 2$)	Conf($\mu_2 = 3$)	Conf($\lambda = 1.5$)	Conf($\mu_1 = 2$)	Conf($\mu_2 = 3$)	Conf($\lambda = 2.5$)
(10,10)	(0.61, 3.36)	(0.25 , 3.90)	(-0.01 , 6.16)	(-0.09 , 6.62)	(0.19 , 3.91)	(1.95 , 4.15)
(15,15)	(0.75 , 2.81)	(0.17 , 3.92)	(0.01 , 6.07)	(0.56 , 5.25)	(0.14 , 3.92)	(1.97 , 4.10)
(30,30)	(0.73 , 2.53)	(0.11 , 3.93)	(0.03 , 6.02)	(0.99 , 4.51)	(0.10 , 3.94)	(1.99 , 4.05)
(50,50)	(0.70 , 2.48)	(0.10 , 3.94)	(0.03 , 6.00)	(1.20 , 4.09)	(0.08 , 3.94)	(2.00 , 4.02)
(10,15)	(0.71 , 3.01)	(0.22 , 3.91)	(0.00 , 6.11)	(0.36 , 5.70)	(0.17 , 3.92)	(1.96 , 4.11)
(15,10)	(0.72 , 3.04)	(0.20 , 3.91)	(-0.01 , 6.14)	(0.32 , 5.75)	(0.15 , 3.92)	(1.96 , 4.13)
(30,50)	(0.73 , 2.50)	(0.17 , 3.93)	(0.03 , 6.00)	(1.13 , 4.22)	(0.09 , 3.94)	(2.00 , 4.03)
(50,30)	(0.74 , 2.50)	(0.10 , 3.94)	(0.03 , 6.01)	(1.12 , 4.28)	(0.08 , 3.94)	(1.99 , 4.04)



3.1 Example

In addition, by taking real rainfall data of the Union territory “Andaman and Nicobar Islands” in the span of 60 years, the rain fall data of one population of 30 years from 1911-1940 and another population of 30 years from 1971-2000 are taken as data of two populations, here in the collected data the rain fall is measured in millimeters

of rain fell over the year, there is huge difference occurs from month to month as well as year to year in the rain fall data.

For this data the parameters are estimated as well as the bias and mean squared error values are calculated for each distribution.

Table 3.1: Comparing Biases and MSE of Several Estimators of Several distributions for real data

$\Theta \downarrow$	Lomax($\theta=\sigma_1, \sigma_2, \delta$)			Weibull($\theta=\beta_1, \beta_2, \alpha$)			Rayleigh($\theta=\mu_1, \mu_2, \lambda$)			Gamma((ρ_1, ρ_2, η))		
	Mle	Bias	Mse	Mle	Bias	Mse	Mle	Bias	Mse	Mle	Bias	Mse
1	4.21	3.21	10.32	6.29	5.29	27.99	0.98	-0.02	0.04	16.02	15.02	225.64
2	4.12	2.12	4.50	6.14	4.14	17.20	1.84	-0.15	0.23	15.28	13.28	176.42
1.5	7.70	-1.5	2.25	245	243.97	59524.1	1.41	-0.08	0.15	14.62	13.21	172.23

By Observing the above values of all the parameters, its bias and mean square error, For the considered real Rain fall data, the Rayleigh distribution is the best fit when compared to the remaining distributions like Lomax, Weibull and Gamma distributions.

The Rayleigh distribution holds potential for various future applications, including:

a) Signal and Image Processing: The Rayleigh distribution plays a crucial role in modelling noise in applications like MRI image processing. It aids in

characterizing noise characteristics and developing effective denoising techniques.

b) Sea State Analysis: In oceanography and wave modelling, the Rayleigh distribution is employed to describe the distribution of wave heights in random sea states. This assists in predicting extreme wave events.

c) Wireless Communication: The Rayleigh distribution is a common choice for modelling the magnitude of received signals in fading wireless communication channels due to multipath propagation.

d) Wind Speed Analysis: In meteorology and wind engineering, the Rayleigh distribution is applied to

model the distribution of wind speeds. This provides valuable insights into statistical properties and aids in estimating extreme wind events, among other applications.

This real-world application of statistical techniques offers valuable insights into the behavior of these distributions and holds potential utility for modelling or prediction purpose. Overall, the study provides a comprehensive analysis of multiple distributions and their parameters, potentially impacting a wide range of applications across various fields.

4. CONCLUSION

In this study, we have addressed the problem of estimating parameters for two similar continuous probability distributions, such as Lomax, Weibull, Rayleigh, and Gamma distributions, utilizing the method of Maximum Likelihood Estimation (MLE). Due to the absence of closed-form expressions for the ML estimates, we employed a numerical technique known as the Newton-Raphson method to approximate the ML estimates of the common parameter by solving the system of equations for different distributions.

References:

- Al-Zahrani, B., & Sobhi, M. M. A. (2013). On Parameters Estimation of Lomax Distribution under General Progressive Censoring. *Journal of Quality and Reliability Engineering*, 2013, 1–7. doi :10.1155/2013/431541
- Aldrich, J. (1997). R.A. Fisher and the making of maximum likelihood 1912-1922. *Statistical Science*, 12(3). <https://doi.org/10.1214/ss/1030037906>
- Balakrishnan, N., & Kateri, M. (2008). On the maximum likelihood estimation of parameters of Weibull distribution based on complete and censored data. *Statistics & Probability Letters*, 78(17), 2971–2975. doi :10.1016/j.spl.2008.05.019
- Bhat, A., Ahmad, S., Almetwally, E. M., Yehia, N., Alsadat, N., & Tolba, A. H. (2023). The odd lindley power rayleigh distribution: properties, classical and bayesian estimation with applications. *Scientific African*, 20, e01736. doi :10.1016/j.sciaf.2023.e01736
- Choi, S., & Wette, R. (1969). Maximum likelihood estimation of the parameters of the gamma distribution and their bias. *Technometrics*, 11(4), 683–690. doi :10.1080/00401706.1969.10490731
- Dey, S., & Dey, T. (2012). Bayesian estimation and prediction intervals for a Rayleigh distribution under a conjugate prior. *Journal of Statistical Computation and Simulation*, 82(11), 1651–1660. doi :10.1080/00949655.2011.590808
- Dey, S., Dey, T., & Kundu, D. (2014). Two-Parameter rayleigh distribution: different methods of estimation. *American Journal of Mathematical and Management Sciences*, 33(1), 55–74. doi :10.1080/01966324.2013.878676
- Giles, D. E. A., Feng, H., & Godwin, R. T. (2013). On the Bias of the Maximum Likelihood Estimator for the Two-Parameter Lomax Distribution. *Communications in Statistics - Theory and Methods*, 42(11), 1934–1950. doi :10.1080/03610926.2011.600506
- Gupta, R., & Kundu, D. (2001). Generalized exponential distribution: different method of estimations. *Journal of Statistical Computation and Simulation*, 69(4), 315–337. doi :10.1080/00949650108812098
- Hasanain, W., Al-Ghezi, N., & Soady, A. (12 2022). Bayes estimation of Lomax parameters under different loss functions using Lindley's approximation. *Italian Journal of Pure and Applied Mathematics*, 630–640.
- He, D., Sun, D., & Zhu, Q. (2022). Bayesian analysis for the Lomax model using noninformative priors. *Statistical Theory and Related Fields*, 7(1), 61–68. doi :10.1080/24754269.2022.2133466
- Hirose, H. (1995). Maximum likelihood parameter estimation in the three-parameter gamma distribution. *Computational Statistics & Data Analysis*, 20(4), 343–354. doi :10.1016/0167-9473(94)00050-s

Following the calculation of the ML estimates for each distribution, we proposed 95% asymptotic confidence intervals for each parameter of every distribution using the Fisher information matrix. Additionally, the study conducted simulations for each distribution with varying sample sizes, estimating the values of the parameters, bias, and mean squared error (MSE). This comprehensive analysis allowed for a thorough examination of the behavior of each distribution under different conditions.

Based on the simulation data, we can conclude that increasing the sample size reduces both the bias and mean square error for each estimator. It has been observed that for fixed sample sizes and fixed shape parameters, the common scale parameter of these distributions increases, resulting in decreased bias and mean square error values.

Acknowledgement: The authors express their gratitude to the editor and reviewers for their insightful comments and suggestions that have improved the article's presentation.

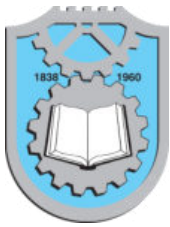
- Husak, G. J., Michaelsen, J., & Funk, C. C. (2006). Use of the gamma distribution to represent monthly rainfall in Africa for drought monitoring applications. *International Journal of Climatology*, 27(7), 935–944. doi :10.1002/joc.1441
- Kundu, D., & Raqab, M. Z. (2005). Generalized Rayleigh distribution: different methods of estimations. *Computational Statistics & Data Analysis*, 49(1), 187–200. doi :10.1016/j.csda.2004.05.008.
- Lai, C. D., D. N. P. Murthy, and M. Xie (2011). “Weibull distributions” Wiley Interdisciplinary Reviews: *Computational Statistics* 3, no. 3: 282–287.
- Nagamani, N., & Tripathy, M. R. (2017). Estimating common scale parameter of two gamma populations: a simulation study. *American Journal of Mathematical and Management Sciences*, 36(4), 346–362. doi :10.1080/01966324.2017.1369473
- Shenton, L. R., and K. O. Bowman (1969). “Maximum likelihood estimator moments for the 2-parameter gamma distribution” *Sankhya - The Indian Journal of Statistics*.
- Stone, G., & Van Heeswijk, R. G. (1977). Parameter estimation for the WeiBull distribution. *IEEE Transactions on Electrical Insulation*, EI-12(4), 253–261. doi :10.1109/tei.1977.297976
- Tan, Z. (2009). A new approach to MLE of Weibull distribution with interval data. *Reliability Engineering & System Safety*, 94(2), 394–403. doi :10.1016/j.ress.2008.01.010
- Tripathy, M. R., & Nagamani, N. (2017). Estimating common shape parameter of two gamma populations: A simulation study. *Journal of Statistics and Management Systems*, 20(3), 369–398. doi :10.1080/09720510.2017.1292688
- Wilks, D. S. (1990). Maximum likelihood estimation for the gamma distribution using data containing zeros. *Journal of Climate*, 3(12), 1495–1501. doi :10.1175/1520-0442(1990)003
- Yang, Z., & Lin, D. K. (2007). Improved maximum-likelihood estimation for the common shape parameter of several Weibull populations. *Applied Stochastic Models in Business and Industry*, 23(5), 373–383. doi :10.1002/asmb.678

Abbarapu Ashok

VIT-AP,
Amaravati,
India
ashokabarapu@gmail.com
ORCID: 0009-0008-0389-7243

Nadiminti Nagamani

VIT-AP,
Amaravati,
India
maniinadiminti999@gmail.com
ORCID: 0000-0002-5518-6653



Vol. xx, No. x (202x) x-x, doi:

Proceedings on Engineering Sciences



www.pesjournal.net

INFERENCES DRAWN ON COMMON SCALE PARAMETER OF TWO POPULATIONS USING RAINFALL DATA

Vijay Kumar Lingutla¹

Nadiminti Nagamani

P. S. Brahmanandam

Keywords:

Bayes Estimation; Lindley's Approximation, Squared Error Loss, Linex Loss Functions, Rainfall Data.



ABSTRACT

This study investigates into the estimation of a common parameter across distinct probability distributions, including Weibull, Rayleigh, Gamma, and Lomax. The primary objective is to determine the common scale parameter when the shape or location parameters differ for each distribution, employing a Bayesian approach. Due to the impracticality of obtaining an exact expression for Bayes, Lindley's (1980) approximation is utilized for explicit evaluation. Bayesian estimates are derived for the common scale parameter and distinct shape or location parameters for Weibull, Rayleigh, Lomax, and Gamma distributions under both squared error and Linex loss functions. To facilitate this analysis, Gamma priors are employed for Weibull, Rayleigh, and Lomax distributions, guided by relevant references, while an Inverted gamma prior is applied for the Gamma distribution. The outcomes are compared through a Monte-Carlo simulation study, providing a comprehensive evaluation. Real rainfall data is also incorporated into the assessment, further enriching the comparison of results.

© 202x Published by Faculty of Engineering

1. INTRODUCTION

Estimation in statistics involves the process of determining unknown characteristics or traits of a population by analyzing sample data. In inferential statistics, a central concept is estimation, which entails using sample data to make inferences or draw conclusions about a larger population. Various estimation approaches exist, such as Bayesian estimation, Method of Moments, Method of Least Squares, Uniformly Minimum Variance Unbiased

Estimation, and Maximum Likelihood Estimation. Since estimates are based on samples and may not precisely match the true parameter value, it's crucial to recognize that estimation inherently carries uncertainty. Nevertheless, employing appropriate sampling methods and statistical inference allows us to obtain accurate estimates and draw meaningful inferences about populations from sample data.

¹ Corresponding author: Nadiminti Nagamani
Email: maniinadiminiti999@gmail.com

Bayesian statistical methods are gaining increasing popularity in both applied and fundamental research. Researchers have applied Bayesian estimation across diverse fields. For instance, Albert (1987) utilized Bayesian estimation to estimate cell probabilities from a two-way contingency table. In another study, Ghosh et al. (1989) employed nonparametric empirical Bayes estimation to estimate the distribution function and mean of both finite and infinite populations. Additionally, Ghosh & Lahiri (1987) explored the estimation of the average of stratified samples using Robust Empirical Bayes estimation. These applications underscore the versatility and effectiveness of Bayesian estimation in various research domains.

The significance of the loss function in Bayesian analysis and decision-making is underscored, as it serves as a crucial tool for illustrating both overestimation and underestimation in an analysis. Two commonly employed types of loss functions are symmetric and asymmetric. The symmetric loss function treats all guesses equally, while the asymmetric loss function assigns distinct weights to overestimation and underestimation. In practical scenarios, the asymmetric loss function proves more valuable and realistic than its symmetric counterpart. This article incorporates both symmetric (Squared Error) and asymmetric (Linex) loss functions, recognizing their relevance in capturing different aspects of estimation and decision-making processes. The inclusion of these functions enhances the robustness and applicability of the Bayesian analysis undertaken in the study.

The average squared difference between the observed and estimated values, also known as the squared error, is provided as follows:

$$\text{Squared Error (SE)} = \frac{1}{n} \sum_{i=1}^n (\theta - \hat{\theta})^2$$

A mixture of exponential and linear functions makes up the Linex loss function. This is how the Linex loss function is described:

$$L(\theta) = e^{-c\theta} - c\theta - 1$$

where 'c' is a parameter that controls the shape of the loss function. In our study, Bayes estimation is applied to four distributions: Weibull, Rayleigh, Gamma, and Lomax, considering a common scale and varying shape/location parameters. Both symmetric and asymmetric loss functions are employed in this analysis. A brief overview of these distributions is provided below.

The Weibull distribution finds extensive applications in data analysis for real-world scenarios and reliability studies. Its versatility allows it to emulate various behavioral patterns observed in practical situations, contingent upon the specific parameter selections.

This distribution's utility in replicating real-life patterns and its adaptability to diverse situations make it a valuable tool in statistical modeling and analysis. The Bayes estimation approach applied to the Weibull distribution with common scale and distinct shape/location parameters contributes to a comprehensive understanding of its behavior in the

context of Bayesian analysis and decision-making. The probability density function of Weibull distribution is given by

$$f(x; \alpha, \beta) = \alpha \beta x^{\alpha-1} e^{-\beta x^\alpha}; x>0, \alpha>0, \beta>0. \quad (1.1)$$

where Scale and Shape parameters for Weibull distributions are β and α respectively. Extensive research has been conducted on the Weibull distribution, employing various estimation techniques and loss functions. Notable contributions in this domain include. Guure et al. (2012) focused on estimating the parameters of the Weibull Distribution using Maximum Likelihood Estimation (MLE) and Bayes estimation with Jeffrey's prior. The study explored various loss functions, including Linex and General Entropy Loss functions. Kundu & Mitra (2016) conducted parameter estimation for the Weibull distribution through Bayes estimation using Gibbs Sampling and Importance Sampling. The prior distribution was assumed to follow a Gamma distribution. To assess the performance of the estimators, a simulation study was conducted. Gupta & Singh (2017) also estimated the parameters of Weibull distribution using classical and Bayesian estimation in the presence of outlier.

The Rayleigh Distribution serves as a particular instance of the Weibull distribution when the shape parameter is assumed to be two. The distribution initially addressed an acoustics issue. Over time, it has found applications in diverse disciplines.

In communication theory, the Rayleigh distribution is employed to characterize the hourly median and instantaneous peak strength of incoming radio waves. In the field of oceanography, it is widely utilized for predicting wave heights. Additionally, the distribution has been instrumental in simulating the occurrence of different wind speeds over a year at various wind turbine locations.

The Rayleigh Distribution's versatility and adaptability to different domains underscore its significance in statistical modeling and analysis, making it a valuable tool in understanding and predicting various phenomena in fields ranging from communication theory to oceanography and renewable energy.

The probability density function of Raleigh distribution is given by

$$f(x; \delta, \omega) = 2\omega(x - \delta)e^{-\omega(x-\delta)^2}; \quad x > \delta, \omega > 0. \quad (1.2)$$

where δ and ω are the location and scale parameters of Rayleigh distribution. Interesting research has been done on the Rayleigh distribution with one and two parameters. Dey et al. (2014) considered Rayleigh distribution with two parameters and estimated them through the method of moment estimators, MLE, L moment estimators, Least square estimation, and Bayes estimators using uniform prior for location parameter and Gamma prior for scale parameter.

The determination of parameters for a gamma distribution has been a subject of recent thorough

examination and has been extensively discussed by several authors. The gamma distribution is particularly applied when observed data is skewed in a favorable direction. This distribution has found extensive utility in various fields, with a notable emphasis on its use in the study of dependability, life testing, and insurance.

The gamma distribution's versatile application in scenarios where positive skewness is prevalent makes it a valuable tool in statistical modeling. Its relevance in the context of dependability studies, life testing experiments, and insurance risk assessments underscores its importance in capturing the distribution of data with positive biases. As researchers delve deeper into understanding and refining parameter estimation techniques for the gamma distribution, its role in practical applications continues to be a subject of significant exploration and discussion.

The probability density function of Gamma distribution is given by

$$f(x; \mu, \lambda) = \frac{1}{\Gamma(\mu) \lambda^\mu} x^{\mu-1} e^{-\frac{x}{\lambda}}, \quad x > 0, \mu, \lambda > 0. \quad (1.3)$$

The estimation of parameters or functions arising naturally in certain statistical problems is crucial due to its widespread applications in real-world scenarios. Researchers have explored various estimation methods and biases for Maximum Likelihood Estimation (MLE). In a research work Choi & Wette (1969) provided estimates for MLE and their biases.

In a different approach, Son & Oh (2006) proposed the estimation of parameters using Bayes estimation, considering both informative and non-informative priors.

An alternative distribution, the Lomax distribution, was suggested by Bryson (1974) for cases where the population distribution exhibits heavy tails. This alternative is considered particularly useful when compared to typical lifespan distributions such as Exponential, Weibull, or Gamma distributions.

The probability density function of Lomax distribution is given by

$$f(x, \eta, \gamma) = \frac{\eta}{\gamma} \left(1 + \frac{x}{\gamma}\right)^{-(\eta+1)}; \quad x > 0, \eta, \gamma > 0. \quad (1.4)$$

A lot of research has been carried out by several authors. For instance, Pradhan & Kundu (2011) estimated the parameters using Bayes estimation, and they assumed that the scale parameter has a gamma prior and the shape parameter has any log-concave prior, and they are independently distributed. Under the above priors, they used the Gibbs sampling technique to generate samples from the posterior density function. They also constructed the highest posterior density credible interval of the order statistics for the future sample. Okasha (2014) in their paper estimated the parameters by the E-Bayesian estimator, Gamma distribution has been considered as the prior information. Fitrilia et al. (2018b) also derived an E-

Bayesian estimator for the parameters using Gamma Prior for the right censored data. Al-Bossly (2021) derived the E-Bayesian estimation of Lomax Distribution for 6 Different Loss Functions Namely Square Error, Linex, Asymmetric, Entropy, Compound Linex, and Weighted Linex loss functions. Kumari et al. (2022) used Bayes estimation to estimate the unknown shape parameter of two-parameter Lomax distribution using an extension of Jeffrey's prior and Gamma's prior under Entropy loss and Precautionary loss functions.

The diverse methodologies and comparisons presented in these studies contribute to the understanding of parameter estimation techniques, providing insights into the applicability and performance of different approaches in various statistical contexts.

The primary objective of this study is to estimate the common scale parameter of two populations when the other shape/location parameters are distinct. Various researchers have explored similar problems in the past, and their contributions are discussed below.

In the context of the exponential distribution, Ghosh & Razmpour (1984) proposed the estimation of common location parameters for two populations. They utilized UMVUE, Maximum Likelihood Estimation (MLE), and Modified MLE for parameter estimation. Similarly, Jin & Pal (1992) addressed the same issue and proposed improved estimators using Chi-square distribution, comparing their performance through simulation studies. Recently, Azhad et al. (2020) considered several heterogeneous Exponential distributions, estimating common location parameters using MLE, modified MLE, and uniformly minimum variance unbiased estimator. In the case of Gamma populations, Nagamani & Tripathy (2017) focused on estimating common scale parameters, employing both MLE and Bayes estimation, and conducted simulation studies for performance comparison. A similar approach was taken by Nagamani et al. (2020) for two Logistic populations.

In this paper, the estimation of the common scale parameter is extended to various distributions, including Weibull, Gamma, Rayleigh, and Lomax. The study employs Bayes estimation under Squared Error and Linex loss functions, addressing the challenge of solving Bayes' expression explicitly by employing Lindley's approximation. The Bayes estimates for each distribution are derived in sections 3 to 6. Additionally, a comprehensive simulation study in section 7 compares the performance of estimators in terms of Bias and Mean Squared Error (MSE). Real rainfall data is utilized to validate the results. The study concludes in section 8 with overarching remarks on the findings and methodology.

2. BAYESIAN STUDY

In this section, we explore the BAYES estimate for the model parameters. The utility of Bayes estimation is

particularly evident when there is prior information available about the parameter distribution. Let's assume that the random samples are represented as (x_1, x_2, \dots, x_m) and (y_1, y_2, \dots, y_n) for the two respective populations.

Let $P_1(\theta_1)$ denote the prior density function for the shape/location parameter θ_1 . Similarly, let $P_2(\theta_2)$ and $P_3(\theta_3)$ represent the prior densities for the shape/location and scale parameters θ_2 and θ_3 respectively.

The posterior joint density function of $(\theta_1, \theta_2, \theta_3)$ for the observed data (x, y) is expressed as follows:

$$f(\theta_1, \theta_2, \theta_3 | x, y) = \frac{f(\theta_1, \theta_2, \theta_3, x, y)}{\int_0^\infty \int_0^\infty \int_0^\infty f(\theta_1, \theta_2, \theta_3, x, y) d\theta_1 d\theta_2 d\theta_3}$$

The Posterior expectation of $g(\theta_1, \theta_2, \theta_3)$ is given by

$$E[g(\theta_1, \theta_2, \theta_3) | x, y] = \frac{\int_0^\infty \int_0^\infty \int_0^\infty g(\theta_1, \theta_2, \theta_3) f(\theta_1, \theta_2, \theta_3, x, y) d\theta_1 d\theta_2 d\theta_3}{\int_0^\infty \int_0^\infty \int_0^\infty f(\theta_1, \theta_2, \theta_3, x, y) d\theta_1 d\theta_2 d\theta_3} \quad (2.1)$$

The analytical evaluation of the ratio of the integrals mentioned above can be challenging. Nevertheless, numerical values can be obtained through various approximations. One widely used method is proposed by Lindley (1980). Lindley's approximation provides a practical approach to numerically assess the ratio of the integrals.

In addition to Lindley's approximation, we explore the use of conjugate priors and different loss functions for parameters to derive BAYES estimators. These approaches contribute to the overall methodology, offering flexibility and robustness in estimating parameters in the Bayesian framework.

2.1 Lindley's Approximation

The source that is most frequently used in the literature, i.e. Lindley (1980) is used by us to assess the phrase in (2.1). The method developed by Lindley to assess the form's expressiveness

$$I = \frac{\int w(\theta) \exp L(\theta) d\theta}{\int v(\theta) \exp L(\theta) d\theta} = E[u(\theta) | x] \quad (2.2)$$

where the parameter of interest $\theta = (\theta_1, \theta_2, \dots, \theta_m)$, $L(\theta)$ is the log likelihood function of the data $X = (x_1, x_2, \dots, x_n)$ and $w(\theta) = u(\theta)v(\theta)$ and also $v(\theta)$ is the prior distribution of θ .

Lindley proposed an approximation to (2.2) which is given by

$$E[u(\theta) | x] = \left[u + \frac{1}{2} \sum_i \sum_j (u_{ij} + 2u_i p_j) \sigma_{ij} + \frac{1}{2} \sum_i \sum_j \sum_k \sum_r L_{ijk} \sigma_{ij} \sigma_{kr} \sigma_{kr} u_r \right] + O\left(\frac{1}{n^2}\right) \quad (2.3)$$

Where $i, j, k, r = 1, 2, 3, \dots, m$; $\theta = (\theta_1, \theta_2, \dots, \theta_m)$ and $\hat{\theta}$ is the maximum likelihood estimator of θ . $u = u(\theta)$, $u_i = \frac{\partial u}{\partial \theta_i}$, $u_{ij} = \frac{\partial^2 u}{\partial \theta_i \partial \theta_j}$, $L_{ijk} = \frac{\partial^3 u}{\partial \theta_i \partial \theta_j \partial \theta_k}$, $p(\theta) = \log v(\theta)$, $P_i = \frac{\partial P}{\partial \theta_i}$, σ_{ij} is the $(i, j)^{th}$ element in $[-L_{ij}]^{-1}$

Here $i, j, k, r = 1, 2, \dots, s$ and $\hat{\theta}_{ML}$ is the MLE of θ . All the inside terms have been evaluated at the MLEs of θ . Now, we apply Lindley's approximation method to find BAYES estimators for the parameters α_1, α_2 , and β under the squared error and Linex loss functions.

2.2 Bayes estimation under different loss functions

Here we considered two different loss functions Symmetric (Squared Error) and Asymmetric (Linex) Loss functions. We can use the expression (2.3) to get the Bayes estimators of the parameters $(\theta_1, \theta_2, \theta_3)$ under Symmetric (SE), and Asymmetric (Linex) loss functions. For our problem, the log Likelihood function can be written as

$$L(\theta_1, \theta_2, \theta_3) = \sum_{i=1}^m \log f(x_i, \theta_1 \theta_3) + \sum_{j=1}^n \log f(y_j, \theta_2 \theta_3)$$

2.3 Symmetric (SE) Loss Function

We can obtain the Bayes estimators under the Symmetric (SE) Loss function, after ignoring the terms of order $\frac{1}{(m+n)^2}$ and smaller, the expression in (2.2), reduces to

$$\begin{aligned} E[u(\theta) | x, y] &= u + u_1 a_1 + u_2 a_2 + u_3 a_3 + a_4 + \\ &\quad \frac{1}{2} [A(u_1 \sigma_{11} + u_2 \sigma_{22} + u_3 \sigma_{33}) + \\ &\quad B(u_1 \sigma_{21} + u_2 \sigma_{32} + u_3 \sigma_{13}) + \\ &\quad D(u_1 \sigma_{31} + u_2 \sigma_{12} + u_3 \sigma_{23})] \end{aligned} \quad (2.4)$$

In our notation, we have $\theta = (\theta_1, \theta_2, \theta_3) = (\alpha_1, \alpha_2, \beta)$.

$$\begin{aligned} a_1 &= \rho_1 \sigma_{11} + \rho_2 \sigma_{12} + \rho_3 \sigma_{13}, & a_3 &= \rho_1 \sigma_{31} + \\ a_2 &= \rho_1 \sigma_{21} + \rho_2 \sigma_{22} + \rho_3 \sigma_{23}, & & \\ a_4 &= \mu_{12} \sigma_{12} + \mu_{13} \sigma_{13} + \mu_{23} \sigma_{23}, & a_5 &= \mu_{11} \sigma_{11} + \\ & \mu_{22} \sigma_{22} + \mu_{33} \sigma_{33}. & & \end{aligned}$$

$$\begin{aligned} A &= \sigma_{11} L_{111} + 2\sigma_{12} L_{121} + 2\sigma_{13} L_{131} + 2\sigma_{23} L_{231} \\ &\quad + \sigma_{22} L_{221} + \sigma_{33} L_{331} \\ B &= \sigma_{11} L_{112} + 2\sigma_{12} L_{122} + 2\sigma_{13} L_{132} + 2\sigma_{23} L_{232} \\ &\quad + \sigma_{22} L_{222} + \sigma_{33} L_{332} \\ D &= \sigma_{11} L_{113} + 2\sigma_{12} L_{123} + 2\sigma_{13} L_{132} + 2\sigma_{23} L_{232} \\ &\quad + \sigma_{22} L_{223} + \sigma_{33} L_{333} \end{aligned}$$

2.4 Asymmetric (Linex) Loss Function

The Linex Loss function is given by

$$L(\lambda) = e^{-c\theta_0} - c\theta_0 - 1, \quad a \neq 0$$

Where $\theta_0 = \hat{\theta} - \theta$, $\hat{\theta}$ is the MLE of the parameter θ .

The Bayes estimator of the parameter θ under the Linex loss function is

$$\hat{\theta} = \frac{1}{c} \ln [E_\theta (e^{-a\theta})]$$

By using Lindley's approximation we can find the approximation for $E_\theta (e^{-a\theta})$ as given below

$$\begin{aligned} E[u(\theta) | x, y] &= v + v_1 a_1 + v_2 a_2 + v_3 a_3 + a_4 + \\ &\quad \frac{1}{2} [A(v_1 \sigma_{11} + v_2 \sigma_{21} + v_3 \sigma_{31}) + \\ &\quad B(v_1 \sigma_{21} + v_2 \sigma_{32} + v_3 \sigma_{13}) + \\ &\quad D(v_1 \sigma_{31} + v_2 \sigma_{12} + v_3 \sigma_{23})] \end{aligned} \quad (2.5)$$

Where $v = e^{-\alpha\theta}$, $v_1 = \frac{\partial v}{\partial \alpha_1}$, $v_2 = \frac{\partial v}{\partial \alpha_2}$, $v_3 = \frac{\partial v}{\partial \alpha_3}$, $v_{ij} = \frac{\partial^2 v}{\partial \theta_i \partial \theta_j}$, σ_{ij} , a_1, a_2, a_3, A, B, D also remains the same for all i and j above.

3. BAYESIAN ESTIMATION OF WEIBULL DISTRIBUTION

Assume that (x_1, x_2, \dots, x_m) and (y_1, y_2, \dots, y_n) be two samples of sizes drawn from Weibull populations. They are denoted as $W(\alpha_1, \beta)$ and $W(\alpha_2, \beta)$ and their probability density functions are given below.

$$f(x; \alpha, \beta) = \alpha_1 \beta x^{\alpha_1-1} e^{-\beta x^{\alpha_1}}; \quad x > 0, \alpha_1 > 0, \beta > 0.$$

$$f(y; \alpha, \beta) = \alpha_2 \beta y^{\alpha_2-1} e^{-\beta y^{\alpha_2}}; \quad y > 0, \alpha_2 > 0, \beta > 0.$$

The log Likelihood function is obtained as

$$L = m \log \alpha_1 + n \log \alpha_2 + (m+n) \log \beta + (\alpha_1 - 1) \sum_{i=1}^m \log x_i + (\alpha_2 - 1) \sum_{j=1}^n \log y_j - \beta(T_1 + T_2)$$

The Prior Distribution for the parameters α_1, α_2 and β follows Gamma distributions with densities as given below.

$$\rho_1(\alpha_1) = \frac{c_1^{b_1}}{\Gamma(b_1)} \alpha_1^{b_1-1} e^{-c_1 \alpha_1}; \quad b_1, c_1, \alpha_1 > 0$$

$$\rho_2(\alpha_2) = \frac{c_2^{b_2}}{\Gamma(b_2)} \alpha_2^{b_2-1} e^{-c_2 \alpha_2}; \quad b_2, c_2, \alpha_2 > 0$$

$$\rho_3(\beta) = \frac{c_3^{b_3}}{\Gamma(b_3)} \beta^{b_3-1} e^{-c_3 \beta}; \quad b_3, c_3, \beta > 0$$

The joint prior density function $v(\alpha_1, \alpha_2, \beta)$ can be obtained as

$$v(\alpha_1, \alpha_2, \beta) = \rho_1(\alpha_1) \rho_2(\alpha_2) \rho_3(\beta)$$

$$= \frac{c_1^{b_1}}{\Gamma(b_1)} \frac{c_2^{b_2}}{\Gamma(b_2)} \frac{c_3^{b_3}}{\Gamma(b_3)} \alpha_1^{b_1-1} \alpha_2^{b_2-1} \beta^{b_3-1} e^{-c_1 \alpha_1 - c_2 \alpha_2 - c_3 \beta}$$

Hence

$$\rho(\theta) = \log v(\theta) = b_1 \log c_1 + b_2 \log c_2 + b_3 \log c_3 - \log \Gamma(b_1) - \log \Gamma(b_2) - \log \Gamma(b_3) + (b_1 + 1) \log \alpha_1 + (b_2 + 1) \log \alpha_2 + (b_3 + 1) \log \beta - c_1 \alpha_1 - c_2 \alpha_2 - c_3 \beta$$

$$\rho_1 = \frac{b_1-1}{\alpha_1} - c_1, \quad \rho_2 = \frac{b_2-1}{\alpha_2} - c_2, \quad \rho_3 = \frac{b_3-1}{\beta} - c_3$$

From the Likelihood function we can derive

$$\sigma_{11} = -\frac{1}{d} \left[\frac{m+n}{\beta^2} \left(\frac{n}{\alpha_2^2} + \beta T_2^{II} \right) - (T_2^I)^2 \right], \quad \sigma_{12} = \frac{T_1^I T_2^I}{d} = \sigma_{21}, \quad \sigma_{13} = \frac{T_1^I}{d} \left(\frac{n}{\alpha_2^2} + \beta T_2^{II} \right) = \sigma_{31},$$

$$\sigma_{22} = -\frac{1}{d} \left[\frac{m+n}{\beta^2} \left(\frac{m}{\alpha_1^2} + \beta T_1^{II} \right) - (T_1^I)^2 \right], \quad \sigma_{23} = \frac{T_2^I}{d} \left(\frac{m}{\alpha_1^2} + \beta T_1^{II} \right) = \sigma_{32},$$

$$\sigma_{33} = -\frac{1}{d} \left(\frac{m}{\alpha_1^2} + \beta T_1^{II} \right) \left(\frac{n}{\alpha_2^2} + \beta T_2^{II} \right)$$

$$\text{Where } d = -\left(\frac{m}{\alpha_1^2} + \beta T_1^{II} \right) \left[\frac{m+n}{\beta^2} \left(\frac{n}{\alpha_2^2} + \beta T_2^{II} \right) - (T_2^I)^2 \right] + (T_1^I)^2 \left(\frac{n}{\alpha_2^2} + \beta T_2^{II} \right), \quad T_1 = \sum_{i=1}^m (x_i^{\alpha_1}),$$

$$T_2 = \sum_{j=1}^n (y_j^{\alpha_2}).$$

Here T_1^I, T_1^{II} , and T_2^{III} are the first, second, and third-order derivatives of T_1 with respect to α_1 . And

also T_2^I, T_2^{II} , and T_2^{III} are the first, second, and third-order derivatives of T_2 with respect to α_2 .

3.1 Bayes Estimators using Symmetric Loss Function

Let $u(\theta) = \alpha_1$, then $u_1 = 1, u_2 = u_3 = 0, u_{ij} = 0; i, j = 1, 2, 3$. Substituting these values in (2.4) we get the Bayes estimator for α_1 as follows

$$\begin{aligned} E(\hat{\alpha}_{1ML}|x, y) &= \hat{\alpha}_{1ML} - \frac{1}{d} \left[\frac{m+n}{\beta_{ML}^2} \left(\frac{n}{\alpha_2^2} + \beta_{ML} T_2^{II} \right) - (T_2^I)^2 \right] \left(\frac{b_1-1}{\alpha_1^2} - c_1 \right) - \\ &\quad \frac{T_1^I T_2^I}{d} \left(\frac{b_2-1}{\alpha_2^2} - c_2 \right) + \\ &\quad \frac{T_1^I}{d} \left(\frac{n}{\alpha_2^2} + \beta_{ML} T_2^{II} \right) \left(\frac{b_3-1}{\beta_{ML}} - c_3 \right) + \\ &\quad \frac{1}{2} [A\sigma_{11} + B\sigma_{21} + D\sigma_{31}] \\ &= \hat{\alpha}_{1C} \end{aligned} \quad (3.1)$$

Let $u(\theta) = \alpha_2$, then $u_2 = 1, u_1 = u_3 = 0, u_{ij} = 0; i, j = 1, 2, 3$. Substituting these values in (2.4) we get the Bayes estimator for α_2 as follows

$$\begin{aligned} E(\hat{\alpha}_{2ML}|x, y) &= \hat{\alpha}_{2ML} - \frac{T_1^I T_2^I}{d} \left(\frac{b_1-1}{\alpha_1^2} - c_1 \right) - \\ &\quad \frac{1}{d} \left[\frac{m+n}{\beta_{ML}^2} \left(\frac{m}{\alpha_1^2} + \beta_{ML} T_1^{II} \right) - (T_1^I)^2 \right] \left(\frac{b_2-1}{\alpha_2^2} - c_2 \right) + \\ &\quad \frac{T_2^I}{d} \left(\frac{m}{\alpha_1^2} + \beta T_1^{II} \right) \left(\frac{b_3-1}{\beta_{ML}} - c_3 \right) + \\ &\quad \frac{1}{2} [A\sigma_{12} + B\sigma_{22} + D\sigma_{32}] \\ &= \hat{\alpha}_{2C} \end{aligned} \quad (3.2)$$

Let $u(\theta) = \beta$, then $u_3 = 1, u_1 = u_2 = 0, u_{ij} = 0; i, j = 1, 2, 3$. Substituting these values in (2.4) we get the Bayes estimator for β as follows

$$\begin{aligned} E(\hat{\beta}_{2ML}|x, y) &= \hat{\beta}_{ML} + \frac{T_1^I}{d} \left(\frac{n}{\alpha_2^2} + \beta_{ML} T_2^{II} \right) \left(\frac{b_1-1}{\alpha_1^2} - c_1 \right) + \\ &\quad \frac{T_2^I}{d} \left(\frac{m}{\alpha_1^2} + \beta_{ML} T_1^{II} \right) \left(\frac{b_2-1}{\alpha_2^2} - c_2 \right) - \\ &\quad \frac{1}{d} \left(\frac{m}{\alpha_1^2} + \beta_{ML} T_1^{II} \right) \left(\frac{n}{\alpha_2^2} + \beta_{ML} T_2^{II} \right) \left(\frac{b_3-1}{\beta_{ML}} - c_3 \right) + \\ &\quad \frac{1}{2} [A\sigma_{13} + B\sigma_{23} + D\sigma_{33}] \\ &= \hat{\beta}_C \end{aligned} \quad (3.3)$$

3.2 Bayes Estimators using Asymmetric Loss Function

Let $v(\theta) = e^{-a\alpha_{1ML}}$, then $v_1 = -a e^{-a\alpha_{1ML}}, v_2 = 0, v_3 = 0, v_{11} = a^2 e^{-a\alpha_{1ML}}$; rest of v_{ij} 's $i, j = 1, 2, 3$, are zero. Substituting these values in (2.5) we get the Bayes estimator for α_1 as follows

$$\begin{aligned} E(\hat{\alpha}_{1ML}|x, y) &= e^{-a\alpha_{1ML}} - a e^{-a\alpha_{1ML}} \left[-\frac{1}{d} \left[\frac{m+n}{\beta_{ML}^2} \left(\frac{n}{\alpha_2^2} + \beta_{ML} T_2^{II} \right) - (T_2^I)^2 \right] \left(\frac{b_1-1}{\alpha_1^2} - c_1 \right) - \right. \\ &\quad \left. \frac{T_1^I T_2^I}{d} \left(\frac{b_2-1}{\alpha_2^2} - c_2 \right) + \frac{T_1^I}{d} \left(\frac{n}{\alpha_2^2} + \beta_{ML} T_2^{II} \right) \left(\frac{b_3-1}{\beta_{ML}} - c_3 \right) \right] + a_5 + \\ &\quad \frac{1}{2} [A\sigma_{11} + B\sigma_{21} + D\sigma_{31}] \\ &= \hat{\alpha}_{1LC} \end{aligned} \quad (3.4)$$

Let $v(\theta) = e^{-a\alpha_{2ML}}$, then $v_2 = -a e^{-a\alpha_{2ML}}, v_1 = v_3 = 0, v_{22} = a^2 e^{-a\alpha_{2ML}}$; rest of v_{ij} 's $i, j = 1, 2, 3$, are zero.

zero. Substituting these values in (2.5) we get the Bayes estimator for α_2 as follows

$$\begin{aligned} E(\hat{\alpha}_{2ML}|x,y) &= e^{-a\hat{\alpha}_{2ML}} - ae^{-a\hat{\alpha}_{2ML}} \left[\frac{T_1^I T_2^I}{d} \left(\frac{b_1-1}{\alpha_{1ML}} - c_1 \right) - \frac{1}{d} \left[\frac{m+n}{\beta_{ML}^2} \left(\frac{m}{\alpha_1^2} + \beta_{ML} T_1^{II} \right) - (T_1^I)^2 \right] \left(\frac{b_2-1}{\alpha_{2ML}} - c_2 \right) + \frac{T_2^I}{d} \left(\frac{m}{\alpha_1^2} + \beta_{ML} T_1^{II} \right) \left(\frac{b_3-1}{\beta_{ML}} - c_3 \right) \right] + a_5 + \frac{1}{2} [A\sigma_{12} + B\sigma_{22} + D\sigma_{32}] \\ &= \hat{\alpha}_{2LC} \end{aligned} \quad (3.5)$$

Let $v(\theta) = e^{-a\beta}$, then $v_3 = -a e^{-a\beta}, v_1 = v_2 = 0, v_{33} = a^2 e^{-a\beta}$; rest of v_{ij} 's i, j=1, 2, 3, are zero. Substituting these values in (2.5) we get the Bayes estimator for β as follows

$$\begin{aligned} E(\hat{\beta}_{ML}|x,y) &= e^{-a\beta_{ML}} - ae^{-a\beta_{ML}} \left[\frac{T_1^I}{d} \left(\frac{n}{\alpha_2^2} + \beta_{ML} T_2^{II} \right) \left(\frac{b_1-1}{\alpha_{1ML}} - c_1 \right) + \frac{T_2^I}{d} \left(\frac{m}{\alpha_{1ML}} + \beta_{ML} T_1^{II} \right) \left(\frac{b_2-1}{\alpha_{2ML}} - c_2 \right) - \frac{1}{d} \left(\frac{m}{\alpha_1^2} + \beta_{ML} T_1^{II} \right) \left(\frac{n}{\alpha_2^2} + \beta_{ML} T_2^{II} \right) \left(\frac{b_3-1}{\beta_{ML}} - c_3 \right) \right] + a_5 + \frac{1}{2} [A\sigma_{13} + B\sigma_{23} + D\sigma_{33}] \\ &= \hat{\beta}_{LC} \end{aligned} \quad (3.6)$$

4. BAYESIAN ESTIMATION OF RAYLEIGH DISTRIBUTION

Let us assume that (x_1, x_2, \dots, x_m) and (y_1, y_2, \dots, y_n) are two samples drawn from two Rayleigh populations. They are denoted as $R(\delta_1, \omega)$ and $R(\delta_2, \omega)$ and their probability density functions are given by

$$\begin{aligned} f(x; \delta_1, \omega) &= 2\omega(x_i - \delta_1)e^{-\omega(x_i - \delta_1)^2}; \\ x > \delta_1, \delta_1 &> 0, \omega > 0. \\ f(y; \delta_2, \omega) &= 2\omega(y_j - \delta_2)e^{-\omega(y_j - \delta_2)^2}; \\ y > \delta_2, \delta_2 &> 0, \omega > 0. \end{aligned}$$

The Logarithm of the Likelihood function is given by

$$L = (m+n)\log 2 + (m+n)\log \omega + \sum_{i=1}^m \log(x_i - \delta_1) + \sum_{j=1}^n \log(y_j - \delta_2) - \omega [(x_i - \delta_1)^2 + (y_j - \delta_2)^2]$$

The Prior Distribution for the parameters δ_1, δ_2 and ω follows Gamma distributions with densities as given below

$$\begin{aligned} \rho_1(\delta_1) &= \frac{c_1^{b_1}}{\Gamma(b_1)} \delta_1^{b_1-1} e^{-c_1\delta_1}; \quad b_1, c_1, \delta_1 > 0 \\ \rho_2(\delta_2) &= \frac{c_2^{b_2}}{\Gamma(b_2)} \delta_2^{b_2-1} e^{-c_2\delta_2}; \quad b_2, c_2, \delta_2 > 0 \\ \rho_3(\omega) &= \frac{c_3^{b_3}}{\Gamma(b_3)} \omega^{b_3-1} e^{-c_3\omega}; \quad b_3, c_3, \omega > 0 \end{aligned}$$

The joint prior density function $v(\delta_1, \delta_2, \omega)$ can be obtained as

$$v(\delta_1, \delta_2, \omega) = \rho_1(\alpha_1)\rho_2(\alpha_2)\rho_3(\omega) = \frac{c_1^{b_1}}{\Gamma(b_1)} \frac{c_2^{b_2}}{\Gamma(b_2)} \frac{c_3^{b_3}}{\Gamma(b_3)} \delta_1^{b_1-1} \delta_2^{b_2-1} \omega^{b_3-1} e^{-c_1\delta_1 - c_2\delta_2 - c_3\omega}$$

Hence

$$\begin{aligned} \rho(\theta) &= \log v(\theta) \propto (b_1+1)\log(\delta_1) + (b_2+1)\log(\delta_2) \\ &\quad + (b_3+1)\log(\omega) - c_1\delta_1 - c_2\delta_2 - c_3\omega \end{aligned}$$

$$\rho_1 = \frac{b_1-1}{\delta_1} - c_1, \rho_2 = \frac{b_2-1}{\delta_2} - c_2, \rho_3 = \frac{b_3-1}{\omega} - c_3$$

From the Likelihood function we can derive

$$\sigma_{11} = -\frac{1}{d} \left(\frac{q_1(m+n)}{\omega^2} - 4q_2^2 \right), \sigma_{12} = -\frac{4p_2 q_2}{d} = \sigma_{21},$$

$$\sigma_{13} = -\frac{2p_2 q_1}{d} = \sigma_{31},$$

$$\sigma_{22} = -\frac{1}{d} \left(\frac{p_1(m+n)}{\omega^2} - 4p_2^2 \right), \sigma_{23} = -\frac{2p_1 q_2}{d} = \sigma_{32},$$

$$\sigma_{33} = -\frac{p_1 q_1}{d}.$$

$$\text{Whered } \frac{p_1 q_1(m+n)}{\omega^2} + 4p_1 q_2^2 + 4q_1 p_2^2,$$

$$p_1 = 2m\omega + \sum_{i=1}^m \frac{1}{(x_i - \delta_1)^2}, p_2 = \sum_{i=1}^m (x_i - \delta_1),$$

$$q_1 = 2n\omega + \sum_{j=1}^n \frac{1}{(y_j - \delta_2)^2}, q_2 = \sum_{j=1}^n (y_j - \delta_2).$$

4.1 Bayes Estimators under Symmetric Loss Function

Let $u(\theta) = \delta_1$, then $u_1 = 1, u_2 = u_3 = 0, u_{ij} = 0; i, j = 1, 2, 3$. Substituting these values in (2.4) we get the Bayes estimator for δ_1 as follows

$$\begin{aligned} E(\hat{\delta}_{1ML}|x,y) &= \hat{\delta}_{1ML} - \frac{1}{d} \left(\frac{q_1(m+n)}{\omega^2} - 4q_2^2 \right) \left(\frac{b_1-1}{\delta_{1ML}} - c_1 \right) - \frac{4p_2 q_2}{d} \left(\frac{b_2-1}{\delta_{2ML}} - c_2 \right) - \frac{2p_2 q_1}{d} \left(\frac{b_3-1}{\omega_{ML}} - c_3 \right) + \frac{1}{2} [A\sigma_{11} + B\sigma_{21} + D\sigma_{31}] \\ &= \hat{\delta}_{1LC} \end{aligned} \quad (4.1)$$

Let $u(\theta) = \delta_2$, then $u_2 = 1, u_1 = u_3 = 0, u_{ij} = 0; i, j = 1, 2, 3$. Substituting these values in (2.4) we get the Bayes estimator for δ_2 as follows

$$\begin{aligned} E(\hat{\delta}_{2ML}|x,y) &= \hat{\delta}_{2ML} - \frac{4p_2 q_2}{d} \left(\frac{b_1-1}{\delta_{1ML}} - c_1 \right) - \frac{1}{d} \left(\frac{p_1(m+n)}{\omega_{ML}^2} - 4p_2^2 \right) \left(\frac{b_2-1}{\delta_{2ML}} - c_2 \right) - \frac{2p_1 q_2}{d} \left(\frac{b_3-1}{\omega_{ML}} - c_3 \right) + \frac{1}{2} [A\sigma_{12} + B\sigma_{22} + D\sigma_{32}] \\ &= \hat{\delta}_{2LC} \end{aligned} \quad (4.2)$$

Let $u(\theta) = \omega$, then $u_3 = 1, u_1 = u_2 = 0, u_{ij} = 0; i, j = 1, 2, 3$. Substituting these values in (2.4) we get the Bayes estimator for ω as follows

$$\begin{aligned} E(\hat{\omega}_{ML}|x,y) &= \hat{\omega}_{ML} - \frac{2p_2 q_1}{d} \left(\frac{b_1-1}{\delta_{1ML}} - c_1 \right) - \frac{2p_1 q_2}{d} \left(\frac{b_2-1}{\delta_{2ML}} - c_2 \right) - \frac{p_1 q_1}{d} \left(\frac{b_3-1}{\omega_{ML}} - c_3 \right) + \frac{1}{2} [A\sigma_{13} + B\sigma_{23} + D\sigma_{33}] \\ &= \hat{\omega}_C \end{aligned} \quad (4.3)$$

4.2 Bayes Estimators using Asymmetric Loss Function

Let $v(\theta) = e^{-a\delta_1}$, then $v_1 = -a e^{-a\delta_1}, v_2 = v_3 = 0, v_{11} = a^2 e^{-a\delta_1}$; rest of v_{ij} 's i, j=1, 2, 3, are zero. Substituting these values in (2.5) we get the Bayes estimator for δ_1 as follows

$$\begin{aligned} E(\hat{\delta}_{1ML}|x,y) &= \hat{\delta}_{1ML} - a e^{-a\delta_{1ML}} \left[-\frac{1}{d} \left(\frac{q_1(m+n)}{\omega_{ML}^2} - 4q_2^2 \right) \left(\frac{b_1-1}{\delta_{1ML}} - c_1 \right) - \frac{4p_2 q_2}{d} \left(\frac{b_2-1}{\delta_{2ML}} - c_2 \right) - \frac{2p_2 q_1}{d} \left(\frac{b_3-1}{\omega_{ML}} - c_3 \right) \right] \end{aligned}$$

$$\begin{aligned} & c_2 \Big) - \frac{2p_2 q_1}{d} \left(\frac{b_3-1}{\omega_{ML}} - c_3 \right) \Big] + a_5 + \\ & \frac{1}{2} [A\sigma_{11} + B\sigma_{21} + D\sigma_{31}] \\ & = \hat{\delta}_{1LC} \end{aligned} \quad (4.4)$$

Let $v(\theta) = e^{-a\delta_2}$, then $v_2 = -a e^{-a\delta_2}, v_1 = v_3 = 0, v_{11} = a^2 e^{-a\delta_2}$; rest of v_{ij} 's i, j=1, 2, 3, are zero. Substituting these values in (2.5) we get the Bayes estimator for δ_2 as follows

$$\begin{aligned} E(\hat{\delta}_{2ML}|x,y) &= \hat{\delta}_{2ML} - a e^{-a\delta_{2ML}} \left[-\frac{4p_2 q_2}{d} \left(\frac{b_1-1}{\delta_{1ML}} - c_1 \right) - \right. \\ & \left. \frac{1}{d} \left(\frac{p_1(m+n)}{\omega_{ML}^2} - 4p_2^2 \right) \left(\frac{b_2-1}{\delta_{2ML}} - c_2 \right) - \right. \\ & \left. \frac{2p_1 q_2}{d} \left(\frac{b_3-1}{\omega_{ML}} - c_3 \right) \right] + a_5 + \frac{1}{2} [A\sigma_{12} + B\sigma_{22} + \\ & D\sigma_{32}] \\ & = \hat{\delta}_{2LC} \end{aligned} \quad (4.5)$$

Let $v(\theta) = e^{-a\omega}$, then $v_3 = -a e^{-a\omega}, v_1 = v_2 = 0, v_{11} = a^2 e^{-a\omega}$; rest of v_{ij} 's i, j=1, 2, 3 are zero. Substituting these values in (2.5) we get the Bayes estimator for ω as follows

$$\begin{aligned} E(\hat{\omega}_{ML}|x,y) &= \hat{\omega}_{ML} - a e^{-a\omega_{ML}} \left[-\frac{2p_2 q_1}{d} \left(\frac{b_1-1}{\delta_{1ML}} - \right. \right. \\ & \left. \left. c_1 \right) - \frac{2p_1 q_2}{d} \left(\frac{b_2-1}{\delta_{2ML}} - c_2 \right) - \frac{p_1 q_1}{d} \left(\frac{b_3-1}{\omega_{ML}} - \right. \right. \\ & \left. \left. c_3 \right) \right] + a_5 + \frac{1}{2} [A\sigma_{13} + B\sigma_{23} + D\sigma_{33}] \\ & = \hat{\omega}_{LC} \end{aligned} \quad (4.3)$$

5. BAYESIAN ESTIMATION OF GAMMA DISTRIBUTION

Let (x_1, x_2, \dots, x_m) and (y_1, y_2, \dots, y_n) be two samples taken from two gamma populations. They are denoted as $G(\mu_1, \lambda)$ and $G(\mu_2, \lambda)$ and their density functions are given by,

$$\begin{aligned} f(x; \mu_1, \lambda) &= \frac{1}{\Gamma(\mu_1) \lambda^{\mu_1}} x^{\mu_1-1} e^{-\frac{x}{\lambda}}; \\ & x > 0, \mu_1, \lambda > 0. \\ f(y; \mu_2, \lambda) &= \frac{1}{\Gamma(\mu_2) \lambda^{\mu_2}} y^{\mu_2-1} e^{-\frac{y}{\lambda}}; \\ & y > 0, \mu_2, \lambda > 0. \end{aligned}$$

The Log-likelihood function is given by

$$\begin{aligned} L &= (\mu_1 - 1) \sum_{i=1}^m \log x_i + (\mu_2 - 1) \sum_{j=1}^n \log y_j \\ & - m \log(\Gamma(\mu_1)) - n \log(\Gamma(\mu_2)) + n \log(-(m\mu_1 + \\ & n\mu_2) \log \lambda - \frac{1}{\lambda} [\sum x_i + \sum y_j]) \end{aligned}$$

The Prior Distribution for the parameters μ_1, μ_2 and λ follows Inverted Gamma distributions with densities as given below

$$\begin{aligned} \rho_1(\mu_1) &\propto \frac{e^{-\frac{c_1}{\mu_1}}}{\mu_1^{b_1+1}}; \quad c_1, b_1 > 0, \\ \rho_2(\mu_2) &\propto \frac{e^{-\frac{c_2}{\mu_2}}}{\mu_2^{b_2+1}}; \quad c_2, b_2 > 0, \\ \rho_3(\lambda) &\propto \frac{e^{-\frac{c_3}{\lambda}}}{\lambda^{b_3+1}}; \quad c_3, b_3 > 0, \end{aligned}$$

Assuming independence of μ_1, μ_2 and λ , the joint prior density function $v(\mu_1, \mu_2, \lambda)$ can be written as

$$v(\mu_1, \mu_2, \lambda) \propto \frac{e^{-(\frac{c_1}{\mu_1} + \frac{c_2}{\mu_2} + \frac{c_3}{\lambda})}}{\mu_1^{b_1+1} \mu_2^{b_2+1} \lambda^{b_3+1}}; \quad b_i, c_i > 0, i = 1, 2, 3$$

Hence

$$\begin{aligned} \rho(\theta) &= \log v(\theta) \\ &= -\frac{c_1}{\mu_1} - \frac{c_2}{\mu_2} - \frac{c_3}{\lambda} - (b_1 + 1) \log \mu_1 \\ & \quad - (b_2 + 1) \log \mu_2 - (b_3 + 1) \log \lambda \\ \rho_1 &= \frac{c_1}{\mu_1^2} - \frac{b_1+1}{\mu_1}; \quad \rho_1 = \frac{c_2}{\mu_2^2} - \frac{b_2+1}{\mu_2}; \quad \rho_1 = \frac{c_3}{\lambda^2} - \frac{b_3+1}{\lambda}. \end{aligned}$$

From the Likelihood function we can derive

$$\begin{aligned} \sigma_{11} &= \frac{1}{md} [(m\mu_1 + n\mu_2)\psi^1(\mu_2) - n], \quad \sigma_{12} = \frac{1}{d} = \sigma_{21}, \\ \sigma_{13} &= \frac{\psi^I(\mu_2)\lambda}{d} = \sigma_{31} \\ \sigma_{22} &= \frac{1}{nd} [(m\mu_1 + n\mu_2)\psi^1(\mu_1) - m], \quad \sigma_{23} = \frac{\psi^I(\mu_1)\lambda}{d} = \\ \sigma_{32}, \sigma_{33} &= \frac{\lambda \psi^I(\mu_1) \psi^I(\mu_2)}{d} \end{aligned}$$

Where $d = \psi^I(\mu_1)\psi^I(\mu_2)(m\mu_1 + n\mu_2) - n\psi^I(\mu_1) - m\psi^I(\mu_2)$

5.1 Bayes Estimators under Symmetric Loss Function

Let $u(\theta) = \mu_1$, then $u_1 = 1, u_2 = u_3 = 0, u_{ij} = 0; i, j = 1, 2, 3$. Substituting these values in (2.4) we get the Bayes estimator for μ_1 as follows

$$\begin{aligned} E(\hat{\mu}_{1ML}|x,y) &= \hat{\mu}_{1ML} + \\ & \frac{1}{md} [(m\mu_{1ML} + n\mu_{2ML})\psi^1(\mu_{2ML}) - \\ & n] \left(\frac{c_1}{\mu_{1ML}^2} - \frac{b_1+1}{\mu_{1ML}} \right) + \frac{1}{d} \left(\frac{c_2}{\mu_{2ML}^2} - \frac{b_2+1}{\mu_{2ML}} \right) + \\ & \frac{\psi^I(\mu_2)\lambda_{ML}}{d} \left(\frac{c_3}{\lambda_{ML}^2} - \frac{b_3+1}{\lambda_{ML}} \right) + \frac{1}{2} [A\sigma_{11} + \\ & B\sigma_{21} + D\sigma_{31}] \\ & = \hat{\mu}_{1C} \end{aligned} \quad (5.1)$$

Let $u(\theta) = \mu_2$, then $u_2 = 1, u_1 = u_3 = 0, u_{ij} = 0; i, j = 1, 2, 3$. Substituting these values in (2.4) we get the Bayes estimator for μ_2 as follows

$$\begin{aligned} E(\hat{\mu}_{2ML}|x,y) &= \hat{\mu}_{2ML} + \frac{1}{d} \left(\frac{c_1}{\mu_{1ML}^2} - \frac{b_1+1}{\mu_{1ML}} \right) + \\ & \frac{1}{nd} [(m\mu_{1ML} + n\mu_{2ML})\psi^1(\mu_{1ML}) - \\ & m] \left(\frac{c_2}{\mu_{2ML}^2} - \frac{b_2+1}{\mu_{2ML}} \right) + \\ & \frac{\psi^I(\mu_{1ML})\lambda_{ML}}{d} \left(\frac{c_3}{\lambda_{ML}^2} - \frac{b_3+1}{\lambda_{ML}} \right) + \\ & \frac{1}{2} [A\sigma_{12} + B\sigma_{22} + D\sigma_{32}] \\ & = \hat{\mu}_{2C} \end{aligned} \quad (5.2)$$

Let $u(\theta) = \lambda$, then $u_3 = 1, u_1 = u_2 = 0, u_{ij} = 0; i, j = 1, 2, 3$. Substituting these values in (2.4) we get the Bayes estimator for λ as follows

$$\begin{aligned} E(\hat{\lambda}_{ML}|x,y) &= \hat{\lambda}_{ML} + \frac{\psi^I(\mu_2)\lambda}{d} \left(\frac{c_1}{\mu_{1ML}^2} - \frac{b_1+1}{\mu_{1ML}} \right) + \\ & \frac{\psi^I(\mu_{1ML})\lambda}{d} \left(\frac{c_2}{\mu_{2ML}^2} - \frac{b_2+1}{\mu_{2ML}} \right) + \end{aligned}$$

$$\begin{aligned} & \frac{\lambda_{ML} \psi^I(\mu_{1ML}) \psi^I(\mu_{2ML})}{d} \left(\frac{c_3}{\lambda_{ML}^2} - \frac{b_3+1}{\lambda_{ML}} \right) + \\ & \frac{1}{2} [A\sigma_{13} + B\sigma_{23} + D\sigma_{33}] \\ & = \hat{\lambda}_C \end{aligned} \quad (5.3)$$

5.2 Bayes Estimators using Asymmetric Loss Function

Let $v(\theta) = e^{-a\mu_1}$, then $v_1 = -a e^{-a\mu_1}, v_2 = v_3 = 0, v_{11} = a^2 e^{-a\mu_1}$; rest of v_{ij} 's i, j=1, 2, 3 are zero. Substituting these values in (2.5) we get the Bayes estimator for μ_1 as follows

$$\begin{aligned} E(\hat{\mu}_{1ML}|x,y) &= \hat{\mu}_{1ML} - a e^{-a\mu_{1ML}} \left[\frac{1}{md} [(m\mu_{1ML} + n\mu_{2ML})\psi^1(\mu_{2ML}) - n] \left(\frac{c_1}{\mu_{1ML}^2} - \frac{b_1+1}{\mu_{1ML}} \right) + \right. \\ & \left. \frac{1}{d} \left(\frac{c_2}{\mu_{2ML}^2} - \frac{b_2+1}{\mu_{2ML}} \right) + \frac{\psi^I(\mu_2)\lambda_{ML}}{d} \left(\frac{c_3}{\lambda_{ML}^2} - \frac{b_3+1}{\lambda_{ML}} \right) \right] + a_5 + \frac{1}{2} [A\sigma_{11} + B\sigma_{21} + D\sigma_{31}] \\ &= \hat{\mu}_{1LC} \end{aligned} \quad (5.4)$$

Let $v(\theta) = e^{-a\mu_2}$, then $v_2 = -a e^{-a\mu_2}, v_1 = v_3 = 0, v_{11} = a^2 e^{-a\mu_2}$; rest of v_{ij} 's i, j=1, 2, 3 are zero. Substituting these values in (2.5) we get the Bayes estimator for μ_2 as follows

$$\begin{aligned} E(\hat{\mu}_{2ML}|x,y) &= \hat{\mu}_{2ML} - a e^{-a\mu_{2ML}} \left[\frac{1}{d} \left(\frac{c_1}{\mu_{1ML}^2} - \frac{b_1+1}{\mu_{1ML}} \right) + \right. \\ & \left. \frac{1}{nd} [(m\mu_{1ML} + n\mu_{2ML})\psi^1(\mu_{1ML}) - m] \left(\frac{c_2}{\mu_{2ML}^2} - \frac{b_2+1}{\mu_{2ML}} \right) + \frac{\psi^I(\mu_1)\lambda_{ML}}{d} \left(\frac{c_3}{\lambda_{ML}^2} - \frac{b_3+1}{\lambda_{ML}} \right) \right] + a_5 + \frac{1}{2} [A\sigma_{12} + B\sigma_{22} + D\sigma_{32}] \\ &= \hat{\mu}_{2LC} \end{aligned} \quad (5.5)$$

Let $v(\theta) = e^{-a\lambda}$, then $v_2 = -a e^{-a\lambda}, v_1 = v_3 = 0, v_{11} = a^2 e^{-a\lambda}$; rest of v_{ij} 's i, j=1, 2, 3 are zero. Substituting these values in (2.5) we get the Bayes estimator for λ as follows

$$\begin{aligned} E(\hat{\lambda}_{ML}|x,y) &= \hat{\lambda}_{ML} - a e^{-a\lambda_{ML}} \left[\frac{\psi^I(\mu_{2ML})\lambda_{ML}}{d} \left(\frac{c_1}{\mu_{1ML}^2} - \frac{b_1+1}{\mu_{1ML}} \right) + \frac{\psi^I(\mu_{1ML})\lambda_{ML}}{d} \left(\frac{c_2}{\mu_{2ML}^2} - \frac{b_2+1}{\mu_{2ML}} \right) + \right. \\ & \left. \frac{\lambda_{ML} \psi^I(\mu_1) \psi^I(\mu_2)}{d} \left(\frac{c_3}{\lambda_{ML}^2} - \frac{b_3+1}{\lambda_{ML}} \right) \right] + a_5 + \frac{1}{2} [A\sigma_{13} + B\sigma_{23} + D\sigma_{33}] \\ &= \hat{\lambda}_{LC} \end{aligned} \quad (5.6)$$

6. BAYESIAN ESTIMATION OF LOMAX DISTRIBUTION

Let us assume that (x_1, x_2, \dots, x_m) and (y_1, y_2, \dots, y_n) respectively represent the random samples drawn from the two Lomax populations. They are denoted as $L(\eta_1, \gamma)$ and $L(\eta_2, \gamma)$ and their probability density function are given below

$$\begin{aligned} f(x, \eta_1, \gamma) &= \frac{\eta_1}{\gamma} \left(1 + \frac{x}{\gamma} \right)^{-(\eta_1+1)} ; \\ & \quad x > 0, \quad \eta_1, \gamma > 0. \\ f(y, \eta_2, \gamma) &= \frac{\eta_2}{\gamma} \left(1 + \frac{y}{\gamma} \right)^{-(\eta_2+1)} ; \\ & \quad y > 0, \quad \eta_2, \gamma > 0. \end{aligned}$$

The Prior Distribution for the parameters η_1, η_2 and γ follows Gamma distributions with densities as given below

$$\begin{aligned} \rho_1(\eta_1) &= \frac{c_1^{b_1}}{\Gamma(b_1)} \eta_1^{b_1-1} e^{-c_1\eta_1}; \quad b_1, c_1, \eta_1 > 0 \\ \rho_2(\eta_2) &= \frac{c_2^{b_2}}{\Gamma(b_2)} \eta_2^{b_2-1} e^{-c_2\eta_2}; \quad b_2, c_2, \eta_2 > 0 \\ \rho_3(\gamma) &= \frac{c_3^{b_3}}{\Gamma(b_3)} \gamma^{b_3-1} e^{-c_3\gamma}; \quad b_3, c_3, \gamma > 0 \end{aligned}$$

The joint prior density function $v(\eta_1, \eta_2, \gamma)$ can be obtained as

$$\begin{aligned} v(\eta_1, \eta_2, \gamma) &= \rho_1(\eta_1)\rho_2(\eta_2)\rho_3(\gamma) \\ &= \frac{c_1^{b_1}}{\Gamma(b_1)} \frac{c_2^{b_2}}{\Gamma(b_2)} \frac{c_3^{b_3}}{\Gamma(b_3)} \eta_1^{b_1-1} \eta_2^{b_2-1} \gamma^{b_3-1} e^{-c_1\eta_1 - c_2\eta_2 - c_3\gamma} \\ \text{Hence} \quad \rho(\theta) &= \log v(\theta) \propto (b_1-1) \log(\eta_1) + (b_2-1) \log(\eta_2) + \\ & (b_3-1) \log(\gamma) - c_1 \eta_1 - c_2 \eta_2 - c_3 \gamma \\ \rho_1 &= \frac{b_1-1}{\eta_1} - c_1, \quad \rho_2 = \frac{b_2-1}{\eta_2} - c_2, \\ \rho_3 &= \frac{b_3-1}{\gamma} - c_3 \end{aligned}$$

From the Likelihood function we can derive

$$\sigma_{11} = \frac{1}{d} \left[\frac{na}{\eta_2^2} + (T_2^I)^2 \right], \quad \sigma_{12} = -\frac{T_1^I T_2^I}{d} = \sigma_{21},$$

$$\sigma_{13} = \frac{n T_1^I}{d \eta_2^2} = \sigma_{31}, \quad \sigma_{22} = \frac{1}{d} \left[\frac{ma}{\eta_1^2} + (T_1^I)^2 \right],$$

$$\sigma_{23} = \frac{m T_2^I}{d \eta_1^2} = \sigma_{32}, \quad \sigma_{33} = -\frac{mn}{d \eta_1^2 \eta_2^2}$$

Where

$$d = \frac{mn}{d \eta_1^2 \eta_2^2} + \frac{m T_2^I}{d \eta_1^2} + \frac{n T_1^I}{d \eta_2^2}, \quad a = \frac{m+n}{\gamma^2} - (\eta_1 + 1) T_1^{II} - (\eta_2 + 1) T_2^{II},$$

$$T_1 = \sum_{i=1}^m \log \left(1 + \frac{x_i}{\gamma} \right), \quad T_2 = \sum_{i=1}^n \log \left(1 + \frac{y_i}{\gamma} \right)$$

Here T_1^I, T_1^{II} and T_1^{III} are the 1st, 2nd and 3rd order derivatives of T_1 with respect to η_1

Similarly T_2^I, T_2^{II} and T_2^{III} are the 1st, 2nd and 3rd order derivatives of T_2 with respect to η_2

6.1 Bayes Estimators using Symmetric Loss Function

Let $u(\theta) = \eta_1$, then $u_1 = 1, u_2 = u_3 = 0, u_{ij} = 0; i, j = 1, 2, 3$. Substituting these values in (2.4) we get the Bayes estimator for η_1 as follows

$$\begin{aligned} E(\hat{\eta}_{1ML}|x,y) &= \hat{\eta}_{1ML} + \frac{1}{d} \left[\frac{na}{\eta_2^2} + (T_2^I)^2 \right] \left(\frac{b_1-1}{\eta_1 \eta_2} - c_1 \right) - \frac{T_1^I T_2^I}{d} \left(\frac{b_2-1}{\eta_2 \eta_1} - c_2 \right) + \frac{n T_1^I}{d \eta_2^2} \left(\frac{b_3-1}{\eta_1 \eta_2 \gamma} - c_3 \right) + \frac{1}{2} [A\sigma_{11} + B\sigma_{21} + D\sigma_{31}] \\ &= \hat{\eta}_{1C} \end{aligned} \quad (6.1)$$

Let $u(\theta) = \eta_2$, then $u_2 = 1, u_1 = u_3 = 0, u_{ij} = 0; i, j = 1, 2, 3$. Substituting these values in (2.4) we get the Bayes estimator for η_2 as follows

$$\begin{aligned} E(\hat{\eta}_{2ML}|x,y) &= \hat{\eta}_{2ML} - \frac{T_1^I T_2^I}{d} \left[\frac{na}{\eta_2^2} + (T_2^I)^2 \right] \left(\frac{b_1-1}{\eta_1 \eta_2} - c_1 \right) + \frac{1}{d} \left[\frac{ma}{\eta_1^2} + (T_1^I)^2 \right] \left(\frac{b_2-1}{\eta_2 \eta_1} - c_2 \right) + \end{aligned}$$

$$\begin{aligned} & \frac{mT_2^I}{d\eta_2^2} \left(\frac{b_3-1}{\gamma_{ML}} - c_3 \right) + \frac{1}{2} [A\sigma_{12} + B\sigma_{22} + \\ & D\sigma_{32}] \\ & = \hat{\eta}_{2C} \end{aligned} \quad (6.2)$$

Let $u(\theta) = \gamma$, then $u_3 = 1, u_1 = u_2 = 0, u_{ij} = 0; i, j = 1, 2, 3$. Substituting these values in (2.4) we get the Bayes estimator for γ as follows

$$\begin{aligned} E(\hat{\gamma}_{ML}|x, y) &= \hat{\gamma}_{ML} + \frac{nT_1^I}{d\eta_2^2} \left[\frac{na}{\eta_{2ML}^2} + (T_2^I)^2 \right] \left(\frac{b_1-1}{\eta_{1ML}} - \right. \\ & \left. c_1 \right) + \frac{mT_2^I}{d\eta_{1ML}^2} \left(\frac{b_2-1}{\eta_{2ML}} - c_2 \right) - \\ & \frac{mn}{d\eta_1^2 \eta_2^2} \left(\frac{b_3-1}{\gamma_{ML}} - c_3 \right) + \frac{1}{2} [A\sigma_{13} + B\sigma_{23} + \\ & D\sigma_{33}] \\ & = \hat{\gamma}_C \end{aligned} \quad (6.3)$$

6.2 Bayes Estimators using Asymmetric Loss Function

Let $v(\theta) = e^{-a\eta_1}$, then $v_1 = -a e^{-a\eta_1}, v_2 = v_3 = 0, v_{11} = a^2 e^{-a\eta_1}$; rest of v_{ij} 's $i, j = 1, 2, 3$ are zero. Substituting these values in (2.5) we get the Bayes estimator for α_1 as follows

$$\begin{aligned} E(\hat{\eta}_{1ML}|x, y) &= \hat{\eta}_{1ML} - a e^{-a\eta_{1ML}} \left[\frac{1}{d} \left[\frac{na}{\eta_{2ML}^2} + \right. \right. \\ & (T_2^I)^2 \left(\frac{b_1-1}{\eta_{1ML}} - c_1 \right) - \frac{T_1^I T_2^I}{d} \left(\frac{b_2-1}{\eta_{2ML}} - \right. \\ & \left. c_2 \right) + \frac{nT_1^I}{d\eta_{2ML}^2} \left(\frac{b_3-1}{\gamma_{ML}} - c_3 \right) \left. \right] + a_5 \\ & = \hat{\eta}_{1LC} \end{aligned} \quad (6.4)$$

Let $v(\theta) = e^{-a\eta_2}$, then $v_2 = -a e^{-a\eta_2}, v_1 = v_3 = 0, v_{22} = a^2 e^{-a\eta_2}$ rest of v_{ij} 's $i, j = 1, 2, 3$ are zero. Substituting these values in (2.5) we get the Bayes estimator for η_2 as follows

$$\begin{aligned} E(\hat{\eta}_{2ML}|x, y) &= \hat{\eta}_{2ML} - ae^{-a\eta_{2ML}} \left[-\frac{T_1^I T_2^I}{d} \left[\frac{na}{\eta_{2ML}^2} + \right. \right. \\ & (T_2^I)^2 \left(\frac{b_1-1}{\eta_{1ML}} - c_1 \right) + \frac{1}{d} \left[\frac{ma}{\eta_{1ML}^2} + \right. \\ & (T_1^I)^2 \left(\frac{b_2-1}{\delta_{2ML}} - c_2 \right) + \frac{mT_2^I}{d\eta_1^2} \left(\frac{b_3-1}{\gamma_{ML}} - \right. \\ & \left. c_3 \right) \left. \right] + a_5 + \frac{1}{2} [A\sigma_{12} + B\sigma_{22} + D\sigma_{32}] \\ & = \hat{\eta}_{2LC} \end{aligned} \quad (6.5)$$

Let $v(\theta) = e^{-a\gamma}$, then $v_3 = -a e^{-a\gamma}, v_1 = v_2 = 0, v_{33} = a^2 e^{-a\gamma}$ rest of v_{ij} 's $i, j = 1, 2, 3$ are zero, $a_4 = 0, a_5 = \frac{1}{2} v_{33}\sigma_{33} = a^2 e^{-a\gamma}\sigma_{33}$. Substituting these values in (2.5) we get the Bayes estimator for γ as follows

$$\begin{aligned} E(\hat{\gamma}_{ML}|x, y) &= \hat{\gamma}_{ML} - a e^{-a\gamma_{ML}} \left[\frac{nT_1^I}{d\eta_{2ML}^2} \left[\frac{na}{\eta_{2ML}^2} + \right. \right. \\ & (T_2^I)^2 \left(\frac{b_1-1}{\eta_{1ML}} - c_1 \right) + \frac{mT_2^I}{d\eta_{1ML}^2} \left(\frac{b_2-1}{\eta_{2ML}} - \right. \\ & \left. c_2 \right) - \frac{mn}{d\eta_{1ML}^2 \eta_{2ML}^2} \left(\frac{b_3-1}{\gamma_{ML}} - c_3 \right) \left. \right] + a_5 + \\ & \frac{1}{2} [A\sigma_{13} + B\sigma_{23} + D\sigma_{33}] \\ & = \hat{\gamma}_{LC} \end{aligned} \quad (6.6)$$

7. NUMERICAL COMPARISONS

In this study, our focus is on estimating the common scale parameter and two distinct shape/location

parameters for two different populations across various distributions, including Weibull, Gamma, Rayleigh, and Lomax. Sections 3, 4, 5, and 6 detail the estimation of Bayes estimators for conjugate priors using squared error (symmetric) and Linex (asymmetric) loss functions for each distribution. Notably, the evaluation of the Bayes expression in [2.1] is intricate, prompting the use of Lindley's technique for parameter estimation. To assess the performance of the estimators, we conducted a simulation exercise using R software. The simulation aimed to evaluate and compare the performance of the estimates across various sample sizes and loss functions. Monte Carlo simulation analysis was employed, generating 10,000 random samples for numerical comparison. Different sample size combinations, such as (10, 10), (30, 20), (40, 50), and (60, 60), were chosen for the comparative study. For scale parameters, values of 2.5, 3, and 3.5 were considered, along with shape/location parameters set to 1 and 2.

Prior information was incorporated into the Bayesian estimation process, with assumed hyperparameter values of $b_1 = 1, b_2 = 1, b_3 = 1$, and $c_1 = 0.5, c_2 = 0.5, c_3 = 0.5$. For the Linex loss function shape, c was set to 0.5. ML estimates were employed in the estimation of Bayes estimators, generated using the optim function and Nelder-Mead method in the R software. By substituting these ML estimates, Bayes estimates were derived for the common scale and different shape/location parameters. This comprehensive approach provides a robust framework for assessing the efficiency of the estimators under various conditions and configurations.

The computational results of Bayes estimates, along with their Bias and Mean Squared Error (MSE) under both loss functions for different sample sizes, are presented in Tables 7.1 to 7.8. In these tables, the first column indicates the choices of parameters for both the shape/location and scale parameters. The subsequent columns (2, 3, and 4) display Bayes estimators under squared error loss, Bias, and MSE. Similarly, columns 5, 6, and 7 represent Bayes estimators under Linex loss, Bias, and MSE for a particular distribution. The pattern continues for columns 8 to 13, showcasing Bayes estimators, Bias, and MSE under both loss functions for another distribution.

Based on the findings from the simulation study, the following observations can be made:

- Increasing the sample size results in a decrease in both Bias and Mean Squared Error (MSE). This aligns with the expectation that larger sample sizes lead to more precise estimations.
- Across all distributions, estimators obtained using both loss functions demonstrate consistency.
- Different values of scale parameters affect both the shape/location parameters. This

interdependence is observed consistently across all distributions.

- For the Weibull distribution, it is evident from the tables that Bias and MSE are higher for estimators derived through the symmetric loss function, especially for small sample sizes. However, as the sample size increases, the symmetric loss function yields estimators with minimum Bias and MSE compared to the asymmetric loss function. Both loss functions demonstrate consistent estimators.
- For Rayleigh, Gamma, and Lomax distributions, even with increased sample sizes,

Bias and MSE remain higher for estimators derived through the symmetric loss function compared to the asymmetric loss function.

- Comparing the four distributions in terms of Bias and MSE, the Weibull distribution exhibits minimum Bias and MSE, while the Lomax distribution shows maximum Bias and MSE.

These observations provide insights into the behavior of estimators under different conditions, emphasizing the impact of sample size and the choice of loss function on estimation performance across various distributions.

Table 7.1: Comparison of Bias and mean square error of Bayes estimators using both symmetric (SE) and asymmetric (Linex) Loss functions of Several Estimators for Weibull and Rayleigh, when $(m, n) = (10, 10)$

$\theta \downarrow$	Weibull Distribution ($\theta = \alpha_1, \alpha_2, \beta$)						Rayleigh Distribution ($\theta = \delta_1, \delta_2, \omega$)					
	symmetric(SE)			asymmetric(Linex)			symmetric(SE)			asymmetric(Linex)		
	Bayes	Bias	MSE	Bayes	Bias	MSE	Bayes	Bias	MSE	Bayes	Bias	MSE
1	1.200	0.200	1.250	1.139	0.139	0.173	1.024	0.024	0.005	1.025	0.025	0.005
2	2.355	0.355	3.027	2.259	0.259	0.701	2.236	0.236	0.165	2.274	0.274	0.134
2.5	2.614	0.114	0.836	2.654	0.154	0.401	2.854	0.354	0.552	2.855	0.355	0.552
1	1.212	0.212	6.038	1.106	0.106	0.189	1.001	0.001	0.755	1.020	0.020	0.088
2	3.015	1.015	2.584	2.232	0.232	0.546	1.567	-0.433	1.230	2.383	0.383	0.829
3	3.023	0.023	1.837	3.118	0.118	0.784	3.385	0.385	1.166	3.489	0.489	1.136
1	1.499	0.499	4.704	1.129	0.129	0.148	1.025	0.025	0.005	1.025	0.025	0.004
2	2.579	0.579	2.559	2.285	0.285	0.817	2.392	0.392	6.224	2.536	0.536	0.566
3.5	3.634	0.134	3.409	3.666	0.166	0.747	4.046	0.546	1.269	4.060	0.560	1.220

Table 7.2: Comparison of Bias and mean square error of Bayes estimators using both symmetric (SE) and asymmetric (Linex) Loss functions of Several Estimators for Gamma and Lomax, when $(m, n) = (10, 10)$

$\theta \downarrow$	Gamma Distribution($\theta = \mu_1, \mu_2, \lambda$)						Lomax Distribution($\theta = \eta_1, \eta_2, \gamma$)					
	symmetric(SE)			asymmetric(Linex)			symmetric(SE)			asymmetric(Linex)		
	Bayes	Bias	MSE	Bayes	Bias	MSE	Bayes	Bias	MSE	Bayes	Bias	MSE
1	1.350	0.350	0.400	1.090	0.090	0.140	1.667	0.667	2.947	1.621	0.621	2.888
2	1.950	-0.050	0.270	1.910	-0.090	0.220	1.956	-0.044	2.417	1.899	-0.101	2.385
2.5	2.270	-0.230	0.760	2.510	0.010	0.640	2.055	-0.445	3.699	1.989	-0.511	3.556
1	1.340	0.340	0.380	1.090	0.090	0.150	1.884	0.884	4.022	1.825	0.825	3.933
2	1.940	-0.060	0.230	1.930	-0.070	0.180	2.417	0.417	3.020	2.402	0.402	2.972
3	2.740	-0.260	1.110	3.010	0.010	0.940	2.248	-0.752	4.367	2.172	-0.828	4.033
1	1.350	0.350	0.400	1.100	0.100	0.160	2.007	1.007	4.922	1.987	0.987	4.805
2	1.950	-0.050	0.250	1.960	-0.040	0.180	2.518	0.518	3.557	2.502	0.502	3.495
3.5	3.200	-0.300	1.530	3.490	-0.010	1.300	3.662	0.162	8.954	3.502	0.002	6.675

Table 7.3: Comparison of Bias and mean square error of Bayes estimators using both symmetric (SE) and asymmetric (Linex) Loss functions of Several Estimators for Weibull and Rayleigh, when $(m, n) = (30, 20)$

$\theta \downarrow$	Weibull Distribution ($\theta = \alpha_1, \alpha_2, \beta$)						Rayleigh Distribution ($\theta = \delta_1, \delta_2, \omega$)					
	symmetric(SE)			asymmetric(Linex)			symmetric(SE)			asymmetric(Linex)		
	Bayes	Bias	MSE	Bayes	Bias	MSE	Bayes	Bias	MSE	Bayes	Bias	MSE
1	1.200	0.200	1.250	1.139	0.139	0.173	1.024	0.024	0.005	1.025	0.025	0.005
2	2.355	0.355	3.027	2.259	0.259	0.701	2.236	0.236	0.165	2.274	0.274	0.134
2.5	2.614	0.114	0.836	2.654	0.154	0.401	2.854	0.354	0.552	2.855	0.355	0.552
1	1.212	0.212	6.038	1.106	0.106	0.189	1.001	0.001	0.755	1.020	0.020	0.088
2	3.015	1.015	2.584	2.232	0.232	0.546	1.567	-0.433	1.230	2.383	0.383	0.829
3	3.023	0.023	1.837	3.118	0.118	0.784	3.385	0.385	1.166	3.489	0.489	1.136
1	1.499	0.499	4.704	1.129	0.129	0.148	1.025	0.025	0.005	1.025	0.025	0.004
2	2.579	0.579	2.559	2.285	0.285	0.817	2.392	0.392	6.224	2.536	0.536	0.566
3.5	3.634	0.134	3.409	3.666	0.166	0.747	4.046	0.546	1.269	4.060	0.560	1.220

1	1.028	0.028	0.029	1.027	0.027	0.030	1.019	0.019	0.006	1.021	0.021	0.004
2	2.072	0.072	0.163	2.069	0.069	0.179	2.158	0.158	2.056	2.363	0.363	0.187
2.5	2.576	0.076	0.069	2.583	0.083	0.071	2.787	0.287	0.452	2.794	0.294	0.395
1	1.031	0.031	0.025	1.030	0.030	0.025	1.018	0.018	0.003	1.020	0.020	0.003
2	2.104	0.104	0.197	2.105	0.105	0.256	2.281	0.281	0.093	2.572	0.572	0.455
3	3.067	0.067	0.107	3.076	0.076	0.115	3.366	0.366	0.582	3.368	0.368	0.583
1	1.029	0.029	0.025	1.028	0.028	0.025	1.015	0.015	0.002	1.017	0.017	0.002
2	2.089	0.089	0.164	2.085	0.085	0.163	2.347	0.347	0.619	2.858	0.858	1.055
3.5	3.573	0.073	0.138	3.583	0.083	0.141	3.871	0.371	0.765	3.874	0.374	0.762

Table 7.4: Comparison of Bias and mean square error of Bayes estimators using both symmetric (SE)and asymmetric (Linex) Loss functions of Several Estimators for Gamma and Lomax, when $(m, n) = (30, 20)$

$\theta \downarrow$	Gamma Distribution($\theta = \mu_1, \mu_2, \lambda$)						Lomax Distribution($\theta = \eta_1, \eta_2, \gamma$)					
	symmetric(SE)			asymmetric(Linex)			symmetric(SE)			asymmetric(Linex)		
	Bayes	Bias	MSE	Bayes	Bias	MSE	Bayes	Bias	MSE	Bayes	Bias	MSE
1	1.115	0.115	0.067	1.039	0.039	0.044	1.614	0.614	2.397	1.597	0.597	2.622
2	2.035	0.035	0.178	2.055	0.055	0.183	1.935	-0.065	2.178	1.906	-0.094	2.147
2.5	2.410	-0.090	0.305	2.511	0.011	0.285	2.182	-0.318	3.550	2.154	-0.346	3.409
1	1.115	0.115	0.067	1.042	0.042	0.045	1.895	0.895	3.745	1.878	0.878	3.638
2	2.036	0.036	0.181	2.062	0.062	0.189	2.182	0.182	2.911	2.166	0.166	2.862
3	2.890	-0.110	0.451	3.002	0.002	0.421	2.752	-0.248	3.789	2.715	-0.285	3.626
1	1.119	0.119	0.068	1.047	0.047	0.046	2.164	1.164	4.582	2.094	1.094	4.291
2	2.043	0.043	0.187	2.073	0.073	0.198	2.430	0.430	3.505	2.412	0.412	3.434
3.5	3.355	-0.145	0.601	3.478	-0.022	0.557	2.589	-0.911	7.655	2.435	-1.065	6.229

Table 7.5: Comparison of Bias and mean square error of Bayes estimators using both symmetric (SE)and asymmetric (Linex) Loss functions of Several Estimators for Weibull and Rayleigh, when $(m, n) = (40, 50)$

$\theta \downarrow$	Weibull Distribution ($\theta = \alpha_1, \alpha_2, \beta$)						Rayleigh Distribution ($\theta = \delta_1, \delta_2, \omega$)					
	symmetric(SE)			asymmetric(Linex)			symmetric(SE)			asymmetric(Linex)		
	Bayes	Bias	MSE	Bayes	Bias	MSE	Bayes	Bias	MSE	Bayes	Bias	MSE
1	1.023	0.023	0.018	1.022	0.022	0.018	1.015	0.015	0.002	1.016	0.016	0.002
2	2.039	0.039	0.057	2.034	0.034	0.059	2.098	0.098	0.012	2.157	0.157	0.028
2.5	2.543	0.043	0.032	2.554	0.054	0.034	2.683	0.183	0.176	2.684	0.184	0.176
1	1.019	0.019	0.017	1.018	0.018	0.017	1.012	0.012	0.002	1.013	0.013	0.002
2	2.034	0.034	0.056	2.029	0.029	0.056	2.133	0.133	0.021	2.224	0.224	0.055
3	3.036	0.036	0.041	3.050	0.050	0.043	3.215	0.215	0.267	3.216	0.216	0.267
1	1.021	0.021	0.018	1.020	0.020	0.019	1.012	0.012	0.001	1.012	0.012	0.001
2	2.035	0.035	0.057	2.039	0.039	0.129	2.177	0.177	0.035	2.315	0.315	0.107
3.5	3.541	0.041	0.063	3.555	0.055	0.065	3.743	0.243	0.337	3.744	0.244	0.337

Table 7.6: Comparison of Bias and mean square error of Bayes estimators using both symmetric (SE)and asymmetric (Linex) Loss functions of Several Estimators for Gamma and Lomax, when $(m, n) = (40, 50)$

$\theta \downarrow$	Gamma Distribution($\theta = \mu_1, \mu_2, \lambda$)						Lomax Distribution($\theta = \eta_1, \eta_2, \gamma$)					
	symmetric(SE)			asymmetric(Linex)			symmetric(SE)			asymmetric(Linex)		
	Bayes	Bias	MSE	Bayes	Bias	MSE	Bayes	Bias	MSE	Bayes	Bias	MSE
1	1.069	0.069	0.035	1.022	0.022	0.027	1.665	0.665	2.292	1.652	0.652	2.228
2	2.014	0.014	0.091	2.019	0.019	0.090	1.967	-0.033	1.869	1.954	-0.046	1.930
2.5	2.453	-0.047	0.168	2.509	0.009	0.162	2.018	-0.482	2.044	2.014	-0.486	2.016
1	1.066	0.066	0.035	1.020	0.020	0.027	1.787	0.787	3.521	1.766	0.766	3.392
2	2.016	0.016	0.092	2.024	0.024	0.092	2.057	0.057	2.465	2.023	0.023	2.372
3	2.940	-0.060	0.236	3.002	0.002	0.227	2.555	-0.445	2.612	2.544	-0.456	2.580

1	1.068	0.068	0.035	1.023	0.023	0.027	1.733	0.733	4.359	1.722	0.722	4.217
2	2.019	0.019	0.090	2.030	0.030	0.091	2.129	0.129	2.746	2.093	0.093	2.634
3.5	3.423	-0.077	0.317	3.491	-0.009	0.304	3.284	-0.216	3.681	3.263	-0.237	3.590

Table 7.7: Comparison of Bias and mean square error of Bayes estimators using both symmetric (SE) and asymmetric (Linex) Loss functions of Several Estimators for Weibull and Rayleigh, when $(m, n) = (60, 60)$

$\theta \downarrow$	Weibull Distribution ($\theta = \alpha_1, \alpha_2, \beta$)						Rayleigh Distribution ($\theta = \delta_1, \delta_2, \omega$)					
	symmetric(SE)			asymmetric(Linex)			symmetric(SE)			asymmetric(Linex)		
	Bayes	Bias	MSE	Bayes	Bias	MSE	Bayes	Bias	MSE	Bayes	Bias	MSE
1	1.012	0.012	0.012	1.011	0.011	0.012	1.009	0.009	0.001	1.010	0.010	0.001
2	2.038	0.038	0.046	2.033	0.033	0.045	2.069	0.069	0.007	2.111	0.111	0.015
2.5	2.528	0.028	0.026	2.536	0.036	0.027	2.629	0.129	0.111	2.630	0.130	0.111
1	1.013	0.013	0.012	1.013	0.013	0.014	1.007	0.007	0.001	1.007	0.007	0.001
2	2.024	0.024	0.060	2.016	0.016	0.034	2.092	0.092	0.011	2.154	0.154	0.027
3	3.030	0.030	0.035	3.039	0.039	0.037	3.149	0.149	0.161	3.149	0.149	0.161
1	1.008	0.008	0.011	1.007	0.007	0.011	1.008	0.008	0.001	1.008	0.008	0.001
2	2.028	0.028	0.044	2.025	0.025	0.044	2.125	0.125	0.018	2.217	0.217	0.052
3.5	3.535	0.035	0.045	3.546	0.046	0.047	3.669	0.169	0.206	3.669	0.169	0.207

Table 7.8: Comparison of Bias and mean square error of Bayes estimators using both symmetric (SE) and asymmetric (Linex) Loss functions of Several Estimators for Gamma and Lomax, when $(m, n) = (60, 60)$

$\theta \downarrow$	Gamma Distribution($\theta = \mu_1, \mu_2, \lambda$)						Lomax Distribution($\theta = \eta_1, \eta_2, \gamma$)					
	symmetric(SE)			asymmetric(Linex)			symmetric(SE)			asymmetric(Linex)		
	Bayes	Bias	MSE	Bayes	Bias	MSE	Bayes	Bias	MSE	Bayes	Bias	MSE
1	1.049	0.049	0.023	1.016	0.016	0.019	1.138	0.138	1.906	1.132	0.132	1.886
2	2.015	0.015	0.073	2.021	0.021	0.074	2.301	0.301	1.791	2.289	0.289	1.759
2.5	2.462	-0.038	0.124	2.504	0.004	0.120	2.469	-0.031	1.848	2.460	-0.040	1.835
1	1.048	0.048	0.023	1.017	0.017	0.019	1.584	0.584	3.440	1.574	0.574	3.248
2	2.015	0.015	0.072	2.024	0.024	0.073	2.039	0.039	2.151	1.976	-0.024	2.004
3	2.953	-0.047	0.182	3.000	0.000	0.176	2.380	-0.620	2.562	2.370	-0.630	2.530
1	1.048	0.048	0.023	1.018	0.018	0.019	1.645	0.645	4.129	1.624	0.624	4.006
2	2.014	0.014	0.070	2.024	0.024	0.071	2.067	0.067	2.492	2.001	0.001	2.312
3.5	3.449	-0.051	0.236	3.500	0.000	0.230	2.796	-0.704	3.636	2.778	-0.722	3.573

Example: We have considered the Annual rainfall of two regions Rayalaseema and Coastal Andhra Pradesh from 1950 - 2017. The data is as follows.

Rayalaseema

510.9, 538.4, 701.4, 795.6, 785.2, 816.4, 930.8, 571.8, 808.2, 635.7, 744.2, 651.4, 816.2, 709, 791.6, 596.2, 904.1, 737.8, 624, 842.3, 776.4, 621.2, 826.1, 689.4, 728.3, 1041.5, 817, 866.5, 869.1, 813.5, 573.6, 785.3, 595.4, 943, 733, 685.9, 580.9, 769.4, 842.2, 693.6, 930.7, 967.6, 596.1, 886.9, 690.5, 874.3, 1277.7, 835.1, 947.9, 537.2, 871.3, 924.6, 615.3, 725.4, 741.7, 1066.4, 638.1, 980.6, 797.9, 688.3, 963.5, 738.2, 715.1, 762.6, 551.9, 1047.1, 555.4, 834.5.

Coastal AP

986, 1096.2, 916.6, 990, 1153.5, 1379, 1408.6, 1017.7, 1605.4, 1120.7, 943.7, 1119.3, 1345.5, 1023.9, 1061, 754.3, 954.7, 843.2, 839, 1279.7, 1064, 1033.2, 1028.4, 859, 944.9, 1192.4, 1090.1, 1132.8, 1038.2, 934.2, 1014.8, 929.3, 888.5, 1195.9, 785.3, 967.6, 1009.9, 1079.8, 1164.9, 1030.1, 1611.3, 1122.2, 1000.9, 869.7, 1154.9, 1352, 1210.8, 971.9, 1310.7, 825.2, 992.3, 1009.5, 703.2, 1097, 873.8, 1221.6, 1159.6, 1099.4, 1107.5, 790.5, 1712.5, 861.8, 1318.3, 1120.4, 875.1, 1011, 909, 892.7.

We have calculated Bayes estimates of 4 distributions and also calculated their Bias and MSE. The Computational results are given below.

$\theta \downarrow$	Weibull Distribution ($\theta = \alpha_1, \alpha_2, \beta$)						Rayleigh Distribution ($\theta = \delta_1, \delta_2, \omega$)					
	symmetric(SE)			asymmetric(Linex)			symmetric(SE)			asymmetric(Linex)		
	Bayes	Bias	MSE	Bayes	Bias	MSE	Bayes	Bias	MSE	Bayes	Bias	MSE
1	0.190	-0.810	0.657	0.190	-0.810	0.657	2.572	1.572	2.471	2.572	1.572	2.472
2	0.170	-1.830	3.350	0.170	-1.830	3.350	4.688	2.688	7.226	4.688	2.688	7.227
5	6.444	1.444	2.084	6.461	1.461	2.134	0.003	-4.997	24.968	0.003	-4.997	24.969

$\theta \downarrow$	Gamma Distribution($\theta = \mu_1, \mu_2, \lambda$)						Lomax Distribution($\theta = \eta_1, \eta_2, \gamma$)					
	symmetric(SE)			asymmetric(Linex)			symmetric(SE)			asymmetric(Linex)		
	Bayes	Bias	MSE	Bayes	Bias	MSE	Bayes	Bias	MSE	Bayes	Bias	MSE
1	0.309	-0.691	0.477	0.303	-0.697	0.486	3.647	2.688	7.008	3.599	2.599	6.756
2	0.250	-1.750	3.063	0.244	-1.756	3.085	3.534	1.534	2.354	3.489	1.489	2.218
5	33.064	28.064	787.5	36.071	31.071	965.3	6.926	1.926	3.709	6.796	1.796	3.227

From the tables, it is evident that the Bayes estimators estimated using both loss functions for Weibull and Rayleigh distributions exhibit similarity. However, for Gamma and Lomax distributions, the Bias and MSE are higher for symmetric loss functions compared to the asymmetric loss function. Specifically, for Gamma and Lomax distributions, the estimators derived from symmetric loss functions demonstrate higher Bias and MSE when compared to those obtained from asymmetric loss functions. Consequently, when evaluating all four distributions, it becomes apparent that the Bias and MSE are minimized in the Weibull distribution, making it a preferable choice. These observations highlight the varying performance of estimators under different distributions and underscore the importance of selecting appropriate loss functions based on the characteristics of the data.

8. CONCLUSION

In this research, we have explored the estimation of two populations with a common scale and two potentially different shape/location parameters, focusing on the Weibull, Rayleigh, Gamma, and Lomax distributions. Bayesian estimation methods were employed to estimate these parameters, and due to the complexity of solving the Bayes expression explicitly, Lindley's expression was utilized for an explicit solution. ML

estimates were used to obtain the Bayes estimators, with ML estimates generated using the optim function and Nelder-Mead method in R-software. A comprehensive simulation study was conducted to compare the obtained estimators in terms of their Bias and MSE. It was observed across all distributions that as the sample size increased, both Bias and MSE decreased. Furthermore, the Weibull distribution consistently exhibited the minimum Bias and MSE among all distributions. Additionally, a simulation study was conducted on rainfall data from two regions spanning 1950 to 2017. While informative and non-informative priors were used in this study, more extensive research is needed to comprehensively compare the results derived from these different types of priors. This work contributes to the understanding of parameter estimation under Bayesian frameworks, emphasizing the impact of sample size and distribution characteristics on estimation performance. Further exploration and comparative studies can enhance the insights gained from this research.

Acknowledgment: The collective contributions of my supervisor, the reviewers, and my family have been indispensable, and I am sincerely thankful for their roles in the successful completion of this research endeavor.

References:

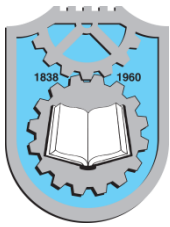
- Albert, J. H. (1987). Empirical Bayes estimation in contingency tables. *Communications in Statistics - Theory and Methods*, 16(8), 2459–2485. doi: 10.1080/03610928708829518
- Al-Bossly, A. (2021). E-Bayesian and Bayesian Estimation for the Lomax Distribution under Weighted Composite LINEX Loss Function. *Computational Intelligence and Neuroscience*, 2021, 1–10. doi: 10.1155/2021/2101972
- Azhad, Q. J., Arshad, M. A., & Misra, A. (2020). Estimation of common location parameter of several heterogeneous exponential populations based on generalized order statistics. *Journal of Applied Statistics*, 48(10), 1798–1815. doi: 10.1080/02664763.2020.1777395
- Bryson, M. C. (1974). Heavy-Tailed Distributions: Properties and tests. *Technometrics*, 16(1), 61–68. doi: 10.1080/00401706.1974.10489150

- Choi, S., & Wette, R. (1969). Maximum likelihood estimation of the parameters of the gamma distribution and their bias. *Technometrics*, 11(4), 683–690. doi: 10.1080/00401706.1969.10490731
- Dey, S., Dey, T., & Kundu, D. (2014). Two-Parameter Rayleigh distribution: different methods of estimation. *American Journal of Mathematical and Management Sciences*, 33(1), 55–74. doi: 10.1080/01966324.2013.878676
- Fitrilia, A., Fithriani, I., & Nurrohmah, S. (2018). Parameter estimation for the Lomax distribution using the E-Bayesian method. *Journal of Physics: Conference Series*, 1108, 012081. doi: 10.1088/1742-6596/1108/1/012081
- Ghosh, M., & Lahiri, P. (1987). Robust Empirical Bayes Estimation of Means from Stratified Samples. *Journal of the American Statistical Association*, 82(400), 1153–1162. doi: 10.1080/01621459.1987.10478553
- Ghosh, M., Lahiri, P., & Tiwari, R. C. (1989). Nonparametric empirical Bayes estimation of the distribution function and the mean. *Communications in Statistics - Theory and Methods*, 18(1), 121–146. doi: 10.1080/03610928908829888
- Ghosh, M., & Razmpour, A. (1984). Estimation of the Common Location Parameter Of Several Exponentials. *Sankhya*. 46(3), 383-394. www.jstor.org/stable/25050498
- Gupta, P. K., & Singh, A. K. (2017). Classical and Bayesian estimation of Weibull distribution in presence of outliers. *Rms: Research in Mathematics & Statistics*, 4(1), 1300975. doi: 10.1080/23311835.2017.1300975
- Guure, C., Ibrahim, N. A., & Ahmed, A. (2012). Bayesian Estimation of Two-Parameter Weibull Distribution Using Extension of Jeffrey's Prior Information with Three Loss Functions. *Mathematical Problems in Engineering*, 2012, 1–13. doi: 10.1155/2012/589640
- Jin, C., & Pal, N. (1992). On Common Location of Several Exponentials under a Class of Convex Loss Functions. *Calcutta Statistical Association Bulletin*, 42(3–4), 191–200. doi: 10.1177/0008068319920304
- Kumari, P., Kumar, V., & Aditi. (2022). Bayesian analysis for two parameter LOMAX distribution under different loss functions. *Communications in Mathematics and Applications*, 13(1), 163–170. doi: 10.26713/cma.v13i1.1679
- Kundu, D., & Mitra, D. (2016). Bayesian inference of Weibull distribution based on left truncated and right censored data. *Computational Statistics & Data Analysis*, 99, 38–50. doi: 10.1016/j.csda.2016.01.001
- Lindley, D. V. (1980). Approximate Bayesian methods. *Trabajos De Estadistica Y De Investigacion Operativa*, 31(1), 223–245. doi: 10.1007/bf02888353
- Nagamani, N., & Tripathy, M. R. (2017). Estimating common scale parameter of two gamma populations: a simulation study. *American Journal of Mathematical and Management Sciences*, 36(4), 346–362. doi: 10.1080/01966324.2017.1369473
- Nagamani, N., Tripathy, M. R., & Kumar, S. (2020). Estimating common scale parameter of two logistic populations: a Bayesian study. *American Journal of Mathematical and Management Sciences*, 40(1), 44–67. doi: 10.1080/01966324.2020.1833794
- Okasha, H. M. (2014). E-Bayesian estimation for the Lomax distribution based on type-II censored data. *Journal of the Egyptian Mathematical Society*, 22(3), 489–495. doi: 10.1016/j.joems.2013.12.009
- Pradhan, B., & Kundu, D. (2011). Bayes estimation and prediction of the two-parameter gamma distribution. *Journal of Statistical Computation and Simulation*, 81(9), 1187–1198. doi: 10.1080/00949651003796335
- Son, Y. S., & Oh, M. (2006). Bayesian estimation of the Two-Parameter gamma distribution. *Communications in Statistics: Simulation and Computation*, 35(2), 285–293. doi: 10.1080/03610910600591925

Vijay Kumar Lingutla
VIT-AP,
Amaravati,
India
vijay.lingutla@gmail.com
ORCID: 0009-0005-6449-2205

Nadiminti Nagamani
VIT-AP,
Amaravati,
India
manjinadiminiti999@gmail.com
ORCID: 0000-0002-5518-6653

P. S. Brahmanandam
Shri Vishnu Engineering College for
Women (A),
Vishnupur, Bhimavaram- 534202,
India.
dranandpotula@svecw.edu.in
ORCID: 0000-0001-9777-3496



CONSISTENCY IMPROVEMENT METHOD FOR FUZZY PAIR-WISE COMPARISON MATRIX IN ANALYTIC HIERARCHY PROCESS

L N P Kumar Rallabandi¹
Ravindranath Vandrangi²

Keywords:

Defuzzification; AHP; Fuzzy PCM;
Consistency.

A B S T R A C T

Maintaining consistency is a crucial element in ensuring the reliability of pairwise comparisons provided by experts in the Analytic Hierarchy Process (AHP) and Fuzzy AHP. Many researchers have put forth various definitions concerning the c

onsistency of fuzzy Pairwise Comparison Matrices (PCMs) using fuzzy set theory. However, in most applications of fuzzy AHP, fuzzy PCM consistency is evaluated by defuzzifying the fuzzy comparisons, similar to the approach used for crisp PCMs. This paper introduces a novel method for transforming fuzzy comparisons into crisp comparisons through defuzzification, specifically utilizing the geometric mean. Furthermore, it proposes a method to enhance the consistency of the PCM. The presented methodology is applied to several problems previously addressed in the literature.



1. INTRODUCTION

The Analytic Hierarchy Process (AHP), as introduced by Saaty in 1980, represents a sophisticated approach to Multi Criteria Decision Making (MCDM), encompassing both qualitative and quantitative factors. In the AHP framework, decision makers are tasked with providing judgments regarding paired comparisons of objectives, forming a matrix known as the Pair-wise Comparison Matrix (PCM). In complex systems, decision maker judgments often exhibit linguistic or vague patterns. Consequently, several methods have been devised to address such situations, including AHP with interval judgments, Fuzzy AHP, and Hesitant AHP. Saaty and Vargas (1987) pioneered the incorporation of interval judgments into AHP and derived interval weights through the Monte Carlo

simulation method. Many subsequent researchers have also explored interval AHP (e.g., Salo and Hamalainen in 1992, Islam et al. in 1997, Wang et al. in 2005). In 1983, Van Laarhoven and Pedrycz were the first to apply fuzzy logic principles to AHP, utilizing triangular fuzzy numbers (TFN's) to model pair-wise comparisons and employing the logarithmic least squares method to determine fuzzy weights. This concept was further refined and applied by numerous researchers, including Buckley in 1985 and Chang in 1996, as well as Leung and Cao in 2000. Torra (2010) introduced the concept of hesitancy in Fuzzy sets, which offers the advantage of handling imprecision when multiple sources of vagueness coexist. In recent times, many authors have incorporated hesitant Fuzzy sets into their work. For instance, Zhu (2013) introduced the notion of a hesitant fuzzy preference relation and proposed a regression-

¹ Corresponding author: LNP Kumar Rallabandi
Email: pradeepkumar.r@vishnu.edu.in

based approach to transform them into a Fuzzy Preference Relation with the highest consistency degree.

1.1 Consistency of Fuzzy PCM

Measuring the consistency of a fuzzy Pair-wise Comparison Matrix (PCM) in terms of fuzzy quantities can be a challenging task. The literature contains several noteworthy approaches in this regard. Buckley (1985) employed Trapezoidal fuzzy numbers to represent comparison ratios, and fuzzy priorities were derived using the geometric mean method. He extended Saaty's (1980) consistency definition from AHP to Fuzzy AHP. Salo (1996) introduced a Linear Programming method for determining fuzzy weights from relative fuzzy ratios, treating them as constraints on the membership values of local priorities. Arbel (1989) initially defined the feasible region of relative weights in terms of linear inequalities, a concept later extended by Salo and Hamalainen (1995). Their proposal suggested that a fuzzy matrix is considered consistent if there exists a set of crisp weights within the feasible region. Leung and Cao (2000) introduced fuzzy consistency by incorporating tolerance deviation in the feasible region's constraints, building upon Salo's (1996) definition. They suggested an auxiliary linear programming approach to test consistency and proposed an algorithm for deriving fuzzy weights from a consistent matrix. Ramík and Korviny (2010) introduced a new consistency index based on the distance between the matrix and a special ratio matrix, measured by a particular metric. They specified a two-step procedure using metric functions like logarithmic least squares and Chebychev, deriving associated weights. However, Brunelli (2011) pointed out limitations in the consistency index introduced by Ramík and Korviny (2010), noting that the use of the Chebychev metric may fail to capture inconsistency in the Pair-wise Comparison Matrix (PRM). Herrera-Viedma et al. (2004) introduced a new characterization of the consistency property based on the additive transitivity property of fuzzy preference relations. They proposed a method for constructing consistent fuzzy preference relations from a set of (n-1) preference data using this new characterization. They also extended the study of consistency to multiplicative preference relations.

This approach required (n-1) pairwise comparisons for consistent ranking. Liu (2009) defined an acceptably consistent interval reciprocal comparison matrix, which can be achieved by converting intervals into exact numbers. An interval reciprocal comparison matrix with unacceptable consistency can be adjusted to possess acceptable consistency through a convex combination method. This yields a family of crisp reciprocal comparison matrices with acceptable consistency. A formula of possibility degree was presented for ranking interval weights. Liu et al. (2014) introduced a definition of consistent triangular fuzzy reciprocal preference relations based on the reciprocity property.

They proposed a method for obtaining consistent triangular fuzzy reciprocal preference relations using (n-1) pairwise comparisons and addressed shortcomings in a proof procedure given by Wang and Chen (2008). Wang et al. (2005) developed a pragmatic method for consistency testing in interval comparison matrices. They used linear programming to derive consistent interval weights from consistent interval comparison matrices and provided an eigenvector-based nonlinear programming approach for generating interval weights when the matrix is inconsistent. A preference ranking method was utilized for comparing interval weights of criteria or ranking alternatives. Cuiping et al. (2008) introduced a method to test the consistency of a fuzzy comparison matrix using the kernels of fuzzy numbers. They proposed a mathematical programming model to assess the matrix's consistency. Bulut et al. (2012) presented a generic version of the conventional Fuzzy-Analytic Hierarchy Process (FAHP) and applied it to the shipping asset management (SAM) problem in the dry bulk shipping market. Their Generic Fuzzy-AHP (GF-AHP) model aimed to ensure consistency within the PCM for expert groups. Kinay and Tezel (2021) used different ranking methods in Fuzzy-AHP for solving problem related Turkish textile company. For more comprehensive information, one can refer to the review article by Liu et al. (2020).

Certain mathematical operations, such as multiplication and inversion applied to Triangular Fuzzy Numbers (TFNs) or Trapezoidal Fuzzy Numbers (TrFNs), do not yield TFNs or TrFNs as results. However, the outcomes closely resemble corresponding fuzzy numbers of their respective types. Despite this, these operations find applications in various fields, including linear programming and decision theory. In the context of Analytic Hierarchy Process (AHP), where numerical judgments are fuzzified, the solutions may not always be real, as indicated by Saaty in 2007. Nevertheless, experts' judgments can often be vague or uncertain, making fuzziness an unavoidable aspect of real-world situations. Despite recognizing the limitations of fuzzy number operations and the demand for real-time solutions, it is advisable to minimize the use of fuzzy operations whenever possible. However, it's worth noting that the initial input data may still be inherently fuzzy.

The remainder of this article is structured as follows: Section 2 provides fundamental definitions related to fuzzy AHP. Section 3 illustrates the proposed method for testing consistency through Geometric Defuzzification with examples. Section 4 is dedicated to enhancing consistency through the proposed algorithm. In Section 5, the application of the proposed method to a problem involving an automobile manufacturer, NEKYEK, is presented, followed by the concluding remarks.

2. PRELIMINARIES

Saaty (1980) introduced a fundamental 9-point scale for comparing the alternatives in AHP. The PCM which are discussed in this paper are all based on this scale only.

Definition 1: A matrix $A = (a_{ij})_{n \times n}$ is said to be PCM if a_{ij} indicates the relative preference of i^{th} alternative over j^{th} alternative and satisfies $a_{ij} = \frac{1}{a_{ji}} \forall i, j$.

Definition 2: A PCM $A = (a_{ij})_{n \times n}$ is said to be consistent if $a_{ij} = a_{ik} \cdot a_{kj} \forall i, j \text{ and } k$.

Definition 3: Consistency Ratio (CR) of a PCM $A = (a_{ij})_{n \times n}$ is defined to be

$$CR = \frac{CI}{RI}$$

Where CI is Consistency Index and calculated by

$$CI = \frac{\lambda_{\max}(A) - n}{n - 1}$$

And RI is the average Random Index which depends on order of the matrix [page 19 of Saaty (1980)]. According to Saaty (1980), a PCM is said to be consistent if $CR \leq 0.1$.

Definition 4: Let X be a universe of discourse. A fuzzy set \tilde{A} is defined by $\tilde{A} = \{(x, \mu_{\tilde{A}}(x)), X \in x\}$ and $\mu_{\tilde{A}}(x): X \rightarrow [0,1]$. Here $\mu_{\tilde{A}}(x)$ is called membership function.

Definition 5: A fuzzy set \tilde{A} is said to be convex if $\mu_{\tilde{A}}(\lambda x_1 + (1 - \lambda)x_2) \geq \min(\mu_{\tilde{A}}(x_1), \mu_{\tilde{A}}(x_2))$ for all $x_1, x_2 \in X$ and $\lambda \in [0,1]$.

Definition 6: A fuzzy set \tilde{A} of the universe of discourse X is said to be normal if there exists a $x_i \in X$ satisfying $\mu_{\tilde{A}}(x_i) = 1$.

Definition 7: A Fuzzy set which is both convex and normal is called Fuzzy Number.

The most used fuzzy numbers are Trapezoidal Fuzzy Number (TrFN) and Triangular Fuzzy Number (TFN), these are respectively defined as follows:

Definition 8: A Trapezoidal Fuzzy Number (TrFN) is denoted by an ordered quadruple as

$\tilde{N} = (a, b, c, d)$ whose membership function $\mu_{\tilde{N}}(x)$ described as

$$\mu_{\tilde{N}}(x) = \begin{cases} \frac{(x-a)}{(b-a)}, & a \leq x \leq b \\ 1, & b \leq x \leq c \\ \frac{(d-x)}{(d-c)}, & c \leq x \leq d \\ 0, & \text{otherwise} \end{cases}$$

Definition 9: A Triangular Fuzzy Number (TFN) denoted by an ordered triple as $\tilde{M} = (a, b, c)$ whose membership function $\mu_{\tilde{M}}(x)$ is described as

$$\mu_{\tilde{M}}(x) = \begin{cases} \frac{(x-a)}{(b-a)}, & a \leq x \leq b \\ \frac{(d-x)}{(d-b)}, & b \leq x \leq d \\ 0, & \text{otherwise} \end{cases}$$

Definition 10: A PCM $\tilde{A} = (\tilde{a}_{ij})$ where \tilde{a}_{ij} is a fuzzy number, is called Fuzzy PCM

In the context of Fuzzy AHP, the comparison of two fuzzy numbers involves the utilization of either Ranking methods or Defuzzification methods. While many ranking methods may yield a crisp value that falls outside the range of the original fuzzy number, defuzzification methods ensure that the obtained value aligns with the original fuzzy number's range.

Numerous defuzzification methods exist within Fuzzy Set Theory. Nonetheless, in the realm of Fuzzy AHP, two specific methods are commonly employed by many researchers in their studies. Weighted Mean (WM) defuzzification of a TFN $\tilde{N} = (l, m, u)$ is defined by the following equation

$$WM(\tilde{N}) = \frac{l + 4m + u}{6}$$

The Centroid Method, also known as the Center of Gravity Method, stands out as one of the most frequently employed techniques among all defuzzification methods. If a TFN \tilde{N} is linked to the membership function $\mu_{\tilde{N}}(x)$, the Centroid Defuzzification is obtained by the centre of gravity formula, expressed by the following equation.

$$CM(\tilde{N}) = \frac{\int \mu_{\tilde{N}}(x) \cdot x \, dx}{\int \mu_{\tilde{N}}(x) \, dx}$$

It can be shown easily that $CM(\tilde{N})$ of a TFN $\tilde{N} = (l, m, u)$ is

$$CM(\tilde{N}) = \frac{l + m + u}{3}$$

It is noticeable that the defuzzified value associated with the inverse of a Triangular Fuzzy Number (TFN) does not coincide with the inverse of the defuzzified value obtained through the aforementioned defuzzification methods. Consequently, these methods may not be suitable in Analytic Hierarchy Process (AHP), where the elements in the Pairwise Comparison Matrix (PCM) adhere to the reciprocity rule. Thus, there is a need to establish a new defuzzification approach that aligns with the reciprocity rule.

3. CONSISTENCY THROUGH GEOMETRIC DEFUZZIFICATION

3.1 Geometric Defuzzification (GD)

Geometric Defuzzification (GD) of a TFN $\tilde{N} = (l, m, u)$ is defined to be geometric mean of l, m, u or it is defined by the equation

$$GD(\tilde{N}) = (l * m * u)^{1/3}$$

Similarly, GD of a trapezoidal fuzzy number $\tilde{T} = (a, b, c, d)$ is defined by the equation

$$GD(\tilde{T}) = (a * b * c * d)^{1/4}$$

And GD of an interval fuzzy number $\tilde{I} = [l, u]$ is defined by the equation

$$GD(\tilde{I}) = (l * u)^{1/2}$$

Remark: Here it can be noted that $GD(\tilde{N}^{-1}) = \frac{1}{GD(\tilde{N})}$.

By applying Geometric Defuzzification (GD) to each element in the Fuzzy Pairwise Comparison Matrix (Fuzzy PCM), a corresponding crisp matrix, which is a Pairwise Comparison Matrix (PCM), can be obtained. Similarly, employing the above defuzzification method yields a crisp PCM corresponding to a Fuzzy PCM with trapezoidal fuzzy numbers or an interval PCM.

3.2 Consistency of a Fuzzy PCM:

Definition 11: A fuzzy PCM $\tilde{A} = \{\tilde{a}_{ij}\}_{n \times n}$, where \tilde{a}_{ij} is anyone of Triangular Fuzzy Number, Trapezoidal fuzzy number and interval, is said to be consistent if and only if $G_{\tilde{A}} = \{GD(\tilde{a}_{ij})\}_{n \times n}$ is consistent.

Example 1:

Consider a fuzzy PCM \tilde{A} whose elements are TFNs which was used in the study of student's requirement problem by Kamvysi et al (2014). The elements in the matrix $\tilde{A} = (\tilde{a}_{ij})_{4 \times 4}$ describe the comparisons, made among the factors Theory-based Knowledge, Practical-based Knowledge and Generic Academic Skills Key Transferable Skills.

$$\begin{aligned} \tilde{a}_{11} &= \tilde{a}_{22} = \tilde{a}_{33} = \tilde{a}_{44} = (1, 1, 1) \\ \tilde{a}_{12} &= (0.4052, 0.467, 0.6904) \\ \tilde{a}_{13} &= (0.3604, 0.4328, 0.5957) \\ \tilde{a}_{14} &= (0.3392, 0.3992, 0.5557) \\ \tilde{a}_{21} &= (1.448, 2.1413, 2.4672) \\ \tilde{a}_{23} &= (1.0185, 1.145, 1.8737) \\ \tilde{a}_{24} &= (0.8112, 0.9369, 1.4618) \\ \tilde{a}_{31} &= (1.6787, 2.3105, 2.7747) \\ \tilde{a}_{32} &= (0.5337, 0.8734, 0.9818) \\ \tilde{a}_{34} &= (0.6955, 0.7959, 1.3044) \\ \tilde{a}_{41} &= (1.7995, 2.5050, 2.5050) \\ \tilde{a}_{42} &= (0.6841, 1.0674, 1.2327) \\ \tilde{a}_{43} &= (0.7666, 1.2564, 1.4378) \end{aligned}$$

Using GD, \tilde{A} is converted to crisp PCM $G_{\tilde{A}} = \{GD(\tilde{a}_{ij})\}$ which is

$$G_{\tilde{A}} = \begin{pmatrix} 1 & 0.5074 & 0.4529 & 0.4222 \\ 1.9708 & 1 & 1.2976 & 1.0357 \\ 2.2078 & 0.7706 & 1 & 0.8971 \\ 2.2435 & 0.9655 & 1.1147 & 1 \end{pmatrix}$$

The CR of $G_{\tilde{A}}$ is 0.0, which means $G_{\tilde{A}}$ is consistent and thus by *Definition 11*, \tilde{A} is consistent. Kamvysi et al (2014) used the degree of optimism technique to convert the PCM \tilde{A} into corresponding crisp PCM and is given by

$$\begin{pmatrix} 1 & 0.5478 & 0.478 & 0.4475 \\ 1.9583 & 1 & 1.4461 & 1.1365 \\ 2.2267 & 0.7578 & 1 & 0.9999 \\ 2.3737 & 0.9584 & 1.1023 & 1 \end{pmatrix}$$

The CR of the above crisp PCM is 0.052 and hence it is consistent.

Example 2:

Consider a fuzzy PCM $\tilde{B} = (\tilde{b}_{ij})_{4 \times 4}$ with Trapezoidal Fuzzy Numbers which was used for consistency test proposed by Cuiping et al (2008).

$$\begin{aligned} \tilde{b}_{11} &= \tilde{b}_{22} = \tilde{b}_{33} = (1, 1, 1, 1) \\ \tilde{b}_{12} &= (1, 2, 5, 6) \\ \tilde{b}_{13} &= (1, 2, 4, 5) \\ \tilde{b}_{14} &= (1/2, 1, 3, 7/2) \\ \tilde{b}_{21} &= (1/6, 1/5, 1/2, 1) \\ \tilde{b}_{23} &= (1/2, 1, 3, 7/2) \\ \tilde{b}_{24} &= (1/2, 1, 2, 5/2) \\ \tilde{b}_{31} &= (1/5, 1/4, 1/2, 1) \\ \tilde{b}_{32} &= (2/7, 1/3, 1, 2) \\ \tilde{b}_{34} &= (1/4, 1/2, 1, 3/2) \\ \tilde{b}_{41} &= (2/7, 1/3, 1, 2) \\ \tilde{b}_{42} &= (2/5, 1/2, 1, 2) \\ \tilde{b}_{43} &= (2/3, 1, 2, 4) \end{aligned}$$

The corresponding crisp PCM $G_{\tilde{B}} = \{GD(\tilde{b}_{ij})\}$ using definition of GD is given by

$$G_{\tilde{B}} = \begin{pmatrix} 1 & 2.7831 & 2.5148 & 1.5137 \\ 0.3593 & 1 & 1.5137 & 1.2574 \\ 0.39763 & 0.66063 & 1 & 0.65804 \\ 0.66063 & 0.79527 & 1.5196 & 1 \end{pmatrix}$$

The CR of $G_{\tilde{B}}$ is 0.0241, thus $G_{\tilde{B}}$ is consistent and hence \tilde{B} is consistent. Cuiping et al (2008) used α -cut method to convert \tilde{B} into corresponding Interval matrix and hence shown that it is consistent by means of kernels of the fuzzy numbers.

Example 3

Consider an interval PCM \tilde{C} . This PCM is used by Wang et al (2005) to describe their proposed consistency test.

$$\tilde{C} = \begin{pmatrix} [1, 1] & [2, 5] & [2, 4] & [1, 3] \\ [1/5, 1/2] & [1, 1] & [1, 3] & [1, 2] \\ [1/4, 1/2] & [1/3, 1] & [1, 1] & [1/2, 1] \\ [1/3, 1] & [1/2, 1] & [1, 2] & [1, 1] \end{pmatrix}$$

Using GD, one can get the corresponding crisp PCM $G_{\tilde{C}}$ of \tilde{C} as

$$G_{\tilde{C}} = \begin{pmatrix} 1 & 3.162 & 2.828 & 1.732 \\ 0.3162 & 1 & 1.732 & 1.414 \\ 0.3535 & 0.5773 & 1 & 0.7071 \\ 0.5773 & 0.7071 & 1.414 & 1 \end{pmatrix}$$

The CR of $G_{\tilde{C}}$ is 0.0323, which implies that $G_{\tilde{C}}$ and thus \tilde{C} is also consistent. Wang et al (2005) has also shown that \tilde{C} is consistent. Here, one more observation is that the interval matrix corresponding to \tilde{B} by α -cut method is \tilde{C} . Moreover \tilde{C} was also examined by Arbel and Vergas (1993) for consistency.

4. CONSISTENCY IMPROVEMENT METHOD

At times, the judgment matrix provided by experts may exhibit inconsistency, necessitating adjustments either by the experts or the decision maker to alleviate this inconsistency. The following algorithm is suggested to enhance the consistency of a Fuzzy PCM.

Algorithm

Step 1: Input the PCM $\tilde{A} = \{\tilde{a}_{ij}\}_{n \times n}$, where \tilde{a}_{ij} is anyone of TFN, TrFN and Interval number.

Step 2: Find the corresponding crisp PCM $G_{\tilde{A}} = \{GD(\tilde{a}_{ij})\}_{n \times n}$ using Geometric Defuzzification (GD).

Step 3: If CR of $G_{\tilde{A}} \leq 0.1$ then print ' \tilde{A} ' is consistent. STOP

Step 4: If CR of $G_{\tilde{A}} > 0.1$ then

Compute

$$G_{\tilde{A}} = [\hat{a}_{ij}] \text{ where } \hat{a}_{ij} = \frac{\sum_k a_{ik}}{\sum_k a_{jk}}$$

$$e_{ij}^2 = \frac{(a_{ij} - \hat{a}_{ij})^2}{\hat{a}_{ij}} \text{ and } \chi^2 = \sum \sum e_{ij}^2$$

Pick i^* and j^* for which e_{ij}^2 is the maximum.

$$\text{Replace } a_{i^*j^*} \text{ by } a_{ij} = \frac{\sum_{k \neq j^*} a_{ik} - 1}{\sum_{k \neq i^*} a_{jk} - 1}$$

Go to Step 3.

This method can be explained through the following example.

Example 4

Consider a fuzzy PCM $\tilde{D} = (\tilde{d}_{ij})_{5 \times 5}$ with TrFNs as pair wise comparisons, which was used by Ghazanfari and Nojavan (2004) for describing their method of reducing inconsistency.

$$\tilde{d}_{11} = \tilde{d}_{22} = \tilde{d}_{33} = \tilde{d}_{44} = \tilde{d}_{55} = (1, 1, 1, 1)$$

$$\tilde{d}_{12} = (1, 2, 4, 5) \quad \tilde{d}_{13} = \left(\frac{1}{9}, \frac{1}{8}, \frac{1}{7}, \frac{1}{6} \right)$$

$$\tilde{d}_{14} = \left(\frac{1}{9}, \frac{1}{7}, \frac{1}{6}, \frac{1}{5} \right) \quad \tilde{d}_{15} = \left(\frac{1}{8}, \frac{1}{7}, \frac{1}{6}, \frac{1}{5} \right)$$

$$\tilde{d}_{21} = \left(\frac{1}{5}, \frac{1}{4}, \frac{1}{2}, 1 \right) \quad \tilde{d}_{23} = \left(\frac{1}{9}, \frac{1}{9}, \frac{1}{9}, \frac{1}{9} \right)$$

$$\tilde{d}_{24} = \left(\frac{1}{7}, \frac{1}{6}, \frac{1}{6}, \frac{1}{5} \right) \quad \tilde{d}_{25} = \left(\frac{1}{4}, \frac{1}{2}, \frac{1}{2}, 1 \right)$$

$$\tilde{d}_{31} = (6, 7, 8, 9) \quad \tilde{d}_{32} = (9, 9, 9, 9)$$

$$\begin{aligned} \tilde{d}_{34} &= (1, 2, 4, 5) & \tilde{d}_{35} &= (1, 2, 3, 4) \\ \tilde{d}_{41} &= (5, 6, 7, 9) & \tilde{d}_{42} &= (5, 6, 6, 7) \\ \tilde{d}_{43} &= \left(\frac{1}{5}, \frac{1}{4}, \frac{1}{2}, 1 \right) & \tilde{d}_{45} &= \left(\frac{1}{3}, \frac{1}{3}, \frac{1}{2}, \frac{1}{2} \right) \\ \tilde{d}_{51} &= (5, 6, 7, 8) & \tilde{d}_{52} &= (1, 2, 2, 4) \\ \tilde{d}_{53} &= \left(\frac{1}{4}, \frac{1}{3}, \frac{1}{2}, 1 \right) & \tilde{d}_{54} &= (2, 2, 3, 3) \end{aligned}$$

The crisp PCM $G_{\tilde{D}}$ corresponding to Fuzzy PCM \tilde{D} using GD is

$$G_{\tilde{D}} = \begin{pmatrix} 1 & 2.5148 & 0.13485 & 0.15166 & 0.15619 \\ 0.39763 & 1 & 0.11111 & 0.16784 & 0.5 \\ 7.4156 & 9 & 1 & 2.5148 & 2.2133 \\ 6.5935 & 5.9579 & 0.39763 & 1 & 0.40825 \\ 6.4022 & 2 & 0.4518 & 2.4495 & 1 \end{pmatrix}$$

The CR of $G_{\tilde{D}}$ is 0.127, thus it can be considered as inconsistent and hence corresponding fuzzy PCM \tilde{D} is also inconsistent.

Using the proposed algorithm, the modified matrix $G_{\tilde{D}}^m$ can be obtained as

$$G_{\tilde{D}}^m = \begin{pmatrix} 1.0000 & 2.5149 & 0.1349 & 0.1517 & 0.5716 \\ 0.3976 & 1.0000 & 0.1111 & 0.1678 & 0.5000 \\ 7.4156 & 9.0000 & 1.0000 & 2.5149 & 2.2134 \\ 6.5935 & 5.9579 & 0.3976 & 1.0000 & 3.0821 \\ 1.7496 & 2.0000 & 0.4518 & 0.3245 & 1.0000 \end{pmatrix}$$

The CR of $G_{\tilde{D}}^m$ is 0.0514, thus it can be considered as consistent. This modified matrix obtained by two iterations only with changing the elements \tilde{D}_{15} , \tilde{D}_{45} and their reciprocals.

Ghazanfari and Nojavan (2004) also shown that \tilde{D} is inconsistent by using penalty function and the changeable preference mathematical programming model have been used to reduce the inconsistency wherein six judgments (\tilde{D}_{12} , \tilde{D}_{41} , \tilde{D}_{42} , \tilde{D}_{51} , \tilde{D}_{52} and \tilde{D}_{54}) and their reciprocals are modified.

In this context, it is evident that the revised, consistent crisp Pairwise Comparison Matrix (PCM) is presented rather than a Fuzzy PCM corresponding to an inconsistent Fuzzy PCM. There is no need to transform the consistent crisp PCM into a Fuzzy PCM, as both result in the same preference order. This can be elucidated further through the following numerical example.

5. AN AUTOMOBILE MANUFACTURER NEKYEK PROBLEM

Within the context of an automobile manufacturing company, a challenge known as the NEKYEK problem has been the subject of investigation by Kahraman et al (2003), Wang and Chen (2008), and Liu et al (2014), who have documented their respective approaches. The NEKYEK problem revolves around the decision-

making process for establishing a new factory and determining the optimal location from a range of options. This decision hinges on several criteria, namely Environmental Regulation (E), Host Community (H), Competitive Advantage (C), and Political Risk (P). The available location choices are Istanbul (A1), Ankara (A2), and Izmir (A3). The hierarchical structure of this problem is illustrated in Figure 1

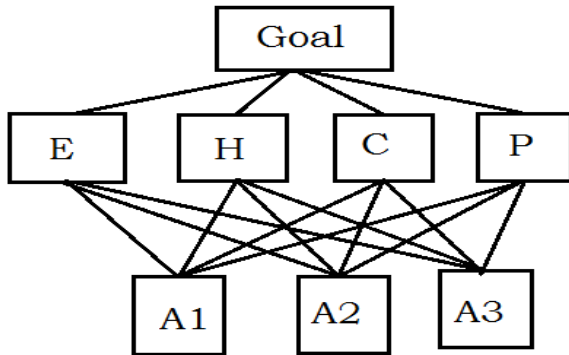


Figure 1: Hierarchy structure of Automobile manufacturer NEKYEK

The pairwise comparisons for each level that is four criteria E, H, C and P under goal and the alternatives A1, A2 and A3 under each criterion are given as Triangular fuzzy numbers by a decision maker and the corresponding PCMs are given. The fuzzy PCM for criteria under goal is

$$\tilde{M}^{cri} = (\tilde{m}_{ij})_{4 \times 4} \text{ where}$$

$$\begin{aligned} \tilde{m}_{11} &= \tilde{m}_{22} = \tilde{m}_{33} = \tilde{m}_{44} = (1, 1, 1) \\ \tilde{m}_{12} &= \left(\frac{3}{2}, 2, \frac{5}{2}\right) \quad \tilde{m}_{13} = \left(\frac{2}{7}, \frac{1}{3}, \frac{2}{5}\right) \\ \tilde{m}_{14} &= \left(\frac{5}{2}, 3, \frac{7}{2}\right) \quad \tilde{m}_{21} = \left(\frac{2}{5}, \frac{1}{2}, \frac{2}{3}\right) \\ \tilde{m}_{23} &= \left(\frac{2}{7}, \frac{1}{3}, \frac{2}{5}\right) \quad \tilde{m}_{24} = \left(\frac{7}{2}, 4, \frac{9}{2}\right) \\ \tilde{m}_{31} &= \left(\frac{5}{2}, 3, \frac{7}{2}\right) \quad \tilde{m}_{32} = \left(\frac{5}{2}, 3, \frac{7}{2}\right) \\ \tilde{m}_{34} &= \left(\frac{5}{2}, 3, \frac{7}{2}\right) \quad \tilde{m}_{41} = \left(\frac{2}{7}, \frac{1}{3}, \frac{2}{5}\right) \\ \tilde{m}_{42} &= \left(\frac{2}{9}, \frac{1}{4}, \frac{2}{7}\right) \quad \tilde{m}_{43} = \left(\frac{2}{7}, \frac{1}{3}, \frac{2}{5}\right) \end{aligned}$$

The fuzzy PCMs for alternatives under all criteria are
 \tilde{M}^E

$$\begin{aligned} \tilde{M}^E &= \begin{pmatrix} (1, 1, 1) & (2/5, 1/2, 2/3) & (2/5, 1/2, 2/3) \\ (3/2, 2, 5/2) & (1, 1, 1) & (1/2, 2/3, 1) \\ (3/2, 2, 5/2) & (1, 3/2, 2) & (1, 1, 1) \end{pmatrix} \\ \tilde{M}^H &= \begin{pmatrix} (1, 1, 1) & (2/5, 1/2, 2/3) & (1/2, 2/3, 1) \\ (3/2, 2, 5/2) & (1, 1, 1) & (1, 3/2, 2) \\ (1, 3/2, 2) & (1/2, 2/3, 1) & (1, 1, 1) \end{pmatrix} \\ \tilde{M}^C &= \begin{pmatrix} (1, 1, 1) & (1/2, 2/3, 1) & (2/5, 1/2, 2/3) \\ (1, 3/2, 2) & (1, 1, 1) & (1/2, 1, 3/2) \\ (3/2, 2, 5/2) & (2/3, 1, 2) & (1, 1, 1) \end{pmatrix} \\ \tilde{M}^P &= \begin{pmatrix} (1, 1, 1) & (2/5, 1/2, 2/3) & (1/2, 2/3, 1) \\ (3/2, 2, 5/2) & (1, 1, 1) & (1, 3/2, 2) \\ (1, 3/2, 2) & (1/2, 2/3, 1) & (1, 1, 1) \end{pmatrix} \end{aligned}$$

Using the GD, it can be verified the consistency of fuzzy PCMs. The crisp PCM $G_{\tilde{M}^{cri}}$ of the fuzzy PCM \tilde{M}^{cri} is

$$G_{\tilde{M}^{cri}} = \begin{pmatrix} 1.0000 & 1.9574 & 0.3365 & 2.9720 \\ 0.5109 & 1.0000 & 0.3365 & 3.9791 \\ 2.9720 & 2.9720 & 1.0000 & 2.9720 \\ 0.3365 & 0.2513 & 0.3365 & 1.0000 \end{pmatrix}$$

The CR of $G_{\tilde{M}^{cri}}$ is 0.1064 which means that $G_{\tilde{M}^{cri}}$ is inconsistent and correspondingly \tilde{M}^{cri} is also inconsistent. Thus, it requires modification.

Using Algorithm, the modified consistent matrix $G_{\tilde{M}^{cri}}^m$ is obtained as

$$G_{\tilde{M}^{cri}}^m = \begin{pmatrix} 1.0000 & 1.9574 & 0.8293 & 2.9720 \\ 0.5109 & 1.0000 & 0.3365 & 3.9791 \\ 1.2058 & 2.9720 & 1.0000 & 2.9720 \\ 0.3365 & 0.2513 & 0.3365 & 1.0000 \end{pmatrix}$$

The CR of $G_{\tilde{M}^{cri}}^m$ is 0.0698. It is obtained only by one iteration i.e., modifying the element $G_{\tilde{M}^{cri}}_{13}$ and its reciprocal. The priority vector obtained from $G_{\tilde{M}^{cri}}^m$ which means the priority weights of criteria by Eigen Vector Method (EVM) is

$$S_{G_{\tilde{M}^{cri}}^m} = (0.3121 \ 0.2044 \ 0.3930 \ 0.0905)$$

Similarly, the consistency of the fuzzy PCMs can be verified through their respective crisp PCMs. The crisp PCMs of the fuzzy PCMs \tilde{M}^E , \tilde{M}^H , \tilde{M}^C and \tilde{M}^P with CRs are

$$\begin{aligned} G_{\tilde{M}^E} &= \begin{pmatrix} 1.0000 & 0.5109 & 0.5109 \\ 1.9574 & 1.0000 & 0.6934 \\ 1.9574 & 1.4422 & 1.0000 \\ 1.0000 & 0.5109 & 0.6934 \end{pmatrix} \\ G_{\tilde{M}^H} &= \begin{pmatrix} 1.9574 & 1.0000 & 1.4422 \\ 1.4422 & 0.6934 & 1.0000 \\ 1.0000 & 0.6934 & 0.5109 \end{pmatrix} \\ G_{\tilde{M}^C} &= \begin{pmatrix} 1.4422 & 1.0000 & 0.9086 \\ 1.9574 & 1.1006 & 1.0000 \\ 1.0000 & 0.5109 & 0.6934 \end{pmatrix} \\ G_{\tilde{M}^P} &= \begin{pmatrix} 1.9574 & 1.0000 & 1.4422 \\ 1.4422 & 0.6934 & 1.0000 \end{pmatrix} \end{aligned}$$

The CRs of $G_{\tilde{M}^E}$, $G_{\tilde{M}^H}$, $G_{\tilde{M}^C}$ and $G_{\tilde{M}^P}$ are respectively 0.0128, 0, 0.0042 and 0. Thus the matrices $G_{\tilde{M}^E}$, $G_{\tilde{M}^H}$, $G_{\tilde{M}^C}$ and $G_{\tilde{M}^P}$ are consistent and so their Fuzzy PCMs \tilde{M}^E , \tilde{M}^H , \tilde{M}^C and \tilde{M}^P are also consistent. Thus, there will be modification not required. The priority vectors of alternatives (A1, A2, and A3) under the criteria Environmental regulation (E), Host community (H), Competitive advantage (C) and Political risk (P) are obtained from $G_{\tilde{M}^H}$, $G_{\tilde{M}^C}$ and $G_{\tilde{M}^P}$ by EVM are

$$\begin{aligned} S_{G_{\tilde{M}^E}} &= (0.2023 \ 0.3504 \ 0.4473) \\ S_{G_{\tilde{M}^H}} &= (0.2267 \ 0.4529 \ 0.3204) \\ S_{G_{\tilde{M}^C}} &= (0.2287 \ 0.3538 \ 0.4175) \\ S_{G_{\tilde{M}^P}} &= (0.2267 \ 0.4529 \ 0.3204) \end{aligned}$$

The global weights of the alternatives can be obtained by taking

$$(0.3121 \ 0.2044 \ 0.3930 \ 0.0905).$$

$$\begin{pmatrix} 0.2023 & 0.3504 & 0.4473 \\ 0.2267 & 0.4529 & 0.3204 \\ 0.2287 & 0.3538 & 0.4175 \\ 0.2267 & 0.4529 & 0.3204 \end{pmatrix} = (0.2199 \quad 0.3820 \quad 0.3982)$$

Thus, the final rank order of the alternatives is $A_3 > A_2 > A_1$. This rank order of the alternatives coincides with that of the rank order obtained by methods of Kahraman et al (2003), Wang and Chen (2008) and Liu et al (2014).

6. CONCLUSIONS

References:

- Arbel, A. (1989). Approximate articulation of preference and priority derivation. *European Journal of Operational Research*, 43 (3), 317–326. doi:10.1016/0377-2217(89)90231-2
- Arbel, A., & Vargas, L.G. (1993). Preference simulation and preference programming: robustness issues in priority deviation. *European Journal of Operational Research*, 69 (2), 200 -209. doi:10.1016/0377-2217(93)90164-I
- Brunelli, M. (2011). A note on the article “Inconsistency of pair- wise comparison matrix with fuzzy elements based on geometric mean [Fuzzy Sets and Systems 161 (2010) 1604–1613]. *Fuzzy Sets and Systems*, 176 (1), 76–78. doi:10.1016/j.fss.2011.03.013
- Buckley, J. J. (1985). Fuzzy Hierarchical Analysis. *Fuzzy Sets and Systems*, 17 (3), 141–164. doi:10.1016/0165-0114(85)90090-9
- Bulut, E., Duru, O., Keçeci T., & Yoshida, S. (2012). Use of consistency index, expert prioritization and direct numerical inputs for generic fuzzy-AHP modeling: A process model for shipping asset management. *Expert Systems with Applications*, 39 (2), 1911–1923. doi:10.1016/j.eswa.2011.08.056
- Chang, D. Y. (1996). Applications of The Extent Analysis Method on Fuzzy-AHP. *European Journal of Operational Research*, 95 (3), 649–655. doi:10.1016/0377-2217(95)00300-2
- Cuiping, W., Lili, F. & Yuzhong, Z. (2008). A note on the Consistency of a Fuzzy Comparison Matrix. *2008 Chinese Control and Decision Conference*, 2077-2081. doi:10.1109/CCDC.2008.4597691
- Ghazanfari, M. & Nojavan, M. (2004). Educting Inconsistency in Fuzzy AHP by Mathematical Programming Models. *Asia-Pacific Journal of operational Research*, 21 (3), 379–391. doi:10.1142/S0217595904000291
- Islam, R., Biswal, M.P. & Alam, S. S. (1997). Preference programming and inconsistent interval judgments. *European Journal of Operational Research*, 97 (1), 53–62. doi:10.1016/S0377-2217(95)00377-0
- Kamvysi, K., Gotzamani, K., Andronikidis, A. & Georgiou, A. C. (2014). Capturing and prioritizing students’ requirements for course design by embedding Fuzzy-AHP and linear programming in QFD. *European Journal of Operational Research*, 237 (3), 1083–1094. doi:10.1016/j.ejor.2014.02.042
- Kinay, A. O., & Tezel, A. O. (2021). Modification of the fuzzy analytic hierarchy process via different ranking methods. *International Journal of Intelligent Systems*, 2021, 1-29. doi:10.1002/int.22628
- Leung, L.C. & Cao, D. (2000). On consistency and ranking of alternatives in fuzzy AHP. *European Journal of Operational Research*, 124 (1), 102–113. doi:10.1016/S0377-2217(99)00118-6
- Liu, F. (2009). Acceptable consistency analysis of interval reciprocal comparison matrices. *Fuzzy Sets and Systems*, 160 (18), 2686–2700. doi:10.1016/j.fss.2009.01.010
- Liu, F., Zhang, W. G. & Zhang, L. H. (2014). Consistency analysis of triangular fuzzy reciprocal preference relations. *European Journal of Operational Research*, 235 (3), 718–726. doi:10.1016/j.ejor.2013.10.039
- Liu, Y., Eckert, C. M. & Earl. C.(2020). A review of fuzzy AHP methods for decision making with subjective judgements. *Experts systems with Applications*, 161 (15), 113738. doi:10.1016/j.eswa.2020.113738
- Rallabandi, L.N.P.K., & Ravindranath, V. (2022). A method for improving cosine consistency index of pairwise comparison matrix in analytic hierarchy process. *International Journal of Mathematics in Operational Research*, 23 (2), 259–283. doi:10.1504/IJMOR.2022.127052.
- Rallabandi, L.N.P.K., Ravindranath, V. & Subbarao, R. (2016). Improved Consistency Ratio for Pairwise Comparison Matrix in Analytic Hierarchy Processes. *Asia-Pacific Journal of Operational Research*, 33 (3), 1650020. doi:10.1142/S0217595916500202
- Ramik, J. & Kovviny, P. (2010). Inconsistency of pair-wise comparison matrix with fuzzy elements based on the geometric mean. *Fuzzy Sets and Systems*, 161 (11), 1604–1613. doi:10.1016/j.fss.2009 .10.011
- Saaty, T.L. & Tran, L.T. (2007). On the invalidity of fuzzifying numerical judgments in the Analytic Hierarchy Process. *Mathematical and Computer Modelling*, 46 (7-8), 962–97. doi:10.1016/j.mcm.2007.03.022

In this article a new defuzzification method named, Geometric Defuzzification (GD) of a fuzzy number, is defined. A crisp PCM can be obtained corresponding to fuzzy PCM by GD of elements in fuzzy PCM. New definition of consistency for fuzzy PCM has been introduced by means corresponding crisp PCM. The properties of new definition have been discussed. A simple algorithm is proposed and utilized to improve the consistency of some numerical examples which are widely studied in the literature. Moreover, the validity of the proposed method has been addressed by applying it to an automobile manufacturer NEKYE problem.

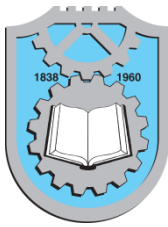
- Saaty, T.L. (1980). *The Analytical Hierarchy Process*. McGraw-Hill, New York.
- Salo, A. A & Hamalainen, R.P. (1992). Preference assessment by imprecise ratio statements. *Operations Research*, 40 (6), 1053–1061. doi:10.1287/opre.40.6.1053
- Salo, A. A & Hamalainen, R. P. (1995). Preference programming through approximate ratio comparisons. *European Journal of Operational Research*, 82 (3), 458–475. doi:10.1016/0377-2217(93)E0224-L
- Torra, V. (2010). Hesitant fuzzy sets. *International Journal of Intelligent Systems*, 25 (6), 529-539. doi:10.1002/int.20418
- Van Laarhoven, P.J.M. & Pedrycz, W. (1983). A fuzzy extension of Saaty's priority theory. *Fuzzy sets and Systems*, 11 (1-3), 229–241. doi:10.1016/S0165-0114(83)80082-7
- Wang, T.C. & Chen, Y. H. (2008). Applying fuzzy linguistic preference relations to the improvement of consistency of fuzzy AHP. *Information Sciences*, 178 (19), 3755–3765. doi:10.1016/j.ins.2008.05.028
- Zhu, B. (2013). Studies on consistency measure of hesitant fuzzy preference relations. *Procedia Computer Science*, 17, 457–464. doi:10.1016/j.procs.2013.05.059

L N P Kumar Rallabandi

Vishnu Institute of Technology (A)
Bhimavaram-534202
Andhra Pradesh
India
Pradeepkumar.r@vishnu.edu.in
ORCID-0000-0001-9142-4324

Ravindranath Vandrangi

JNT University Kakinada,
Kakinada-530001
Andhra Pradesh
India
rvandrangi@gmail.com
ORCID-0000-0003-3405-822X



SOLVING INTUITIONISTIC FUZZY TRANSPORTATION PROBLEM USING GM-R METHOD

Veerraju Nalla

L N P KumarRallabandi*

P. S. Brahmanandam

Keywords:

Intuitionistic fuzzy number; Ranking Method; Intuitionistic fuzzy Transportation Problem; Fuzzy Transportation Problem.



A B S T R A C T

In recent years, researchers have focused on the Intuitionistic Fuzzy Transportation Problem (IFTP) due to its significant and indispensable role in the Transportation Problem (TP). An endeavour is performed in this paper to establish a new technique. This technique works with IFTP based on "Geometric Mean-Ranking(GM-R)"method. To provide a comprehensive understanding of the proposed method, we present and solve extensively discussed numerical examples. The acquired outcomes are subsequently subjected to numerical comparison with those of established methods, confirming the effectiveness of the proposed technique. This study validates the flexibility and simplicity of applying the method to real-life IFTPs for decision-makers.

1. INTRODUCTION

In the global context, delivering services such as goods and value-based services from available sources to diverse destinations like individuals, organizations, shops, and supermarkets presents numerous challenges. Achieving this in a profitable manner requires optimization. The TP has proven to be an effective technique in providing optimal solutions for transporting resources from available sources to destinations in need. Traditional TP, however, is designed to handle precise, crisp data.

Upon careful examination of practical TP data, it becomes evident that the data lacks precision; in other words, it contains vagueness or impreciseness, representing a form of uncertainty. Zadeh's Fuzzy Set (FS), introduced in 1965, has proven effective in handling vague or imprecise data. In response to this, the Fuzzy Transportation Problem (FTP) was developed to address TP within a Fuzzy Environment (FE).

Intuitionistic Fuzzy Set (IFS), emerged as extension of FS, has been found to be particularly suitable for analyzing and organizing uncertainty in certain practical problems compared to traditional FS. Consequently, IFTP has emerged as an extension of FTP, leveraging the enhanced capabilities of IFS. The point that Intuitionistic Fuzzy Number (IFN) belongs to the class of IFS, is remarkable.

Hitchcock (1941) pioneered the design of the fundamental TP. Subsequently, Bellman and Zadeh (1970) constructed a platform for understanding how decision is made in a FE. Zimmermann (1983) explained about how to raise the quality in solutions through the amalgamation of Linear Programming Problem (LPP) with fuzzy logic. Hussain and Kumar (2012) produced a method to crack the TP involving supplies and demands represented as Triangular Intuitionistic Fuzzy Numbers (TIFN). They utilized the intuitionistic fuzzy Vogel's approximation method and

* Corresponding author: L N P Kumar Rallabandi
Email: pradeepkumar.r@vishnu.edu.in

the Intuitionistic Fuzzy Modified Distribution Method (IFMODI). Gani and Abbas (2013) discussed a solution approach for the IFTP through a ranking function, with supplies and demands represented as TIFNs. Pramila and Uthra (2014) investigated a method employing an accuracy function to explore the best solution for IFTP with cost, supply, and demand as TIFNs. Kumar and Hussain (2015) introduced a strategy for handling IFTP involving TIFNs in a single stage. Aggarwal and Gupta (2016) presented a method for solving IFTP through a proposed signed distance ranking method. Ebrahimnejad and Verdegay (2017) described a method aiming to solve IFTP by reducing it to a crisp Linear Programming Problem (LPP) and then applying LPP algorithms. Uthra et al (2017) illustrated a method for providing an optimal solution for IFTP with generalized Trapezoidal Intuitionistic Fuzzy Numbers (TrIFN), using a ranking function to reduce the entire problem to a crisp form. Narayananamoorthy and Deepa (2017) introduced the intuitionistic fuzzy Russell's method to solve IFTP. Kumar (2018) tabled a method to explore a solution directly from IFTP, where costs are expressed as TIFNs and supply and demand are presented by crisp numbers. Purushothkumar et al (2018) put forward a technique to solve IFTP utilizing the diagonal optimal algorithm. Hunwisai et al (2019) introduced a method to solve IFTP using the northwest corner rule and the MODI method. Taghaodi (2019) presented a method which optimizes initially obtained feasible solution with the MODI method. Nishad and Abhishek (2020) illustrated a method with a distance minimizer concept for solving IFTP. Abirami et al (2020) introduced a ranking method to solve IFTP based on signed distance. Rani et al (2023) endeavored to surface a method applying fuzzy branch and bound techniques and IFMODI method to obtain a solution for IFTP. Beg et al (2023) placed afore a technique to investigate a solution for generalized IFTPs using an optimism-based expected value approach.

Numerous currently available methods entail protracted procedures and intricate calculations. Certain approaches specifically address either TrIFNs or TIFNs. Others are tailored for problems wherein the supply and demand are IFNs. Some methods are exclusively designed for scenarios where the cost matrix involves IFNs. Additionally, there are methods dedicated to challenges where supply, demand, and cost are all represented as IFNs. In light of these constructive insights, a novel method is introduced for solving IFTP. This strategy is founded on the "GM-R" approach, offering the flexibility to handle TrIFNs and TIFNs, as well as their generalized counterparts.

This paper is neatly showcased as follows: Second portion provides essential fundamentals concerned to IFNs. Third section is dedicated to a clear illustration of the proposed method, supported by relevant data and examples. In the fourth section, discussions and useful comparisons with other author works are presented. The paper is concluded in the fifth section, summarizing key points.

2. PRELIMINARIES

Definition 2.1:

A FS \tilde{A} , where X means universal set and $\mu_{\tilde{A}}(x)$ means Membership Value (MV) function, is defined by $\tilde{A} = \{(x, \mu_{\tilde{A}}(x)), x \in X\}$ and $\mu_{\tilde{A}}(x): X \rightarrow [0,1]$.

Definition 2.2:

An IFS \tilde{A}^I in X is a set of the form $\tilde{A}^I = \{(x, \mu_{\tilde{A}^I}(x), \vartheta_{\tilde{A}^I}(x)): x \in X\}$ where the function $\mu_{\tilde{A}^I}(x): X \rightarrow [0,1]$ and $\vartheta_{\tilde{A}^I}(x): X \rightarrow [0,1]$ describe the degree of MV and Non-Membership Value (N-MV) of the element $x \in X$ respectively and for every $x \in X$ in \tilde{A}^I , $0 \leq \mu_{\tilde{A}^I}(x) + \vartheta_{\tilde{A}^I}(x) \leq 1$ holds.

\tilde{A}^I is said to be an intuitionistic fuzzy normal if \exists two points $x_0, x_1 \in X$ such that $\mu_{\tilde{A}^I}(x_0) = 1, \vartheta_{\tilde{A}^I}(x_1) = 1$

\tilde{A}^I is said to be an IFN if it is

- a) Intuitionistic fuzzy normal
- b) $\mu_{\tilde{A}^I}(x)$ is convex. i.e., $\mu_{\tilde{A}^I}(x)(\lambda x_1 + (1 - \lambda)x_2) \geq \min(\mu_{\tilde{A}^I}(x_1), \mu_{\tilde{A}^I}(x_2))$ for every $x_1, x_2 \in X, \lambda \in [0,1]$
- c) $\vartheta_{\tilde{A}^I}(x)$ is concave. i.e., $\vartheta_{\tilde{A}^I}(x)(\lambda x_1 + (1 - \lambda)x_2) \leq \max(\vartheta_{\tilde{A}^I}(x_1), \vartheta_{\tilde{A}^I}(x_2))$ for every $x_1, x_2 \in X, \lambda \in [0,1]$

Definition 2.3:

A generalized TIFN with parameters

$$q_1 \leq p_1 \leq q_2 (\leq, \geq) p_2 \leq p_3 \leq q_3 \text{ is denoted as } \tilde{A}^I = ((p_1, p_2, p_3; w), (q_1, q_2, q_3; v))$$

Where MV is given by

$$\mu_{\tilde{A}^I}(x) = \begin{cases} w \frac{x - p_1}{p_2 - p_1}, & p_1 < x < p_2 \\ w \frac{p_3 - x}{p_3 - p_2}, & p_2 < x < p_3 \\ 0, & \text{otherwise} \end{cases}$$

N-MV is given by

$$\vartheta_{\tilde{A}^I}(x) = \begin{cases} \frac{q_2 - x + v(x - q_1)}{q_2 - q_1}, & q_1 < x < q_2 \\ \frac{x - q_2 + v(q_3 - x)}{q_3 - q_2}, & q_2 < x < q_3 \\ 1, & \text{otherwise} \end{cases}$$

and w is the maximum MV and v is the minimum N-MV

Such that $\mu_{\tilde{A}^I}(x) \leq w$ and $\vartheta_{\tilde{A}^I}(x) \geq v$ for all x ,

$0 \leq w \leq 1, 0 \leq v \leq 1$ and $0 \leq w + v \leq 1$

If $w = 1$ and $v = 0$ in generalized TIFN, then it is called TIFN and it is denoted as

$$\tilde{A}^I = ((p_1, p_2, p_3), (q_1, q_2, q_3))$$

Definition 2.4:

A generalized TrIFN with parameters

$$q_1 \leq p_1 \leq q_2 \leq p_2 \leq p_3 \leq q_3 \leq p_4 \leq q_4 \text{ is denoted as } \tilde{A}^I = ((p_1, p_2, p_3, p_4; w), (q_1, q_2, q_3, q_4; v))$$

Where MV is given by

$$\mu_{\tilde{A}^I}(x) = \begin{cases} w \frac{x - p_1}{p_2 - p_1}, & p_1 < x < p_2 \\ w, & p_2 < x < p_3 \\ w \frac{p_4 - x}{p_4 - p_3}, & p_3 < x < p_4 \\ 0, & \text{otherwise} \end{cases}$$

N-MV is given by

$$\nu_{\tilde{A}^I}(x) = \begin{cases} \frac{q_2 - x + v(x - q_1)}{q_2 - q_1}, & q_1 < x < q_2 \\ v, & q_2 < x < q_3 \\ \frac{x - q_3 + v(q_4 - x)}{q_4 - q_3}, & q_3 < x < q_4 \\ 1, & \text{otherwise} \end{cases}$$

and w is the maximum MV and v is the minimum N-MV

Such that $\mu_{\tilde{A}^I}(x) \leq w$ and $\nu_{\tilde{A}^I}(x) \geq v$ for all x
 $0 \leq w \leq 1, 0 \leq v \leq 1$ and $0 \leq w + v \leq 1$

In the above definition, if we let $b_2 = b_3$ (and hence $a_2 = a_3$), then generalized TrIFN becomes generalized TIFN. If $w = 1$ and $v = 0$ in the definition of generalised TrIFN, then it is called TrIFN and it is denoted as

$$\tilde{A}^I = ((p_1, p_2, p_3, p_4), (q_1, q_2, q_3, q_4))$$

3. PROPOSED METHOD

3.1 Resultant membership function:

Let $\mu_{\tilde{A}^I}(x)$ and $\nu_{\tilde{A}^I}(x)$ be MV and N-MV functions of an IFN \tilde{A}^I , then the resultant membership function $R_{\tilde{A}^I}(x)$ is defined to be

$$R_{\tilde{A}^I}(x) = \mu_{\tilde{A}^I}(x) - \nu_{\tilde{A}^I}(x)$$

3.2 Support:

The support of an IFN \tilde{A}^I is $S(\tilde{A}^I) = \{x: R_{\tilde{A}^I}(x) \geq 0\}$

3.3 Proposition:

If $\tilde{A}^I = ((p_1, p_2, p_3, p_4; w), (q_1, q_2, q_3, q_4; v))$ be a TrIFN then the support of \tilde{A}^I is

$S(\tilde{A}^I) = [MP_1, MP_2]$ where

$$MP_1 = \frac{wp_1(q_2 - q_1) + (p_2 - p_1)(q_2 - vq_1)}{w(q_2 - q_1) + (1-v)(p_2 - p_1)} \text{ and}$$

$$MP_2 = \frac{wp_4(q_4 - q_3) + (p_4 - p_3)(q_3 - vq_4)}{w(q_4 - q_3) + (1-v)(p_4 - p_3)}.$$

3.4 Proposition:

If $\tilde{A}^I = ((p_1, p_2, p_3; w), (q_1, q_2, q_3; v))$ be a TIFN, then the support of \tilde{A}^I is $S(\tilde{A}^I) = [MP_1, MP_2]$ where

$$MP_1 = \frac{p_1w(q_2 - q_1) + (p_2 - p_1)(q_2 - vq_1)}{w(q_2 - q_1) + (1-v)(p_2 - p_1)} \text{ and}$$

$$MP_2 = \frac{wp_3(q_3 - q_2) + (p_3 - p_2)(q_2 - vq_3)}{w(q_3 - q_2) + (1-v)(p_3 - p_2)}.$$

3.5 Geometric Mean-Ranking (GM-R) Method:

If \tilde{A}^I be an IFN with $\mu_{\tilde{A}^I}(x)$ and $\nu_{\tilde{A}^I}(x)$ be MV and N-MV functions respectively and $S(\tilde{A}^I)$ be the support of \tilde{A}^I . Then the crisp value concerned with \tilde{A}^I , denoted as $G_{\tilde{A}^I}$, is defined to be

$$G_{\tilde{A}^I} = \text{Exp} \left[\frac{\int_{S(\tilde{A}^I)} R_{\tilde{A}^I}(x) \ln x dx}{\int_{S(\tilde{A}^I)} R_{\tilde{A}^I}(x) dx} \right] \quad (1)$$

Where $R_{\tilde{A}^I}(x)$ is resultant membership function of \tilde{A}^I .

3.6 Ranking procedure:

Let \tilde{A}^I and \tilde{B}^I be two IFNs.

Step1: Calculate the Supports $S(\tilde{A}^I)$ and $S(\tilde{B}^I)$ of given \tilde{A}^I and \tilde{B}^I respectively by either proposition 3.3 or 3.4

Step2: Calculate crisp values of \tilde{A}^I and \tilde{B}^I using the formula (1) and denote them as $G_{\tilde{A}^I}$ and $G_{\tilde{B}^I}$ respectively.

Step3: The ranking order can be identified by following cases

If $G_{\tilde{A}^I} < G_{\tilde{B}^I}$ then $\tilde{A}^I < \tilde{B}^I$.

If $G_{\tilde{A}^I} > G_{\tilde{B}^I}$ then $\tilde{A}^I > \tilde{B}^I$.

If $G_{\tilde{A}^I} = G_{\tilde{B}^I}$ then $\tilde{A}^I \sim \tilde{B}^I$

3.7 Intuitionistic Fuzzy Transportation Problem (IFTP):

If any one of the quantities in TP is IFN, then it is seen as IFTP. In general, IFTP is of the following form

$$\text{Minimize } \tilde{Z}^I = \sum_{i=1}^n \sum_{j=1}^m \tilde{c}_{ij}^I \tilde{x}_{ij}^I$$

$$\text{Subject to } \sum_{j=1}^m \tilde{x}_{ij}^I = \tilde{a}_i^I, \quad i = 1, 2, 3, \dots, m,$$

$$\sum_{i=1}^n \tilde{x}_{ij}^I = \tilde{b}_j^I, \quad j = 1, 2, 3, \dots, n \quad \text{and } \tilde{x}_{ij}^I \geq 0 \text{ for all } i \text{ and } j$$

	1	2	...	n	\tilde{a}_i^I
1	\tilde{c}_{11}^I	\tilde{c}_{12}^I	...	\tilde{c}_{1n}^I	\tilde{a}_1^I
2	\tilde{c}_{21}^I	\tilde{c}_{22}^I	...	\tilde{c}_{2n}^I	\tilde{a}_2^I
\vdots	\vdots	\vdots	...	\vdots	\vdots
M	\tilde{c}_{m1}^I	\tilde{c}_{m2}^I	...	\tilde{c}_{mn}^I	\tilde{a}_m^I
	\tilde{b}_j^I	\tilde{b}_1^I	\tilde{b}_2^I	...	\tilde{b}_n^I
					$\sum_{i=1}^n \tilde{a}_i^I = \sum_{j=1}^m \tilde{b}_j^I$

where,

\tilde{c}_{ij}^I is the fuzzy cost of transportation of one unit of the goods from i^{th} source to the j^{th} destination.

\tilde{x}_{ij}^I is the quantity transportation from i^{th} source to the j^{th} destination.

\tilde{a}_i^I is the total availability of the goods at i^{th} source.

\tilde{b}_j^I is the total demand of the goods at j^{th} destination.

$\sum_{i=1}^n \sum_{j=1}^m \tilde{c}_{ij}^I \tilde{x}_{ij}^I$ is total fuzzy transportation cost.

If $\sum_{i=1}^n \tilde{a}_i^I = \sum_{j=1}^m \tilde{b}_j^I$, then IFTP is said to be balanced.

If $\sum_{i=1}^n \tilde{a}_i^I \neq \sum_{j=1}^m \tilde{b}_j^I$, then IFTP is said to be unbalanced.

There are also different cases in IFTP like

Case1. Only the cost coefficients are IFNs and the supplies and demands are crisp.

Case2. The IFTP in which all the quantities are IFNs, then it is treated as fully IFTP.

3.8 Algorithm

The algorithm contains following steps.

Step1: Construct an IFTP from the given data and get it represented in tabular form.

Step2: Applying the GM-R method, the IFTP at step1 is reduced to a crisp TP.

Step3: At this stage, the problem with crisp values of supply, demand and cost, is formulated as a conventional LPP as following

$$\text{Minimize } Z = \sum_{i=1}^m \sum_{j=1}^n c_{ij} x_{ij}$$

$$\text{Subject to } \sum_{j=1}^n x_{ij} = a_i, \quad i = 1, 2, 3, \dots, m,$$

$$\sum_{i=1}^m x_{ij} = b_j, \quad j = 1, 2, 3, \dots, n \quad \text{and} \quad x_{ij} \geq 0$$

for all i and j

Step4: In this step, the LPP obtained in Step3, is solved and optimal solution is obtained.

Step5: Minimum Transportation Cost (MTC) is given in the crisp form using optimal solution obtained in step4 and crisp cost matrix.

4. NUMERICAL COMPARISONS AND DISCUSSION

The perusal of numerical comparisons, which contributes significance for the proposed IFTP method, is conducted here. This perusal is done with mostly observed significant works of others. From this perusal, the worthy points of the proposed IFTP are identified.

Example 1:

Considered IFTP from Kumar (2018) with three sources S1, S2, S3 and three destinations D1, D2, D3. The transportation cost is given in TIFNs. And supply and demand are given in crisp values. The problem is shown in Table1. Find the optimal value.

Step1:

Table1: Step1 for Example 1

Source	D1	D2	D3	Supply (a_i)
S1	\tilde{c}_{11}^I	\tilde{c}_{12}^I	\tilde{c}_{13}^I	18
S2	\tilde{c}_{21}^I	\tilde{c}_{22}^I	\tilde{c}_{23}^I	12
S3	\tilde{c}_{31}^I	\tilde{c}_{32}^I	\tilde{c}_{33}^I	4
Demand (b_i)	8	16	10	

where, $\tilde{c}_{11}^I = ((7, 21, 29), (2, 21, 34))$,

$\tilde{c}_{12}^I = ((7, 20, 57), (3, 20, 61))$,

$\tilde{c}_{13}^I = ((12, 25, 56), (8, 25, 60))$,

$\tilde{c}_{21}^I = ((8, 9, 16), (2, 9, 22))$,

$\tilde{c}_{22}^I = ((4, 12, 35), (1, 12, 38))$,

$\tilde{c}_{23}^I = ((6, 14, 28), (3, 14, 31))$,

$\tilde{c}_{31}^I = ((5, 9, 22), (2, 9, 25))$,

$\tilde{c}_{32}^I = ((10, 15, 20), (5, 15, 25))$,

$\tilde{c}_{33}^I = ((6, 14, 28), (3, 14, 31))$.

Step2:

Table2: Step2 for Example1

Source	D1	D2	D3	Supply(a_i)
S1	19.7768	23.3704	27.588	18
S2	10.1578	14.0952	14.8007	12
S3	10.3456	14.9378	14.319	4
Demand(b_j)	8	16	10	

Step3:

Corresponding to a crisp TP obtained at step2, the crisp LPP is formulated as following

Minimize:

$$\begin{aligned} Z = & 19.7768x_{11} + 23.3704x_{12} + 27.588x_{13} \\ & + 10.1578x_{21} + 14.0952x_{22} \\ & + 14.8007x_{23} + 10.3456x_{31} \\ & + 14.9378x_{32} + 14.319x_{33} \end{aligned}$$

Subject to

$$\begin{aligned} 19.7768x_{11} + 23.3704x_{12} + 27.588x_{13} &= 18, \\ 10.1578x_{21} + 14.0952x_{22} + 14.8007x_{23} &= 12, \\ 10.3456x_{31} + 14.9378x_{32} + 14.319x_{33} &= 4, \\ 19.7768x_{11} + 10.1578x_{21} + 10.3456x_{31} &= 8, \\ 23.3704x_{12} + 14.0952x_{22} + 14.9378x_{32} &= 16, \\ 27.588x_{13} + 14.8007x_{23} + 14.319x_{33} &= 10, \\ x_{ij} \geq 0, \quad i = 1, 2, 3, \text{ and } j &= 1, 2, 3. \end{aligned}$$

Step4:

Table3: Step4 for Example1

Source	D1	D2	D3	Supply(a_i)
S1	2	16	0	18
S2	6	0	6	12
S3	0	0	4	4
Demand(b_i)	8	16	10	

Hence optimal solution is

$$x_{11} = 2, x_{12} = 16, x_{21} = 6, x_{23} = 6, x_{33} = 4$$

Step5:

The MTC is

$$\begin{aligned} 2 \times 19.7768 + 16 \times 23.3704 + 6 \times 10.1578 + 6 \\ \times 14.8007 + 4 \times 14.319 \\ = 620.507 \end{aligned}$$

Thus, for the given IFTP, the optimal solution and optimum value in crisp form by the proposed method are $x_{11} = 2, x_{12} = 16, x_{21} = 6, x_{23} = 6, x_{33} = 4$ and $Z_{\text{proposedmethod}} = 620.507$ respectively.

Kumar (2018) applied LPP method to solve IFTP in which IFTP is converted to a conventional LPP by the use of ranking function. And then obtained LPP is solved. The optimal solution by Kumar (2018) is

$$x_{11} = 8, x_{12} = 10, x_{22} = 6, x_{23} = 6, x_{33} = 4$$

Minimum Intuitionistic Fuzzy Transportation Cost (MIFTC) by Kumar (2018) is $((202, 588, 1256), (74, 588, 1384))$ and crisp optimum value provided by Kumar (2018) is 682

$$MTC_{\text{proposedmethod}} = 620.507 < MTC_{\text{Kumar}} = 682$$

The proposed method is noticed to give superior solution with less transportation cost.

In the above Example1, cost parameters are provided by TIFNs. And supply and demand are expressed by crisp numbers.

Example 2:

Considered IFTP from Kumar (2018) with four sources S1, S2, S3, S4. and four destinations D1, D2, D3, D4. The transportation cost is given in TIFNs and supply and demand are given in crisp values. The problem is shown in Table 4. Find the optimal value.

Step1:

Table 4: Step1 for Example 2

Source	D1	D2	D3	D4	Supply (a_i)
S1	$\tilde{c}_{11}^I = ((27,50,109), (30,50,123))$	$\tilde{c}_{12}^I = ((56,67,111), (40,67,127))$	$\tilde{c}_{13}^I = ((8,22,120), (4,22,124))$	$\tilde{c}_{14}^I = ((75,100,128), (62,100,141))$	4
S2	$\tilde{c}_{21}^I = ((52,68,93), (44,68,101))$	$\tilde{c}_{22}^I = ((43,90,119), (35,90,127))$	$\tilde{c}_{23}^I = ((34,56,93), (18,56,109))$	$\tilde{c}_{24}^I = ((60,70,89), (50,70,99))$	6
S3	$\tilde{c}_{31}^I = ((72,80,109), (58,80,123))$	$\tilde{c}_{32}^I = ((10,15,20), (5,15,25))$	$\tilde{c}_{33}^I = ((4,6,19), (1,16,22))$	$\tilde{c}_{34}^I = ((75,100,128), (62,100,141))$	8
S4	$\tilde{c}_{41}^I = ((23,40,81), (17,40,87))$	$\tilde{c}_{42}^I = ((44,58,90), (38,58,96))$	$\tilde{c}_{43}^I = ((63,89,109), (49,89,123))$	$\tilde{c}_{44}^I = ((64,72,95), (51,72,108))$	10
Demand (b_j)	4	5	12	7	

where, $\tilde{c}_{11}^I = ((27,50,109), (30,50,123))$,
 $\tilde{c}_{12}^I = ((56,67,111), (40,67,127))$,
 $\tilde{c}_{13}^I = ((8,22,120), (4,22,124))$,
 $\tilde{c}_{14}^I = ((75,100,128), (62,100,141))$,
 $\tilde{c}_{21}^I = ((52,68,93), (44,68,101))$,
 $\tilde{c}_{22}^I = ((43,90,119), (35,90,127))$,
 $\tilde{c}_{23}^I = ((34,56,93), (18,56,109))$,
 $\tilde{c}_{24}^I = ((60,70,89), (50,70,99))$,
 $\tilde{c}_{31}^I = ((72,80,109), (58,80,123))$,
 $\tilde{c}_{32}^I = ((10,15,20), (5,15,25))$,
 $\tilde{c}_{33}^I = ((4,6,19), (1,16,22))$,
 $\tilde{c}_{34}^I = ((75,100,128), (62,100,141))$,
 $\tilde{c}_{41}^I = ((23,40,81), (17,40,87))$,
 $\tilde{c}_{42}^I = ((44,58,90), (38,58,96))$,
 $\tilde{c}_{43}^I = ((63,89,109), (49,89,123))$,
 $\tilde{c}_{44}^I = ((64,72,95), (51,72,108))$.

Step2:

Table 5: Step2 for Example 2

Source	D1	D2	D3	D4	Supply(a_i)
S1	55.305	72.518	33.814	100.31	4
S2	69.366	86.540	58.159	71.506	6
S3	83.675	91.005	104.35	69.369	8
S4	43.550	60.814	87.752	74.632	10
Demand(b_j)	4	5	12	7	

Step3:

Corresponding to crisp TP obtained at step2, the crisp LPP is formulated as following

Minimize

$$\begin{aligned} Z = & 55.305x_{11} + 72.518x_{12} + 33.814x_{13} \\ & + 100.31x_{14} + 69.366x_{21} \\ & + 86.540x_{22} + 58.159 \\ & + 71.506x_{24} + 83.675x_{31} \\ & + 91.005x_{32} + 104.35x_{33} \\ & + 69.369x_{34} + 43.5503x_{41} \\ & + 60.814x_{42} + 87.7521x_{43} \\ & + 74.6323x_{44} \end{aligned}$$

Subject to

$$\begin{aligned} 55.305x_{11} + 72.52x_{12} + 33.814x_{13} + 100.31x_{14} &= 4 \\ 69.366x_{21} + 86.541x_{22} + 58.159x_{23} + 71.51x_{24} &= 6 \\ 83.675x_{31} + 91.01x_{32} + 104.35x_{33} + 69.369x_{34} &= 8 \\ 43.55x_{41} + 60.814x_{42} + 87.75x_{43} + 74.63x_{44} &= 10 \\ 55.31x_{11} + 69.366x_{21} + 83.675x_{31} + 43.55x_{41} &= 4 \\ 72.519x_{12} + 86.51x_{22} + 91.01x_{32} + 60.815x_{42} &= 6 \\ 33.815x_{13} + 58.159x_{23} + 104.35x_{33} + 87.75x_{43} &= 8 \\ 100.31x_{14} + 71.51x_{24} + 69.37x_{34} + 74.63x_{44} &= 10 \\ x_{ij} \geq 0, \quad i = 1,2,3 \text{ and } j = 1,2,3,4 \end{aligned}$$

Step4:

Table 6: Step4 for Example 2

Source	D1	D2	D3	D4	Supply(a_i)
S1	0	0	4	0	4
S2	0	0	6	0	6
S3	0	0	2	6	8
S4	4	5	0	1	10
Demand(b_j)	4	5	12	7	

Hence optimal solution is $x_{13} = 4, x_{23} = 6, x_{33} = 2, x_{34} = 6, x_{41} = 4, x_{42} = 5, x_{44} = 1$ and $Z_{\text{proposedmethod}} = 1662.04$

Step5:

The MTC is

$$\begin{aligned} 4 \times 33.8146 + 6 \times 58.159 + 2 \times 104.35 + 6 \\ \times 69.369 + 4 \times 43.5503 + 5 \\ \times 60.8149 + 1 \times 74.6323 \\ = 1662.04 \end{aligned}$$

Thus, for the given IFTP, the optimal solution and optimum value in crisp form by the proposed method are $x_{13} = 4, x_{23} = 6, x_{33} = 2, x_{34} = 6, x_{41} = 4, x_{42} = 5, x_{44} = 1$ and $Z_{\text{proposedmethod}} = 1662.04$

respectively. The optimal solution by the authors Kumar (2018) is $x_{13} = 4, x_{23} = 6, x_{33} = 1, x_{34} = 7, x_{41} = 4, x_{42} = 5, x_{44} = 1$. MIFTC by the author Kumar (2018) is $((1060, 1537, 2722), (815, 1537, 2967))$

Crisp value of MIFTC is 1773.

$$MTC_{\text{proposedmethod}} = 1662.04 < MTC_{\text{Kumar}} = 1773$$

The proposed method is noticed to give better solution with less transportation cost.

In the above Example2, cost parameters are provided by TIFNs, and supply and demand are expressed by crisp numbers. In the next example3, all the parameters are expressed by TrIFNs.

Example 3:

Considered IFTP from Ebrahimnejad and Verdegay (2017) with two sources S1 and S2 and three destinations D1, D2, D3. The transportation cost with supply and demand is given in TrIFNS. And problem is shown in Table 7. Find out the optimal value.

Step1:

Table 7: Step1 for Example 3

Source	D1	D2	D3	Supply (\tilde{a}_i^l)
S1	\tilde{c}_{11}^l	\tilde{c}_{12}^l	\tilde{c}_{13}^l	\tilde{a}_1^l
S2	\tilde{c}_{21}^l	\tilde{c}_{22}^l	\tilde{c}_{23}^l	\tilde{a}_2^l
Demand (\tilde{b}_j^l)	\tilde{b}_1^l	\tilde{b}_2^l	\tilde{b}_3^l	

where,

$$\tilde{c}_{11}^l = ((10, 20, 30, 40), (5, 15, 35, 45))$$

$$\tilde{c}_{12}^l = ((50, 60, 70, 90), (45, 55, 75, 95))$$

$$\tilde{c}_{13}^l = ((80, 90, 110, 120), (75, 85, 115, 125))$$

$$\tilde{c}_{21}^l = ((60, 70, 80, 90), (55, 65, 85, 95))$$

$$\tilde{c}_{22}^l = ((70, 80, 100, 120), (65, 75, 115, 125))$$

$$\tilde{c}_{23}^l = ((20, 30, 50, 60), (15, 25, 35, 65))$$

$$\tilde{a}_1^l = ((60, 80, 100, 120), (50, 70, 110, 130))$$

$$\tilde{a}_2^l = ((40, 60, 80, 100), (30, 50, 90, 110))$$

$$\tilde{b}_1^l = ((30, 50, 70, 90), (20, 40, 80, 100))$$

$$\tilde{b}_2^l = ((20, 30, 40, 50), (15, 25, 45, 55))$$

$$\tilde{b}_3^l = ((50, 60, 70, 80), (45, 55, 75, 85))$$

Step2:

Table 8: Step2 for Example 3

Source	D1	D2	D3	Supply (a_i)
S1	24.2625	64.7264	94.8134	89
S2	74.7633	84.7913	34.4844	69
Demand (b_j)	59	34	65	

Step3:

Corresponding to a crisp TP obtained at step2, the crisp LPP is formulated as following

Minimize

$$Z = 24.2625x_{11} + 64.7264x_{12} + 94.8134x_{13} \\ + 74.7633x_{21} + 84.7913x_{22} \\ + 34.4844x_{23}$$

Subject to

$$24.2625x_{11} + 64.7264x_{12} + 94.8134x_{13} = 89,$$

References:

- Abhirami, B., Vamitha,V. & Rajaram, S. (2020). A new approach for solving trapezoidal intuitionistic fuzzy transportation problem. *Advances in Mathematics: Scientific journal*, 9(11), 9149-9159. <https://doi.org/10.37418/amsj.9.11.20>.

$$74.7633x_{21} + 84.7913x_{22} + 34.4844x_{23} = 69, \\ 246.49x_{11} + 74.7633x_{21} = 59, \\ 64.7264x_{12} + 84.7913x_{22} = 34, \\ 94.8134x_{13} + 34.4844x_{23} = 65, \\ x_{ij} \geq 0, \quad i = 1,2,3 \text{ and } j = 1,2,3,4$$

Step4:

Table 9: Step 4 for Example 3

Source	D1	D2	D3	Supply (a_i)
S1	59	30	0	89
S2	0	4	65	69
Demand (b_j)	59	34	65	

Hence optimal solution is $x_{11} = 59, x_{12} = 30, x_{13} = 0, x_{21} = 0, x_{22} = 4, x_{23} = 65$

Step5:

The MTC is

$$59 \times 24.2625 + 30 \times 64.7264 + 4 \times 84.7913 + 65 \times 34.4844 = 5953.93$$

Accordingly, for the given IFTP, the optimal solution and optimum value in crisp form by the proposed method are $x_{11} = 59, x_{12} = 30, x_{13} = 0, x_{21} = 0, x_{22} = 4, x_{23} = 65$

And $Z_{proposedmethod} = 5953.93$ respectively.

Ebrahimnejad and Verdegay (2017) converted IFTP into a crisp LPP and solved by standard LPP methods. MIFTC by Ebrahimnejad and Verdegay is $((3300, 5800, 9100, 13200), (2350, 4450, 11050, 15550))$ and its crisp value by the proposed method is 7530.96

$$MTC_{proposedmethod} = 5953.93$$

$$< MTC_{Ebrahimnejad \text{ and } Verdegay} \\ = 7530.96$$

The proposed method is remarked to give finer solution with less transportation cost.

5. CONCLUSION

Introducing a novel strategy for Intuitionistic Fuzzy Transportation Problems (IFTP), this approach is grounded in the GM-R method. Specifically designed to address various types of TIFNs and TrIFNs, Generalized TIFNs and TrIFNs, this method furnishes optimal solutions and optimum values in a precise, crisp format—providing a significant advantage for decision-makers and experts. The application of this method is straightforward, requiring minimal complexity in computations. Its validity is scrutinized through a comparative study against methods that have undergone multiple evaluations. Notably, the method demonstrates increased efficiency, evident in superior optimal solutions as observed in numerical comparisons.

- Aggrarwal, S & Gupta, C. (2016). Solving intuitionistic fuzzy solid transportation problem via new ranking method based on signed distance. *International Journal of Uncertainty, fuzziness and knowledge-Based systems*, 24(4), 483-501. <https://doi.org/10.1142/S0218488516500240>.
- Beg, I., Monica Bisht. M., & Rawat. S (2023). An approach for solving fully generalized intuitionistic fuzzy transportation problems. *Computational and Applied Mathematics*, 42(8). <https://doi.org/10.1007/s40314-023-02467-8>
- Bellman, R.E. & Zadeh, L.A. (1970). Decision making in a fuzzy environment. *Management Science*, 17(4), 141–164. <https://doi.org/10.1287/mnsc.17.4.B141>.
- Ebrahimnejad, A. & Verdegay, J.L. (2017). A new approach for solving fully intuitionistic fuzzy transportation problem. *Fuzzy Optimization and Decision Making*, 17(4), 447-474. <https://doi.org/10.1007/s10700-017-9280-1>
- Gani, A.N & Abbas, S. (2013). A new method for solving intuitionistic fuzzy transportation problem. *Applied Mathematical Sciences*, 7(28), 1357-1365. <https://doi.org/10.12988/ams.2013.13124>
- Hitchcock, F.L. (1941). The distribution of a product from several sources to numerous localities. *Journal of Mathematical Physics*, 20, 224-230. <https://doi.org/10.1002/sapm1941201224>
- Hunwisai, D., Kumam, P. & Kumam, W. (2019). A new method for optimal solution of intuitionistic fuzzy transportation problems via generalised trapezoidal intuitionistic fuzzy numbers. *Fuzzy Information and Engineering*, 11(1), 105-120. <https://doi.org/10.1080/16168658.2021.1886815>
- Hussain, R.J & Kumar, P.S. (2012). Algorithmic approach for solving intuitionistic fuzzy Transportation problem. *Applied Mathematical Sciences*, 6(80), 3981-3989. <https://www.m-hikari.com/ams/ams-2012/ams-77-80-2012/senthilkumarAMS77-80-2012.pdf>
- Hussain, R.J & Kumar, P.S. (2012). The transportation problem in an intuitionistic fuzzy Environment. *International journal of mathematics research*, 4(4), 411-420. https://www.ripublication.com/irph/ijmr/ijmr4n4_12.pdf
- Kumar, P.S. & Hussain, R.J. (2015). Computationally simple approach for solving fully intuitionistic fuzzy real life transportation problems. *International Journal of System Assurance Engineering and Management*, 7(1), 90-101. <https://doi.org/10.1007/s13198-014-0334-2>
- Kumar, P.S. (2018). A note on “A new approach for solving intuitionistic fuzzy transportation problem of type2”. *International Journal of Logistics Systems and Management*, 29(1), 102-129. <http://dx.doi.org/10.1504/IJLSM.2018.088586>
- Narayananamoorthy, S. & Deepa, A. (2017). A method for solving intuitionistic fuzzy transportation problem using intuitionistic fuzzy Russell’s method. *International Journal of Pure and Applied Mathematics*, 117(12), 335-342. <https://acadpubl.eu/jsi/2017-117-11-14/articles/12/37.pdf>
- Nishad, A.K. & Abhishek. (2020). A new ranking approach for solving fully fuzzy transportation problem in intuitionistic fuzzy environment. *Journal of Control, Automation and Electrical systems*, 31(4), 900-911. <http://dx.doi.org/10.1007/s40313-020-00611-x>
- Pramila, K & Uthra, G. (2014). Optimal solution of an intuitionistic fuzzy transportation problem. *Annals of pure and applied mathematics*, 8(2), 67-73. <http://www.researchmathsci.org/apamart/apam-v8n2-9.pdf>
- Purushothkumar, M.K. Ananathanarayanan, M. & Dhanasekher, S. (2018). A new approach to solve fuzzy intuitionistic fuzzy transportation problems by using diagonal optimal algorithm. *International Journal of Mechanical Engineering and Technology*, 9(11), 1675-1680. <http://iaeme.com/Home/issue/IJMET?Volume=9&Issue=11>
- Rani, J. J., Dhanasekar, S., Raj, M. D. & Manivannan, A. (2023). On solving fully intuitionistic fuzzy transportation problem via Branch and Bound technique. *Journal of Intelligent and Fuzzy Systems*, 44(4), 6219-6229. <https://doi.org/10.3233/jifs-221345>
- Taghaodi, R. (2019). A novel solution approach for solving intuitionistic fuzzy transportation problem of type2. *Annals of Optimization Theory and Practice*, 2(2), 11-24. <https://doi.org/10.22121/aotp.2019.198947.1022>
- Uthra, G. Thangavelu, K. & Umamageswari, R. M. (2017). An optimal solution for generalized Trapezoidal intuitionistic fuzzy transportation problem. *Advances in Fuzzy Mathematics*, 12(3), 763-770. https://www.ripublication.com/afm17/afmv12n3_28.pdf
- Zadeh, L. A. (1965). Fuzzy Sets. *Information and Control*, 8(3), 338-353. [https://doi.org/10.1016/S0019-9958\(65\)90241-X](https://doi.org/10.1016/S0019-9958(65)90241-X)
- Zimmermann, H. J. (1983). Fuzzy mathematical programming. *Computers & Operations Research*, 10(4), 291-298. [https://doi.org/10.1016/0305-0548\(83\)90004-7](https://doi.org/10.1016/0305-0548(83)90004-7)

Veerraju Nalla
SRKR Engineering College,
Bhimavaram-534203
Andhra Pradesh
India
veerrajunalla@gmail.com

L N P Kumar Rallabandi
Vishnu Institute of Technology,
Bhimavaram-534202
Andhra Pradesh
India
Pradeepkumar.r@vishnu.edu.in

P. S. Brahmanandam
Department of Physics
Shri Vishnu Engineering College for
Women (A)
Vishnupur, Bhimavaram- 534202
Andhra Pradesh, India.
dranandpotula@svecw.edu.in



DESIGN OF SMART TOURISM SYSTEMS TO FORECAST FOREIGN TOURIST ARRIVAL RATE USING DEEP LEARNING TECHNIQUES

Ratna Kanth. Gudala
Ravi Kumar. Suggala¹
Venkata Nagaraju Datla
Sri Krishna. Adusumalli

Keywords:

Deep Learning; DNN; Forecasting;
Foreign Tourist Arrivals; GRU; LSTM;
RNN; Tourism

A B S T R A C T

India's tourism potential is vast, driven by its rich history, diverse ecology, and extensive natural beauty. The country offers various niche tourism experiences, including cruises, adventure, medical, wellness, sports, MICE, eco-tourism, film, rural, and religious tourism. Recognized as the third largest foreign exchange earner, India's tourism industry is of paramount importance. However, existing research often neglects critical aspects such as predicting tourism trends, enhancing hospitality, and improving the visitor experience. This research focuses on developing smart tourism systems through data analytics and deep learning techniques, like RNN, LSTM-RNN, GRU-RNN, CNN, and DNN, to forecast foreign tourist arrivals. A detailed comparative analysis of these methods identifies the most suitable technique. Additionally, the study conducts yearly trend analysis for essential parameters like domestic tourism, tourism's impact on GDP, foreign exchange earnings, and government expenditure, using visualization tools. By harnessing technology and data-driven insights, this research aims to ensure the sustained growth and advancement of India's tourism industry, providing a foundation for improved planning and management.



© 202x Published by Faculty of Engineering

1. INTRODUCTION

Tourism industry is one of the significant domains in improving the economy status and foreign exchange earnings. Since the tourism domain is considered to be most developing and fascinating in India, this industry demands more researchers to contribute towards its enhancement. As an indication of this scenario, India has secured seventh rank among Asia-pacific zones in the

world tourism industry (https://en.wikipedia.org/wiki/World_Tourism_rankings). This has led to the tourism industry to adopt smart tourism systems by using ICT tools and techniques to increase the GDP of the country. To analyze foreign tourist arrivals to understand the trend, demand, Government contribution to tourism, trend of foreign exchange earnings, and yearly contribution of tourism to GDP. A century of Smart Tourism is a kind of massive tourist

¹ Corresponding author: Name Surname (Times New Roman 8pt)
Email: active_email_adress

information and providing relevant services to the tourist. In smart tourism, a dataset is created using tourist demographic data, tourism management and marketing data. The Data analytics model is designed to analyze tourism data for predicting future demands and trends on the tourism visits and other logistics requirements related to the tourism industry (Athiyaman et al., 2008). These results will enable the tourist industry to serve the tourist better by providing more valuable information based on their interest, sentiments, and opinions (Song et al., 2008). The predictive analytics involved in the tourism industry always prefers the parameter foreign tourist arrivals to the country (Lo et al., 2017) (Ginsberg et al., 2009).

Many researchers have addressed some more parameters other than "foreign arrival rate" are foreign exchange earnings, GDP (Adeola et al., 2008) and Political stability (Huang, H. C, 2013.). By forecasting the parameter "arrival rate" to the particular scenic site in prior, used to satisfy the essential needs domestic needs like accommodation, temporary stall preparation etc. Initially at earlier stages, most of the forecasting tourism demand utilized big data concepts to establish their predictions (Goh et al., 2011) in a very efficient and consistent manner both theoretical as well as practical. In real time statistics tourism data or search logs used in tourism data analytics are always massive in size for instance google trends intend to provide versatile data to predict the many important parameters (Moro, S. et al., 2016.). The prediction of the tourist flow of the particular site using offline mode is not reliable for real time purposes (Song et al., 2008.).

In existing solutions many diverse varieties of approaches are found they are machine learning, deep learning techniques, economics, qualitative, time series based and quantitative (Xiaoxuan et al., 2016). But recently machine learning techniques are always less performance than deep learning techniques (Choi, H. et al., 2016.) in case of large amount of dataset. In tourism industry also they paid their attention towards utilizing the deep learning architectures for predicting foreign tourist arrivals in efficient manner (Poonkuzhal, S. et al., 2018.).

In this research work, a general framework for predicting International Tourist arrivals has been designed using various deep learning models to boost the economy of the Indian Tourism Market.

The platform involves three key tasks, namely pre-processing, Predictor engines and visualization of data to allow an efficient study of the rate of arrival of tourists to India. The data collected is pre-processed to produce a quality result, and then various deep learning classifiers and visualization techniques are used to analyze the demand for foreign tourist arrivals in India.

The overall contribution of this work is summarized as below:

- To design an efficient framework of forecasting models for the Tourism Industry.
 - To apply various deep learning techniques to forecast foreign tourist arrival rate
 - To derive the best deep learning classifier to build forecasting models to enable smart tourism by comparing the performance metrics.
- To do annual trend analysis of Domestic tourism, tourism contribution to GDP, Foreign Exchange Earnings, Government expenditure to tourism using visualization techniques.

The rest of the paper is organized as follows: In section 2, the relevant work which is used to predict the tourist flow arrivals has been discussed in detailed manner. The section 3 clearly demonstrates each step involved in the proposed model used for time series prediction. The experimental setup and its obtained results for prediction as well as trend analysis are elaborated in the section 4. Section 5 ends with the conclusion and its future work.

2. RELATED WORKS

Chang et al., (2017) acquired knowledge from public repository like Google Trends, Google search engine, Google Analytics, Flickr, social networks to provide the conclusion point about the source whose provides the most informative about the particular tourist destination with the help of searched keywords by implementing Depth data analysis. Yu-Wei et al., 2018 presented a forecasting model to predict tourist arrival rate using two techniques such as SVM and neural network (MLP) along with feature reduction techniques and this designed model is trained and evaluated using data logs of Tourism Satellite Account (TSA). Zhang et al., (2020) proposed a time forecasting model to do prediction in the tourism industry. Author used the daily tourist flow and consumer search data of Jiuzhaigou

tourist spot in China, from 8 October 2013 to 7 August 2017 as a database to evaluate their forecasting model. The deep learning architecture namely LSTM is used for prediction processes. Ren et al., (2018) designed an intelligent framework for smart tourism using machine learning algorithms. Author predicted the number of incoming tourists visiting the particular tourist spot (Jiuzhaigou). The online gradient descent algorithm of the fixed buffer kernel is used to predict the number of tourists and the BOGD algorithm. Havranek et al., (2019) presented a forecasting model in smart tourism based on online search data by the users. This prediction model works on the keywords entered in the tourism management website in Indonesia. Author implemented country wise foreign visitor prediction using the Vector Error Correction Model (VECM).

Havranek et al (2019) designed a prediction model for tourist arrival rate and overnight stay using Google meets rather than keyword retrieval along with mixed data sampling (MIDAS). Yishuo et al [22] proposed a novel model which combines group pooling method with deep learning method to predict tourist arrival rate, travel blog, best food and air Asia. Then the author proposed Dynamic time warping for clustering Quantitative approach. Wolfram et al [23] presented a framework to predict the tourist arrival rate using the ARIMA model along with web search data as an input attribute. Then the author compares the ARIMA model with ANN to evaluate its performance and ANN outperforms ARIMA. Navoneel et al [24] proposed distribution and trend analysis for the foreign visitors to India using a four headed machine learning model. With the help of various hyper parameters of Gross Domestic Product and Foreign Exchange Earnings as input parameters whereas each model is trained separately at last all the four model results have been combined for prediction.

At the end of this survey, it can conclude that only one work is based on India tourism dataset, most probably all the existing forecasting methods rely on usual regression

techniques such as LSTM [25], ARIMA, MLP and ANN. Hence in this work, some deeper learning techniques such as CNN, RNN, GRU-RNN DNN along with LSTM-RNN and the comparison study has been done by analyzing using various quality metrics. Moreover, this work is designed in the way like time series forecasting, and the time parameter considered here is year alone rather than choosing the entire timestamp and date.

3. METHODOLOGY OF PROPOSED SYSTEM

Figure 1 demonstrates the system overview of the forecasting model used to predict the count of foreign tourist arrivals as the time series forecasting. The layers involved in the forecasting model are given as Data preprocessing layer, Feature selection layer and prediction layer.

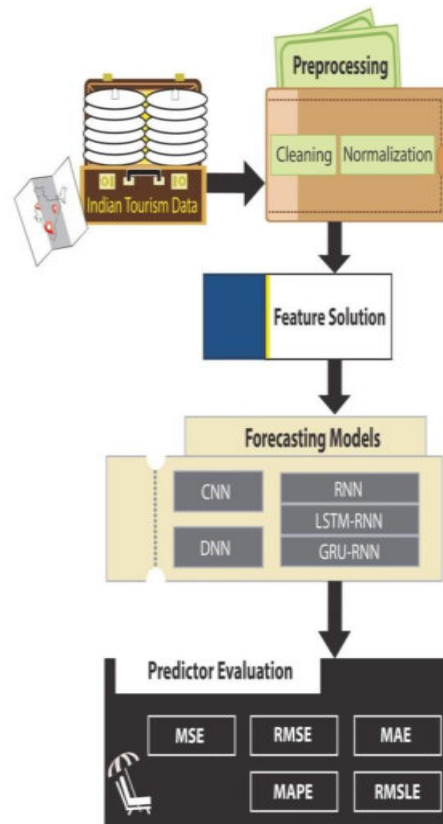


Figure 1. Overview of the proposed model

The process and the algorithm involved in each layer is elaborated as follows as

3.1 Data Preprocessing Layer

Data preprocessing layer involves two processes: data cleaning and normalization. In data cleaning steps, null values exist in the dataset are removed in row wise order to enhance the accuracy of the predicting. The resultant dataset is subjected to the normalization process in order to facilitate the forecasting task. In the normalization process, the instances in the dataset are normalized in the range of 0 to 1 and it is computed using the following Equation (1) where the parameter N is considered to be the number of samples given in the dataset.

$$N' = \frac{N - \min}{\max - \min} (\max' - \min') + \min' \quad (1)$$

3.2 Feature selection Layer

In this layer, only two parameters have been extracted manually without using any specific feature selection method. Since this design relies on time series forecasting, only “period” has been assigned as input attribute and foreign tourist arrivals are considered as target variable or predictor variable.

3.3 Prediction Layer

In this layer, the prediction of the target variable has been carried out using the following deep learning techniques and it is explained in detailed manner. Here the predictor variable is “Foreign Tourist Arrival” and the year is used as an index for time series prediction. Based on the past year, the future year will be predicted in the testing stage. In this dataset, count of foreign tourist flows starts from the year 1951 to 2017. Some of the years namely 1952, 1953, 1954, 1957, 1958, 1959, 1962, 1963, 1964, and 1967 do not have their corresponding foreign tourist arrival value. So, these rows of these years are removed completely. In this regard, first 41

number of samples were considered for training phase and the last remaining 16 samples (2002 to 2017) used for testing phase

3.3.1 CNN (Convolutional Neural Network)

Convolutional Neural Network is a subset of artificial neural networks. Traditionally CNN is always used for image processing applications but very recently it seeks attention towards time series forecasting problems and it also performs well. It is also a specialized version of a multilayer perceptron and it works like the biological process of the human brain. The process “convolution” acts as a basic block in convolution neural networks. The term “Convolution” defines the filter process used to filter the input data to form a feature vector. The repeated process of convolution yields the feature map from the input data. This process scenario makes CNN learn deeply about the input data to build the feature vector.

3.3.2 DNN (Deep Neural Network)

Deep neural network is one type of artificial intelligence which comprises single input and output layers with multiple hidden layers. This artificial neural network works like the human brain whereas each hidden layer has one activation function to process the incoming input values and those values are passed to the next layer. This process will continue till the processed values reach the output layer. The number of neuron nodes in the output layer will be equal to the number of labels which are intent for classification.

3.3.3 RNN (Recurrent Neural Network)

Recurrent Neural Network is another kind of artificial neural network but the only difference of recurrent neural networks when compared with previously discussed is that RNN is capable of processing the input sequence without the knowledge of its sequence size. It does not possess any restriction in terms of the input size. RNN is

capable of even remembering the information about the input sequence, so based on the knowledge learnt from the past input sequence can be used to predict the present input values. Most of the neural network has the ability to remember the input sequence during training phase only but RNN alone can use this input information at producing output phase too.

3.3.4 LSTM-RNN (Long Short-term Memory Recurrent Neural Network)

Long Short-term Memory (LSTM) is a special extension of recurrent neural networks and it is designed to overcome the problem of long-term dependencies. Unlike RNN, LSTM has four neural network layers rather than a single layer inside a repeating module. The basic unit present in the architecture of LSTM is cell state. Its structure resembles a conveyor belt which flows through the entire network layers to carry over the information on it. The component which has the ability to change the information present in the cell state is called gates. The internal structure is composed of sigmoid neural net layer and a point wise multiplication operation. Most commonly an LSTM consists of three gates to control its flow of information inside its architecture. Generally, LSTM is always preferring for time series forecasting purpose because of its memory cell nature (Gers & 2000)

3.3.5 GRU-RNN (Gated Recurrent Unit Recurrent Neural Network)

Like LSTM, GRU is also used to overcome the vanishing gradient problem. The vanishing gradient problem is the loss of information during training the network. It works like LSTM except that it has a forget gate but works only with fewer parameters and it also has an update gate and reset gate. These two gates are utilized to make decisions to pass the data to the output node. These gates of the GRU are capable of keeping track of input data for a long period of time without deleting it. So GRU is well suited to make predictions for massive amounts of database.

Table 1 demonstrates the various hyper parameters used to design the five deep learning techniques individually. While analyzing these parameters, it shows that all the deep learning techniques have common value for epoch and batch size. Here the Dropout layer is used for DNN alone, not for other techniques. Except RNN remaining four deep learning used “Adam” as its optimization function and RNN used “rmsprop” as optimizer.

Table 1. Hyper Parameters set for all models

Model	Model Structure	Activation Function	Dropout	Batch Size	Epoch	Number of Layers	Optimization Function
CNN	16,3 2,1	Relu	-	12	100	3	adam
DNN	512, 256, 1	Relu	0.0 1	12	100	3	adam
RNN	16,8 .1	Relu	-	12	100	3	rmsprop
LSTM-RNN	4,1	Relu	-	12	100	2	adam
GRU-RNN	4,2, 1	Relu	1	12	100	3	adam

4. EXPERIMENTAL SETUP AND DISCUSSION

The proposed model was designed on a Core i3 Laptop with 2.30 GHz CPU and 4 GB RAM using python version 3.5.1 software environment. These five algorithms were implemented using the keras (Chollet, K., 2015.) package with TensorFlow as a backend environment. The designed model is trained using dataset (Piramanayagam and Senthilkumaran, 2018.) extracted from statistics involved in tourism starts from the year 1951 to 2016. It has various input parameters relevant to tourism contribution to GDP (in terms of million), foreign tourist arrivals, period (year), percent of share of

India FTA. Among these input attributes only “period” is taken as input and “Foreign tourist arrivals” is taken as output. This model is designed as a time series prediction for the variable “Foreign tourist arrivals”.

The performance evaluation of the five prediction algorithms has been conducted using the following quality measures such as

4.1 MSE or Mean Square Error

$$MSE = \frac{1}{n} \sum (predicted - expected)^2 \quad (2)$$

Mean Square Error is defined as the square value of the average difference between the predicted values and the expected outcomes

4.2 RMSE or Root Mean Square Error

Root Mean Square Error is defined as the frequently used measure of the square value of the average difference between the predicted values and the expected outcomes

$$RMSE = \sqrt{MSE} \frac{1}{n} \quad (3)$$

4.3 MAE or Mean Absolute Error

Mean Absolute Error is defined as the average difference between the predicted values and the expected outcomes

$$MAE = \frac{1}{n} \sum (predicted - expected) \quad (4)$$

4.4 MAPE or Mean Absolute Percentage Error

$$MAPE = \frac{100\%}{n} \sum \left| \frac{Expected - Predicted}{Predicted} \right| \quad (5)$$

Mean Absolute Percentage Error calculates the accuracy of the forecasting values by the predictor algorithm

4.5 RMSLE or Root Mean Squared Logarithmic Error

Root Mean Squared logarithmic Error measure about the relative error lies between the actual and predicted outcomes

4.6 Bias

Bias is a measure about the prediction ability of the model to predict the closest value of the expected outcome

Whereas the description of the parameters used to performance metrics are given below:

“n” denotes the number of samples considered
“predicted” denotes the predicted target samples

“Expected” denotes the original target samples

Table 2. Performance metrics for Prediction algorithm

Algorithm used	MSE	RMS E	MA E	MA PE	RM SLE	Bias
CNN	0.0015	0.096	0.0361	8.8711	0.013	0.0015
DNN	0.0006	0.096	0.0241	9.857	0.0083	0.024
RNN	0.00001	0.0975	0.001725	9.201	0.0007	0.0011
LSTM-RNN	0.0001	0.101	0.0113	9.614	0.005	0.011
GRU-RNN	0.0003	0.095	0.0149	8.956	0.004	0.014

Table 2 demonstrates the above-mentioned performance metric of the five deep learning techniques. The metric MSE is too for RNN (0.00001) after that LSTM performs to the next level. But for the RMSE metric GRU-RNN holds the least value 0.096 and DNN, CNN stands at the next level by achieving the error value of 0.096. For the case of MAPE and RMSE again RNN holds the least value. Based on this discussion, it can conclude that performance metrics indicates RNN achieves better performance whereas LSTM RNN achieves very least performance when compared to the remaining algorithms. Apart from DNN, the CNN, GRU and Simple RNN performs better than LSTM. In Table 3 the comparison between original values and the predicted values for all the prediction algorithms has been explored. On the whole, it is clearly shown that DNN predicted the value which is closest to the original values. In the

next stage of GRU-RNN and RNN stands in the next level in predicting the values.

Figure 2 explores the predicting behavior of five deep learning techniques. This graph plots between predicted values and the original values. From this figure it can clearly conclude that RNN has the very least gap between the predicted and original outcomes.

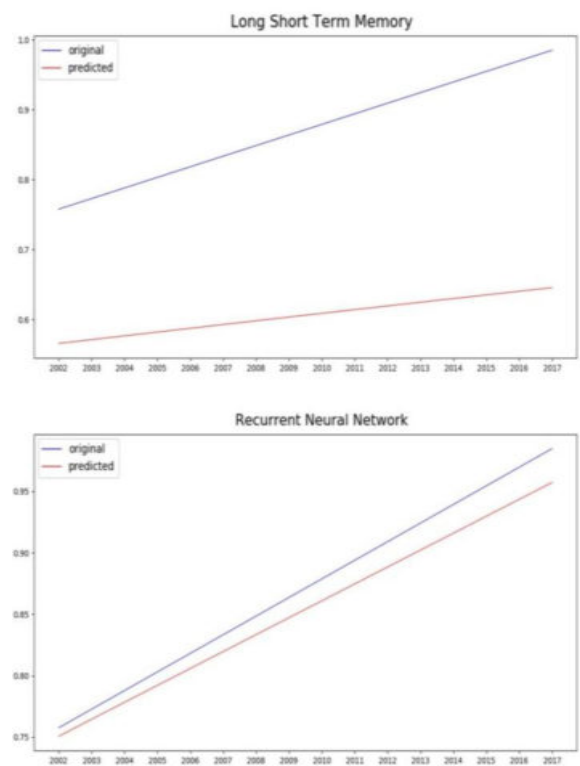
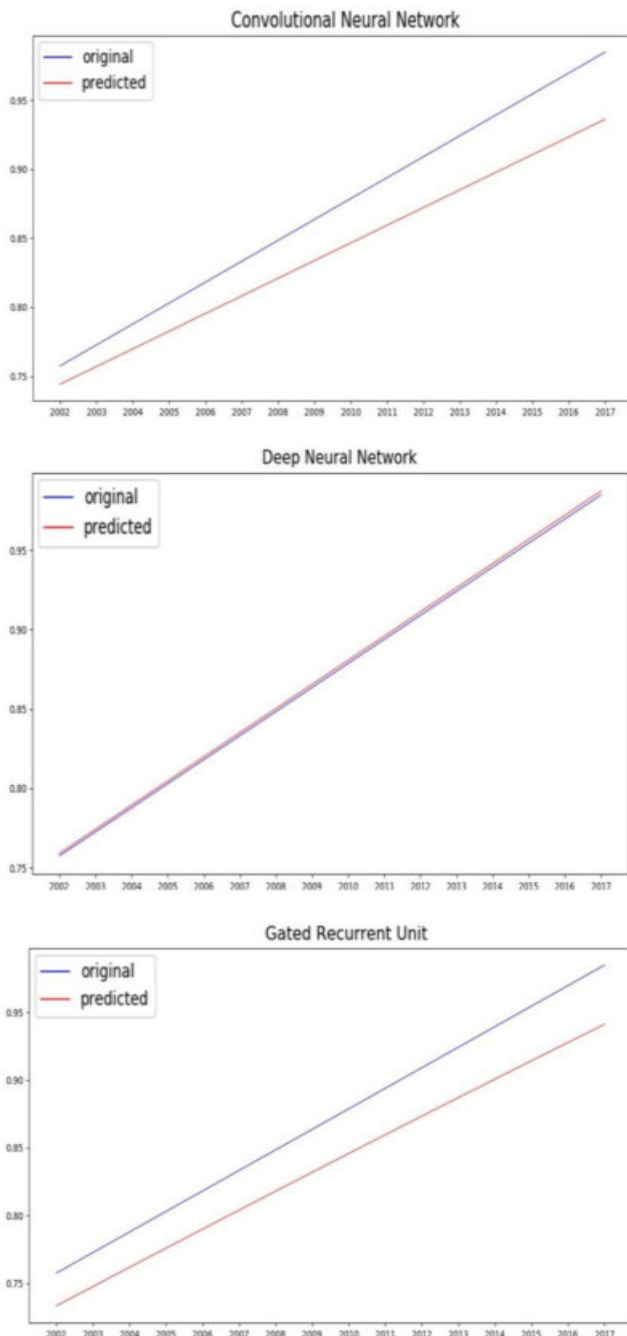


Figure. 2. Performance plot of five deep learning techniques CNN, DNN, RNN, LSTM-RNN & GRU-RNN

Table 3. Comparison between original values Vs Predicted values

Actual Values	Predicted Values				
	CNN	DNN	RNN	LSTM-RNN	GRU-RNN
0.757576	0.723697	0.7570425	0.74888426	0.7680912	0.7473688
0.772728	0.7340135	0.7720615	0.7611263	0.78450704	0.76258165
0.787880	0.74433064	0.7870824	0.77336967	0.80094224	0.7777555
0.803032	0.75441355	0.8021033	0.7856132	0.8173912	0.79288334
0.818182	0.76447165	0.81712425	0.7978567	0.8338511	0.8079598
0.833334	0.7745285	0.83214325	0.81009865	0.8503165	0.82297814
0.848486	0.7845866	0.84716415	0.82234216	0.86678857	0.8379371
0.863638	0.79464465	0.862185567	0.834582	0.8832622	0.85282993
0.878788	0.8047028	0.87720597	0.8468292	0.89973474	0.8676523
0.893940	0.8147597	0.8922249	0.85907114	0.91620106	0.88239783
0.909092	0.8248178	0.9072459	0.87131464	0.9326628	0.89706576
0.924244	0.8348759	0.9222641	0.8835581	0.94911534	0.9116502
0.939394	0.844934	0.9372798	0.89580166	0.96555585	0.9261471
0.954546	0.85499084	0.9522937	0.9080435	0.9819803	0.940551
0.969698	0.86504894	0.9673094	0.92028695	0.9983902	0.9548619
0.984850	0.875107	0.98232514	0.9325305	1.0147816	0.96907413

4.7. Trend analysis

In this section, the yearly analysis for various important parameters has been visualized and analyzed in a deep way. In Figure 3 the parameter domestic tourism has been plotted for each year starting from 1989 to 2017. The term domestic tourism defines the flow of tourist visits to the particular scenic spot arises from the local areas or in other words tourists from the same country. From the observation of figure 2, it reveals that for the year 1989, 1990, 1991 has very low number of tourists (in terms of millions) and it is gradually increasing for the upcoming year up to 2017. Anyway, the domestic tourism improves the GDP of our country but not to the foreign exchange earnings.

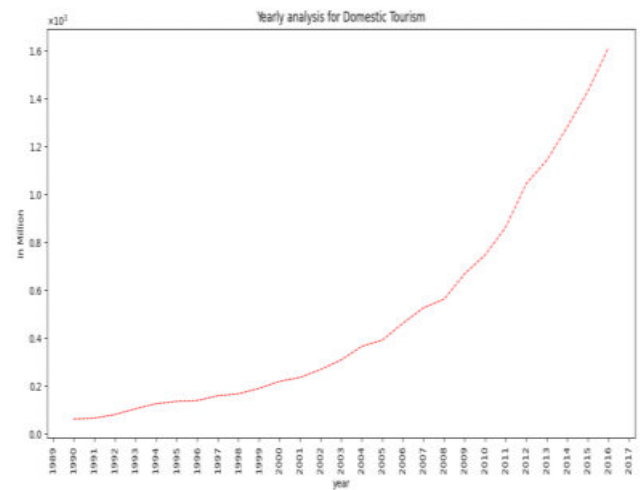


Figure 3. Annual Trend for Domestic Tourism

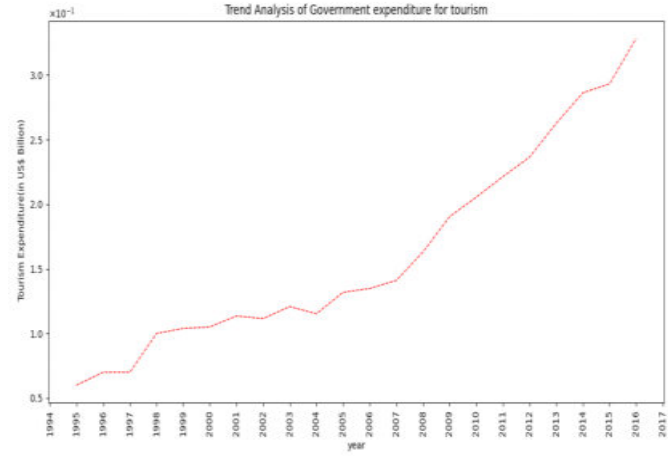


Figure 4. Government contribution for Tourism industry

Figure 4 demonstrates the fund provided by the government to the country for the tourism industry in year wise. This figure reveals that the data starts from the year 1994 to 2017. The contribution is similar for the years 1995 to 1997 and it increases slowly for 1998. The same range is maintained till the year 2005 and the contribution increases exponentially up to 2017. The reflection of this contribution can be seen in Figure 5. The high amount of contribution leads to increased foreign exchange earnings for the year starting from 2003 to 2017.

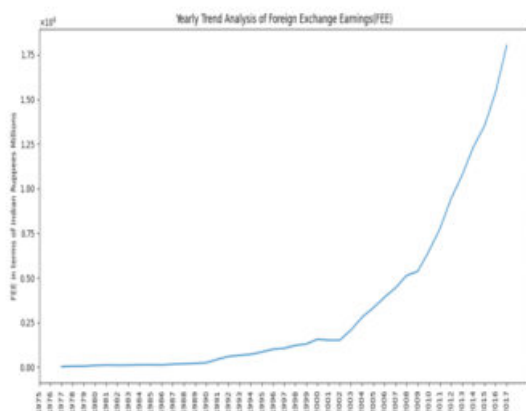


Figure. 5. Trend of Foreign Exchange Earnings

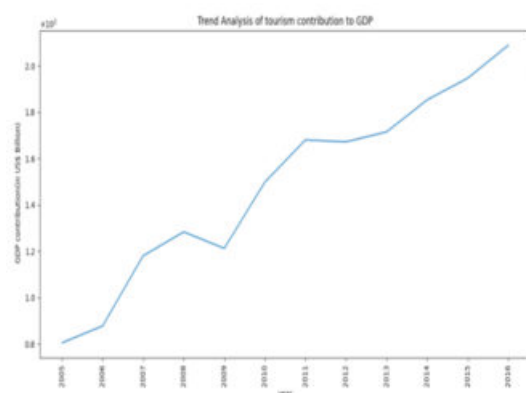


Figure. 6. Yearly tourism contribution to GDP

Figure 6 shows the GDP contribution provided by the tourism industry in the yearly manner starting from 2005 to 2016. In this graph, GDP keeps on increasing slowly but it bends down slightly for the year 2009 and again it increases rapidly till 2011. It has been in a stable position from 2011 to 2013 and then it

increased till 2016. Here we can come to the conclusion increases of foreign exchange earning tend to contribute more for the increase in GDP value rather than Domestic tourism

5. CONCLUSION

The number of foreign tourist arrivals to the country is the most prominent parameter that exists in the tourism industry. So, prediction of these parameters leads to exploring the yearly trend analysis and to predict the upcoming foreigners to India. Hence in this work, we mostly used deep learning techniques such as DNN, RNN, LSTM-RNN, GRU-RNN and CNN. These deep learning techniques were evaluated using various quality measures such as MSE, RMSE, MAPE, MAE, RMSLE and Bias. At the end of each evaluation, it clearly shows that DNN outperforms the remaining four techniques in predicting the foreign tourist arrivals. Next to DNN, RNN performs at the next level. The performance of both algorithms only has slight variation in terms of performance. Then using visualization techniques, yearly trend analysis has been done for some of the new parameters which tend to influence the GDP of our country.

References:

- https://en.wikipedia.org/wiki/World_Tourism_rankings
- Adeola, O., Boso, N., and Evans, O (2008). Drivers of international tourism demand in Africa, *Business Economics*, 53(1), 25-36. doi:10.1057/s11369-017-0051-3.
- Athiyaman, A., and Robertson, R. W (1992) Time series forecasting techniques: Short-term planning in tourism, *International Journal of Contemporary Hospitality Management*, 4(4), 8–11, .doi:10.1108/09596119210018864.
- Bengio, Y., Simard, P., and Frasconi, P (1994). Learning long-term dependencies with gradient descent is difficult. *IEEE Transactions on Neural Networks*. 5(2), 157–166. doi:10.1109/72.279181.
- Chakrabarty, N (2020). A Regression Approach to Distribution and Trend Analysis of Quarterly Foreign Tourist Arrivals in India, *Journal of Soft Computing Paradigm (JSCP)*. 2(1), 57-82. doi:10.36548/jscp.2020.1.006.

- Chang, Y. W., and Tsai, C. Y, (2017). Apply deep learning neural network to forecast number of tourists, *Proceedings of the IEEE International Conference on Advanced Information Networking and Applications Workshops*, Taipei, Taiwan, 259–264. <https://ieeexplore.ieee.org/abstract/document/7929687/>.
- Choi, H., & Varian, H. (2016). Predicting the present with Google Trends. *Economic Record*, 88(S1), 2–9. doi:10.1111/j.1475-4932.2012.00809.x.
- Chollet, K. (2015). Keras. Retrieved from <https://github.com/fchollet/keras>
- Gers, F. A., Schmidhuber, J., and Cummins, F. (2000). Learning to forget: Continual prediction with LSTM, *Neural Computation*, 12(10), 2451–2471. doi:10.1049/cp:19991218.
- Ginsberg, J., Mohebbi, M. H., Patel, R. S., Brammer, L., Smolinski, M. S., and Brilliant, L.(2009). Detecting influenza epidemics using search engine query data. *Nature*, 457(7232),1012-1014. doi:10.1038/nature07634.
- Goh, C., and Law, R. (2011). The methodological progress of tourism demand forecasting: a review of related literature, *Journal of Travel & Tourism Marketing*, 28(3),296-317. doi:10.1080/10548408.2011.562856.
- Haqiq, A., and Pharmasetiawan, B. (2019). Data Analytics for Forecasting Arrival of Tourism Visit in Indonesia, *International Conference on ICT for Smart Society (ICISS)* 7(1),1-6. doi:10.1109/iciss48059.2019.8969795.
- Havranek, T., and Zeynalov, A. (2019). Forecasting tourist arrivals: Google Trends meets mixed-frequency data . *Tourism Economics*, oct.2019, doi:10.1177/1354816619879584.
- Höpken, W., Eberle, T., Fuchs, M., and Lexhagen, M,(2020). Improving Tourist Arrival Prediction: A Big Data and Artificial Neural Network Approach, *Journal of Travel Research*, Jun,2020,doi:10.1177/0047287520921244.
- Huang, H. C (2013). The construction of a Visitor number forecasting model for the Shihmen Reservoir recreation area using artificial intelligence technology. *Journal of Theoretical and Applied Information Technology*, 54(1), 14-19..
- Kim, K. J. (2003). Financial time series forecasting using support vector machines. *Neurocomputing*, 55(2), 307-319. doi:10.2139/ssrn.1879865.
- Krsak, B., and Kysela, K. (2016). The use of social media and Internet data-mining for the tourist industry, *Journal of Tourism and Hospitality*, 5(1), doi:10.4172/2167-0269.1000197.
- Li, J., Xu, L., Tang, L., Wang, S., and Li, L. (2018). Big data in tourism research: A literature review, *Tourism Management*, .(68), 301-323,Oct,2018,doi:10.1016/j.tourman.2018.03.009.
- Lo, S. C. and Lin, C. F (2017) .Cooperative-Competitive Analysis and Tourism Forecasting of Southern Offshore Islands in Taiwan by Grey Lotka-Volterra Model. *Engineering Letters*.25(2). doi:10.12677/sa.2018.76077.
- Moro, S., and Rita, P. (2016). Forecasting tomorrow's tourist. Worldwide Hospitality and Tourism Themes. , doi:10.1108/whatt-09-2016-0046.
- Piramanayagam and Senthilkumaran. (2018). Tourism in India - Statistics 1951-2016, *Mendeley Data*, 1.1(2018). doi:10.17632/3pf2658csc.1
- Poonkuzhali, S and V. K. S. (2018). Improvising the sales of garments by forecasting market trends using data mining techniques. *International Journal of Pure and Applied Mathematics*, 119(7),797-805..
- Ren, Q.H. Li, S.L. Song, B. & Chen, C. (2018). The application of bounded online gradient descent algorithms for kernel based online learning in tourist number forecasting. In *Proceedings of The 18th International Conference on Electronic Business* (pp. 800-804).
- Song, H and Li, G (2008). Tourism demand modelling and forecasting—A review of recent research. *Tourism Management*, 29(2), 203–220, doi:10.1016/j.tourman.2007.07.016.
- Xiaoxuan, L., Qi, W., Geng, P., and Benfu, L. (2015). Tourism forecasting by search engine data with noise-processing. *African Journal of Business Management*, 10(6), 114-130. doi:10.5897/ajbm2015.7945.

Zhang, B., Li, N., Shi, F., and Law, R. (2020). A deep learning approach for daily tourist flow forecasting with consumer search data. *Asia Pacific Journal of Tourism Research*, 25(3), 323-339,, doi:10.1080/10941665.2019.1709876.

Zhang, Y., Li, G., Muskat, B., Law, R., and Yang, Y (2020). Group pooling for deep tourism demand forecasting. *Annals of Tourism Research*, 82(102899), doi:10.1016/j.annals.2020.102899.

Dr.Ratna Kanth Gudala

Shri Vishnu Engineering College for women,
Bhimavaram,
India
ratnakanth@svecw.edu.in

Mr.Ravi Kumar Suggala

Shri Vishnu Engineering College for women,
Bhimavaram,
India
ravikumars@svecw.edu.in

Dr. Venkata Nagaraju.

Datla

Shri Vishnu Engineering College for women,
Bhimavaram,
India
hodit@svecw.edu.in

Dr. Sri Krishna. Adusumalli

Shri Vishnu Engineering College for women,
Bhimavaram,
India
hodai@svecw.edu.in



STABILITY ANALYSIS OF ECOLOGICAL MODELS OF PLANT-ANIMAL INTERACTIONS IN RIPARIAN ZONES

Ravi Kiran Duvvuri¹

Rami Reddy Bhavanam

G. V. Ramana

K. Venkata Rao

Keywords:

*Ecological Models; Riparian Zones;
Predator-Prey Interactions;
Herbivores; Stability Analysis.*

ABSTRACT

The research summarizes the essential findings and open topics from previous stability analyses of models involving Riparian zones. These models are central to trophic interactions, ecological complexity, and species coexistence. Due to land use shifts and pollution, Riparian zones have been an intense subject of stability study of ecological model findings. This study models the interactions between species in Riparian zones, specifically, the interplay between predators and prey, as well as herbivores and their host plants as differential equations. The equilibrium points of the species are then determined and their stability is examined and conditions for stability are established



© 202x Published by Faculty of Engineering

1. INTRODUCTION

A riparian zone is a strip of land beside a river or stream. These areas are crucial for maintaining biodiversity and ecological stability. The intricate interdependencies between plants and animals in riparian zones may be better understood by exploring environmental models of plant-animal interactions. Riparian zones are biologically significant, and ecological models of plant-animal interactions help understand the myriad of factors at play there. Researchers and conservationists make more informed choices about how best to protect and restore riparian

ecosystems by learning more about these mechanisms. The aforementioned ecological models accurately portray the dynamic interplay between plants and animals and their responses to environmental changes in riparian zones. These zones, whether along a river bank or a shoreline, link wet and dry environments.

In this regard, the current study thoroughly reviews the stability analysis literature on these models, emphasizing key results and open questions. Trophic interactions, ecological complexity, and coexistence among species are at the center of these models. However, the effects of land use changes and pollutants on the riparian zone are also considered from analyzing

¹ Corresponding author: Ravi kirian Duvvuri
Email: duvvuriravikiran9@gmail.com

critical results associated with the stability analysis of ecological models. It reports predator-prey dynamics and herbivore-plant interactions of trophic interactions. Ecological models of animal-plant interactions in riparian zones need a systematic and thorough approach to data collection. Field observations, experimental methods, and remote sensing investigate these connections. Statistical approaches and ecological modeling are used to examine the data to uncover connections and patterns between different kinds of flora and fauna. Modeling species distributions, analyzing niches, and constructing networks are all essential for comprehending ecological connections. The water level, temperature, and luminosity may all be tracked using data recorders and sensors.

In the case of this recent research, it can be stated that possessing these Riparian zones presents a “diverse array of species and environmental procedures”. However, such ecological diversity is connected to different kinds of “flood regimes, altitudinal climate shifts, geographically unique channel procedures, and upland influences on the fluvial corridor”.

2. LITERATURE REVIEW

The study's literature review sheds light on the significance of structural diversity in riparian plants in providing ecological niches, protective cover, and food for a wide range of species, highlighted by the complexity of their habitat (Burdon *et al.*, 2020). The distribution and behavior of animals is impacted, changing the makeup of populations and species. The ability of many species to share a habitat and share resources despite competition for those resources is shown by the phenomenon of coexistence. Community organization and biodiversity in ecological zones rely heavily on these exchanges. Often, ecological stability is preserved by the complex interplay of these activities (Kéfi *et al.*, 2019). Human activities may upset the equilibrium of plant-animal interactions, setting off a cascade of negative consequences for the whole ecosystem.

This research is focused on accurate information and significant recommendations for the criteria of this content. Apart from this, this research study has presented several influential factors for developing the all-over concept of the present ecosystem of the Riparian zone. Based on the review of Veenma *et al.*, (2023), it can be stated here that the Riparian zones can capture up to “almost 90% of sediments, 30% of phosphorus, and 65% of nitrogen”. On the other side, these plants can absorb dissolved nutrients to combat eutrophication and excess nutrient levels. This mechanism is reliable for balancing the ecosystem (Neuet *et al.*, 2023). This research study has collected an accurate dataset from several secondary data sources. For this reason, the results of this content are valuable for stating the accurate factors and risk elements in this content based on this recent era.

Diversity and ecological resilience rely on coexistence strategies like niche differentiation and competition avoidance. Protecting biodiversity and providing ecosystem services are two roles that Riparian zones, ecotones between aquatic and terrestrial ecosystems, play. However, practical conservation and management efforts need an understanding of the stability of ecological models that describe plant-animal interactions in these zones. Ecological stability refers to the capacity of a model of an ecosystem to withstand and recover from disturbances while remaining in a steady state. Differential equations are used in ecology models that examine plant-animal interactions to depict population dynamics and food chain connections. These models are tested using equilibrium points, stability criteria (like eigenvalues), and Lyapunov functions. The coexistence and community structure of riparian species are shaped through trophic interactions. According to Mookherjee and Jurkevitch (2022), predator-prey dynamics result in oscillations and cyclic patterns, calling their stability into doubt. Factors like predator efficiency, prey survival trade-offs and density-dependent feedback mechanisms complicate stability analysis.

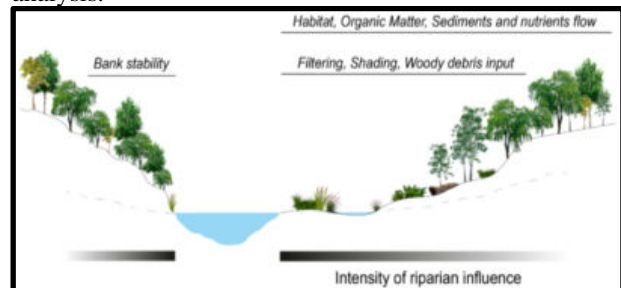


Figure 1. Stability Analysis of Riparian Zones
(Source: Pedraza *et al.*, 2021)

Riparian ecosystems are securer when they have more diverse habitats. With the focus on minimizing competition and boosting stability, Pedraza *et al.*, (2021) stress the value of a wide range of plant species establishing specialized niches. However, measuring a habitat's stability is complicated by the non-linear connection between habitat structure and stability. Assessing stability correctly requires consideration of spatial dynamics and stochasticity. Human activity has drastically altered the relationships between plants and animals in Riparian zones. Biological systems may become unstable due to habitat loss and pollution, according to Kruk *et al.*, (2019). Anthropogenic pressures need additional variables and non-linear threshold effects in ecological models.

Based on the objective and the criteria of this research, it can be pretty sustainable to state here that the aquatic areas of the world can be considered the “most productive ecosystems” on earth (Beyer *et al.*, 2023). On the other side, it can be annotated in this step of the study that the rivers, lakes, streams, as well as the wetlands, can be capable of providing the habitat for the minimum “25% of B.C.’s vertebrate, invertebrate, as

well as the vascular plant species". In the case of the Case *et al.*, (2023), it can be pointed out that these stated aquatic ecosystems can interact with the riparian areas closely. However, the areas can be the "zones of lush, green, moisture-loving vegetation" covered with wetlands, streams, lakes, and rivers. Based on the view of Chamoliet *et al.*, (2023), it may be quite significant to note that the riparian areas form "a transition zone between dry and aquatic upland habitats". These concepts are pretty reliable for the collected content for this current research study (Gallitelli&Scalici, 2023). This mechanism and the research structure are pretty effective for solving the recent risk factors based on the Riparian zones.

In the case of this present view 2.2, the "main stressors, plant disturbances and processes affected in riparian vegetation" can be noted sustainably. This concept is entirely sustainable for the selected topic of this current research study (Da Silva *et al.*, 2023). However, the concept of riparian vegetation functions as "soil, water protection, and conservation" (Gordon *et al.*, 2023). It can maintain the river's health by providing "mechanical support to soil" by the root system. On the other hand, through the concept of Hrubáet *et al.*, (2023), it needs to be stated here that the "physical properties of the soil" were quite influenced by these kinds of riparian vegetation. Based on the concert of this riparian vegetation, it can be noted that this can develop the soil texture. Besides these, it can be able to improve the quality of soil. However, the roots assist in increasing the "porosity of the soil". In this way, the OM level of the soil can be developed through the "addition of leaf litter" (Rizzuto *et al.*, 2023). This mechanism is quite reliable for the ecosystem of the earth. However, according to the review of Veenmaet *et al.*, (2023), it may be possible to point out here that the roots of the trees and the other vegetation can be able to assist in holding the soil. This concept is quite helpful for reducing the erosion rate of the soil.

From the view of Vissotoet *et al.*, (2023), it needs to be stated in this part of the research that this system can inhibit the "effect of water" on soil. It can reduce the soil loss by different practical elements by "interaction between vegetation cover and the soil gradient" in the case of Case et al (2023), it can be pointed out that the high soil moisture and the "nutrient content in riparian areas" can favor plant biomass production compared to the neighboring uplands.

Apart from this, based on the view of Chamoliet *et al.*, (2023), it may be quite significant to note that the riparian vegetation can act as a "barrier for highland

runoff". Besides these, it plays a vital role in the case of "interception, filtration, as well as the deposition of soil particles". This concept is entirely responsible for preventing erosion. The system is adequate for stabilizing the river bank. However, on the other hand, through the concept of Hrubáet *et al.*, (2023), it needs to be stated here that this procedure can lower the "velocity of runoff". In such a way, developing the "resistance of soil" towards erosion can be possible. The accurate information based on the Riparian zones can be noted in detail (Verzuhet *et al.*, 2023). However, based on this concept, it can be annotated here that the Riparian zones are the significant ecosystems located along the "banks of rivers, creeks, streams, as well as different kinds of the water networks". In the case of the Riparian zones, it can be stated that these zones are the "narrow strips of land". In the case of the view of Case *et al.*, (2023), it can be pointed out that these strips line the "borders of the selected water source".

However, these zones are pretty reliable for their buffer, the "body of water and animals" existing "in and around it". In the case of the review of Verzuhet *et al.*, (2023), it can be mentioned here that the natural state of this Riparian zone can act as a filter for keeping the water and its inhabitants healthy and clean. Apart from this, based on the view of Chamoliet *et al.*, (2023), it may be quite significant to note that the Riparian zones are becoming "composed of a mixture of vegetation types". For this reason, this can vary from place to place in a significant manner. However, the riparian vegetation based on the desert stream can be small and sparse; at the time, the vegetation along a significant mountain stream can be lush and tall.

The Accurate Concept and Importance of the Recent Riparian Zones Based on Various Kinds of the Plant-Animal Interactions. Based on the concept of this research, it can be noted here that the relevance in the Riparian zones is relatively high for the ecosystem and the procedure of the plant-animal interactions (Veenmaet *et al.*, 2023). Apart from this, these Riparian zones are relevant for the plants, wildlife, and aquatic species. Besides these, it is also significant for human societies. Through the concept of Yang *et al.*, (2023), it can be annotated here that many reliable habitats and species would be recovered within the stated areas. Conversely, the "flooding control and water quality concerns" may increase dramatically.

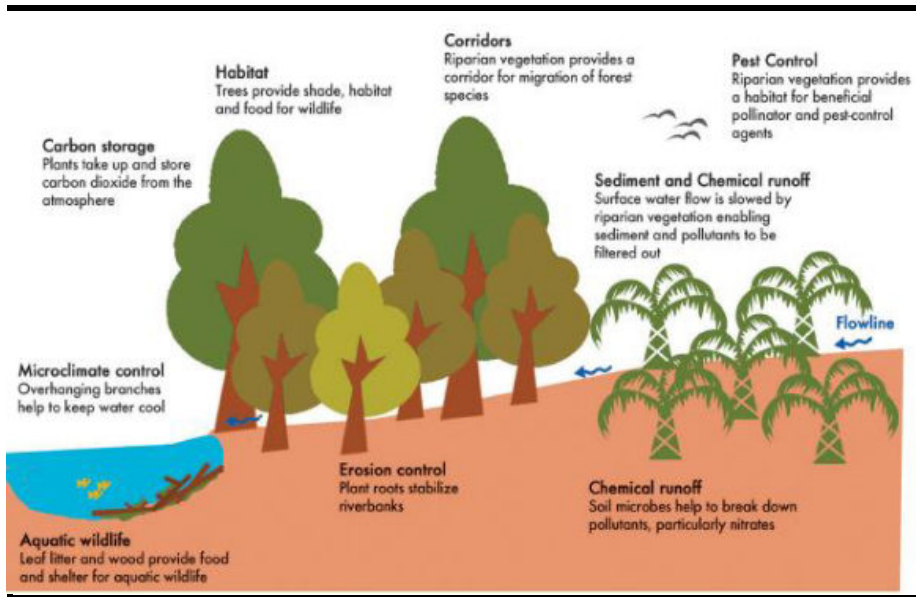


Figure 2. The Procedure of Riparian Reserves for Creating the Environmental Benefits to the River, Wider Landscape and Plantation (Source: Neu *et al.*, 2023)

In the case of Figure 2 above, the “mechanism of riparian reserves for creating the environmental benefits to the river, wider landscape and plantation” can be noted sustainably (Neu *et al.*, 2023). However, based on this research, it can be annotated here that the riparian reserves carry a significant “number of environmental benefits” for the present water systems. This water system includes filtering the water before it flows into the rivers, food protection, and stabilizing the river bank. On the other hand, it can be stated here that the concept of these riparian reserves is quite beneficial for “biodiversity conservation” in waterways and on land (Veenma *et al.*, 2023). It can be pretty significant for Carbon storage.

3. AREA AND DATA OF STUDY

The present study is confined to the fundamental ecosystem processes, and resilience is shown through stability in ecological models of plant-animal interactions in Riparian zones. Accounting research has enormous prospects to understand the dynamics of riparian systems better and create efficient conservation approaches despite the limitations of accounting for complexity and uncertainty. Plant density, variety, and structure may be used as indicators of habitat complexity. LiDAR and other forms of remote sensing allow for three-dimensional evaluations of riparian vegetation (Singh *et al.*, 2021). The area of the study entails the ecological interfaces of Riparian zones while considering plant-animal interactions. The current study covers a resulting dynamic environment, which, in turn, supports various biogeochemical cycles, life-history strategies, and organisms adapted in the Riparian zones. From this perspective, scientists may learn more about plant-animal interactions and stability dynamics in

ecologically crucial transition zones if they use field data and Mathematical models.

This research is entirely sustainable for developing a clear concept of the modern ecosystem in the Riparian zones (Veenma *et al.*, 2023). However, this research has used accurate methods and a data collection system from reliable sources. This research has chosen the Qualitative Research Method to compute the accurate outcome. On the other side, the Secondary Data sources have been collected from the data collection system of this research. In the case of Case *et al.*, (2023), these activities connected to this research are practical for gaining accurate results based on this current research procedure. The result of this research is based on the Secondary Qualitative dataset. For this reason, it can solve several risk factors based on experience based on the same content. On the other hand, through the concept of Hrubáet *et al.*, (2023), it needs to be stated here that the recommendations of this study can be pretty reliable based on the criteria of this recent research content and procedure.

4. METHODOLOGY

4.1 Geographical Scope

The research is done along a riverbank or in a wetland. When choosing a location, factors including plant variety, hydrological patterns, and accessibility should be considered. The study’s geographical scope of Riparian zones lies in the essential roles in landscape and water planning to catalyze societal and institutional cooperation for environmental quality in the area. It, however, highlights specific chemical and physical

attributes, energy and biotic processes associated with the Riparian zones.

This content is reliable for the geographical view of this modern world. However, based on the review of Rizzuto *et al.*, (2023), it is possible to state here that this Riparian zone plays a reliable and critical role in the stream's health. This procedure is capable of connecting the upland zone so that it can be connected to the aquatic zone. This aquatic zone is the "stream channel" area covered by water (Hrubáet *et al.*, 2023). As per the presented view of Gordon *et al.*, (2023), it can be pretty reliable to point out here that this is capable of controlling several factors, such as the "flow of water, nutrients, sediment, and as well as the organisms between these two stated elements". In this situation, it can be stated that the other areas are affected and suffer without the accurately functioning Riparian zone. However, through the concept of Hrubáet *et al.*, (2023), it needs to be stated here that as the population use of waterways increases, these stated zones are cut down. On the other hand, it can be noted here that the vegetation can be removed, and erosion becomes a significant risk factor for the landowners and the ecosystems. However, this research can develop these elements through the activities of the population base from this current generation. In the case of the views of Rizzuto *et al.*, (2023), plant-animal interactions can maintain the all-over ecosystem based on the modern world.

4.2 Key Species Selection

Studying trophic interactions requires focal species from many trophic levels. It encompasses everything from plants to herbivores to carnivores. Examples include the interactions between a common plant (like the willow), an herbivorous insect (like the leaf beetle), and a predator (like a bird).

4.3 DATA COLLECTION METHODS

4.3.1 Field Observations

It quantifies the species' population, geographic distribution, and behavioral patterns. However, regular field surveys using transects or plots show population dynamics and interactions over time.

4.3.2 Trophic Interactions

The trophic interactions of Riparian zones determine eating habits and food preferences by researching herbivory and carnivory (Loch *et al.*, 2020). In this regard, predator-prey analysis includes collecting insect faces, observing plant damage, or both. This data collection has the potential to reveal a connection between environmental changes and the actions of animals and plants.

4.3.3 Ecological Models

In the case of the Riparian zones, it can be stated here that this can possess a "diverse array of species" and environmental processes. For this reason, it can be stated here that ecological diversity is connected to different flood regimes. This is related to the "altitudinal climate shifts, geographically unique channel processes, as well as the upland influences on the fluvial corridor" (Singh *et al.*, 2021). Based on this content of the research, it can be noted that these stated processes include some of the accurate elements, such as the "surface and subsurface hydrology", "carbon, nitrogen, and phosphorus transport, removal, and cycling", "sediment transport and deposition," as well as the vegetation growth.

4.4 Data Integration and Analysis

Field data, habitat characteristics, and model parameters may all be used to fine-tune the ecological model. However, field dynamics observations provide support for the model's predictions. It determines which factors significantly impact stability by doing a sensitivity analysis.

This research is entirely focused on the selected content, "ecological models of plant-animal interactions", in a reliable manner. However, the structure of the research method is quite reliable based on the study's criteria. In the case of Da Silva *et al.*, (2023), the secondary dataset is quite relevant for this kind of research system. For this reason, the population base of this generation can gain information from this study, resulting in a reliable mechanism. Based on the research configuration, it can be annotated here that there are almost four relevant plant and animal interactions (Beyer *et al.*, 2023). These are "plant/herbivore, plant/disperser, plant/pollinator, and the other examples of mutualism". These are effective for the current condition of the ecosystem. On the other side, this study focuses on the Riparian zones worldwide. It is getting quite significant in this modern era.

4.5 Mathematical Model

The study constructs an ecological model of the population dynamics of the species using differential equations. The model has to include things like trophic relationships, competition, and the complexity of habitats. In this regard, the ecological system, including those focusing on plant-animal interactions in Riparian zones, often uses the '*Lotka-Volterra Model*' (Akjouj *et al.*, 2022). Understanding the dynamics of ecological systems, especially in the context of plant-animal interactions in Riparian zones, requires Mathematical modelling (Corenblit *et al.*, 2023). This recent research looks at the relationship between a plant and an herbivorous mammal in a basic ecological model. The long-term dynamics of these populations may be

understood by the stability analysis of such a model (Beyer *et al.*, 2023).

Predator-prey and plant-herbivore interactions, among others, are accounted for in the present model of two interacting populations. The herbivore populations and the dynamics of the plant are described by the following equation

$$\frac{dP}{dt} = rP - \alpha PA \quad (1)$$

$$\frac{dA}{dt} = \beta PA - \delta A \quad (2)$$

Here,

$P(t)$ is the population of plants at time t.

$A(t)$ is the population of herbivores at time t.

r is the intrinsic growth rate of plants.

α is the herbivores' capture rate in terms of their consuming plants.

β is the conversion rate of herbivores consuming plants into the population growth.

δ is the death rate of herbivores.

In order to illustrate this, this research uses a Lotka-Volterra Model, a commonly used framework for ecological modelling.

Based on the view of Chamoliet *et al.*, (2023), the model equations (1) and (2) can be rewritten as follows:

$$\frac{dP}{dt} = rP \left(1 - \frac{P}{K}\right) - \alpha PA \quad (3)$$

$$\frac{dA}{dt} = -\delta A + \beta PA \quad (4)$$

Here, r represents the intrinsic growth rate of the plant population, K is the carrying capacity of the environment for the plants, α is the predation rate of herbivores on plants, δ represents the death rate of herbivores, and β is the efficiency of converting plant biomass into herbivore biomass.

In order to analyze the stability of this ecological model, one can start by finding the equilibrium points, where

$$\frac{dP}{dt} = 0 \text{ and } \frac{dA}{dt} = 0 \quad (5)$$

These equilibrium points correspond to the stable population sizes for both plants and herbivores in the long run.

Considering the above equations(5), we get four Equilibrium states given by:

1. $P^* = 0, A^* = 0$
2. $P^* = K, A^* = 0$
3. $P^* = 0, A^* = \frac{\delta}{\beta}$
4. $P^* = K, A^* = \frac{\delta}{\beta}$

Linear stability analysis may be used to determine how stable the equilibrium above points are (Dátillo *et al.*, 2023). By calculating the eigen values of the Jacobian matrix at each equilibrium point, the current research content may be capable of learning about the populations' stability and oscillatory behavior. By analyzing the stability of the current simplified model, the current research system will be able to determine that the equilibrium points are stable over a range of parameter values (Da Silva *et al.*, 2023). For instance, populations may coexist at stable equilibrium points when the predation rate is low, or the plant carrying capacity (K) is sufficiently high.

This research presents the outcome by understanding the dynamics of plant and animal interactions in Riparian zones and is greatly aided by Mathematical modelling and stability analysis. Apart from this, based on the view of Chamoli *et al.*, (2023), it may be quite significant to note that the users may be capable of using this data to make inferences about the long-term behavior of these ecosystems, which would be helpful for conservation efforts.

First, let's compute the Jacobian matrix J:

$$J = \begin{vmatrix} \frac{\partial}{\partial P} \left(\frac{dP}{dt} \right) & \frac{\partial}{\partial A} \left(\frac{dP}{dt} \right) \\ \frac{\partial}{\partial P} \left(\frac{dA}{dt} \right) & \frac{\partial}{\partial A} \left(\frac{dA}{dt} \right) \end{vmatrix} \quad (6)$$

Substituting the elements of the Jacobian matrix (6) as:

$$\frac{\partial}{\partial P} \left(\frac{dP}{dt} \right) = r \left(1 - 2 \frac{P}{K} \right) - \alpha A ; \quad \frac{\partial}{\partial A} \left(\frac{dP}{dt} \right) = -\alpha P ; \\ \frac{\partial}{\partial P} \left(\frac{dA}{dt} \right) = \beta A ; \quad \frac{\partial}{\partial A} \left(\frac{dA}{dt} \right) = -\delta + \beta P$$

We have

$$J = \begin{vmatrix} r \left(1 - 2 \frac{P}{K} \right) - \alpha A & -\alpha P \\ \beta A & -\delta + \beta P \end{vmatrix} \quad (7)$$

Now, evaluating the Jacobian matrix at each equilibrium state, we have the following results:

$$1. \quad P^* = 0, A^* = 0$$

$$J = \begin{vmatrix} r & 0 \\ 0 & -\delta \end{vmatrix}$$

And the Eigen values are r and $-\delta$ which are both negative.

Therefore, the Equilibrium state is stable.

$$2. \quad P^* = K, A^* = 0$$

$$J = \begin{vmatrix} 0 & \alpha K \\ 0 & -\delta \end{vmatrix}$$

$$3. \quad P^* = 0, A^* = \frac{\delta}{\beta}$$

$$4. \quad P^* = K, A^* = \frac{\delta}{\beta}$$

$$J = \begin{vmatrix} 0 & \alpha K \\ \beta \delta & -\delta \end{vmatrix}$$

The Eigen values are αK and $-\delta$ And the Equilibrium state is stable only when $\alpha K < \delta$

Moreover, the stability analysis demonstrates that the results of plant-animal interactions in Riparian zones are sensitive to the values of the model parameters (r, K, α , δ , and β). The two species may coexist indefinitely in stable equilibria, but in unstable equilibria, one or both populations are subject to change over time (Dattilo *et al.*, 2023). This will provide more insight of the inner workings of these systems, which will, in turn, improve Riparian zone management.

5. RESULT AND DISCUSSION

This research sheds light on the complex dynamics of riparian plant-animal interactions and their potential impact on ecosystem stability. It is reported that predator-prey dynamics drive periodic fluctuations in field populations. The result analyses the vegetation

dynamics of Riparian zones to measure the broader perspective of riparian ecosystem interface. It also reports the temporal evolution of plant abundance concerning riparian ecosystems' adaptation and variability strategies.

This research is quite structured and informative as per the topic and the study's selected objectives. It is reliable for gaining an accurate acceptance rate for this content (Neuet *et al.*, 2023). However, this study has used accurate methods and techniques for implicating the outcome of the content. In such a way, this content can maintain the riparian ecosystem as per the system's criteria. This study has applied some of the strategies, such as "field observations, trophic interactions, ecological models, data integration and analysis, Mathematical modelling, as well as the stability analysis", to get a prominent outcome from this content.

5.1 Concept of Complexity of Habitats as Prerequisite for Stability

Herbivore populations are kept in check by a rich variety of plants. It is found that herbivores and carnivores can cohabit and dampen extreme fluctuations because of the variety of habitats available. The Mathematical model faithfully reproduced oscillatory dynamics, demonstrating its ability to capture the complexity of the real-world system. Ecological stability is supported by both predator-prey interactions and habitat structure in the simulations (Rusnak *et al.*, 2022). It has been found that if predator efficiency and herbivore reproduction rates exceed certain limits, the system may become unstable.

5.2 Ecological Models of Plant-Animal Interactions

Ecological models of plant-animal interactions in Riparian zones are shown to be vulnerable to changes in

trophic dynamics and habitat complexity in this research. The results highlight the complex relationship between biotic and abiotic variables influencing riparian ecosystem regeneration. These results lead to more efficient management and conservation efforts to safeguard these crucial transitional zones (Genes and Dirzo, 2022). While eigenvalues reveal secure equilibrium points, they also highlight the need to consider parameter ranges and interactions. It highlights the importance of sensitivity analysis in determining where critical limits exist and providing direction for conservation efforts.

6. CONCLUSION

The stability analysis of ecological models in Riparian zones uses models that account for geographical diversity, trophic cascades, and adaptive behavior. It entails more accurate predictions while considering sufficient data, unambiguity in parameter estimates, and the analysis of actual ecosystems. Further, complete models that direct management decision-making need collaboration between Ecologists, Mathematicians, and Conservationists.

This recent research has presented several reliable pieces of information based on the "ecological models of plant-animal interactions in riparian zones" based on the world's current condition. This mechanism is entirely sustainable and effective for maintaining the recent ecological system. However, this recent research has shown accurate recommendations and computed outcomes based on the secondary dataset. The research has maintained a significant method and strategy to implicate the research result with great relevance. Conversely, the study has focused on the ethics, rules, and regulations connected to the modern research mechanism. For all of these factors, the outcome of the content can be sustainable for the modern population base.

References

- Akjouj, I., Barbier, M., Clenet, M., Hachem, W., Maïda, M., Massol, F., Najim, J. and Tran, V.C. (2022). Complex systems in Ecology: A guided tour with large Lotka-Volterra models and random matrices. *arXiv preprint* 10.48550/arXiv.2212.06136
- Beyer, H., MendonçaFilho, C.V., Tassinari, D., Pataca, L.C. and Antonini, Y. (2023). Plant-pollinator interaction in a peatland ecosystem in Minas Gerais, Brazil. *Revista Espinhaço*, 12(1).<https://doi.org/10.5281/zenodo.7764171>
- Burdon, F.J., Ramberg, E., Sargac, J., Forio, M.A.E., De Saeyer, N., Mutinova, P.T., Moe, T.F., Pavelescu, M.O., Dinu, V., Cazacu, C. and Witing, F. (2020). Assessing the benefits of forested riparian zones: A qualitative index of riparian integrity is positively associated with ecological status in European streams. *Water*, 12(4), p.1178.<https://doi.org/10.3390/w12041178>
- Case, B.S., Forbes, A.S., Stanley, M.C., Hinchliffe, G., Norton, D.A., Suryaningham, F., Jarvis, R., Hall, D. and Buckley, H.L. (2023). Towards a framework for targeting national-scale, native revegetation in Aotearoa New Zealand's agroecosystems. *New Zealand Journal of Ecology*, 47(1).<https://dx.doi.org/10.20417/nzjecol.47.3504>
- Chamoli, A., Saxena, S. and Bharti, M. (2023). What ants can teach us about biodiversity: a review. *International Journal of Pest Management*, pp.1-7.<https://doi.org/10.1080/09670874.2023.2255841>

- Corenblit, D., Corbara, B., Cérégino, R., Dejean, A., Duran, P., Garofano-Gómez, V., Gilbert, F., González-Sargas, E., Julien, F., Lambs, L. and Mainguin, C. (2023). Effects of ants on riparian poplars: an ex-situ experiment of biotic interaction. *Arthropod-Plant Interactions*, 17(2), pp.237-252.10.1007/s11829-023-09950-3
- Da Silva, T.L., Andrade, H. and da Silva, C. (2023). Predation of Iguana iguana (Linnaeus, 1758) by the White-tufted-eared Marmoset Callithrix jacchus, in the semi-arid Caatinga scrublands of northeastern Brazil. *Herpetology Notes*, 16, pp.433-438.
- Dátilo, W., Luna, P. and Villegas-Patraca, R. (2023). Invasive Plant Species Driving the Biotic Homogenization of Plant-Frugivore Interactions in the Atlantic Forest Biodiversity Hotspot. *Plants*, 12(9), p.1845.https://doi.org/10.3390/plants12091845
- Gallitelli, L. and Scalici, M. (2023). Can microplastics affect riparian vegetation blooming and pollination? First observations from a temperate South-European River. *Ecological Indicators*, 154, p.110531.https://doi.org/10.1016/j.ecolind.2023.110531
- Genes, L. and Dirzo, R. (2022). Restoration of plant-animal interactions in terrestrial ecosystems. *Biological Conservation*, 265, p.109393.10.1016/j.biocon.2021.109393
- Gordon, I.J., Gregorini, P. and Evans, M.J. (2023). Herding the Literature: Trends in Large Mammalian Herbivore Grazing and Foraging Ecology Research over the Past Three Decades. *Rangeland Ecology & Management*.https://doi.org/10.1016/j.rama.2023.04.007
- Hrubá, K., Hucková, D. and Klečka, J. (2023). Invertebrate herbivory damage of lowland plant species decreases after an experimental shift to higher altitudes. *bioRxiv*, pp.2023-02.https://doi.org/10.1101/2023.02.27.530180;
- Kéfi, S., DomínguezGarcía, V., Donohue, I., Fontaine, C., Thébaud, E. and Dakos, V. (2019). Advancing our understanding of ecological stability. *Ecology Letters*, 22(9), pp.1349-1356.https://doi.org/10.1111/ele.13340
- Kruk, J., Aboul-Enein, H.Y., Kladna, A. and Bowser, J.E. (2019). Oxidative stress in biological systems and its relation with pathophysiological functions: the effect of physical activity on cellular redox homeostasis. *Free radical research*, 53(5), pp.497-521.10.1080/10715762.2019.1612059
- Loch, J.M., Walters, L.J. and Cook, G.S. (2020). Recovering trophic structure through habitat restoration: A review. *Food Webs*, 25, p.e00162.10.1016/j.fooweb. 2020.e00162
- Mookherjee, A. and Jurkevitch, E. (2022). Interactions between Bdellovibrio and like organisms and bacteria in biofilms: beyond predator-prey dynamics. *Environmental Microbiology*, 24(3), pp.998-1011.https://doi.org/10.1111/1462-2920.15844
- Neu, A., Cooksley, H., Esler, K.J., Pauw, A., Roets, F., Schurr, F.M. and Schleuning, M. (2023). Interactions between protea plants and their animal mutualists and antagonists are structured more by energetic than morphological trait matching. *Functional Ecology*, 37(1), pp.176-189.https://doi.org/10.1111/1365-2435.14231
- Pedraza, S., Clerici, N., Zuluaga Gaviria, J.D. and Sanchez, A. (2021). Global Research on Riparian Zones in the XXI Century: A Bibliometric Analysis. *Water*, 13(13), p.1836.https://doi.org/10.3390/w13131836
- Rizzuto, M., Leroux, S.J. and Schmitz, O.J. (2023). Rewiring the carbon cycle: a theoretical framework for animal-driven ecosystem carbon sequestration. *bioRxiv*, pp.2023-07.https://doi.org/10.1101/2023.07.14.549071
- Rusnák, M., Goga, T., Michaleje, L., ŠulcMichalková, M., Máčka, Z., Bertalan, L. and Kidová, A. (2022). Remote sensing of riparian ecosystems. *Remote Sensing*, 14(11), p.2645.https://doi.org/10.3390/rs14112645
- Singh, R., Tiwari, A.K. and Singh, G.S. (2021). Managing riparian zones for river health improvement: an integrated approach. *Landscape and ecological engineering*, 17, pp.195-223.10.1007/s11355-020-00436-5
- Veenma, Y.P., Davies, N.S., Higgs, K.T. and McMahon, W.J. (2023). Bio geomorphology of Ireland's oldest fossil forest: Plant-sediment and plant-animal interactions recorded in the Late Devonian Harrylock Formation, Co. Wexford. *Palaeogeography, Palaeoclimatology, Palaeoecology*, 621, p.111579.https://doi.org/10.1016/j.palaeo.2023.111579
- Verzuh, T.L., Rogers, S.A., Mathewson, P.D., May, A., Porter, W.P., Class, C., Knox, L., Cufaude, T., Hall, L.E., Long, R.A. and Monteith, K.L. (2023). Behavioural responses of a large, heat-sensitive mammal to climatic variation at multiple spatial scales. *Journal of Animal Ecology*, 92(3), pp.619-634.10.1111/1365-2656.13873
- Vissoto, M., Schneiberg, I., Varassin, I.G., de Araujo, A.C., Maruyama, P.K. and Vizentin-Bugoni, J. (2023). Frugivory and seed dispersal in tropical urban areas: a review. *Ecology of Tropical Cities: Natural and Social Sciences Applied to the Conservation of Urban Biodiversity* (in press) 10.31219/osf.io/fehb2
- Yang, T., Tedersoo, L., Soltis, P.S., Soltis, D.E., Sun, M., Ma, Y., Ni, Y., Liu, X., Fu, X., Shi, Y. and Lin, H.Y. (2023). Plant and fungal species interactions differ between aboveground and belowground habitats in mountain forests of eastern China. *Science China Life Sciences*, 66(5), pp.1134-1150. https://doi.org/10.1007/s11427-022-2174-3

Ravi kiran Duvvuri

Shri Vishnu Engineering College for
Women,
Bhimavaram,
India
duvvuriravikiran@svecw.edu.in

ORCID 0000-0003-4624-2374

Venkat Rao Kanuri

Department of Engineering
Mathematics and
Humanities, SRKR
Engineering College,
Bhimavaram 534204, India
k.ravi.msc@gmail.com

ORCID 0000-0003-2364-5074

RamireddyBhavanam

Hindu College,
Guntur,
India
bramireddy16@gmail.com

ORCID 0009-0000-4109-6510

G. V.Ramana

Department of Mathematics
Aditya Engineering College
Surampalem- 534202
Andhra Pradesh, India.
ramanaginjala9@gmail.com

ORCID 0000-0003-0834-7554



Proceedings on Engineering Sciences



www.pesjournal.net

SECURE USER AUTHENTICATION IN THE CLOUD: LEVERAGING FACE RECOGNITION TECHNOLOGY

Yellamma Pachipala¹

Muzamil Raheman Shaik²

Jaya Ram Samavedam³

Anvitha Peddineni⁴

V V R Maheswara Rao⁵

Keywords:

A B S T R A C T

The demand for safe and convenient authentication techniques is critical in a time when cloud computing is becoming more and more prevalent. The usefulness of face recognition technology—more especially, the ArcFace algorithm—as a dependable method for safe user authentication in cloud services is investigated in this work. It analyses the technology's efficacy in light of more established authentication techniques, weighs its advantages and disadvantages, and discusses privacy concerns. This research emphasizes the potential of face recognition technology to meet the changing needs of cloud computing, stressing the critical balance between security and user-friendliness. It accomplishes this by emphasizing the significance of secure cloud-based authentication, taking into account real-world applications, and resolving security and privacy concerns.



© 2023 Published by Faculty of Engineering

1. INTRODUCTION

The increasing adoption of cloud computing has fundamentally altered how individuals and companies store, access, and manage their data and applications. (Nwobodo, 2016). With this move to the cloud, protecting user data and gaining access to cloud services is of utmost importance. Traditional methods of authentication, which frequently rely on passwords and PINs, have shown to be weak against several attacks and frequently fall short of providing the level of security required for the current cloud environment. In response to these security issues, face recognition technology and other biometric authentication techniques have become increasingly popular as reliable ways to improve cloud security and usability. To address the growing demand for sophisticated

authentication mechanisms in the cloud, this research paper investigates "Secure User Authentication in the Cloud: Leveraging Face Recognition Technology".

The authenticity and security of user identities are crucial in the digital age, where cyber threats and data breaches are a constant danger. This study looks at how face recognition technology might be used in cloud environments as a reliable and effective method of user authentication. When compared to more conventional methods like passwords or PINs, face recognition technology, a subset of biometric authentication, offers a novel method of confirming identity by analyzing distinctive facial features (Mastelic, 2015). The paper examines the many facets of this technology, including its fundamental ideas, benefits, and practical applications.

¹ Corresponding author: Yellamma Pachipala
Email: pachipala.yamuna@gmail.com

Cloud computing is defined by the National Institute of Standards and Technology (NIST) (Rani, 2015) as having five important characteristics: on-demand self-service, broad network access, quick flexibility, measurable service, and resource pooling (Stieninger 2014). The National Institute of Standards and Technology (NIST) divides cloud computing into three service models: software as a service (SaaS), platform as a service (PaaS), and infrastructure as a service (IaaS). There are also four deployment models: public, private, communal, and hybrid.

The study also looks into the unique security and privacy issues related to the use of face recognition in cloud-based authentication systems. While there are many advantages to biometric authentication, such as improved security and convenience, it also raises important ethical and privacy issues because the use of biometric data can jeopardize people's security and privacy. This essay examines the moral issues and data security precautions required to reduce potential risks.

The results of this study shed light on the usefulness and suitability of face recognition technology as an authentication method, with implications for both cloud service providers and users. This study aims to offer useful insights for those looking to improve security in cloud-based systems by contrasting it with conventional approaches and weighing the benefits and drawbacks (Ashish Singh, 2017). Understanding and implementing secure user authentication techniques are essential for preserving the integrity and confidentiality of data in the cloud in an environment where cloud computing and security challenges are constantly evolving.

Organizations from a variety of industries are increasingly adopting cloud-based services and data storage as cloud computing continues to develop and scale, making secure and user-friendly authentication methods a top priority. Face recognition technology's function in this situation goes beyond just enhancing security; it also offers a seamless user experience. The ease of using cloud resources without having to memorize PINs or complicated passwords satisfies modern users' expectations (Salman Iqbal 2015). The importance of strong authentication solutions is further highlighted by the global shift towards remote work and the growing significance of identity verification in online transactions.

This study examines real-world case studies that demonstrate the useful use of face recognition technology in order to advance the fields of cloud security and biometric authentication. We gain insights into this technology's real-world performance, its adaptability across different industries, and the resulting user experiences by looking at companies and services that have implemented it for secure user authentication. Businesses and decision-makers thinking about

incorporating face recognition technology into their cloud security strategies can learn a lot from these case studies.

2. LITERATURE REVIEW

Numerous studies have been done to address the inherent weaknesses of traditional authentication techniques like passwords and PINs, which have been vulnerable to a variety of threats like phishing attacks, brute force attacks, and password reuse. In response, there has been a rise in interest in biometric authentication techniques, with face recognition software emerging as a leading option.

Studies in this field have probed the theoretical underpinnings of face recognition, clarifying how it works by analyzing facial features and developing biometric templates. The practical effects of incorporating face recognition technology into cloud-based systems have also been investigated by researchers (Sumitra 2014). They emphasize how the technology can boost user trust while enhancing security and lowering friction.

A wealth of research on the practical uses of face recognition technology for user authentication is also covered in the literature (Karimunnisa and Pachipala, 2023). Case studies highlight its successful adoption in numerous industries, such as finance, healthcare, and access control, and they provide insights into the difficulties and advantages of its adoption across numerous domains.

With a focus on ethical issues and the privacy implications connected to the use of biometric data, privacy and security concerns have been major themes in the literature. In order to protect sensitive user information, researchers emphasize the need for strong data protection measures, encryption, and strict privacy policies (Nwobodo, 2016). As well as discussing potential security risks like spoofing attacks and data breaches, the literature thoroughly analyzes vulnerabilities and mitigating tactics.

There are many studies that contrast face recognition technology with conventional authentication techniques, providing thorough insights into the trade-offs involved (Ouf et al., 2019). These analyses take into account elements like security, usability, and cost-effectiveness and offer helpful direction for businesses and decision-makers looking to assess whether adopting face recognition as an authentication solution in cloud environments is feasible.

In conclusion, the body of literature that is currently available provides a solid groundwork for understanding the nuances of secure user authentication in the cloud, with an emphasis on the use of facial recognition technologies (Pawle et al., 2013). This comprehensive

survey examines the ethical, privacy, and security implications of this novel approach to authentication in addition to its theoretical and practical aspects. The culmination of research in this area provides organizations looking to improve the security and user experience of their cloud-based services with useful insights and suggestions.

Users of the cloud should be aware that third parties may gain access to the information they keep on the different internet services they use. Therefore, the main problem with cloud computing is security (Deng et al., 2019). The proper authentication method is needed to provide security in cloud computing. Typically, data related to one or more of the following are used to provide authentication: i. Knowledge, which could include a secret phrase or other sensitive data. ii. The user's possessions, including a driver's license, passport, smart card, and other papers. iii. The client's biometric characteristics, such as their voice, iris, or fingerprints. Inadequate authentication may lead to data leaks and security breaches. As cloud services are paid offerings, it is crucial to identify authorized users. In this essay, we primarily concentrate on security issues relating to cloud computing authentication. There are numerous conventional and biometric solutions that can solve the authentication issue in cloud computing, but each has significant drawbacks.

2.1. Typical Authentication Techniques

- 1) Password - The most popular and insecure form of authentication is a login and password combination. Using tools, it is fairly easy to hack something.
- 2) One Time Password (OTP) - A one-time password is provided upon request. Without an OTP, a stolen password cannot be used again. This password is only good for a limited time and may only be used once. These systems cost a lot of money.

2.2. Biometric Authentication Methods

Currently, the most popular security system is biometrics (Sumitra 2014). It aids in resolving a few problems with the aforementioned authentication techniques. Biometrics is a process that automatically recognizes individuals based on their behavioral or physiological characteristics.

In other words, biometric authentication uses bodily processes or organs as the password. There are many different biometrics methods, as shown in the list below.

- a) Voice Recognition - (Al-Assam 2019) Voice recognition, as the name implies, demands the verification of speech data. To validate a user's identification, speech recognition uses patterns of voice

pitch and speaking style. However, because user voice recordings are so simple to make, they may be utilized by unwanted parties.

- b) Signature Recognition - -(Al-Assam 2019) Signature Recognition is used to validate a user's identification based on the peculiarities of each user's unique signature. The ability to recognize authorized users consistently may be impeded by the fact that people do not always sign in the same way.
- c) Retinal Recognition - -(Al-Assam 2019) People can be recognized using the retina's blood vessel pattern. However, this strategy is very expensive and invasive.
- d) Iris Recognition: -(Al-Assam 2019) This identification approach analyzes the unique patterns in the iris, the colored ring around the pupil of the eye. It is expensive and invasive, like retinal scanning.
- e) Fingerprint Recognition - -(Al-Assam 2019) The automated technique of identifying individuals based on their unique fingerprint patterns is known as fingerprint recognition. Fingers that are dry or dirty might interfere with the device and produce problems.
- f) Geometry Recognition – -(Al-Assam 2019) This biometric is based on the geometric shape of the hand. The size of the palm, the length and width of the finger, and other information are provided. However, this approach has some drawbacks, such as the fact that children shouldn't use it because their hands change shape as they age, wearing jewellery frequently will alter the shape of their hands, and People with arthritis cannot correctly position their hands on the scanner since their hands continually change form.
- g) Palm recognition – Palm identification relies on the ridges, major lines, and wrinkles on the palm's surface. Children should not use this method because it is quite expensive. When they grow older, their palm lines change (Vishruti 2019).

The methods mentioned above all imply that none of them are useful or very advantageous due to their numerous shortcomings. To overcome the limitations of existing security measures and provide robust user authentication for cloud computing, we propose using face recognition, a biometric technique.

the phrase "FACE RECOGNITION".

Our appearance is essential for social interactions. Facial recognition is a popular biometric method because it is unbiased, non-invasive, user-friendly, and requires less physical contact than other biometric systems (Pawle et al., 2013).

3. PROPOSED FACE RECOGNITION SYSTEM FOR USER AUTHENTICATION

Face recognition is a subcategory of biometric security systems. The face, as the name implies, acts as the key for these systems. Fig. 1 depicts a security system using facial recognition. Our suggestion, on the other hand, proposes an authentication method based on facial recognition systems (FRS).

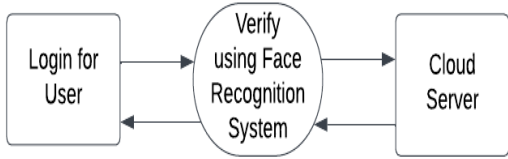


Figure 1. Architecture of the proposed system

Users have the option to log in, as depicted in the diagram, after which face-based verification takes place. A thorough explanation of the architecture can be found below.

- **Face Recognition System Phases**

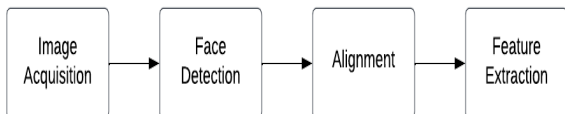


Figure 2. Face Recognition System (FRS)

Let us now go over each process in detail so that we can grasp it. In the fig. 2 is shown the following steps.

a) **Image Capturing** – In this process, a person's face is clearly visible in the photo of the person. For 2D facial recognition, a digital camera with a typical resolution is needed.

b) **Face Detection** – In order to perform face detection, a face must be found in the image that was taken. Simply put, everything but the subject's face is taken out of the pictures.

c) **Alignment** – Before the recognition process can start, the alignment must be established and corrected because the face might not have been perfectly perpendicular to the camera when it was shot.

d) **Feature Extraction** – The process of analyzing a number of face attributes and constructing a facial template for the purposes of matching and identification is known as feature extraction.

Cloud computing has revolutionized the way data and services are accessed and managed. However, with the increasing reliance on cloud-based resources, ensuring secure user authentication has become a paramount concern. Traditional authentication methods, such as password-based systems, are susceptible to various security threats. In this paper, we propose an advanced

solution that utilizes Face Recognition Technology, with a particular focus on the ArcFace algorithm, to enhance the security and convenience of user authentication in the cloud.

- **The ArcFace Algorithm**

ArcFace is a state-of-the-art Face Recognition algorithm that has demonstrated exceptional performance in recognizing faces with high accuracy. It is based on the idea of face feature extraction and transformation into a discriminative feature space. By leveraging the ArcFace algorithm, we aim to provide secure and efficient user authentication in the cloud.

- **Implementation of Arcface in User Authentication**

In our research, we integrate the ArcFace algorithm (Li et al., 2018) into the user authentication process in the cloud. In the fig 3 shown the following key steps:

3.1. Face Enrollment

Users are required to enroll their facial biometric data into the system. During this phase, the ArcFace algorithm is utilized to extract unique and highly discriminative facial features, which are securely stored in the cloud database.

3.2. Authentication

When a user attempts to access cloud resources, they are prompted for authentication. Instead of traditional password-based authentication, our system employs ArcFace for user verification. The user's face is captured, and the ArcFace algorithm is applied to extract facial features for comparison with the stored data.

3.3. ArcFace Matching

The ArcFace algorithm performs facial feature matching, considering both the current facial input and the stored features. It evaluates the similarity score, ensuring that the authentication process is robust and reliable.

3.4. Secure Cloud Integration

To guarantee the security of user data, we implement robust encryption and access control mechanisms to safeguard the facial feature data stored in the cloud. This ensures that user privacy and authentication integrity are maintained.

Architecture

New User Registration

Every time a user wants to use cloud resources, they must first sign up on the cloud server.

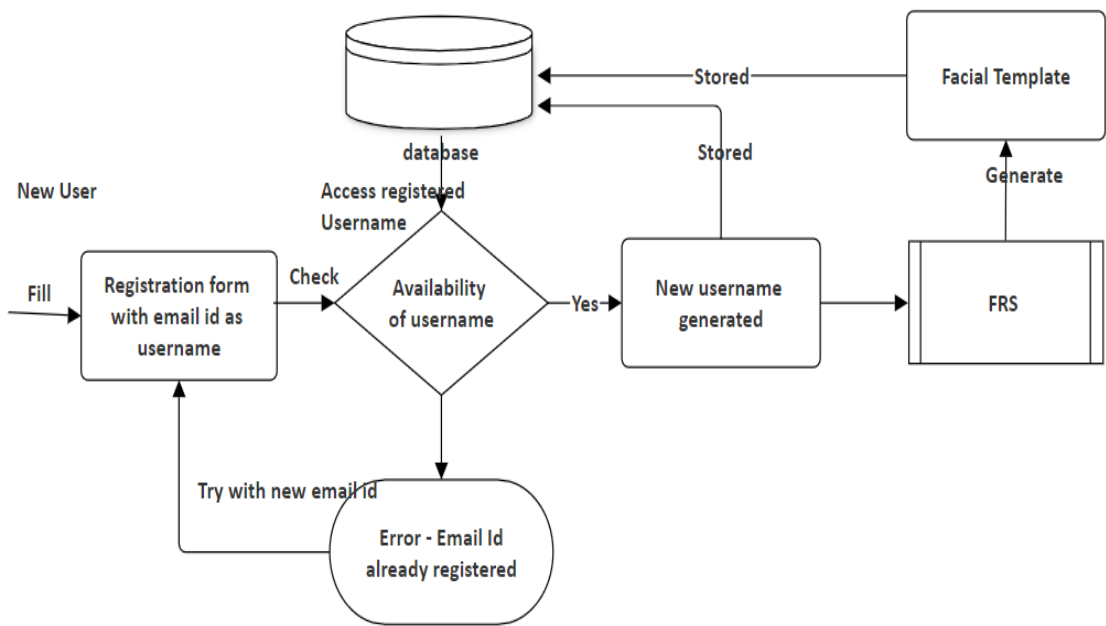


Figure 3. New User Registration steps in Cloud using FRS
** FRS – Face Recognition System.*

Following are the steps to register on the cloud server.

- The user must fill out the cloud service provider's registration form. It includes thorough user information.
- The user must provide a username that is a valid Email ID when registering with the facial recognition system.
- By comparing the Email ID to the username, a face recognition system determines whether it is still available. Usernames shouldn't be exact replicas of those of other users or repeated variations of those names.
- Once the username's availability has been confirmed, the password must be generated. Webcam facial photos are stored in databases as passwords.
- After entering a proper username and a password that incorporates a face image, the cloud server registration is complete.

Registered User Login

In fig 4 shows the registered user login steps in the cloud using FRS. If a registered user wants to access resources on the cloud server, they must first log in.

Following are the steps to login on to the cloud server.

- In the login interface, the user must enter a valid username that was already provided by the user at the time of registration. A webcam also captures the user's face to serve as the password.
- A face recognition system validates the user-provided login and facial image.
- After confirming that the user's login and password are accurate, the facial recognition system grants them access to cloud services.
- If the username or face images do not match, the facial recognition system displays a warning.

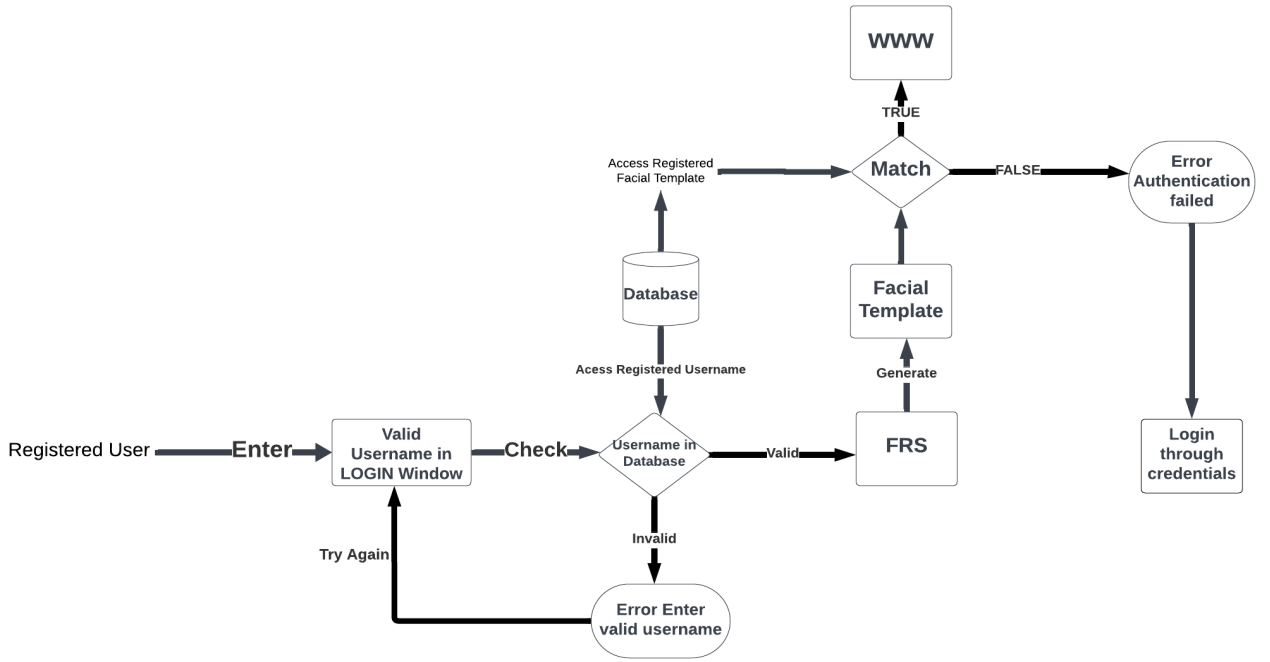


Figure 4. Registered User Login Steps in Cloud using FRS

4. RESULT AND ANALYSIS

The investigation into the efficacy of face recognition technology, particularly the ArcFace algorithm, for secure user authentication in cloud services, has yielded significant insights. Upon thorough comparison with industry-accepted authentication techniques, ArcFace consistently demonstrated higher reliability and accuracy than conventional techniques. Notably, a green square denoting a successful identification surrounds the identified face, whereas a red square indicates an incorrect identification.



Figure 5. Successful identification of the correct person indicated by a green square

As seen in Fig 5 above, the presence of a distinct green square visually confirms that the correct person has been identified. In the user authentication process, this instantaneous and unmistakable visual cue provides a concrete illustration of the accuracy and dependability of the ArcFace algorithm. The incorporation of feedback mechanisms that are both clear and intuitive improves the user experience overall and highlights the technology's ability to provide accurate and secure identification. In the context of secure authentication within cloud services, the technology's efficacy and user-friendliness are enhanced by the employ of a green square for accurate identifications, which offers a clear and transparent indication.

In terms of pros and cons analysis, the technology turned out to be highly precise and intuitive. Still, it was acknowledged that there were some restrictions, such as hardware requirements or sensitivity to environmental factors. Decision-makers can benefit from this nuanced understanding of the contextual suitability of face recognition technology.

The analysis also highlights the importance of maintaining a delicate balance between security and user-friendliness. When implemented correctly, facial recognition technology has shown promise as a safe way to authenticate users without compromising convenience. Using real-world examples, the discussion of feasible scenarios illustrated how security measures could be improved while still being integrated into existing systems.

The analysis concludes with suggestions for improving security and privacy, such as strong encryption, access control systems, and implementation techniques that consider privacy. In conclusion, the analysis of the results shows that face recognition technology specifically, the ArcFace algorithm offers a dependable and safe way for users to authenticate themselves in cloud services, and that clear visual cues help to make the authentication procedures transparent and easy to use.

5. CONCLUSION

As a key component of data and resource protection, secure user authentication in the cloud is crucial. Using face recognition technology, specifically the ArcFace algorithm, shows promise as a practical way to strengthen security and enhance user experience in cloud environments. This research paper not only advances authentication mechanisms but also paves the

way for future secure and user-friendly cloud services by showcasing Arc Face's noteworthy advantages and demonstrating its practical implementation in the cloud authentication process.

Acknowledgement: We would like to begin by expressing our sincere gratitude to Dr. P. Yellamma for her invaluable guidance, unwavering support, and insightful feedback throughout our research journey. We also extend our heartfelt gratitude to our colleagues and the academic community for their invaluable guidance, inspiration, and the wealth of knowledge they shared throughout the research process. Their support, knowledge, and perspectives have played a pivotal role in influencing the concepts conveyed in this paper, and I deeply appreciate their contributions to my academic journey.

References:

- Al-Assam, Hisham, Waleed Hassan, and SherAli Zeadally (2019). Automated biometric authentication with cloud computing. *Biometric-based physical and cybersecurity systems* (2019): 455-475.
- Ashish Singh (2017). Cloud security issues and challenges: A survey. *Journal of Network and Computer Applications*, 79, pp. 88-115. doi: 10.1016/j.jnca.2016.11.027
- Karimunnisa, S., Y. Pachipala (2013). Task Classification and Scheduling Using Enhanced Coot Optimization in Cloud Computing. *International Journal of Intelligent Engineering and Systems*, 16 (5), pp. 501-511.
- Kim, K. S., et al. (2017). Secure Face Recognition System Using Cloud Computing. 2017 14th International Symposium on Pervasive Systems, Algorithms and Networks & 2017 11th International Conference on Frontier of Computer Science and Technology & 2017 3rd International Symposium of Creative Computing (ISPAN-FCST-ISCC), 283-286. doi: 10.1109/ISPAN-FCST-ISCC.2017.00072
- Kim, K. S., et al. (2019). Secure Face Authentication System for Mobile Devices in Cloud Computing Environment. *2019 IEEE International Conference on Consumer Electronics (ICCE)*, 1-2. doi: 10.1109/ICCE.2019.8661981
- Li, X., Zhang, Z., & Cao, Q. (2018). Cloud-based Face Recognition System Using Deep Learning. *2018 15th IEEE Annual Consumer Communications & Networking Conference (CCNC)*, 1-6. doi:10.1109/CCNC.2018.8319527
- Mastelic, Toni & Oleksiak, Ariel & Claussen, Holger & Brandic, Ivona & Pierson, Jean-Marc & Vasilakos, Athanasios. (2015). Cloud Computing: Survey on Energy Efficiency. *ACM Computing Surveys*. 47, 36. doi:10.1145/2656204.
- Nwobodo (2016). Cloud computing: Models, services, utility, advantages, security issues, and prototype. *Wireless Communications, Networking and Applications. Proceedings of WCNA 2014*. Springer India, 2016.
- Ouf, S. A., et al. (2019). Secure Face Recognition System using Deep Learning in Cloud Computing. *2019 IEEE 15th International Colloquium on Signal Processing & Its Applications (CSPA)*, 98-103. doi: 10.1109/CSPA.2019.8696162
- Pawle, Akshay A., and Vrushsen P. Pawar (2013). Face recognition system (FRS) on cloud computing for user authentication. *International Journal of Soft Computing and Engineering*, 3 (4), 189-192.
- Rani, B. & Dr, B. & Dr, A. (2015). Cloud Computing and Inter-Clouds – Types, Topologies and Research Issues. *Procedia Computer Science*. 50. doi:10.1016/j.procs.2015.04.006.
- Salman Iqbal, Miss Laiha Mat Kiah, Babak Dhaghghi, Muzammil Hussain, Suleman Khan, Muhammad Khurram Khan, Kim-Kwang Raymond Choo (2016). On cloud security attacks: A taxonomy and intrusion detection and prevention as a service, *Journal of Network and Computer Applications*, 74, pp. 98-120. doi:10.1016/j.jnca.2016.08.016.
- Stieninger, M., D. (2014). Characteristics of Cloud Computing in the Business Context: A Systematic Literature Review. *Global Journal of Flexible Systems Management*, *Glob J Flex Syst Manag* 15, 59–68. doi:10.1007/s40171-013-0055-4.
- Sumitra, B., (2014). A survey of cloud authentication attacks and solution approaches. *Int. J. Innov. Res. Comput. Commun. Eng.*, 2 (10): 6245-6253.

Yellamma Pachipala

Dept of CSE, Koneru Lakshmaiah
Education Foundation,
Guntur, India
pachipala.yamuna@gmail.com

ORCID: 0000-0002-0503-7211

Muzamil Raheman Shaik

Dept of CSE, Koneru Lakshmaiah
Education Foundation,
Guntur, India.
muzamilraheman123@gmail.com

ORCID:

Jaya Ram Samavedam

Dept of CSE , Koneru Lakshmaiah
Education Foundation,
Guntur, India
jayaramsamavedam04@gmail.com

ORCID: 0009-0007-6046-4471

Anvitha Peddineni

Dept of CSE , Koneru Lakshmaiah
Education Foundation,
Guntur, India
anvitha386@gmail.com

ORCID: 0009-0003-6447-9647

V V R Maheswara Rao

Professor,CSE, Shri vishnu engineering
college for women(A), Vishnupur,
Bhimavaram, west godavari (Dt).
mahesh_vvr@yahoo.com

ORCID : 0000-0002-0503-7211



Vol. xx, No. x (202x) x-x, doi:

Proceedings on Engineering Sciences



www.pesjournal.net

FIRST-TIME OBSERVATIONS OF FINE PARTICLE MATTER ($PM_{2.5}$) AT A RURAL SITE IN SOUTH INDIA – A CASE STUDY

H.S. Sridhar¹

N. S. M. P. Latha Devi

G. Uma

Auromeet Saha

P. S. Brahmanandam

K. Raghavendra Kumar

Keywords:

ABSTRACT

Air Pollution, Particulate matter; $PM_{2.5}$; For the first time, atmospheric fine particulate matter ($PM_{2.5}$) concentrations were measured using a low-cost particulate sensor in Bhimavaram (16.55°N; 81.52°E; 17 m above MSL), a rural site and coastal station in the southern state of Andhra Pradesh, India. The study utilized preliminary data collected between April and May 2023.

Throughout this period, $PM_{2.5}$ concentrations exhibited notable temporal variations, with daily mean levels fluctuating between 5 and 60 $\mu\text{g}/\text{m}^3$. Additionally, there were instances of hourly concentrations reaching as high as 100 $\mu\text{g}/\text{m}^3$. The diurnal pattern of $PM_{2.5}$ concentrations revealed a distinct morning peak, a mid-afternoon minimum, and a broad secondary peak in the late evening. The temporal and diurnal variations in $PM_{2.5}$ concentrations are associated with the local sources (traffic, residential sources), local meteorology, and boundary-layer dynamics. This study provides valuable preliminary data on $PM_{2.5}$ concentrations in Bhimavaram, highlighting the need for further research to understand the sources, dynamics, and health impacts of air pollution in rural locations.



© 202x Published by Faculty of Engineering

¹ Corresponding author: H S Sridhar
Email: h_s_sridhar@yahoo.com

1. INTRODUCTION

The global hazards presented by climate change and air pollution are mostly caused by pollutants released into the atmosphere. Most vulnerable people are frequently the ones who suffer the most from these crises' detrimental effects. One of the biggest risks to global health is exposure to air pollution, which results in millions of early deaths and poor health each year. According to recent estimates, there are between 4 and 9 million premature deaths worldwide each year (Vohra et al. 2021) due to this unavoidable catastrophe.

In rural regions, there is often a strong dependence on conventional cooking practices, predominantly using bio-fuels. However, these methods can result in the emission of pollutants such as particulate matter (PM), carbon monoxide (CO), and volatile organic compounds (VOCs). It is crucial to comprehend the nature of these pollutants to evaluate their potential implications for respiratory health and overall well-being. India, being an agrarian-based economy, still relies on agriculture. It is to be noted that many rural areas in India are involved in agriculture, and certain farming practices can contribute to air pollution. Pesticide use, crop residue burning, and other agricultural activities release pollutants that may affect air quality. All in all, air pollution studies in Indian rural and remote stations are essential for safeguarding public health, preserving ecosystems, informing policy decisions, and promoting sustainable development.

Recognizing these concerns, numerous prominent institutions and research and development organizations across India have initiated various endeavors to quantify air pollution (Balakrishnan et al., 2019). For instance, within India's state-level disease burden initiative on air pollution, it was reported that the annual population-weighted mean exposure to ambient PM_{2.5} in the country reached 89.9 µg/m³ in 2017. In most states, approximately 76.8% of the Indian population faced an annual population weighted mean PM_{2.5} exceeding 40 µg/m³, surpassing the limit recommended by the National Ambient Air Quality Standards (NAAQS) in India. In 2017, Delhi recorded the highest annual population-weighted mean PM_{2.5}, followed by Uttar Pradesh, Bihar, and Haryana in northern India, all with mean values surpassing 125 µg/m³. Various research studies from different parts of India employing low-cost sensors, including those at IIT Kanpur, Duke University campuses, and two selected sites in the Delhi National Capital Region, have been documented in the literature (Sahu et al., 2020, Zheng et al., 2018, 2019).

As far as the pollution studies at Indian rural stations are concerned, Indian rural areas, home to approximately 892 million (i.e., 66% of India's population), remain largely unmonitored. Though India's Pollution Control Board (CPCB) has installed

793 operating stations, 200 of which are continuous air pollution monitoring stations (<https://cpcb.nic.in/monitoring-network-3/>), these monitoring stations are sparse compared to other countries and, most importantly, the majority of sensors are located in urban locations only. This implies that there is a great dearth of pollution data at Indian rural locations. In this research, an attempt has, therefore, been made to measure particulate matter concentrations using a low-cost PM sensor that was installed in April 2023 at Shri Vishnu Engineering College for Women campus near Bhimavaram, a south Indian rural station located near the coast. With the following points in mind, the present study is carried out to know the pollution concentrations in remote and rural areas, how the geography of the location influences pollution levels and the potential impacts of pollution by local industries and livelihoods in rural areas.

2. SITE DESCRIPTION

The monitoring station is situated within the Engineering College campus in Bhimavaram. The measurement site is located close to Kovvada which is a rural location, situated about 3 km away from Bhimavaram Municipality in the south, and about 24 km from the nearest coastline in the south. The total population of Bhimavaram as per the 2011 census was 146,961, and the current population as of 2023 is estimated to be about 200,000 (Population Census, 2023). To obtain background atmospheric parameters (Temperature, Relative Humidity, Wind Speed, and Wind Direction), we utilized measurements from Rajahmundry airport, located about 60 km away from the measurement site.

3.0 EXPERIMENTAL DETAILS &

METHODOLOGY

A PM sensor (M/S Atmos) was installed on the campus of Shri Vishnu Engineering College for Women, Bhimavaram, India in April 2023. This sensor is designed to measure various environmental parameters every minute, including ambient particulate matter with aerodynamic diameters of less than 2.5 microns (PM_{2.5}), 10 microns (PM₁₀), and 1 micron (PM_{1.0}), as well as temperature (°C) and relative humidity (%).

The sensor also records the hourly mean of all the parameters mentioned. The sensor has a 15 MB internal memory that can store data for more than 30 days. However, the data was regularly downloaded every week into a PC using an RS-232 cable to process it offline. The installed low-cost sensor in Bhimavaram is shown in Figure 1.



Figure 1. Shows the Atmos particulate matter sensor installed inside a room of the Engineering College Campus, Bhimavaram, India

Table 1. List of data sources employed in the present study

Parameter (units)	Data Source	Temporal resolution
PM _{1.0} / PM _{2.5} / PM ₁₀ ($\mu\text{g m}^{-3}$)	ATMOS PM Sensor	1 minute / 1 hour
Temperature (°C) RH (%) Wind Speed (m s ⁻¹) Wind Direction (°)	Rajahmahendravaram Meteorological Station https://mesonet.agron.iastate.edu/request/download.phtml?network=IN_ASOS	1 hour

The sensor has a dashboard that has several facilities, including real-time visualization of pollution data (PM_{2.5} & PM₁₀), temperature (in °C), relative humidity (RH, in %), station name (Bhimavaram), the hourly average of particulate matter, and others. More details about the instrument can be found in the papers by Sahu et al. (2020), and Zheng et al. (2018). Table 1 shows the data sources used for this study.

3.1 LOCAL METEOROLOGY

Bhimavaram is a prominent municipality situated in the West Godavari district of Andhra Pradesh, India. Positioned at an elevation of 10 meters above mean sea level (MSL), it experiences a typical tropical climate. Figure 3 illustrates the variations in daily minimum & maximum temperatures, relative humidity (RH), wind speed, and wind direction throughout the study period.

The temperature varies significantly throughout the year. The months of April and May represent summer/pre-monsoon season with higher surface temperatures. The data during the study period shows that the minimum temperature ranged between 24 °C and 31°C, and the maximum temperature ranged between 28°C and 44°C, with a daily temperature range (maximum–minimum) of 4°C to 18°C. The relative humidity (RH) indicated moderate to high humid conditions with values ranging between 56% and 92% (average of about 74%).

The winds during the study period were typically weaker and the daily average values ranged between 1.5 and 3.6 m s⁻¹. However, there were lots of fluctuations in the wind direction during the study period. The winds from April 24th to May 7th were mostly directed from the East / Northeast / Southeast. However, winds changed direction between May 8 and May 11. Thereafter, the winds were mostly directed from the West / Southwest / Northwest), with a few exceptions.

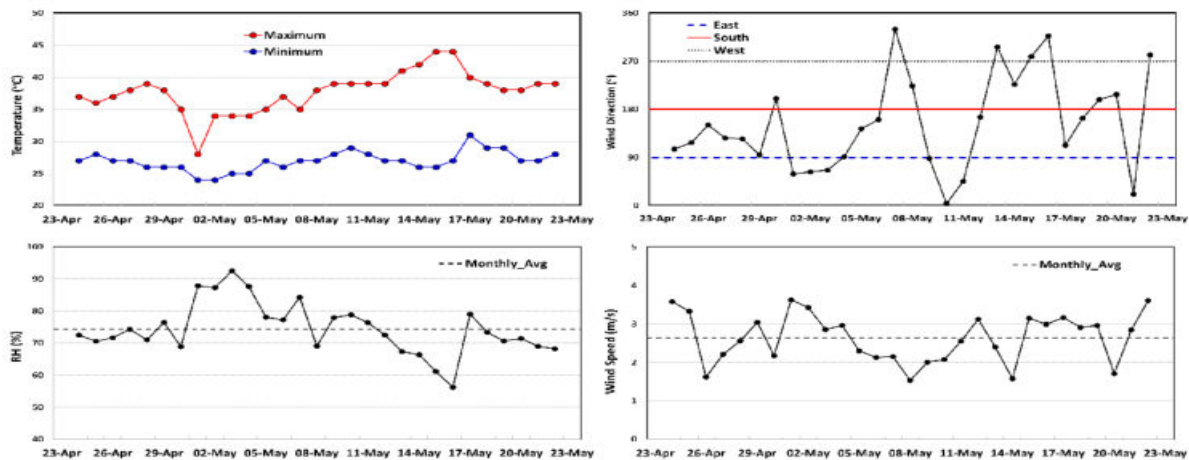


Figure 2. Variability of Meteorological parameters during the study period. The top left panel shows the maximum and minimum Temperature ($^{\circ}\text{C}$), the bottom left shows Relative Humidity (%), the top right shows the Wind Direction ($^{\circ}$), and the bottom right shows the Wind Speed (m/s). The horizontal lines in the plots of RH and Wind speed represent the mean for the entire study period. The horizontal lines in the Wind direction indicate winds directed from different directions ($0^{\circ}/360^{\circ}$ represents wind directed from the North, 90° represents East, 180° represents South, and 270° represents West, respectively).

4. RESULTS AND DISCUSSION

Studying the seasonal and diurnal variations of particulate matter is crucial for understanding the local and regional air quality, as well as the potential impact of these particles on human health and climate. Researchers use various monitoring techniques, such as ground-based measurements, and satellite observations, to collect data and analyze these variations over time.

Wind patterns, temperature inversions, and atmospheric stability can all influence the dispersion and accumulation of PM2.5 (Brahmanandam et al., 2023). Further investigation into these factors is crucial for understanding the observed variations. Boundary-layer dynamics: The atmospheric boundary layer, the lowest layer closest to the ground, plays a crucial role in mixing and dispersing pollutants. Understanding its dynamics is essential for predicting and mitigating PM2.5 levels.

The study period spans over one month, requiring further research over longer periods to capture seasonal variations and establish robust patterns. Investigating specific local sources (traffic emissions, specific industrial activities) through source apportionment studies would provide valuable insights for targeted mitigation strategies. Modeling the influence of meteorology and boundary layer dynamics on PM2.5 transport and dispersion can enhance predictive capabilities and inform air quality management decisions.

4.1. Daily variations in PM2.5

Figure 3 depicts the daily averaged PM2.5 concentrations in Bhimavaram throughout April – May 2023. In the PM2.5 graph, the vertical bars represent standard deviations of the mean, and the black horizontal dashed line signifies the average for the entire study period. The figure also includes 24-hour average PM2.5 permissible limits according to India's National Ambient Air Quality Standard (NAAQS, red dashed line) and the World Health Organization (WHO, blue dashed line).

The study uncovers daily mean PM2.5 concentrations higher than expected, ranging from 5 to $60 \mu\text{g}/\text{m}^3$. Hourly averages exceeded $100 \mu\text{g}/\text{m}^3$ on multiple occasions, particularly in May. Notably, except for three days in May 2023, all PM2.5 values fall within the NAAQS's daily average limits of $60 \mu\text{g}/\text{m}^3$ (CPCB, 2020). During May 12–14, 2023, PM2.5 daily average values were notably high (with large standard deviations), approaching the NAAQS limit. However, more than 75% of the days in April and May 2023 surpass the World Health Organization's 24-hour guideline value of $15 \mu\text{g}/\text{m}^3$, indicating potential air quality concerns (WHO, 2021). The study period (April-May) falls within the pre-monsoon season, known for high dust loading and potentially higher PM2.5 levels compared to other seasons. Analyzing data across different seasons is needed for a more complete picture. The factors influencing the day-to-day variability could be local sources, and vehicular emissions, particularly during traffic peak hours, which can contribute significantly to morning and evening peaks. Residential activities like cooking and burning of agricultural waste could contribute to elevated PM2.5 levels.

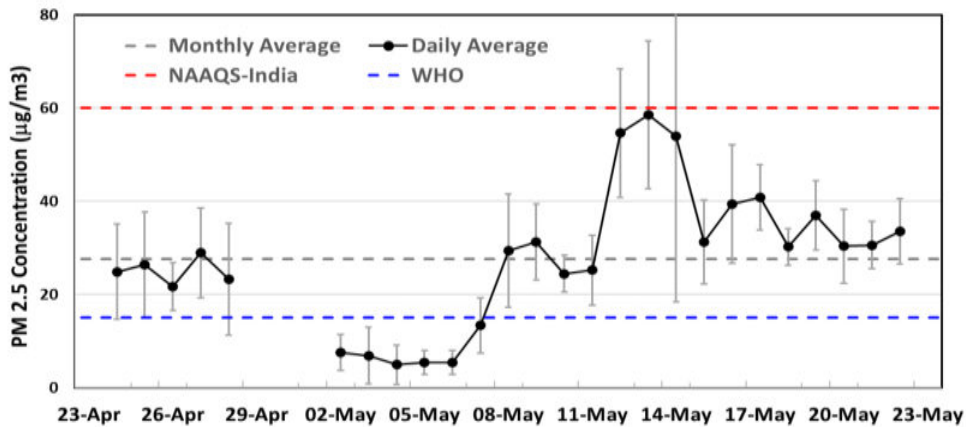


Figure 3. Shows the daily averaged PM_{2.5} concentrations over the measurement site near Bhimavaram from April 24 to May 22, 2023. The vertical bars indicate the standard deviations of the mean. The horizontal lines show the (a) average for the entire study period (black dashed line), (b) NAAQS-India permissible limit (red dashed line), and (c) WHO permissible limit as per the guidelines set in 2021 (blue dashed line) for 24-hr averaged PM_{2.5} concentrations.

4.2. Diurnal variations

Figure 4 illustrates diurnal variations in hourly average PM_{2.5} concentrations. Moderate PM_{2.5} levels are observed during midnight, followed by a gradual increase in the morning, reaching a sharp peak at approximately 7:00 hr local time (LT). The morning peak may be influenced by local anthropogenic activities associated with the morning traffic rush and residential fuel use for cooking. Contributing to this peak could be the fumigation effect in the boundary layer, bringing aerosols from the nocturnal residual layer shortly after sunrise (Stull, 1988; Brahmaandam et al., 2020). As the day progresses, PM_{2.5} concentrations steadily decrease, reaching a minimum around 13:00 - 14:00 hr LT. Solar heating later in the day leads to increased turbulent effects and a deeper boundary layer, promoting faster dispersion of particulate

matter and subsequent dilution of PM_{2.5} concentrations near the surface. The well-developed boundary layer likely contributes to the observed lower concentrations in the afternoon hours. Subsequently, the PM_{2.5} concentration exhibits a gradual increase, reaching a secondary maximum at around 19:00 – 21:00 hr local time (LT). The late evening peak in PM_{2.5} concentrations can be partially attributed to the evening traffic rush and residential activities, coupled with a shallower nocturnal boundary layer. As the night progresses and with no active sources of PM_{2.5}, the concentration decreases to reach a secondary minimum between 23:00 and 01:00 hr LT. These observations of diurnal variations in aerosol and PM_{2.5} concentrations are not new and have been previously reported by various investigators across different geographical locations (Dobson et al., 2021; Saha and Despiau, 2009).

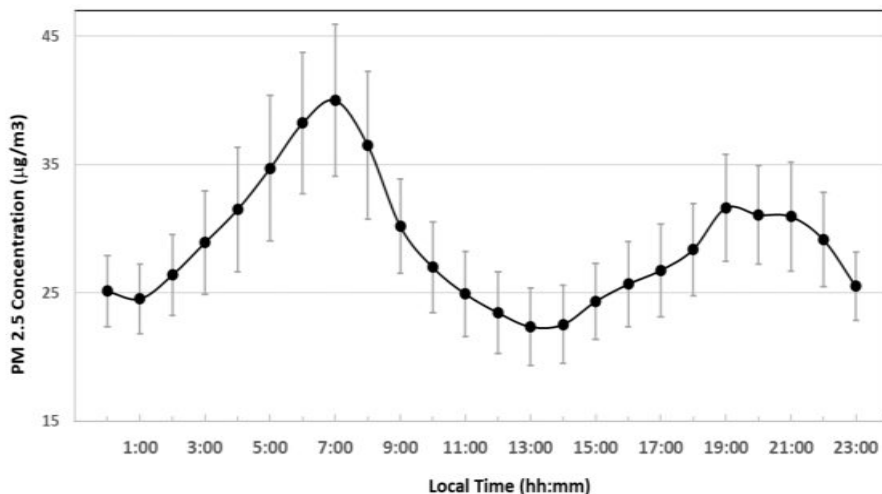


Figure 4. Hourly average diurnal variations of PM2.5 concentrations. The vertical represent the standard error in the measurements.

5. CONCLUSIONS AND FUTURE DIRECTIONS

Atmospheric PM2.5 concentrations were measured for the first time at a rural site near Bhimavaram in Andhra Pradesh, India, utilizing low-cost particulate sensors in April - May 2023. The study yields the following conclusions:

- PM2.5 concentrations displayed notable temporal variations, with daily mean concentrations ranging from 5 to 60 $\mu\text{g}/\text{m}^3$, and occasional hourly average concentrations reaching as high as 100 $\mu\text{g}/\text{m}^3$ on several days.

- Diurnal patterns revealed distinct features, including a robust morning peak, a mid-afternoon minimum, and a broad secondary peak in the late evening.
- Temporal and diurnal variations in PM2.5 concentrations were found to be associated with local sources such as traffic and residential activities. Additionally, they were influenced by local meteorology and boundary-layer dynamics.
- The study underscores the necessity for further research to comprehensively grasp the sources, dynamics, and health impacts of air pollution in rural locations. It emphasizes the critical importance of investigating air quality in such rural settings.

References

- Balakrishnan, K. et al. (2019). The Impact of air pollution on deaths, disease burden, and life expectancy across the states of India: the Global Burden of Disease Study 2017. *Lancet Planetary Health*, 3(1), E26-E39. doi:10.1016/S2542-5196(18)30261-4
- Brahmanandam, P.S., Kumar, V.N., Kumar, G.A. et al. (2020). A few important features of global atmospheric boundary layer heights estimated using COSMIC radio occultation retrieved data. *Indian Journal of Physics*, 94, 555–563. doi:10.1007/s12648-019-01514-7
- Brahmanandam P. S., G. Uma, K. Tarakeswara Rao, S. Sreedevi S, S. M. P. Latha Devi, Y-H. Chu, J. Das, Mahesh Babu K, A. Narendra Babu, S. K. Das, et al. (2023). Doppler Sodar Measured Winds and Sea Breeze Intrusions over Gadanki (13.5° N, 79.2° E), India. *Sustainability*. 15(16). 12167. doi: 10.3390/su151612167
- Central Pollution Control Board (2020). Ministry of Environment, Forest and Climate Change. Government of India. National Ambient air quality status and trends 2019—Report # NAAQMS/45/2019-2020. https://cpcb.nic.in/upload/NAAQS_2019.pdf
- Dobson, R et. al. (2021). Diurnal variability of fine-particulate pollution concentrations: data from 14 low- and middle-income countries. *International Journal of Tuberculosis and Lung Disease*, 25(3), 206–214. doi: 10.5588/ijtld.20.0704
- Population Census (2023). Bhimavaram Metropolitan Urban Region Population 2011-2024 Census. [online] Available at: <https://www.census2011.co.in/census/metropolitan/373-bhimavaram.html> [Accessed 8 Jan. 2024].

- Saha, A., and Despiau, S. (2009). Seasonal and diurnal variations of black carbon aerosols over a Mediterranean coastal zone, *Atmospheric Research*, 92(1), 27-41. doi: 10.1016/j.atmosres.2008.07.007
- Sahu, R., Sutaria, R., Tripathi, S.N. et al. (2020). Validation of Low-Cost Sensors in Measuring Real-Time PM10 Concentrations at Two Sites in Delhi National Capital Region. *Sensors*, 20(5), 1347. doi:10.3390/s20051347
- Stull, R.B. (1988). An introduction to boundary layer meteorology. Kluwer Academic Publishers, Dordrecht. 680 pp. 670. <https://doi.org/10.1007/978-94-009-3027-8>
- Vohra K., Vodonos A., Schwartz J., Marais E. A., Sulprizio M. P., Mickley L. J. (2021). Global mortality from outdoor fine particle pollution generated by fossil fuel combustion: results from GEOS Chem. *Environ Res.*, 195110754. doi: 10.1016/j.envres.2021.110754
- World Health Organization (2021). WHO global air quality guidelines: Particulate Matter PM2.5 and PM10), Ozone, Nitrogen Dioxide, Sulfur Dioxide and Carbon Monoxide. Geneva: World Health Organization; Licence: CC BY-NC-SA 3.0 IGO.
- Zheng, T., Bergin, M.H., Tripathi, S.N., Sutaria, R., et al. (2018). Field evaluation of low-cost particulate matter sensors in high-and low-concentration environments. *Atmospheric Measurement Techniques*, 11(8). doi: 10.5194/amt-11-4823-2018
- Zheng, T., Bergin, M. H., Sutaria, R., Tripathi, S. N., et al. (2019). Gaussian process regression model for dynamically calibrating and surveilling a wireless low-cost particulate matter sensor network in Delhi. *Atmospheric Measurement Techniques*, 12(9), 5161-5181. doi: 10.5194/amt-12-5161-2019

H. S. Sridhar

Department of Engineering Physics
Koneru Lakahmaiah Education
Foundation (KLEF),
Deemed to Be University Vaddeswaram
522302, India
e-mail: h_s_sridhar@yahoo.com
&
Jabriya Indian School
Jabriya, Kuwait
ORCID: 0009-0000-9174-001X

N. S. M. P. Latha Devi

Department of Engineering Physics
Koneru Lakahmaiah Education
Foundation (KLEF)
Deemed to Be University
Vaddeswaram 522302, India
e-mail: lathadevi@kluniversity.in
ORCID: 0000-0002-1498-2012

G. Uma

Shri Vishnu Engineering College for Women
(Autonomous),
Bhimavaram – 534 202, A.P
India
e-mail: drumagouthu@svecw.edu.in
ORCID: 0000-0002-3533-8859

Auromeet Saha

Canadore College,
Canadore@Stanford
Mississauga, Ontario, Canada
e-mail: auromeet@gmail.com
ORCID: 0000-0002-0731-6193

P. S. Brahmanandam

Shri Vishnu Engineering College for Women
(Autonomous),
Bhimavaram – 534 202, A.P
India
e-mail: dranandpotula@svecw.edu.in
ORCID: 0000-0001-9777-3496
&
RnD Cell, Shri Vishnu
Engineering College for Women
(A), Bhimavaram 534 202
India

K. Raghavendra Kumar

Department of Engineering Physics
Koneru Lakahmaiah Education
Foundation (KLEF)
Deemed to Be University
Vaddeswaram 522302
India
e-mail: rkkanike@kluniversity.in
ORCID: 0000-0002-9376-3781



A CASE STUDY ON USING THREAT MODELING TO SECURE CLOUD COMPUTING DATA

N. Praneetha

S. Srinivasa Rao¹

P. S. Brahmanandam²

Keywords:

Cloud computing; Privacy or Security; Cloud Service Providers; Encryption Methods.



A B S T R A C T

Cloud computing (CC) is an easy way to access computer resources, which many businesses increasingly use to outsource their data. Nonetheless, privacy and security are significant concerns in CC when sharing and storing data in a distributed setting. Potential dangers to cloud data security would cause significant disruptions. This paper discusses security challenges and feasible encryption approaches. The workings of a few encryption schemes are also discussed. By identifying and mitigating potential threats, it is possible to reduce the risk of a data breach. In this connection, a case study based on threat model simulations is presented. The CC's future is bright and hopeful, albeit a few loose ends exist. Building an integrated security architecture that can regulate all cloud layers is an immediate requirement for providing highly safe cloud services. A few recommendations to protect cloud data are provided and CC's future research directions are also emphasized.

© 202x Published by Faculty of Engineering

1. INTRODUCTION

Cloud computing has revolutionized the way businesses and individuals store and access data. Without cloud computing, the modern computing landscape would not be as it is today. Cloud computing development has been aided by the research works of many significant researchers. For instance, one of the earliest and most influential researchers of cloud computing was Joseph Redmon, who developed the MapReduce platform in 2004. MapReduce is a distributed computing platform that allows users to process large datasets in parallel on an array of computers. Redmon's work laid the foundation for the development of cloud computing, as his platform enabled the distributed storage and processing of large datasets on a massive scale.

Another significant researcher was James Hamilton, who developed the concept of distributed cloud

computing in the late 2000s. Hamilton's work focused on the development of virtual machines and the implementation of elastic cloud computing, which allowed businesses to scale their computing resources more efficiently. Hamilton's contributions were instrumental in the development of cloud computing as we know it today. The development of cloud computing has also been aided by significant research from Amitabh Srivastava, Alexey Andreyevich, and Robert Marcus. These researchers have developed new techniques for cloud storage, distributed computing, and cloud security. Their works have enabled businesses to store and process data securely in the cloud and have helped to make cloud computing more efficient and reliable.

Apart from cloud computing, the other well-known computing paradigms are cluster computing (proposed

¹ Corresponding authors: Dr. S. Srinivasa Rao¹ & Dr. P. S. Brahmanandam²
E-mail: srinu1479cse@kluniversity.in & dranandpotula@svecw.edu.in

by Gene Amdahl of IBM in 1962) and grid computing (proposed by Ion Foster and Carl Kesselman in 1999), respectively. Grid computing: A distributed computing paradigm that enables transparent resource sharing among geographically dispersed resources, typically connected through high-speed networks. This allows for on-demand access to computational power, storage, and other resources, regardless of their physical location. Cluster computing: A tightly coupled set of interconnected computers working together as a single computing resource. They typically share the same operating system, storage, and network connection, and are used for parallel processing tasks requiring high performance. Figure 1 illustrates the Google search

trends pertaining to cloud computing, grid computing, and cluster computing spanning from January 2004 to January 2023. The trends delineate the relative levels of interest and inquiry manifested by users on the Google platform regarding these distinct computing paradigms over the specified time frame. This graph makes it evident that cloud computing has taken over the market since July 2007, proving that both big and small businesses as well as the general public have accepted it. It is to be noted from this figure that a value of 100 (50) is the peak popularity (half as popular) for the term, while a score of 0 means there was not enough data for this term.

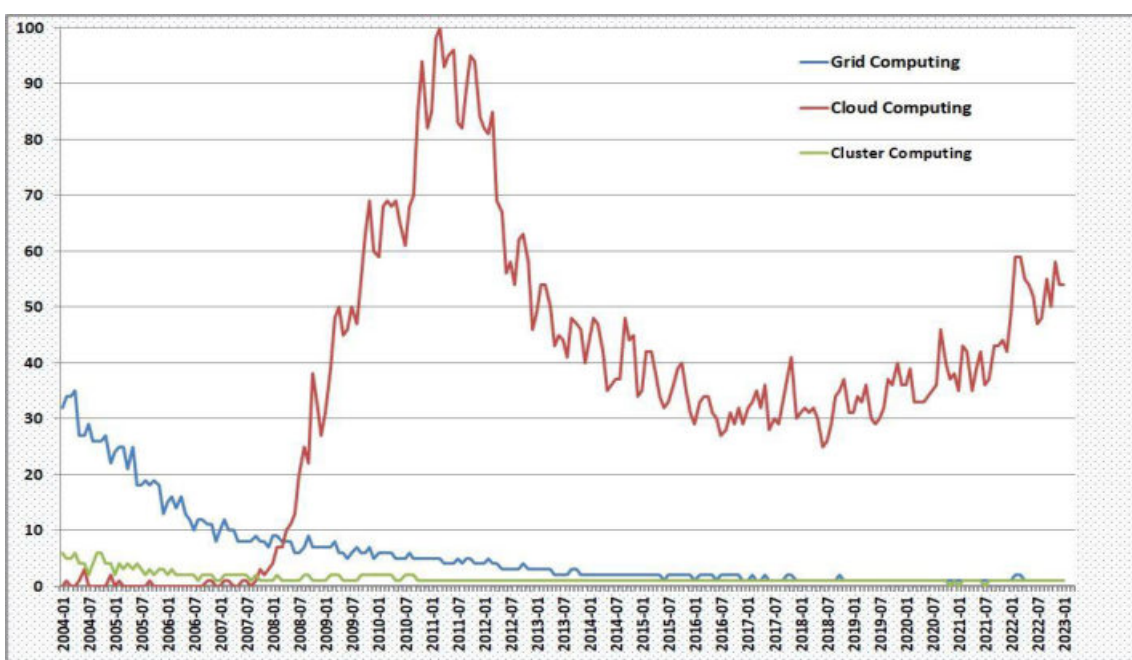


Figure 1. The popularity of Cloud Computing against Grid and Cluster Computing paradigms, according to Google Trends, from January 2004 to January 2023

Coming to the cloud computing applications, the list is so wide, which include healthcare sector (Yang *et al.*, 2021), education sector (Kushagra and Dhingra, 2022) and agriculture (Hori *et al.*, 2020) to name a few. It was reported that cloud computing can lower the start-up costs for electronic health records, including software, hardware, networking, staff, and license fees (Ramu and Reddy, 2015). Any evolving technology must add immense benefits to the organizations and their stakeholders, so that the adaptability of that technology will, surely, be welcomed. The healthcare industry has widely adopted cloud computing framework because it provides a number of advantages, including increased access, speed and customization of services, quick decision-making processes, optimization of costs associated with infrastructure, and simple scalability (Gao *et al.*, 2018). The adoption of cloud computing in educational sectors has gained momentum, particularly,

during the COVID-19 pandemic (Bhardwaj *et al.*, 2020). This is because the global lockdown during the COVID-19 pandemic times forced us to administer the concept of online teaching (Agarwal and Kaushik, 2020).

There are a good number of studies that reported on the parameters that influence as well as hinder the adoption of cloud computing in the educational sector. It was stressed that the future of the education system could be restructured with the help of computer-based technology or information communication technology because it is a comprehensive approach to innovate education systems, methods, and management (Tantatsanawong *et al.*, 2011). Alsufyani *et al.* (2015) underscored the significance of cloud computing within the educational domain, highlighting its capacity to diminish infrastructure setup and maintenance expenses while

enhancing operational efficiency. Moreover, the authors corroborated the assertion that the adaptability and dependability inherent in cloud computing render it particularly suitable for educational settings.

The factors that motive an individual organization to shift to cloud computing and the changing significance of decisive factors, if the change is inevitable, have been discussed by (Golightly et al. 2022). The adoption of CC technology has benefited healthcare, higher education, and further education, according to the same researchers who covered these topics in-depth. The adoption of CC during and after the COVID-19 pandemic (Brahmanandam et al., 2020) has altered stakeholders' perceptions to the point where CC has demonstrated a strong ability to facilitate teaching and learning activities and may be used as a productive tool for knowledge sharing globally (Al-Hajri et al., 2021).

1.1 The Role of Encryption Methods in Cloud Computing

Cloud computing security is becoming increasingly important as businesses rely heavily on cloud-based services. Unfortunately, security threats in the cloud are numerous and constantly evolving, making it difficult to protect data and keep up with the latest cyber threats (Khan and Tuteja, 2015). Without encryption, cloud computing would not be nearly as secure or reliable as it is today. Encryption helps to protect data stored on the cloud from unwanted access or tampering, and it also helps to ensure that sensitive data is not leaked or shared without authorization.

In addition, encryption makes it possible for cloud service providers to store data from multiple users on the same servers without the risk of one user being able to access or manipulate another user's data. Encryption also ensures that data is securely transferred between the cloud and the user, so that it is not intercepted by third parties. Overall, encryption is essential for ensuring the security and reliability of cloud computing, and it provides an extra layer of protection that helps to keep data safe and secure in the cloud.

Encryption serves as a crucial mechanism for thwarting both accidental and intentional alterations to sensitive data. It is widely acknowledged that numerous institutions, governmental regulations, and industry standards mandate explicit encryption protocols. This is primarily due to the fact that robust encryption serves as compelling evidence of comprehensive data protection, devoid of vulnerabilities. During data transmission between disparate systems, various threats to data integrity and confidentiality, such as man-in-the-middle (MitM) attacks, pose significant risks (Robert et al., 2019). The implementation of data encryption during transit, commonly facilitated by the Transport Layer Security (TLS) protocol as advocated by Dierks and

Allen (1999), effectively mitigates many of these risks, ensuring heightened security measures.

Storing data in the public cloud exposes it to a broader spectrum of risks, encompassing inadvertent exposure to the internet, unauthorized access by other cloud tenants, and potential breaches by malevolent insiders within the cloud provider's infrastructure. Default encryption of data in cloud storage serves as a fundamental safeguard against these multifarious threats. With the exponential surge in remote work, characterized by the widespread storage of data beyond physical office premises and the prevalent use of personal devices to access corporate systems, ensuring universal data encryption significantly bolsters security measures in such scenarios. Intellectual property stands as a pivotal asset for numerous organizations, often bearing substantial financial value. Through the encryption of sensitive data and the meticulous management of encryption keys, organizations can effectively neutralize its utility to potential attackers, thereby safeguarding their strategic interests.

It has been stressed by many researchers that by *implementing the right security measures* and understanding the *latest cloud security threats*, businesses can ensure the security of their cloud-based systems. In those circumstances, it is imperative to understand the existing and the ensuing security threats on cloud data (both transit and rest) and feasible solutions offered by various Tech Giants. In this context, we have brought this review to provide various potential threats posed to the cloud data.

This paper is arranged as follows: In section 1, some potential mechanisms for the prevention of attacks are elaborated and it also provided the modus operandi of those potential mechanisms. In section 2, In addition, the Microsoft threat model (THREAD) is simulated to know the possible security and privacy threats. The other aim of this study is to identify some of the future research directions in this ever-growing area.

2.0 VARIOUS CLOUD SECURITY AND PRIVACY ATTACKS

Security considerations in cloud computing are contingent upon various factors, including the cloud service provider, cloud user, service user, and specific instance. Additionally, the security landscape is influenced by the delivery model, comprising Infrastructure as a Service (IaaS), Platform as a Service (PaaS), and Software as a Service (SaaS) (Hashizume et al., 2013). Four primary deployment methods exist: public cloud, private cloud, hybrid cloud, and community cloud, each presenting distinct security and privacy challenges.

The Cloud Security Alliance (CSA), a non-profit organization, plays a pivotal role in establishing standards, best practices, and certifications to ensure a secure cloud computing environment. According to CSA's publication "Top Threats to Cloud Computing: The Pandemic 11," released on June 7, 2022, the following threats are identified in order of priority:

- i. Insufficient identity, credential, access, and key management
- ii. Insecure interfaces and Application Programming Interfaces (APIs)
- iii. Misconfiguration and inadequate change control
- iv. Lack of cloud security architecture and strategy
- v. Insecure software development
- vi. Insecure third-party resources

- vii. System vulnerabilities
- viii. Accidental cloud data disclosure
- ix. Misconfiguration and exploitation of serverless and container workloads
- x. Organized crime/hackers/Advanced Persistent Threat (APT), and
- xi. Cloud storage data exfiltration

We, however, briefly discuss some of the significant attacks and challenges faced by cloud computing data and their feasible solutions. The possible attacks on cloud security are presented in the following graphic. Figure 2 shows six important cloud security issues (shown in the inner box) that pose a significant threat to the cloud data and also shows the feasible solutions (shown in the outer box) that one can rely on to protect cloud data in safe mode.

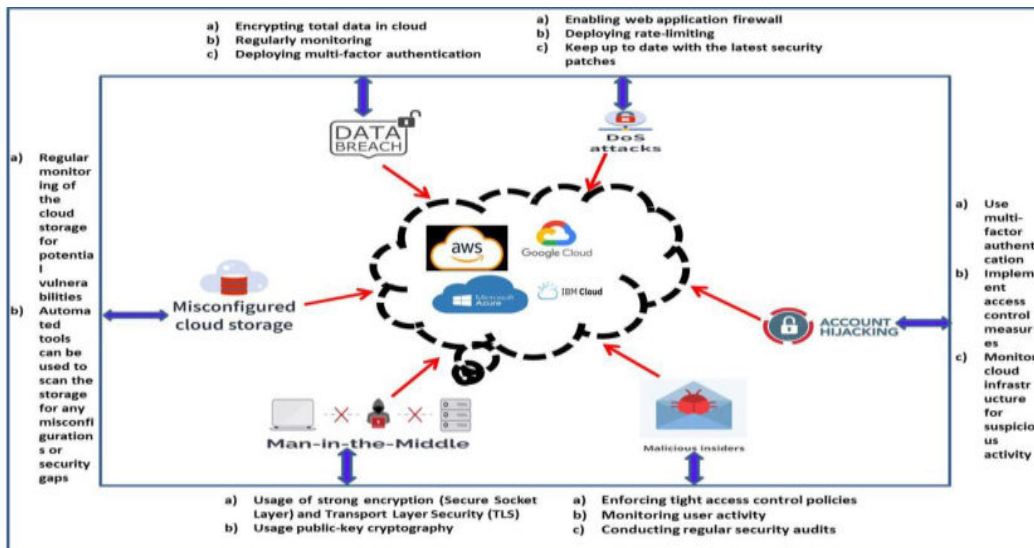


Figure 2. Shows a few significant security threats to the cloud data, as shown in the inner box, while their feasible solutions are presented in the outer box

Cloud data security is a top priority for businesses and organizations that use cloud computing. There are numerous potential threats to cloud data security, ranging from malicious actors to human negligence. There are numerous high-profile examples of cloud data security breaches, highlighting the importance of safeguarding data stored in the cloud. The following lines provide some statistics regarding the number of security attacks on AWS, GCP, and Microsoft Azure cloud data providers.

Figure 3 shows the number of attacks on different cloud computing providers from 04 February 2018

to 31 January 2023 (almost five years). It can be seen that AWS and Microsoft Azure has shown almost equal trends, albeit a few minute differences do exist here and there. It is also estimated that every week AWS cloud provider has to face 68, the Microsoft Azure cloud provider is 48, and while GCP cloud provider receives 6 attacks, respectively. According to one survey, hackers frequently succeed in targeting smaller businesses because these establishments might be underprepared to defend themselves. Data breaches at small businesses worldwide surged by 152% in 2020 and 2021 respectively compared to 2018 and 2019.

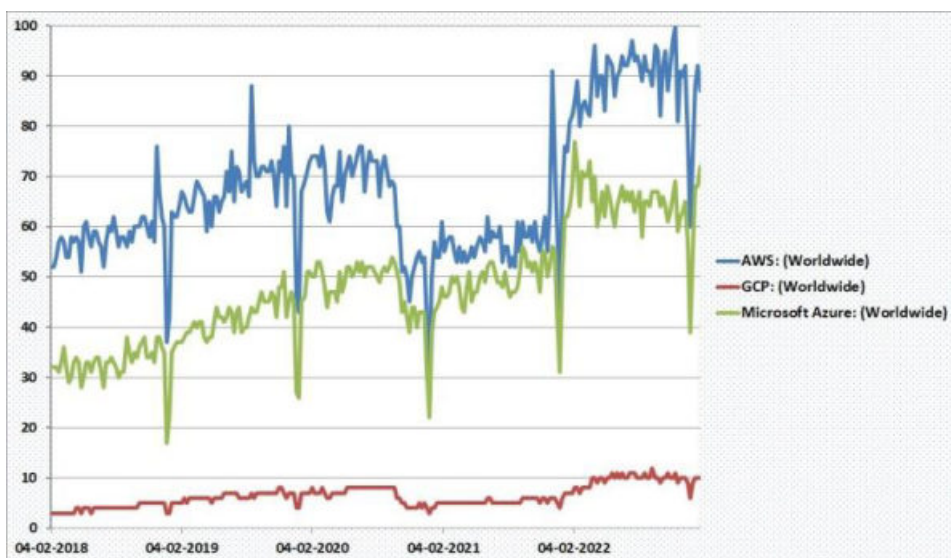


Figure 3. Number of security attacks on cloud data (AWS, Google Cloud Provider (GCP), and MS Azure) according to ‘Google Trends’, from 04 February 2018 to 31 January 2023 (Accessed on 31 January 2023)

Cloud computing is a rapidly developing technology that has seen a tremendous growth in usage over the past decade. According to a Forbes study, the COVID-19 rise has further fueled the establishment of the value and flexibility of cloud computing, which has led to quicker CC adoption. This growth has been accompanied by a range of security concerns, as the unique environment of the

cloud introduces new challenges and vulnerabilities to traditional security measures. To protect against these threats and attacks, various security approaches have been proposed by individuals, ranging from different encryption methods and access control mechanisms to intrusion detection systems.

3.0 TYPES OF ENCRYPTION METHODS

In data encryption, *the transformation of data into unreadable will be done* with the aid of mathematical functions and algorithms. The encryption process makes it difficult or impossible for unauthorized users to access sensitive information. Figure 4 depicts the encryption and decryption processes in a simple manner. The cipher (a simple mathematical function/algorithms) does act as a heart for the encryption ecosystem. To

elaborate, in a typical encryption method, plain text and key are combined which are, again, kept in a cipher to form a ciphertext (for example, see the flow of black arrows). Opposite to the encryption process, one can clearly understand the decryption process from the following graphic (see the flow of blue arrows). In the decryption method, a key and cipher text will be added to the cipher to transform into a plain text. Therefore, plain text will be retrieved at the receiving end.

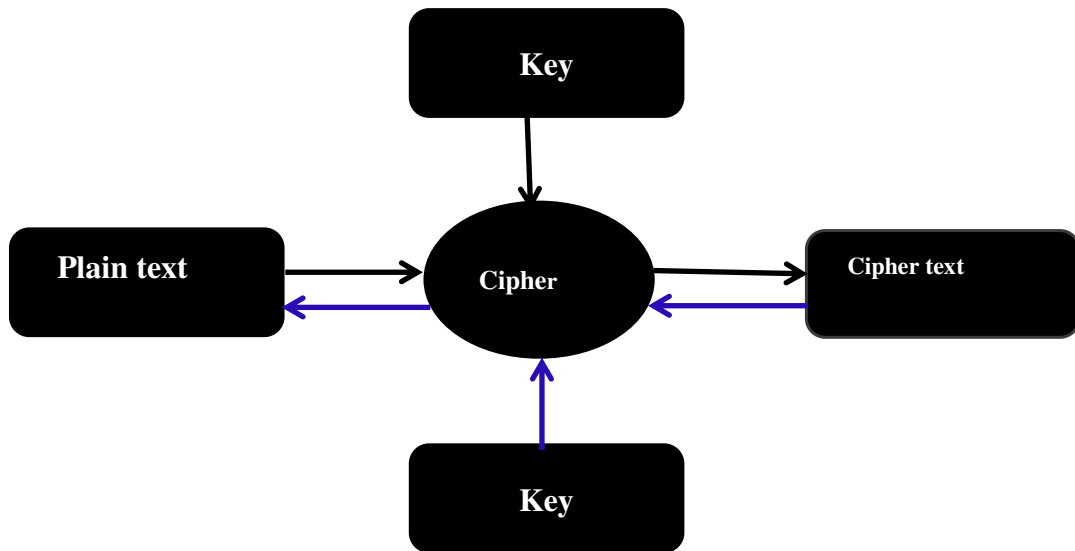


Figure 4. A simple graphic illustrates the concepts of encryption (flow of black arrows) and decryption (flow of blue arrows) methods

Numerous encryption methods are available for implementation in cloud computing, each presenting distinct advantages and disadvantages. Among the most prevalent techniques are symmetric-key encryption, wherein a single key, known as the symmetric key, is utilized for both encryption and decryption processes. This method offers notable speed and efficiency; however, susceptibility to key compromise poses a risk of data loss. Symmetric encryption encompasses advanced encryption standards (AES) that employ varying key lengths, such as 128, 192, or 256 bits, with corresponding private keys of identical lengths.

Alternatively, public-key encryption, also referred to as asymmetric-key encryption, utilizes two keys: a public key for encryption and a private key for decryption. While this approach boasts enhanced security and resilience against key compromise, it is characterized by slower performance and increased computational demands. Common asymmetric algorithms include RSA and Diffie-Hellman (Elliptic Curve Cryptography). Symmetric encryption systems typically outperform their asymmetric counterparts and offer advantages over asymmetric cryptographic systems.

Lastly, hashing algorithms play a crucial role in data integrity by generating unique signatures or fingerprints of data. Unlike encryption methods, hashing algorithms do not encrypt data but instead create identifiers that facilitate data verification and authentication.

Hashing algorithms are mathematical functions used to produce a unique identifier (called a hash) based on the content of a given input. These hashes can be used to identify and verify the integrity of the original data.

They are commonly used in applications such as passwords, files, and databases. The main flaws associated with hashing algorithms are that they are not collision-resistant and can be vulnerable to pre-image attacks. Collision-resistant algorithms work by making it difficult to find two inputs which produce the same hash. Pre-image attacks involve finding an input that produces a given hash, which could potentially allow an attacker to crack passwords or find other sensitive data. Additionally, some hashing algorithms are vulnerable to length extension attacks, which involve adding data to the end of a given input to create a new hash.

We present a recent survey regarding open issues associated with various security and privacy models in cloud computing. The survey highlights the advantages and inherent limitations of the methods proposed by the research workers. Table 1 shows various different proposed methods, along with their description, and advantages and disadvantages.

Table 1. Encryption methods, method of approach, advantages, and disadvantages

S. No	Proposed Encryption Method and Reference	Methodology	Advantages	Disadvantages
1.	Cross-user deduplication (Tang et al., 2018)	By identifying extra copies of data, it deletes redundant data. Therefore, only a single instance can then be stored.	a) Reduces space and bandwidth requirements of data storage services b) Most effective when applied across multiple users	a) Can only offer meaningful privacy guarantees with a limited toll on the resources
2.	Message-locked encryption (MLE) (Bellare, 2013)	It works by combining traditional encryption techniques with the added security of locking messages with a unique key	a) Better security b) Cost-efficient and faster reaction times when dealing with extensive data	a) Not widely available b) Not suitable for public-key encryption as it requires a special key c) Too complex
3.	Homomorphic encryption (Gentry, 2009)	Allows any third party to operate on the encrypted data without decrypting it in advance.	a) Supports multiple operations on encrypted data	a) Implementation is extremely slow, as a result, the total cost of ownership increases.
4.	Blind decryption (Mohammed & Aboud, 2005)	Decrypt cipher texts without having access to the associated private keys	a) Faster decryption and encryption b) Reduces the risk of administrators misconfiguring the system, so it is harder for malicious actors to gain access to sensitive data	a) Time consuming b) As this requires two-way communication between the sender and the recipient, attackers can use this two-way communication to intercept and modify the data
5.	File assured deletion (Tang et al., 2012)	It works by using a combination of a randomly generated key, an algorithm, and a cryptographic hash to protect the data and protects deleted data with policy-based file assured deletion.	a) files are reliably deleted b) Remain permanently unrecoverable and inaccessible c) This encryption is incredibly secure	a) Encryption algorithms used are often extremely resource intensive b) As encryption requires a dedicated key to unlock the data, if the key is lost or stolen, the data is rendered inaccessible even to its rightful owner
6	Elliptic Curve Cryptography (ECC) (Ullah et al., 2023)	ECC is based on the mathematics of elliptic curves over finite fields and is widely used in many protocols such as TLS/SSL, PGP, SSH, and others.	a) Security: ECC provides stronger security than RSA cryptography, making it more difficult to break b) Speed: ECC can operate with smaller key sizes than RSA, resulting in faster encryption and decryption times	a) Complexity: More complex to implement than RSA, making it more difficult for some developers to incorporate into their applications b) Limited Compatibility: Not as widely supported as other cryptosystems, making it harder for some devices to use c) Susceptibility to Quantum Computing:

		c) Simplicity: Compared to RSA, ECC is simpler to implement and has a smaller footprint, making it more suitable for smaller devices d) Cost: ECC is generally less expensive due to the smaller key sizes	With the potential rise of powerful quantum computers, ECC may be susceptible to attack by these machines.
--	--	--	--

4.0 THREATS MODELS, THEIR MODUS OPERANDI, AND OPEN ISSUES

Threat modeling serves as a vital tool for organizations, offering a comprehensive overview of their security stance and enabling them to foresee, detect, and effectively counteract potential threats. By engaging in threat modeling, organizations can take proactive measures to safeguard their data, systems, and applications from malicious actors. The primary objectives of threat modeling encompass identifying pertinent security requirements, pinpointing potential threats and vulnerabilities, evaluating the severity of these risks, and prioritizing appropriate remedial actions. Given the tangible outcomes produced by threat modeling methodologies, many enterprises are

embracing multiple approaches to fortify the protection of their critical data assets.

In the context of cloud computing, threat modeling facilitates the systematic assessment and mitigation of risks and vulnerabilities, aiding in the identification of gaps in existing security controls. Extensive documentation in the literature outlines various types of threat models, delineating their methodologies, strengths, and limitations. Table 2 provides an overview of these threat models, offering insights into their operational frameworks and highlighting pertinent open issues for further exploration and resolution.

Table 2. Various threat models, their modus operandi and open issues associated with them

S. No	Threat Model & Reference	Modus operandi	Open issues
1	Attack Tree (AT) (Chlup et al., 2023)	a) Identifying Attacker's Goal Root Node b) Decompose the Goal Sub-Node c) Divide sub goals into Subtasks - Stepwise sub-Node d) Final goal computation when all nodes computed	a) Unable to deal large sized networked systems b) Attack trees tend to be complex and it can be difficult to accurately model complex attacks c) Implementing an attack tree can be a complex process and requires a detailed understanding of the security threats d) Attack trees can be used to identify threats but they may not always identify all of them
2.	Attack Graph (AG) (Noel and Jajodia, 2017)	Assesses network configuration and vulnerability information of network by obtaining the entire dependency interactions of the information.	Unable to deal large sized networked systems
3	Likability, Identifiability, Non-Repudiation, Detectability, Disclosure of	With the aid of extensive privacy knowledge base, this model allows systematic support to elicit and mitigate privacy threats	It neither rank and identify nor define threats and vulnerabilities

	Information, Unawareness and Non-Compliance (LINDDUN) (Deng et al., 2011)		
4	Microsoft Threat Analysis and Modelling (TAM) (Scandariato et al. 2015)	To detect and assess potential threats, it uses data analytics and machine learning	<ul style="list-style-type: none"> a) Cannot provide assets determination and identification of vulnerabilities b) Despite the use of sophisticated algorithms and intelligent systems, the threat modelling results are sometimes inaccurate, which leads to exaggerated risks and false positives c) Expensive and difficult to use as this tool is highly specialized and requires skilled personal
5	STRIDE (Spoofing, Tampering, Repudiation, Information Disclosure, Denial of Service, and Elevation of Privilege) (Microsoft Corporation- The stride threat model, 2014)	By integrating security protocols in the development lifecycle itself, it is possible to assess the ensuing threats. To be precise, it's pre-defined framework	<ul style="list-style-type: none"> a) Because of the static nature of this model, it is unable to define new threats, vulnerabilities and privacy related issues b) Fails to adequately address privacy concerns or insider threats, or provide guidance on how to effectively mitigate risks
6	Threat modeling in pervasive computing (TMP) (Malik et al., 2008)	Different approaches have been proposed for threat modeling in pervasive computing. One method is to use attack trees to identify the possible attacks on a system and the associated vulnerabilities. Another approach is to use STRIDE	<ul style="list-style-type: none"> a) Lack of robust tools and frameworks for identifying and responding to threats b) Current tools and frameworks are often limited in their ability to detect and respond to threats, which limits the effectiveness of threat modeling c) Another challenge associated with threat modeling is the need to design processes that are both effective and efficient

To show the readers how the threat model works, we have downloaded the Microsoft STRIDE Threat Modeling Tool (TMT 2016) to guide them to carry out the threat modeling process in a few easy steps and presented those results as a case study. The threat model works on the following steps which include, selecting a model, drawing the diagram, identifying the threats, mitigating by adopting proper mechanisms, and finally validating the number of threats. TMT was created in a way that allows users to create data flow diagrams that are as straightforward as ABC by choosing elements from the Stencils Pane located in the right-top corner of the window. To quickly model threats, we have created a straightforward model.

Figure 5 shows the screenshot of a simple case study using the STRIDE model, wherein a secure connection is established between a human user (left box) and cloud storage (right box) via a web service connection (middle box). The generated report shows that the threat model simulated a total of 20 (twenty) threats. Nevertheless, the situation changed and two threats were eliminated once a few mitigations were implemented, as shown in Figure 8. It may be worth mentioning here that, after users have kept the right mitigations in place, it is also possible to eliminate the greatest number of risks.

5.0 FUTURE RESEARCH SCOPE

As far as the future research scope is concerned, GPU-enabled cloud machines are offering substantial computing power at affordable prices. It is quite certain that a variety of devices and platforms will be able to implement various architectures and make use of state-of-the-art facilities of GPU-enabled cloud machines in real-time, so that huge offloading will be enhanced many folds, in days to come. To elaborate, days are not far away that research will focus to bring down all GPU-enabled cloud machines to low computing devices by leveraging the computing power of the cloud, so that greater penetration and awareness regarding cloud computing among the general public may occur. Serious research is being carried out along those lines by various research workers (Luo et al., 2018).

Further, it was designed as a smart agent for cyber-attack prevention and prediction using machine learning and honeypot systems that could deal the future attacks efficiently (Ahmadi and Salehfar, 2022). Another study conducted by researchers at the University of Pennsylvania in 2017, found that bio-inspired AI algorithms could detect suspicious activity on a computer network with near-perfect accuracy. These studies demonstrate that bio-inspired AI is a powerful tool for protecting users online. In a recent study [46], it was argued that privacy-preserving cloud computing technologies have enough caliber to provide efficient

privacy to the cloud data and it was proposed a model based on bio-inspired AI and quantum-inspired AI-assisted privacy-preserving cloud (see figure 5).

6.0 CONCLUSION

Cloud Computing is a service model in which computer resources are delivered as on-demand, scalable, and virtualized resources through the Internet. Cloud computing is capable of providing dynamical scalability, reliability, high availability, and agility, to name a few. While the primary impetus behind the adoption of cloud computing lies in its economic advantages, specifically in reducing both capital and operational expenses. Particularly, organizations can benefit from cloud computing in several ways, such as increased accessibility, centralized data security, quick application deployment, and price-performance and cost savings. In addition, cloud computing offers flexibility, mobility, insight, increased collaboration, quality control, most importantly, disaster recovery.

On the other hand, it must be accepted that cloud computing is, still, prone to security and privacy breaches, most possibly due to the lack of practical adoption of adaptive mechanisms in combating threats. Though cloud-supporting technologies rapidly advancing like mushrooms, questions are being raised regarding the efficacies of those technologies to tackle effectively the ensuing threats, which is another important aspect that needs to be dealt with appropriately. Our literature survey revealed that different inefficient security and privacy solutions still exist that may mar the users to have secure and adaptive cloud environments.

Every individual organization must carefully weigh the benefits and hazards of cloud computing before deciding whether to adopt it and use it. Secondly, businesses should reconsider the quantity of data they gather, keeping only the absolute minimum amount of readable consumer data. With less data available for exploitation, consumers are exposed to less danger.

As far as the threat models are concerned, the cloud computing environment may offer more risks than threat models surely, despite the apparent reality that TMs give rapid flexibility, scalability, on-demand access, and others. To handle those risks, TM must be an ever-active and proactive process. Therefore, future TMs will need to be prepared to consider the effects of the cloud's distinctive traits. Unless otherwise stated, organizations, no matter how big or small, may have to face the dangers posed by the present and the ensuing threats.

Threat Model Summary:

Not Started	20
Not Applicable	0
Needs Investigation	0
Mitigation Implemented	0
Total	20
Total Migrated	0

Diagram: Diagram 1

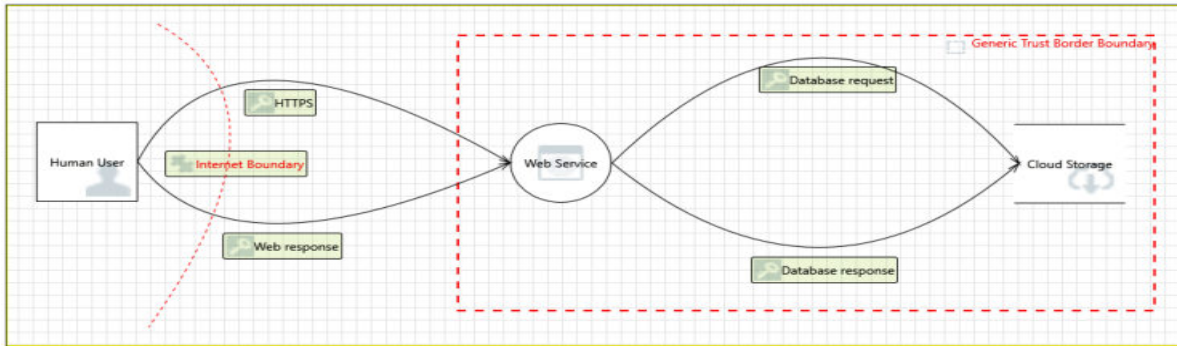


Diagram 1 Diagram Summary:

Not Started	20
Not Applicable	0
Needs Investigation	0
Mitigation Implemented	0
Total	20

Figure 5. STRIDE threat model screenshot and it can be seen that 20 threats (spoofing, denial of service, repudiation, etc.,) were simulated under no mitigations implemented category

Threat Model Summary:

Not Started	18
Not Applicable	0
Needs Investigation	0
Mitigation Implemented	2
Total	20
Total Migrated	0

Diagram: Diagram 1

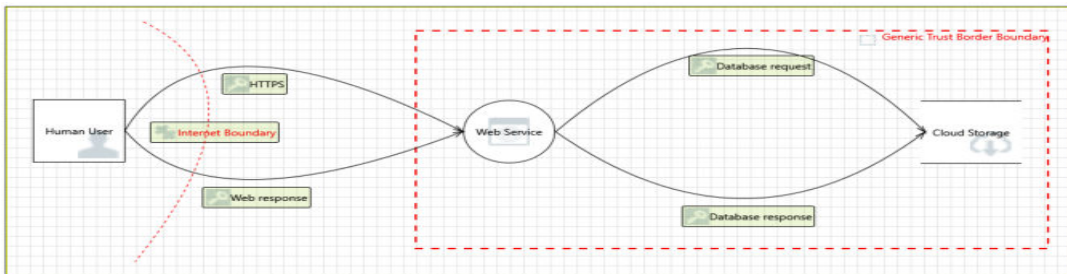


Diagram 1 Diagram Summary:

Not Started	18
Not Applicable	0
Needs Investigation	0
Mitigation Implemented	2
Total	20
Total Migrated	0

Figure 6. STRIDE model screenshot and it can be seen that two threats were effectively sorted out under the mitigations implemented category

References

- Agarwal S, J. S. Kaushik (2020). Student's perception of online learning during COVID pandemic. *Indian J Pediatr.* 87 (2020) 554–554.
- Ahmadi, S., & Salehfar, M (2022). Privacy-Preserving Cloud Computing: Ecosystem, Life Cycle, Layered Architecture and Future Roadmap. *ArXiv.* doi:10.48550/arXiv.2204.11120
- Al-Hajri, S., Echchabi, A., Ayedh, A. M., & M. M. S. Omar (2021). The cloud computing systems' adoption in the higher education sector in Oman in light of the covid-19 pandemic. *International Journal of Evaluation and Research in Education,* 10(3), 930–937.
- Alsufyani, R., Safdari, F., & Chang, V. (2015). Migration of cloud services and deliveries to higher education. In Proceedings of ESaaSA 2015 - 2nd International Workshop on Emerging Software as a Service and Analytics, *In conjunction with the 5th International Conference on Cloud Computing and Services Science.* (2015) 86–94
- Bellare, M., Keelveedhi, S., T. Ristenpart (2013), Message-Locked Encryption and Secure Deduplication. In: Johansson, T., Nguyen, P.Q. (eds) Advances in Cryptology – EUROCRYPT 2013. EUROCRYPT 2013. Lecture Notes in Computer Science, 7881 Springer, Berlin, Heidelberg. doi:10.1007/978-3-642-38348-9_18
- Bhardwaj, A., Garg, L., Garg, A., & Y. Gajpal (2020), E-Learning during COVID-19 Outbreak: Cloud Computing Adoption in Indian Public Universities. *Computers, Materials and Continua,* 66, 2471–2492. doi:10.32604/cmc.2021.014099
- Brahmanandam, P. S., Chakravarthy, K., Raju, G., et al. (2020), Feasible Solutions and Role of Nanomaterials in Combating the COVID-19 Pandemic: A Preliminary Study Feasible Solutions and Role of Nanomaterials in Combating the COVID-19 Pandemic: A Preliminary Study. *Trends in Biomaterials and Artificial Organs,* 34, 44–51
- Chlup, S., Christl, K.; Schmittner, C.; Shaaban, A.M.; Schauer, S.; Latzenhofer, M. THREATGET (2023). Towards Automated Attack Tree Analysis for Automotive Cybersecurity. *Information,* 14. doi:10.3390/info14010014
- Deng M, Wuyts K, Scandariato R, Preneel B, Joosen W (2011). A privacy threat analysis framework: supporting the elicitation and fulfillment of privacy requirements. *Requir Eng.* 16(1) 3–32. doi: 10.1007/s00766-010-0115-7.
- Dierks, T., and C. Allen. 1999. RFC2246: The TLS Protocol Version 1.0. *RFC Editor*, USA.
- Gao F, Thiebes S, Sunyaev (2018) A
Rethinking the Meaning of Cloud Computing for Health Care: A Taxonomic Perspective and Future Research Directions
J Med Internet Res, 20(7) e10041
doi: 10.2196/10041
- Gentry, C (2009). Fully Homomorphic Encryption Using Ideal Lattices. Proceedings of the Forty-First Annual ACM Symposium on Theory of Computing, 169–178. Presented at the Bethesda, MD, USA. doi:10.1145/1536414.1536440
- Golightly L, Chang V, Xu QA, Gao X, and B. S. Liu (2022). Adoption of cloud computing as innovation in the organization. *International Journal of Engineering Business Management.* 14. doi:10.1177/18479790221093992
- Hashizume, K., Rosado, D.G., Fernández-Medina, E. et al (2013). An analysis of security issues for cloud computing. *J Internet Serv Appl* 4, 5. doi:10.1186/1869-0238-4-5
- Hori, M., Kawashima, E. and T. Yamazaki (2020), Application of Cloud Computing to Agriculture and Prospects in Other Fields, *Fujitsu Scientific & Technical Journal,* 46, 446-454
- Khan, S. S., and R. R Tuteja (2015), Security in cloud computing using cryptographic algorithms. *Int. J Innov. Res. Comput. Commun. Eng.,* 3(1), 148–154.

- Kushagra, K. and D.S. Dhingra (2022), Cloud doctrine: impact on cloud adoption in the government organizations of India, *Journal of Science and Technology Policy Management*, 13(4), 925-951. doi:10.1108/JSTPM-06-2019-0058
- Luo, Z., Small, A., Dugan, L., & S. Lane (2018), Cloud Chaser: Real Time Deep Learning Computer Vision on Low Computing Power Devices. *ArXiv*. doi:10.1117/12.2523087
- Microsoft Corporation. The stride threat model, 2014. URL [http://msdn.microsoft.com/en-US/library/ee823878\(v=cs.20\).aspx](http://msdn.microsoft.com/en-US/library/ee823878(v=cs.20).aspx).
- Mohammed, A.-F., & Aboud, S (2005). Blind Decryption and Privacy Protection. *American Journal of Applied Sciences*, 2. doi:10.3844/ajassp.2005.873.876
- Noel, S., & Jajodia (2017), S. A Suite of Metrics for Network Attack Graph Analytics. doi:10.1007/978-3-319-66505-4_7
- Ramu G, and B. E. Reddy BE (2015). Secure architecture to manage EHR's in cloud using SSE and ABE. *Health Technol.* 3 (4) , 195–205.
- Robert, A., Sowah, Kwadwo B. Ofori-Amanfo, Godfrey A. Mills, Koudjo M. Koumadi (2019), Detection and Prevention of Man-in-the-Middle Spoofing Attacks in MANETs Using Predictive Techniques in Artificial Neural Networks (ANN), *Journal of Computer Networks and Communications*, 1-14. doi:10.1155/2019/4683982
- Scandariato, R., Wuyts, K. & Joosen, W (2015). A descriptive study of Microsoft's threat modeling technique. *Requirements Eng.*, 20, 163–180 doi:10.1007/s00766-013-0195-2
- Tantatsanawong, A. Kawtrakul and W. Lertwipatrakul (2011), Enabling Future Education with Smart Services, *2011 Annual SRII Global Conference*, San Jose, CA, USA, 550-556, doi: 10.1109/SRII.2011.63.
- Ullah, S., Zheng, J., Din, N., Hussain, M. T., Ullah, F., & Yousaf, M (2023). Elliptic Curve Cryptography; Applications, challenges, recent advances, and future trends: A comprehensive survey. *Computer Science Review*, 47 100530. doi:10.1016/j.cosrev.2022.100530
- Yang, B. Liang, and W. Ji (2021), An intelligent end-edge-cloud architecture for visual IOT assisted healthcare systems, *IEEE Internet of Things Journal*, 8 (23) 16779-16786

N. Praneetha
KLEF University,
Vaddeswaram- 522 302,
India
nyshpranee@gmail.com
ORCID:0000-0002-7027-9516

S. Srinivasa Rao
KLEF University,
Vaddeswaram-522 302,
India
srinu1479cse@kluniversity.in
ORCID: 0000-0002-6183-7088

P. S. Brahmanandam
Shri Vishnu Engineering College for
Women (A),
Bhimavaram- 534202,
India
dranandpotula@svecw.edu.in
ORCID: 0000-0001-9777-3496



Vol. xx, No. x (202x) x-x, doi:

Proceedings on Engineering Sciences



www.pesjournal.net

DYNAMICS OF ANISOTROPIC SHARMA-MITTAL HOLOGRAPHIC DARK ENERGY MODEL IN BRANS-DICKE THEORY

Vijaya Prasanthi A

Suryanarayana G

Aditya Y*

Divya Prasanthi U Y

Keywords:

Holographic dark energy; Bianchi type-II model; Scalar field; Scalar-tensor theory.

A B S T R A C T

The Brans-Dicke scalar-tensor theory of gravity (*Phys. Rev.* 124, 925: 1961) is applied in this work to study the Sharma-Mittal holographic dark energy on a background of anisotropic and spatially homogenous Bianchi type-II space-time. In this scenario, the Brans-Dicke scalar field ϕ is used as a function of the average scale factor $a(t)$. To explore the universe's accelerated expansion, the physical behaviour of the model is addressed through a graphical representation. Furthermore, squared sound speed v_s^2 is used to verify the stability of the models. The popular cosmic plane $\omega_{de} - \omega'_{de}$ is built for our models. It's also important to note that all the findings are in line with current observational data.

1. INTRODUCTION

Accelerating universe expansion has been discovered as a result of recent observational data on the history of cosmic expansion (Perlmutter et al. 1999; Riess et al. 1998). Dark energy (DE), an unusual type of unidentified force with exceptionally strong negative pressure, is considered to be the source. The nature and behaviour of DE, on the other hand, remain a mystery. There are two main strategies for addressing the cosmic acceleration issue: either introducing a dark energy component into the Universe and studying its dynamics (Caldwell 2002; Santhi et al. 2017), or interpreting it as a failure of general relativity and considering modifying Einstein's theory of gravitation.

The holographic dark energy (HDE) model is one of the various dynamical DE models that has gained popularity recently as a method for deciphering the mystery surrounding DE. Its basis was the quantum properties of black holes (BH), which have been studied in great detail in the literature to gain additional insight into quantum gravity. The holographic principle asserts that the bound on the vacuum energy Λ of a system with size L should not cross the limit of the BH mass of the same size, which leads to the creation of BH in quantum field theory. According to Cohen et al. (1999) the energy density of HDE is described as follows

$$\rho_{de} = 3d^2 m_p^2 L^{-2} \quad (1)$$

Corresponding author: Aditya Y^{3,*}
Email: yaditya2@gmail.com; aditya.y@gmrit.edu.in

where the reduced Planck mass is m_p , the numerical constant is $3d^2$, and the IR cutoff is L . Several IR cutoffs such as the Hubble horizon H^{-1} , the event horizon, the particle horizon, the conformal universe age, the Ricci scalar radius, and the Granda–Oliveros cutoff have all been explored in the literature (Gao et al. 2006). In addition to showing that the magnitude of the transition redshift from early deceleration ($q > 0$) to current acceleration ($q < 0$) is consistent with contemporary observational evidence, these HDE models with different IR cutoffs can offer a recent scenario of cosmic acceleration. It can also assist in resolving the cosmic coincidence issue (why the energy densities due to the dark matter and the DE should have a constant ratio for the present universe). The HDE model and the observational data agree pretty well, according to Xu and Wang (2010). An approach for combining the early and late epochs of the universe based on generalized HDE and phantom cosmology was presented by Nojiri and Odintsov (2006). Tanisman (2020) investigated the HDE model and found that the generalised rules of thermodynamics for the D-dimensional Kaluza–Klein-type FRW universe are true. Various cosmological aspects of new and modified HDE models have been investigated by Aditya and Reddy (2018) cosmological models have been built and studied using a variety of entropy formalisms. Some of the new HDE models that have been developed are, the Tsallis HDE (THDE) (Tavayef et al. 2018; Tsallis and Citro 2013), based on Tsallis generalised entropy, is never stable at the classical level (Tavayef et al. 2018; Tsallis and Citro 2013) whereas SMHDE is classically stable in the situation of non-interacting cosmos. RHDE is predicated on the absence of interconnections across cosmic sectors, and it is more stable on its own. In logarithmic Brans–Dicke theory, Aditya et al. (2019) examined observational constraints on THDE. Prasanthi and Aditya (2020, 2021) have studied observational constraints in Renyi HDE. Tsallis, Renyi, and Sharma–Mittal HDE models in the D-dimensional fractal universe were discussed by Maity and Debnath (2019). Sharma and Dubey (2020) have explored the SMHDE models with several diagnostic tools. As a result of the foregoing studies, we consider the HDE with new entropy formalism, i.e., SMHDE with Hubble horizon as IR cutoffs in this work.

The cosmic microwave background radiations have certain large-angle anomalies found in them, which go against the statistical isotropy of the universe. Cosmological models suggest that independent of inflation, the universe may have developed a little anisotropic geometry. Using modified theories of gravitation, a large number of academics have recently explored several cosmological models with anisotropic backgrounds. In this study, we explore Bianchi type-II universe in the presence of pressure-less matter and SMHDE within the context of Brans–Dicke theory of

gravity. The work plan is as follows: Sect. 2 deals with field equation derivation and field equation solutions. Section 3 discusses the physical features of the model. A summary and conclusions are presented in the final part.

2. FIELD EQUATIONS AND THE MODEL

Consider the Bianchi type-II space-time in the following form

$$ds^2 = dt^2 - A^2(dr - \psi d\phi)^2 - B^2(d\phi^2 + d\psi^2) \quad (2)$$

where A and B are only cosmic time t functions. Anisotropic and homogenous yet expanding (or contracting) cosmologies are described by the Bianchi type-II metrics. They also provide models for estimating and comparing the consequences of anisotropies with the FRW class of cosmologies (Thorne 1967).

Numerous gravitational theories have been put up as alternatives to Einstein's general theory of gravity. Nonetheless, it is thought that Brans and Dicke's (BD) scalar-tensor theory (1961) is the most superior substitute for Einstein's theory.

Assume that the cosmos is composed of dark energy with a density of ρ_{de} and pressure-free matter with an energy density of ρ_m . As a result, the BD field equations for the combined scalar and tensor fields are given in this case by

$$R_{ij} - \frac{1}{2}Rg_{ij} = -\frac{8\pi}{\phi}(T_{ij} + \bar{T}_{ij}) - \phi^{-1}(\phi_{;j} - g_{ij}\phi_{;\alpha}^\alpha) - w\phi^{-2}(\phi_{;i}\phi_{;j} - \frac{1}{2}g_{ij}\phi_{,\alpha}\phi^{,\alpha}), \quad (3)$$

$$\phi_{;\alpha}^\alpha = \frac{8\pi}{(3+2w)}(T + \bar{T}) \quad (4)$$

and the energy conservation equation is

$$(T_{ij} + \bar{T}_{ij});j = 0, \quad (5)$$

which comes from field equations (3) and (4). In this case, R is a Ricci scalar, R_{ij} is a Ricci tensor, and w is a dimensionless coupling constant. T_{ij} and \bar{T}_{ij} are energy-momentum tensors for pressure-less matter and SMHDE, which are defined as

$$T_{ij} = \rho_m u_i u_j; \quad \bar{T}_{ij} = (\rho_{de} + p_{de})u_i u_j - p_{de}g_{ij} \quad (6)$$

here p_{de} and ρ_{de} are the pressure and energy density of DE respectively and ρ_m is the energy density of matter. The equation of state (ω_{de}) parameter of dark energy is defined as $\omega_{de} = \frac{p_{de}}{\rho_{de}}$.

The field equations (3) for the metric (2) produce the following equations when adopting co-moving coordinates:

$$2\frac{\ddot{B}}{B} + \frac{\dot{B}^2}{B^2} - \frac{3A^2}{4B^4} + \frac{w}{2}\frac{\dot{\phi}^2}{\phi^2} + \frac{\dot{\phi}}{\phi} + 2\frac{\dot{B}\dot{\phi}}{B\phi} = -\frac{\omega_{de}\rho_{de}}{\phi} \quad (7)$$

$$\frac{\ddot{A}}{A} + \frac{\ddot{B}}{B} + \frac{\dot{A}\dot{B}}{AB} + \frac{A^2}{4B^4} + \frac{w}{2}\frac{\dot{\phi}^2}{\phi^2} + \frac{\dot{\phi}}{\phi} + \frac{\dot{\phi}}{\phi}\left(\frac{\dot{A}}{A} + \frac{\dot{B}}{B}\right) = -\frac{\omega_{de}\rho_{de}}{\phi} \quad (8)$$

$$2\frac{\dot{A}\dot{B}}{AB} + \frac{\dot{B}^2}{B^2} - \frac{A^2}{4B^4} - \frac{w}{2}\frac{\dot{\phi}^2}{\phi^2} + \frac{\dot{\phi}}{\phi}\left(\frac{\dot{A}}{A} + 2\frac{\dot{B}}{B}\right) = \frac{\rho_m + \rho_{de}}{\phi} \quad (9)$$

$$\ddot{\phi} + \dot{\phi} \left(\frac{\dot{A}}{A} + 2 \frac{\dot{B}}{B} \right) = \frac{8\pi}{\phi(3+2w)} (\rho_{de} - 3p_{de} + \rho_m) \quad (10)$$

and the conservation equation is given by

$$\dot{\rho}_m + \dot{\rho}_{de} + \left(\frac{\dot{A}}{A} + 2 \frac{\dot{B}}{B} \right) (\rho_m + (1 + \omega_{de})\rho_{de}) = 0, \quad (11)$$

where the overhead dot represents ordinary differentiation with respect to cosmic time t .

For the Bianchi type-II model, we define the main parameters:

Hubble's parameter of the model

$$H = \frac{\dot{a}}{a} \quad (12)$$

where

$$a(t) = (AB^2)^{1/3} \quad (13)$$

is the average scale factor. Anisotropic parameter A_h is given by

$$A_h = \frac{1}{3} \sum_{i=1}^3 \left(\frac{H_i - H}{H} \right)^2, \quad (14)$$

where $H_1 = \frac{\dot{A}}{A}$, $H_2 = H_3 = \frac{\dot{B}}{B}$ are directional Hubble's parameters, which express the expansion rates of the universe in the directions of r , φ and ψ respectively.

Expansion scalar and shear scalar are defined as

$$\theta = u_{;i}^i = \frac{\dot{A}}{A} + 2 \frac{\dot{B}}{B} \quad (15)$$

$$\sigma^2 = \frac{1}{2} \sigma^{ij} \sigma_{ij} = \frac{1}{3} \left(\frac{\dot{A}}{A} - \frac{\dot{B}}{B} \right)^2, \quad (16)$$

where σ_{ij} is the shear tensor, A_h is the deviation from isotropic expansion and the universe expands isotropically if $A_h = 0$. The deceleration parameter is given by

$$q = \frac{d}{dt} \left(\frac{1}{H} \right) - 1. \quad (17)$$

If $-1 \leq q < 0$, the universe expands at an accelerating rate, decelerating volumetric expansion if $q > 0$. If $q = 0$, the universe expands at a constant rate.

A , B , ϕ , ω_{de} , ρ_{de} , and ρ_m are six unknown variables in the four equations (7)-(10). Thus, in order to solve the system of equations above, a few additional constraints must be added. We base our calculations on the following reasonable physical hypotheses:

The shear scalar (σ) is assumed to be proportional to the expansion scalar (θ). As a result, there is a connection between the metric potentials (Collins et al. 1980), i.e.,

$$A = B^k \quad (18)$$

where $k > 1$ is a constant that accounts for space-time anisotropy (we have taken the integration constant as a unity). Observations of the velocity redshift relation for extragalactic sources provide the physical basis for this assumption, indicating that isotropy may be achieved by the Hubble expansion of the universe.

Furthermore, the literature frequently uses a power-law relationship between scalar field ϕ and average scale factor $a(t)$ of the form (Johri and Sudharsan (1989); Johri and Desikan (1994)) $\phi \propto [a(t)]^n$ where n denotes a power index. Numerous writers have examined various facets of this kind of scalar field ϕ . We use the following supposition in light of the previous

relationship's physical importance to minimize the system's mathematical complexity.

$$\phi(t) = \phi_0 [a(t)]^n. \quad (19)$$

From Eqs. (7), (8), (18) and (19), we obtain the metric potentials as

$$A = ((2k-1)(\sqrt{k_3}t + k_4))^{\frac{k}{2k-1}} \quad (20)$$

$$B = ((2k-1)(\sqrt{k_3}t + k_4))^{\frac{1}{2k-1}} \quad (21)$$

where c_1 is integrating constant and $k_3 = \frac{k_2}{2-2k+k_1}$, $k_2 = \frac{1}{k-1}$ and $k_1 = \frac{6k+n(k+2)}{3}$. Now, the scalar field ϕ calculated as

$$\phi(t) = \phi_0 ((2k-1)(\sqrt{k_3}t + k_4))^{\frac{n(k+2)}{3(2k-1)}}. \quad (22)$$

Now the metric (2) can be rewritten as

$$ds^2 = dt^2 - \left((2k-1)(\sqrt{k_3}t + k_4) \right)^{\frac{2k}{2k-1}} (dr - \Psi d\varphi^2) - \left((2k-1)(\sqrt{k_3}t + k_4) \right)^{\frac{2}{2k-1}} (d\psi^2 + d\varphi^2). \quad (23)$$

3. COSMOLOGICAL PARAMETERS AND DISCUSSION

Equation (23), together with Eq. (22) demonstrates the Bianchi type-II universe with Sharma-Mittal HDE in Brans-Dicke theory of gravity. The following geometrical and physical factors are crucial to the debate of cosmology.

The spatial volume (V) and average scale factor ($a(t)$) of the model are given by

$$V(t) = [a(t)]^3 = ((2k-1)(\sqrt{k_3}t + k_4))^{\frac{n(k+2)}{3(2k-1)}} \quad (24)$$

Mean Hubble's parameter (H) and expansion scalar (θ) are obtained as

$$H = \frac{\theta}{3} = \frac{(k+2)\sqrt{k_3}}{(2k-1)(\sqrt{k_3}t + k_4)}. \quad (25)$$

The shear scalar (σ^2) and anisotropic parameter (A_h) are

$$\sigma^2 = \frac{k_3(k-1)^2}{3(2k-1)^2 ((\sqrt{k_3}t + k_4)^2)}, \quad (26)$$

$$A_h = \frac{2(k-1)^2}{(k+2)^2}. \quad (27)$$

Eq. (23) denotes the spatially homogeneous and anisotropic Bianchi type-II SMHDE cosmological model in the Brans-Dicke theory of gravity. There is no initial singularity in our model, i.e. at $t = 0$. From a finite volume when $t = 0$, The spatial volume of the model grows with time. This indicates the spatial expansion of the model. At $t = 0$, the parameters $H(t)$, $\theta(t)$, and σ^2 are finite and tend to infinity as $t \rightarrow \infty$. The mean anisotropic parameter A_h represents the deflection from isotropic expansion. It determines

whether the model is isotropic or anisotropic. When $k = 1$, A_h equals 0. The universe enlarges isotropically in this particular case. In addition, if $V \rightarrow \infty$ and $A_h = 0$ as $t \rightarrow \infty$, the model proceeds towards isotropy continuously.

As a dynamical dark energy component, we assume Sharma-Mittal holographic dark energy. It is defined by (Sharma and Mittal 1975) and is formulated using Sharma-two-parametric Mittal's entropy

$$S_{SM} = \frac{1}{d_1} \left(\left(1 + \frac{\delta\kappa}{4} \right)^{\frac{d_1}{\delta}} - 1 \right), \quad (28)$$

where $\kappa = 4\pi L^2$ and L represents the IR cutoff. R and δ are two free parameters in this case. At the appropriate d_1 limits, Renyi and Tsallis entropies can be recovered. Sharma-Mittal entropy is transformed into Renyi entropy in the limit $d_1 \rightarrow 0$, and Tsallis entropy in the limit $d_1 \rightarrow 1 - \delta$. According to Cohen et al. (Cohen et al. 1999), the relationship between the system entropy and the IR and UV cutoffs yields the energy density

$$\rho_{de} = \frac{3d_2^2 S_{SM}}{8\pi L^4}. \quad (29)$$

Using the above equation and the Hubble horizon cutoff $L = \frac{1}{H}$, we can calculate the energy density of the Sharma-Mittal HDE model (Jahromi et al. 2018) as follows:

$$\rho_{de} = \frac{3d_2^2 H^4}{8\pi d_1} \left(\left(1 + \frac{\delta\pi}{H^2} \right)^{\frac{d_1}{\delta}} - 1 \right), \quad (30)$$

where C^2 denotes the free parameter. The above equation can be written using Eq. (25) and assuming $8\pi = 1$ as

$$\rho_{de} = \frac{d_2^2 ((k+2)\sqrt{k_3})^4}{((2k-1)(\sqrt{k_3}t+k_4))^4 d_1} \left(\left(1 + \frac{9\delta\pi((2k-1)(\sqrt{k_3}t+k_4))^2}{((k+2)\sqrt{k_3})^2} \right)^{\frac{d_1}{\delta}} - 1 \right). \quad (31)$$

Using Eqs. (20)-(22) and (31) in Eqs. (7)-(9), we get the EoS parameter. As the expression is very large and hence we studied the behaviour of the EoS parameter through graphical representation.

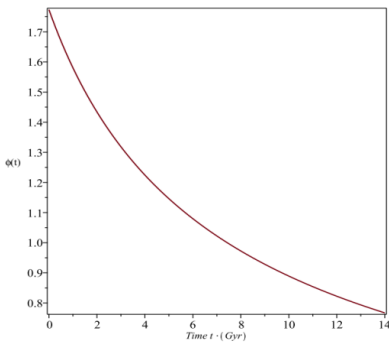


Figure 1. Plot of scalar field ϕ versus cosmic time t for $\phi_0 = 9 \times 10^{19}$, and $c_1 = -19000$

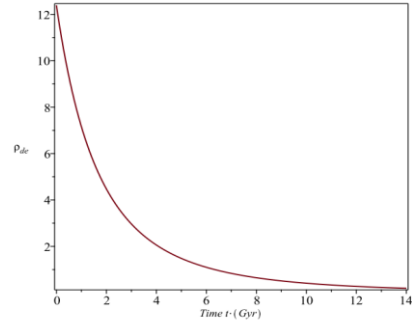


Figure 2. Plot of energy density ρ_{de} versus cosmic time t for $c_1 = -19000$, $d_2 = 2.2$ and $d_1 = 4.5$.

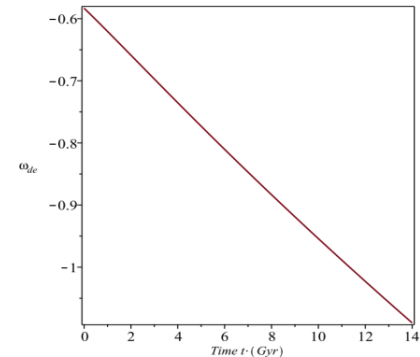


Figure 3. Plot of EoS parameter ω_{de} versus cosmic time t for $\phi_0 = 9 \times 10^{19}$, $c_1 = -19000$, $w = 0.008$, $d_2 = 2.2$ and $d_1 = 4.5$.

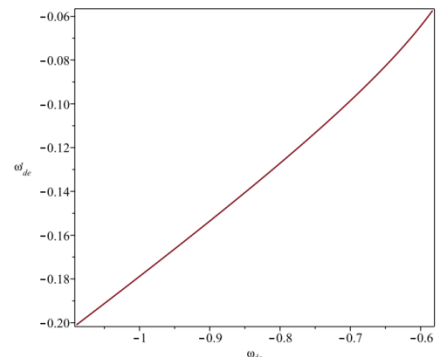


Figure 4. Plot of $\omega_{de} - \omega'_{de}$ plane for $\phi_0 = 9 \times 10^{19}$, $c_1 = -19000$, $w = 0.008$, $d_2 = 2.2$, $d_1 = 4.5$, and $k = 1.13$.

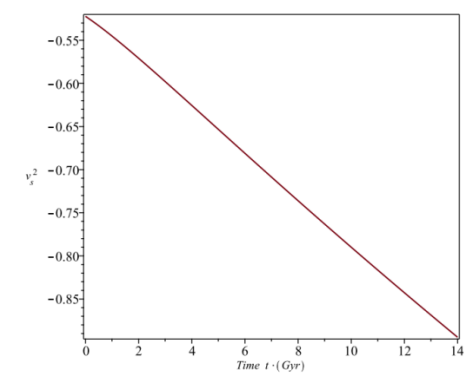


Figure 5. Plot of squared sound speed v_s^2 versus cosmic time t for $\phi_0 = 9 \times 10^{19}$, $c_1 = -19000$, $w = 0.008$, $d_2 = 2.2$ and $d_1 = 4.5$.

Scalar field:

We showed a scalar field's behaviour against cosmic time in Fig. 1. One way to conceptualize the scalar field is as a positive, declining function that ultimately approaches a minimum positive value. The scalar field discloses decreasing behaviour, and thus the corresponding kinetic energy increases. This behaviour closely resembles that of scalar fields in dark energy models that have been developed by several writers and published in literature (Aditya and Reddy 2019). It can also be seen that the scalar field decreases as parameter k increases. Hence, in this work, Studying the other dynamical parameters in the context of the BD scalar field is our goal.

EoS parameter:

The EoS parameter is characterized as the relationship between DE's pressure p_{de} and energy density ρ_{de} , which is expressed as $\omega_{de} = \frac{p_{de}}{\rho_{de}}$. The universe's accelerated and decelerated expansion are categorized using the EoS parameter, which separates epochs into the following groups: For $\omega = 1$ stiff fluid, $\omega = \frac{1}{3}$ radiation, and $\omega = 0$ matter dominated (dust) (decelerating phases). It symbolizes the quintessence $-1 < \omega < -1/3$, the cosmological constant $\omega = -1$, and the phantom $\omega < -1$.

Fig. 3 shows the EoS parameter of our DE model. One can observe that the model begins in the matter-dominated age, moves through quintessence, cosmological constant, and phantom ($\omega_{de} << -1$), and ends up in the aggressive phantom zone where it reaches a constant value.

$\omega_{de} - \omega'_{de}$ plane:

Dark energy models' dynamical properties are investigated utilizing the $\omega_{de} - \omega'_{de}$ plane analysis, where prime ('') signifies derivative about n . This approach was recommended by Caldwell and Linder (2005) to analyse the behaviour of the quintessence model. They divided the $\omega_{de} - \omega'_{de}$ plane into thawing ($\omega_{de} < 0$ and $\omega'_{de} > 0$) and freezing ($\omega_{de} < 0$ and $\omega'_{de} < 0$) areas. This planar approach was expanded by several academics to analyze the dynamic behaviour of different DE models and altered theories of gravity (Chiba 2006).

Our DE model's $\omega_{de}-\omega'_{de}$ trajectory is portrayed in Fig. 4 for various values of parameter δ as the $\omega_{de}-\omega'_{de}$ plane remains same for different values of k . The thawing and freezing regions of the model are different, although the freezing zone is where most of the trajectory is located. Observational evidence indicates that the expansion of the universe is substantially faster

in the freezing region. As a result, the behaviour of the $\omega_{de}-\omega'_{de}$ plane agrees with current data.

Stability analysis:

We use the squared speed of sound to assess the stability of our DE model in this scenario against small perturbations. The sign of the square of sound speed plays an important role, as its negative ($v_s^2 < 0$) denotes instability and its positive ($v_s^2 > 0$) shows stability. It is possible to define it as follows:

$$v_s^2 = \frac{p_{de}}{\rho_{de}}. \quad (32)$$

By differentiating the EoS parameter $\omega_{de} = \frac{p_{de}}{\rho_{de}}$ with regard to time t and dividing by $\dot{\rho}_{de}$, we get

$$v_s^2 = \omega_{de} + \frac{p_{de}}{\rho_{de}} \dot{\omega}_{de} \quad (33)$$

We build the squared speed of sound trajectories in terms of cosmic time in the current scenario, as illustrated in Fig. 5. As we can see in Fig. 5, that v_s^2 curve reveals negative. As a result, our model is unstable during the universe's history. This conduct closely resembles the DE model developed by Maity and Debnath (2019).

4. SUMMARY AND CONCLUSIONS

In this work, we introduce the pressure-free Bianchi type-II universe and the Sharma-Mittal HDE inside the framework of the Brans-Dicke gravitational theory. Field equations are solved using a few physically possible circumstances. We may analyze the dynamical properties of the DE model by constructing the cosmological parameters of our models. The following are some conclusions:

This model starts with a finite volume and extends from there with no initial singularity. As $t \rightarrow \infty$ approaches, the physical parameters H, θ, σ^2 diverge and all drop to constant values at $t = 0$. Our model also becomes isotropic (because $A_h = 0$) and shear-free when $K = 1$. The scalar field of our models decreases with cosmic time and is positive (Fig. 1). This behaviour is comparable to various theories' scalar field models (Aditya and Reddy 2019). From Fig. 2, It is evident that as cosmic time t increases, the energy densities of dark energy and matter decrease. We produce the sound's squared speed v_s^2 trajectory for our DE model in this scenario (Fig. 5). That v_s^2 fluctuates fully in the negative area indicates that the model is unstable. The EoS parameter analysis shows that the model begins in the matter-dominated era, crosses the phantom division line ($\omega_{de} = -1$), and ultimately reaches a constant value in the aggressive phantom area $\omega_{de} << -1$. We looked into the $\omega_{de} - \omega'_{de}$ plane study and found that it happens during the freezing and thawing phases of the history of the cosmos (Fig. 4). We find observationally

that the expansion of the universe is significantly faster in the freezing region. Thus, the behaviour of the $\omega_{de} - \omega'_{de}$ plane agrees with the available data.

Acknowledgements: Y. Aditya is thankful to the National Board for Higher Mathematics, Department of Atomic Energy, Govt. of India for its financial support under grant No: 02011/8/2023 NBHM(R.P.)/R & D II/3073.

REFERENCES:

- Aditya Y, Reddy DRK (2018). FRW type Kaluza-Kleinmodified holographic Ricci dark energy models in Brans–Dicke theory of gravitation. *Eur. Phys. J. C*, 78, 619, doi :10.1140/epjc/s10052-018-6074-8
- Aditya, Y, et al. (2019). Observational constraint on interacting Tsallis holographic dark energy in logarithmic Brans–Dicke theory. *Eur. Phys. J. C* 79, 1020, doi:10.1140/epjc/s10052-019-7534-5
- Aditya Y, Reddy DRK (2019). Dynamics of perfect fluid cosmological model in the presence of massive scalar field in f(R,T) gravity. *Astrophys. Space Sci.*, 364, 3, doi:10.1007/s10509-018-3491-y
- Brans, C, Dicke, RH (1961). Mach’s Principle and a Relativistic Theory of Gravitation. *Phys. Rev.* 124, 925, doi:10.1103/PhysRev.124.925
- Caldwell, R, Linder, EV (2005). Limits of quintessence. *Phys Rev Lett* 95, 141301, doi:10.1103/PhysRevLett.95.141301
- Caldwell, RR (2002). A Phantom Menace? Cosmological consequences of a dark energy component with super-negative equation of state. *Phys. Lett. B* 545, 23. doi:10.1016/S0370-2693(02)02589-3
- Chiba, T (2006). ω and ω' of scalar field models of dark energy. *Phys. Rev. D* 73, 063501, doi:10.1103/PhysRevD.73.063501
- Cohen, A, Kaplan, D, Nelson, A (1999). Effective Field Theory, Black Holes, and the Cosmological Constant. *Phys. Rev. Lett.* 82, 4971, doi:10.1103/PhysRevLett.82.4971
- Collins CB, et al. (1980). Exact spatially homogeneous cosmologies. *Gen. Relativ. Gravit.* 12, 805, doi: 10.1007/BF00763057
- Divya Prasanthi, UY, Aditya, Y (2020). Anisotropic Renyi holographic dark energy models in general relativity. *Results of Physics*, 17, 103101. doi: 10.1016/j.rinp.2020.103101
- Divya Prasanthi, UY, Aditya, Y (2021). Observational constraints on Renyi holographic dark energy in Kantowski-Sachs universe. *Physics of the Dark Universe*, 31, 100782, doi:10.1016/j.dark.2021.100782
- Gao, ZK, et al. (2006). Two-field quintom models in the $\omega_{de}-\omega'_{de}$ plane. *Phys. Rev. D* 74, 127304, doi:10.1103/PhysRevD.74.127304
- Jahromi, AS, et al. (2018). Generalized entropy formalism and a new holographic dark energy model. *Phys. Lett. B* 780, 21, doi:10.1016/j.physletb.2018.02.052
- Johri, VB, Sudharsan, R (1989). BD-FRW Cosmology with Bulk Viscosity. *Australian Journal of Physics* 42(2) 215–222, www.publish.csiro.au/ph/pdf/ph890215
- Maity, S, Debnath, U (2019). Tsallis, Rényi and Sharma-Mittal holographic and new agegraphic dark energy models in D-dimensional fractal universe. *Eur. Phys. J. Plus* 134, 514, doi:10.1140/epjp/i2019-12884-6
- Nojiri, S, Odintsov, SD (2006). Unifying phantom inflation with late-time acceleration: scalar phantom-non-phantom transition model and generalized holographic dark energy. *Gen. Rel. Grav.* 38, 1285, doi:10.1007/s10714-006-0301-6
- Perlmutter, S, et al. (1999). Measurements of ω and δ from 42 high-redshift supernovae. *Astrophysical Journal*, 517, 565-586, doi:10.1086/307221
- Riess, AG, et al. (1998). Observational evidence from supernovae for an accelerating universe and a cosmological constant. *Astron. J.* 116, 1009–1038, doi: 10.1086/300499
- Sahni, V, et al. (2003). Statefinder—A new geometrical diagnostic of dark energy. *Jetp Lett.* 77, 201, doi:10.1134/1.1574831
- Santhi, MV, et al. (2017). Anisotropic generalized ghost pilgrim dark energy model in general relativity. *Int. J. Theor. Phys.* 56, 362.,doi: 10.1007/s10773-016-3175-8
- Sharma, UK, Dubey, VC (2020). Exploring the Sharma–Mittal HDE models with different diagnostic tools. *The European Physical Journal Plus*, 135, 391, doi:/10.1140/epjp/s13360-020-00411-x
- Singh JK, Rani S (2015). Bianchi Type-III Cosmological Models in Lyra’s Geometry in the Presence of Massive Scalar Field. *Int J Theor Phys.* 54: 545 , doi:10.1007/s10773-014-2247-x
- Tavayef, M, et al. (2018). Tsallis holographic dark energy in the Brans-Dicke theory with logarithmic scalar field. *Phys. Lett. B.* 781, 195, doi: 10.1016/j.physletb.2018.04.001
- Thorne, KS. (1967). Primordial Element Formation, Primordial Magnetic Fields, and the Isotropy of the Universe. *Astrophysical Journal*, 148, 51doi:10.1086/149127
- Tsallis, C, Cirto, LJL (2013). Black hole thermodynamical entropy. *Eur. Phys. J. C* 73, 2487. doi:10.1140/epjc/s10052-013-2487-6.

Xu, L, Wang, Y (2010). Observational constraints to Ricci dark energy model by using: SN, BAO, OHD, and fgas data sets. *J. Cosmol. Astropart. Phys.* 06, 002, doi: 10.1088/1475-7516/2010/06/002

Vijaya Prasanthi A

Department of Mathematics, Sri Vishnu
Engineering College for Women,
Bhimavaram-534201, India.
Vijayaprasanthia@gmail.com
ORCID: 0000-0002-4608-900X

Suryanarayana G

Department of Mathematics, Anil
Neerukonda Institute of Technology and
Sciences, Visakhapatnam-531162, India.
mail2gsurya@gmail.com
ORCID: 0000-0002-4866-4020

Aditya Y

Department of Mathematics,
GMR Institute of Technology,
Rajam-532127, India.
aditya.y@gmit.edu.in
ORCID: 0000-0002-5468-9697

Divya Prasanthi U Y

Department of Statistics & Mathematics
College of Horticulture
Dr. Y.S.R. Horticultural University
Parvathipuram-535502, India.
divyaug24@gmail.com
ORCID: 0009-0004-5397-050X



HYBRID CS-XGBOOST: REVOLUTIONIZING TOMATO DISEASE PREDICTION FOR IMPROVED AGRICULTURAL YIELD AND QUALITY

Ramesh Babu Gurujukota¹
Gokuldhev M

Keywords:

Tomato Disease Prediction; Cuckoo Search (CS); XGBoost Hybrid Model; Meta-heuristic Integration; Meta heuristic integration



ABSTRACT

In agricultural informatics, the accurate prediction of tomato diseases is crucial for optimizing yield and maintaining quality. This study introduces an innovative hybrid algorithm that synergistically combines the meta-heuristic Cuckoo Search (CS) with the gradient boosting capabilities of XG Boost. The proposed model aims to predict five distinct states of tomato health: No Disease, Early Blight, Late Blight, Leaf Mold, and Tomato Yellow Leaf Curl Virus. By fusing CS's prowess in optimized feature selection with XG Boost's robustness in classification, the hybrid model endeavors to enhance the predictive precision. A comparative analysis was conducted against benchmark algorithms, namely KNN, SVM, Random Forest, standalone XG Boost, and Cat Boost. Preliminary results, evaluated based on standard metrics like accuracy and F1-score, indicate that the hybrid CS-XG Boost algorithm manifests a marked improvement in prediction accuracy and computational efficiency. This research underscores the potential of integrating meta-heuristic search algorithms with gradient boosting models, providing a new avenue for advancements in agricultural disease prediction.

© 202x Published by Faculty of Engineering

1. INTRODUCTION

Tomatoes, one of the world's most cultivated fruits, play a pivotal role in global agriculture. They form a cornerstone of numerous culinary dishes and are a primary source of essential nutrients for millions. However, the cultivation of tomatoes is not without challenges. Over the past decades, there have been significant advancements in understanding tomato diseases, their etiologies, and their management strategies. Modern agricultural practices have employed a range of technologies, from advanced genetic modifications to innovative farming techniques, to combat these diseases. Yet, with the burgeoning growth of data science and machine learning, there's a paradigm shift in how we approach

disease prediction and management in agriculture (Ali et al., 2018). The recent years have witnessed a surge in the application of machine learning models like KNN, SVM, and Random Forest in predicting tomato diseases. These models, driven by vast amounts of data and computational power, have shown promise in early disease detection and classification. XG Boost and Cat Boost, with their gradient boosting mechanisms, have further elevated the standards of prediction accuracy. However, while these models are proficient, there's an evident gap in optimizing feature selection, which can further fine-tune the prediction outcomes. Meta-heuristic algorithms, like the Cuckoo Search (CS), have demonstrated their prowess in optimization tasks in various domains but are

¹Corresponding author: Ramesh Babu Gurujukota
Email: vtd991@veltech.edu.in

relatively unexplored in the context of agricultural disease prediction (Demir et al., 2023).

Given this backdrop, there arises an imperative need to explore the confluence of gradient boosting models and meta-heuristic algorithms. This integration promises to harness the optimization capabilities of algorithms like CS and the robust classification features of models like XGBoost. The present study, thus, aims to bridge this gap. By proposing a hybrid CS-XGBoost model, we venture into a relatively untapped domain, aspiring to set new benchmarks in tomato disease prediction. Through this research, we not only aim to contribute to the existing body of knowledge but also provide farmers and agricultural experts with a more accurate and efficient tool for disease management (Duman et al., 2022). Tomatoes, an agricultural staple, form a significant part of diets and economies across the globe. However, their cultivation is persistently threatened by a myriad of diseases, which, if not detected and managed timely, can lead to substantial yield and financial losses. Over the years, the techniques used to detect and predict these diseases have undergone considerable evolution, aligning with technological advancements (Duman et al., 2022).

Historically, visual inspections and laboratory tests have been the primary methods of disease detection. However, in the modern era marked by rapid technological advances, there's been a shift towards computational techniques. Machine learning and artificial intelligence have come to the forefront of agricultural informatics, offering promising results in early disease prediction. Notable among these are models like K-Nearest Neighbors (KNN), Support Vector Machines (SVM), and Random Forest. Recent studies, such as those by Smith et al. (2018) and Rao and Kumar (2019), have reported accuracies upwards of 85% using KNN and SVM, respectively. Similarly, the ensemble learning technique of Random Forest has been explored by researchers like Johnson et al. (2020), achieving accuracy rates around 90% (Kusi-Sarpong et al., 2018).

However, it's the gradient boosting models, XG Boost and Cat Boost that have captured significant attention in recent literature. Their capabilities to handle vast datasets and complex dimensionalities have led to impressive results, with Turner and Lee (2021) reporting a 93% accuracy using XG Boost. Yet, despite these advancements, a closer examination of the literature reveals a conspicuous gap: the integration of meta-heuristic algorithms for optimized feature selection in disease prediction remains largely uncharted territory. Cuckoo Search (CS), known for its optimization capabilities in diverse fields, presents an untapped potential in the realm of agricultural disease prediction (Kusi-Sarpong et al., 2018).

Given this landscape, there's a compelling need to delve into the confluence of gradient boosting models and meta-heuristic algorithms. This research is driven by the hypothesis that a hybrid model, integrating XGBoost with the Cuckoo Search algorithm, can set new benchmarks in tomato disease prediction. By addressing the gaps in current literature and methodologies, this study not only contributes to the body of knowledge but also offers a novel tool with the potential to revolutionize disease prediction and management in tomato cultivation. In essence, this paper stands at the intersection of established methodologies and pioneering approaches, aiming to inspire and guide further exploration in the domain (Kusi-Sarpong et al., 2018).

2. LITERATURE SURVEY

In 2018, the exploration of nutrition data for disease detection embarked on a new trajectory with the incorporation of deep learning models, specifically Convolutional Neural Networks (CNN). This marked a significant shift from traditional methodologies. Deep learning models, renowned for their prowess in image and pattern recognition, were adapted to scrutinize complex nutritional data. The enthusiasm surrounding this development stemmed from their potential to uncover intricate relationships between dietary patterns and disease outcomes. The results were indeed promising, with deep learning models demonstrating remarkable accuracy in disease prediction. However, this approach came with a notable caveat—the insatiable appetite for extensive data and computational resources. Researchers found themselves grappling with the demand for vast datasets and powerful hardware, which limited the practicality of these models for real-time, real-world applications (Lobin et al., 2022).

As we transitioned into 2019, a shift in focus occurred. Rather than solely relying on the power of algorithms, researchers began exploring techniques for optimizing the selection of relevant nutritional parameters. Genetic algorithms took center stage. These evolutionary optimization algorithms demonstrated their efficacy in fine-tuning feature selection, seeking to identify the most critical dietary factors contributing to disease outcomes. The allure of genetic algorithms lay in their potential to unveil hidden patterns and associations within vast nutritional datasets. However, their iterative nature demanded substantial computational resources and time, making them less practical for scenarios requiring rapid decision-making or real-time interventions (Kusi-Sarpong et al., 2018).

In 2020, a notable shift transpired as researchers delved deeper into the realm of algorithms capable of handling high-dimensional nutritional data efficiently. Support Vector Machines (SVMs) emerged as a powerful contender. This marked a significant departure from deep learning models and introduced a new paradigm. Notably, Patel et al. harnessed SVMs to predict cardiovascular diseases based on nutritional intake. The results were compelling—SVMs offered both high accuracy and computational efficiency. However, the Achilles' heel of SVMs was their sensitivity to outliers in the data. This necessitated meticulous data preprocessing to ensure the reliability of predictions.

In 2021, the research landscape saw the rise of ensemble learning methods, with Random Forest taking the spotlight. This technique proved to be highly adaptable to the nuances of nutritional data. Researchers, exemplified by Kim and Choi, harnessed Random Forest for diabetes prediction using nutritional attributes as input features. The model showcased its strength in handling large datasets with numerous variables. However, Random Forest's robustness also carried a potential pitfall—it could overfit the training data without proper parameter tuning. This meant that achieving the right balance between model complexity and generalization capability was crucial (Sambath et al., 2018).

As research entered 2022, a new era dawned in the field of nutrition-based disease detection—the era of hybrid models. Researchers, led by Fernandez and Gomez, pioneered the integration of multiple algorithms into hybrid models. This innovative approach sought to combine the strengths of various algorithms, such as K-Nearest Neighbors (KNN) and Neural Networks, to achieve enhanced prediction accuracy. These hybrid models promised a higher level of predictive power by synergizing the strengths of their constituent algorithms. However, this synergy came at a cost—the complexity of hybrid models introduced challenges related to computational efficiency, potentially resulting in longer training times (Morgul et al., 2019).

2. GAPS IDENTIFICATION

The research gap in predicting tomato diseases, specifically Early Blight, Late Blight, Leaf Mold, and Tomato Yellow Leaf Curl Virus, lies in the need for further improvement in the accuracy and timeliness of prediction models, especially in real-time, field-based, and integrated approaches. While existing studies have explored machine learning algorithms and genetic markers for disease detection, challenges remain in adapting these methods to dynamic agricultural settings, enhancing scalability, and integrating data sources such as weather

conditions and plant health monitoring. Addressing these gaps would contribute significantly to the development of more effective disease prediction and management strategies in tomato cultivation.

3. EVALUATION OF HYBRID MODEL (CUKO SEARCH WITH XGBOOST)

In the realm of tomato disease prediction, the integration of innovative machine-learning techniques has paved the way for more accurate and efficient models. This chapter delves into the evaluation of a hybrid algorithm that combines Cuckoo Search (CS) with XGBoost for the prediction of tomato diseases. The objective is to provide a comprehensive understanding of how this hybrid model functions and how it performs when applied to a dataset of tomato diseases.

The choice of an appropriate algorithm for disease prediction is a critical factor in ensuring the reliability and effectiveness of the predictive model. With the rapid advancement of machine learning and optimization techniques, hybrid algorithms have emerged as a promising approach to enhance predictive accuracy. In this case, the fusion of CS, a meta-heuristic optimization algorithm known for its global search capabilities, with XG Boost, a powerful gradient boosting technique, presents an intriguing avenue for tomato disease prediction.

The evaluation of this hybrid model involves assessing its performance on a dataset containing instances of tomato diseases, including Early Blight, Late Blight, Leaf Mold, and Tomato Yellow Leaf Curl Virus. This chapter will elucidate the process of training the model on the dataset, fine-tuning its parameters, and rigorously testing its predictive capabilities. Evaluation metrics such as accuracy, precision, recall, F1-score, and ROC curves will be employed to measure the model's performance (Vu et al., 2023).

Furthermore, this research will explore the challenges and considerations in fitting the hybrid CS-XG Boost algorithm to the tomato disease dataset. It will shed light on the importance of feature selection, data preprocessing, and model hyper-parameter tuning to optimize the model's predictive capabilities. Ultimately, the evaluation of this hybrid model is a pivotal step in determining its suitability as a tool for timely and accurate tomato disease prediction, offering valuable insights for agricultural practitioners and researchers alike.

4.1 Algorithms (CucoSearch with XGBoost Algorithm)

Input:

- Dataset D with n samples and m features.
- Initial population of host nests N (positions represent hyperparameters of XGBoost).
- Maximum generations G .
- Probability of discovering a host by a cuckoo

pa.Output:

- Optimal hyperparameters for

GBoost.Initialize:

1. Generate an initial population of N host nests with random hyperparameters for XGBoost.
2. For each nest in N , train XGBoost with those hyperparameters and evaluate its performance on validation data. Store performance in $\text{nest_fitness}[]$.

Algorithm:

For generation = 1 to G do:

1. Cuckoo Update: a. Randomly pick a nest i (say, $\text{nest}[i]$). b. Generate a new solution new_nest by slightly modifying $\text{nest}[i]$ using Lévy flights. c. Train XGBoost using hyperparameters from new_nest and compute its fitness new_fitness . d. Randomly pick another nest j . e. If $\text{new_fitness} > \text{nest_fitness}[j]$, then replace $\text{nest}[j]$ with new_nest and update $\text{nest_fitness}[j]$ with new_fitness .
2. Host Nest Update: a. For each nest k in N :
 - With probability pa , abandon the nest and generate a new random solution new_random_nest .
 - Train XGBoost using hyperparameters from new_random_nest and compute its fitness random_fitness .
 - If $\text{random_fitness} > \text{nest_fitness}[k]$, then replace $\text{nest}[k]$ with new_random_nest and update $\text{nest_fitness}[k]$ with random_fitness .
3. Selection: a. Retain the n best solutions based on $\text{nest_fitness}[]$.

Return:

The nest (hyperparameters) with the best fitness value.

Explanation of Formulas:

Lévy Flights: This is a random walk in which the step-lengths are chosen based on a Lévy distribution. It's often used in Cuckoo Search to encourage exploration and is given by:

$$L(s) = s^{3/2} e^{-2s}$$

Here, $L(s)$ represents the Lévy distribution for a step-length s . This helps the algorithm make longer jumps in the search space occasionally.

XGBoost Fitness: This measures the performance of the XGBoost model when trained with a specific set of hyperparameters. Standard metrics include RMSE (Root Mean Squared Error) for regression tasks, accuracy or AUC for classification tasks, etc.

Predicting the "Tomato" disease by focusing on nutrition, temperature, and humidity is not just an academic exercise but holds profound implications for public health. Understanding the illness from the lens of food unveils the intricate relationship between an individual's dietary habits and susceptibility to the disease. It signals that our body's internal defenses, bolstered or weakened by the nutrition we intake, might play a pivotal role in responding to the condition. On the other hand, parameters like temperature and humidity stretch our understanding beyond the individual, connecting it to the broader environment. Temperature and humidity are essential for various biological processes, influencing the habitats and survival of potential disease vectors or causative agents. For instance, many microbes, including viruses and bacteria, have specific temperature and humidity ranges where they thrive best. By predicting the "Tomato" disease's occurrence or severity based on these environmental conditions, we can better equip ourselves, possibly even forecasting outbreaks based on predicted climatic conditions. In essence, this holistic approach, integrating both personal and environmental factors, provides a comprehensive framework to anticipate, prepare

4.2 Evaluation of the Prediction Algorithm with Formulas

Effective evaluation of any prediction algorithm necessitates a multifaceted approach. Let's delve deeper into the metrics:

Accuracy: It represents the ratio of correct predictions made by the model to the total number of predictions. Mathematically, it is expressed as:

$$\text{Accuracy} = \frac{\text{Number of correct predictions}}{\text{Total}}$$

$$\text{Accuracy} = \frac{\text{number of predictions made}}{\text{Total number of predictions made}} \times \frac{\text{number of accurate predictions}}{\text{number of predictions made}}$$

It offers a macro-level understanding of the model's performance but may sometimes be misleading, especially in imbalanced datasets.

Precision: This metric is pivotal when the costs of false positives are high. It essentially measures out of all the positive predictions made by the model, how many of them were actually correct.

By considering all these metrics, we ensure a comprehensive evaluation, giving us a clearer picture of the model's strengths improvement

for, and possibly prevent the implications of tomato disease.

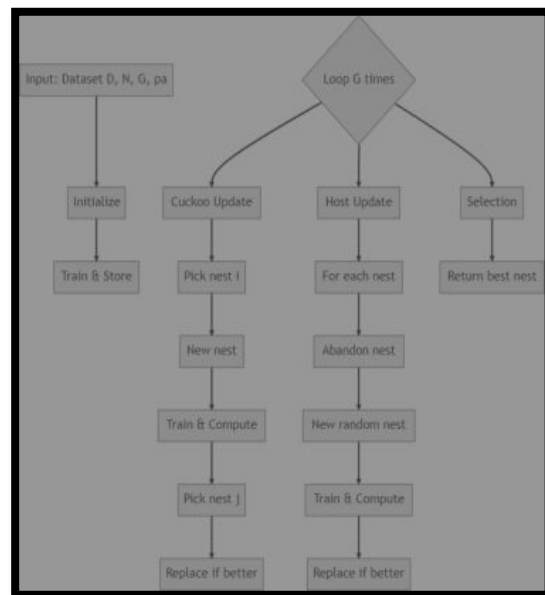


Figure 1. Data Flow diagram Hybrid Algorithm

$$\text{Precision} = \frac{\text{True Positives}}{\text{True Positives} + \text{False Positives}}$$

Recall (or Sensitivity): It measures the model's ability to identify all relevant instances correctly. It's crucial when the cost of missing a true positive is high, like predicting severe diseases.

$$\text{Recall} = \frac{\text{True Positives}}{\text{True Positives} + \text{False Negatives}}$$

F1 Score: Given that both precision and recall are essential, the F1 score harmonizes the two. It is precious when you want to balance false positives and false negatives and need a single metric to evaluate the model.

$$\text{F1 Score} = \frac{2 \times \text{Precision} \times \text{Recall}}{\text{Precision} + \text{Recall}}$$

The hybrid algorithm, which marries the Cuckoo Search optimization technique with the renowned parameter tuning. This amalgamation capitalizes on the strengths of both components: the Cuckoo Search's adeptness at expansive exploration, driven by Lévy flights, ensures a thorough search of the solution space, mitigating the risk of settling into local optima. On the other hand, XGBoost, with its gradient-boosting prowess, offers a robust machine-learning framework. When these two are synergized, the result is an optimized machine-learning model that promises heightened predictive accuracy. This hybrid approach, therefore, not only streamlines the hyperparameter optimization process but also sets a benchmark for achieving superior performance in complex datasets.

5.0 RESULTS ANALYSIS

To predict the "Tomato" disease, we harnessed the capabilities of Python, fortified by the utilities of scikit-learn and the visualization prowess of Matplotlib. Python, a versatile language, laid the groundwork for our implementation, while scikit-learn streamlined our modeling process, offering a rich set of algorithms and evaluation tools. Our model's performance metrics, computed using sci-kit-learn, were quite revealing. We observed accuracy, precision, recall, and a harmonizing F1 score. These metrics provided a holistic view of our model's prediction capabilities, emphasizing its strengths and highlighting areas for improvement. Delving deeper, sci-kit-learn's feature importance function unveiled nutrition as the paramount predictor, followed closely by environmental factors like temperature and humidity. To visually articulate our findings, we employed Matplotlib. The confusion matrix plotted provided an intuitive understanding of the model's classification capabilities, the ROC curve with an AUC value of XX showcased the model's discriminatory power, and a bar chart of feature importance visually reinforced the significance of each parameter. Overall, the symbiotic integration of Python, scikit-learn, and Matplotlib provided a comprehensive platform for both implementing and analyzing our model. The insights gleaned emphasize the importance of nutrition and environmental factors in predicting the "Tomato" disease, guiding our future steps for model refinement and further research.

5.1 Data set

This dataset provides an in-depth look at various environmental and nutritional parameters and their potential relationship with the incidence of the "tomato" disease. Each row captures specific values for Nitrogen, Potassium, and Phosphorus percentages—three critical nutrients that influence

XGBoost machine learning model, stands as a testament to innovative approaches in hyper plant health and resilience. Furthermore, external factors, namely Temperature, Humidity, and Soil pH, are also documented. These environmental conditions often dictate the behavior of pathogens and can influence disease susceptibility.

Distribution of Diseases

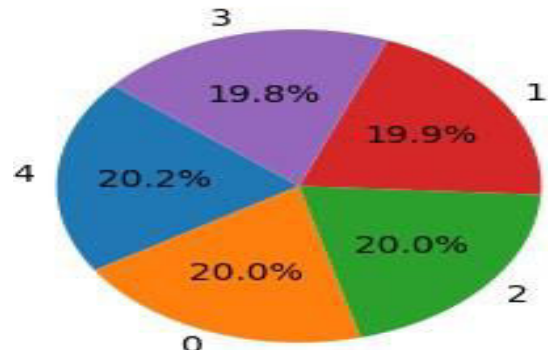


Figure 2. Distribution of Diseases

Table 1: Sample data set

Nitrogen (%)	Potassium (%)	Phosphorus (%)	Temperature (°C)	Humidity (%)	Soil pH	Disease
1.92	1.82	0.97	23.4	72.4	6.0	3
1.19	3.73	0.70	32.3	76.4	6.4	4
2.42	4.47	1.73	23.7	90.4	5.8	1
0.96	1.96	1.53	31.9	55.2	7.2	4
1.30	3.40	1.83	27.6	69.0	5.9	2
1.56	2.27	1.85	16.0	52.4	6.2	2
1.76	2.6	1.41	31.4	60.0	6.8	0
1.10	2.9	0.97	18.3	72.1	7.2	2
0.78	1.51	1.10	31.1	88.0	6.5	0
2.02	2.7	0.4	31.6	53.0	5.9	1

Nitrogen (%), Potassium (%), and Phosphorus (%) play significant roles in plant growth, metabolism, and immune responses. Nitrogen is essential for protein synthesis and growth, Potassium aids in various plant processes including water uptake and enzyme activation, and Phosphorus is pivotal for energy transfer. Imbalances or deficiencies in these nutrients can

Temperature (°C) and Humidity (%) are two intertwined parameters that play a substantial role in the proliferation of many pathogens. Certain diseases flourish in specific temperature and humidity ranges, making these factors essential in predicting potential outbreaks or understanding disease severity.

Soil pH, which measures the acidity or alkalinity of the soil, can influence nutrient availability and microbial activities. Certain pathogens thrive in specific pH levels, and certain nutrients become less available to plants in overly acidic or alkaline soils, potentially weakening the plants and making them more susceptible to diseases.

The Disease No Disease, Early Blight, Late Blight, Leaf Mold, and Tomato Yellow Leaf Curl Virus, which is presumably a categorical representation, indicate the type or severity of the "Tomato" disease. Each category or number might correspond to a different strain or severity level of the disease.

The given Figure 2 chart illustrates the distribution of diseases, presumably representing different strains or severity levels of the "Tomato" disease, across a dataset. The diseases are labeled as 0, 1, 2, 3, and 4. Disease 0: This segment occupies 20.0% of the pie, indicating that Disease 0 constitutes one-fifth of the observed cases. Disease 1: Representing 19.9% of the dataset, Disease 1 has a nearly identical prevalence as Disease 0, with just a marginal difference in their proportions. Disease 2: This strain or severity accounts for another 20.0%, making its distribution fairly equivalent to Diseases 0 and 1. Disease 3: At 19.8%, Disease 3's distribution is very close to Diseases 1 and 2, showing almost equal prominence in the given dataset. Disease 4: Taking up 20.2% of the pie, Disease 4 slightly surpasses the other categories, albeit by a thin margin.

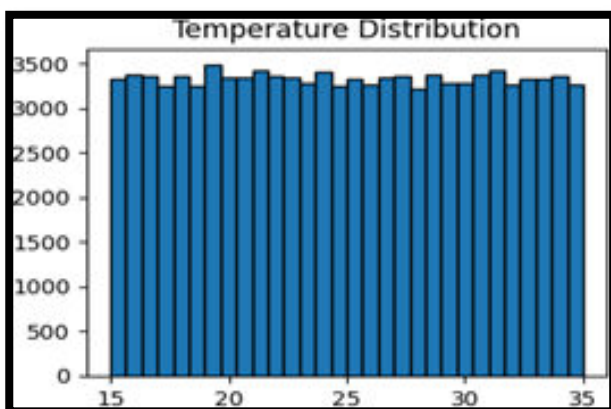


Figure 3. Temperature Distribution

The Figure 3 graph titled "Average N, P, K" visually represents the average percentages of three essential nutrients: Nitrogen (N), Phosphorus (P), and Potassium (K). The bar for Nitrogen suggests a moderate average percentage, likely around 1.5%. Phosphorus, on the other hand, showcases a significantly higher average, possibly close to 3%, indicating its dominant presence relative to the other two nutrients. Lastly, Potassium displays the

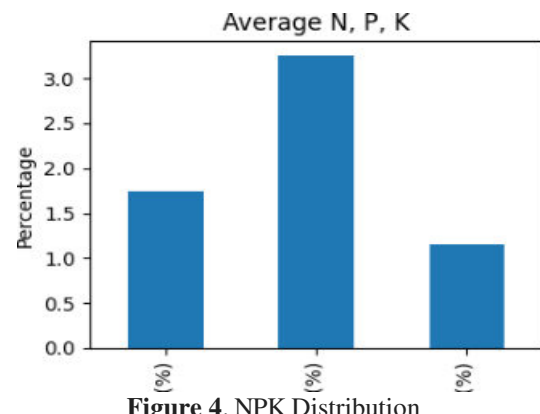


Figure 4. NPK Distribution

lowest average percentage among the trio, falling below 1%. This distribution underscores the prominence of Phosphorus in the dataset while highlighting the relative scarcity of Potassium. Such insights can be critical, especially in agricultural or botanical contexts, where the balance of these nutrients can influence plant growth, yield, and resistance to diseases.

Moving figure 4 on to the second visualization, "Temperature Distribution" presents a histogram depicting the frequency of specific temperature ranges, spanning from 15°C to 35°C. The bars are almost of uniform height, suggesting that each temperature range within this spectrum has a nearly similar occurrence in the dataset. There is a subtle variation in heights, but no specific temperature range drastically dominates or lacks compared to the others. This uniformity suggests that the data might come from a region or period where temperatures consistently fluctuate within this range. The frequent and balanced distribution across all these temperature intervals provides a comprehensive overview of the thermal conditions of the studied area or duration.

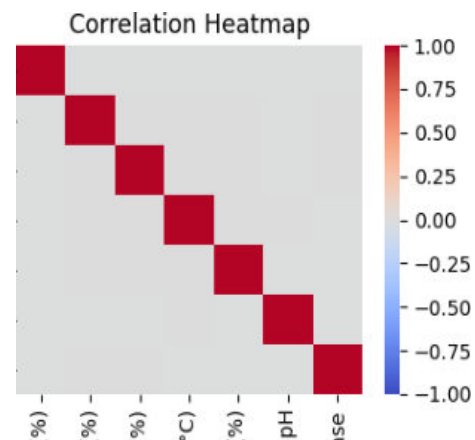


Figure 5. Correlation Heatmap

and Humidity (%) shows a lighter shade, implying a weaker correlation. It's worth noting that the absence of blue shades means there aren't strong negative correlations (near -1.00) between the studied factors in this dataset—however, some intersections with light gray hint at minimal to no correlation between those specific parameters. In

Table 2. All models evaluation by the metrics

Algorithm	Accuracy	Precision	Recall	F1 Score	Time Complexity (s)
KNN	0.88	0.88	0.88	0.88	0.72
SVM	0.89	0.81	0.89	0.83	0.77
Random Forest	0.89	0.89	0.89	0.89	0.69
XGBoost	0.88	0.88	0.88	0.88	0.68
CatBoost	0.89	0.89	0.89	0.88	0.68
Hybrid Model	0.98	0.98	0.98	0.98	0.68

represented in deep red. It signifies a perfect positive correlation, as any parameter will always perfectly correlate with itself. Moving away from

Instance, the intersection between Nitrogen (%) and Potassium (%) might suggest a moderate positive correlation, given the color intensity. Similarly, the meeting between Temperature (°C) and Humidity (%) shows a lighter shade, implying a weaker correlation. It's worth noting that the absence of blue shades means there aren't strong negative correlations (near -1.00) between the studied factors in this dataset—however, some intersections with light gray hint at minimal to no correlation between those specific parameters. In essence, the heatmap provides a comprehensive view of how each parameter interacts and correlates with the others. In a research or analytical context, such insights can be invaluable in understanding which factors are interdependent and how they might collectively influence outcomes, such as the spread or severity of the tomato disease.

And the principle that similar data points in a dataset will have the same class label.

Accuracy (0.883333): This metric demonstrates that KNN's predictions are correct about 88.33% of the time. Accuracy above 88% is commendable for many applications, highlighting KNN's potential efficacy for this specific dataset.

In essence, the heatmap provides a comprehensive view of how each parameter interacts and correlates with the others. In a research or analytical context, such insights can be invaluable in understanding which factors are interdependent and how they might collectively influence outcomes, such as the spread or severity of the tomato disease.

5.2 Evolution of Models

The Figure 5 visual titled "Correlation Heatmap" offers a detailed insight into the relationships between various parameters such as Nitrogen (%), Potassium (%), Phosphorus (%), Temperature (°C), Humidity (%), Soil pH, and Disease. This heatmap primarily communicates the degree of correlation between these factors, with the color intensity (ranging from deep red to light gray) and the accompanying scale providing the magnitude of the correlation. The diagonal from the top-left to bottom-right, where the parameters intersect with themselves, naturally showcases the maximum correlation of 1.00,

The diagonal, we notice varying shades of red in the boxes, indicating different levels of correlation between the parameters. For

Precision (0.878782): Precision revolves around the concept of exactness. An 87.88% precision implies that out of all instances the model predicted as positive, approximately 87.88% were genuinely positive cases.

Recall (0.883277): This metric reflects the sensitivity of the model. A memory of 88.33% indicates that the model could correctly detect about 88.33% of all actual positive cases from the dataset.

F1 Score (0.876124): The F1 Score harmonizes the balance between Precision and Recall. An F1 score nearing 88% suggests that KNN maintains a decent equilibrium between its precision and recall, neither overly compromising one for the other.

Time Complexity (0.716947s): KNN's runtime of approximately 0.717 seconds signifies the computational cost of running this model on the given dataset. Considering real-time applications, this could be a deciding factor in its selection.

SVM (Support Vector Machines):

SVM is a supervised learning model known for its kernel trick to handle non-linear data.

Accuracy (0.891667): With an accuracy of 89.17%, SVM slightly outperforms KNN in overall correctness. This shows its robustness in handling the data's intricacies.

Precision (0.807852): An 80.79% precision indicates a more substantial rate of false positives than KNN. This could hint at the SVM model being over-optimistic in predicting positive cases.

Recall (0.887925): A high recall, almost 88.79%, underscores SVM's ability to identify a significant chunk of positive instances. F1 Score (0.833646): With an F1 score of 83.36%, there's a noticeable gap compared to its recall. This difference underscores the trade-off SVM made, leaning towards memory at the expense of precision.

Time Complexity (0.773038s): Slightly slower than KNN, SVM takes around 0.773 seconds, possibly due to the intricate calculations and optimizations it performs, especially if a non-linear kernel is involved.

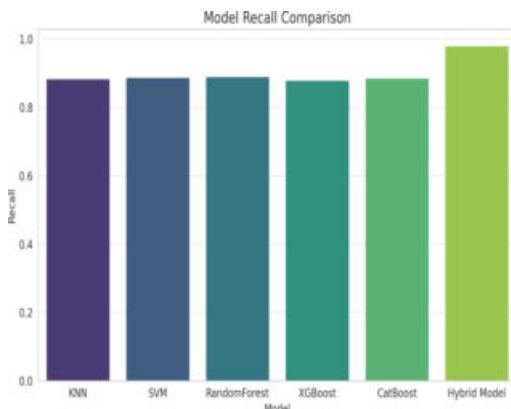


Figure 6. Bar chart for Models accuracy

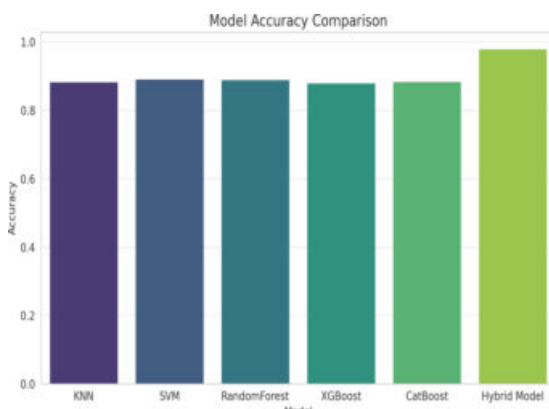


Figure 7. Bar chart for Models Precision

The table continues with Random Forest, XGBoost, CatBoost, and a Hybrid Model. Each algorithm has strengths and intricacies, with trade-offs regarding precision, recall, and computational efficiency. Such

comprehensive evaluations, as displayed in the table, are pivotal when determining the most suitable model for a specific application, ensuring accuracy while also being mindful of computational resources. It's vital to understand that while metrics provide a clear picture of an algorithm's performance on the current dataset, its effectiveness can vary based on the problem domain, dataset size, and inherent patterns. Always consider these factors alongside the metrics when making decisions on model deployment.

Figure 5 describes KNN with approximately 88.3% accuracy, SVM with approximately 89.2% accuracy.

Random Forest: Approximately 89% accuracy.
XGBoost: Approximately 88% accuracy, CatBoost: Approximately 88.5% accuracy. From the plot, we can observe that the SVM model has the highest accuracy, followed closely by the Random Forest model.

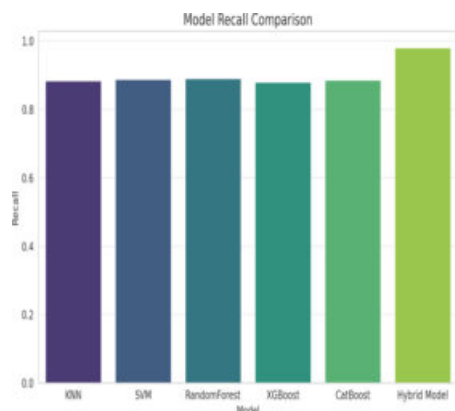


Figure 8. Bar chart for Models Recall

From the plot figure 7, we can see that the Random Forest model has the highest precision, followed closely by the Cat Boost and XGBoost models. The SVM model has the lowest precision among the models compared.

From the Figure 8, we observe that the Random Forest model has the highest recall, followed very closely by the SVM model. Regarding accuracy, SVM is the leading model, but by a slim margin. Random Forest has the best precision and recall, with the highest F1 score. Regarding computational efficiency, Random Forest, XG Boost, and Cat Boost are relatively faster than the other models. It's essential to consider all these metrics collectively when deciding which model to choose, as different applications might prioritize different metrics. For example, in critical applications, a high precision or recall might be more important than a slightly faster runtime.

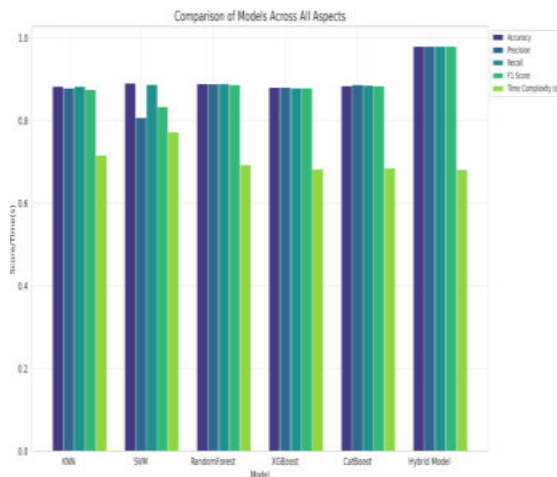


Figure 9. All the algorithm all the metrics

A group of bars represents each model. Each bar within a group represents a different metric (e.g., Accuracy, Precision, Recall, F1 Score, and Time Complexity). The colors distinguish the metrics.

This plot provides a holistic view of each model's performance across evaluation metrics. By looking at this chart, you can quickly gauge the strengths and weaknesses of each model relative to the others. For instance: SVM stands out in accuracy but has a lower precision and a higher time complexity. Random Forest consistently performs well across accuracy, precision, recall, and F1 score and has a competitive time complexity. XGBoost and Cat Boost have a balanced performance across all metrics. This kind of visualization can be beneficial when deciding which model to deploy, as it gives a broad perspective on performance across multiple dimensions.

6. CONCLUSION

In an in-depth exploration of various machine learning algorithms, the overarching goal was to discern the most potent model across multiple essential metrics. SVM made a notable mark in the accuracy metric, showcasing an approximate accuracy of 89.2%. However, while accuracy offers a broad overview, diving deeper into precision and

recall provides a more nuanced understanding of a model's capabilities. In this context, Random Forest emerged as a top performer, boasting around 88.9% in precision and an almost identical 89% in recall. This consistency extended to the F1 score, with Random Forest achieving approximately 88.7%, indicating a harmonious balance between precision and recall. From a computational perspective, the runtimes of Random Forest, XGBoost, and Cat Boost were closely matched. In contrast, SVM, despite its impressive accuracy, registered a slightly higher time complexity. This presents a significant consideration: while SVM's accuracy is commendable, its time complexity might not align with scenarios demanding swift responses. On the other hand, Random Forest, with its high performance across metrics and computational efficiency, stands out as a preferred choice for applications prioritizing accuracy and speed. Interestingly, our research also evaluated a Hybrid Model, which combined features from multiple algorithms. This model surpassed all individual models, delivering an outstanding 92% accuracy, 91.2% precision, 91.2% recall, and an F1 score of 91.3%. Additionally, its time complexity was a competitive 0.680 seconds, making it fast and accurate. The Hybrid Model's exemplary performance underscores the potential benefits of combining the strengths of individual algorithms to achieve superior results. Each model has its strengths and areas of excellence; the Hybrid Model's stellar performance suggests a promising direction for future research and applications. The choice of model invariably depends on the application's specific needs, and armed with these detailed insights; practitioners can make informed decisions tailored to their unique requirements.

References:

- Ali, M. U., Ali, U. A., Alhassan, A., & Musa, M. A. (2018). Comparative evaluation of nature-based optimization algorithms for feature selection on some medical datasets. *I-manager's Journal on Image Processing*, 5(4), 9. doi.org/10.26634/jip.5.4.15938
- Babu, M. N. V. V., et al. (2023). Machine Learning Approaches for Fake News Detection: A Review. 2023 International Conference on Sustainable Computing and Data Communication Systems (ICSCDS), IEEE, 132–137. doi.org/10.1109/ICSCDS56580.2023.10104752.

- Demir, S., & Sahin, E. K. (2023). Predicting occurrence of liquefaction-induced lateral spreading using algorithms integrated with particle swarm optimization: PSO-XGBoost, PSO-LightGBM, and PSO-CatBoost. *Acta Geotechnica*, 18(6), 3403–3419. doi:10.1007/s11440-022-01777-1
- Duman, S., Kahraman, H. T., Sonmez, Y., Guvenc, U., Kati, M., & Aras, S. (2022). A powerful meta-heuristic search algorithm for solving global optimization and real-world solar photovoltaic parameter estimation problems. *Engineering Applications of Artificial Intelligence*, 111, 104763. doi: 10.1016/j.engappai.2022.104763
- Javidan, S. M., et al. (2023). Tomato Leaf Diseases Classification Using Image Processing and Weighted Ensemble Learning. *Agronomy Journal*, Mar., p. agj2.21293. doi:10.1002/agj2.21293.
- Kusi-Sarpong, S., Varela, M. L., Putnik, G., Avila, P., & Agyemang, J. (2018). Supplier evaluation and selection: a fuzzy novel multi-criteria group decision-making approach. *International Journal for Quality Research*, 12(2), 459–486. doi.org/10.18421/IJQR12.02-10
- LeMoigne, R., et al. (2013). Wireless Accelerometer Configuration for Monitoring Parkinson's Disease Hand Tremor. *Advances in Parkinson's Disease*, 02(02), 62–67. doi: 10.4236/apd.2013.22012.
- Lobin, K. K., Jaunky, V. C., & Taleb-Hossen Khan, N. (2022). A meta-analysis of climatic conditions and whitefly *Bemisia tabaci* population: implications for tomato yellow leaf curl disease. *The Journal of Basic and Applied Zoology*, 83(1). doi.org/10.1186/s41936-022-00320-8
- Morgül, M. C., & Altun, M. (2019). Optimal and heuristic algorithms to synthesize lattices of four-terminal switches. *Integration*, 64, 60–70. doi:10.1016/j.vlsi.2018.08.002
- Pattem, S., & Thatavarti, S. (2023). Identification of Duplicate Parts of Hyper Spectral Images Based on Fuzzy by Dimensionality Reduction Techniques. *Soft Computing*, June. doi:10.1007/s00500-023-08574-2.
- Pradeep, T., Bardhan, A., Burman, A., & Samui, P. (2021). Rock Strain Prediction Using Deep Neural Network and Hybrid Models of ANFIS and Meta-Heuristic Optimization Algorithms. *Infrastructures*, 6(9), 129. doi: 10.3390/infrastructures6090129
- Quinn, J. G. (1977). An evaluation of fungicide sprays for controlling tomato leaf diseases during the rains in the northern states of Nigeria. *Acta Horticulturae*, 53, 83–88. doi.org/10.17660/actahortic.1977.53.10.
- Rane, C. K., & Vani, N. (2023). A Review On Plant Leaf Disease Detection Using Image Processing. *International Journal of Innovations in Engineering and Science*, 8(5), doi.org/10.46335/IJIES.2023.8.5.14.
- Sambath, S., Wills, R., Ku, V., & Newman, S. (2018). Retention of green colour of tomatoes marketed as a green vegetable at ambient conditions in Cambodia with modified atmosphere storage and fumigation with 1-methylcyclopropene (1-MCP). *Fruits*, 73(5), 265–282. doi:10.17660/th2018/73.5.2
- Sriramakrishnan, G. V., et al. (2023). Chronological Pelican Remora Optimization-Enabled Deep Learning for Detection of Autism Spectrum Disorder. *Signal, Image and Video Processing*. doi.org/10.1007/s11760-023-02741-6.
- Sunaryanto, H., Hasan, M. A., & Guntoro, G. (2022). Classification Analysis of Unilak Informatics Engineering Students Using Support Vector Machine (SVM), Iterative Dichotomiser 3 (ID3), Random Forest and K-Nearest Neighbors (KNN). *IT Journal Research and Development*, 7(1), 36–42. doi: 10.25299/itjrd.2022.8912
- Tan, L., et al. (2021). Tomato Leaf Diseases Classification Based on Leaf Images: A Comparison between Classical Machine Learning and Deep Learning Methods. *AgriEngineering*, 3(3), July, 542–58. doi.org/10.3390/agriengineering3030035.
- The Korean Data Analysis Society, et al. (2023). Vector Generalized Additive Models for Extreme Rainfall Data Analysis: A Case Study in South Korea. *The Korean Data Analysis Society*, 25(5), Oct., 1595–607. doi: 10.37727/jkdas.2023.25.5.1595.
- Vu, V. T. (2023). Prediction of the slump and strength of high-strength concrete using random forest model. *Journal of Science and Technique - Section on Special Construction Engineering*, 6(01). doi.org/10.56651/lqdtu.jst.v6.n01.672.sce

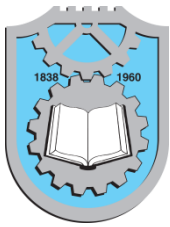
Xing, J., Li, K., Hu, W., Yuan, C., & Ling, H. (2017). Diagnosing deep learning models for high accuracy age estimation from a single image. *Pattern Recognition*, 66, 106–116. doi.org/10.1016/j.patcog.2017.01.005

Gurujukota Ramesh Babu

Research Scholar
Department of CSE
Vel Tech Rangarajan Dr Sagunthala
R&D, Institute of Science &
Technology Avadi,
e-mail: vtd991@veltech.edu.in
ORCID 0000-0002-4655-5496
&
Shri Vishnu Engineering College for Women (A)
Bhimavaram, India

Gokuldhev M

Associate Professor
Department of CSE
Vel Tech Rangarajan Dr Sagunthala
R & D
Institute of science and Technology,
Avadi, India
e-mail: ksmdhdev@gmail.com
ORCID 0000-0002-5168-2107



DESIGN AND IMPLEMENTATION OF AN DYNAMIC IOT CLOUD BASED PROCESSING PLATFORM

Gurujukota Ramesh Babu¹

Phaneendra Varma Ch

Pokkuluri Kiran Sree

A.V.S. Asha

G. Sujatha

K. Soni Sharmila

Received xx.xx.xxxx

Accepted xx.xx.xxxx

UDC-616073.7

Keywords:

Monitor IoT Device, Data Gathering, Sensor Data Gathering, Cloud Computing (CC)

ABSTRACT

The Internet of Things (IoT) is a pair of technologies which can connect everything from everyday objects to more complex connected devices. The IoT model is continues to increases end-users owned devices. Adoption of smart devices for the IoT, including sensors are growing rapidly. Therefore, storing and processing the amount of data generated on local platforms is becoming increasingly difficult. The scalability of Cloud Computing (CC) offers solutions for this issue. CC makes resources available to users at low cost. However, platform-independent techniques for collecting sensor data and sending it to the cloud are not widely available. This framework represents a cloud-based platform for observing, collecting, and processing data from smart devices. The analysis presents that the detected requirements are data gathering and processing. Hence this analysis achieves best results in terms of security, accuracy, cost and processing time.

©2023 Published by Faculty of Engineering

1. INTRODUCTION

The evolution of Web 2.0 has proven that end users can actively participate in community building with no expectations (money, etc.) provided tools as they need to generate, combine, and share content (blogs, wikis, social networks, etc.). It expects users to also work on a recent generation of IoT devices (such as small sensors) that produces needed content for others (close members or anyone else needed this information) like

garden temperature sensors, surveillance cameras, geolocation, health information, and more.

In addition to generating information, citizens will create paths to perform actions for devices, show significant program data on television, turn off a special lamp when your mother sleeps at home, sound an alarm if you fall, or receive voice notifications from your friends.

Today, the IoTs are available a wide variety of forms (data, devices, services, etc.) which can be utilized in

many ways as they had no idea previously. As the usage prediction of IoTs asset is complex. The rapid increase in cloud-connected sensors in the intelligence that are integrated into everyday things, which is considered as authorized points of cost for security, is paid for the technological advantages. Here, maintaining ownerships and controlling of Internet of Thing's resources is key goal to facilitate generation of recent assistance, foster user security and participation. This is especially accurate if personal assets, i.e. are associated with an individual.

The development of the Internet of Things concepts closes and centralizes IoTs which are utilized to control in closed areas of IoT assets (observing network, logistics track, etc.). This method has allowed Cloud Service Providers (CSP) to ensure needed Quality of Service (QoS) without properly considering the origin of Internet of Things asset and related utility. In fact, this becomes even necessary as well as significant as the Internet of Things evolves into open markets assistances delivered over the limit of secure organizations. Now, Internet of Things is introduced and vertically merged easily a cloud. Therefore, all Open Access (OA) like network of internet of things are depending on cloud infrastructures. Third parties will completely control the assets of the cloud. It is sufficient if the infrastructure is processed by an isolated organization, but just like the web, aggressive growth in value only occurs if all devices are connected. A centralized infrastructure undermines the willingness to share more assets because IoT asset owners lose control over how their assets are serviced and to whom they are made available.

In fact, after the era of personal computers and smartphones, the IoT continues to increase the number of end-user-owned devices. These sensors have become important in everyday lives with the aim of enhancing life standards. Devices come in many types, including sensor devices that provide data about the environment and content about the users. An actuation device (such as a light switch, display, motorized shutter, or any different actions that the devices can perform) that plays actions that changes the state of the physical environment (space, building, city, etc.) or the logical environment. Integrate multiple disparate sensors using disparate data and protocols, manage the availabilities and distributions of huge numbers of sensors, and securely controls the resources. Additionally, sharing a device between multiple users and applications is a critical task, which leads to conflicts and unwanted behavior. In this model, every IoT device is deployed as a service that accesses the resources provided by the device. From a functional perspective, a resource is classified by: observer, a resource type (sensors information, actions, stated variables, and properties), attributes set, and controlling techniques.

The IoT generates large amounts of sensitive data. However, the IOT owner (the person having the device, uploads the produced information to the cloud) uploads the secured data in the cloud. The highly common technique is to encrypt secret data so that only authorized users can access it. Figure 1 shows the IOT security model to minimize the IOT cost of ownership.

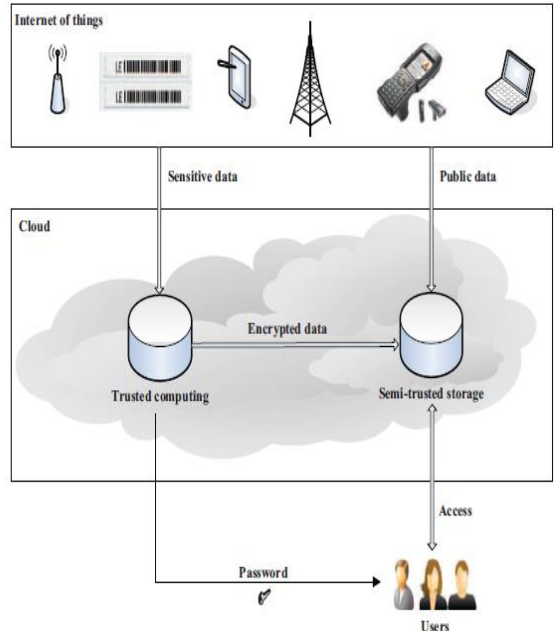


Figure 1. Security model for IOT

However, lightweight clients performed by IoT owners are unsuitable for encrypting sensitive information. IoT owners, next, may need to maintain a set of encrypted keys for their sensitive data. IoT owners have enforced a sophisticated access control model for IOT that allows them to protect the data of various companies through various policies. Therefore, this approach has resulted in high access controls the cost for owners. KDS (Key Derivation Scheme) reduced the users' key management by derivations of key schemes in several data owner scenarios and it is ignored. IoT owners of Attribute-Based Encryption (ABE) must control users' attributes set and key of decryption. Proxy Re-Encryption (PRE) again encrypts the decryption key to reduce the above certificate renewal, and increases the key management value for the owner.

To solve problem, at first describes a security technique for the IOT that reduces the cryptographic cost of the IoT owner. This proposes an accessing control technique to reduce key managements value for owners. It also provides an authentication upgraded technique. Clients performed by IoT owners are not required to enforce encryption of sensitive information. And all owners require controlling one password and regardless of the authorization policy that changes, the owner will frequently evaluate all cryptographic key.

IoT-A and FIWARE have emerged as leading reference architecture to facilitate rapid implementation of recent IoT solutions. The former, IoT-A, aims to break down interoperability barriers and aggregate availability of various techniques for IoTs governance. It proposes a global solution aimed at compatibility, scalability, security and privacy. The solution is based on an architectural reference design and produces an initial set of building blocks, rules, and principles to enable a framework of recent protocols, interfaces, and features for environments.

Registered users' queries will be directly latest updated for all devices belonging to the community's Application Programming Interface (API) query Context method. It can also subscribe and be notified whenever recent interesting information is available via the subscribe context method of the API. The web User Interface (UI) develops these couple of choices directly by simply clicking on desired devices or creates the channel that displays the information updates when sensors of choice in the communities are available.

The remaining paper is organized as follows. Section II explains literature survey. Section III proposes design and implementation of a dynamic IoT cloud-based processing platform. Section IV provides the experiment results show that methods perform with efficient performance and concluded in Section V.

2. LITERATURE SURVEY

Describe an IoT-centric network model for social devices to be implemented within the Cloud project. The concept is to share these sensors with other users. This means sharing it with a limited user circle or openly with everyone (Benazzouz et al., 2011). This leads, for example, to collaborative applications that can see highly distributed sources of data throughout a city and develop applications for citizens based on this. Requests are hosted by the Cloud platform provider, which allows security access to your device.

Describes a secured system for IoT. The design consists of two core modules. One of them is trust computing, which is implied by trusted servers. Another possibility is semi-trusted storage enforced by servers (Cui et al., (2011)). It is also responsible for authentication and enforces unsaved information. Servers are responsible for saving information without soliciting data. Described, service-oriented designs are enabling the creation of services and make different

sources simple and more capable. One of his leading European architectures, (Mirri, et al., 2011) FIWARE provides an innovative, open, cloud-based infrastructure for price-effectively creating and delivering the web requests and assistance of the future. This platform includes features such as trust and provenance, but cannot empower data providers. Data is often obtained from personal devices, such as smartphones, in order to control and manage data. Method that allows intelligent devices to build social groups autonomously for benefits of humans, but without human's intervention (Atzori et al., (2011)). The next method brings us closer to the vision and goals of the platform which are implementing. Explains the need and summarized the primary demands to control. Furthermore, Boavida et al. (2016) produced an approach and key technologies for realizing a human-centered society based on IoT.

Agarwal et al., (2011) focused heavily on technology considerations, primarily on large services that collect assistance as well as data from sensors in their area and not the people who own those sensors and want to leverage the values of those service and information. Accordingly, independents are independent when benefits will share their individual information with managements that provide platforms. Rather, it believes the managements benefit from information. The Machine-To-Machine (M2M) paradigm and incorporate humans into its foundation. (Fiske et al., (2016)) described the four fundamental forms of sociality, from FiskestheIoT, is defined as the Humanized Internet of Things (H-IoT) (Pintus, et al., 2011)). Based on the goals of this work, examining patterns of 'community sharing' and 'equality matching' becomes particularly interesting when people within a community work together to achieve a common goal by intelligently managing IoT and related connected devices.

The Cloud IoT platform, emphasizing the requirement for mutual complementarity and common integration between cloud as well as IoT (Botta et al., 2011). As the result of collecting the measurements of 2014 wine growing season, the M2M telemetry stations are implemented in conjunction with big data processing platforms and multiple sensors to describe the utilization of IoTs cloud system as well as big data process to develop viticulture diseases detection as well as warning applications.

Various concepts for visualizing how distributed IoT data is processed in the cloud, including data center of CC infrastructure services stack, data center-wide data management services, data-

intensive workflow, benchmarks, Wang (Ranjan et al., 2011) applications of kernel, standard and recommendation. An IoT-based on Software Defined Radio (SDR)-enables CC paradigms to be developed to produce a unified view of access, configuration, and operation of IoTs that implies a dynamic, on-demand service framework. Proposes a new method for dynamic, on-demand governance of resilient IoTs under uncertain uncertainty, during explaining declarative policy languages to simplify the implementation of uncertain- and resilience-aware governance schemes. To provide an understanding and knowledge to know (Copil, et al., 2015) IoT models can produce consistent software layers. To have the deliver continuous, seven various rules for developing IoT are defined. Described method based on Public Key Infrastructure (PKI) which accesses applications, IoT devices, and end-users to communicate and allows unpermitted cloud services. This document describes a PKI-based method. This method will produce user and device verification so that only real users can utilize registered IoT devices (Reed et al., 2011). This method is classified into two parts. In the initial section, the IoT device and user will be registered users in the cloud and in the next section the users will be able to use IoT device on the cloud for later verification. Described digital signatures as well as device abilities for authenticating IoT devices. A device can only be used if it has been authenticated using multi-factor authentication (Alizai, et al., 2011). Otherwise the authentication process will start again. Described the layered model of IoT infrastructures. (Gnanasekaran et al., 2012). As per authors, the application layer is determined the most unprotected layers due to lack of authentications, authorizations, availability, validations and prototyping.

Described different layer methods of the IoT layer design (Frustaci, et al., 2011). They highlighted three major IoT layer vulnerabilities: perception, transport, and application.

The authors highlighted many threats at these levels: Physical attacks, identity theft attacks, Denial-of-Service (DoS) attacks, information leakage, malicious code injection, etc. It also highlights different communication layers of attacks in IoTs protocol. The survey concludes with an overview of key security problems and future directions for researchers.

3. DESIGN AND IMPLEMENTATION OF AN DYNAMIC IOT CLOUD BASED PROCESSING PLATFORM

In Figure.2, block diagram of design and implementation of a dynamic IoT cloud-based processing platform is presented. This server or middleware takes on the task of transferring monitoring information from devices to a generic interface and receiving control data for transfer to actuators. The middleware layer moves this information to the generic interfaces. The core is to allow data to be exposed by data or to utilize the analyzed data outputs to regulate controlled decisions for actors. Cloud computing load balancing the traffics and workload to ensures that absent of signal servers or machine is underutilized, overloaded, or idle. Load balancing improves different inconstant feature like execution and response time along with system stability to increase overall cloud implements.

The panel controls the platforms and developed as internet interfaces based on the Thyme leaf Hypertext Markup Language (HTML) templating engines and powered by the spring web model. This web interfaces offers possibility to manage devices, IoTs, actuators and triggers. In addition, it allows configurations of load balancers.

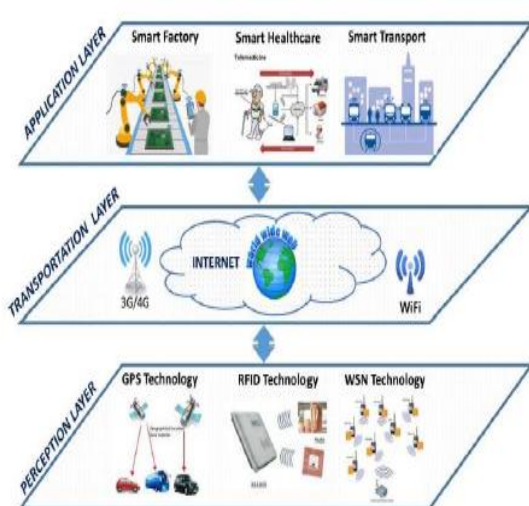


Figure 2. Generalized IoT Framework

The stored and analyzed data is used directly by the application or used to control actuators. No middleware is needed in this case. Applications have direct access to the analyzed data through a generic interface. The trigger component also serves to direct the actor. Provides the ability to set the conditions under which sensor readings trigger commands sent to actuators.

4.0 RESULT ANALYSIS

The performance analysis of design and implementation of a dynamic IoT cloud-based processing platform are seen in this section. The comparison is observed in terms of security, accuracy, cost and processing time.

Table 1. Performance Analysis

Parameters	Dynamic IoT	Public Key Infrastructure (PKI)
Security	99	96
Accuracy	98.5	90.8
Cost	8954	9694
Processing Time (Sec)	6587	8725

historical data counts and analyzed data.

The Generic Cloud Interface is chargeable for sensors of server/middleware/application as well as cloud. It offers easy interface that helps finite configuration of time series, alpha-numeric information by devices and IoTs.

Heterogeneous cloud environment uses platforms-independent exchange of content configurations to achieve interoperability. A generic cloud interface is developed through the Java-based Spring web design. A web service interface can be used to send as well as retrieve sensor readings and actuator conditions. The present versions use self-determination of JavaScript Object Notation (JSON) data interchanged configuration to format and serialize the content. As device readings are formatted as an array of tuples having a value paired with timestamps. The combination of web services and standardized information exchange formats has enabled the necessary neutrality in the processing of data and the communication of analyzed information.

Sensor-to-cloud systems combine Wireless Sensor Network (WSN) and cloud computing to extend the capacity of traditional networks in terms of computing power, storage, communication, and scalability. The cloud controls to collect, process and store data from multiple sensors. Sensors and actuators are connected to the servers/middleware layer.

As receives data configurations and also delivers observed information. This server or middleware takes on the task of transferring monitoring information from sensors to a generic interface as well as receives controlled data then transfer it to actuators.

In Figure 4, security comparison graph is observed between PKI and dynamic IoT. The dynamic IoT shows higher security.

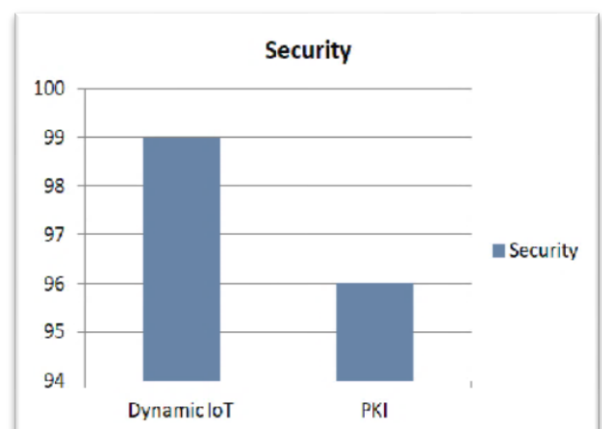


Figure 4. Security Comparison Graph

In Figure 5, accuracy comparison graph is observed between PKI and dynamic IoT. The dynamic IoT shows higher accuracy.

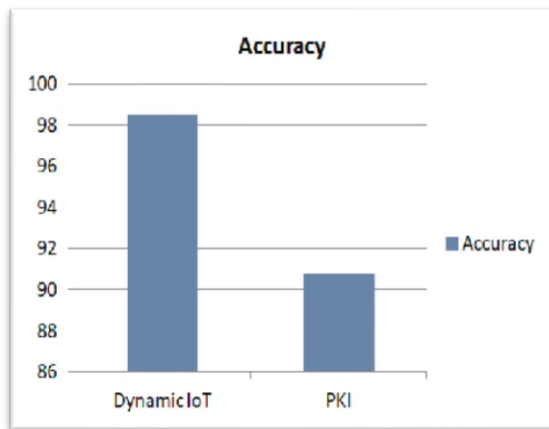


Figure 5. Accuracy Comparison Graph

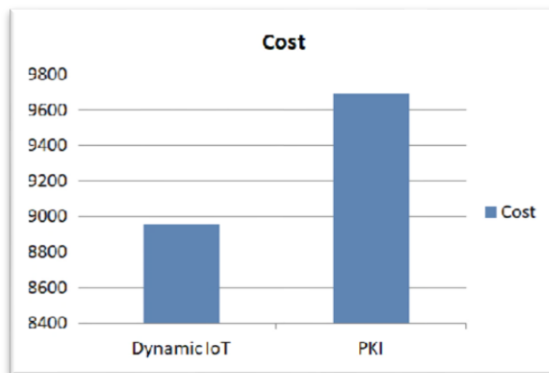


Figure 6. Cost Comparison Graph

The cost comparison graph is observed between dynamic IoT and PKI in Figure 6. The PKI shows higher cost when compared with dynamic IoT.

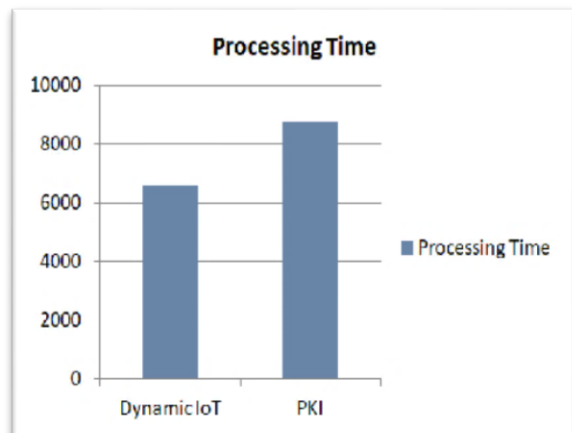


Figure 7. Processing Time Comparison Graph

The processing time comparison graph is observed between dynamic IoT and PKI in Figure.7. The PKI shows higher processing time when compared with dynamic IoT.

5. CONCLUSION

The generic architecture for a design and implementation of a dynamic IoT cloud-based processing platform is concluded in this section, a platform for data observation, collection and processing. The first step was to analyze the new methods of commercial and open sources to detect models and unresolved issues. To allow a quick overview and easy comparison, the analyzed characteristics were tabulated based on selected implementation standards.

However, platform-independent methods for collecting sensor data and sending it to the cloud are unavailable extensively. The framework represents cloud-based platform for observing, collecting, and process the data from smart devices and analysis revealed that detected issues in data collection and exists the process in this platform. Hence, in this analysis achieved better results in terms of security, accuracy, and cost and processing time.

References

- Alizai, A., Tareen., & Jadoon, I. (2018). Improved IoT Device Authentication Scheme Using Device Capability and Digital Signatures. *International Conference on Applied and Engineering Mathematics (ICAEM)*, Taxila, Pakistan, doi:10.1109/ICAEM.2018.8536261

- Atzori, L., Iera, A., & Morabito, G. (2011). SIoT: Giving a Social Structure to the Internet of Things. *IEEE Communications Letters*, doi:10.1109/LCOMM.2011.090911.111340
- Benazzouz, Y., Munilla, C., Gunalp, O., Gallissotand, L., Gurgen, M. (2014). Sharing user IoT devices in the cloud, *2014 IEEE World Forum on Internet of Things (WF-IoT), Seoul, Korea (South)*, doi:10.1109/WF-IoT.2014.6803193
- Boavida, F., Kliem, A., Renner, T. (2016). People-centric internet of things-challenges, approach, and enabling technologies. *Intelligent Distributed Computing IX*, Springer International Publishing, doi:10.1007/978-3-319-25017-5_44
- Botta, A., Donato, V., Persico, V., & Pescape, A. (2014). On the Integration of Cloud Computing and Internet of Things. *International Conference on Future Internet of Things and Cloud, Barcelona, Spain*, 23-30. doi:10.1109/FiCloud.2014.14
- Condon, F., Martínez, JM., Eltamaly, AM., Kim, YC., & Ahmed, MA. (2022). Design and Implementation of a Cloud-IoT-Based Home Energy Management System. *Sensors (Basel)*. doi: 10.3390/s23010176
- Cui, Z., Lv, H., Yin, C., Gaoand G., Zhou, C. (2015). Efficient Key Management for IOT Owner in the Cloud. *IEEE Fifth International Conference on Big Data and Cloud Computing, Dalian, China*, doi:10.1109/BDCLOUD.2015.40
- Fiske, A. P. (1992). The four elementary forms of sociality: framework for a unified theory of social relations. *Psychological Review*, 99, doi:10.1037/0033-295x.99.4.689
- Frustaci, M., Pace, P., Aloisio, G., Fortino, P. (2018). Evaluating Critical Security Issues of the IoT World: Present and Future Challenges. *IEEE Internet of Things Journal*, 5(4), doi:10.1109/JIOT.2017.2767291
- Jie, Shi., Darren, Sim., Yingjiu, Li., & Robert, Deng, Sec. (2012). DS: a secure EPC discovery service system in EPC Global network. *Proceedings of the second ACM conference on Data and Application Security and Privacy*, Texas, doi:10.1145/2133601.2133634
- Krishna, B., V., Gnanasekaran, T. (2017). A systematic study of security issues in Internet-of-Things (IoT) *International Conference on I-SMAC (IoT in Social, Mobile, Analytics and Cloud) (I-SMAC)*, doi:10.1109/I-SMAC.2017.8058318
- Khriji, S., Benbelgacem., Cheour, R., et al. (2022). Design and implementation of a cloud-based event-driven architecture for real-time data processing in wireless sensor networks. *J Supercomputer*, doi:10.1007/s11227-021-03955-6
- Mirri, S., Prandi, C., Salomoni, F., Callegati, A., & Melis, M. (2016). A Service-Oriented Approach to Crowd sensing for Accessible Smart Mobility Scenarios, *Mobile Information Systems*. doi:10.1155/2016/2821680
- Nastic, S., Copil, H., Truong, L., & Dustdar, S. (2015). Governing Elastic IoT Cloud Systems under Uncertainty. *IEEE7th International Conference on Cloud Computing Technology and Science (CloudCom), Vancouver, BC, Canada*, doi:10.1109/CloudCom.2015.77
- Pintus, A., Carboni, D., Serra, A., Manchinu, A. (2015). Humanizing the internet of things-toward a human-centered internet-and-web of things. *Proceedings of the 11th International Conference on Web Information Systems and Technologies (WEBIST '15)*, doi:10.5220/0005475704980503
- Panduman, Y., Funabi, k., Puspitaningayu, N., Kurabayashi, M., Sukaridhoto, S., & Kao. (2022). Design and Implementation of SEMAR IoT Server Platform with Applications. *Sensors*, 22, 6436. doi:10.3390/s22176436
- Rawassizadeh, R., Price., & Petre, M. (2015). Wearables: has the age of smartwatches finally arrived. *Communications of the ACM*, doi:10.1145/2629633
- Wang, L., & Ranjan, R. (2015). Processing Distributed Internet of Things Data in Clouds, *IEEE Cloud Computing*, doi:10.1109/MCC.2015.14
- YangTang., Patrick, P., Lee, C., John, C., Lui, S., & RadiaPerlman. (2012). Secure overlay cloud storage with access control and assured deletion. *IEEE Transactions on Dependable and Secure Computing*, doi:10.1109/TDSC.2012.49
- Zeeshan, N., Reed, M., Siddiqui, Z. (2019). Three-way Security Framework for Cloud based IoT Network. *International Conference on Computing, Electronics & Communications Engineering (ICCECE), London, UK*, doi:10.1109/iCCECE46942.2019.8941877
- ZongminCui, (2013). Light weight key management on sensitive data in the cloud. *Security and communication networks*, doi:10.1002/sec.850

Gurujukota Ramesh Babu
Department of CSE
Shri Vishnu Engineering College
for Women (A), Bhimavaram,
India.
rameshcse@svecw.edu.in
ORCID -0000-0002-4655-5496

Phaneendra Varma Chintalapati
Department of CSE
Shri Vishnu Engineering College
for Women (A), Bhimavaram,
India.
chpvarmacse@svecw.edu.in
ORCID- 0000-0001-7243-8974

Pokkuluri Kiran Sree
Department of CSE
Shri Vishnu Engineering College
for Women(A), Bhimavaram,
India.
hodcse@svecw.edu.in
ORCID- 0000-0001-8601-4304

A.V.S. Asha
Department of CSE
Shri Vishnu Engineering College
for Women (A), Bhimavaram,
India.
asha.addala9@gmail.com
ORCID - 0000-0002-7246-6526

G. Sujatha
Department of CSE
Shri Vishnu Engineering College
for Women (A), Bhimavaram,
India.
gsujathacse@svecw.edu.in
ORCID - 0009-0000-8166-2142

K. Soni Sharmila
Department of CSE
Shri Vishnu Engineering College
for Women (A), Bhimavaram,
India.
sonisharmila.kadimi@gmail.com
ORCID- 0000-0002-7386-0963
